NUREG/CP-0058
Vol. 4

Proceedings of the U.S. Nuclear Regulatory Commission

Twelfth Water Reactor Safety Research Information Meeting

Volume 4
- Materials Engineering Research

Held at
National Bureau of Standards
Gaithersburg, Maryland
October 22-26, 1984

U.S. Nuclear Regulatory Commission

Office of Nuclear Regulatory Research

Available from

GPO Sales Program
Division of Technical Information and Document Control
U.S. Nuclear Regulatory Commission
Washington, D.C. 20555

Printed copy price: $8.00

and

National Technical Information Service
Springfield, VA 22161

NUREG/CP-0058
Vol. 4
R5 and R5

Proceedings of the U.S. Nuclear Regulatory Commission

Twelfth Water Reactor Safety Research Information Meeting

Volume 4
- Materials Engineering Research

Held at
National Bureau of Standards
Gaithersburg, Maryland
October 22-26, 1984

Date Published: January 1985

Compiled by: Stanley A. Szawlewicz, Consultant

Office of Nuclear Regulatory Research
U.S. Nuclear Regulatory Commission
Washington, D.C. 20555

ABSTRACT

The papers published in this six volume report were presented at the Twelfth Water Reactor Safety Research Information Meeting held at the National Bureau of Standards, Gaithersburg, Maryland during the week of October 22-26, 1984. The papers describe progress and results of programs in nuclear safety research conducted in this country and abroad. Foreign participation in the meeting included twenty-six different papers presented by researchers from seven European countries, Japan, and Canada.

PROCEEDINGS OF THE
TWELFTH WATER REACTOR SAFETY RESEARCH
INFORMATION MEETING

October 22-26, 1984

Published in Six Volumes

GENERAL INDEX

VOLUME 1
- Plenary Session - I
- Integral System Tests
- Separate Effects
- International Programs in Thermal Hydraulics
- Calculation of Appendix K Conservatisms

VOLUME 2
- Pressurized Thermal Shock
- Code Assessment and Improvement
- 2D/3D Research Program
- Nuclear Plant Analyzer Program

VOLUME 3
- Containment Systems Research
- Fuel Systems Research
- Accident Source Term Assessment
- Japanese Industry Safety Research

VOLUME 4
- Materials Engineering Research

VOLUME 5
- Mechanical Engineering
- Structural Engineering
- Seismic Research
- Process Control
- Instrumentation and Control Program
- Equipment Qualification and Nuclear Plant Aging

VOLUME 6
- Plenary Session - II
- Human Factors and Safeguards Research
- Health Effects and Radiation Protection
- Risk Analysis
- EPRI Safety Research

PROCEEDINGS OF THE
TWELFTH WATER REACTOR SAFETY RESEARCH
INFORMATION MEETING

held at the

NATIONAL BUREAU OF STANDARDS
Gaithersburg, Maryland
October 22-26, 1984

TABLE OF CONTENTS - VOLUME 4

PREFACE ix

MATERIALS ENGINEERING RESEARCH
Pressure Vessel Materials and Fracture Analysis
Chairman: M. Vagins, NRC

Irradiation Effects in Low-Alloy Reactor Pressure Vessel Steels (Heavy-Section Steel Technology Program Series 4 and 5)
R. G. Berggren, et al., ORNL and B. H. Menke, MEA . . . 1

Fracture Properties of a Neutron-Irradiated Stainless Steel Submerged Arc Weld Cladding Overlay
W. R. Corwin, R. G. Berggren, R. K. Nanstad, ORNL . . . 26

Composition Influences and Interactions in Radiation Sensitivity of Reactor Vessel Steels
J. R. Hawthorne, MEA 48

Fatigue Crack Growth Rates of Low-Carbon and Stainless Piping Steels in PWR Environment
W. H. Cullen, MEA 63

The Effects of Material and Environmental Variables on Corrosion Fatigue Crack Growth in Pressure Vessel Steels
W. H. Bamford, et al., Westinghouse Electric Corp. . . . 82

Dosimetry and Annealing
Chairman: A. Taboada, NRC

LWR Surveillance Dosimetry Improvement Program: PSF Metallurgical Blind Test Results
F. W. Stallmann, et al., ORNL 109

Thermal and Structural Analysis of Light-Water Reactor Vessel In-Place Annealing
W. L. Server, INEL and J. P. Houstrup, CE, Inc. . . . 137

Annealing of the BR3 Reactor Pressure Vessel
A. Fabry, et al., SCK/CEN, Belgium 144

Piping Research and Fracture Mechanics
Chairman: M. Vagins, NRC

Investigation of the Ductile Fracture Properties of Type 304 Stainless Steel Plate, Welds, and 4-Inch Pipe
M. G. Vassilaros, R. A. Hays, J. P. Gudas, USNRDC . . . 176

MATERIALS ENGINEERING RESEARCH
Piping Research and Fracture Mechanics (Cont'd)

BWR Pipe Crack and Weld Clad Overlay Studies
W. J. Shack, et al., ANL 190

Metallurgy and Steam Generators
Chairman: J. Muscara, NRC

Aging of Cast Duplex Stainless Steels in LWR Systems
O. K. Chopra and H. M. Chung, ANL 211

Sensitization Development in Austenitic Stainless Steel Piping
S. M. Bruemmer, R. E. Page, D. G. Atteridge, PNL . . . 231

Steam Generator Tube Vibration Tests
W. I. Enderlin, PNL 251

Surry Steam Generator Program and Baseline Eddy Current Examination
R. A. Clark and P. G. Doctor, PNL 260

NDE Research
Chairman: J. Muscara, NRC

Integration of Nondestructive Examination Reliability and Fracture Mechanics
S. R. Doctor, et al., PNL 286

Development and Validation of a Real-Time SAFT-UT System for Inservice Inspection of LWRs
S. R. Doctor, et al., PNL 319

Evaluation of Methods for Leak Detection in Reactor Primary Systems and NDE of Cast Stainless Steel
D. S. Kupperman and T. N. Claytor, ANL and
D. W. Prine and T. A. Mathieson, Chamberlain Mfg. Corp. . . 342

Summary of Detection, Location, and Characterization Capabilities of AE for Continuous Monitoring of Cracks in Reactors
P. H. Hutton, et al., PNL 362

PREFACE

This report, published in six volumes, contains 176 papers out of the 205 that were presented at the Twelfth Water Reactor Safety Research Information Meeting. The papers are printed in the order of their presentation in each session. The titles of the papers and the names of the authors have been updated and may differ from those which appear in the final agenda for the meeting. The papers listed under the session on Human Factors and Safeguards Research did not appear in the agenda but were prepared for the panel discussions that made up that session.

IRRADIATION EFFECTS IN LOW-ALLOY REACTOR PRESSURE VESSEL STEELS (HEAVY-SECTION STEEL TECHNOLOGY PROGRAM SERIES 4 AND 5)*

R. G. Berggren, J. J. McGowan, B. H. Menke,†
R. K. Nanstad, and K. R. Thoms‡

Metals and Ceramics Division
OAK RIDGE NATIONAL LABORATORY
Oak Ridge, Tennessee 37831

INTRODUCTION

Numerous studies of the effects of impurities and fast neutron irradiation on fracture toughness of nuclear reactor pressure vessel materials (plates, forgings, and welds) have been reported in the literature.[1-9] Most such studies have included a minimum number of tests for each material and/or combination of irradiation parameters. Statistical analysis of neutron irradiation effects has been possible only by using a large body of data representing a variety of materials and neutron exposure conditions. However, such analytical methods do not address the question of accuracy of each datum in the large set, or the accuracy and reliability of results from a single small data set such as might be obtained in a nuclear reactor pressure vessel surveillance study. The present studies address this question by multiple testing at two laboratories of typical nuclear pressure vessel materials (both irradiated and unirradiated) and statistical analyses of the test results. Multiple tests are conducted at each of several test temperatures for each material, standard deviations are determined, and results from the two laboratories are compared.

The Fourth Heavy-Section Steel Technology (HSST) Irradiation Series, almost completed, was aimed at elastic-plastic and fully plastic fracture toughness of low-copper weldments ("current practice welds"). A typical nuclear pressure vessel plate steel was included for statistical purposes.

The Fifth HSST Irradiation Series, now in progress, is aimed at determining the shape of the K_{IR} curve after significant radiation-induced shift of the transition temperatures. This series includes irradiated test specimens of thicknesses up to 100 mm and weldment compositions typical of early nuclear power reactor pressure vessel welds.

These two series will be discussed separately.

---

*Research sponsored by the Office of Nuclear Regulatory Research, U.S. Nuclear Regulatory Commission, under Interagency Agreements DOE 40-551-75 and 40-552-75 with the U.S. Department of Energy under contract DE-AC05-84OR21400 with Martin Marietta Energy Systems, Inc.

†Materials Engineering Associates, Lanham, Maryland.

‡Engineering Technology Division, Oak Ridge National Laboratory.

FOURTH HSST IRRADIATION SERIES

This irradiation program was conducted on four submerged-arc welds and one plate of A-533 grade B class 1 pressure vessel steel. The welds were made by commercial vendors using current welding practices and contained relatively low copper contents. The target fast neutron fluence was 2×10^{23} neutrons/m^2 (>1 MeV) and the irradiation temperature was 288°C (550°F). Charpy V-notch, tensile, and fracture toughness tests (1TCS specimens) were conducted. Sufficient numbers of specimens were included in the irradiations to permit statistical analyses of the results.

MATERIALS

The plate material was from a 305-mm-thick plate of ASTM A-533 grade B class 1 manganese-molybdenum-nickel steel produced by Lukens Steel Company for the HSST Program.[10] This plate material was designated HSST plate 02 and portions of it have been used in many investigations. All test specimens were prepared in the transverse (TL) orientation.

All four submerged-arc weldments were made in ASTM A-533 grade B class 1 plate. Two of the submerged-arc weldments were supplied by the Electric Power Research Institute (EPRI) and had been fabricated by Combustion Engineering, Inc. HSST weld 68W was produced as a 178-mm-thick submerged-arc weldment using Linde 0091 flux and 4.8-mm-diam MIL-B-4 (low copper and phosphorus) wire and was designated "CGS" in EPRI studies.[11] HSST weld 69W was produced as a 300-mm-thick submerged-arc weldment using Linde 0091 flux and 4.8-mm-diam MIL-B-4 wire and was designated "CHS" in EPRI studies.[11] Both welds were postweld heat treated 25 h at 621°C.

The other two welds were supplied by Babcock and Wilcox Company.[12] Both welds were produced as 174-mm-thick submerged-arc weldments using Mn-Mo-Ni (SFA-5.23EF2N) filler wire. HSST weld 70W was fabricated using Linde 0124 flux and HSST weld 71W was fabricated using Linde 0080 flux. Both welds were postweld heat treated 48 h at 607°C.

All test specimens were prepared with longitudinal axes transverse to the weld centerline and crack propagation direction parallel to the surface.

The four weldments are considered "current practice" and are of low or medium low-copper content. Two of the welds (EPRI material) also had low-nickel contents.

Chemical compositions of the five materials are presented in Table 1.

MATERIAL IRRADIATION

All irradiations were conducted at two faces of the Bulk Shielding Reactor (BSR) at Oak Ridge National Laboratory (ORNL), a 2-MW pool-type reactor. Thermal shields of 42.5-mm-thick stainless steel were used between the reactor core and the specimen capsules to reduce gamma heating

Table 1. Chemical compositions of plate and submerged-arc welds

Material	Composition, wt %									
	C	Mn	P	S	Si	Cr	Ni	Mo	Cu	V
Plate, A533 grade B class 1 (HSST-02)	0.23	1.55	0.009	0.014	0.20	0.04	0.67	0.53	0.14	0.003
Weld HSST-68W, Linde 0091 flux	0.15	1.38	0.008	0.009	0.16	0.04	0.13	0.60	0.04	0.007
Weld HSST-69W, Linde 0091 flux	0.14	1.19	0.010	0.009	0.19	0.09	0.10	0.54	0.12	0.005
Weld HSST-70W, Linde 0124 flux	0.10	1.48	0.011	0.011	0.44	0.13	0.63	0.47	0.056	0.004
Weld HSST-71W, Linde 0080 flux	0.124	1.58	0.011	0.011	0.54	0.12	0.63	0.45	0.046	0.005

in the irradiation capsules. Each capsule contained 60 1TCS fracture toughness specimens, 80 to 90 Charpy V-notch impact test specimens, and 10 to 20 tensile test specimens in an arrangement shown in Fig. 1.

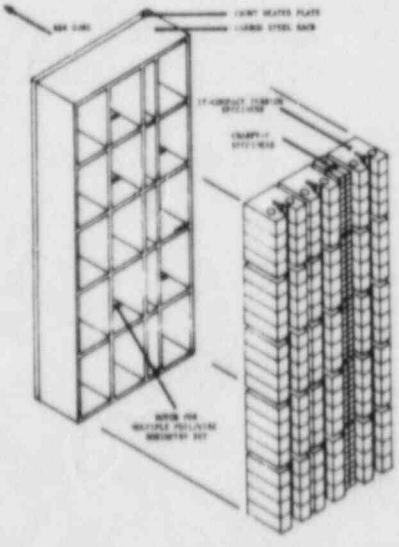

Fig. 1. BSR-HSST-4 irradiation capsule specimen rack assembly.

Specimen temperatures during irradiation were controlled by a combination of electrical heaters and controlled sweep gas composition (helium and nitrogen). Specimen temperatures during irradiation were controlled at 288 ± 5°C. Irradiation times for the capsules ranged from 4300 to 5400 h.

Complete spatial maps of damage exposure parameter values were determined for each capsule. The dosimetry in the capsules consisted of multiple foil sets and gradient wires. The dosimetry and spectral adjustment procedures are completely presented elsewhere.[13-14] The values of fluences greater than 1 MeV, 0.1 MeV, and displacements per atom (dpa) were determined for each specimen. Uncertainties for the damage exposure parameters were less than 8% (standard deviation).

TEST PROCEDURES

The Charpy V-notch impact testing was apportioned between Materials Engineering Associates (MEA), Lanham, Maryland, and ORNL, Oak Ridge, Tennessee, such that both laboratories tested equivalent specimens insofar as possible.

The impact testing machines at both laboratories were calibrated in conformance with ASTM Standard Method E23, including proof tests using "standardized specimens."

Preliminary tests of both unirradiated and irradiated specimens were conducted to approximate the Charpy transition curve and specific temperatures were selected for the balance of the testing. Specimens were selected such that, insofar as possible, tests at each selected temperature were conducted by both laboratories of specimens that came from adjacent positions in the original plate or weld, adjacent positions in the irradiation capsules, and about the same neutron exposure.

Mean Charpy-V energies of unirradiated specimens and standard deviations were first determined for each selected test temperature for each laboratory and for the combined data set. This permitted determination of any bias between the laboratories and also provided data on scatter of results inherent in the materials and the Charpy test.

Least-squares regressions were then conducted on the data from unirradiated specimen tests using several fitting expressions:

$$E = A + BT \quad . \tag{1}$$

$$E = (A + BT)\left\{1 + \tanh[(C/2)(T - D)]\right\} \quad . \tag{2}$$

$$E = (A + BT)\left\{1 - \exp[-C(T + 273)D]\right\} \quad . \tag{3}$$

where

E = fracture energy, J,

T = test temperature, °C, and

A, B, C, D = parameters determined in the fitting process.

Equation (1) is a bilinear expression that was fitted separately for the transition and upper-shelf regions. Results that were in the lower and upper "knee" temperature regions were deleted for this analysis. Equations (2) and (3) are "sloping upper-shelf" representations of the

Charpy curves. "Flat upper-shelf" representations of the Charpy curves were also obtained by deleting the BT term in Eqs. (2) and (3).

The results of tests on irradiated specimens (energy-temperature pairs) were then converted to transition temperature shifts (ΔT) or upper-shelf energy changes (ΔE), depending on whether the irradiated specimen test was in the transition or upper-shelf region. Transition temperature shifts are the test temperature minus the temperature at which the mean unirradiated curve gives the same energy as was obtained in the test of the irradiated specimen. The upper-shelf energy change was simply the energy from the irradiated specimen tests minus the mean energy for the unirradiated specimen tests conducted at the same temperature. A positive ΔT is an irradiation-induced transition temperature increase and a positive ΔE is a radiation-induced upper-shelf energy increase.

We then attempted to analyze the radiation-induced changes as a power law function of neutron fluence. However, with the maximum neutron fluence range of only ±50%, the scatter of the data was such that a reliable analysis was not obtained. We therefore determined the mean fluence, mean fracture energy, and mean test temperature for transition region and upper-shelf region data for each material and compared these with the unirradiated specimen data to obtain transition temperature and upper-shelf energy changes.

Testing of compact toughness (CT) specimens was performed by the single specimen compliance (SSC) technique with each laboratory testing approximately half the specimens. All compact specimens designated for upper-shelf testing were side-grooved on each side by 10% of the specimen thickness. The SSC technique provides a method to determine the amount of specimen crack extension by means of small unloadings (<15% of maximum load) conducted at regular intervals throughout the test.

Values of the J-integral were calculated using the modified version of the J-integral, known as J_M, as proposed by Ernst.[15] J_M is given by:

$$J_M = J_D - \int_{a_0}^{a} \frac{\partial [J_D - G]}{\partial a} \Bigg|_{\delta_{pl}} da \ , \qquad (4)$$

where

J_D = deformation theory J,

G = Griffith linear elastic energy release rate = $K_I^2(1 - \nu^2)/E$,

a_0, a = the initial and current crack lengths,

$J_D - G = J_{pl}$, the plastic part of the deformation theory J,

δ_{pl} = the plastic part of the displacement, and

ν = Poisson's ratio.

Deformation theory J (J_D) contained in Eq. (4) is the formation of the J-integral specified for use in the ASTM Standard Test for J_{Ic}, a

measure of fracture toughness, E813-81, and in the tentative ASTM J-integral resistance (J-R) curve test procedure.[16] Modified J (J_M) was used in this program because Ernst has shown it to be more specimen-size independent when the crack extension exceeds the J-controlled crack growth regime.

A typical R curve produced with the SSC technique is illustrated in Fig. 2. The R curve format of Fig. 2 is in accordance with that of ASTM Standard E813, i.e., J_{Ic}, the initiation elastic-plastic fracture toughness, is defined by the intersection with the blunting line of the linear regression fit to the data between the 0.15- and 1.5-mm exclusion lines. The use of linear least-squares fit stems from the multispecimen nature of ASTM E813 where a minimum of only four data points are required. Thus, with only a few data points, the nonlinear nature of the R curve cannot be evaluated. For this study, we used the procedure proposed by Loss et al.,[17-18] whereby a power law, $J = C(\Delta a)^N$, is fit to the data between the 0.15- and 1.5-mm exclusion lines with the constants C and N chosen to optimize the curve fit. The initiation fracture toughness, J_{Ic}, is defined with this procedure as the intersection of the power law R curve with the 0.15-mm exclusion line as indicated in Fig. 2. J_{Ic}, as defined by the two methods, is nearly identical for nuclear grade pressure vessel steels. In addition to more closely describing the nonlinear behavior of the R curve, the power law J_{Ic} definition provides a consistent means for determining the initiation toughness when fast fracture, i.e., brittle fracture by a cleavage micromode, occurs prior to development of a full R curve. To address this cleavage phenomenon, the power law method classifies the R curve into three types: types A, B, and C. With type A, failure occurs before the slow ductile crack extension is sufficient to cross the 0.15-mm exclusion line. In this case, J_{Ic} is taken as the value of J_M at failure. Type B covers cases where testing was terminated by fast fracture after ductile crack extension exceeded the 0.15-mm exclusion line, but prior to reaching the 1.5-mm exclusion line. In this case, a power law is fit to the available data and J_{Ic} is taken as the intersection of the fit with the 0.15-mm exclusion line. Type C covers cases where the R curve extends beyond the 1.5-mm exclusion line.

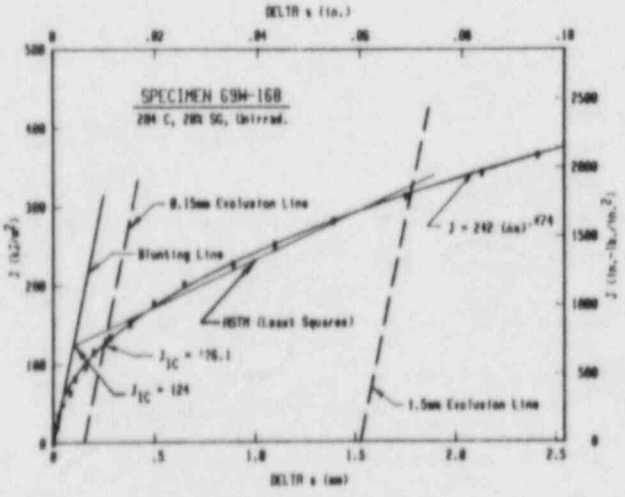

Fig. 2. Power law representation of the J-R curve using the SSC test technique and comwith the ASTM E813 procedure.

Another effect resulting from the nonlinear nature of the R curve is that the tearing modulus is not constant as was originally envisioned by ASTM E813. For comparison purposes and consistency with ASTM E813, a single value for the tearing modulus (T_{avg}) can be computed from the power law equation for type C R curves. The tearing modulus is defined as:

$$T = \frac{E}{\sigma_f^2} \frac{dJ}{da} , \tag{5}$$

where σ_f = (yield stress + ultimate stress)/2.

To obtain an average value for the slope of the power law R curve, the power law equation is fit in closed form with a linear regression of the form $J = J_o + (dJ/da)\Delta a$ to that part of the curve lying between the exclusion lines. This technique is directly analogous to the E813 method of fitting a linear line to the discrete data points. However, fitting the power law equation has the effect of including an infinite number of points. Little difference in magnitude is observed between the values of T obtained by the two techniques.

The power law and E813 methodologies produce similar results in regions covered by the E813 standard.[19-20] The procedure is to convert the elastic-plastic J_{Ic} power law initiation toughness to a quasielastic K_{Jc} value using the following relationship:

$$K_{Jc} = [EJ_{Ic}]^{0.5} . \tag{6}$$

ASTM Standard E813 gives an equation for converting J_{Ic} to K_{Jc}, which incorporates a plane-strain term. Equation (6) is identical to the E813 equation, but with the plane-strain term removed. This term was removed because in this program specimens tested in the upper transition region and those tested on the upper shelf experienced net section yielding. Such behavior is closer to plane stress than it is to plane strain. In the lower transition region, however, the specimen through-thickness constraint is greater and more nearly plane strain. Thus, it is unclear just where one should use the E813 equation. Since most of the data generated in this study were more nearly plane stress and for consistency of presentation, all K_{Jc} values were calculated using Eq. (6).

At toughness levels too great to allow measurement of a valid K_{Ic} with a small specimen, K_{Jc} values can be determined as stated above; however, these data tend to be of greater magnitude than that which would be obtained with a larger specimen capable of measuring the linear elastic toughness level by E399 criteria. A similar observation was made by Irwin[21] in that the plane stress fracture toughness (K_c) overestimates K_{Ic}. Irwin developed an empirical relationship from which K_{Ic} could be estimated once K_c was known. Recently, Merkle[22] has shown that reasonable estimates of K_{Ic} can be determined using K_{Jc} as a substitute for K_c. In this study, K_{Jc} values in the brittle-to-ductile transition region were

corrected to $K_{\beta c}$ using the Irwin-Merkle β_{Ic} correction to provide another means of determining the shift to higher temperature of the brittle-to-ductile transition with irradiation.

RESULTS — CHARPY TESTS

Charpy impact test results for unirradiated specimens are summarized Figs. 3 and 4 and Table 2. In Table 2 the results for the two laboratories can be compared. The means for the two laboratories are, in almost all cases, within one standard deviation of each other, indicating good reproducibility. There may be a tendency for the ORNL results to give slightly higher energies in the transition region and MEA results to give slightly higher energies in the upper-shelf region. The standard deviations do not show any consistent trends with laboratory, material, or region of the curve. They do, however, indicate the possible errors that might be encountered if only a few tests are conducted in the transition or upper-shelf regions. In Fig. 3 the results of fitting the data for HSST plate 02 to all five Charpy curve expressions can be seen to give virtually identical transition temperatures and upper-shelf energies. The greatest differences are in the lower- and upper-knee regions where there are few data. In this plate material the upper shelf is very nearly a constant value over a range of 150°C. The results of fitting data for submerged-arc weld HSST 70W are presented in Fig. 4. In this case a positively sloping upper shelf is indicated by the analysis. The transition temperatures, however, were almost identical for all fitting expressions. These examples are typical of most of the analyses. The only exceptions were for a few data sets where the distribution or quantity of data were such that the fitting was affected. In both these figures one can visualize the possible effects on the shape and position of the curves if few tests had been conducted.

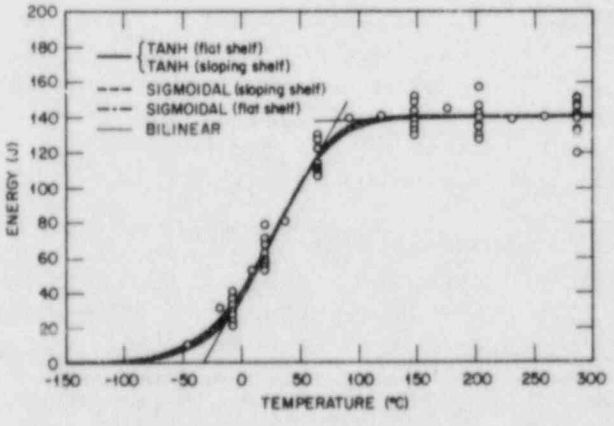

Fig. 3. Several functions fitted to Charpy V-notch impact data for unirradiated A-533 grade B class 1 steel plate (HSST-02).

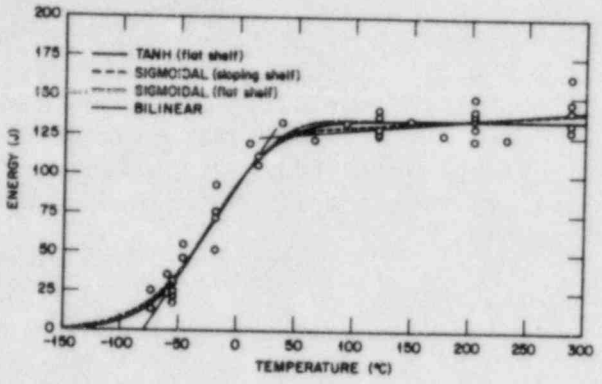

Fig. 4. Several functions fitted to Charpy V-notch impact data for unirradiated submerged-arc weld metal (HSST-70W).

Table 2. Comparison of Charpy impact test results for unirradiated pressure vessel plate and submerged-arc welds from ORNL and MEA

Test temperature (°C)	Mean energy ($\bar{x}$), J			Standard deviation (σ_n), J			Number of tests	
	ORNL	MEA	Combined	ORNL	MEA	Combined	ORNL	MEA
A533 grade B class 1 (HSST-02)								
−7	31.5	28.7	30.1	5.0	5.7	5.5	5	5
21	64.8	61.3	63.0	7.9	7.2	7.7	5	5
66	119.7	116.9	118.5	8.2	8.9	8.6	6	5
149	143.0	135.6	139.6	5.8	4.9	6.6	6	5
204	138.4	138.3	138.3	5.1	10.6	8.1	6	5
288	137.9	145.9	141.5	10.6	3.9	9.2	6	5
Submerged-arc weld (HSST-68W)								
−62	36.2	[a]		5.5			3	0
−46	70.5	[a]		23.0			2	0
121	186.4	[a]		8.6			2	0
200	190.5	[a]		10.7			3	0
288	209.5	[a]		37.4			2	0
Submerged-arc weld (HSST-69W)								
−18	41.9	41.2	41.6	12.7	10.5	11.7	6	5
10	98.7	98.2	98.4	14.5	17.8	16.4	5	6
121	144.0	148.9	146.4	6.1	4.7	6.0	5	5
204	143.0	151.2	146.7	6.7	4.0	6.9	5	4
288	147.8	161.3	154.6	1.5	8.5	9.1	5	5
Submerged-arc weld (HSST 70W)								
−54	25.8	24.4	24.9	4.1	5.5	5.0	2	3
−18	73.5	66.4	70.0	16.9	10.7	14.6	3	3
121	131.9	129.8	130.8	6.5	5.2	6.0	3	3
204	131.9	140.1	136.0	7.1	7.8	8.5	3	3
288	134.2	150.1	142.1	5.1	9.2	10.9	3	3
Submerged-arc weld (HSST 71W)								
−9	38.0	37.3	37.7	8.1	2.0	5.9	2	2
10	60.6	58.3	59.7	11.5	6.9	10.0	3	2
121	99.4	97.2	98.3	10.2	5.2	8.2	3	3
204	102.6	111.6	107.1	1.7	1.7	4.8	3	3
288	99.9	115.2	107.5	7.4	8.8	11.2	3	3

[a]No tests by MEA.

As stated earlier, fluences greater than 1 MeV, greater than 0.1 MeV, and dpa were determined. However, in this study it was found that the ratio of fluence greater than 0.1 MeV to fluence greater than 1 MeV was 3.629 with a standard deviation of 0.104 and the ratio of dpa to fluence greater than 1 MeV was 1.616×10^{-23} with a standard deviation of 0.024×10^{-23}. In view of these standard deviations, any effect of exposure parameter was undetectable and test results will be presented in terms of neutrons of energy greater than 1 MeV.

Tensile strength changes, due to irradiation, are given in Table 3 (ref. 23). In Figs. 5 through 8, typical examples are presented of the results of Charpy V-notch impact tests on the irradiated materials. Inherent in the experiment is a fluence variation due to the fast neutron flux gradients at the reactor. The standard deviation of fluence values was about 30% of the mean fluence for each material. Figure 5 presents the results for the material, HSST plate 02, and a hyperbolic tangent [sloping shelf, Eq. (2)] fit for the mean fluence and in Fig. 6 a similar fit for the submerged-arc weld HSST 71W. It can be seen in Figs. 7 and 8 that the amount of scatter in the results is not exclusively a result of fluence differences. Power law functions were fitted to the data in these figures and the best fit equations in these examples were

$$\Delta T = 55.2(\Phi/10^{23})^{0.443} \quad \text{(Fig. 7)} ,$$

and

$$\Delta T = 33.1(\Phi/10^{23})^{0.206} \quad \text{(Fig. 8)} ,$$

where

ΔT = transition temperature increase, °C, and

Φ = fluence, 10^{23} n/m^2, >1 MeV.

Table 3. Average tensile strengths

Material	Average yield strength from 22 to 288°C (MPa)		Change (%)	Average ultimate tensile strength from 22 to 288°C (MPa)		Change (%)
	Unirradiated	Irradiated		Unirradiated	Irradiated	
Plate HSST-02	432	564	31	590	707	20
Weld HSST-68W	496	590	19	604	620	3
Weld HSST-69W	584	672	15	692	752	9
Weld HSST-70W	440	493	12	562	608	8
Weld HSST-71W	430	489	14	563	602	7

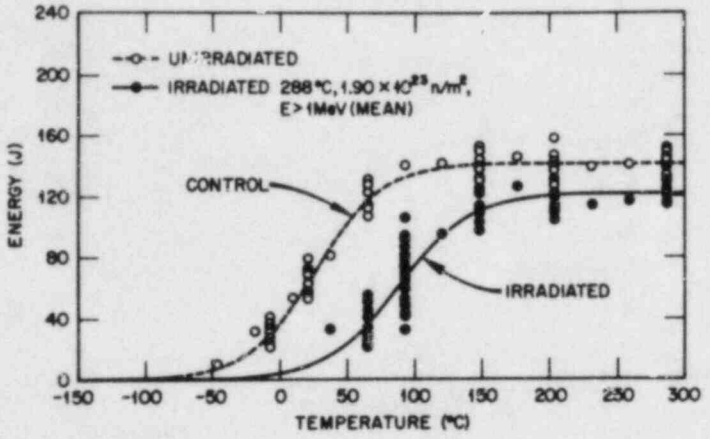

Fig. 5. Charpy V-notch impact data for A-533 grade B class 1 steel plate (HSST-02) before and after irradiation; fitted to hyperbolic tangent (sloping upper-shelf) function.

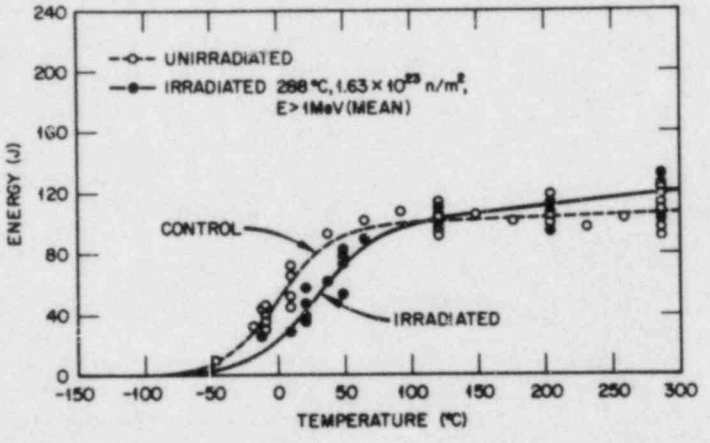

Fig. 6. Charpy V-notch impact data for submerged-arc weld metal (HSST-71W) before and after irradiation; fitted to hyperbolic tangent (sloping upper-shelf) function.

The exponents on neutron fluence given in the above equations are within the range of exponents obtained in other studies.[4-6] However, other exponents were tried in a sensitivity analysis and almost any exponent gave nearly the same standard deviations. Attempts to fit a power law function to the other transition temperature shift data and to the upper-shelf change data yielded exponents that ranged from greater than unity to negative values (concave upward). These results were due to several factors: the scatter in the data, the rather restricted fluence range, and the low sensitivity of these "current practice" welds.

The results are, therefore, presented in Table 4 in terms of mean fluence, mean transition temperature increase, and mean upper-shelf change. The plate material, having the greatest copper and nickel

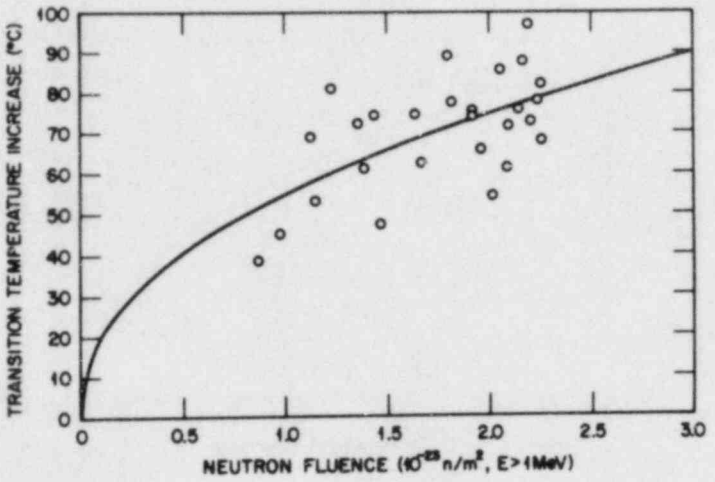

Fig. 7. Transition temperature increase of A-533 grade B class 1 steel plate (HSST-02) irradiated to 288°C.

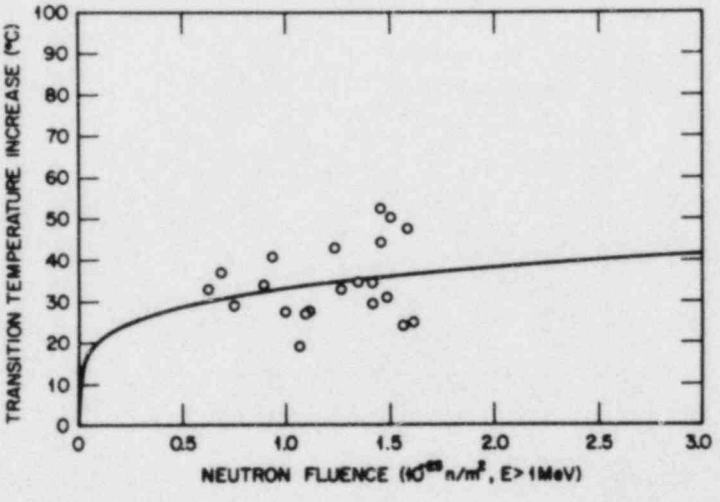

Fig. 8. Transition temperature increase of submerged-arc weld metal (HSST-69W) irradiated at 288°C.

contents, had the largest changes in both transition temperature increase and upper-shelf energy decrease. Weld HSST 68W with both low-copper and low-nickel contents showed the smallest transition temperature increase while the other three welds gave intermediate transition temperature increases. Of interest is the observation that welds HSST 70W and 71W with low copper and normal nickel contents had transition temperature increases only slightly less than for weld HSST 69W, which had medium copper and low nickel contents. The upper-shelf energy changes for the four welds are within the observed scatter of the data, and are probably not significant.

Table 4. Effect of fast neutron irradiation on Charpy V-notch impact properties of plate and welds

(All values are means for the data sets)

Transition temperature increase		Upper-shelf energy change			Cu (%)	Ni (%)
Fluence, 10^{23} n/m^2 (>1 MeV)	Shift (°C)	Fluence, 10^{23} n/m^2 (>1 MeV)	Average change (J)	Average change (%)		
		Plate HSST-02				
2.04	68.2	1.76	–22.4	–16	0.14	0.67
		Weld HSST-68W				
1.35	6.0	1.14	17.3	9	0.04	0.13
		Weld HSST-69W				
1.22	34.2	1.18	–4.2	–3	0.12	0.10
		Weld HSST-70W				
1.65	30.9	1.69	–13.1	–10	0.056	0.63
		Weld HSST-71W				
1.65	26.4	1.64	8.1	8	0.046	0.63

In Table 5 the transition temperature increases obtained in this study are compared to predictions from several trend curve formulations.[1-6] In making this comparison, several factors must be considered:

1. The predictions of the trend curve formulations are largely or wholly based on surveillance results and represent lower fluxes and much longer irradiation periods than for the present study.

2. The *Regulatory Guide 1.99* (ref. 1) was meant to be conservative.

3. The values based on the Draft Regulatory Guide (ref. 2) do not include the "margin" specified in the draft.

4. In several cases the tabulated predicted values are for compositions outside the limits given by the authors.

Considering the above factors, there is fairly good agreement of the present results with the several predictions.

Table 5. Comparison of several radiation embrittlement predictive expressions with results of present study

Material	Fluence, 10^{23} n/m^2 (>1 MeV)	Transition temperature increase, °C						
		Observed ΔTT	RG 1.99[a]	Draft RG 1.99[b]	V-B[c]	P-W[d]	V-S-K[e]	G[f]
Plate HSST-02	2.04	68	83	68	75	61	66	66
Weld HSST-68W	1.35	6	26	22[g]	−54[g]	20	17	3
Weld HSST-69W	1.22	34	50	36	20	20	29	39
Weld HSST-70W	1.65	31	30	48	47	46	75	16
Weld HSST-71W	1.65	26	30	39	20	38	73	10

[a]Ref. 1, *Regulatory Guide 1.99.*

[b]Ref. 2, *Draft Regulatory Guide 1.99.*

[c]Ref. 3, Varsik and Byrne.

[d]Ref. 4, Perrin, Wullaert, Odette, and Lombrozo.

[e]Ref. 5, Varsik, Schloss, and Koziol.

[f]Reg. 6, Guthrie.

[g]Outside limits of applicability per author.

RESULTS — FRACTURE TOUGHNESS TESTS

All side-grooved specimen J-R curves obtained in this study were valid by ASTM E813 criteria and the agreement between MEA and ORNL data, both in the transition and upper-shelf regimes, is excellent. J-R curves obtained from tests at 200°C are illustrated in Fig. 9 in the tearing instability format.[24] The solid curves result from the power law curve fit plotted in terms of J_M and T material (T_{Mat}). The data symbols indicate crack extension at J_{Ic} (lower right), 0.5, 1, 1.5, and 2 mm, respectively. Extrapolation to larger values is not appropriate since questions remain as to the validity of the data beyond approximately 2 mm of crack extension.

It is clear that for each material the J-R curves are generally lowered by both irradiation and increased test temperature. Note that both the J level, and to a greater extent the tearing modulus, are lowered.

The effect of temperature and irradiation on initiation toughness and tearing modulus is illustrated directly in Figs. 10 and 11, respectively. All data for a given material condition were fit with a linear regression line. Only the line is plotted for clarity. In general, both J_{Ic} and

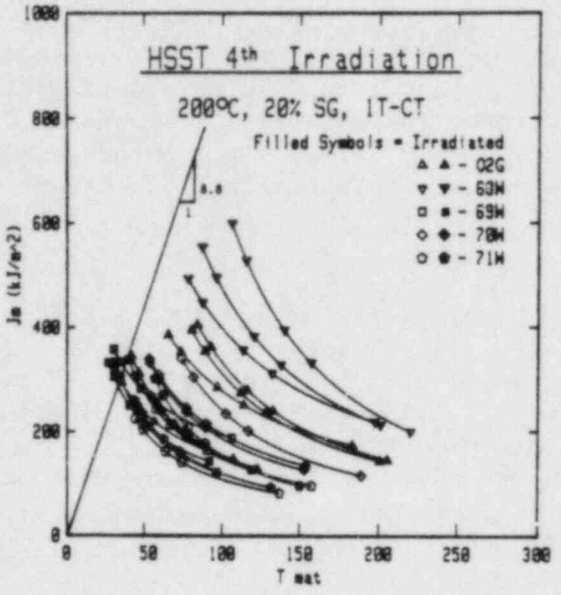

Fig. 9. Effect of irradiation on J-R curve obtained from 200°C tests.

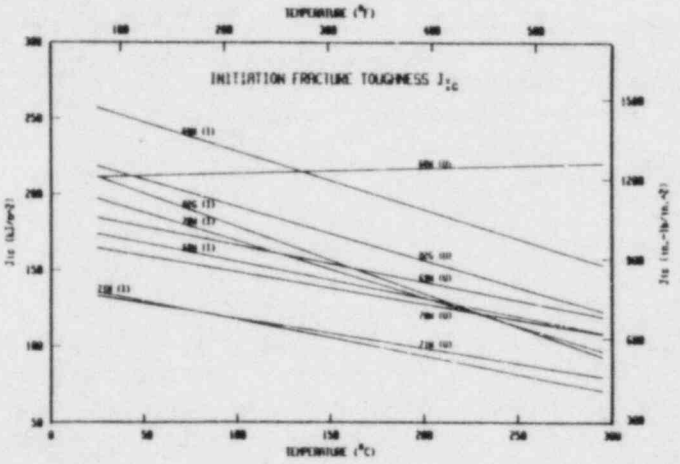

Fig. 10. Variation of initiation fracture toughness, J_{Ic}, with test temperature and irradiation (upper-shelf data).

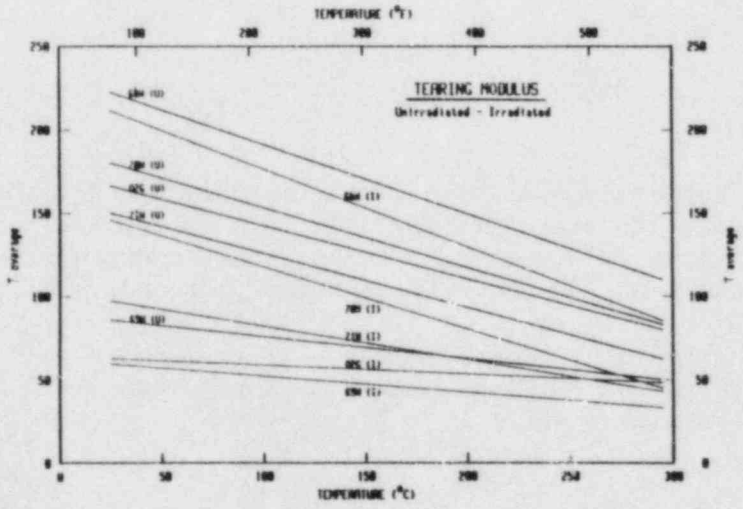

Fig. 11. Variation of tearing modulus, T, with test temperature and irradiation (upper-shelf data).

T_{avg} decrease with increasing temperature and with irradiation; however, the tearing modulus is more sensitive to irradiation. This is evidenced by considering the average change indicated by each parameter for a given material and condition. For instance, the initiation toughness of plate 02, and welds 69W and 71W drop only slightly while the tearing modulus for these same materials drops substantially. The inconsistent behavior evidenced by the unirradiated J_{Ic} line for weld 68W is believed to be due to data scatter.

The fracture toughness behavior in terms of the quasielastic parameter K_{Jc} is illustrated in Figs. 12 through 14. In these figures, the solid line trend curves are the result of regression curves fit to all data points. On the upper shelf, a linear regression was used and in the transition the data were fit with an exponential of the form $K_{Jc} = A[\exp(B \cdot \text{temperature})]$ with the constants A and B chosen to optimize the fit. All shifts in transition temperature were calculated using the exponential curve fit equations.

Data for plate 02 material are depicted in Fig. 12. This material had the highest levels of both copper (0.14%) and nickel (0.67%) and the K_{Jc} data indicate the greatest shift in the transition temperature. There is not, however, a corresponding large change in upper-shelf toughness. Data scatter is low for this material, as would be expected in a homogeneous reference material such as plate 02.

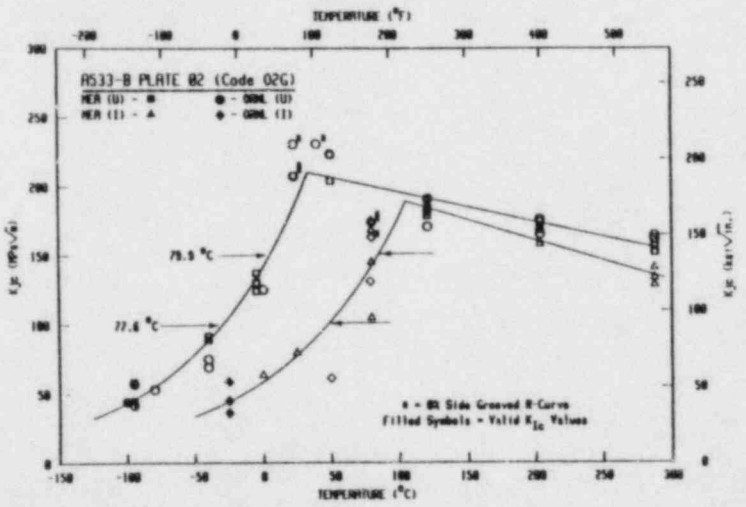

Fig. 12. Variation of initiation fracture toughness, K_{Jc}, of HSST plate 02 material with test temperature and irradiation.

Weld 68W had the lowest copper (0.04%) of all five materials and a low nickel content (0.13%). As illustrated in Fig. 13, this material also showed the least radiation effects. The shift in transition temperature (~6°C) is almost insignificant when compared with that for plate 02.

Figure 14 illustrates the behavior indicated for weld 71W. This weld had essentially the same copper level (0.046%), but a higher nickel level (0.63%) than weld 68W. The transition shift is relatively small compared with that for plate 02, but greater than for weld 68W.

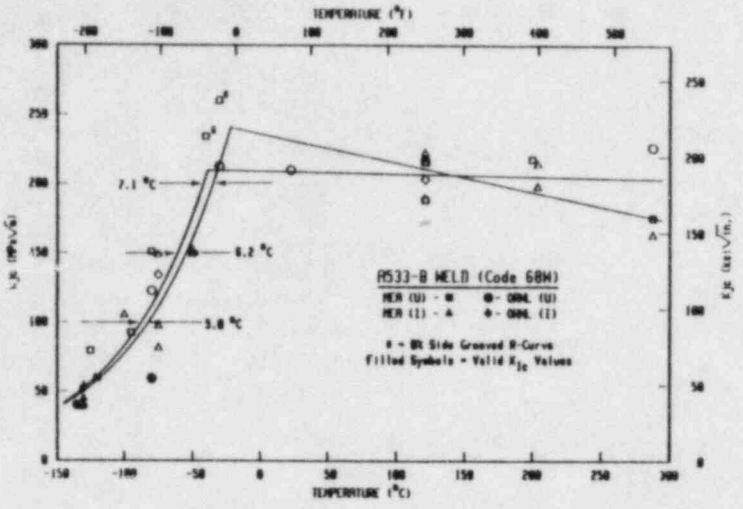

Fig. 13. Variation of initiation fracture toughness, K_{Jc}, of weld HSST-68W material with test temperature and irradiation.

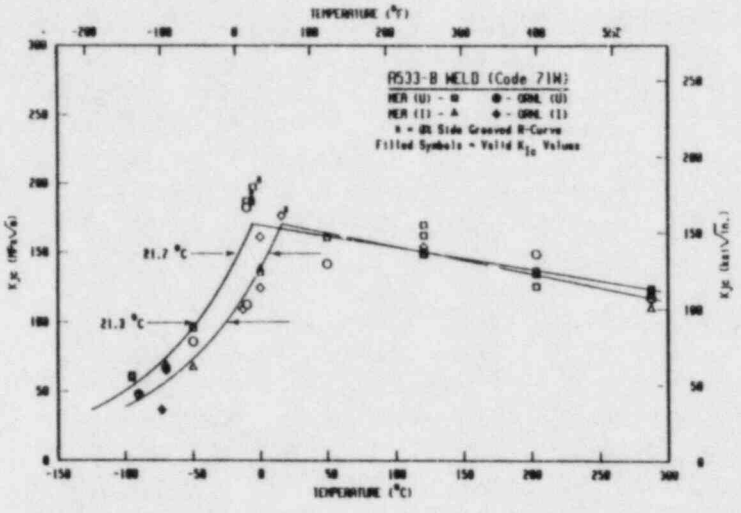

Fig. 14. Variation of initiation fracture toughness, K_{Jc}, of weld HSST-71W material with test temperature and irradiation.

The shift in transition temperature for all five materials is summarized in Fig. 15. In this figure, the shift indicated by Charpy V-notch test results can be directly compared with that of K_{Jc} and $K_{\beta c}$. The CVN shift was indexed at 41 J and K_{Jc} was indexed at 125 MPa$\sqrt{m}$. $K_{\beta c}$ was indexed at 90 MPa$\sqrt{m}$ for all five materials. This $K_{\beta c}$ level roughly corresponds to the β_{Ic}-corrected 125 MPa$\sqrt{m}$ K_{Jc} index for all five materials. Comparison of the CVN shift with K_{Jc}, and $K_{\beta c}$ indexed at 90 MPa$\sqrt{m}$ give similar results since the unirradiated and irradiated K_{Jc} and $K_{\beta c}$ transition curves are essentially parallel.

It is clear in Fig. 15 that the transition temperature shift is reduced by decreasing both the copper and the nickel content. Reducing either one separately does not produce as substantial a change in the shift as reducing both. Only the welds can be compared directly. The highest shift is evidenced by the data from weld 69W with the highest copper and lowest nickel, thus indicating that copper alone has a substantial effect. However, increased nickel with lowered copper

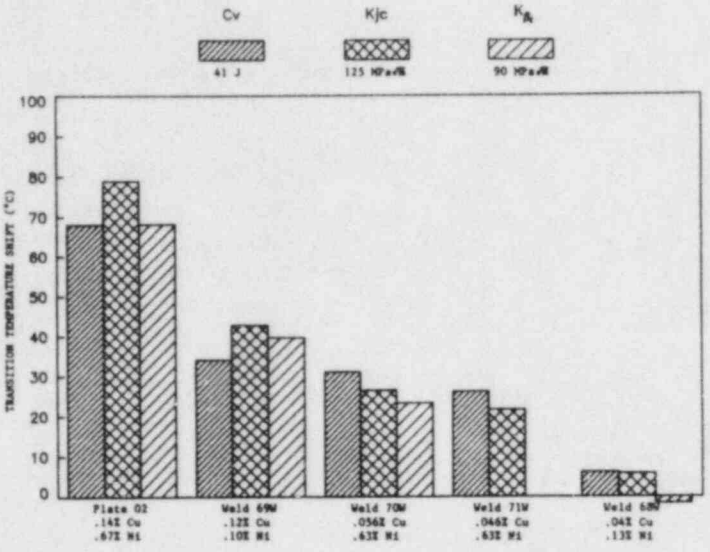

Fig. 15. Summary of the shift in brittle-to-ductile transition temperature indicated by Charpy, K_{Ic}, and $K_{\beta c}$ data.

(welds 70W and 71W) also produces a substantial but lesser shift. The lowest shift was produced in weld 68W where the percentage of both elements was reduced. Although the magnitude of the transition temperature shift varies somewhat for each indicator, all three support these observations.

The results of this irradiation effects study are summarized in Table 6. Primarily, the J-integral results have indicated that reduced levels of copper and nickel will reduce the effect of radiation on the behavior of the brittle-to-ductile transition and will reduce the degradation of the upper-shelf tearing modulus. Significant decreases (>25%) in the tearing modulus were observed in all materials with either copper or nickel contents above those of the weld having the lowest levels of these elements. Only when both elements were reduced was the tearing modulus degradation reduced. In terms of initiation fracture toughness, J_{Ic}, the upper-shelf level was essentially insensitive to all variables, i.e., radiation, copper content, and nickel content appeared to have little or no effect. The transition region, on the other hand, was substantially more sensitive to these variables. Variations were observed that appear to be directly related to changes in either the copper or nickel content. Only when both elements were reduced was the shift in the K_{Jc} brittle-to-ductile transition minimized.

Another observation is made regarding the shape of the K_{Jc} transition curve before and after irradiation. When either small or large shifts occurred, the shape did not appreciably change. This observation is significant since estimates of the K_{Ic} shift currently are based on the assumption that there is no shape change. Historically, the CVN transition curve shape has changed with shifts to higher temperature. In this study with 1TCS specimens, the data indicate that the fracture toughness, K_{Jc}, curve does not follow this pattern.

Table 6. Summary of material properties after irradiation

Material	Fluence, $n/m^2 \times 10^{23}$ (>1 MeV)	Yield strength increase[a] (%)	Transition temperature increase (°C)			Upper-shelf change (%)		Tearing modulus change (%)
			CVN[b]	K_{Jc}[c]	$K_{\beta c}$[d]	CVN	K_{Jc}[a]	
Plate HSST-02, 0.14% Cu, 0.67% Ni	2.0	31	68	79	68	–16	–15	–54
Weld HSST-68W, 0.04% Cu, 0.13% Ni	1.4	19	6	6	–4	9	–7	–5
Weld HSST-69W 0.12% Cu, 0.20% Ni	1.2	15	34	43	40	–3	–8	–32
Weld HSST-70W 0.056% Cu, 0.63% Ni	1.6	12	31	26	23	–10	4	–31
Weld HSST-71W 0.046% Cu, 0.63% Ni	1.6	14	26	22	--	8	–6	–32

[a]Average change.

[b]Increase at 41-J index.

[c]Increase at 125-MPa$\sqrt{m}$ index.

[d]Increase at 90-MPa$\sqrt{m}$ index.

Charpy V-notch data, in general, indicated transition temperature shifts that agree well with the shifts from the fracture toughness tests. The CVN upper-shelf changes also agree well with that indicated by the fracture toughness data, except for the case of plate 02. For plate 02, Charpy data indicated a moderate shelf drop, as did the initiation fracture toughness data; however, the tearing modulus from the J-R tests dropped by roughly 50%.

Additional details on this irradiation series may be found in refs. 25 and 26. Additional statistical analyses will be made when the final tests are completed.

CONCLUSIONS

1. There was excellent agreement between the results from the two laboratories, ORNL and MEA.

2. All five Charpy curve fitting equations gave nearly identical transition temperatures and transition temperature shifts.

3. Upper-shelf energy determinations should consider a possible sloping shelf.

4. A small data set can lead to erroneous conclusions regarding irradiation-induced changes of both transition temperature and upper-shelf energy.

5. The several trend curve formulations were in general agreement with Charpy specimen results of the present study.

6. Upper-shelf elastic-plastic initiation fracture toughness is essentially insensitive to radiation damage for the current production practice welds characterized in this study.

7. Transition temperature shifts to higher temperature with radiation are directly related to the copper and nickel content of the material with copper producing the greatest effect.

8. Upper-shelf initiation fracture toughness and tearing modulus are inversely proportional to temperature.

9. Irradiation degradation in tearing modulus is related to the copper and nickel content of the material.

10. Transition temperature shifts indicated by the CVN data indexed at the 41-J level correlate well with the fracture toughness indicated shift for these materials.

11. Submerged-arc welds with both low copper and low nickel contents show essentially zero radiation embrittlement.

FIFTH HSST IRRADIATION SERIES

The primary objective of this program (Fifth HSST Irradiation Series) is to obtain valid fracture toughness (K_{Ic}) curves to as a high a level as practical for two nuclear pressure vessel materials irradiated at 288°C.

Currently, estimates of the K_{Ic} curve shift are based on results from Charpy impact testing with the assumption that the shift of a Charpy toughness curve to higher temperatures can be applied directly to a K_{Ic} curve. To test this assumption, this program includes Charpy V-notch impact test specimens and drop-weight test specimens in addition to the compact fracture toughness specimens. Tensile specimens are included in the program to provide data for determining test parameters for the fracture toughness tests and for analysis of the fracture toughness data.

Irradiation and material parameters were chosen to (1) provide significant separation of unirradiated and irradiated properties (i.e., a significant radiation-induced temperature shift of toughness properties), (2) represent, as closely as practical, materials used in early nuclear pressure vessel construction (high copper and nickel contents), and (3) permit program conclusion in a reasonable time period. The chosen irradiation parameters are an irradiation temperature of 288°C (550°F) and a neutron fluence of 1.5×10^{23} neutrons/m^2 (>1 MeV). The chosen materials are submerged-arc weldments of 0.23 and 0.32% Cu content

(0.60% Ni in both weldments). The predicted temperature shifts of fracture toughness for these two weldments are 86 and 121°C, respectively, for the above irradiation parameters. The lower bounds (95% confidence level) are 58 and 93°C, respectively. These predictions are based on the Metal Properties Council analyses[27] of weld metals irradiated in test reactors.

The program plan provides sufficient numbers of specimens to permit meaningful statistical analyses of test results.

MATERIALS

In order to provide as uniform a test material as possible, submerged-arc weldments were fabricated using two special heats of AWS type EF-2 welding wire with copper added in the ladle to achieve the two levels of copper content. One lot, well mixed, of Linde 124 flux was used for all the welds. The weldments were fabricated and stress-relieved according to commercial practice. The base plate for the weldments is a single 220-mm-thick plate of SA-533 grade B class 2 steel. The submerged-arc welding was done by the tandem-arc, alternating-current procedure using a 0° bevel weld groove. The width of the deposited weld metal is about 30 mm. All welds were stress-relieved at 607°C for 40 h. About 14 lin m of each weldment were fabricated for the program.

SPECIMEN COMPLEMENT

The largest practical compact (K_{Ic}) specimen that can be irradiated is a 4TCS specimen. The irradiated yield stress will be about 620 MPa (90 ksi), resulting in a valid fracture toughness (K_{Ic}) measuring capacity of 130 MPa$\sqrt{m}$ (120 ksi$\sqrt{in.}$). To achieve this toughness level in the unirradiated specimens, having a yield stress of about 480 MPa (70 ksi), requires 8TCS specimens and these are provided for in the program. Smaller fracture toughness specimens are provided for measuring toughness at lower levels, obtaining K_{Jc} values for predicting test parameters for the larger specimens, and obtaining data for comparisons of K_{Ic} and K_{Jc} results. A series of irradiation capsules will contain a total of 16 each 4TCS, 36 each 2TCS, 60 each 1TCS, 112 each Charpy-V, 32 each drop-weight, and 28 each subsize tensile specimens, divided equally between the two materials. Sufficient numbers of unirradiated specimens will be tested to provide base line properties. The numbers of specimens are based on consideration of statistical analysis requirements and the constraints of the irradiation facility. Sufficient weldments are available for fabrication of additional unirradiated specimens, if found necessary.

IRRADIATION CAPSULE DESIGN AND OPERATION

The Fifth HSST Irradiation Series consists of a total of 12 capsules to be irradiated in the poolside facility of the Oak Ridge Research Reactor (ORR). Neutron dosimetry studies in the facility were conducted in a dummy capsule and a prototype of the 4T capsules was operated in the facility to obtain neutron and gamma heat parameters for final experiment

design. A steel gamma shield was incorporated into the facility to allow control of specimen temperatures. Neutron dosimeter sets are included in each capsule to verify the exposures.

The first two 4T capsules were installed in the irradiation facility and, following extensive checkouts of both the capsules and the facility instrumentation, the irradiation facility was inserted and irradiation began on May 11, 1984. The desired 288°C irradiation temperature was maintained at the quarter-thickness points at the specimen crack fronts. Due to the heat flow patterns in these specimens, temperatures at the center of the crack fronts were 2 to 3°C higher and at 8 mm from the ends of the crack front were 7 to 12°C lower than at the quarter-thickness points. This temperature gradient is due to the gamma heating in these massive specimens and would have been greater except for the use of steel gamma shields. (We are able to orient the small specimens to reduce the temperature gradients along the crack front to very small values.)

After 30 equivalent full-power days of irradiation, the capsules were rotated on June 11, 1984, and, after an additional 30 days, the irradiation was terminated on July 21, 1984. The temperature control during irradiation was very good. The desired 288°C at quarter-thickness position was easily maintained. The recorded temperature data are presently being reduced and average temperatures for all thermocouples, as well as their variation with time, will be reported in the next HSST semiannual progress report.

The second set of 4T capsules began irradiation on August 16, 1984. The assembly of the small specimen (1TCS, Charpy, drop-weight, and tensile) capsules is almost complete and preparations for the 2T capsules are well under way.

TEST PLAN

Two organizations, Materials Engineering Associates, Inc., (MEA) and Oak Ridge National Laboratory (ORNL) will participate in the testing program. Because of testing equipment limitations, all testing of irradiated 4TCS specimens and unirradiated 6TCS and 8TCS specimens will be conducted by MEA and all tensile tests will be conducted by ORNL. The sequence of testing will be:

1. materials characterization,
2. testing of unirradiated Charpy V-notch, tensile, and drop-weight specimens,
3. testing of unirradiated compact specimens, smaller specimens being tested first, and K_{Jc} tests preceding the large specimen tests,
4. testing of irradiated Charpy V-notch, tensile, and drop-weight tests,
5. testing of irradiated compact specimens, smaller specimens being tested first, and K_{Jc} tests preceding the large specimen tests, and
6. statistical analyses of results.

ACKNOWLEDGMENTS

We wish to thank M. Vagins of the U.S. Nuclear Regulatory Commission for supporting this study. We appreciate the assistance of the Electric Power Research Institute and Babcock and Wilcox Company in providing the weldments for the Fourth Series. We also wish to thank F. B. Kam and his co-workers for the dosimetry analyses, J. W. Woods and D. Heatherly for construction and operation of the Fourth Series irradiation capsules, technicians T. N. Jones, T. D. Owings, and R. L. Swain for conducting the tests at ORNL, and J. R. Hawthorne, A. Hiser, E. D'Ambrosio, L. Fletcher, and L. Lamont for conducting the tests at MEA. We thank J. L. Bishop for preparation of the manuscript.

REFERENCES

1. "Effects of Residual Elements on Predicted Radiation Damage to Reactor Vessel Materials," *Regulatory Guide 1.99* (Rev. 1), U.S. Nuclear Regulatory Commission, Washington, D.C., April 1977.

2. Private communication, P. N. Randall, U.S. Nuclear Regulatory Commission, to R. G. Berggren, Oak Ridge National Laboratory, January 1984.

3. J. D. Varsik and S. T. Byrne, "An Empirical Evaluation of the Irradiation Sensitivity of Reactor Pressure Vessel Materials," pp. 252–66 in *Effects of Radiation on Structural Materials*, ASTM-STP 683, J. A. Sprague and D. Kramer, eds., American Society for Testing and Materials, Philadelphia, 1979.

4. J. F. Perrin, R. A. Wullaert, G. R. Odette, and P. M. Lombrozo, *Physically Based Regression Correlations of Embrittlement Data From Reactor Pressure Vessel Surveillance Programs*, EPRI NP-3319, Electric Power Research Institute, Palo Alto, Calif., January 1984.

5. J. D. Varsik, S. M. Schloss, and J. J. Koziol, *Evaluation of Irradiation Response of Reactor Pressure Vessel Materials*, EPRI NP-2720, Electric Power Research Institute, Palo Alto, Calif., November 1982.

6. G. L. Guthrie, "Development of Trend Curve Formulas Using Surveillance Data-II," pp. HEDL-3–4 in *LWR Pressure Vessel Surveillance Dosimetry Improvement Program, Quarterly Progress Report for the Period April–June 1982*, NUREG/CR-2805, Vol. 2, HEDL-TME-82-19, Hanford Engineering Development Laboratory, Richland, Wash., January 1983.

7. U. Potapovs and J. R. Hawthorne, "The Effect of Residual Elements on the Response of Selected Pressure Vessel Steels and Weldments to Irradiation at 550°F," *Nucl. Appl.* 6(1), 27–46 (1969).

8. C. Guionnet et al., "Radiation Embrittlement of PWR Reactor Vessel Weld Metals: Nickel and Copper Synergism Effects," pp. 392–411 in *Effects of Radiation on Materials*, proceedings of the 11th International Symposium held in Scottsdale, Ariz., on June 28–30, 1982, ASTM STP 782, ed. H. R. Brager and J. S. Perrin, American Society for Testing and Materials, Philadelphia, 1982.

9. C. Leitz et al., "Comparative Irradiation Study of Reactor Pressure Vessel Steel Weld Metals," pp. 412–32 in *Effects of Radiation on Materials*, proceedings of the 11th International Symposium held in Scottsdale, Ariz., on June 28–30, 1982, ASTM STP 782, ed. H. R. Brager and J. S. Perrin, American Society for Testing and Materials, Philadelphia, 1982.

10. C. E. Childress, *Fabrication History of the First Two 12-inch Thick ASTM A533 Grade B, Class 1 Steel Plates of the Heavy Section Steel Technology Program, Documentary Report 1*, ORNL-4313, Oak Ridge National Laboratory, Oak Ridge, Tenn., February 1969.

11. T. V. Marston, M. P. Borden, J. H. Fox, and L. D. Reardon, *Fracture Toughness of Ferritic Materials in Light Water Nuclear Reactor Vessels*, MML-75-152, Combustion Engineering, Inc., Chattanooga, Tenn., October 1975.

12. A. L. Lowe, Jr., and J. I. Quresi, *Fabrication of Weldments Using Linde 80 and Linde 124 Weld Fluxes for HSST-4 Irradiation Program*, BAW-1537, Babcock and Wilcox Company, Lynchburg, Va., June 1981.

13. C. A. Baldwin, *Neutron Spectral Characterization Calculations for the Fourth Nuclear Regulatory Commission Heavy Section Steel Technology 1T-CT Irradiation Experiments*, NUREG/CR-3311, ORNL/TM-8782, Oak Ridge National Laboratory, Oak Ridge, Tenn., June 1983.

14. F. W. Stallman, C. A. Baldwin, and F. B. K. Kam, *Neutron Spectral Characterization for the Fourth Nuclear Regulatory Commission Heavy Section Steel Technology 1T-CT Irradiation Experiments: Dosimetry and Uncertainty Analysis*, NUREG/CR-3333, ORNL/TM-8789, Oak Ridge National Laboratory, Oak Ridge, Tenn., July 1983.

15. H. A. Ernst, "Material Resistance and Instability Beyond J-Controlled Crack Growth," Scientific Paper 81-1D7-J1NTF-P6, Westinghouse Research and Development Center, Pittsburgh, Dec. 3, 1981.

16. P. Albrecht et al., "Tentative Test Procedure for Determining the Plane Strain J_I-R Curve," *J. Test. Eval.* 10(6), 245–51 (November 1982).

17. F. J. Loss, ed., *Structural Integrity of Water Reactor Pressure Boundary Components, Quarterly Progress Report for the Period April–June 1979*, NUREG/CR-0943, NRL Memorandum Report 4064, Naval Research Laboratory, Washington, D.C., Sept. 28, 1979.

18. F. J. Loss, ed., *Structural Integrity of Water Reactor Pressure Boundary Components, Annual Report, Fiscal Year 1979*, NUREG/CR-1128, NRL Memorandum Report 4122, Naval Research Laboratory, Sept. 31, 1979.

19. J. R. Hawthorne, ed., *Evaluation and Prediction of Neutron Embrittlement of Reactor Pressure Vessel Materials*, EPRI NP-2782, Final Report, Electric Power Research Institute, Palo Alto, Calif., December 1982.

20. A. L. Hiser et al., *J-R Curve Characterization of Irradiated Low Upper Shelf Welds*, NUREG/CR-3506, MEA-2028, Materials Engineering Associates, Inc., Lanham, Md., April 1984.

21. G. R. Irwin, "Fracture Mode Transition for a Crack Traversing a Plate," ASME J. Basic Eng. 82(2), 417–25 (1960).

22. J. G. Merkle, *An Examination of the Size Effects and Data Scatter Observed in Small-Specimen Cleavage Fracture Toughness Testing*, NUREG/CR-3672, ORNL/TM-9088, Oak Ridge National Laboratory, Oak Ridge, Tenn., April 1984.

23. J. J. McGowan, *Tensile Properties of Irradiated Nuclear Grade Pressure Vessel Plate and Welds for the Fourth HSST Irradiation Series*, NUREG/CR-3978, ORNL-6096, Oak Ridge National Laboratory, Oak Ridge, Tenn., to be published.

24. R. E. Johnson, ed., *Resolution of the Reactor Vessel Materials Toughness Safety Issue*, NUREG/CR-0744, U.S. Nuclear Regulatory Commission, Washington, D.C., September 1981.

25. R. G. Berggren, J. R. Hawthorne, and R. K. Nanstad, "An Analysis of Charpy V-Notch Impact Toughness of Irradiated A-533 Grade B Class 1 Plate and Four Submerged-Arc Welds," presented at the Twelfth International Symposium on the Effects of Radiation on Materials, Williamsburg, Va., on June 18, 1984, to be published.

26. B. H. Menke, J. J. McGowan, R. G. Berggren, R. K. Nanstad, and K. C. Miller, "Effects of Neutron Irradiation on Fracture Toughness of A-533 Grade B Class 1 Plate and Four Submerged-Arc Welds," presented at the Twelfth International Symposium on the Effects of Radiation on Materials, Williamsburg, Va., on June 18, 1984, to be published.

27. Metal Properties Council Subcommittee 6 on Nuclear Materials, "Prediction of the Shift in the Brittle-Ductile Transition Temperature of Light-Water Reactor (LWR) Pressure Vessel Materials," *J. Test. Eval.* 11(4), 327–60 (July 1983).

FRACTURE PROPERTIES OF A NEUTRON-IRRADIATED STAINLESS STEEL SUBMERGED ARC WELD CLADDING OVERLAY*

W. R. Corwin, R. G. Berggren, and R. K. Nanstad
Metals and Ceramics Division
Oak Ridge National Laboratory
Oak Ridge, Tennesseee 37831

ABSTRACT

The ability of stainless steel cladding to increase the resistance of an operating nuclear reactor pressure vessel to extension of surface flaws depends greatly on the properties of the irradiated cladding. Therefore, weld overlay cladding irradiated at temperatures and fluences relevant to power reactor operation was examined. The cladding was applied to a pressure vessel steel plate by the submerged arc, single-wire, oscillating-electrode method. Three layers of cladding provided a thickness adequate for fabrication of test specimens. The first layer was type 309, and the upper two layers were type 308 stainless steel. The type 309 was diluted considerably by excessive melting of the base plate. Specimens were taken from near the base plate-cladding interface and also from the upper layers. Charpy V-notch and tensile specimens were irradiated at 288°C to a fluence of 2×10^{23} neutrons/m^2 (>1 MeV).

When irradiated, both types 308 and 309 cladding increased 5 to 40% in yield strength and slightly increased in ductility in the temperature range from 25 to 288°C. All cladding exhibited ductile-to-brittle transition behavior during impact testing. The type 308 cladding, microstructurally typical of that in reactor pressure vessels, showed very little degradation in either upper-shelf energy or transition temperature due to irradiation. Conversely, the impact properties of the specimens containing the highly diluted type 309 cladding, microstructurally similar to that produced during some off-normal welding conditions in existing reactors, experienced significant increases in transition temperature and drops of up to 50% in upper-shelf energy. The impact energies of the Charpy specimens containing the type 309 layer strongly reflected the amount of the type 309 actually in the specimen, falling into two distinct high- and low-energy populations with the low-energy population corresponding to a higher fraction of type 309 in the specimen.

---

*Research sponsored by Office of Nuclear Regulatory Research, U.S. Nuclear Regulatory Commission under Interagency Agreement DOE 40-551-75 with the U.S. Department of Energy under Contract No. DE-AC05-840R21400 with the Martin Marietta Energy Systems, Inc.

INTRODUCTION

It has been proposed that the existence of a tough surface layer of weld-deposited stainless steel cladding on the interior of a reactor pressure vessel (RPV) can keep a short surface flaw from becoming long, either by impeding the initiation of extension of a static flaw and/or by arresting a running flaw. To obtain preliminary material properties typical of those needed to make such an evaluation for light-water reactors (LWRs), a program has been established to obtain data on the degradation (or lack thereof) of the fracture properties of stainless steel weld overlay cladding. A recent review of the literature[1] has indicated that fracture properties of stainless steel weld metal can degrade significantly under irradiation conditions relevant to LWRs. To evaluate this potential degradation, tensile, Charpy V-notch, and precracked Charpy specimens of stainless steel weld overlay cladding were irradiated to about 2×10^{23} neutrons/m^2 (>1 MeV) at 288°C. The results of tensile and Charpy V-notch tests are reported here and compared with the properties of unirradiated cladding.

MATERIALS

The specimens were all taken from a single laboratory weldment fabricated by the automated single-wire oscillating submerged arc procedure for a companion program investigating structural effects of stainless steel cladding on composite four-point bend specimens.[2,3] The weldment consisted of a lower layer of type 309 stainless steel deposited on A 533 grade B class 1 plate, followed by two upper layers of type 308 stainless steel cladding.

The welding wires for both the types 308 and 309 stainless steel were 4 mm in diameter and chosen to be representative of cladding formerly applied in industry. The cladding was deposited on plates that were 114 mm thick by 406 mm wide by 914 mm long to minimize distortion and provide an adequate heat sink. The clad plates were then postweld heat treated (PWHT) at 621°C for 40 h to represent commercial practice.

The single-wire oscillating submerged arc welding process used involved a preheat temperature of 121°C and an interpass temperature below 288°C. The welding parameters were as follows:

1. wire extension, 27.0 mm;
2. oscillation width, 19.0 mm;
3. frequency, 0.3 Hz;
4. dc, 500 A;
5. dc straight polarity voltage, 36 V; and
6. forward travel speed, 2.1 mm/s.

The three layers of cladding were applied to provide adequate cladding thickness (~20 mm) to obtain test specimens. The material compositions of each layer of weld metal are given in Table 1. This

Table 1. Chemical composition of overlay weldments

Layer	Content[a] (wt %)												
	C	Cr	Ni	Mo	Mn	Si	Co	Cu	V	Al	Ti	P	S
Lower	0.145	13.46	6.90	0.47	1.47	0.56	0.066	0.14	0.02	0.014	<0.005	0.018	0.01
Middle	0.081	18.52	8.81	0.27	1.47	0.70	0.092	0.10	0.04	0.010	<0.005	0.021	0.01
Upper	0.065	20.01	9.36	0.21	1.49	0.76	0.100	0.09	0.04	0.16	0.006	0.022	0.01

[a]Balance Fe, with Nb, <0.01; Ta, <0.01; As, <0.03; and B, <0.001 for all layers.

contrasts with typical commercial practice, in which a single layer of overlay approximately 5 mm thick is applied by either multiple wire or strip-cladding submerged arc procedures. Subsequent metallographic examination showed that the upper layer appeared typical of LWR stainless steel overlay, whereas the lower layer had incurred excessive dilution as a result of base metal melting during welding. Photomicrographs of the three passes illustrate the radically different microstructures in the finished weldment. The upper pass (Fig. 1) shows a distribution of δ-ferrite in an austenite matrix quite typical of microstructures seen in good practice commercial weld overlay cladding in reactor pressure vessels.[4] The effect of the 40-h PWHT on these materials is to partially transform the δ-ferrite to sigma phase. Although this is difficult to resolve in the optical micrographs, magnetic etching with ferrofluid, the use of a colloidal suspension of magnetic particles in the presence of a local magnetic field,[5] and color staining techniques verified that the partial transformation had occurred.

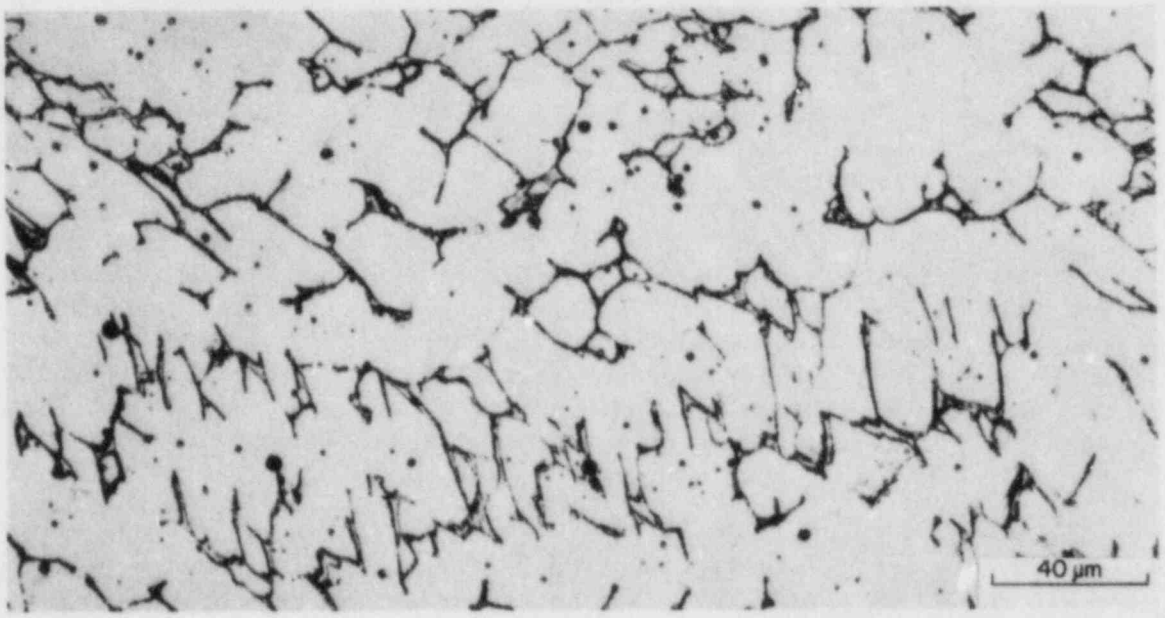

Fig. 1. The microstructure of the top layer of type 308 stainless steel weld overlay is typical of reactor pressure vessel cladding with δ-ferrite in an austenite matrix.

The lower and middle layers of cladding, on the other hand, formed atypical microstructures as a result of the excessive dilution (approximately 50%) by the base metal and lower pass weldment, respectively. Amounts of dilution in good practice cladding are typically in the range of 10 to 25%. The middle layer (Fig. 2) contains δ-ferrite dispersed in austenite but in addition contains limited regions in which martensite is also present. The bottom layer had sufficient dilution to move it

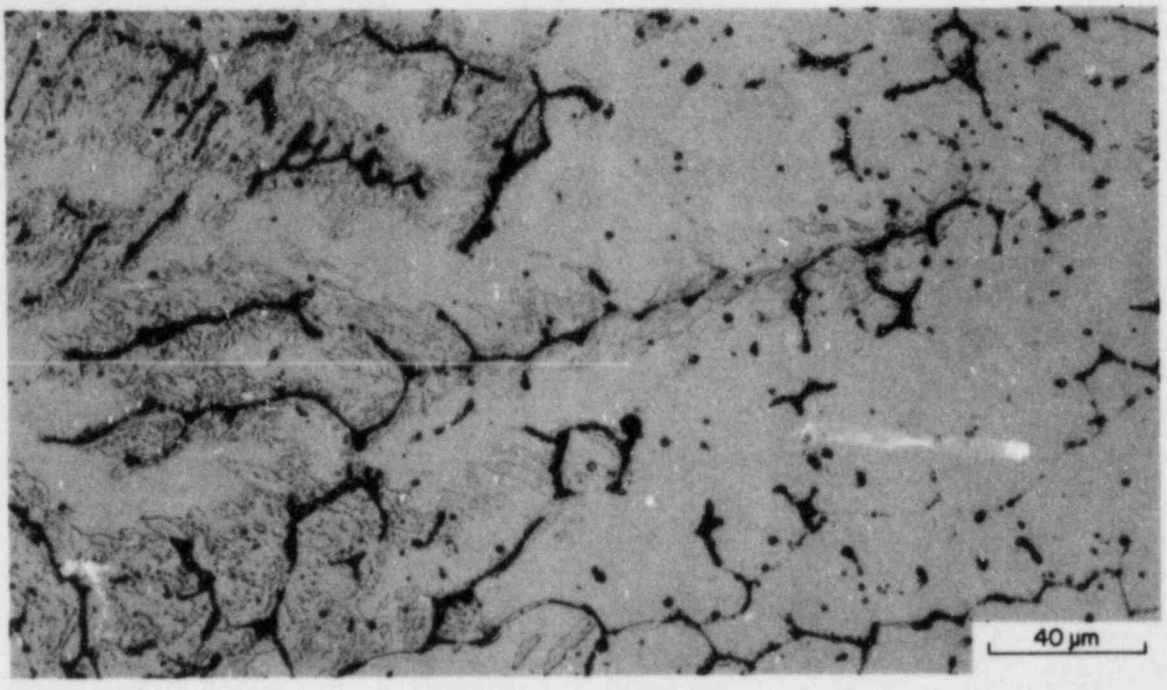

Fig. 2. The middle layer of the overlay (type 308 stainless steel) includes patches of martensite (light gray) in addition to the δ-ferrite in an austenite matrix.

entirely from the δ-ferrite-forming region of the Schaeffler diagram[6] and into the austenite-plus-martensite region (these are the dominant phases). Examination of its microstructure (Fig. 3), however, shows three distinct regions. The use of the ferrofluid magnetic etching technique and studies in the transmission electron microscope verified the lightest regions to be austenite, the light gray regions tempered martensite, and the dark regions δ-ferrite decorated with $M_{23}C_6$.

Although the investigation of high-dilution cladding was not the initial aim of the cladding studies, it may well be highly germane to the question of the effects of cladding on RPV integrity. High base metal dilution of cladding, caused by inadequate control of welding procedures, and the resulting microstructures have been documented[7,8] in commercial RPVs. Typically, the resulting material has poorer mechanical and/or corrosion properties in the unirradiated condition; no information is available on the irradiation damage of such material. The inclusion of such material may provide insight into the behavior of substandard weld overlay cladding representative of irradiated material actually in the field.

To examine the effects of the varying microstructures, two sets of tensile and Charpy V-notch specimens were carefully fabricated to be contained as fully as possible within either the upper two layers (nominally type 308 specimens) or the lower layer (nominally type 309 specimens).

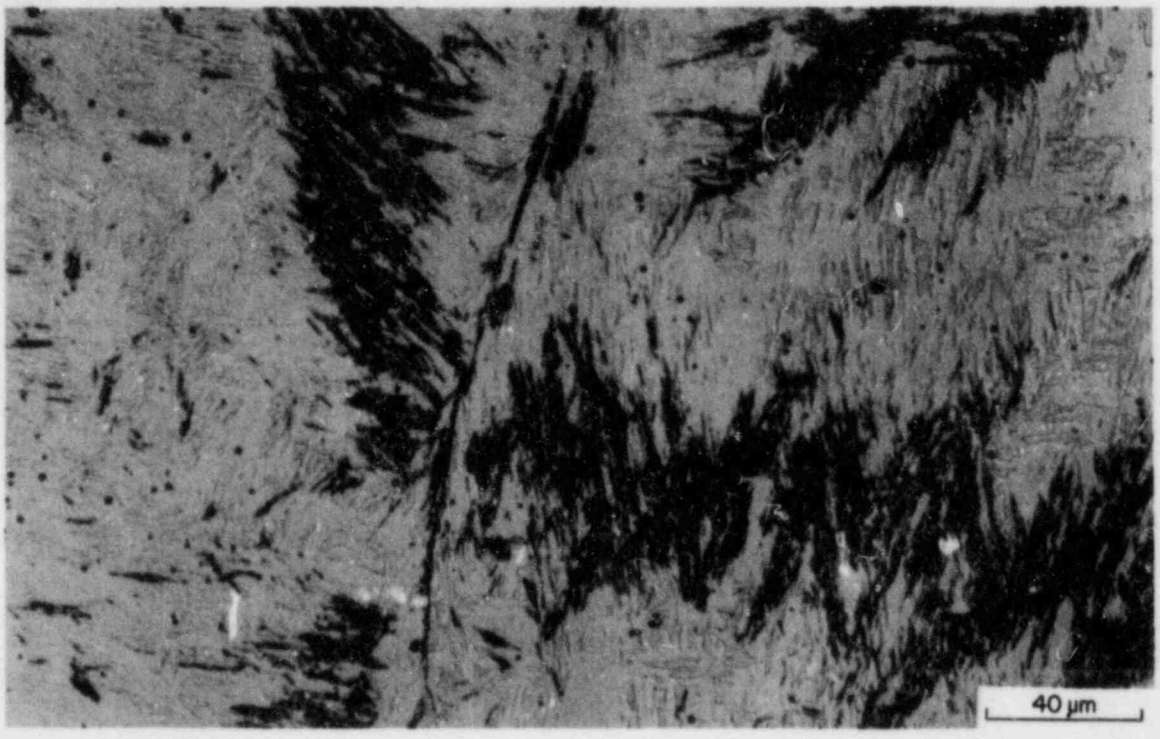

Fig. 3. The high base metal dilution of the lowest layer of cladding, type 309 stainless steel, resulted in a three-phase microstructure of austenite (lightest region), martensite (light gray), and δ-ferrite decorated with additional carbides (black).

All specimens were fabricated with the specimen axis parallel to the welding direction. The Charpy specimens were notched on the surface parallel to and nearer the base metal in all cases.

Ferrite numbers were measured on the finished Charpy specimens with a Ferrite Scope, which locally measures the percentage of ferromagnetic material in the sample. The nominally type 308 specimens consistently had ferrite numbers of 2 to 6 (corresponding roughly to percentages of ferrite), as did the portion of nominally type 309 specimens composed of upper weld pass layers. The notched side of the nominally type 309 specimens closest to the base metal interface exhibited a wide range of ferrite numbers from 2 to greater than 30 (off scale). This wide range was presumably due to the volume of material over which the Ferrite Scope takes a measurement and to the inclusion, in some cases where the amount of type 309 weldment was thin, of some of the type 308 upper layer cladding. Optical examination of the microstructure of the type 309 layer indicates the amounts of martensite and ferrite to be 30 to 45% and 10 to 15%, respectively.

IRRADIATION HISTORY

The specimens were irradiated by Materials Engineering Associates in the core of the 2-MW pool reactor (UBR) at the Nuclear Science and Technology Facility, Buffalo, New York. Two separate capsules were used, one each for the types 308 and 309 stainless steel specimens. The capsules were instrumented with thermocouples and dosimeters and were rotated 180° once during the irradiation for fluence balancing. The capsule containing the type 308 specimens reached an average fluence of 2.09×10^{23} neutrons/m^2 (>1 MeV) ± 10% during 679 h of irradiation. The capsule containing the type 309 specimens reached an average fluence of 2.02×10^{23} neutrons/m^2 (>1 MeV) ± 5% in 508 h. The fluences are for a calculated spectrum based on Fe, Ni, and Co dosimetry wires. Temperatures were maintained at 288 ± 14°C except for the initial week of irradiation. During that time, temperatures as low as 263°C were recorded for the type 308 specimens.

RESULTS AND DISCUSSION

Tensile testing was conducted at room temperature, 149°C, and 288°C. Irradiation increased the yield strength of the type 309 specimens by 30 to 40%, whereas the increase of the type 308 specimens was only 5 to 25% (Fig. 4). Surprisingly, the total elongation and reduction of area of both materials increased during irradiation (Fig. 5). Tensile properties are detailed in Table 2.

The effect of irradiation on the Charpy impact properties of the type 308 weld metal representative of typical weld overlay cladding was relatively small (Fig. 6). Only a very slight upward shift in transition temperature (~15°C) and drop in upper shelf (<10%) were observed. It should be noted for both the control and irradiated specimens that Charpy curves more typical of ferritic materials than of austenitic stainless steel were observed with respect to the abrupt transition from high- to low-energy fracture. Fracture surfaces of selected specimens were examined in the lower transition and upper-shelf regions. Macrographs of the irradiated type 308 specimens tested at temperatures low in the transition show flat fracture with clear definition of some of the large grains produced during welding (Fig. 7). By comparison, specimens at upper-shelf temperatures produced fracture surfaces more typical of wrought stainless steel with deep shear lips and a dull appearance. Scanning electron microscopy (SEM) of unirradiated specimens tested in the lower transition and upper-shelf regions clearly show the transition from a cleavage or quasi cleavage to a fibrous fracture mode (Fig. 8). This behavior compares well with the work of other researchers,[9,10] who have shown that fully ductile fracture occurs in as-welded austenitic weld metal as low as 4 K but that quasi cleavage can occur in weld metal that has received a PWHT in the temperature range in which carbide precipitation and sigma formation occur. Studies on weld metal examined here indicate that the fracture path preferentially follows the ferritic phases.

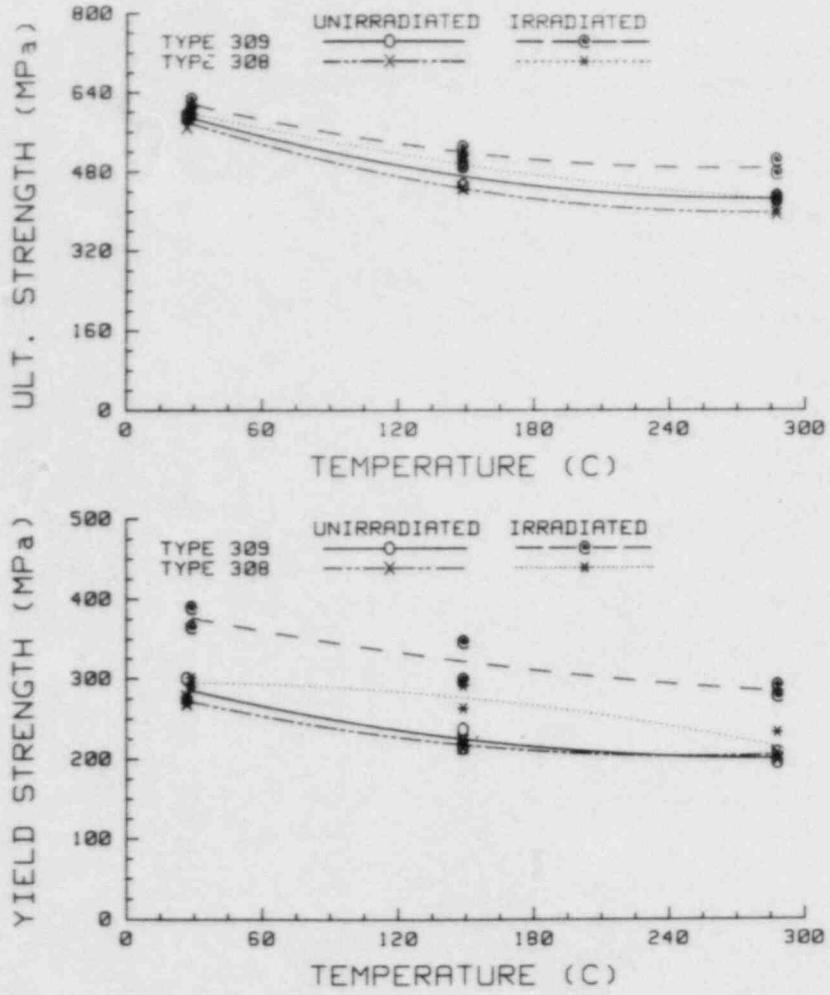

Fig. 4. Effect of irradiation at 288°C to a fluence of 2×10^{23} neutrons/m^2 (>1 MeV) on the tensile strength of the nominally types 308 and 309 stainless steel weld metal.

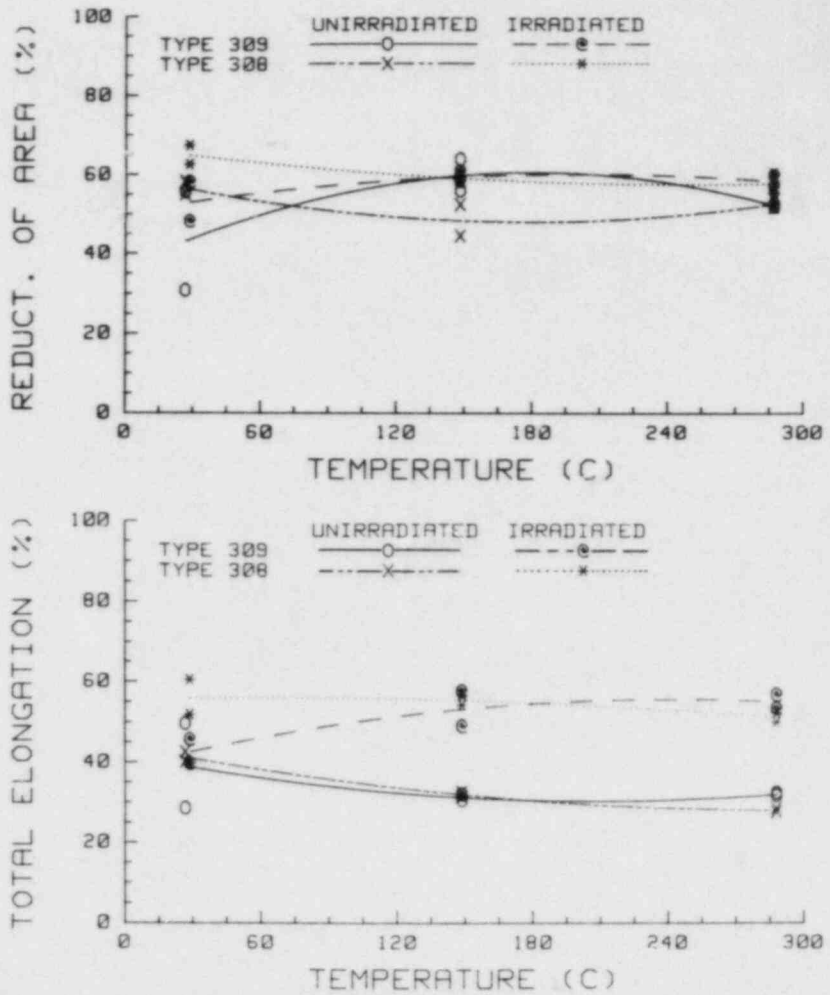

Fig. 5. Effect of irradiation at 288°C to a fluence of 2×10^{23} neutrons/m^2 (>1 MeV) on the tensile ductility of the nominally types 308 and 309 stainless steel weld metal.

Table 2. Tensile properties of stainless steel cladding before and after irradiation at 288 ± 14°C

Specimen	Material type[a]	Fluence, >1 MeV (neutrons/m^2)	Test temperature (°C)	Strength (MPa)		Total elongation[b] (%)	Reduction of area (%)
				Yield	Ultimate		
CPL-80	309	0	27	299	593	28.4	30.6
CPL-83	309	0	27	273	586	49.5	55.5
CPC-72	308	0	27	268	589	40.0	55.0
CPC-73	308	0	27	276	568	42.4	58.0
CPL-81	309	2.0×10^{23}	29	388	606	39.4	48.0
CPL-85	309	2.0	29	364	624	45.4	58.0
CPC-70	308	2.1	29	289	605	51.5	62.3
CPC-75	308	2.1	29	300	589	60.1	67.1
CPL-86	309	0	149	213	448	31.9	55.5
CPL-89	309	0	149	236	450	30.4	63.4
CPC-77	308	0	149	221	445	31.3	44.0
CPC-78	308	0	149	213	444	32.4	52.0
CPL-82	309	2.0	149	297	508	57.2	57.9
CPL-87	309	2.0	149	345	526	48.6	60.4
CPC-71	308	2.1	149	290	501	56.3	59.3
CPC-76	308	2.1	149	262	485	53.8	58.1
CPL-90	309	0	288	195	429	31.7	51.5
CPL-91	309	0	288	207	423	32.4	52.2
CPC-79	308	0	288	205	393	28.5	51.4
CPC-80	308	0	288	205	402	27.6	53.3
CPL-84	309	2.0	288	277	475	52.9	56.6
CPL-88	309	2.0	288	290	501	56.3	59.3
CPC-74	308	2.1	288	198	422	51.9	55.0
CPC-81	308	2.1	288	232	427	49.5	59.8

[a]Type 309 consists primarily of the first metal pass, type 308 primarily the third (last pass).

[b]Gage length/diameter = 7.

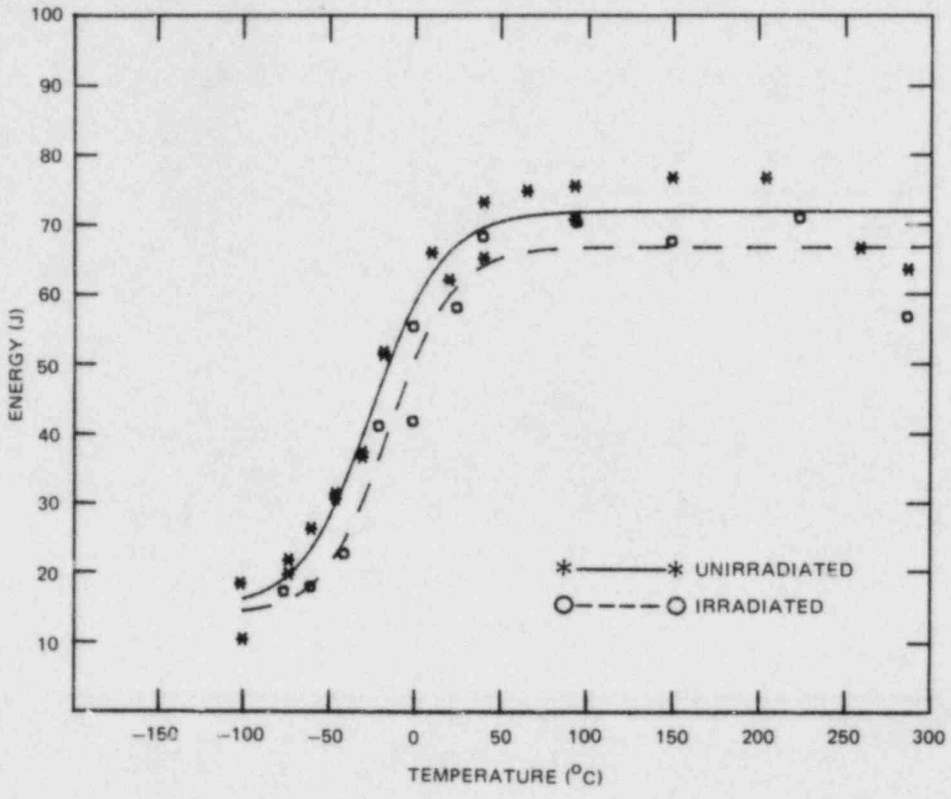

Fig. 6. Effect of irradiation on the Charpy impact energy of type 308 stainless steel cladding.

At low temperatures the fracture appears typically to follow the δ-ferrite in both the type 308 and 309 weld metals, going through the austenite or martensite only where necessary to reach the next δ-ferrite island. On the upper shelf this does not occur because the fracture is no longer dominated by the ferrite but passes through austenitic and ferritic phases with equal ease. Therefore, the failure of ferrite at low temperature, resulting from its inherent ductile-to-brittle behavior, appears to govern the macroscopic transition-type failure behavior of the austenitic weld metal.

The interpretation of the impact results of the nominally type 309 specimens is more complicated. Since the type 309 weld pass was not thick enough to obtain specimens composed entirely of type 309 weld metal, a portion of all the specimens nominally called type 309 is indeed type 308. Macrographs of the irradiated specimen fracture surfaces show that over the range of the full Charpy curve, the portion composed of type 309 weldment remains bright and faceted (Fig. 9). The remainder of the fracture surface, composed of upper cladding layers of type 308 weld metal, exhibits the same behavior seen in the fully type 308 specimens.

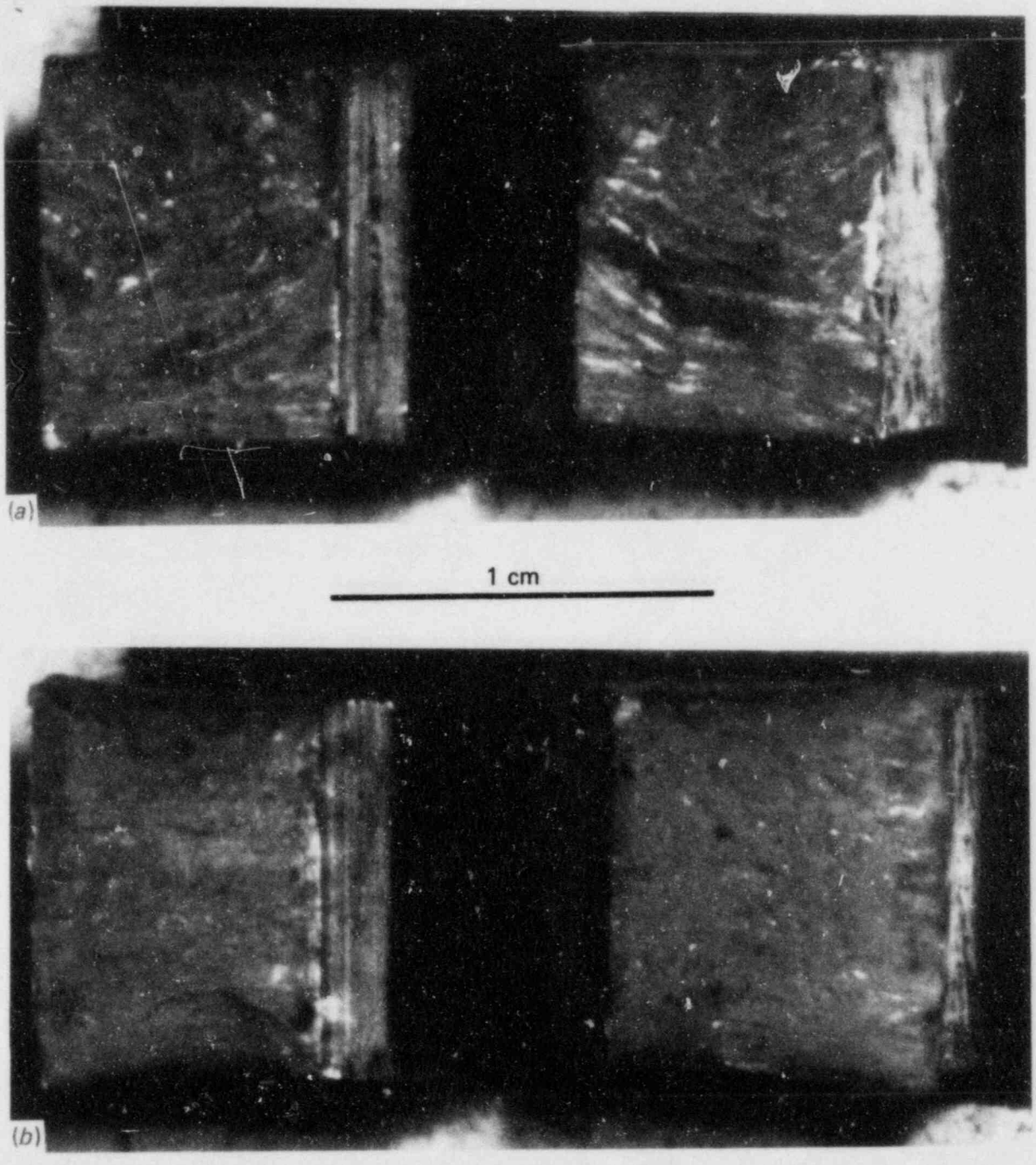

Fig. 7. Fracture surfaces of irradiated type 308 stainless steel cladding Charpy impact specimens. (*a*) Specimen CPC-304 tested at −60°C very low in the transition range. (*b*) Specimen CPC-290 tested at 150°C on the upper shelf.

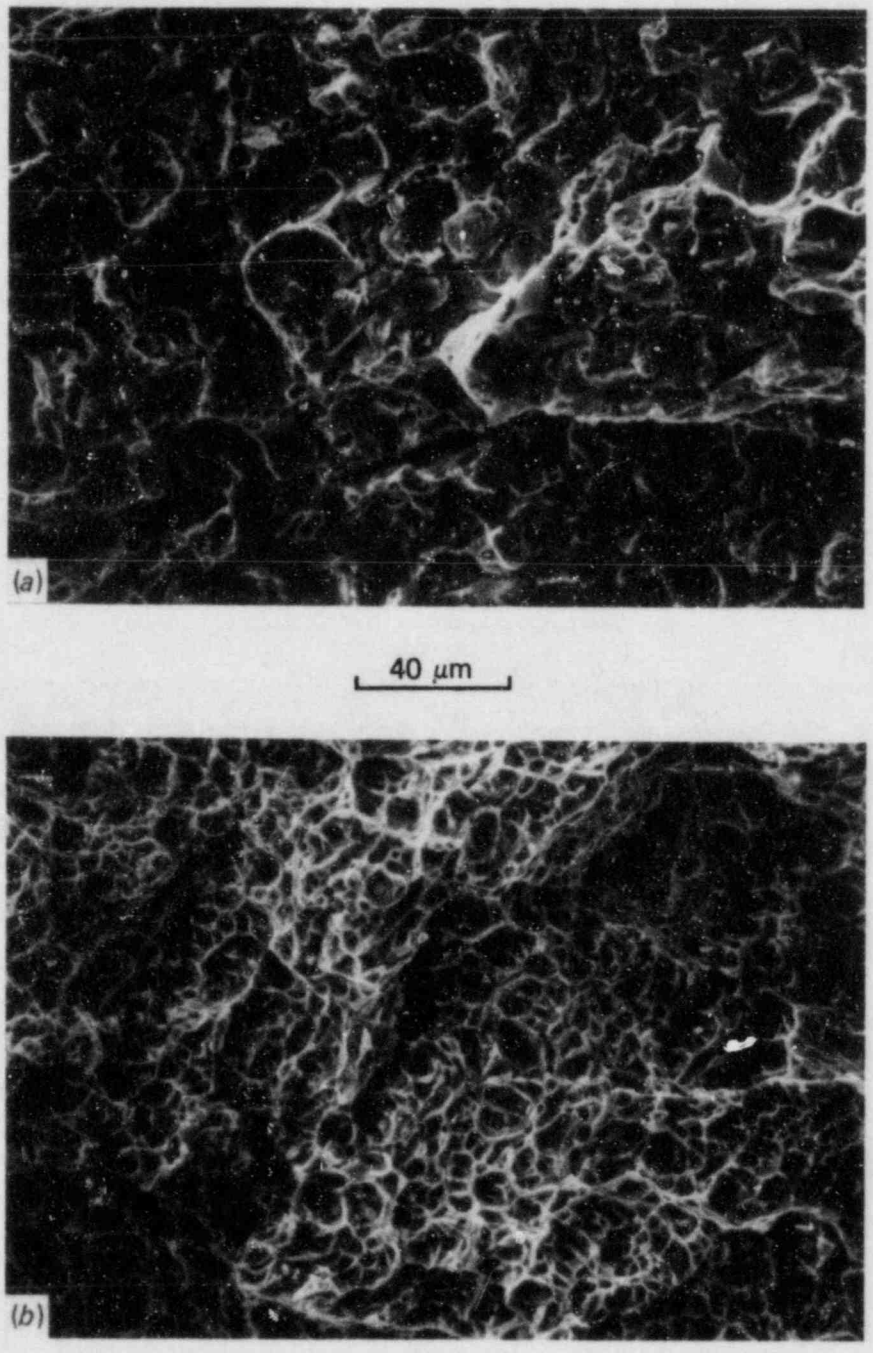

Fig. 8. Scanning electron micrographs of the fracture surfaces of unirradiated type 308 stainless steel cladding Charpy impact specimens. (*a*) Specimen CPC-283 tested at −100°C on the lower shelf, showing predominantly brittle fracture. (*b*) Specimen CPC-298 tested at 150°C on the upper shelf, showing fibrous fracture.

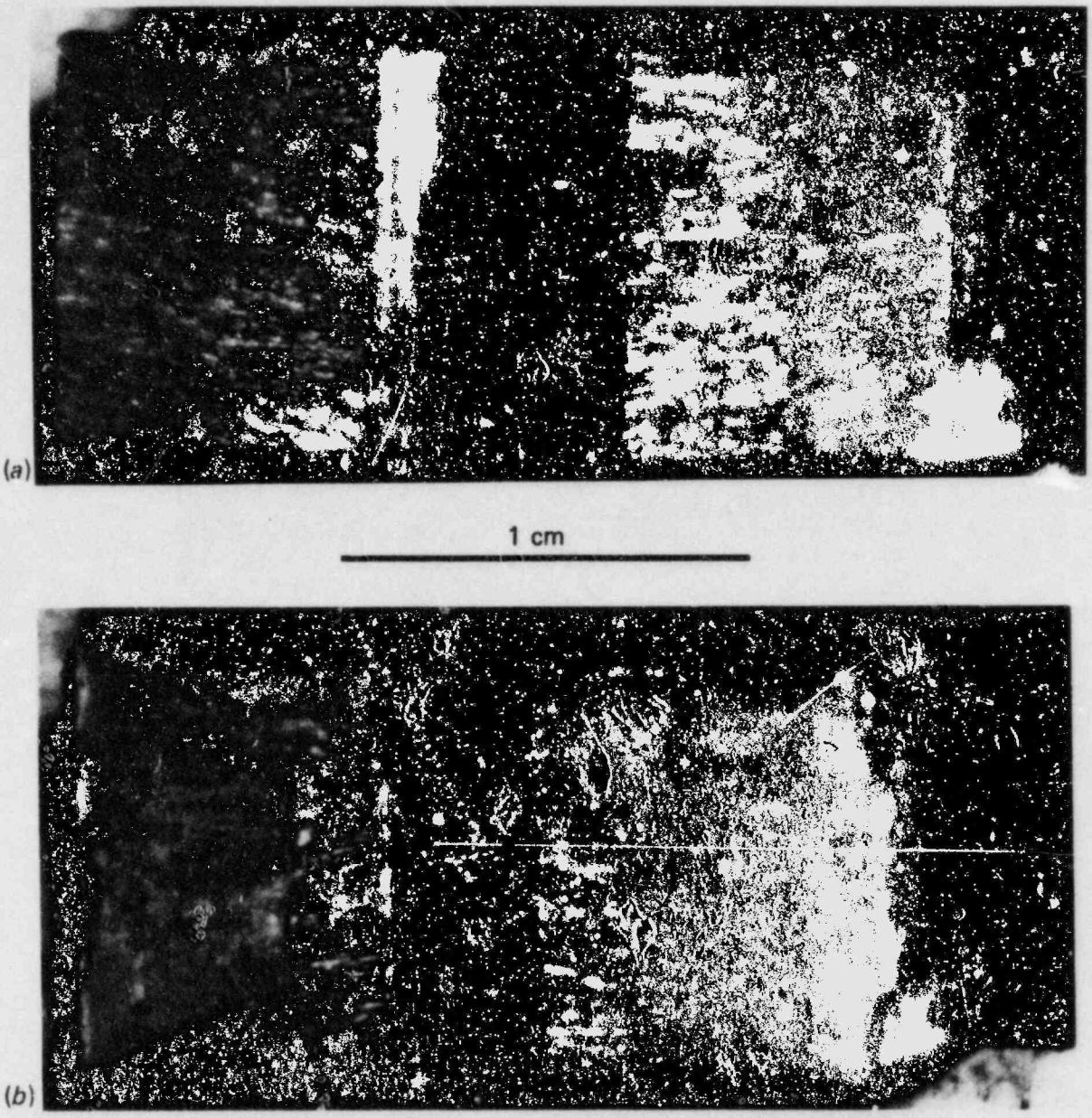

Fig. 9. Fracture surfaces of irradiated stainless steel cladding Charpy impact specimens (nominally type 309) clearly showing the bright faceted type 309 weld metal directly below the notch and the duller type 308 weld metal composing the rest of the specimen. (*a*) Specimen CPL-515 tested at 0°C in the very low transition region. (*b*) Specimen CPL-518 tested at 250°C on the upper shelf.

Scanning electron microscopy of an unirradiated specimen from the lower transition range (Fig. 10) illustrates the very different fracture morphology of the type 309 weld metal just below the notch and the rest of the the fracture surface composed of type 308 weld metal. The type 309 is very flat and formed predominately by cleavage (Fig. 11) at a temperature (−32°C) at which the type 308 weld metal is still mixed mode (Fig. 12). At upper-shelf temperatures, although the type 309 and 308 weld metals can still be distinguished in the SEM, both fail in a fibrous manner (Fig. 13).

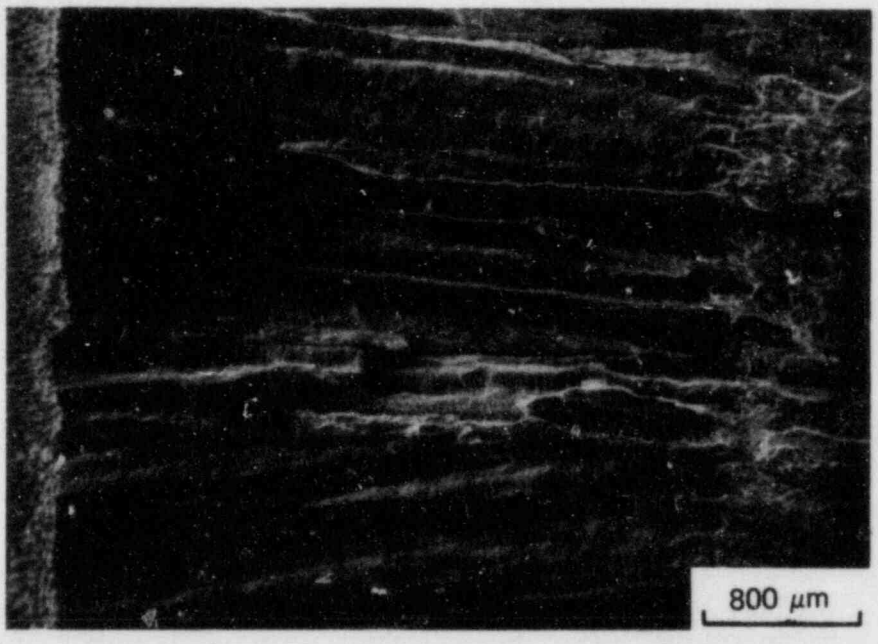

Fig. 10. Scanning electron micrograph of fracture face of unirradiated Charpy specimen CPL-516 (nominally type 309 stainless steel) tested at −32°C in the transition region. The dimpled area at the left is the specimen notch, the central flat portion is the type 309 weld metal, and the rough portion at the right is the first type 308 weld pass.

In the nominally type 309 specimens, interpreting the Charpy impact curves demands that the dual fracture properties of the type 308 and 309 portions of the material be taken into consideration. Examination of the fracture surfaces shows clearly that the type 308 weld metal has a lower transition temperature than does the type 309. Examining the impact data reveals a bimodal population related to the amount of the tougher type 308 weld metal present in the sample. The more type 308 in the specimen, the lower the apparent transition temperature of the specimen. The compilation of the unirradiated and irradiated impact data in Tables 3 and 4, respectively, includes the percentage of type 308 weld metal measured visually on each fracture surface. By using this percentage as a criterion, the impact data were divided into low- and high-energy populations.

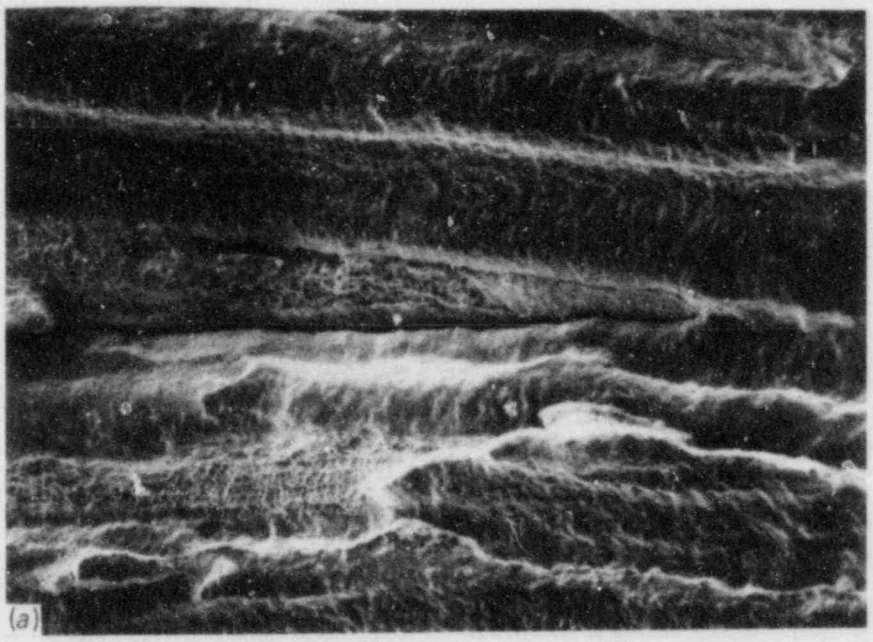

200 μm

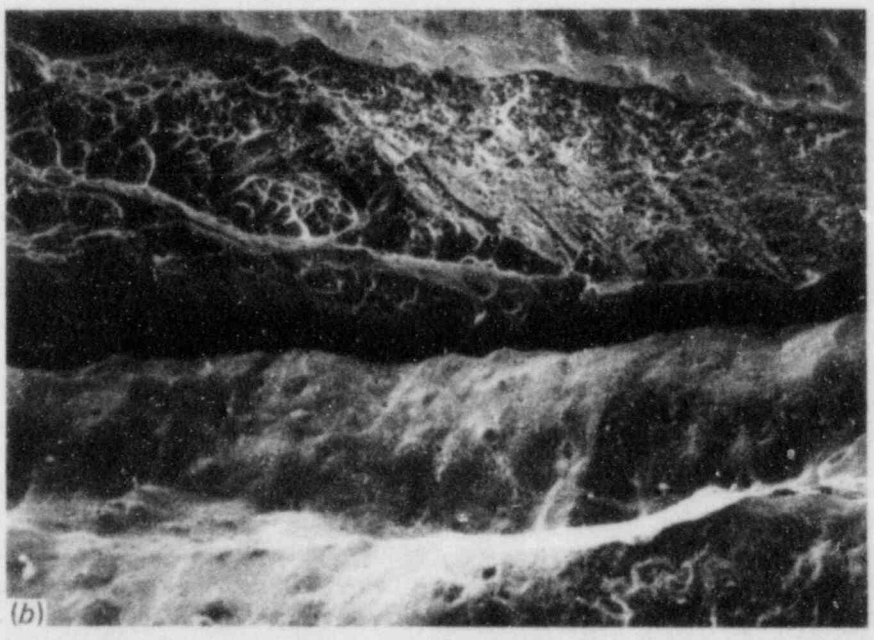

40 μm

Fig. 11. Detailed views of the type 309 stainless steel weld metal fracture surface of specimen CPL-516 (tested at −32°C) showing predominantly flat fracture with islands of fibrous tearing.

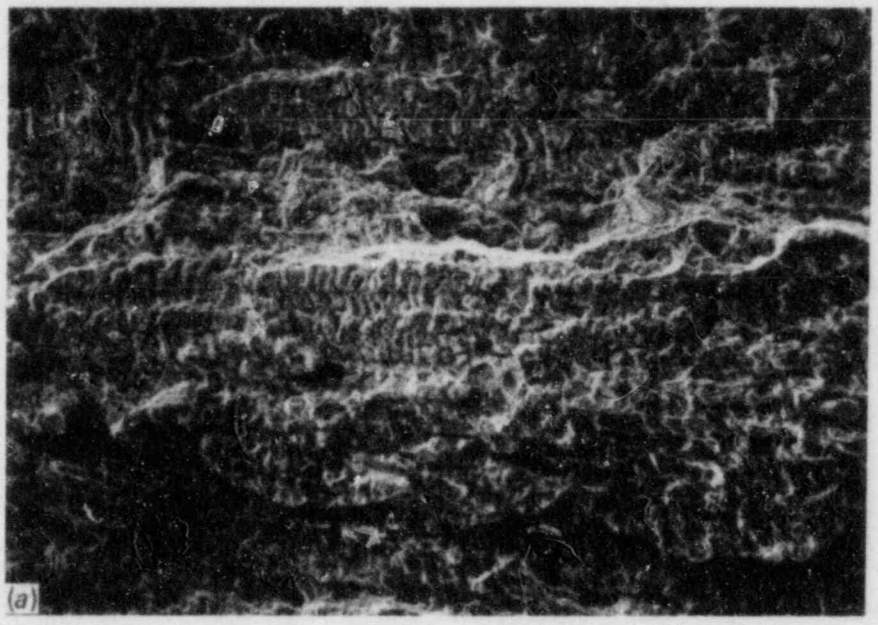

200 μm

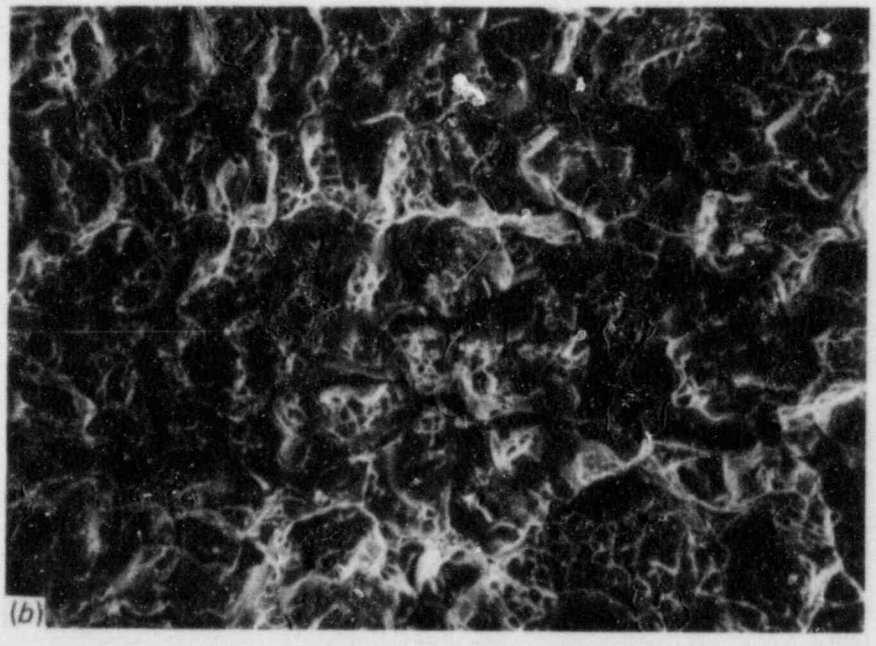

40 μm

Fig. 12. Detailed views of the type 308 stainless steel weld metal fracture surface of specimen CPL-516 (tested at −32°C) showing mixed-mode fracture.

800 μm

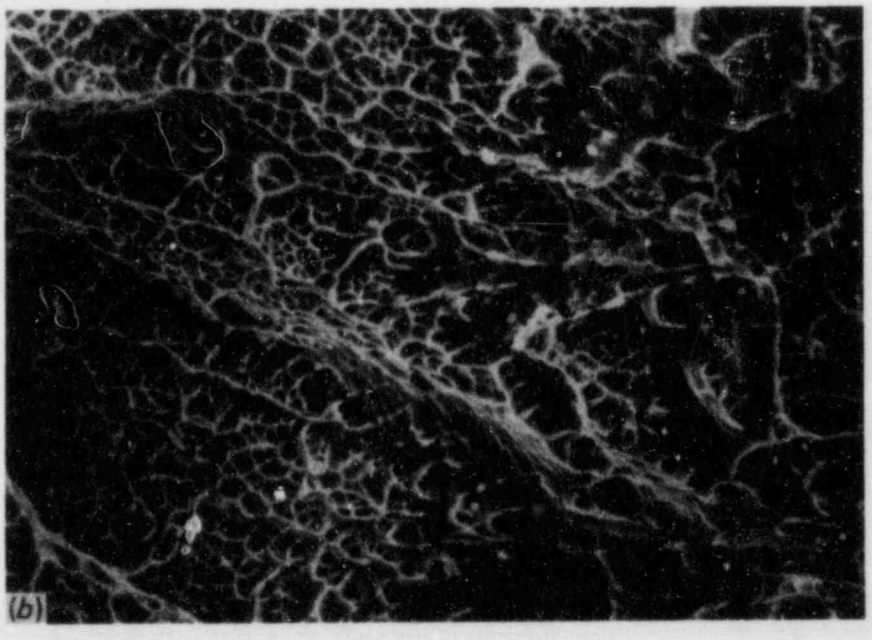

40 μm

Fig. 13. Scanning electron micrograph of the fracture surface of unirradiated nominally type 309 stainless steel Charpy specimen CPL-524 tested at 177°C on the upper shelf. (*a*) Low-magnification view of the notch, the type 309 weld layer, and the type 308 weld layer, each constituting roughly one-third of the micrograph from left to right. (*b*) Detail of the type 309 weld layer showing fibrous fracture.

The most appropriate criteria for separating the low-energy populations were arbitrarily chosen to be less than 70 and 80% type 308 weld metal for the unirradiated and irradiated data sets, respectively (Figs. 14 and 15), because these produced the most distinct difference between the data sets.

Table 3. Charpy impact energy of unirradiated nominally type 309 stainless steel cladding

Specimen	Test temperature (°C)	Impact energy (J)	Amount of type 308 weld metal[a] (%)
Low-energy population[b]			
CPL-516	−32	9.5	65
CPL-530	−30	12.7	65
CPL-534	10	33.4	60
CPL-514	20	28.5	65
CPL-545	50	36.2	60
CPL-542	66	34.6	55
CPL-517	93	67.1	60
CPL-524	177	80.3	60
CPL-522	260	72.3	40
High-energy population[c]			
CPL-519	−100	5.4	85
CPL-539	−73	6.9	75
CPL-520	−40	12.9	75
CPL-540	−30	11.5	75
CPL-529	−4	44.7	95
CPL-532	−4	54.2	95
CPL-547	−4	30.5	70
CPL-544	10	65.1	100
CPL-527	20	63.0	80
CPL-535	50	83.9	80
CPL-525	66	69.2	80
CPL-537	150	93.3	70
CPL-549	150	94.9	70

[a]As measured on the fracture surface.

[b]Less than 70% type 308 weld metal.

[c]At least 70% type 308 weld metal.

Table 4. Charpy impact energy of nominally type 309 stainless steel cladding irradiated to 2×10^{23} neutrons/m^2 (>1 MeV) at 288°C

Specimen	Test temperature (°C)	Impact energy (J)	Amount of type 308 weld metal[a] (%)
Low-energy population[b]			
CPL-515	0	10.8	60
CPL-543	40	17.0	75
CPL-541	65	25.1	65
CPL-548	85	15.6	40
CPL-521	100	25.1	60
CPL-523	150	40.7	65
CPL-518	250	42.7	70
CPL-528	288	36.6	75
High-energy population[c]			
CPL-533	−20	12.0	80
CPL-538	0	21.7	90
CPL-526	28	40.7	100
CPL-531	80	54.2	95
CPL-546	120	51.5	80
CPL-536	130	56.9	85

[a]As measured on the fracture surface.

[b]Less than 80% type 308 weld metal.

[c]At least 80% type 308 weld metal.

Once these populations within the type 309 data were established, the effect of irradiation was seen to be quite appreciable (Fig. 16). Both populations experienced large drops in upper-shelf energy of up to 50% and shifts in transition temperature of up to 100°C.

The extensive toughness degradation seen in the type 309 material as compared with very little in the type 308 is probably due to the higher fraction of ferritic phases in the type 309 resulting from the excessive base metal dilution and their intrinsically higher radiation sensitivity.

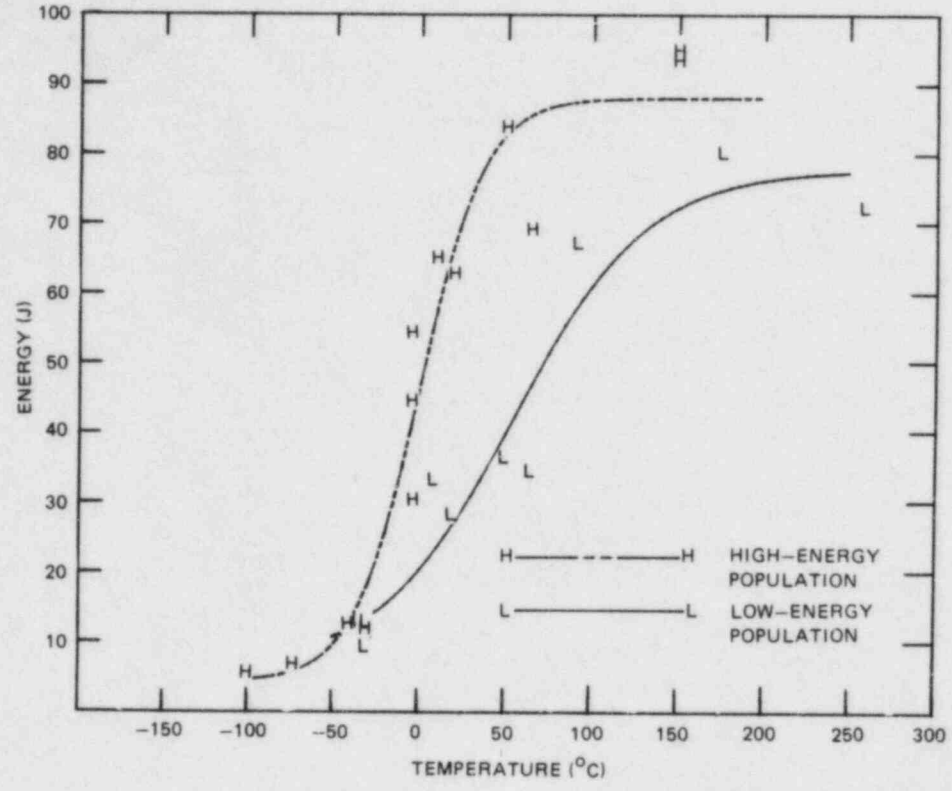

Fig. 14. Charpy impact energy of the unirradiated nominally type 309 stainless steel cladding divided into low- and high-energy populations based on the fraction of type 308 weld metal in the specimen ligament.

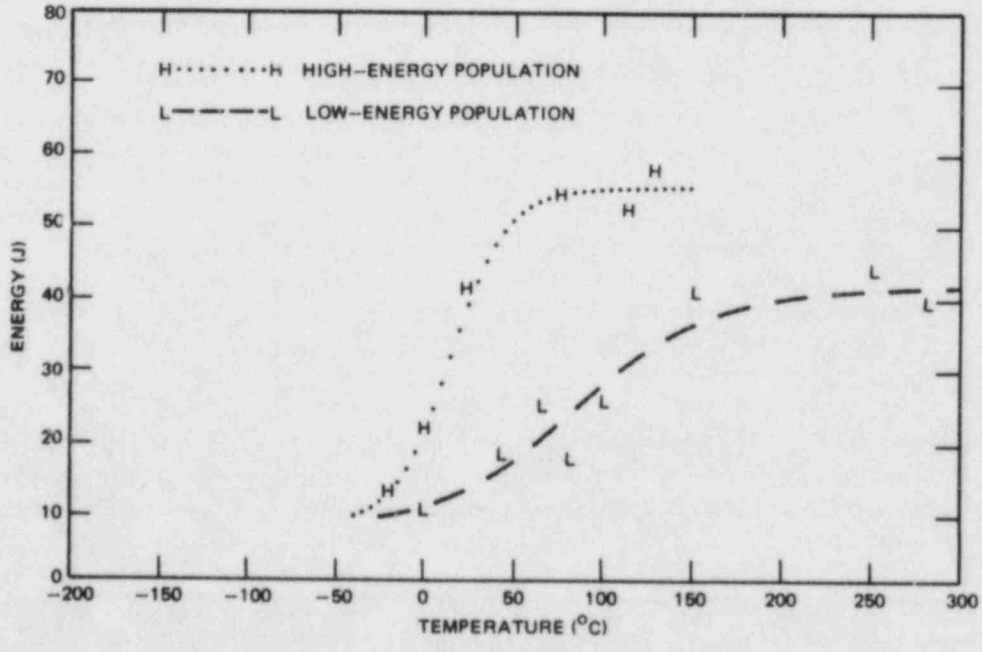

Fig. 15. Charpy impact energy of the irradiated nominally type 309 stainless steel cladding divided into low- and high-energy populations based on the fraction of type 308 weld metal in the specimen ligament.

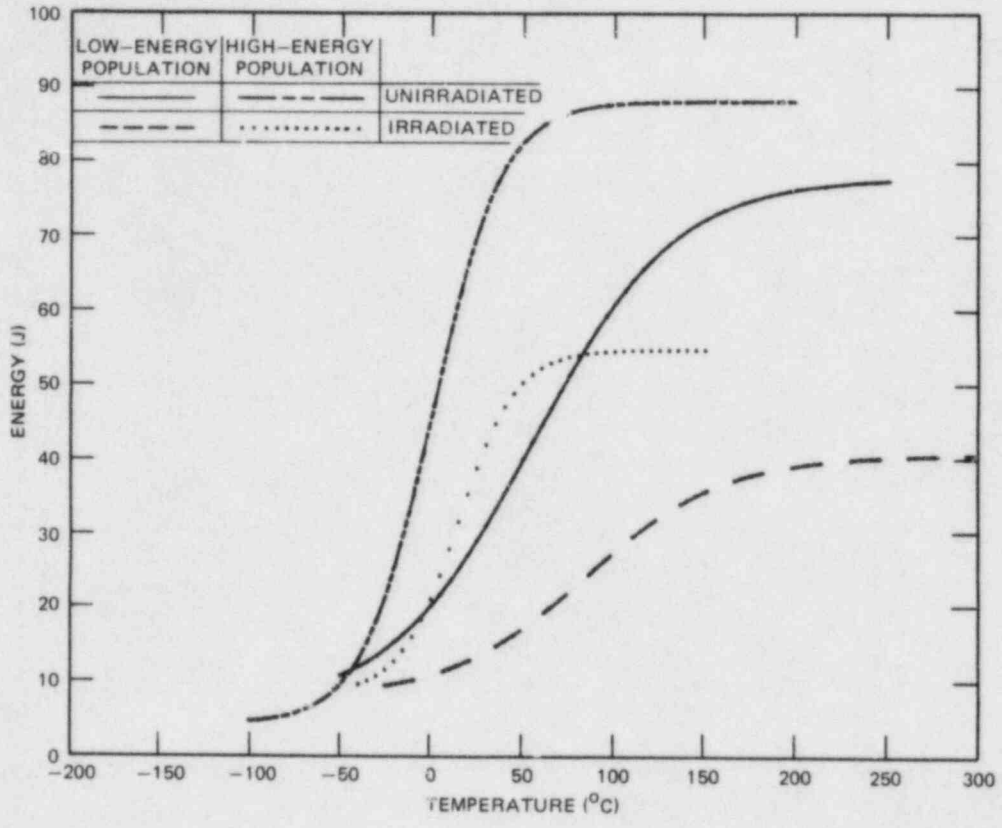

Fig. 16. Effect of irradiation on the Charpy impact energy of high- and low-energy populations of the specimens of nominal type 309 cladding.

CONCLUSIONS AND RECOMMENDATIONS FOR FURTHER WORK

On the basis of irradiation of one weldment of stainless steel overlay at a temperature and fluence similar to those at end of life for an LWR, very little degradation of the notch-impact toughness displayed by good quality cladding would be expected. In fact, both the tensile strength and the fracture ductility were improved slightly by irradiation. It must be stressed, however, that this is only a single case and that no conclusions, positive or negative, can be drawn regarding welding procedures or compositions leading to material appreciably different from that studied here.

It would be very valuable to repeat this type of experiment on cladding overlays produced by other methods similar to those used for existing cladding in LWR reactor pressure vessels (e.g., multiple wire or strip cladding).

Results from the highly diluted type 309 weld metal do show appreciable radiation-induced degradation of notch-impact toughness, even though both the tensile strength and the tensile fracture ductility were

improved slightly by irradiation. In the few known cases where welding has produced abnormal cladding with excessive dilution in operating reactors, the radiation effects on notch-impact toughness may be cause for concern.

ACKNOWLEDGMENTS

The authors gratefully acknowledge the personnel of Materials Engineering Associates, particularly J. R. Hawthorne, for capsule fabrication and irradiation. We also acknowledge T. N. Jones and H. Blevins for their experimental assistance, D. P. Edmonds for reviewing, J. L. Bishop for typing the rough draft, Sigfred Peterson for editing, and D. C. Sammons for preparing the final report. Lastly we would like to acknowledge the support of our technical monitor, Milton Vagins, and the U.S. Nuclear Regulatory Committee.

REFERENCES

1. W. R. Corwin, *Assessment of Radiation Effects Relating to Reactor Pressure Vessel Cladding*, NUREG/CR-3671, ORNL/6047, July 1984.

2. R. K. Nanstad et al., "Stainless Steel Cladding Investigations," pp. 109–29 in *Heavy-Section Steel Technology Program Quarterly Progress Report for Period April–June 1982*, NUREG/CR-2751, Vol. 2, ORNL/TM-8369/V2, December 1982.

3. G. C. Robinson et al., "Stainless Steel Cladding Investigations," pp. 133–38 in *Heavy-Section Steel Technology Program Quarterly Progress Report for Period October–December 1982*, NUREG/CR-2751, Vol. 4, ORNL/TM-8369/V4, May 1983.

4. W. R. Corwin et al., "Stainless Steel Cladding Investigations," pp. 143–56 in *Heavy-Section Steel Technology Program Quarterly Progress Report for Period January–March 1983*, NUREG/CR-3334, Vol. 1, ORNL/TM-8787/V1, September 1983.

5. R. J. Gray, "Magnetic Etching with Ferrofluid," pp. 155–77 in *Metallographic Specimen Preparation*, ed. J. L. McCall and W. M. Mueller, Plenum, New York, 1974.

6. A. Schaeffler, "A Constitution Diagram for Stainless Steel Weld Metal," *Met. Prog.* **56**(5), 680, 680B (1949).

7. E. B. Norris, D. R. Ireland, and C. E. Lautzenheiser, *The Second Inspection of the Elk River Pressure Vessel After Operation*, SWRI-122, Southwest Research Institute, San Antonio, Tex., July 21, 1967, pp. 9–13.

8. T. Kondo, H. Nakajima, and R. Nagasaki, "Metallographic Investigation of the Cladding Failure in the Pressure Vessel of a BWR," *Nucl. Eng. Design* **16**, 205–22 (1971).

9. D. T. Read et al., "Metallurgical Factors Affecting the Toughness of 316L SMA Weldments at Cryogenic Temperatures," *Weld. J.* (Miami) **59**(4), 104–13-s (1980).

10. F. W. Bennett and C. P. Dillon, "Impact Strength of Austenitic Stainless-Steel Welds at –320°F – Effects of Composition, Ferrite Content and Heat Treatment," *J. Basic Eng.* **88**(3), 33–36 (1966).

COMPOSITION INFLUENCES AND INTERACTIONS IN RADIATION SENSITIVITY OF REACTOR VESSEL STEELS

J. Russell Hawthorne

Materials Engineering Associates, Inc.
9700-B George Palmer Highway
Lanham, MD 20706-1837

1.0 INTRODUCTION

It has been established that synergisms can (and do) exist between steel alloying and copper impurities in radiation sensitivity development. A prime example is the modification, that is, enhancement, of the detrimental effect of copper on 288°C radiation resistance by nickel when nickel alloying is greater than ~ 0.4% Ni. This synergism, although long suspect, was confirmed only in 1982. Prior to this time, it was observed that low nickel, low copper steels offered very good radiation resistance and increasing a steel's nickel content to as much as 1% did not alter resistance capabilities. On the other hand, high copper steels as a group exhibited marked sensitivity to radiation-induced embrittlement. Sensitivity level was observed to be even higher when nickel content as well as copper content was high, especially in the case of weld deposits. Confirmation of the suspect synergism was provided by tests of steel plates produced from split laboratory melts (Ref. 1).

Two melts were made for the cited study. From one melt, a series of four high copper content plates depicting a range of nickel contents was obtained. The second melt provided materials with an intermediate copper content but with similar variations in nickel. Charpy-V specimens from each plate were irradiated at 288°C with the results shown in Fig. 1. As expected, the low copper materials exhibited a low radiation sensitivity; increasing the copper content from 0.05% (low) to 0.15% (intermediate) and finally to 0.25% (high) copper produced a progressive increase in radiation sensitivity as determined from the 41 J transition temperature elevation. More importantly, where the nickel content was high, the apparent sensitivity was greater in the intermediate and high copper steels than where the nickel content was low. Since the low copper steels consistently showed a low radiation sensitivity, independent of the nickel content, the aggregate results provide a clear confirmation of the copper-nickel synergism. Data for a shielded metal arc weld (0.05% Cu, 0.96% Ni) were included in Fig. 1 to emphasize the independence of low copper steel performance on % Ni.

Confirmation of the synergism was one reason for the NRC's recent draft revision of Regulatory Guide 1.99 on the "Effects of Residual Elements on Predicted Radiation Damage to Reactor Vessel Materials." The confirmation also raised a new issue of possible interactions between copper impurities and other alloying elements such as manganese, molybdenum and chromium. Furthermore, a possible interaction between alloying and phosphorus content became suspicious. MEA has undertaken studies to explore both possibilities for the NRC. Dual aims are to provide key information for making further refinements to Regulatory Guide 1.99 and for gaining a better understanding of certain power reactor surveillance data.

2.0 MATERIALS

A series of seven (4-way split) laboratory melts of steel were cast and processed to plates as a means of obtaining statistical combinations of specific impurity elements and/or alloying elements. The matrix focus is on binary and tertiary element combinations identified by data bank reviews as having a high probability of correlation with radiation sensitivity level. The primary base composition for melting was ASTM A 302-B or A 533-B. In general, the materials matrix reflects high/low limits of the steel specifications for alloying. Limits for A 508-2 forgings were also considered in setting alloying combinations and composition ranges. Table 1 lists the compositions of the 28 plates produced for the study.

Ingots were rolled to 15-mm gage plates. These, in turn, were heat-treated to microstructures typical of 150-mm or thicker plates at the quarter-thickness location. Other details of melt processing and a summary of preirradiation tensile strength for the plates are given in Reference 2.

2.1 Material Irradiation

The study bases relative radiation sensitivity on comparisons of notch ductility and tensile strength changes wrought by a fluence of $\sim 2.0 \times 10^{19}$ n/cm^2 (E > 1 MeV) at 288°C. Specimen irradiations are being performed in one in-core position of the 2MW pool reactor (UBR) located at the Nuclear Science and Technology Facility in Buffalo, NY. To date, three of the four irradiation experiments planned for the first phase investigation have been completed; completion of the fourth is expected by late 1984.

2.2 Experimental Findings

Data for melts 68 and 69 were presented to the 1983 NRC Water Reactor Safety Research Information Meeting. In brief, these results showed that phosphorus has an influence on radiation sensitivity at 288°C, but its contribution is dependent on the steel's copper content (Fig. 2). The detrimental influence of phosphorus on sensitvity is most pronounced when the copper content is low. While the effect of phosphorus had been isolated earlier through a study of a phosphorus-doped laboratory melt of A 302-B steel (Ref. 3), more recent computer

analyses of existing data banks found no clear correlation between phosphorus content and sensitivity level. The present results provide the explanation. Information supplied to the computer, by-in-large, consisted of results for low phosphorus, low copper steels and welds and high phosphorus, high copper steels. As a result, the proper "mix" needed to reveal the inverse dependence shown by the laboratory results was absent.

The current draft revision of Regulatory Guide 1.99 omits all reference to phosphorus content in its method for projecting radiation sensitivity. The new (improved, low copper) steels, on the other hand, can be expected to be influenced quite heavily by phosphorus content. Therefore, for new steels, phosphorus content should not be ignored when projecting radiation sensitivity in service. Fortunately, data are available which suggest that the level of the phosphorus contribution is not dependent on nickel content as well (Fig. 3).

During the current year (1984), MEA expanded the base of information with the development of postirradiation comparisons for 16 other composition variations (that is, plates from melts 69, 70, 71, 72). Results are summarized in Figs. 4 and 5.

Referring to Fig. 4, the one group of plates having phosphorus contents in the range of 0.016 to 0.018% P showed a small sensitizing influence by a 0.021% tin content, compared to a 0.004% tin content. Not shown in this figure, the effect of this impurity element was much more evident in the upper shelf reduction by irradiation. The addition of 0.035% arsenic to the melt, on the other hand, produced no change in apparent radiation resistance. Likewise, the addition of 0.50% chromium did not change radiation resistance level in the one case tested. Current interest in the influence of chromium content on radiation performance stems from prior comparisons of A 508-2 vs. A 533-B embrittlement susceptibility. The former on balance shows a lower radiation sensitivity than A 533-B which could be a reflection of their difference in alloying (chromium content) or metal working history (forging vs. rolling). A further test of chromium effects will be acquired from the melt 66 series now being irradiated. To complete the evaluation of tin and arsenic, a study with low phosphorus materials and with low copper materials is considered essential in view of the inverse dependence of the phosphorus effect on copper level.

Figure 5 reports findings on the effects of high-low manganese contents and the effects of high-low molybdenum contents on radiation sensitivity for steels having a 0.18% copper content or a 0.33% copper content. For the lower of the two copper contents, a beneficial effect to radiation resistance from a high manganese content and, separately, from a high molybdenum content is observed. As shown in Fig. 6, however, the higher molybdenum content also raised the initial (preirradiation) Charpy-V 41 J temperature index. This, in turn, negates the beneficial effect of molybdenum on radiation resistance if the plates are compared on the basis of final (as-irradiated) 41 J temperature. For the higher copper content materials, Fig. 5

tentatively suggest an adverse effect on radiation resistance by a high manganese content. No effect on radiation sensitivity is apparent for the molybdenum content variation in these materials. In the manganese test series, preirradiation data for one of the plates show relatively large scatter; potential causes are being evaluated.

3.0 DISCUSSION

The most recent determinations reinforce previous evidence that important composition interactions exist in radiation sensitivity development. These most probably are responsible for a large portion of the unexplained scatter found in individual irradiation effects data banks. In the current series, it is recognized that some portion of material-to-material differences could be related to microstructure differences. With low temperature irradiation (< 150°C), tests have demonstrated that radiation sensitivity is closely related to microstructure as well as composition (Refs. 3 and 4). Microstructure examinations are underway to aid the overall assessment of the present materials before and after irradiation. As reported earlier, strength differences among the plates in the preirradiation condition were minimal.

Material composition is also expected to be a factor in postirradiation annealing recovery. Figures 7 and 8 present Charpy-V data for two submerged-arc welds made with Linde 80 flux. Although their copper and nickel contents were essentially the same and their neutron exposures were well matched, a large difference in notch ductility recovery by 399°C-168 hr annealing is indicaced. On the one hand (Fig. 7), recovery was 75°C (135°F) or 69% of the initial shift of 108°C (195°F). In contrast, the second weld (Fig. 8) exhibited only 44°C (80°F) recovery or 37% of the initial shift of 199°C (215°F). The dissimilarity is quite large and, if we are to apply the annealing method with good confidence of the result, reasons for the difference must be identified.

MEA has initiated a study of composition effects on annealing, using materials initially acquired for the radiation sensitivity study (Table 1). Focus of first efforts is on the role of copper, nickel and phosphorus in recovery by 400°C annealing. Specific materials in the exploratory program are identified in Table 2. Phase 1 results are expected in early 1985.

4.0 CONCLUSIONS

Primary observations from the latest evaluations of the laboratory-melted plates were:

1. A change in arsenic content from < 0.01% to 0.035% did not alter the radiation resistance of the melt; however, a change in tin content from 0.004% to 0.024% did decrease radiation resistance at 288°C and was most apparent in upper shelf energy reduction.

2. A change in chromium content from 0.003% to 0.50% did not modify the radiation resistance of the melt.

3. A beneficial effect on radiation resistance of a 0.18% copper content melt was achieved with an increase in molybdenum content from 0.37% to 0.66% and, separately, with an increase in manganese content from 0.88% to 1.63%.

4. A detrimental effect to radiation resistance was found with an increase in manganese content from 0.88% to 1.63% when the copper content was 0.33%; however, no change in resistance was found with an increase in molybdenum content from 0.37% to 0.66%.

5. Improvements to radiation resistance through increased steel alloying can be negated by changes to preirradiation notch ductility properties in some cases.

REFERENCES

1. J. R. Hawthorne, "Significance of Nickel and Copper Content to Radiation Sensitivity and Postirradiation Heat Treatment Recovery of Reactor Vessel Steels," Effects of Radiation on Materials: Eleventh Conference, ASTM STP 782, H. R. Brager and J. S. Perrin, eds., American Society for Testing and Materials. 1982, pp. 375-391.

2. F. J. Loss, ed., "Structural Integrity of Water Reactor Pressure Boundary Components — Annual Report for 1983," USNRC Report NUREG/CR-3228, Vol. , Sept. 1984.

3. U. Potapovs and J. R. Hawthorne, "Effects of Residual Elements on 550°F Irradiation Response of Selected Pressure Vessel Steels and Weldments," Nuclear Applications, Vol. 6(1), Jan. 1969, pp. 27-46.

4. J. R. Hawthorne and L. E. Steele, "Initial Evaluations of Metallurgical Variables as Possible Factors Controlling the Radiation Sensitivity of Structural Steels," NRL Report 6420, Naval Research Laboratory, Sept. 29, 1966.

Table 1 Chemical Compositions of Plates from Laboratory (4-Way Split) Melts of Steel (A 302-B or A 522-B Base Composition)

Melt No.	Plate/ Cast No.	Chemical Composition (Weight-%)												
		C	Mn	P	S	Si	Cu	Ni	Cr	Mo	As	Sn	N	B
1	66A	0.24	1.30	0.018	0.018	0.21	0.16	< 0.002	< 0.003	0.52	-----	< 0.004	0.010	0.0005
	66B						0.16		0.25					
	66C						0.32		0.25					
	66D						0.32		0.52					
2	67A	0.23	1.31	0.003	0.018	0.20	0.002	0.70	< 0.003	0.51	-----	< 0.004	0.009	0.0004
	67B			0.015								< 0.004		
	67C			0.025								< 0.004		
	67D			0.025								0.024		
3	68A	0.23	1.31	0.003	0.017	0.22	0.30	0.70	< 0.003	0.52	-----	0.004	0.010	0.0006
	68B			0.016								0.004		
	68C			0.028								0.004		
	68D			0.028								0.023		
4	69A	0.23	1.23	0.016	0.018	0.24	0.19	0.30	< 0.003	0.53	< 0.010	< 0.004	0.010	0.0005
	69B							0.30			< 0.010	0.021		
	69C							0.70			0.010	0.021		
	69D							0.70			0.033	0.021		
5	70A	0.23	0.88	0.004	0.018	0.22	0.18	0.005	< 0.003	0.37	-----	< 0.004	0.008	0.0005
	70B						0.18			0.66				
	70C						0.33			0.66				
	70D		1.62				0.33			0.66				
6	71A	0.24	0.87	0.003	0.019	0.21	0.18	< 0.002	< 0.003	0.36	-----	< 0.004	0.009	0.0006
	71B		1.63				0.18			0.36				
	71C		1.63				0.32			0.36				
	71D		1.63				0.32			0.67				
7	72A	0.23	1.31	0.020	0.019	0.21	0.33	0.25	< 0.003	0.52	< 0.010	< 0.004	0.009	0.0004
	72B							0.71	< 0.003		< 0.010			
	72C							0.71	0.50		< 0.010			
	72D							0.71	0.50		0.035			

Table 2 Materials Selected for Initial Studies of Composition Effects on Annealing Recovery*

Experiment Number	Material Code	Composition Intercomparisons
1	67B	Low Cu, High Ni, ΔP
	67C	
	68A	High Cu, High Ni, ΔP
	68B	ΔCu, High Ni, High/Low P
	68C	
2	5C	Medium Cu, Low P, ΔNi
	5D	
	6A	High Cu, Low P, ΔNi
	6B	ΔCu, High/Low Ni, Low P
	6C	

* 400°C-168 hr heat treatment

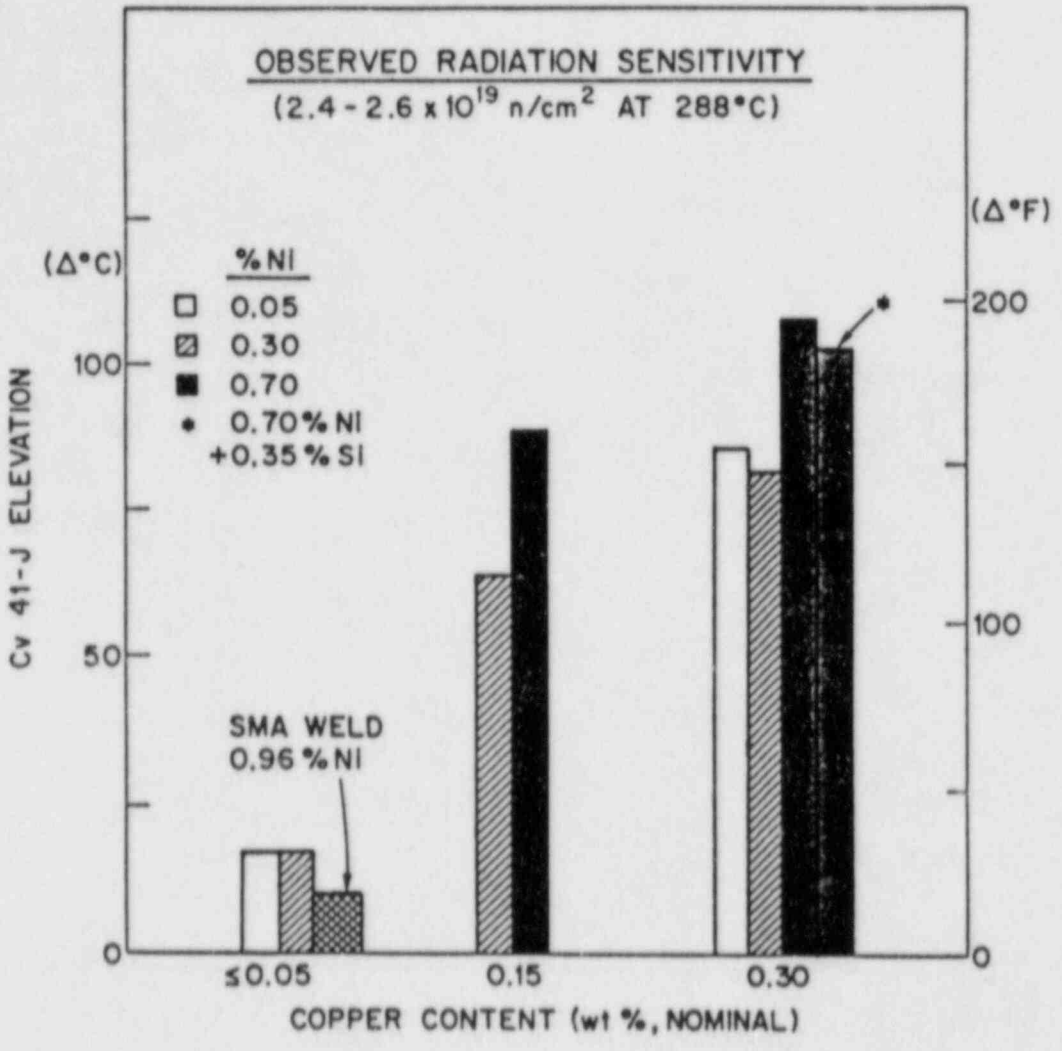

Fig. 1 C. 41 J transition temperature increases observed for plates from two split melts of steel (A 302-B or A 533-B). Results for a high fluence (~ 6.6 x 10^{19}) test of high nickel, low copper weld are also shown.

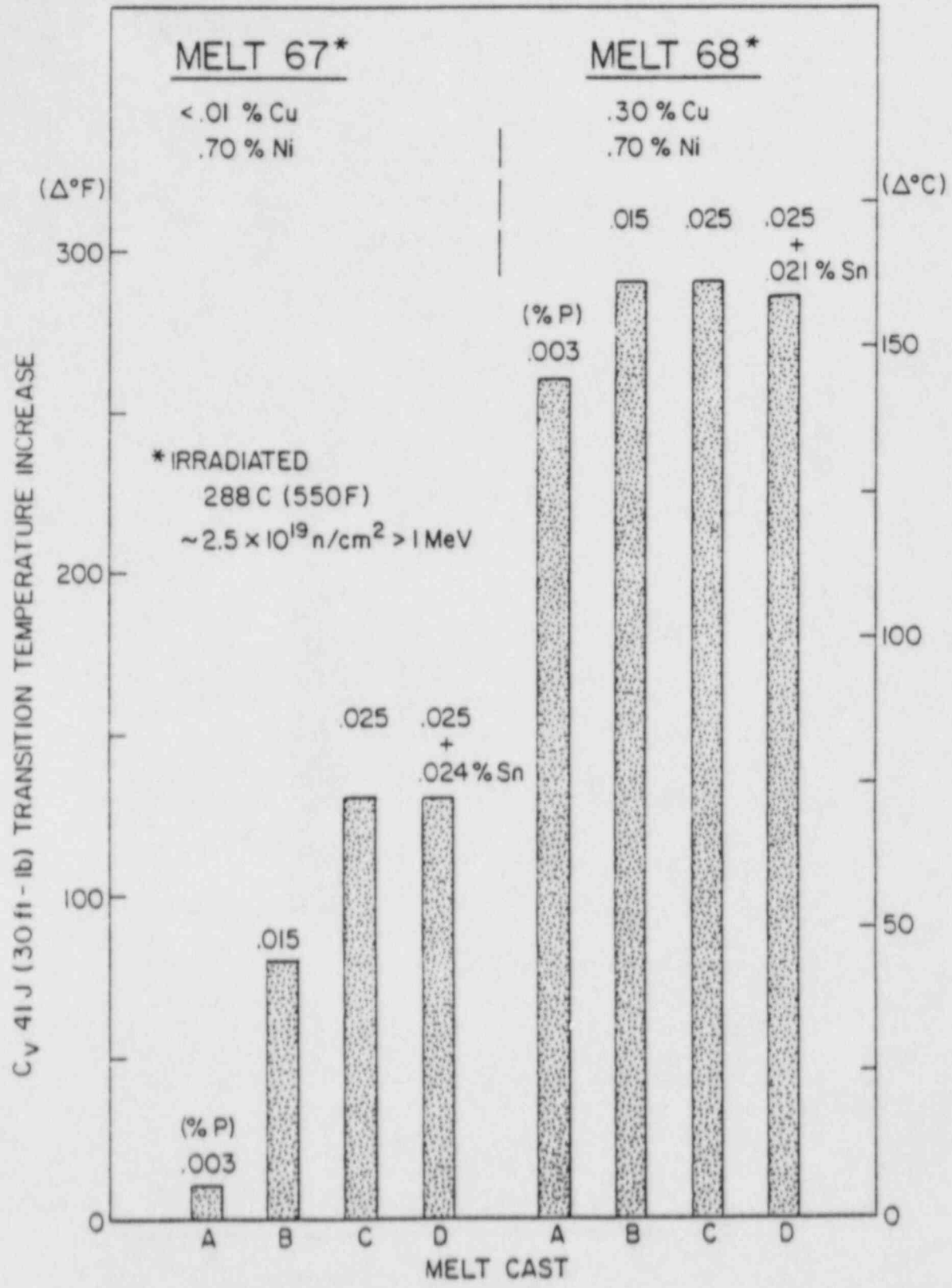

Fig. 2 C_v 41 J transition temperature increases observed for plates from melts 67 and 68 showing the dependence of the phosphorus influence on radiation sensitivity on copper content.

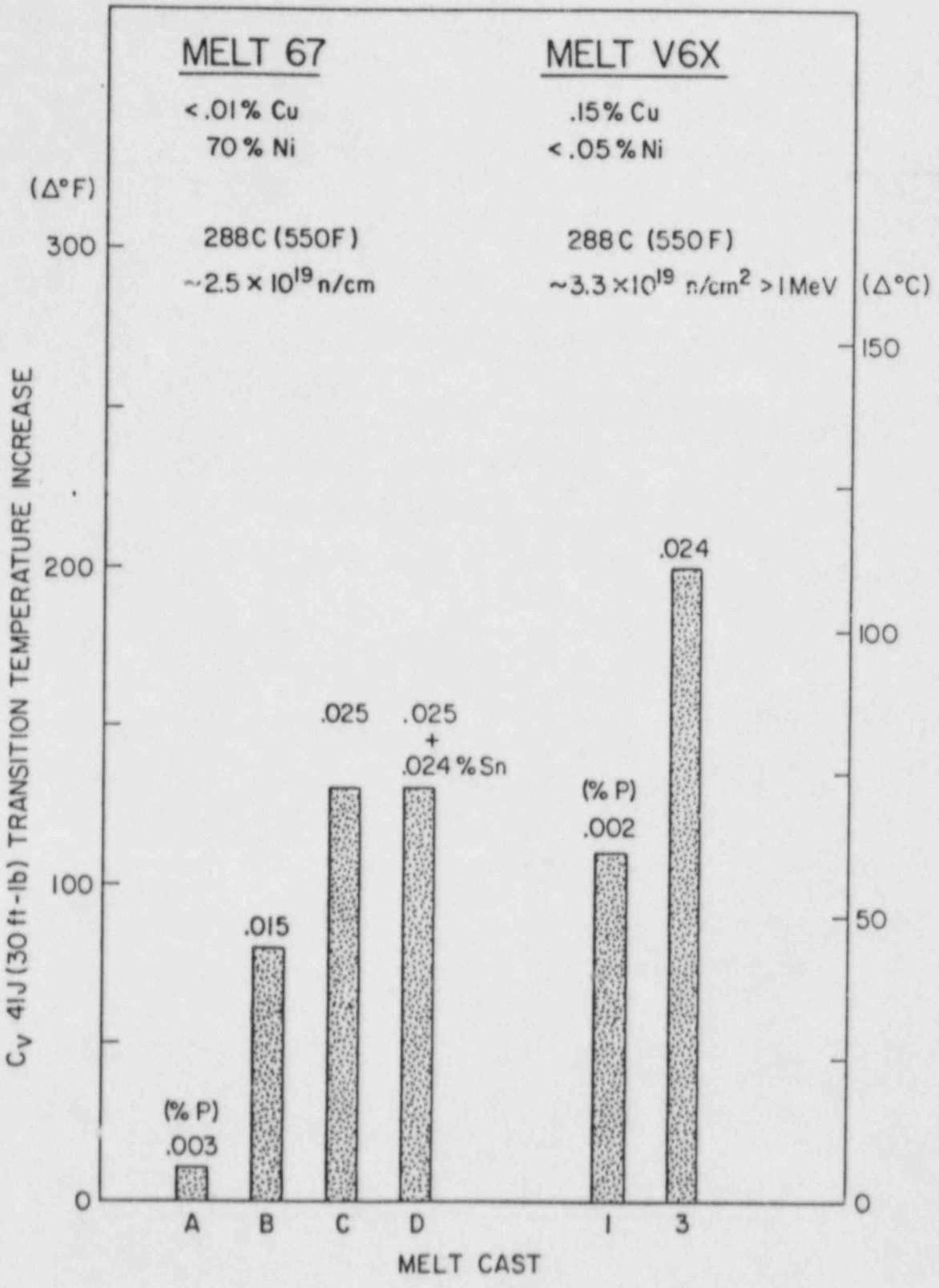

Fig. 3 C_v 41 J transition temperature increases observed for plates from melts 67 (A 533-B steel) and plates from melt V6X (A 302-B steel).

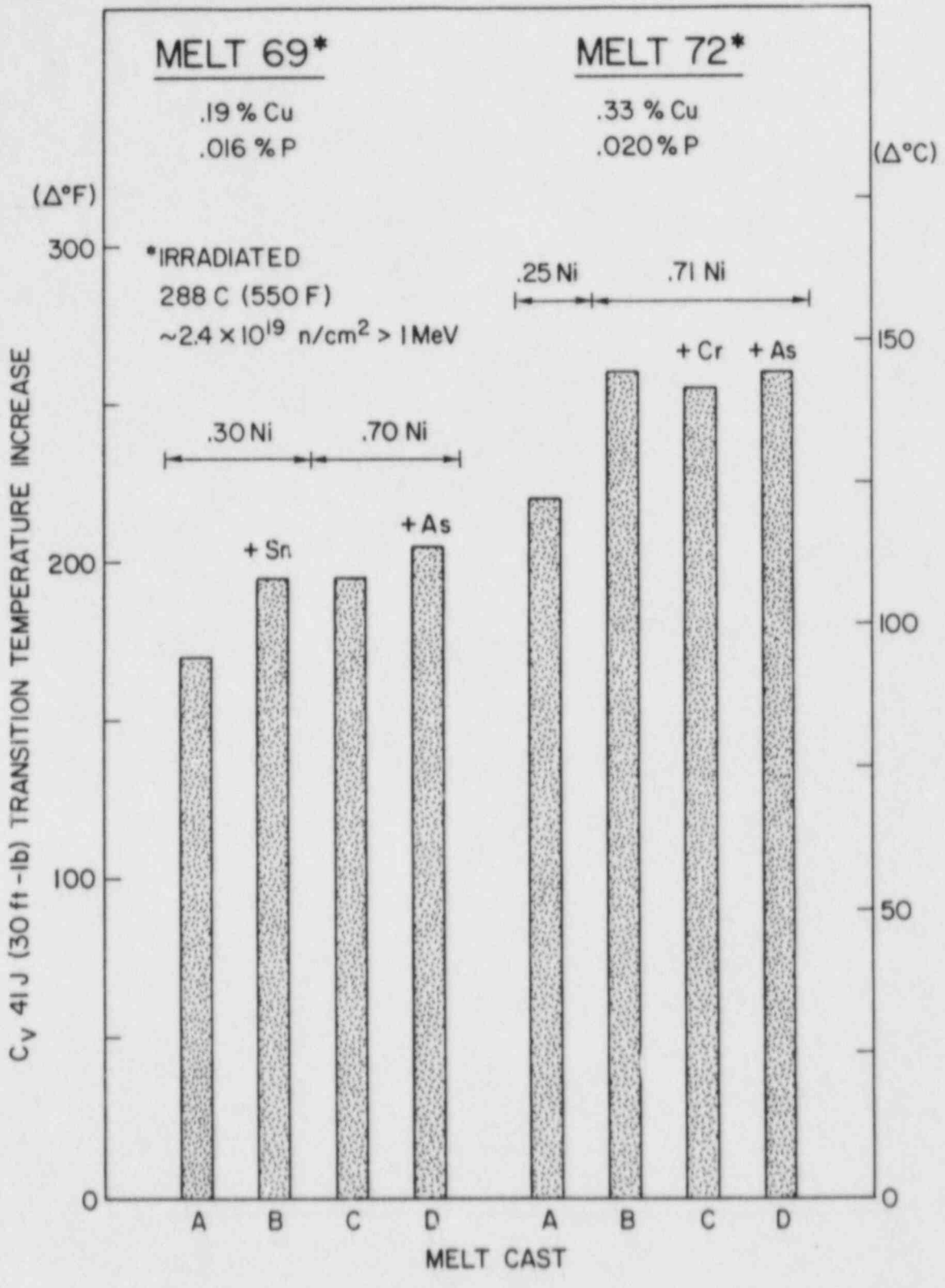

Fig. 4 C_v 41 J transition temperature increases observed for plates from melts 69 and 72.

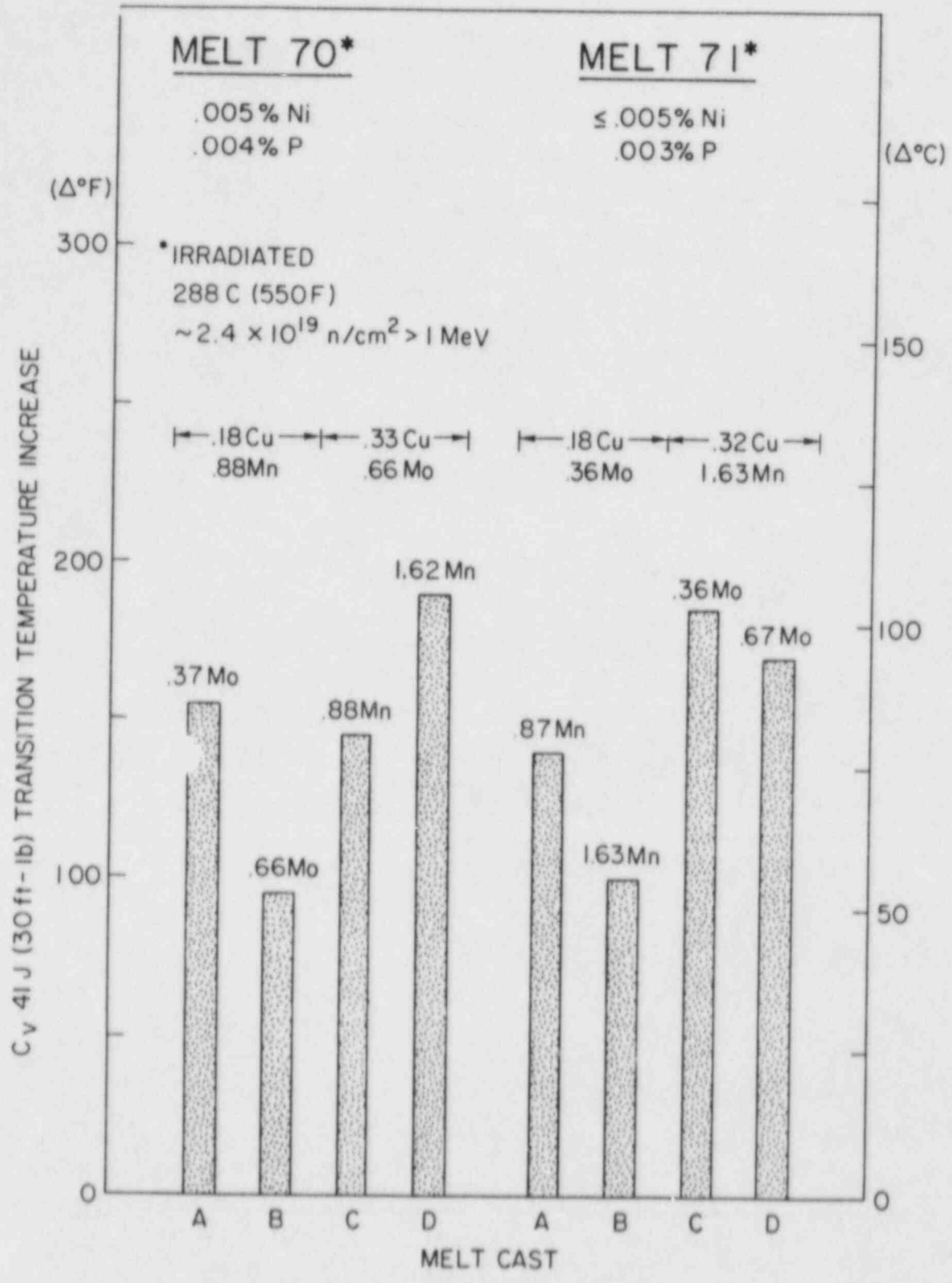

Fig. 5 C_v 41 J transition temperature increases observed for plates from melts 70 and 71.

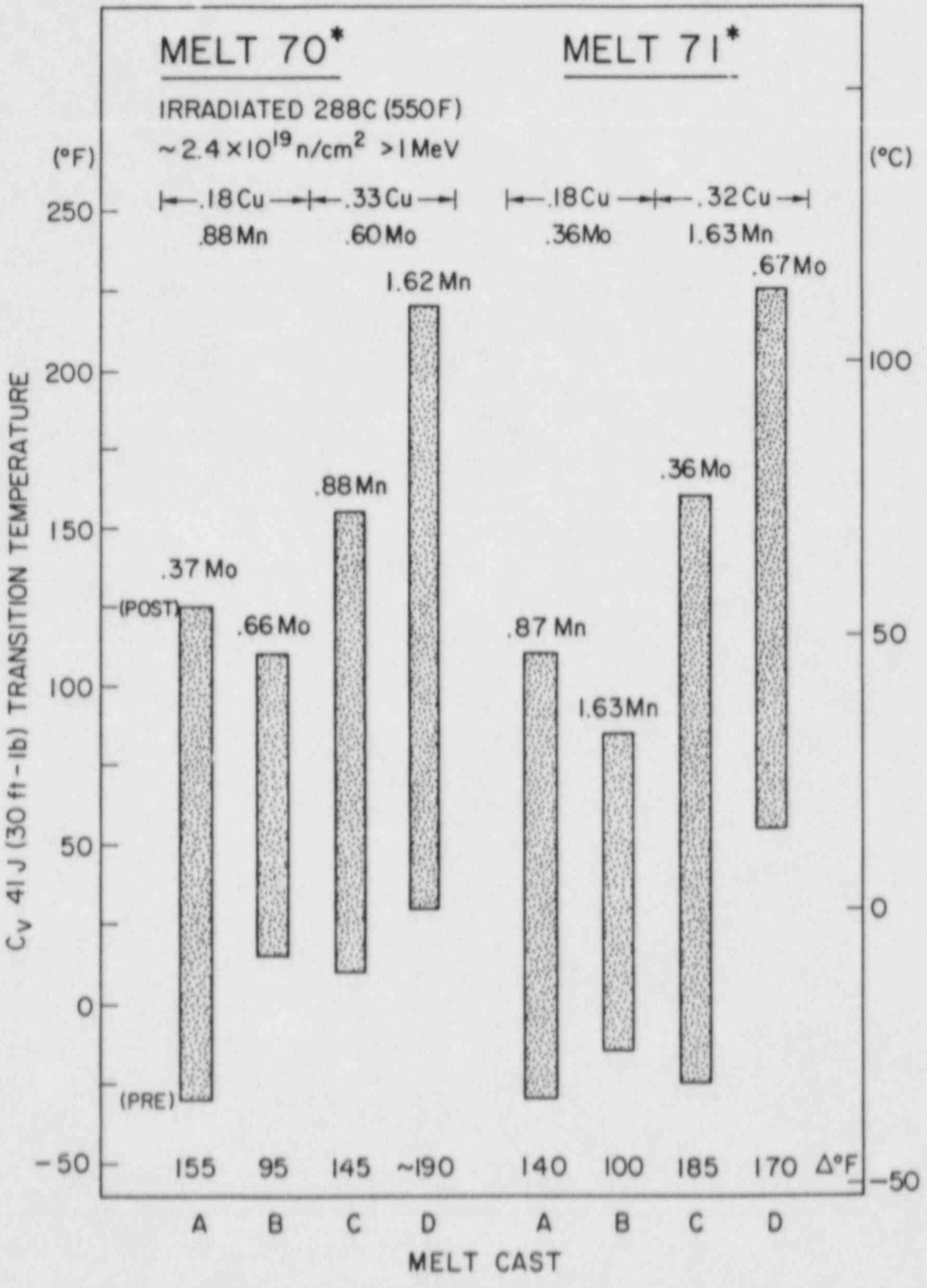

Fig. 6 Absolute C_v 41 J transition temperature of plates from melts 70 and 71 before and after irradiation.

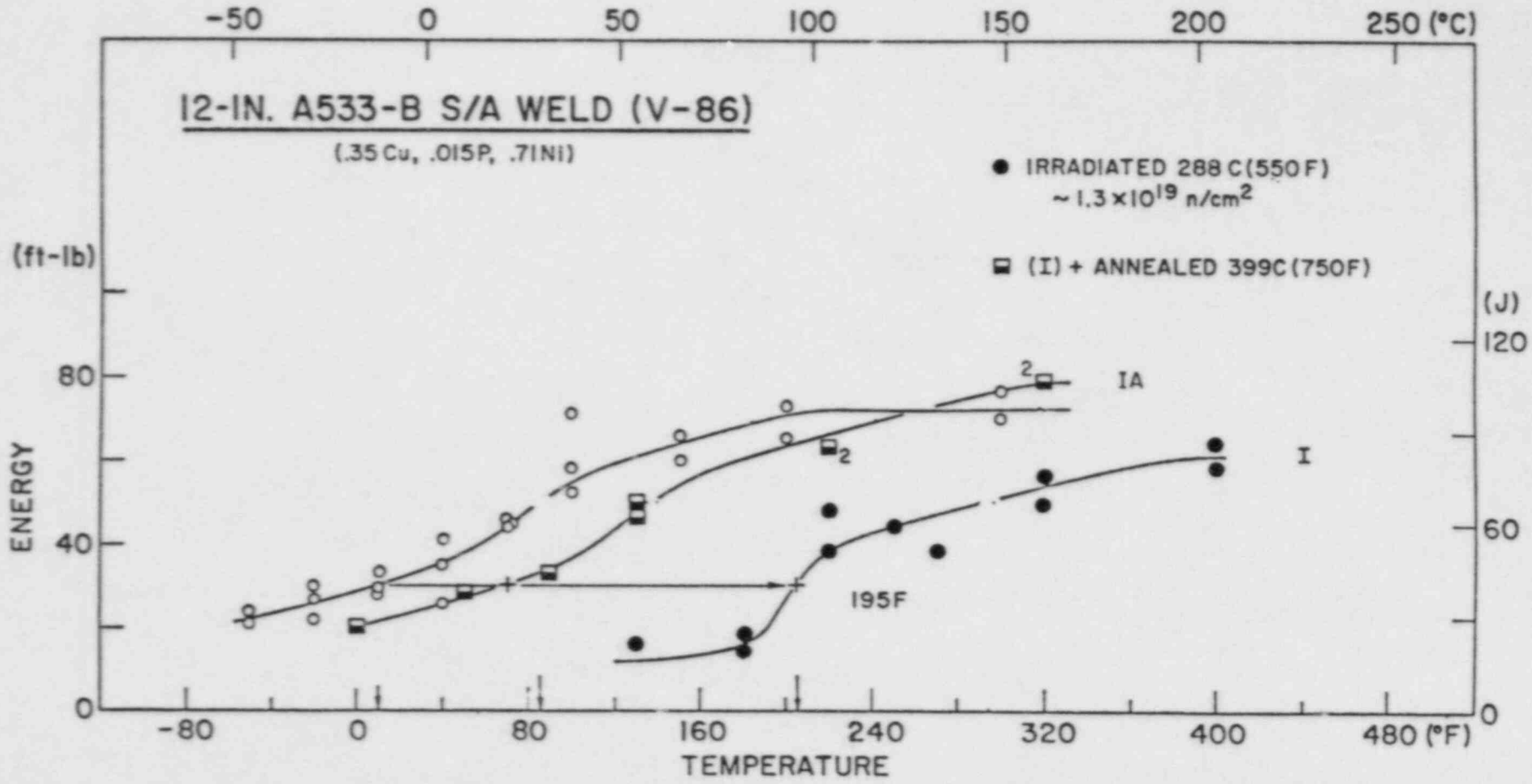

Fig. 7 C_v notch ductility of the commercially-produced, submerged-arc weld, code V-86, before and after 288°C irradiation and after 399°C annealing. The welding flux was Linde 80.

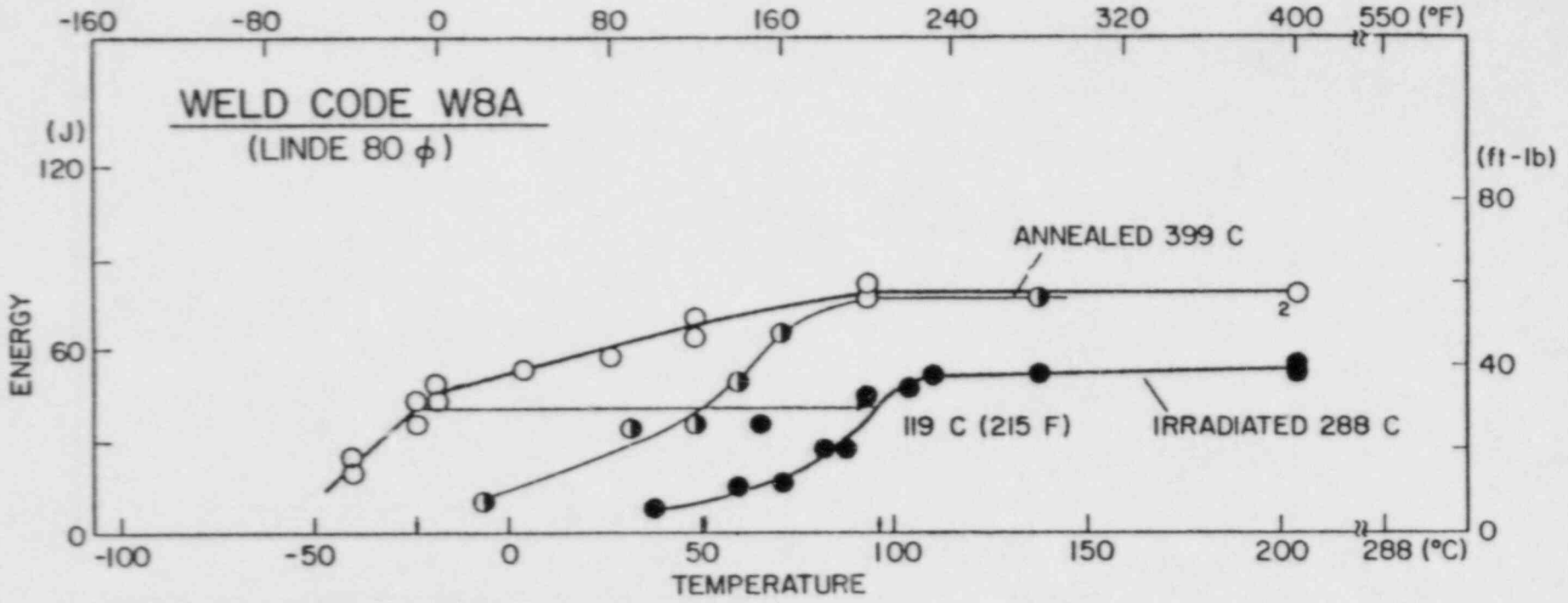

Fig. 8 C_v notch ductility of the commercially-produced, submerged-arc weld, code W8A, before and after 288°C irradiation and after 399°C annealing. The average copper, phosphorus and nickel contents of the weld were 0.38% Cu, 0.010% P and 0.59% Ni.

FATIGUE CRACK GROWTH RATES OF LOW-CARBON AND STAINLESS PIPING STEELS IN PWR ENVIRONMENT

William H. Cullen

Materials Engineering Associates, Inc.
9700-B George Palmer Highway
Lanham, MD 20706

1.0 INTRODUCTION, OBJECTIVE AND SCOPE

Research on the fatigue crack growth characteristics of pressure vessel and piping steels in pressurized, high-temperature, simulated reactor coolants is an important aspect of reactor safety assurance studies. Over the course of the 1970's, most of this work was focused on studies of pressure vessel steels -- A 533, A 508, and compatible welds and heat-affected zone specimens. As a result of that research, many important effects of critical variables have been identified. Among these are the effects of waveform and frequency, temperature steel composition, orientation, and water chemistry, especially dissolved oxygen content (Refs. 1-4). Many of these effects are not in accord with well-known trends, due to these same variables acting on structural steels in a marine environment, or pipeline steels in subterranean water (Refs. 5-9). Several recent reviews have focused on the fatigue crack growth of nuclear reactor pressure vessel steels in their applicative environments, and research is continuing on many yet unexplained phenomenon (Refs. 10-11).

However, as the collection of data on pressure vessel steels increases, and the upper bounds of these data sets become better defined, some research interest has shifted to the piping steel question. The objective of this study was to measure fatigue crack growth rates (FCGR) on low-carbon and stainless steels in a simulated pressurized water reactor environment. The results described below are from an ongoing scoping study, and describe effects of load ratio, temperature and orientation on FCGR results. The scope of this effort was confined to testing on SA 351-CF8A cast stainless steel, A 106 Gr. C and A 516 Gr. 70 carbon steels. In each case, only particular variables were selected for the test matrix. This series of tests was not intended to be an exhaustive matrix to cover both materials and critical variables. The steels selected are in wide use, and this compilation of data provides an index of the fatigue crack growth behavior of these steels relative to the more-investigated pressure vessel steels.

2.0 SPECIMENS AND FACILITIES DESCRIPTION

2.1 Specimens and Materials

The parent material for this study came in three different forms. The A 106 Gr. C came as rings which were 0.81-m (O.D) x 0.2-m long and 83-mm thick (32 in. x 8 in. x 3-1/4 in.). There were two shipments of A 106 received and used in this program. Specimens with serial codes FOP-57 through FOP-62 were from Lot #1; specimens FOP-63 through FOP-94 were from Lot #2. The A 516 Gr. 70 came as a plate which was 0.4 m x 0.9 m x 0.15 m (16 in. x 36 in. 6 in.). The A 351-CF8A was a segment from a research pressure vessel which was 0.8 m (32 in.) in diameter and 57-mm (2-1/4-in.) thick.

Compact specimens and the two-pin, wedge-opening load (CT and WOL) specimens were used throughout this research. Specimens were 25.4-mm or 50.8-mm (1-in. or 2-in.) thick (1T- or 2T-) with machined notches to a normalized depth (crack length to width, or a/W) of 0.25 to 0.35. In all cases, the specimens were precracked in air by at least 1.2 mm (for 1T specimens) or 2.5 mm (for 2T specimens) at a low ΔK with respect to the initial ΔK of the actual test. The material chemistries are given below in Table 1.

Table 1 Chemical Composition of the Low-Carbon Piping Steels Examined in this Study

Element	C	S	Si	Mo	Ni	Mn	Cr	V	P
A 106 Gr. C Code FOP									
Lot #1	0.25	0.017	0.22	0.033	0.25	0.88	0.10	0.003	0.016
Lot #2	0.25	0.016	0.18	0.049	0.26	0.92	0.22	0.003	0.018
A 516 Gr. 70 Code FOK	0.25	0.017	0.23	0.065	0.27	1.05	0.10	0.002	0.018
A 351-CF8A Code A9	0.06	0.018	1.17	-----	8.58	0.68	20.42	-----	0.020

2.2 Test Facilities

All tests were conducted under load-controlled, constant amplitude cycling. Specimens were tested in ovens, for air tests, or in environmental chambers which contain the simulated reactor coolant environments under the required temperature and pressure conditions. Both single specimen tests and multiple-specimen, daisy chain tests were utilized in these studies.

Air tests were conducted in resistance-heated convection ovens with a control thermocouple mounted in the wall of the oven and monitoring thermocouples spot-welded to the specimen itself. In the case of the water environment tests at 93°C, a 6-liter capacity, stainless steel vessel, equipped with an internal LVDT, and a dedicated water circulation loop was employed.

In the case of tests at higher temperatures, autoclaves capable of containing pressurized water were used. Two such autoclave systems were utilized in this study. The smaller of the two contained four liters of water; the larger was a three-chamber, multispecimen system with each autoclave accomodating four specimens and holding about 150 liters of water. The small autoclave is capable of 55-kN loads and the larger autoclaves are capable of 550-kN (10-kips and 100-kips, respectively); an LVDT was attached to each specimen.

Table 2 Water Chemistry Specifications

Boron (as boric acid)	1000 ppm
Lithium (as lithium hydroxide)	1 ppm
Chloride ions	< 0.15 ppm
Fluoride ions	< 0.10 ppm
Dissolved oxygen	~ 1 ppb
Dissolved hydrogen (saturation)	30 to 50 cm^3/kg water

All other metallic or ionic species should be at about trace levels. Some iron, both in solid and soluble form is the inevitable result of a corroding specimen.

3.0 RESULTS AND DISCUSSION

3.1 Low-Carbon Steels -- A 106 Gr. C and A 516 Gr. 70

3.1.1 Frequency and Load Ratio Effects

Data sets which describe effects of frequency, load ratio, orientation, and temperature are included below. In order to establish a baseline against which to compare the aqueous environment test results, 288°C air tests, using a load ratio (R) of 0.2, were conducted on specimens of each of these steels. Those results are shown in Figs. 1a and 1b. In subsequent figures, these essentially linear results are represented by a line which referenced the best fit through the air environment data. Figure 2 shows data for A 106 in a water environment at 288°C, for a 17-mHz sinusoidal waveform and load ratios of 0.2 and 0.7. Here the separation due to load ratio is clearly evident, but in the case of the data for FOP-61, there is a noticable bending over of the data set at the highest growth rates, indicating that the rapid increase in growth rates with ΔK cannot be sustained.

Similar results for A 516 are shown in Figs. 3 and 4. Figure 3 shows data for a 1-Hz test frequency for two orientations of the crack plane, together with 288°C trend line for air results on the same steel. These results demonstrate that there can be a significant environmental effect even at the relatively high test frequency of 1 Hz. Figure 4 contains data from 2T specimens for both 1-Hz and 17-mHz test frequencies, and load ratios of 0.2, 0.7 and 0.85, the last for a test frequency of 50 mHz. There is a general layering of the data sets as a function of load ratio. The 1-Hz and 17-mHz data sets for the R = 0.2 test (specimen FOK-16) blend together quite smoothly, and although the 17-mHz portion started out at slightly lower growth rates than the 1-Hz portion, higher growth rates for the lower test frequency were quickly attained and a maximum in environmental assistance was reached in the midrange of applied ΔK, at about 28 MPa$\sqrt{m}$. Growth rate trends then bend over and slow appreciably. There is a greater degree of variability evident in the results for R = 0.7. The growth rates at 17 mHz for specimens FOK-11 and FOK-13 show a difference of a factor of about 10, which is likely due to a difference in material properties, such as microstructure, since the test practice and environments were essentially the same, although the tests were not conducted at exactly the same time. It is important to note that specimens FOK-11 and FOK-13 are of the same orientation, and in fact were cut from neighboring locations at the same elevation from the parent plate. These common denominators suggest that such variability and the consequent differences in growth rates are difficult characteristics to predict.

The results of the load ratio aspects of this part of the study are quite clear in that higher load ratios produced higher growth rates for equivalent ΔK values, with a trend toward bending over at the higher growth rates. The results of the frequency study are less clear in that for load ratios of 0.7, test frequencies of 1 Hz often produced higher growth rates than test frequencies of 17 mHz.

3.1.2 Temperature Effects in A 106 Gr. C

A study of the effects of temperature on growth rates in A 106 yielded the data sets shown in Figs. 5 through 7, and the trend line plot in Fig. 8. The 93°C data in Fig. 5 were acquired on 1T-CT specimens in a single-specimen test device, while data sets at the higher temperatures were collected from 2T-CT specimens. It is clear from these figures that the growth rates are lowest at the highest temperature, which is typical of primary circuit hot leg operating temperatures.

In an earlier report on temperature effects in A 508-2 pressure vessel steel (Ref. 12). the author showed that a minimum in growth rates was developed at a temperature of about 200°C (~ 390°F). By plotting these results in a similar way, as a function of inverse temperature, the degree of this effect can be seen in Fig. 9. The dotted line shows the previously published trend for A 508-2. The piping steel trend lines indicate that the magnitude of the trend is somewhat similar to that for the pressure vessel steel, but displaced to a higher temperature. The increase in growth rates, if any, would occur at unattainable combinations of pressure and temperature, and do not

bear on any realistic operating transient scenarios. While data sets for two orientations of the crack plane are shown in each of the above figures, there is no discernible dependence of the crack growth rates on this orientation difference.

3.2 Load Ratio and Temperature Effects in SA 351-CF8A Cast Stainless Steel

Tests were carried out on specimens of cast stainless steel to evaluate the response of fatigue crack growth rates to a range of load ratios and temperatures. The complete results of the investigation of temperature dependence are contained in an earlier report (Ref. 13); the results below are a only summary. Figure 10 shows crack growth rate results for load ratios of 0.2 and 0.7. The growth rates for the 0.7 case show the customary increase as compared, on a ΔK basis with the growth rates for the 0.2 cases. However, they show about the same slope, or dependence on ΔK, as do the 0.2 results in high-temperature water. The air test was conducted using a 1T-CT specimen, hence the abbreviated ΔK range as compared with the aqueous environment tests, all carried out with 2T-CT specimens, which support a higher maximum applied ΔK. Many of the appropriate figures also include a trend line which represents a large volume of data for air environment tests, mostly taken from references by James (Refs. 14-15).

Figures 11 to 13 show fatigue crack growth rates for two orientations of the cast stainless specimens at temperatures of 232°C, 288°C and 338°C (450°F, 550°F and 650°F), all at a load ratio of 0.2. On Fig. 12, the data for the highest temperature, trend lines for the 232°C and 288°C data are also shown. It is easily seen that the growth rates at 338°C are considerably higher than growth rates at the other two temperatures. It is interesting to note the roughly sigmoidal shape of the growth rate curves at the temperatures of 232°C and 288°C, indicating that there is a higher proportion of environmental assistance at the lower range of ΔK than at the higher range.

4.0 SUMMARY AND CONCLUSIONS

This section is divided into summary and conclusion sets for the carbon steels, and for the stainless steels.

4.1 Carbon Piping Steels, A 106 Gr. C and A 516 Gr. 70

Fatigue crack growth rate tests in PWR environments have been carried out for these steels under a variety of test frequency, temperature and load ratio conditions. Many combinations of these critical variables produced significant components of environmental assistance. The microstructure of these steels, particularly the manganese sulfide inclusions, played a major role in the progress of the fatigue crack. The increase in growth rates as a function of ΔK with an increase in load ratio is in line with the increase observed in pressure vessel steels. The temperature dependence of crack growth rates in A 106 is different in form from that of A 508-2 pressure vessel steel, but covers basically the same extremes.

The conclusions are as follows:

(1) Crack growth rates in these steels are of the same order of magnitude, and exhibit the same basic dependence on the known critical variables as those of pressure vessel steels.

(2) The frequency dependence of crack growth rates seems to be tied to the load ratio, with 1-Hz test frequencies often resulting in higher growth rates than 17 mHz at the higher load ratios.

(3) The manganese sulfide inclusions play a major role in the crack plane morphology and in the crack growth rates. In a study with a limited sampling of steels such as this one, it is impossible to predict an upper limit which might occur because of a detrimentally high concentration of sulfide inclusions; but rather high growth rates are possible.

(4) Many features of the fractography (described in Ref. 16) of the A 516 specimens suggest that the crack growth rates are affected by a hydrogen-assistance mechanism.

4.2 Cast Stainless Steel, A 351-CF8A

Crack growth rates in the stainless steels lie within the same range as the carbon steels described above, but the dependencies on the critical variables are somewhat different. Crack growth rates at 1 Hz show usually less environmental assistance than at 17 mHz, for load ratios of both 0.2 and 0.7, although the data base at 0.7 suffers from its content of only two tests. The temperature dependence of crack growth rates shows that rates increase as the temperature increases. The fatigue fracture surface morphology shows brittle-like features cover nearly all of the fracture surface, and that the crack progress is not influenced by the delta-ferrite phase.

The conclusions are as follows:

(1) The amount of environmental assistance provided to the fatigue crack growth rates may be directly proportional to the test frequency, and is basically independent of the load ratio. Growth rates at 232°C and 288°C showed relatively little environmental component.

(2) The temperature dependence of crack growth rates shows a modest increase in growth rates with increase in temperature, for load ratios of 0.2.

(3) Fractographic features (described in Ref. 13) show that regions of ductility can abut regions of highly brittle-like fatigue striation formation, suggesting that crack growth rates do not depend directly on the mechanics of crack tip deformation. Overall, brittle-like features cover nearly all of the fatigue fracture surface.

5.0 FUTURE RESEARCH NEEDS

This study, together with some of the references cited in the text, represents the beginning of the accumulation of a data base for fatigue crack growth rates for piping steels in LWR environments. Through these studies, some of the influence of a few key critical variables is beginning to be understood. Some of the areas which should be covered in future research projects are as follows:

For the carbon steels:

(1) The frequency dependence of fatigue crack growth rates, and its interaction with load ratio, needs to be clarified. There are indications that high test frequencies, together with high load ratios, such as 10 Hz at R = 0.9, may provide high growth rates on a da/dN basis. Such a test is feasible from a laboratory test time and equipment standpoint.

(2) The influence of sulfide inclusions on crack growth rates needs to be studied in great depth, from either the macro- or micro-approach. That is to say, "worst-case" steels should be tested to determine the maximum increase in growth rates which might occur. Also, it would be interesting and potentially helpful to understand better the crack tip micromechanism through which the environment in the crack tip enclave is affected by the dissolving MnS inclusions, and the way in which the inclusions promote, if they do, increases in hydrogen-assisted crack growth.

For the cast stainless steels:

(1) Research is needed to define growth rates at the higher load ratios which are more typical of piping steels. The combination of high load ratios and high temperatures (typical of hot leg conditions) should be investigated.

(2) Since the fractographic features are essentially the same for fatigue crack growth and stress-corrosion cracking tests, the time dependence of crack growth rates should be determined. This can be accomplished by carrying out tests at lower test frequencies, together with a choice of other suitable critical variables, such as high load ratio and high temperature. These tests are feasible, but somewhat difficult from a laboratory point-of-view.

REFERENCES

1. W. H. Cullen, "Effects of Loading Rate, Waveform and Temperature on Fatigue Crack Growth Rates of RPV Steels," Aspects of Fracture Mechanics in Pressure Vessels and Piping, S. S. Palusamy and S. G. Sampath, eds., PVP-58, Amer. Soc. Mech. Engineers, New York, NY, 1982, pp. 303-312.

2. P. M. Scott, and A. E. Truswell, "Corrosion Fatigue Crack Growth in Reactor Pressure Vessel Steels in PWR Primary Water," Paper PVP-82-029, Proc. of ASME Pressure Vessels and Piping Conference, Orlando, FL, June 1982, Journal of Pressure Vessel Technology, Vol. 105(3), 1983, p. 245.

3. W. H. Bamford, "Environmental Cracking of Pressure Boundary Materials, and the Importance of Metallurgical Considerations" in Aspects of Fracture Mechanics in Pressure Vessels and Piping, S. S. Palusamy and S. G. Sampeth, eds., PVP-58, Amer. Soc. Mech. Engineers, New York, NY, 1982, pp. 209-228.

4. P. M. Scott, A. E. Truswell and S. G. Druce, "Corrosion Fatigue of Pressure Vessel Steels in PWR Environments — Influence of Steel Sulfur Content," Corrosion, Vol. 40(7), 1984, pp. 350-357.

5. J. M. Barsom, "Effect of Cyclic Stress Form on Corrosion Fatigue Crack Propagation Below K_{Iscc} in a High Yield Strength Steel," Corrosion Fatigue: Chemistry, Mechanics and Microstructures, NACE-2, O. Devereux, A. J. McEvily and R. W. Staehle, eds., National Association of Corrosion Engineers, 1972, pp. 424-433.

6. O. Vosikovsky, "Effects of Mechanical and Environmental Variables on Fatigue Crack Growth Rates in Steel — A Summary of Work Done at CANMET," Canadian Metallurgical Quarterly, Vol. 19, 1980, pp. 87-97.

7. R. J. Selines and R. M. Pelloux, "Effect of Cyclic Stress Wave Form on Corrosion Fatigue Crack Propagation in Al-Zn-Mg Alloys," Metallurgical Transactions, Vol. 3, 1972, pp. 2525-2531.

8. D. B. Dawson and R. M. Pelloux, "Corrosion Fatigue Crack Growth in Titanium Alloys in Aqueous Environments," Metallurgical Transactions, Vol. 5, 1974, pp. 723-731.

9. O. Vosikovsky, W. R. Neill, D. A. Carlyle and A. Rivard, "The Effect of Sea Water Temperature on Corrosion Fatigue Crack Growth in Structural Steels," CANMET Physical Metallurgy Research Laboratories Report ERP/PMRL 83-27 (OP-J), Ottawa, Canada, April 1983.

10. W. H. Cullen and K. Torronen, "A Review of Fatigue Crack Growth of Pressure Vessel and Piping Steels in High-Temperature, Pressurized, Reactor-Grade Water," USNRC Report NUREG/CR-1576, NRL Memorandum Report 4298, Sept. 1980.

11. W. H. Cullen and F. J. Loss, "Interpretation of USA Results on Corrosion Fatigue of RPV Steels in Typical PWR Environments," Structural Integrity of Light Water Reactor Components, Applied Science Publishers, 1982, pp. 275-286.

12. W. H. Cullen, K. Torronen and M. Kemppainen, "Effects of Temperature on Fatigue Crack Growth of A 508-2 Steels in LWR Environment," USNRC Report NUREG/CR-3230, April 1983.

13. W. H. Cullen, et al., "The Temperature Dependence of Fatigue Crack Growth Rates of A 351-CF8A Cast Stainless Steel in LWR Environment," USNRC Report NUREG/CR-3546, April 1984.

14. L. A. James, "Fatigue Crack Propagation in Austenitic Stainless Steels," Atomic Energy Review, Vol. 14(1), 1976, pp. 37-86.

15. L. A. James, "Fatigue-Crack Propagation in a Cast Stainless Steel," Nuclear Technology, Vol. 26(1), 1975, pp. 46-53.

16. W. H. Cullen, "Fatigue Crack Growth Rates of Low-Carbon and Stainless Piping Steels in PWR Environment," USNRC Report NUREG/CR-3945, MEA-2055, Nov. 1984.

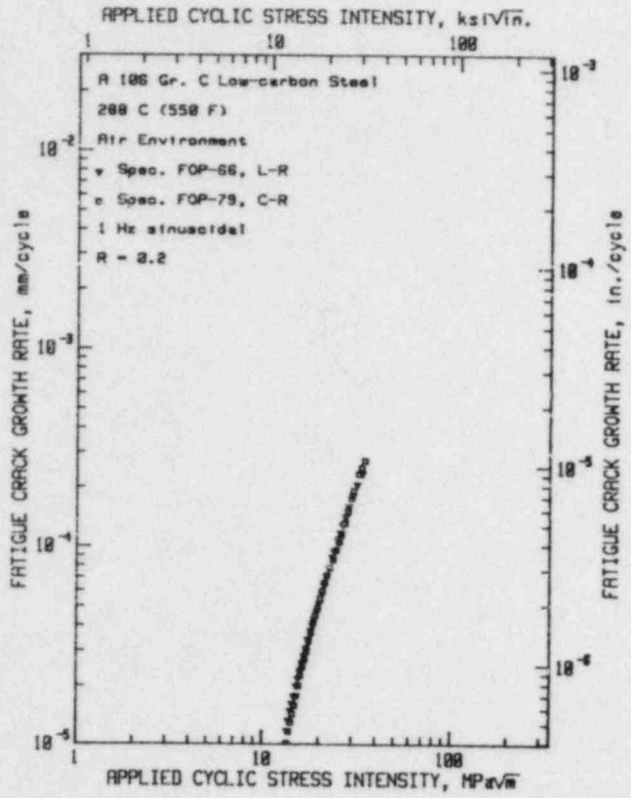

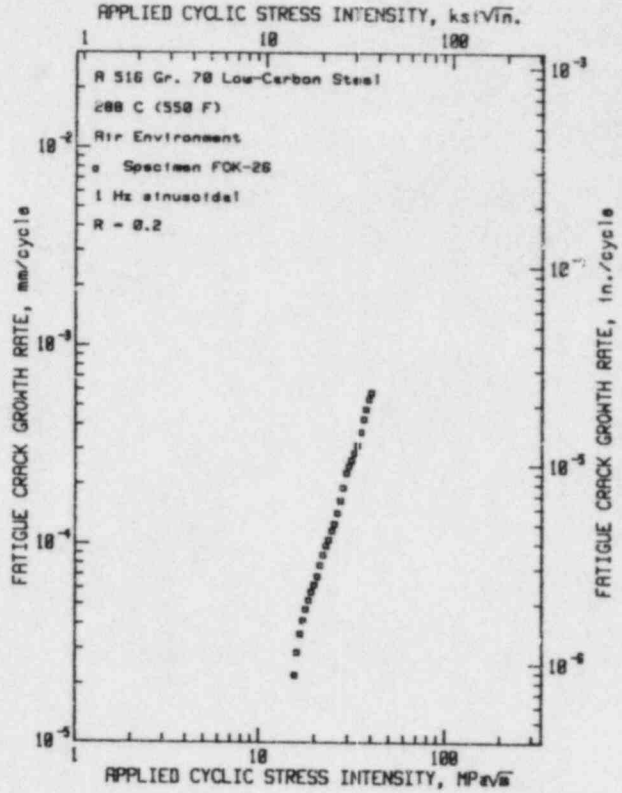

Figure 1 Fatigue crack growth rates vs. applied cyclic ΔK for A 106 Gr. C and A 516 Gr. 70 steels for 288°C (550°F) air environment, and a test frequency of 1 Hz at a load ratio of 0.2. In companion figures later in this report, these data sets are illustrated by the best linear fit.

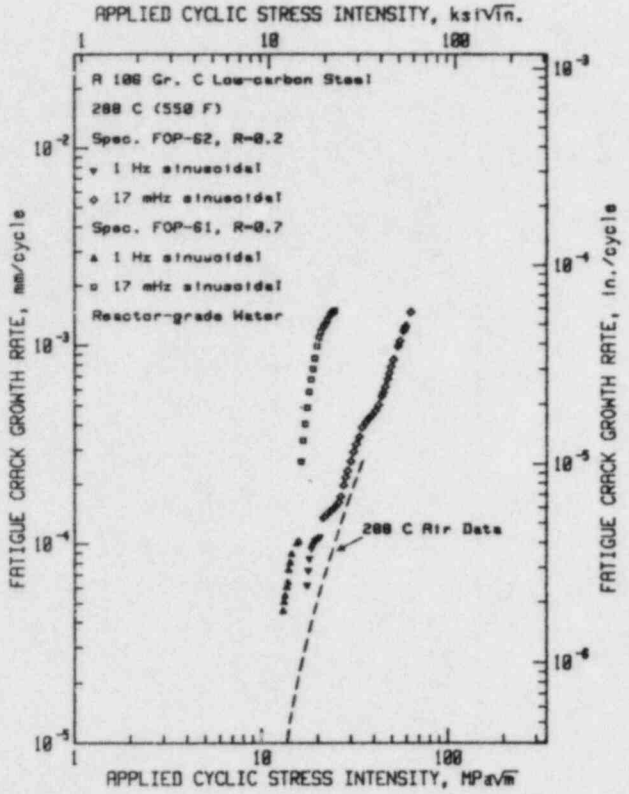

Figure 2 Fatigue crack growth rates vs. applied cyclic ΔK for A 106 Gr. C steel in 288°C PWR environment, for a test frequency of 1 Hz, and load ratios of 0.2 and 0.7.

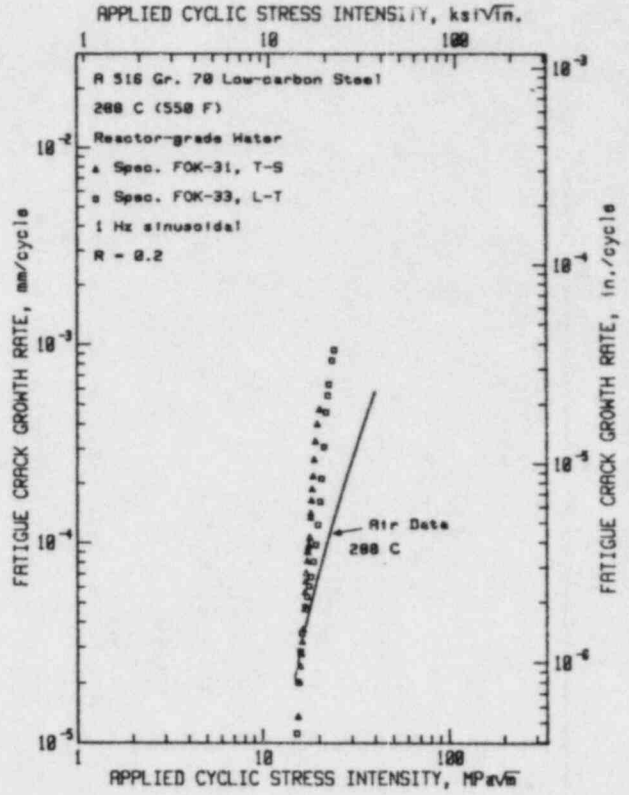

Figure 3 Fatigue crack growth rates vs. applied cyclic ΔK for A 516 Gr. 70 steel in PWR environment for a test frequency of 1 Hz and a load ratio of 0.2. There is little apparent orientation dependence for these data sets, but comparison with the air data shows a considerable environmental component.

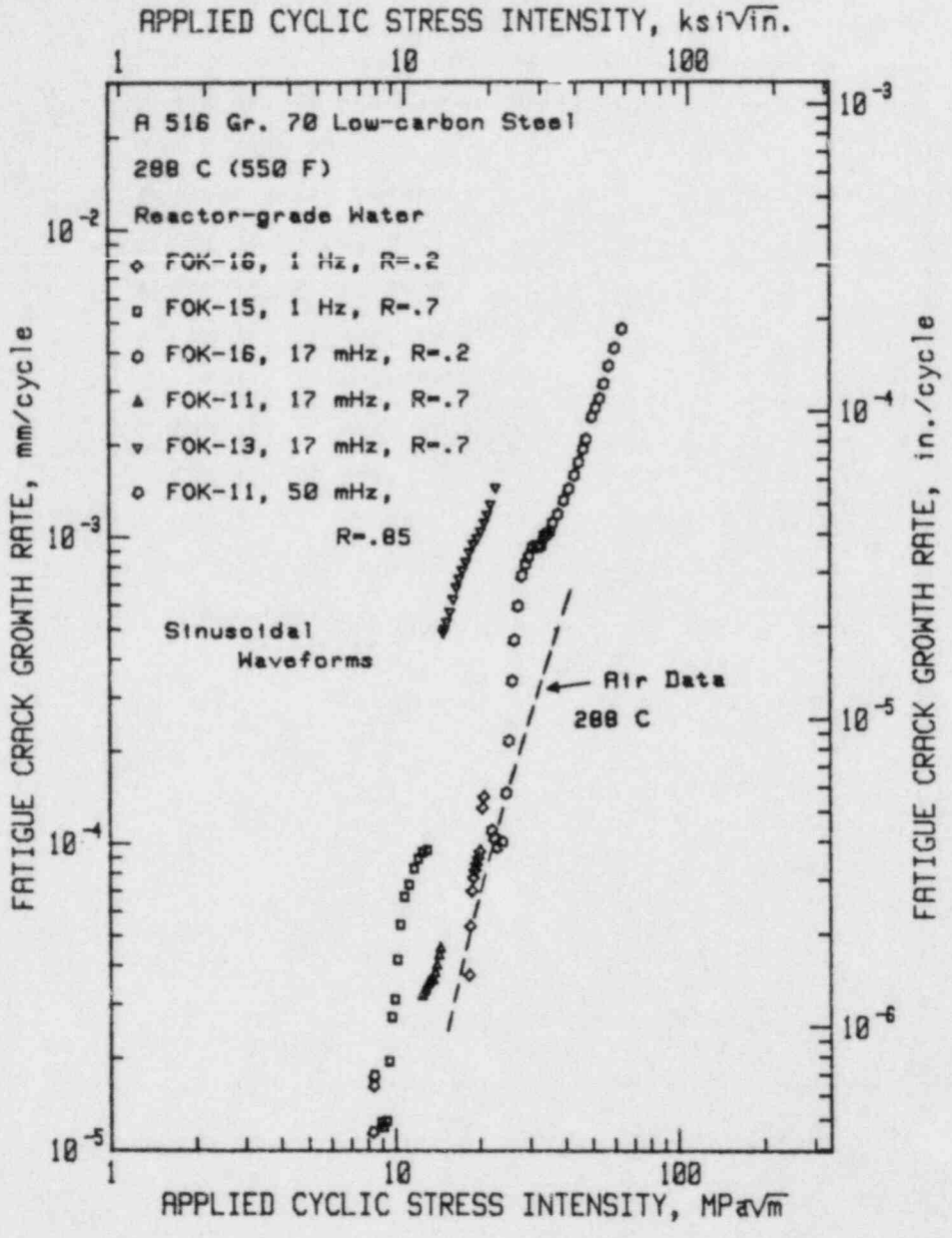

Figure 4 Fatigue crack growth rates vs. applied cyclic ΔK for A 516 Gr. 70 steel in 288°C PWR environment for various test frequencies and load ratios.

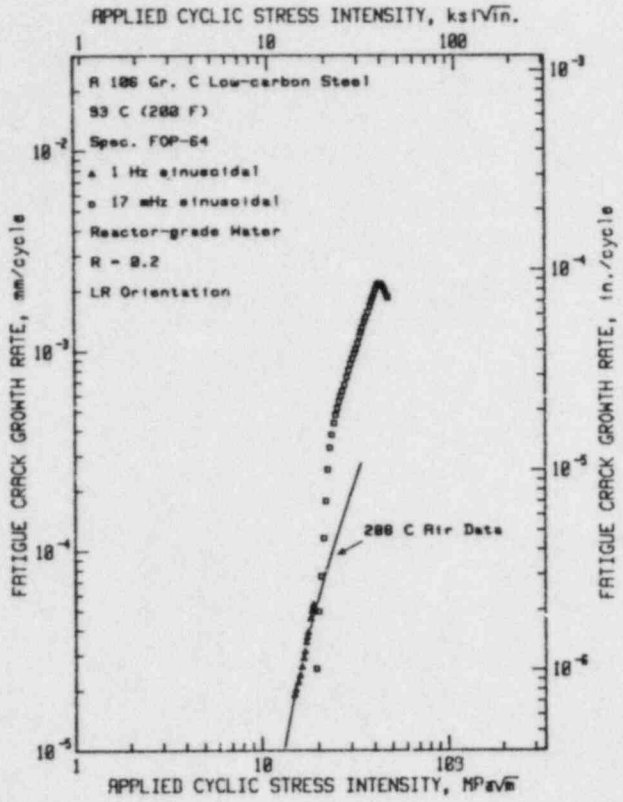

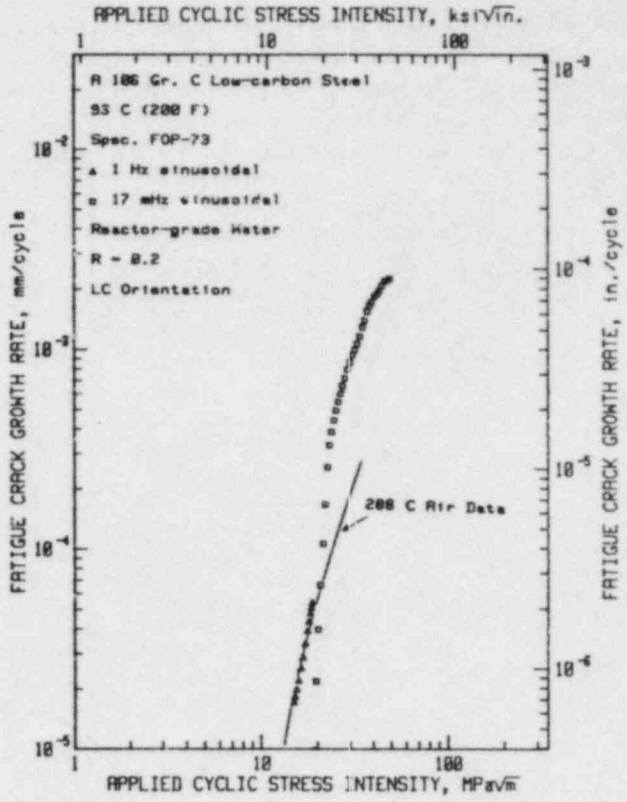

Figure 5 Fatigue crack growth rates vs. applied cyclic ΔK for A 106 Gr. C steel in 93°C PWR environment at 1 Hz and 17 mHz frequencies and a load ratio of 0.2. There is no measurable orientation difference between the two specimens(L-C in a and L-R in b), but there is a considerable environmental enhancement at both test frequencies.

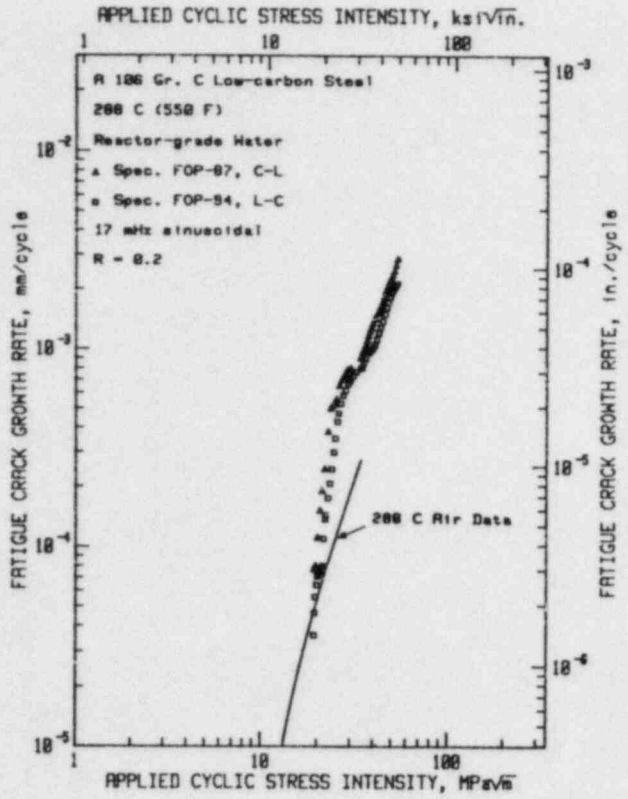

Figure 6 Fatigue crack growth rates vs. applied cyclic ΔK for A 106 Gr. C steel in 288°C PWR environment for 17 mHz test frequency. There is no measurable orientation dependence between the two specimens.

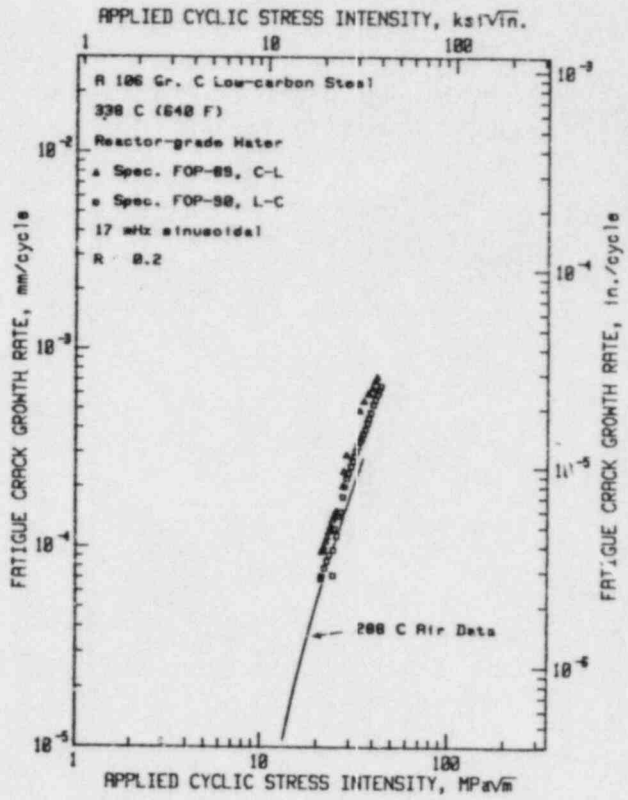

Figure 7 Fatigue crack growth rates vs. applied cyclic ΔK for A 106 Gr. C steel in 338°C PWR environment, for a test frequency of 17 mHz, and a load ratio of 0.2. There is virtually no environmental enhancement shown in these growth rates.

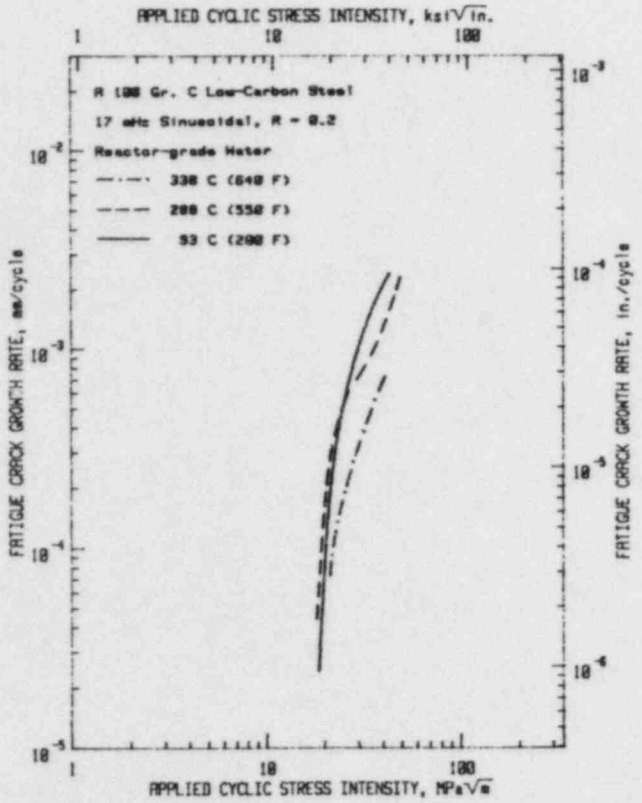

Figure 8 Trend lines for the fatigue crack growth rate data sets shown in Figs. 5, 6 and 7. The test results for 338°C exhibit the lowest crack growth rates.

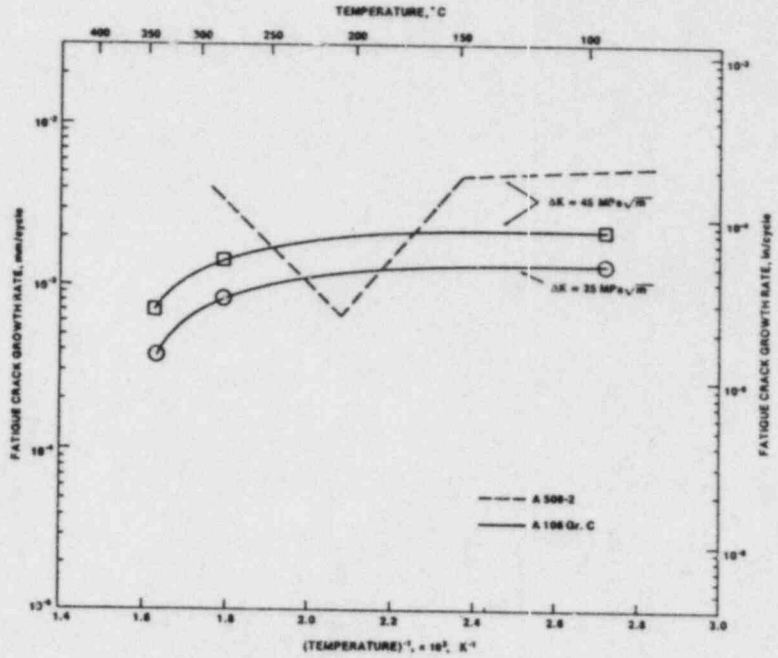

Figure 9 Fatigue crack growth rates vs. inverse temperature, for applied cyclic ΔK's of 35 and 45 MPa$\sqrt{m}$ for A 106 Gr. C steel, at a test frequency of 17 mHz, and a load ratio of 0.2.

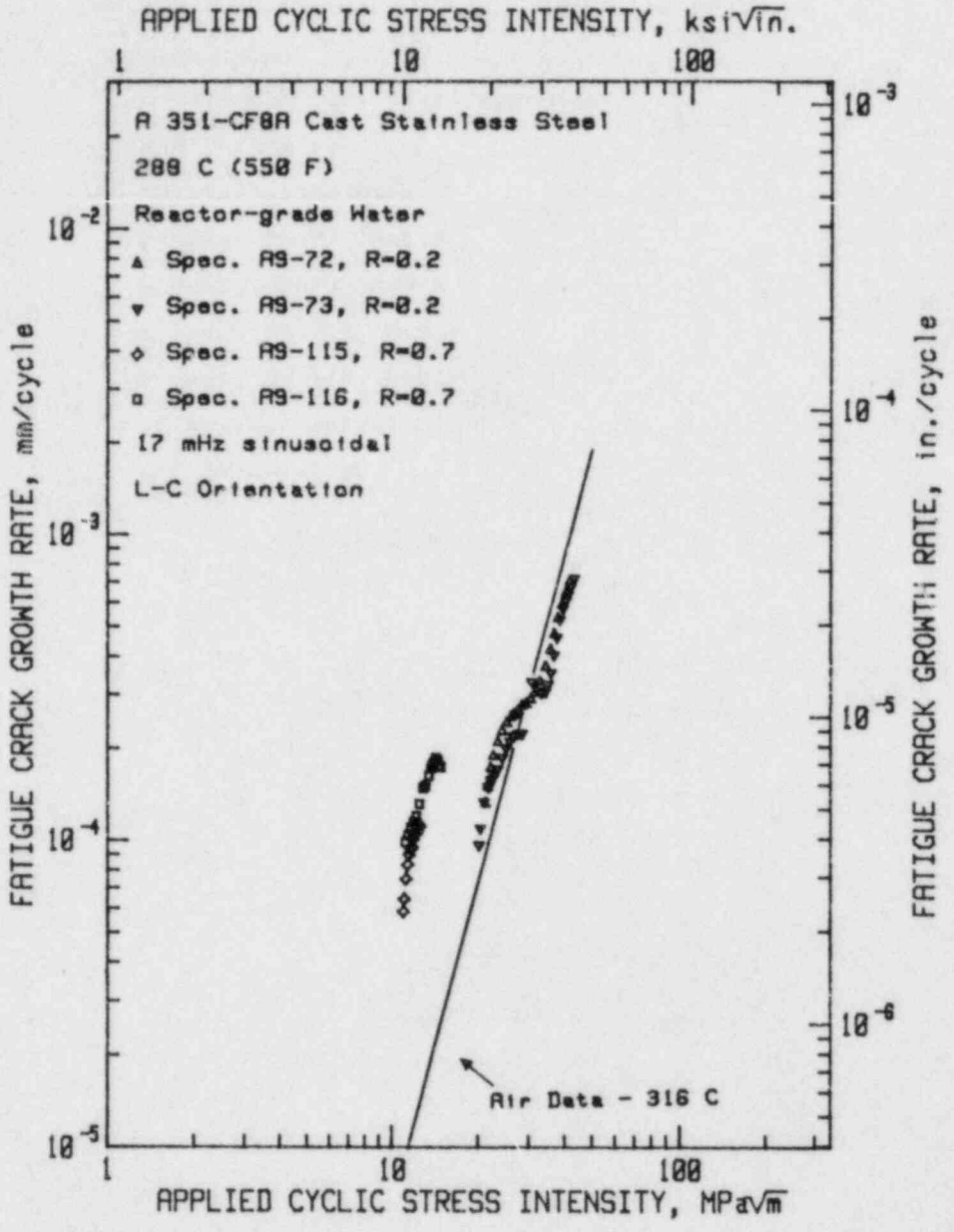

Figure 10 Fatigue crack growth rates vs. applied cyclic stress intensity factor for A 351-CF8A for load ratios of 0.2 and 0.7, 17-mHz test frequency and a temperature of 288°C.

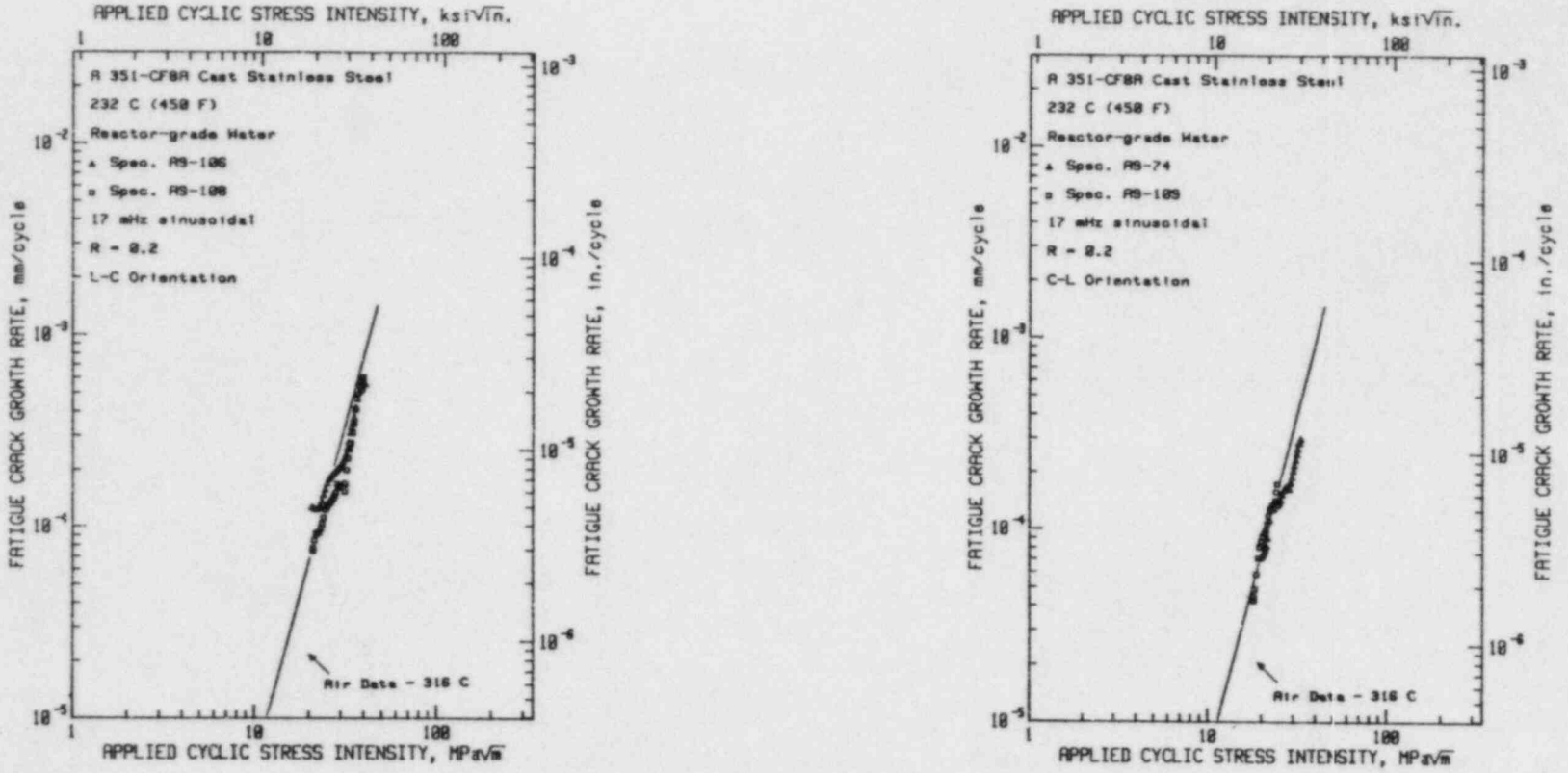

Figure 11 Fatigue crack growth rates vs. applied cyclic stress intensity factor for A 351-CF8A for a load ratio of 0.2, 17-mHz test frequency, and a temperature of 232°C.

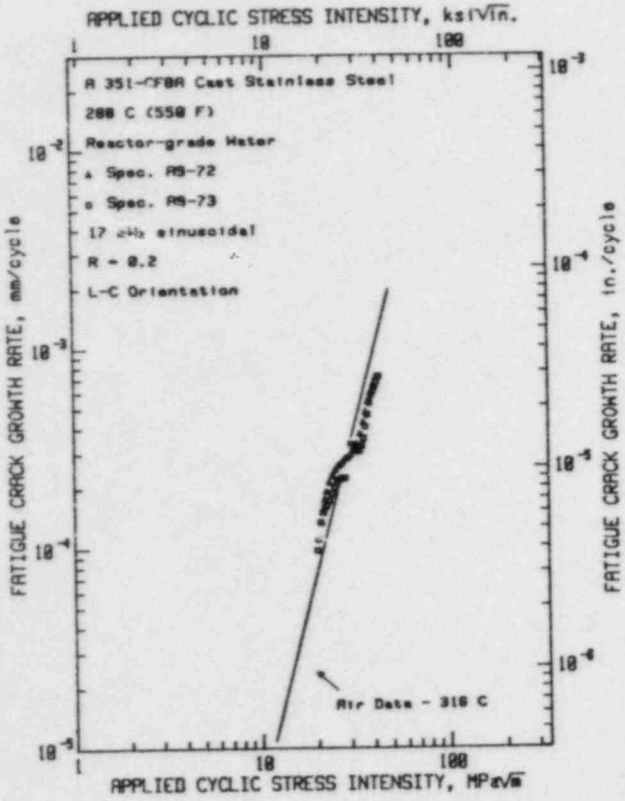

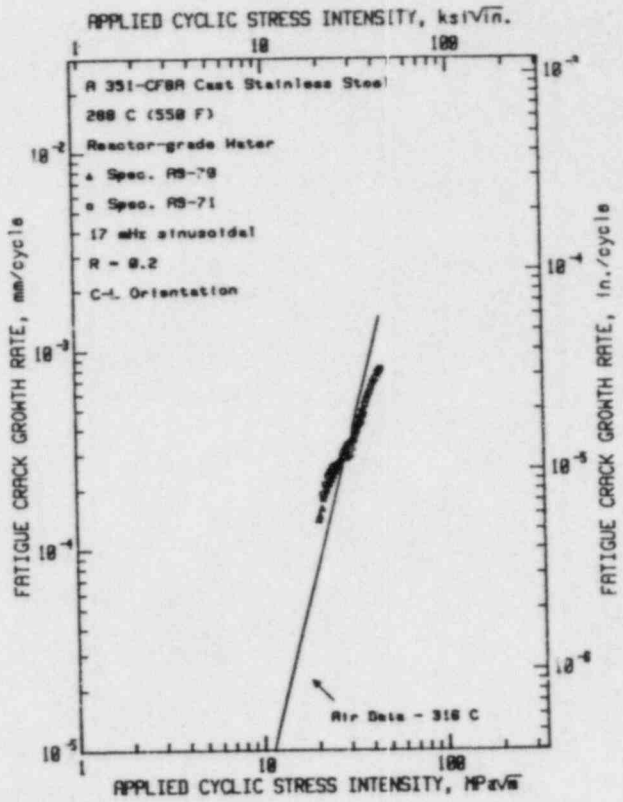

Figure 12 Fatigue crack growth rates vs. applied cyclic stress intensity factor for A 351-CF8A for a load ratio of 0.2, 17-mHz test frequency, and a temperature of 288°C.

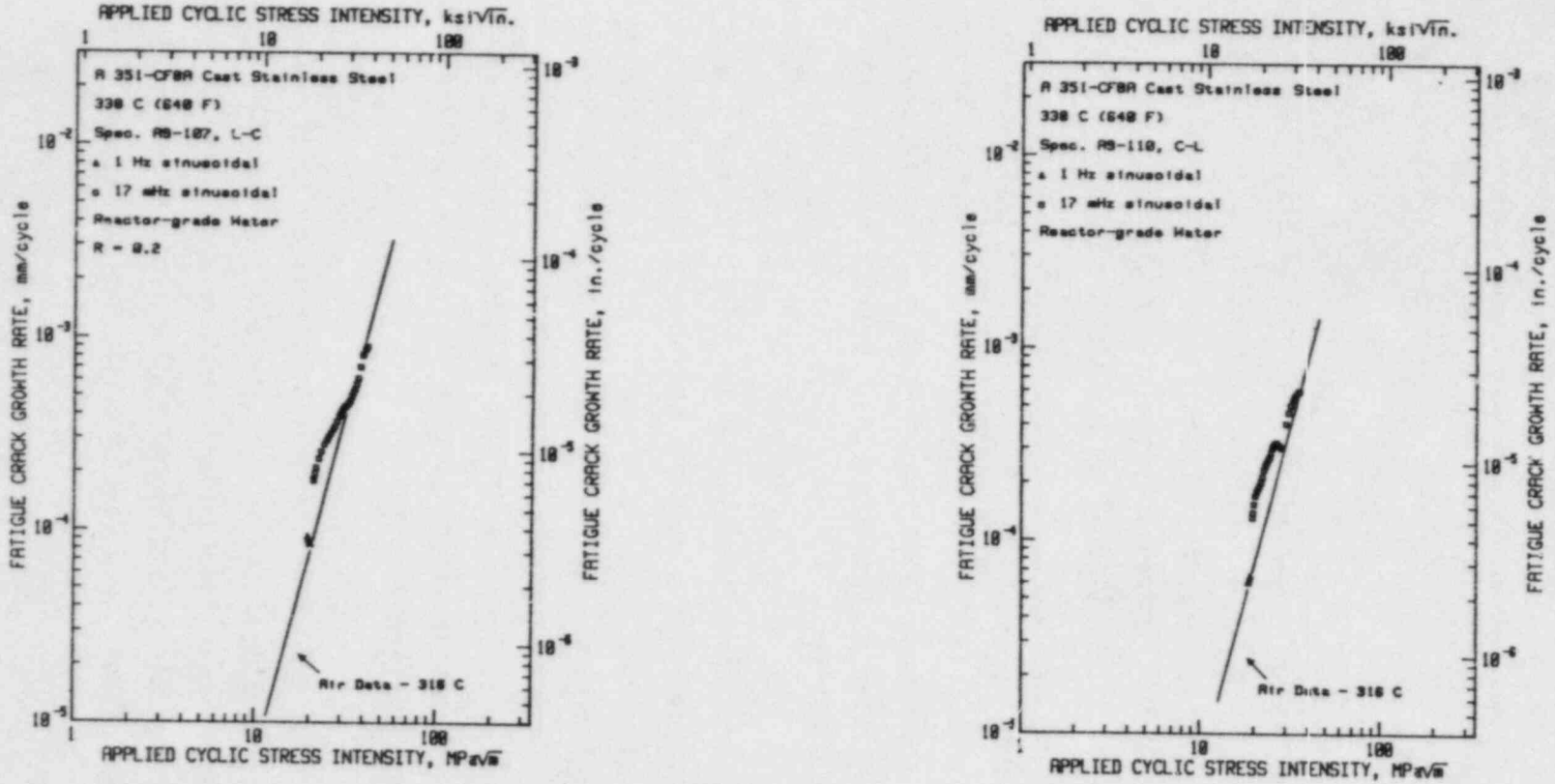

Figure 13 Fatigue crack growth rates vs. applied cyclic stress intensity factor for A 351-CF8A for a load ratio of 0.2, 17-mHz test frequency, and a temperature of 338°C.

THE EFFECTS OF MATERIAL AND ENVIRONMENTAL VARIABLES ON CORROSION FATIGUE CRACK GROWTH IN PRESSURE VESSEL STEELS

W. H. Bamford, R. J. Jacko, I. L. W. Wilson, L. J. Ceschini

WESTINGHOUSE ELECTRIC CORPORATION

Introduction

The objective of the research being carried out in this program is to give improved understanding of the crack growth rate properties of light water reactor materials exposed to primary coolant environments. This understanding can then be used to improve the reference fatigue crack growth laws for the industry which are contained in Section XI of the ASME Code.

The paper begins with a summary of the background and technical basis of the reference fatigue crack growth laws presently contained in Section XI. This discussion will provide a starting point for the rest of the paper, where recent findings will be related to these existing curves, and conclusions reached about their applicability.

Two key variables have emerged from recent work in the field, the effect of material chemistry and microstructure, and the characteristics of the water environment in which crack growth occurs. The material effect is presently believed to be best measured by the sulfur content of the steel, where high sulfur levels have been found to increase environmental acceleration of crack growth, and several examples of this effect will be shown. Work on the mechanisms of environmental acceleration has been done which confirms this effort and provides an explanation for it.

The environmental effect has been found to be best characterized by the free corrosion potential which exists in the system, and a great deal of development work has been done to find reliable measurement techniques. This has been coordinated through the International Cyclic Crack Growth Review Group (ICCGR) and will be discussed in some detail. The results of this work

will be provided, along with examples of measurements taken during crack growth experiments.

One environmental factor which has been shown to be important is the flow rate of the water, and observations on this subject will be made. This factor is closely related to the water chemistry effects, and mechanistic explanations for this will be reviewed.

Finally, the impact of these new observations on potential revision of the reference curves will be discussed, and conclusions reached on the likelihood of such changes.

Background and Technical Basis of the Present ASME Section XI Reference Crack Growth Curves

The present ASME Code reference fatigue crack growth curves for pressure vessel steels in water environments were adopted with the Winter Addendum to the 1980 Code. The technical basis for these curves was provided in reference [1], and will be reviewed briefly here to provide a basis on which to judge recent developments.

The data available in the 1978-79 time period are summarized in Figure 1, along with the first reference curves which were developed. These curves are statistically developed 95 percent global confidence limits on the mean of the data, which corresponds to predictions that the mean behavior of 95 percent of the future data will fall below the reference curves. The original Section XI reference curve for water environments is also shown in Figure 1, for reference.

The general fatigue crack growth behavior of ferritic steels in a water environment is shown schematically in Figure 2. The growth rate increases rapidly with increasing range of stress intensity factor ΔK. At a point which depends on frequency and R ratio the slope changes, and the curve then continues until it reaches the curve corresponding to air behavior. The growth rate curve which is followed is strongly dependent on R ratio and loading rate or cyclic frequency. The R ratio is accounted for directly in

the reference curves, as shown in Figure 3. The effect of welds vs. base metal on the crack growth rate data is shown in Figure 4, where it is seen that weld crack growth data are slightly lower and contain frequent retardations. The reference curves account for frequency or loading rate effects by using data obtained at the frequency for which the highest growth rates were found. This is one cycle per minute, as seen for example in Figure 5. Available data at the time indicated no measurable difference between PWR and BWR environments, so all the data were treated together. Although irradiation effects were unknown in a water environment, they were assumed to be negligible.

The resulting curves were checked for adequacy by using them to predict the individual specimen results on which they were based, and to predict the behavior of two specimens loaded with a range of conditions designed to simulate an operational condition. Loadings and frequencies applied to the two specimens are shown in Table 1. The predictions using the reference curves are shown in Table 1*, and plotted in Figures 6 and 7. Results show that the ASME revised reference curves are conservative predictors of the specimen behavior in both cases. In these figures, curve 1 is the old Section XI law, curve 2 is a graphically determined revision (not adopted) and curve 3 is the revised ASME law.

The reference curves in their present form were based on approximately 25 specimen results, including base metal and welds. Since that time (circa 1978) the available database has increased by nearly an order of magnitude, and many carefully controlled studies have been carried out; including mechanistic studies. This work has resulted in many new findings and revealed the essence of environmental enhancement effects in these materials. These environmental effects are now known to result from these sources, mechanical, metallurgical, and environmental variables, as listed in Table 2. The present reference curves were primarily based on mechanical variables, but have held up remarkably well in light of the new findings in these other areas. The next two sections will consider the new findings in some detail.

* The revised ASME reference curves are labeled "Mean" in Table 1.

Metallurgical Variables

It has recently been found that the level of sulfur in steel can have a remarkable effect on its sensitivity to environmental enhancement of crack growth [2]. This effect was demonstrated in a carefully constructed matrix of tests carried out in this program.

Three different heats of the same material, A533B Cl plate, were utilized, with the only major difference being the sulfur content. The test matrix was devised to study three parameters, sulfur content, crack orientation, and R ratio. All tests have been designed to use the same specimen size and exactly the same loadings for a given R ratio. All tests have been run in simulated PWR environment with the same chemistry, pH = 9 at room temperature. The specific heats chosen were labeled TW, PN and IN, and their complete chemistries are shown in Table 3. As might be expected, the effects of sulfur content and orientation are interrelated, since high levels of manganeses sulfide lead to directionality as a result of the rolling process flattening the inclusions. The orientations chosen for study are shown in Figure 8, and the designations are those used by ASTM.

Results obtained in the matrix of tests have been remarkably consistent, with the same trend observed at both high and low R ratio. The trends in the degree of environmental enhancement are the same as those observed earlier for fracture toughness and Charpy energy, where the materials and orientations which display the lowest toughness also display the highest degree of environmental susceptibility. This is shown for example in Figure 9.

The highest environmental enhancement was found for the transverse (TL) orientation, while the lowest occurred in the through-thickness (LS) orientation. Materials with high sulfur content showed the most enhancement, as well as the strongest orientation effects, as shown for example in Figure 10. The observed behavior of the LS, or through-thickness orientation was about the same regardless of sulfur content and was equivalent to the behavior of all three orientations of the low sulfur heat TW, as shown in Figure 11. This is an important observation, because of the crack orientation which is of most interest from the standpoint of vessel integrity would be the through-thickness direction.

Corrosion fatigue crack growth in submerged arc welds has been found to follow the same pattern as base metal which has similar material chemistry, except that retardation occurs with some regularity, as shown earlier in Figure 4. These retardations are more pronounced at higher R ratios, so the net effect is that crack growth in welds will be somewhat slower.

Although various fluxes have been used for the submerged arc welds, differences in crack growth rate behavior appear to be more dependent on the sulfur content of the weld than on the flux used. This can be seen in Figures 12 and 13, where welds made with two different fluxes with nearly equal levels of sulfur (.012 - .014 wt. pct.) are compared with a lower sulfur weld (.008 wt. pct.) made with a third flux.

Thus, we see that there can be large differences in the degree of environmental enhancement produced by steels which are nominally the same, but have different sulfur contents. As may be seen in the previous figures, even the highest crack growth rates are still covered by the present reference fatigue crack growth curves. Lower growth rates are clearly in evidence for lower sulfur steels, but this effect may be difficult to take advantage of because of environmental interactions, which will be discussed next.

Environmental Variables

The mechanisms of environmental enhancement of crack growth are now being aggressively investigated by many laboratories. A number of important variables have been identified, as seen in Table 2. The key variables include water chemistry, water flow rate and the crack tip strain rate.

One of the early proposed mechanisms of the environmental influence on fatigue crack growth was based on hydrogen effects [3]. It was suggested that the environmental effects on crack growth could be explained based on the surface energy required for the creation of slip steps on the surface. The presence of hydrogen lowers the surface energy associated with cleavage-type crack propagation, as shown in Figure 14. The mechanism of crack advance by ductile plastic deformation forming slip steps is in delicate balance with the

cleaveage mode. The presence of sulfur species changes this balance, as seen in the Figure, making cleavage dominant. This observation was made from a series of tests where hydrogen sulfide was added to the water environment. Results for an example case are shown in Figure 15, and demonstrate accelerated crack growth, with a fracture surface dominated by cleavage facets. Similar behavior has been observed in high sulfur plate materials, in PWR environment with no added sulfur species, with a fracture appearance tending toward more cleavage facets.

The crack tip environment is therefore key in understanding the mechanisms of crack growth enhancement. One of the best methods of characterizing this environment has been found to be the free corrosion potential of the system. One of the first characterizations of the potential of a light water reactor system was produced by Indig [4]. He found that the level of oxygen was clearly reflected by the measured electrochemical potential, as seen in Figure 16. One of the key areas of emphasis in this program has been to determine the most reliable methods of measuring the electrochemical potential, and to implement them. Results of one of our first tests with different measurement systems are shown in Figure 17. This work has been coordinated with a large number of other laboratories through the International Cyclic Crack Growth Rate (ICCGR) international group, which has advanced the state of the art considerably in this area.

Another important variable influencing the crack tip behavior is the flow rate. Faster flow sweeps the water out of the crack tip region, making it more difficult for species (such as sulfur) to concentrate there. An example of this effect is shown in Figure 18, where the same material was tested in a high flow rate rig (UKAFA) and a low flow rate rig (Westinghouse). The crack growth was only slightly accelerated in the high flow rate rig.

Another way of explaining environmental influences has been suggested by Scott [5] and others, and involves the crack tip strain rate. This strain rate affects the ability of the environment to influence the cracking, and does explain the frequency and wave form effects which have been observed. More work is underway in this area, and the approach shows promise of providing a consistent characterization of environmental effects.

Summary and Conclusions

A great deal of study of the issue of environmentally assisted crack growth has been completed since the revision of the ASME reference crack growth curves in 1980. This work has resulted in a database almost an order of magnitude larger than that available at that time. These new data have generally confirmed the adequacy of the present curves, and have provided much more insight into the mechanisms which are operating. It is possible that a modification of the present curves may be possible for newer, low sulfur steels in a tightly controlled environment, but more complete understanding of the operable mechanisms will be necessary before such a step is warranted.

References

1. Bamford, W. H., "Technical Basis for Revised Reference Crack Growth Curves for Pressure Boundary Steels in LWR Environment," in Trans ASME, Journal of Pressure Vessel Technology, November 1980.

2. Bamford, W. H., "Environmental Cracking of Pressure Boundary Materials, and the Importance of Metallurgical Considerations" in Aspect of Fracture Mechanics in Pressure Vessels and Piping, ASME Vol. 58, 1982.

3. Bamford, W. H. and Moon, D. M., "Some Mechanistic Observations on the Crack Growth Characteristics of Pressure Vessel and Piping Steels in PWR Environment," in Corrosion Vol. 36, No. 6, June 1980.

4. Indig, M. E., in "BWR Environmental Cracking Margins for Carbon Steel Piping," First Semi-Annual Progress Report, July-December 1978, General Electric Report NEDC 24625, January 1979.

5. Scott, P. M., "Chemistry Effects in Corrosion Fatigue" in ASTM STP 801 Corrosion Fatigue: Mechanics, Metallurgy, Electrochemistry and Engineering, May 1983, pp. 319-350.

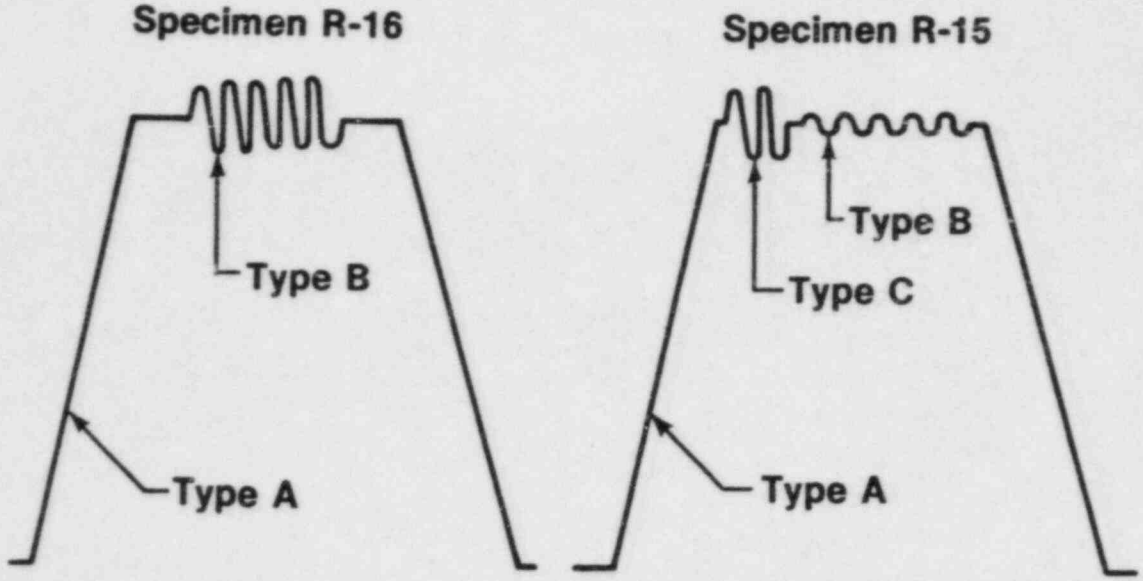

Specimen	Cycle Type	Relative Number of Occurrences	R Ratio	Initial ΔK	Final ΔK	Total Percent of Growth	
						Sect. XI	Mean
R-16	A - 1/2 Min Ramp	1	0.17	33.5	65.4	75%	42%
	B - 1 Cycle/Minute	6	0.68	15.4	30.1	25%	58%
R-15	A - 1/2 Min Ramp	1	0.18	34.6	70.2	91%	61%
	B - 1 Cycle/Minute	10	0.92	3.6	7.4	0.3%	0.3%
	C - 1 Cycle/Minute	5	0.75	12.1	24.6	8.7%	36.7%

TABLE 1 MULTIPLE LOAD EXPERIMENTS

TABLE 2 VARIABLES AFFECTING ENVIRONMENTAL FATIGUE CRACK GROWTH

MECHANICAL	Stress ratio or load ratio R Frequency and Waveform
ENVIRONMENT	Temperature Level of oxygen and other dissolved gases Electrochemical potential Velocity of water
METALLURGICAL	Level and distribution of alloying elements and impurities Microstructure Mechanical properties (strength, toughness)

TABLE 3 MATRIX STUDY OF SULFUR EFFECTS

Material	C	Mn	P	S	Si	Ni	Cr	Mo	Cu	V	Co
A533B Cl 1											
"IN	.21	1.26	.012	.026	.25	.47	-	.47	.19	-	-
"TW"	.21	1.38	.008	.004	.21	.67	-	.56	.08	-	-
"W7"	.23	1.40	.005	.004	.25	.70	-	.57	-	-	-
"PN"	.21	1.33	.012	.016	.22	.56	-	.54	.13	-	-

Material: A533B Class 1	Test Conditions					
	R = 0.2			R = 0.7		
Sulfur content/ Orientation	TL	LT	LS	TL	LT	LS
S = 0.004	TW-1 W7-2C7	TW-4	TW-7	TW-2 W7-2C6	TW-5	TW-8
S = 0.016	PN-1	PN-4	PN-7	PN-2	*PN-6	PN-8
S = 0.026	IN-1	IN-4	IN-7	IN-2	IN-5	*IN-8

NOTE: All the above tests were carried out in sumulated PWR environment at 288°C. All specimens were 2TCT, and the applied loadings were identical for all specimens at a given R ratio. Load form was a one cycle per minute sine wave.

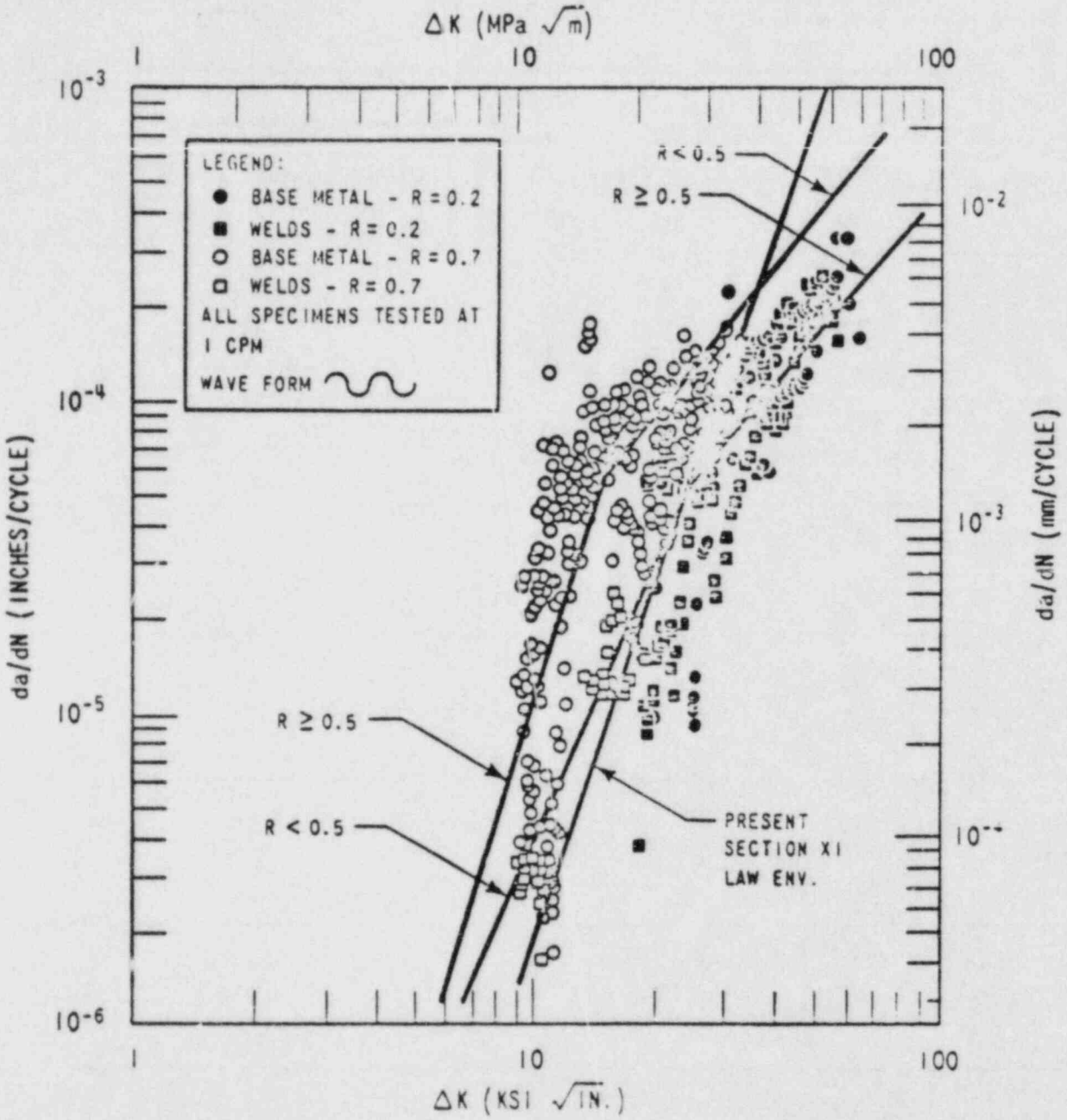

FIGURE 1 SUMMARY OF DATA USED FOR - 95 PERCENT GLOBAL CONFIDENCE LIMIT ON THE MEAN DATA - 1979

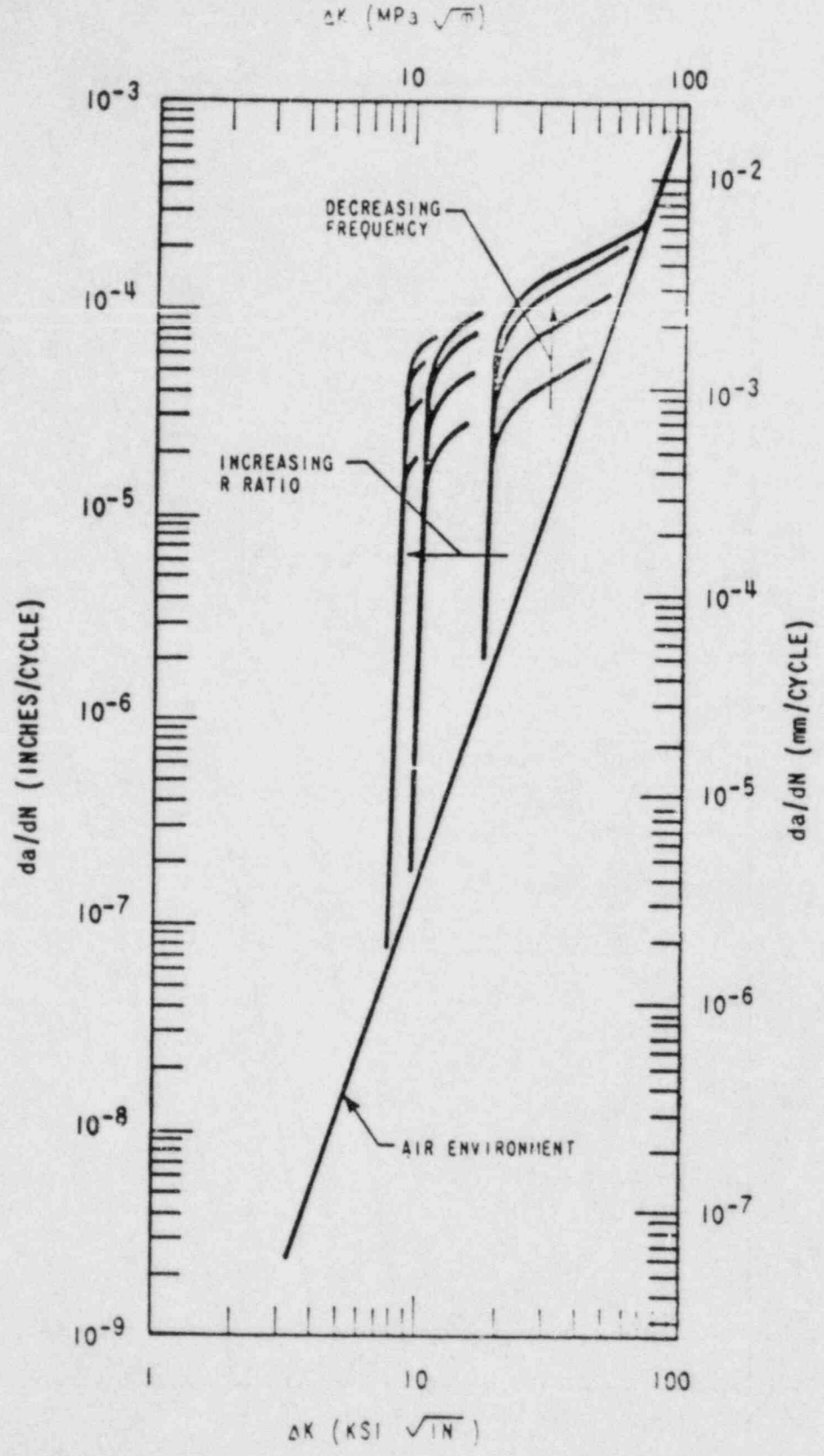

FIGURE 2 SCHEMATIC OF FREQUENCY AND R RATIO EFFECTS - PRESSURE VESSEL STEELS IN LWR ENVIRONMENT

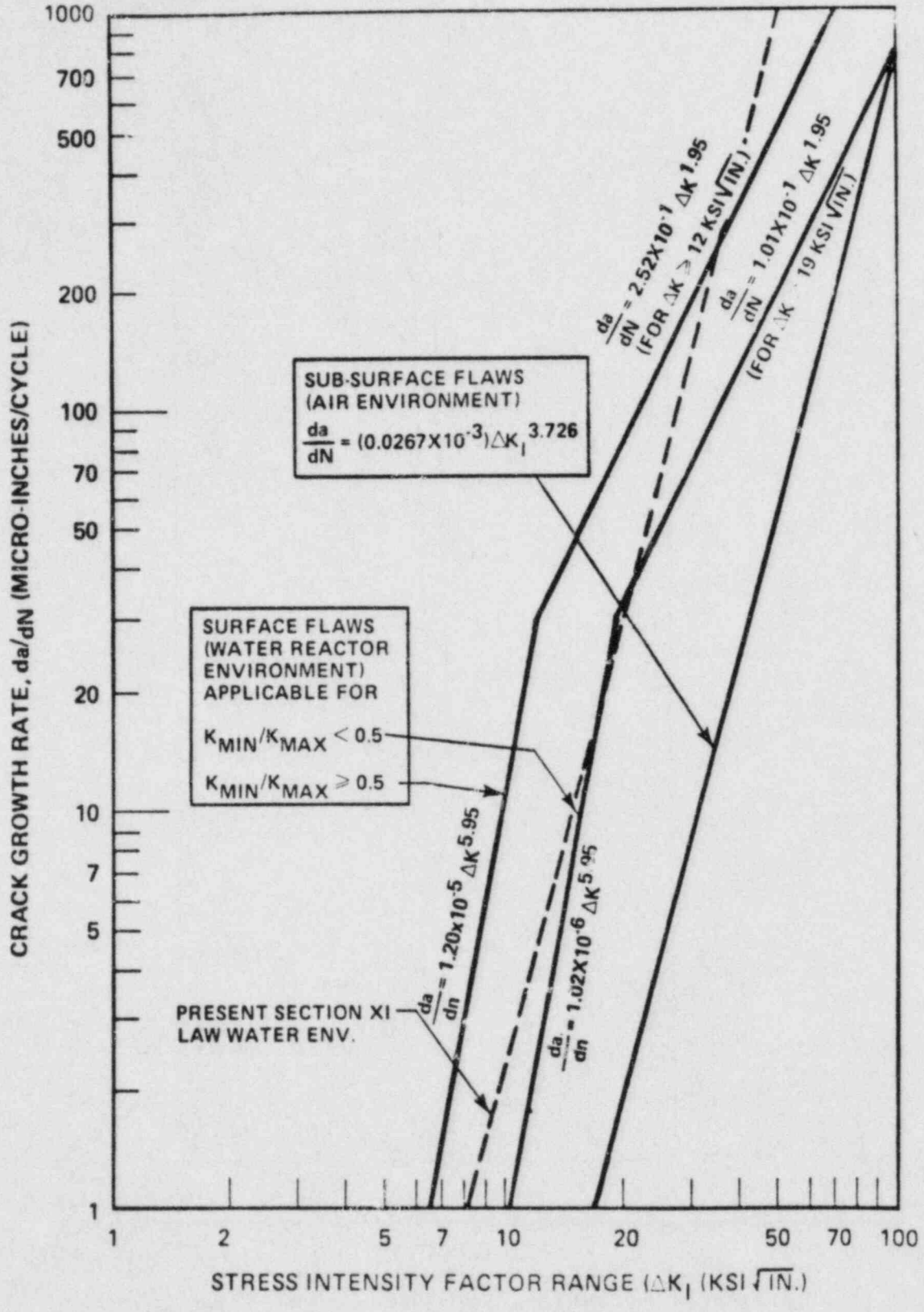

FIGURE 3 COMPARISON OF REVISED CURVES WITH PREVIOUS REFERENCE CURVE

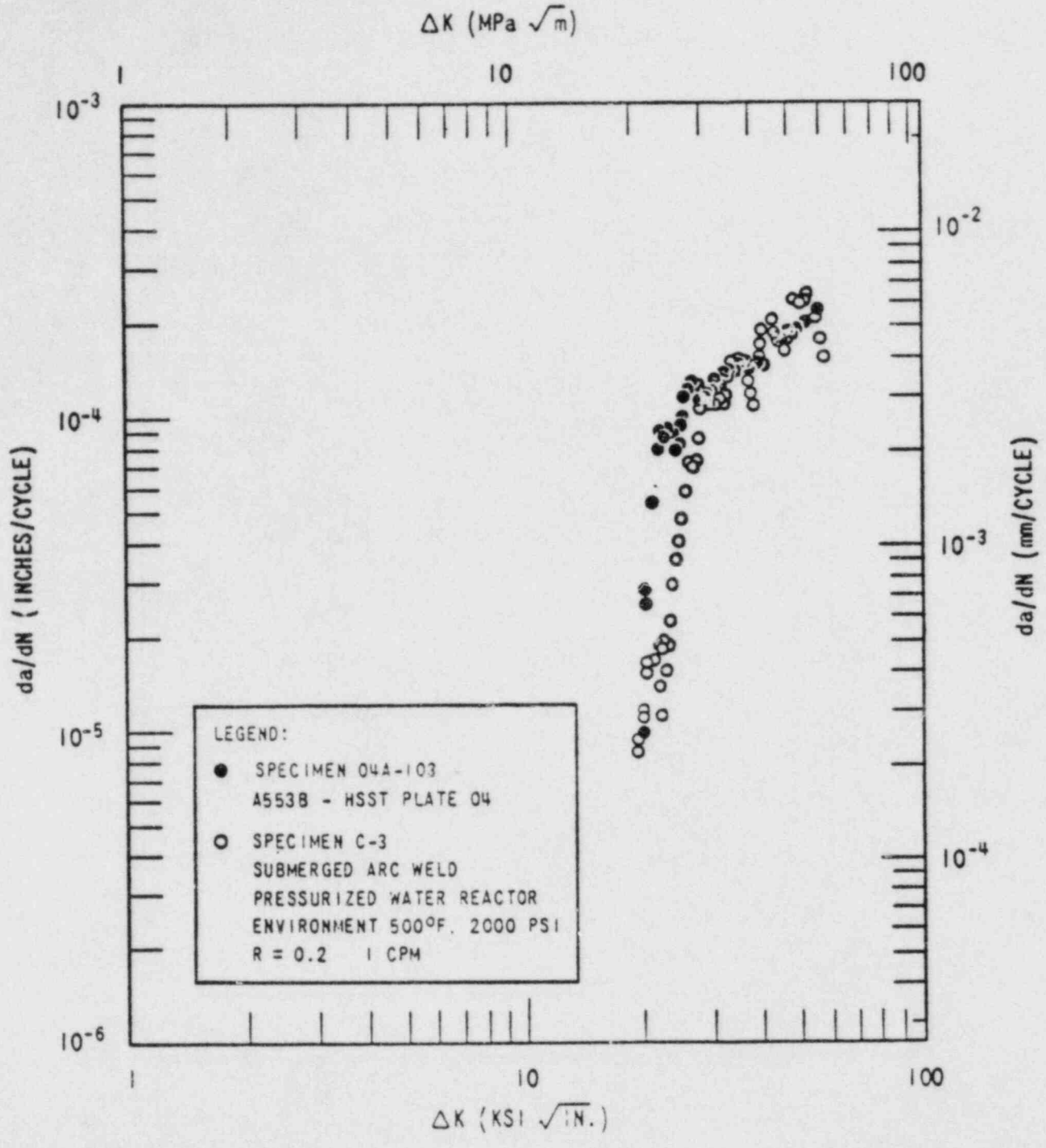

FIGURE 4 COMPARISON OF CRACK GROWTH OF BASE METAL AND SUBMERGED ARC WELDMENTS IN PRESSURIZED WATER ENVIRONMENT

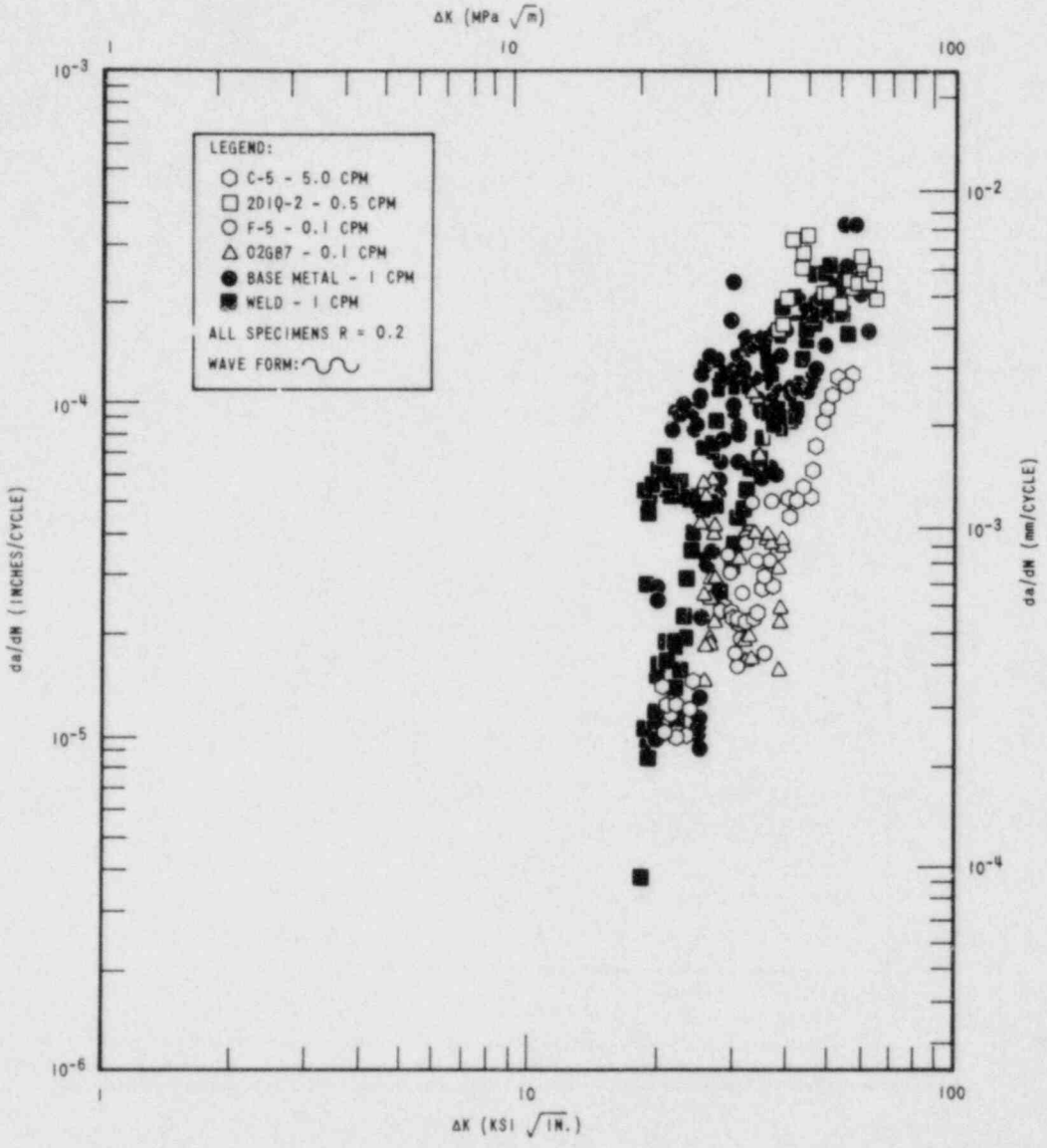

FIGURE 5 EFFECTS OF TEST FREQUENCY ON CRACK GROWTH FOR A SERIES OF MEDIUM AND HIGH SULFUR STEELS

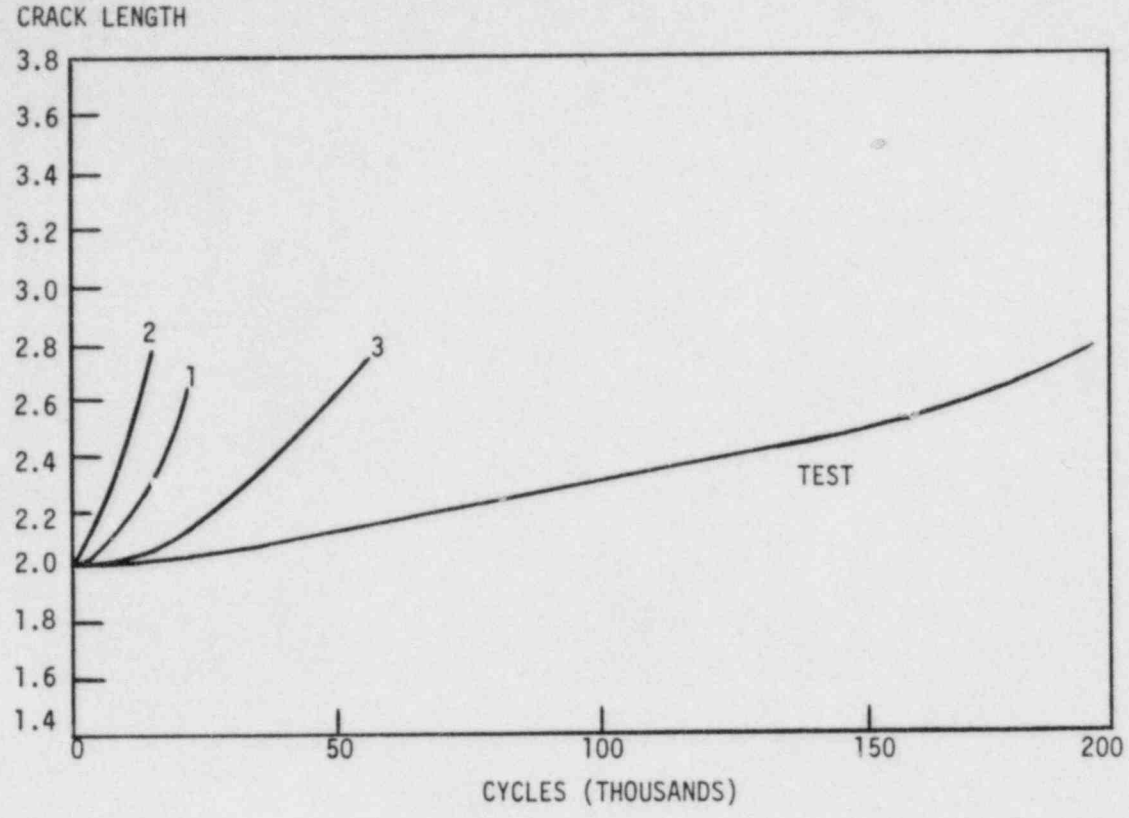

FIGURE 6 RESULTS OF VERIFICATION TEST R-15

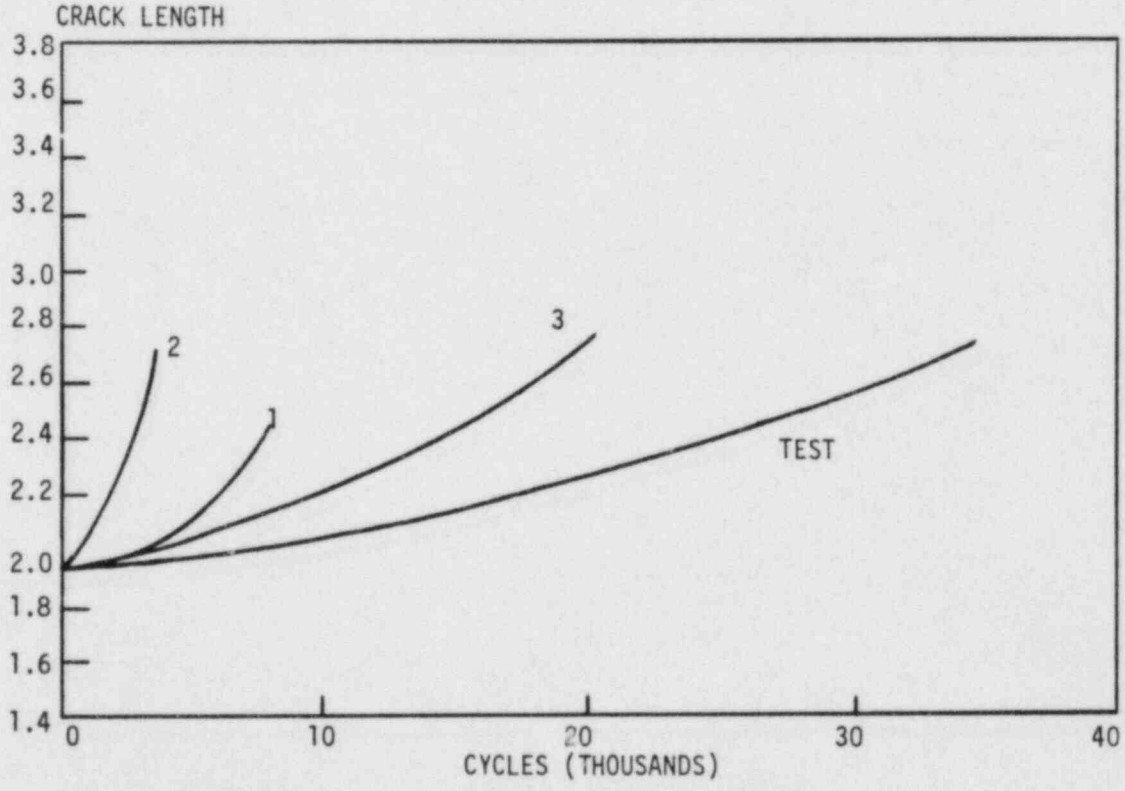

FIGURE 7 RESULTS OF VERIFICATION TEST R-16

NOTE: 1 Prediction from old Section XI reference curve.
2 Prediction with qraphical upper bound method.
3 Prediction with new Section XI reference curve.

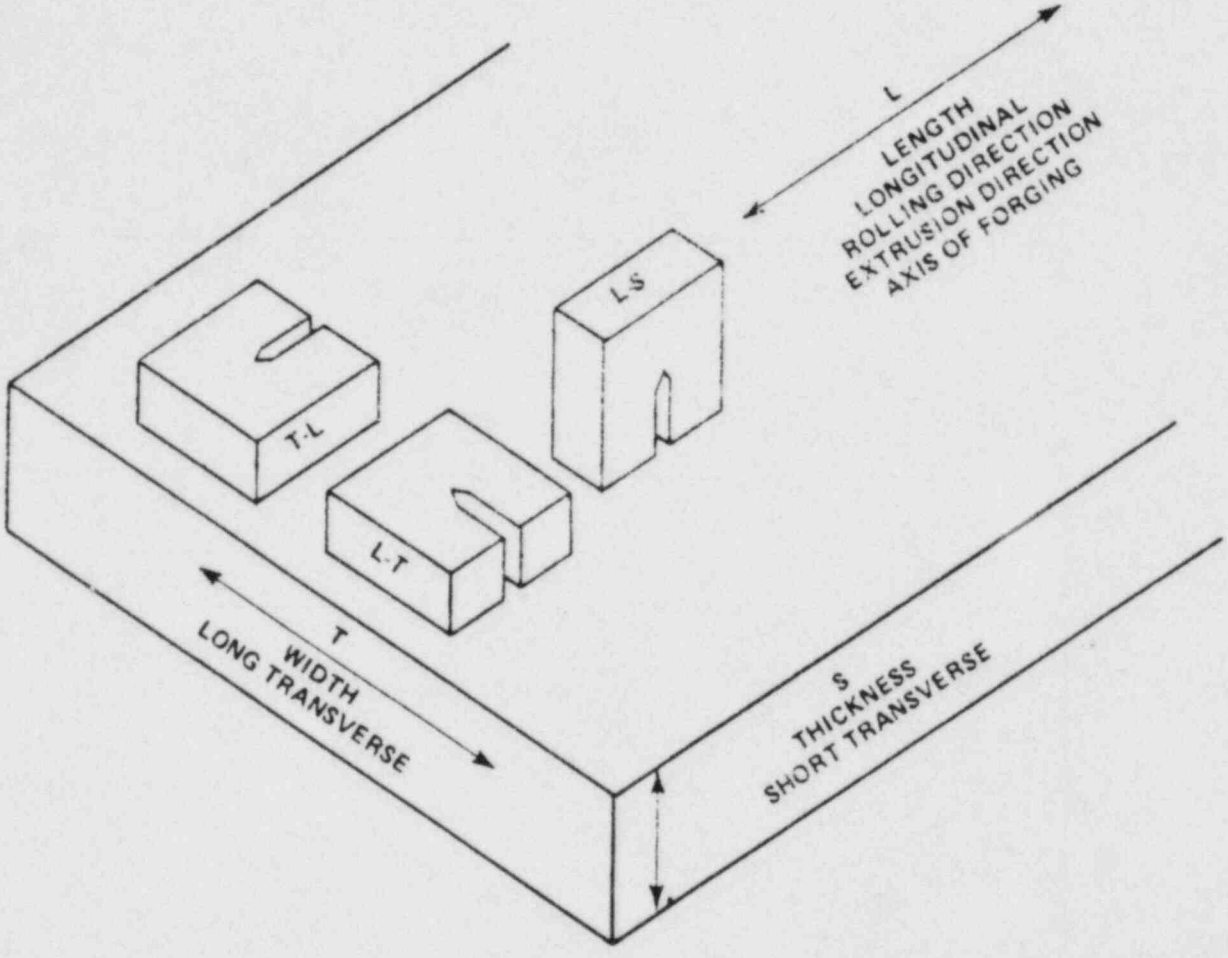

FIGURE 8 CRACK PLANE ORIENTATION IDENTIFICATION CODE FOR PLATE

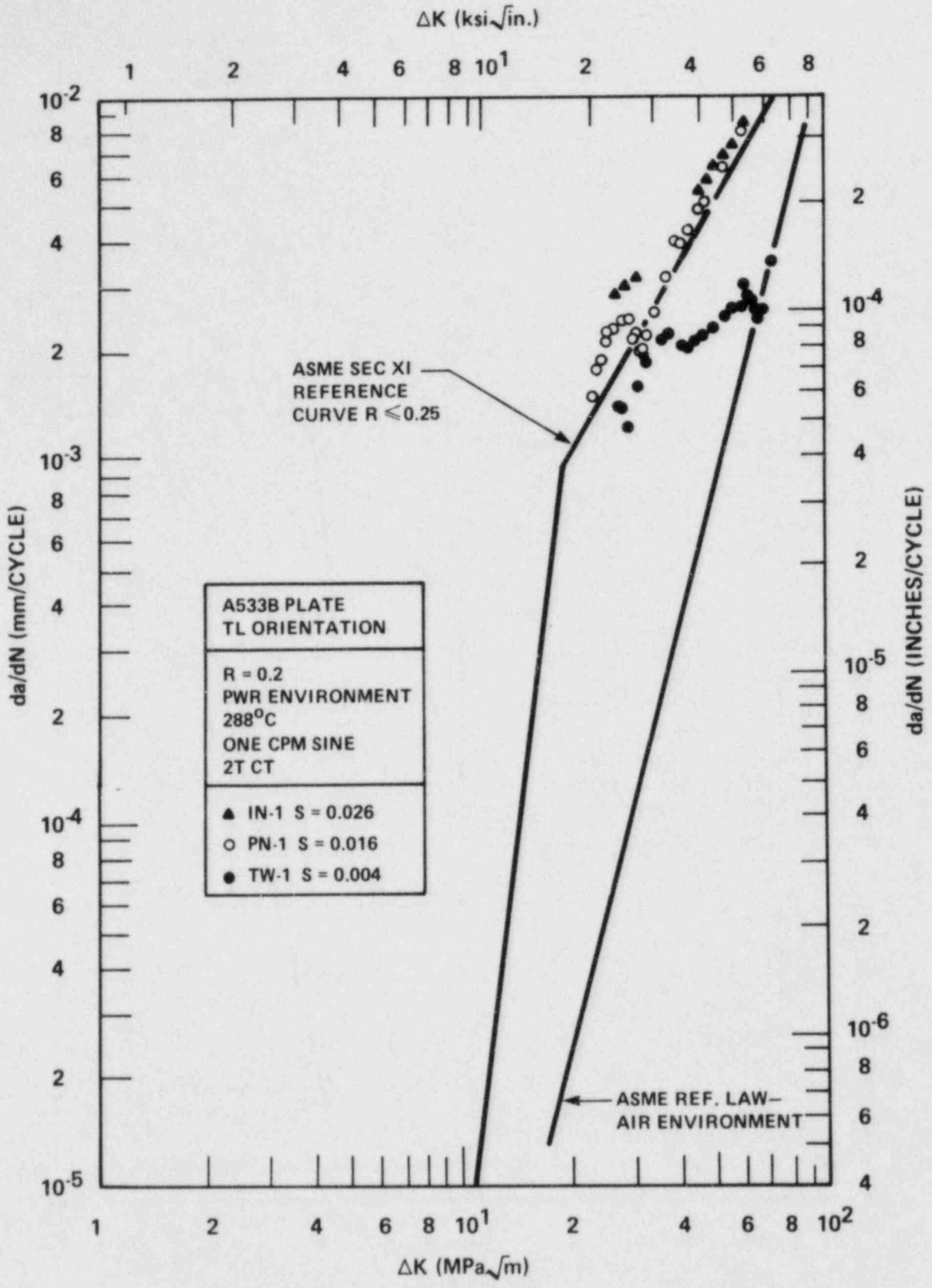

FIGURE 9 THE EFFECT OF SULFUR CONTENT ON FATIGUE CRACK GROWTH IN PWR ENVIRONMENT AT R=0.2, TL ORIENTATION

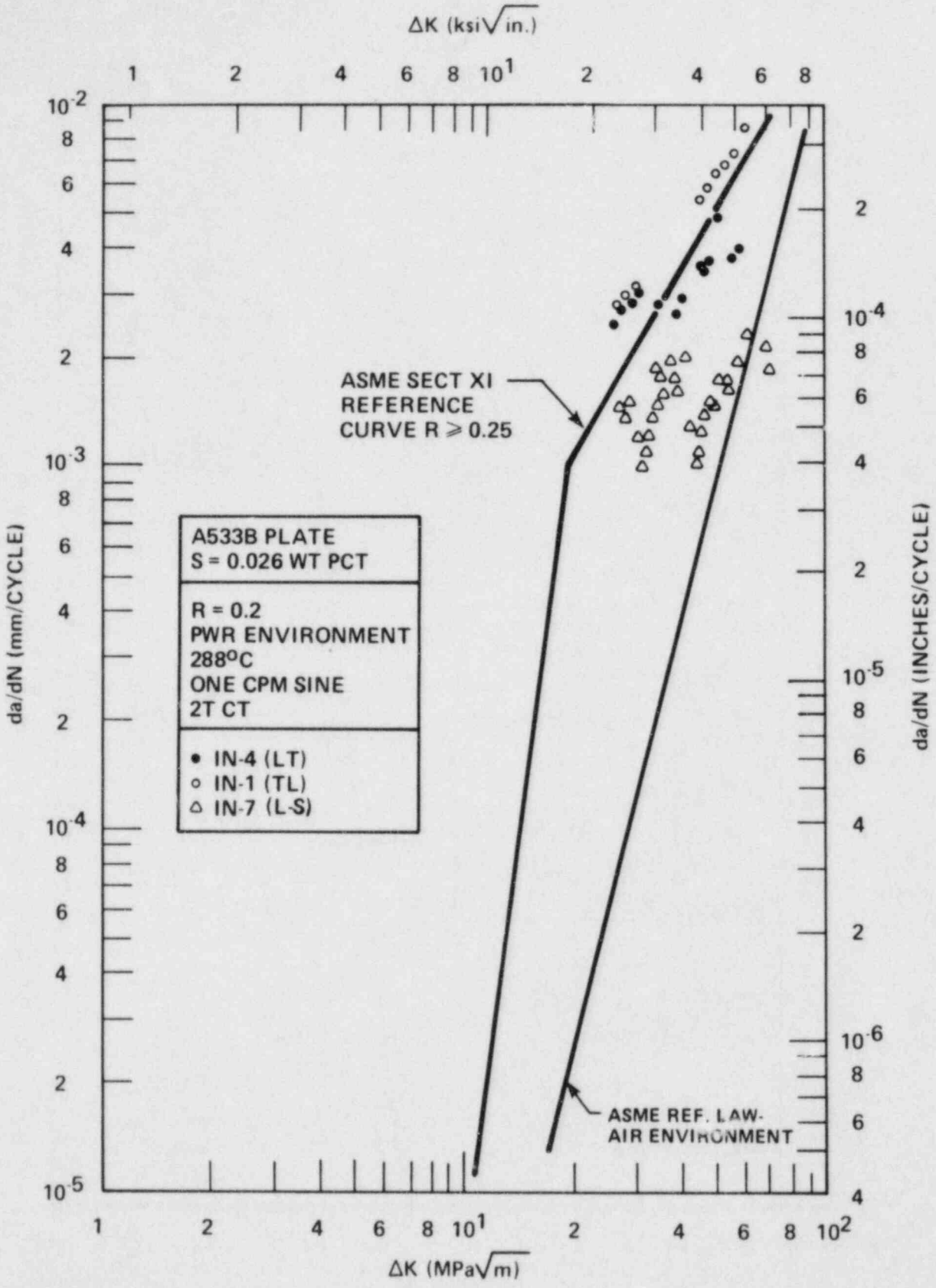

FIGURE 10 THE EFFECT OF SPECIMEN ORIENTATION ON CRACK GROWTH, HIGH SULFUR PLATE MATERIAL (LT, TL, LS REFER TO ASTM DESIGNATIONS OF FLAW ORIENTATION, AS FOUND IN E399)

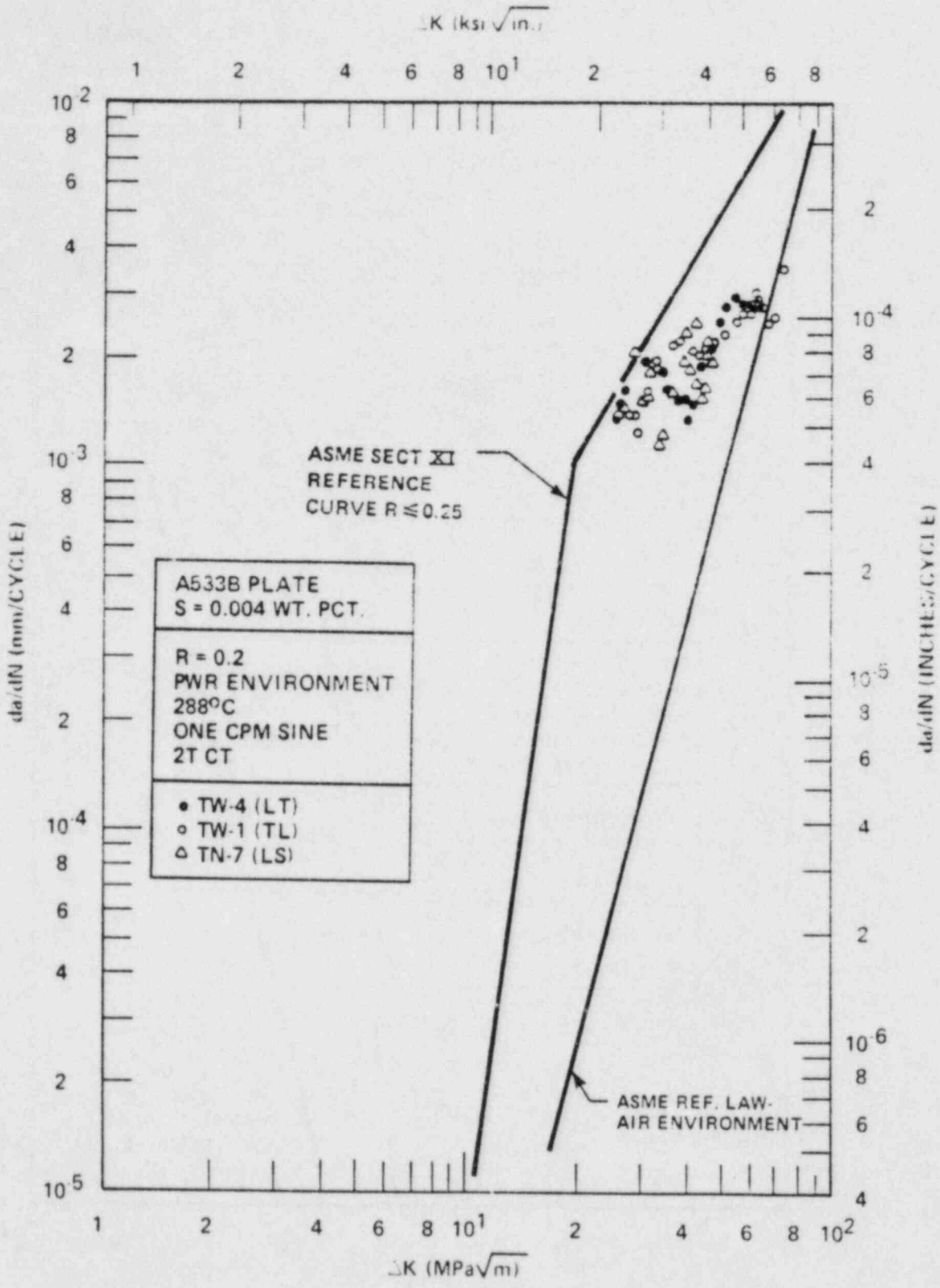

FIGURE 11 EFFECTS OF SPECIMEN ORIENTATION ON CRACK GROWTH RATE, LOW SULFUR PLATE

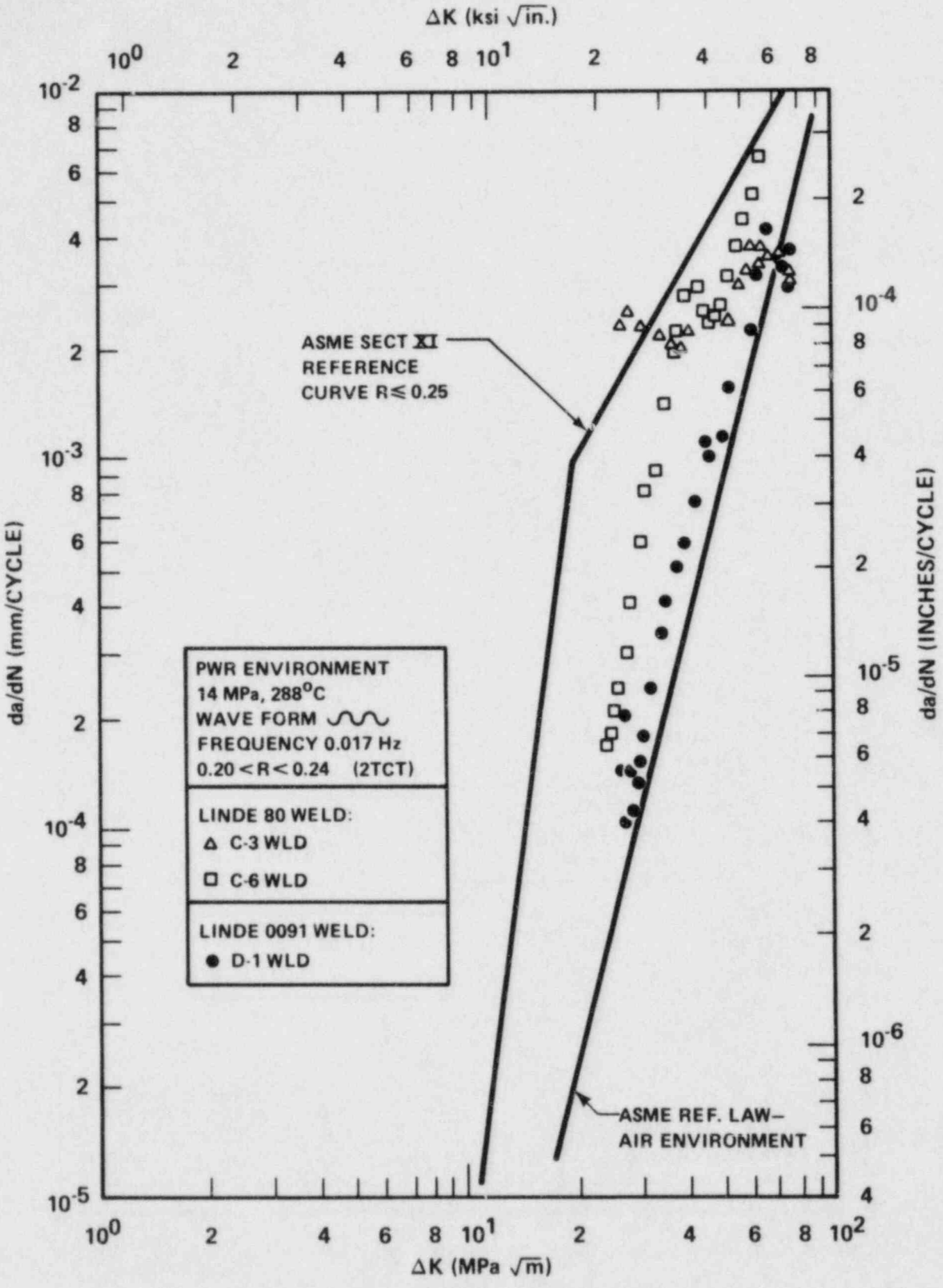

FIGURE 12 COMPARISON OF LINDE 80 AND LINDE 0091 SAMPLE WELD CRACK GROWTH BEHAVIOR

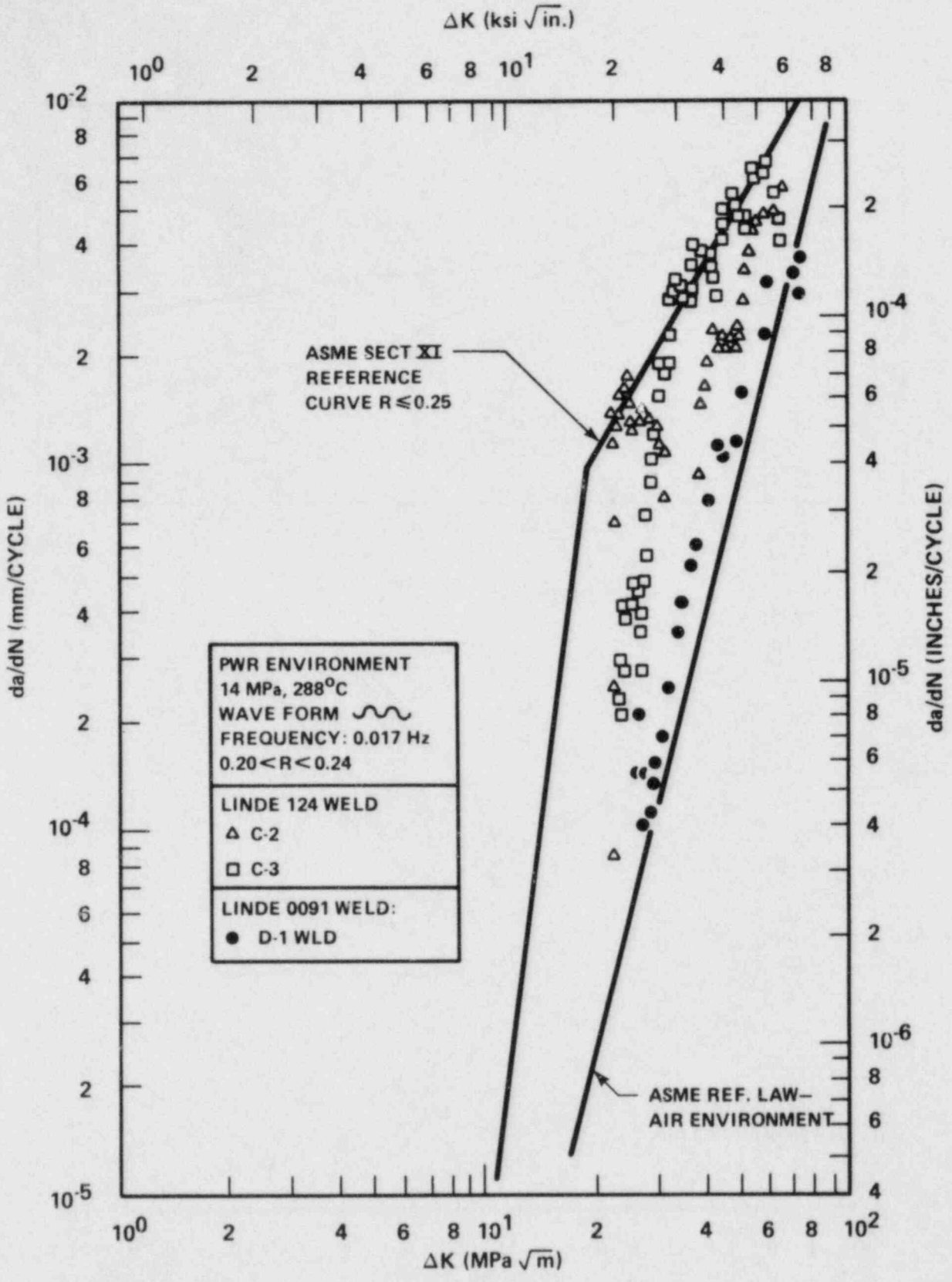

FIGURE 13 COMPARISON OF LINDE 124 AND LINDE 0091 SAMPLE WELD CRACK GROWTH BEHAVIOR

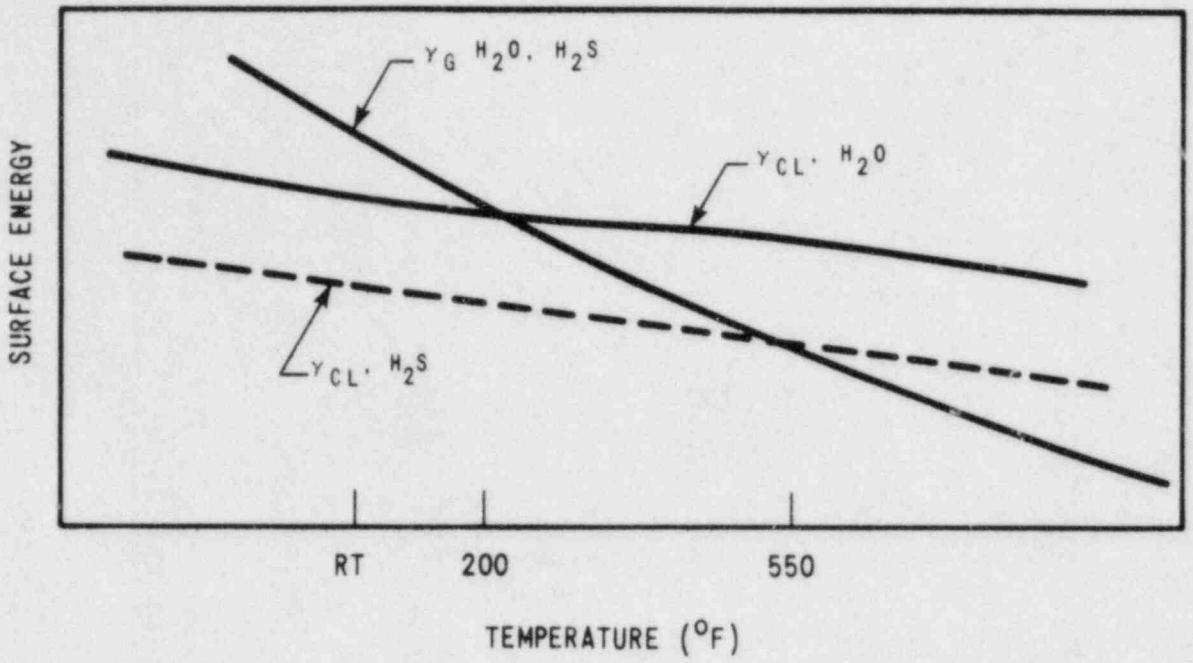

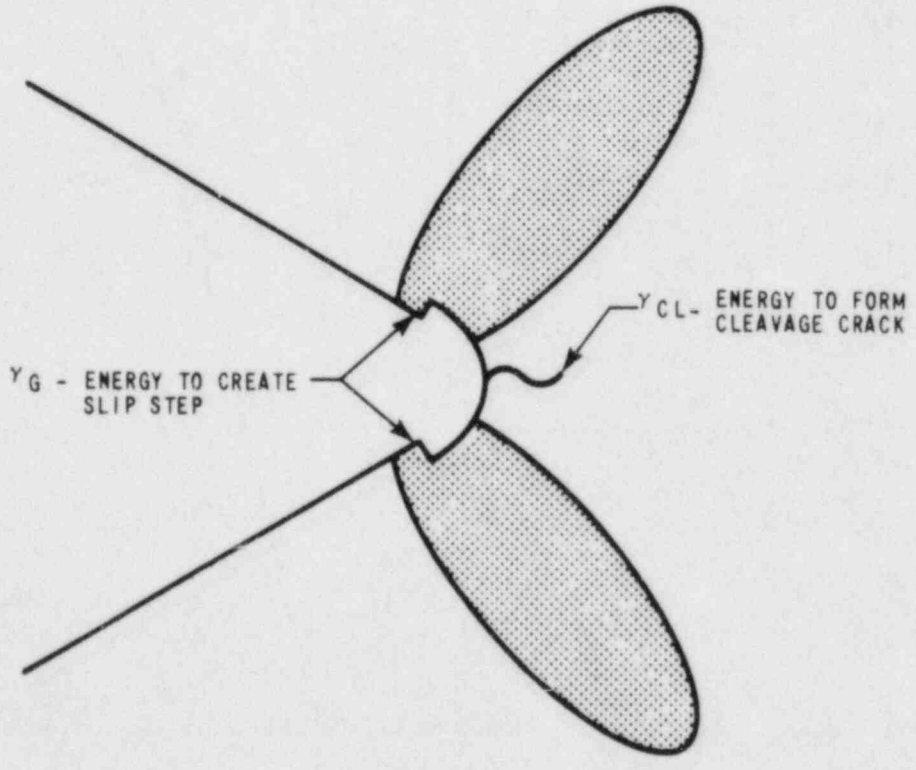

FIGURE 14 INFLUENCE OF ENVIRONMENT ON CRACK TIP BEHAVIOR

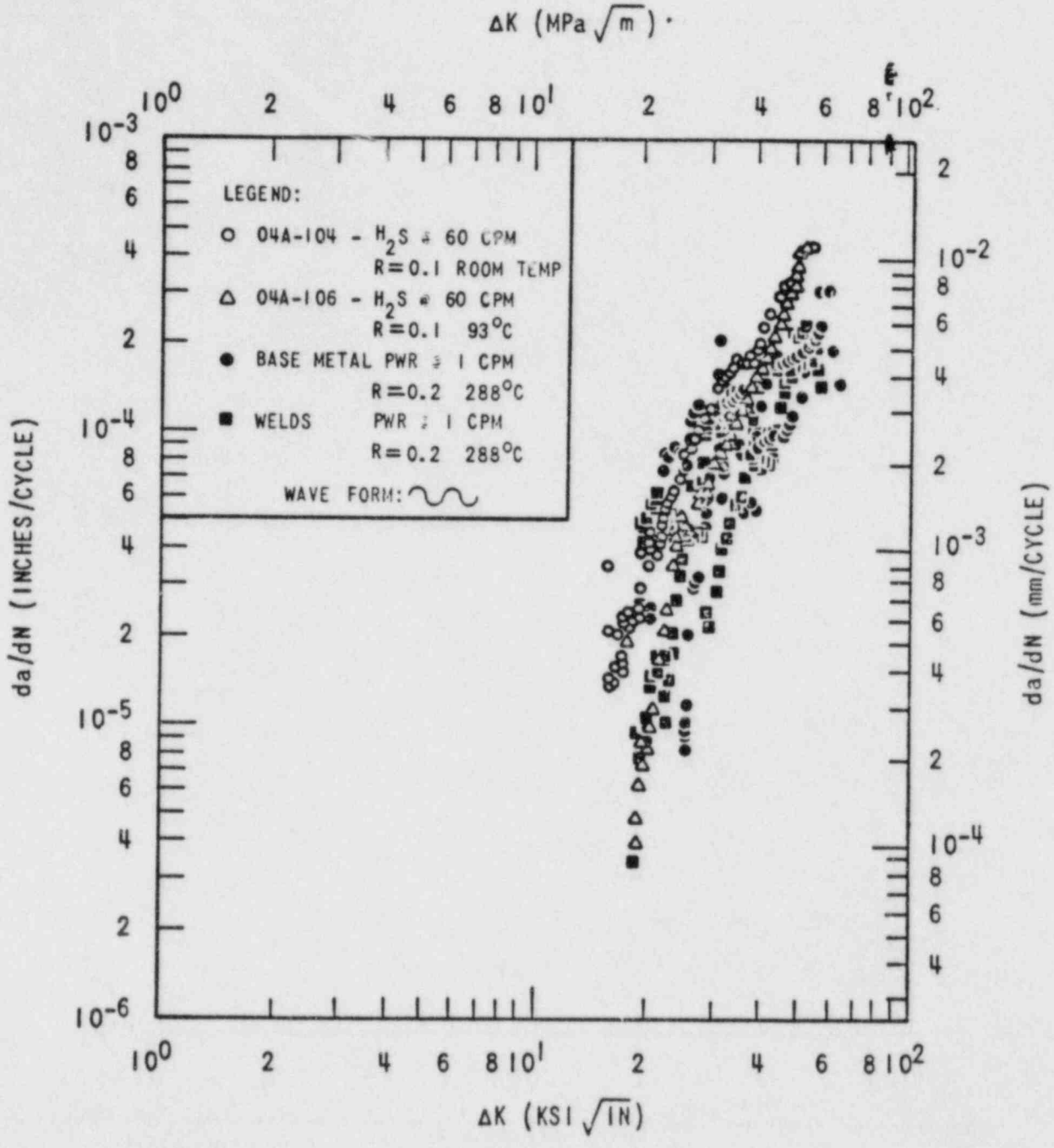

FIGURE 15 COMPARISON OF FATIGUE CRACK GROWTH FOR PRESSURE VESSEL STEELS IN HYDROGEN SULFIDE AND PWR ENVIRONMENT - LOW R RATIO

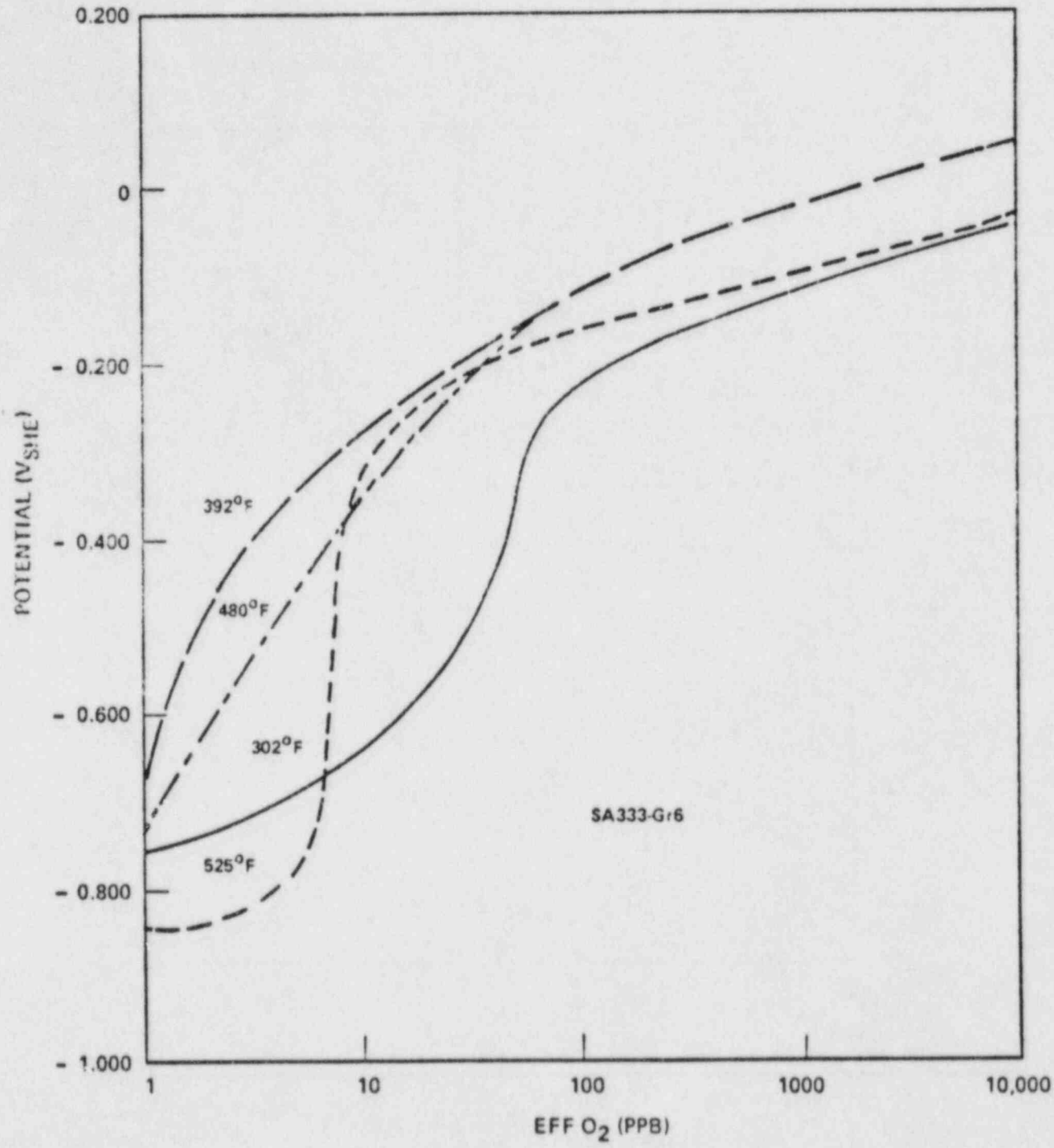

FIGURE 16 EFFECT OF OXYGEN AND TEMPERATURE ON CORROSION POTENTIAL AS DETERMINED BY INDIG, REFERENCE 4

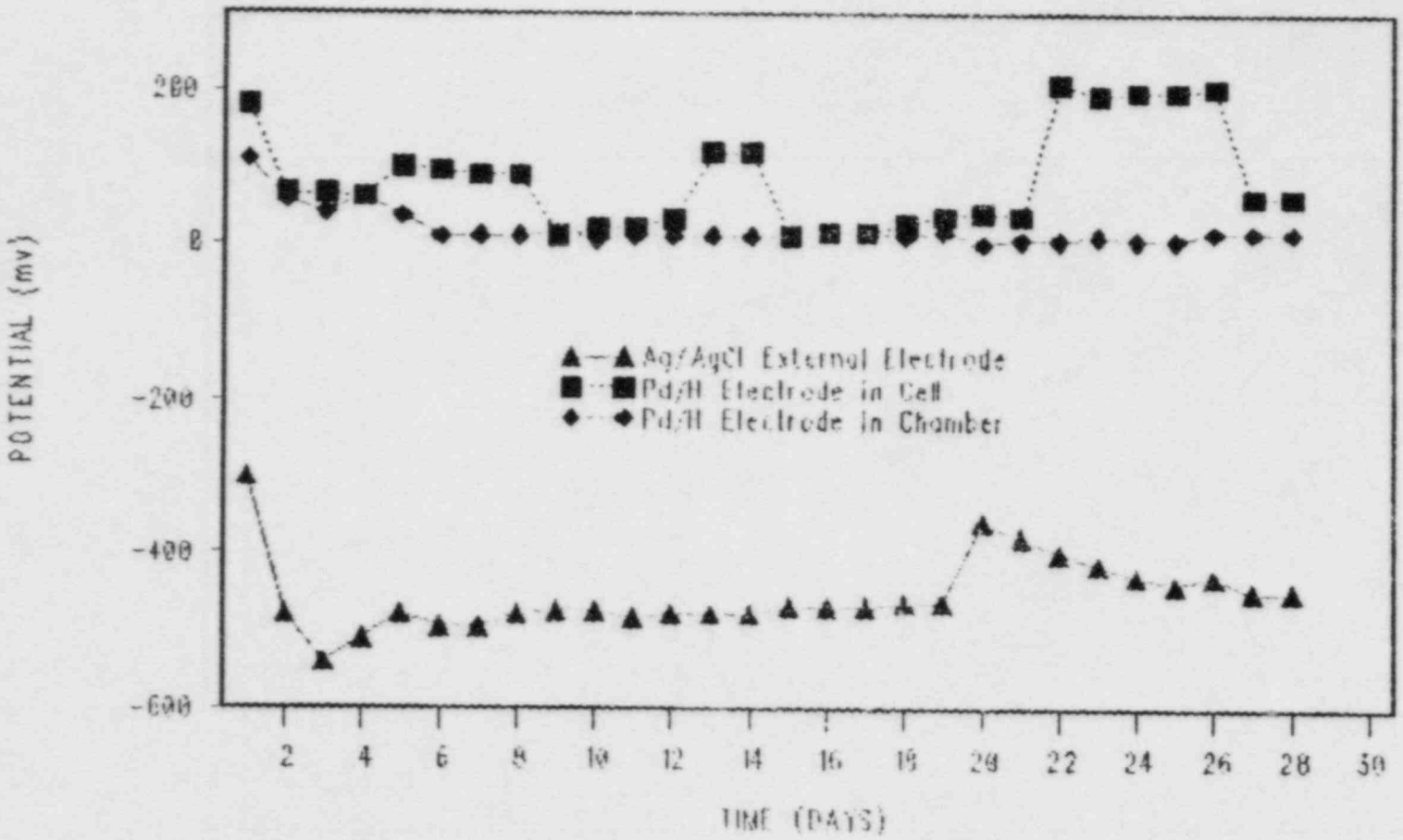

FIGURE 17 SUMMARY OF POTENTIAL READINGS FROM EXPERIMENT #1

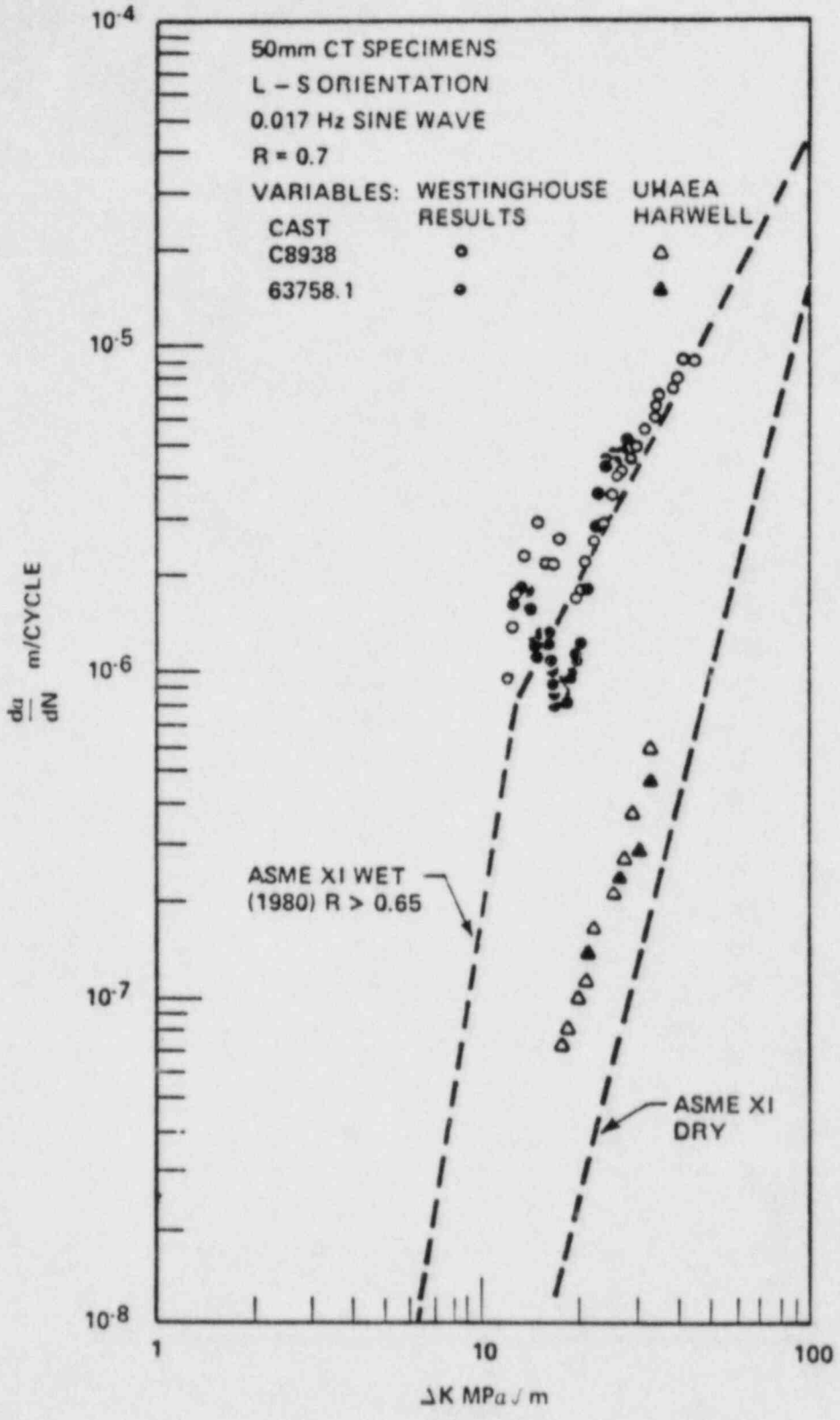

FIGURE 18 CRACK GROWTH RATE DATA OBTAINED ON PRESSURE VESSEL STEELS IN WATER ENVIRONMENT USING TWO DIFFERENT AUTOCLAVE SYSTEMS

LWR SURVEILLANCE DOSIMETRY IMPROVEMENT PROGRAM: PSF METALLURGICAL BLIND TEST RESULTS

F. W. Stallmann
F. B. K. Kam
G. Guthrie*
W. N. McElroy*

Oak Ridge National Laboratory
Oak Ridge, Tennessee 37831, USA

INTRODUCTION

The metallurgical irradiation experiment at the Oak Ridge Research Reactor Poolside Facility (ORR-PSF) is one of the series of benchmark experiments in the framework of the Light Water Reactor (LWR) Surveillance Dosimetry Improvement Program[1] (Fig. 1). The goal of this program is to test, against well-established benchmarks, the methodologies and data bases which are used to predict the irradiation embrittlement of pressure vessels in commercial power reactors at the end of their service life and to determine safe operating limits for these vessels. Knowledge of pressure vessel embrittlement is also essential to determine the resistance of the vessel under thermal shock conditions and to determine if and when annealing of the vessel is needed. The prediction methodology as practiced in pressure vessel surveillance programs includes procedures for neutron physics calculations, dosimetry and spectrum adjustment methods, and metallurgical tests and damage correlation. The benchmark experiments in the framework of the Dosimetry Improvement Program serve to validate, improve, and standardize these procedures. The results of this program are implemented in a set of ASTM Standards (Fig. 2) on pressure vessel surveillance procedures, which are in various stages of completion.[2] These in turn may be used as guides for regulatory procedures of the Nuclear Regulatory Commission (NRC).

The ORR-PSF experiment was specifically designed to simulate the surveillance capsule-pressure vessel configuration in power reactors and to test the validity of procedures which determine the radiation damage in the vessel from test results of surveillance capsules. Emphasis was on radiation embrittlement of reactor vessel steels and damage correlation in order to test current embrittlement prediction methodologies. For this purpose, a PSF metallurgical Blind Test was initiated.[3] Experimental results were withheld from the participants; only the type of information which is normally contained in surveillance reports was given. The goal was to predict from this limited information the metallurgical test results in the pressure vessel wall capsule. Of particular interest was the question, what effects, if any, the differences in fluence rate and fluence spectrum in the surveillance capsule and in the pressure vessel wall may have on the embrittlement prediction.

*Hanford Engineering Development Laboratory

To serve as a benchmark, a very careful characterization of the ORR-PSF experiment is necessary, both in terms of neutron fluence spectra and of metallurgical test results. Statistically determined uncertainties must be given in terms of variances and covariances to make the comparisons between predictions and experimental results meaningful. A description of the characterization program is given in the first part of this paper. The second part discusses the preliminary results of the Blind Test and its implications.

DESCRIPTION OF THE EXPERIMENT

The ORR-PSF (Fig. 3) consists of the ORR reactor core and the ex-core components that are used to mock up pressure vessel surveillance configurations for light water reactors (LWRs). The ex-core components are the thermal shield (TS), the simulated surveillance capsule (SSC), the simulated pressure vessel capsule (SPVC), and the simulated reactor cavity [void box (VB)]. The aluminum window is part of the ORR pressure vessel which separates the core from the ex-core components. The PSF metallurgical Blind Test is concerned with the SSC and the SPVC. Five metallurgical specimen assemblies were prepared for the irradiation experiment. Each assembly (Fig. 4) contains the same mix of plate, forging, and weld material specimens.[4,5] Dosimeters are distributed throughout each assembly to monitor the neutron exposure received by the specimens. Two capsules were fabricated for irradiation in sequence at the simulated surveillance location (SSC1 and SSC2) to fluences (E > 1.0 MeV) of 2×10^{19} and 4×10^{19} neutrons/cm^2, respectively. Each SSC contained one of the metallurgical specimen assemblies. The SPVC contained the other three assemblies which were positioned at locations corresponding to the inner surface (0-T), the quarter thickness (1/4 T), and the half thickness (1/2 T) of a pressure vessel. The fluences for SSC1 and SSC2 are approximately equal to the 1/4T and 0-T positions, respectively. The total irradiation times for SSC1 and SSC2 are approximately 46 days and 92 days while the irradiation time for the SPVC is approximately 600 days. The temperature of the specimens was tightly controlled to 288° $\pm$ 7°C during the irradiation (Ref. 6).

A "startup experiment" with dummy capsules containing only dosimeters was performed prior to the metallurgical experiment in order to determine accurately the irradiation times needed to reach the target fluences. This experiment was also used to test the accuracy of a preliminary neutron transport calculation. Comparison of dosimetry results between the startup and the two-year experiment showed significant differences, which were traced to differences in core loadings.[7,8] A new set of transport calculations, described in the next section, was performed to account for 52 different core loadings.

NEUTRON TRANSPORT CALCULATION

Flux, fluence, and reaction rate calculations were performed for each of the three exposures (two surveillance capsules and a pressure vessel capsule) performed during the two-year metallurgical Blind Test experiment at the ORR-PSF. Motivation for these calculations was prompted by differences of up to 25% between dosimetry measurements performed in the earlier startup scoping experiment and the two-year experiment.

Following the same simplified calculational methods used in a re-analysis of the startup experiment, fission source distributions were obtained from three-dimensional diffusion theory for most of the 52 cycles active during the course of the complete experiment, combined in small groups, and the resultant ex-core group fluxes calculated by two-dimensional discrete ordinate transport theory. More details can be found in Refs. 8 and 9.

Comparisons of the ORNL-calculated dosimeter end-of-irradiation activities with HEDL measurements indicate agreement generally within 15% for the first surveillance capsule, 5% for the second, and 10% for three locations in the pressure vessel capsule, which are as good as, if not somewhat better than, comparisons in the startup experiment. The calculations thus validate the trend of the measurements in both the startup and the two-year experiments and confirm the presence of a significant cycle-to-cycle variation in the core leakage. The tape containing the unadjusted spectral fluences for each of the three exposures that can be used in the metallurgical analysis is thus considered to be accurate to within about 10%.

DOSIMETRY AND ADJUSTMENT PROCEDURES

A 10% accuracy, as quoted in the preceeding section, for the damage parameter values of the metallurgical specimen is quite sufficient for most metallurgical damage correlation studies. However, since the ORR-PSF experiment is intended to be a benchmark, higher accuracies and a more thorough study of the uncertainties is required. Thus, comprehensive statistical analyses with the use of adjustment procedures are being made by program participants to obtain complete three-dimensional fluence-spectrum maps. These maps will include not only the damage parameter values $\phi t > 1.0$ MeV, $\phi t > 0.1$ MeV (ϕt = fluence), and dpa, but also reaction rate values for all major threshold reactions. These reaction rate values are included to test dosimetry measurements from a variety of laboratories and some experimental dosimetry (e.g., damage monitors) which were not used in the adjustment procedure.

Details of the dosimetry sensors in the ORR-PSF experiment are given in Ref. 10. Summary information on the analysis of physics-dosimetry for the ORR-PSF experiment by Blind Test participants is given in Ref. 11. The measurements, which are available to date, can be found in Refs. 10 and 11. Figure 5 gives an overview of the methodology used to obtain the ORNL three-dimensional fluence map discussed in this paper.

Both the LSL-M2 and FERRET adjustment procedures[12,13] have been used for the evaluation, but only the ORNL results are discussed in this paper. In it, data from the ORNL transport calculation were combined with the HEDL dosimetry from the gradient sets (GS), back bone sets (BB), and gradient strips along the Charpy specimens (see Fig. 4 and Ref. 10). Adjusted damage parameter values at capsule centers are listed in Table 1, together with uncertainties. Values at other positions of the capsules are determined through a cosine-exponential fit

$$P(X,Y,Z) = P_0 \cos B_X(X-X_0) \cos B_Z(Z-Z_0)\, e^{-\lambda(Y-Y_0)} \qquad (1)$$

where $P(X,Y,Z)$ is the value of the damage parameter in question at (X,Y,Z). (For the orientation of the coordinate system, see Fig. 6.) There is one set of fitting parameters for each capsule and each damage parameter. The values are listed in Table 2. This interpolation-extrapolation introduces additional uncertainties, which increase with increasing distance from the capsule centers, up to about 5%. More details can be found in Ref. 14.

STATISTICAL EVALUATION OF THE METALLURGICAL TESTS

The need for rigorous statistical evaluation of the experimental results is not restricted to dosimetry and neutron fluence determination. The high standard for accuracy and reliable determination of uncertainties applies also to the metallurgical test results. The primary source for the Blind Test comparisons is the Charpy test results. The raw Charpy data[4] are fitted to continuous curves, impact energy vs. test temperature, in order to determine the shift of nil-ductility temperature (ΔNDT) and upper shelf energy (ΔUSE) with increasing damage fluence. Hand-drawn fits are used in Refs. 4 and 5 but without assigned uncertainties. The HEDL evaluation will make use of hand-drawn and least squares fit.[15] In the ORNL evaluation,[16] a computer fit CV81* was used. This fitting procedure uses separate curves for NDT and USE and is, therefore, more flexible than hyperbolic tangent or error function approximations which are commonly used for computer fits. (These fits were used by some Blind Test participants.) There are no obvious differences between the CV81 evaluations and the hand-drawn fits in Ref. 5, as can be seen in Table 5, but the statistical computer fit allows the calculation of uncertainties. Table 3 lists the different materials used in the metallurgical irradiation and their chemical composition. A summary of the CV81 results is given in Table 4. Details of the procedure are given in Ref. 16.

DISCUSSION OF THE BLIND TEST RESULTS

The participants of the Blind Test received the following information[3]:**

1. Calculated 102-group flux-spectrum, exposure rate parameters, and dosimeter reaction rates for the SSC1, SSC2, and SPVC 0-T PV surface, 1/4T wall, 1/2T wall, 3/4T wall, and SVBC positions. (This calculation is different from the one described in this paper, in that it was done for the "startup" experiment with somewhat different core configuration.)

2. The SSC1 measured in-situ dosimetry as-built information, exposure time history, and post-irradiation sensor results.

3. The SSC1, SSC2, and SPVC 0-T, 1/4T, and 1/2T measured in-situ Co-Al alloy bare and gadolinium-covered sensor results used to determine two additional low-energy group flux-spectral values for the thermal and thermal to 9.8×10^{-2} MeV energy ranges.

4. The SSC1, SSC2, and SPVC measured metallurgical specimen exposure time histories.

5. The SSC1, SSC2, and SPVC measured metallurgical specimen temperature time histories.

*CV81 is a linear least squares procedure, although linear combinations of non-linear functions can be used.

**This information will be made available to those who have an interest in making their own analysis, predictions, and contributions to the PSF experiment studies.

6. The SSC1, SSC2, and SPVC as-built metallurgical specimen dimensional and placement information.

7. The SSC1 metallurgical specimen heat treatment, chemistry, and measured un-irradiated and irradiated properties for different steels.

Participants were asked to predict both the damage parameter values and the metallurgical test results in the SSC2 and SPVC capsules.

To determine damage parameter values, most participants used the calculated fluences normalized with measurements at the SSC1. Adjustment procedures and cosine-exponential fits were also used by some participants. Uncertainties were quoted by some participants and were all on the optimistic side. None of the quoted figures for damage parameter values differed by more than 30% in either direction from the ORNL evaluation, and 65% of the values were within $\pm$10% of ORNL. Differences in the damage parameter determinations had very little impact on the determination of radiation damage. That is, some participants who predicted low damage parameter values quoted high embrittlement values and vice versa.

The prediction of materials property changes, primarily NDT and USE for Charpies vs. fluence, were all based on one of the two formulas

$$\Delta M = C\,(\phi t)^{a} \quad , \text{ or} \tag{2}$$

$$\Delta M = C\,(\phi t)^{(a - b\cdot\log(\phi t))} \tag{3}$$

with ΔM materials change and ϕt fluence > 1.0 MeV (or some other damage parameter such as dpa). C is a "chemistry factor" which is either determined explicitly from the chemical composition and a data base or used as a scale factor based on the SSC1 results. Formula (2) with a = 0.5 is used in NRC Reg. Guide 1.99.[17] Other (usually smaller) values of a are used by some participants as obtained from their data bases. The "Guthrie formula" (3)[18] replaces the straight line in a log-log plot by a parabola, taking into account that damage "saturates" faster than a single exponent would indicate. The parameters a and b were either the ones originally obtained by Guthrie or modifications obtained from their own data bases.

The MEA and ORNL 41J-ΔRT_{NDT} results were compared with Blind Test predictions and summarized in Table 5. Lowest and highest predictions are strikingly close to each other and mostly symmetrically distributed relative to the experimental values. The largest deviation, between measurements and prediction, is for the weld code (R) in the SPVC capsules. The high nickel content places this material outside the data bases from which the prediction formulas were obtained. Aside from this material, no consistent biases nor major deviations between predictions and experimental values were found. Also, none of the prediction formulas was consistently superior.

The explanation for this outcome can be found in the graphs, Figs. 7-12, which plot the experimental shifts against the damage parameter dpa. The data points for each of these graphs can be fitted to a variety of straight lines (2) or slightly curved parabolas (3) within the indicated uncertainty bounds. Since the actual curves show quite different slopes and curvatures for different materials, no single formula will give a good fit for all of them. On the other hand, large uncertainties and variability within the material, due to such factors as heat treatment or position and direction of the specimen, will make it difficult to define any single unique approximation, such as (2) and (3).

To explain the differences in trend curves for different materials quantitatively, much more needs to be known about the physical processes which lead to radiation embrittlement. This can be obtained only with more detailed studies of the microstructure. The current information from this experiment and other metallurgical data bases is purely phenomenological. Any attempt to fit such data to some simple model results in fairly large data scatter which is not likely to improve by adding more parameters to the model. In the Blind Test predictions, a 1σ uncertainty of approximately $\pm$20°C for ΔNDT was observed and this uncertainty was about the same for different prediction formulas. The uncertainty is likely to be somewhat larger for predictions based on surveillance specimen in commercial power reactors. More work is needed to establish reliable safety margins in these cases.[20]

It is informative to compare the metallurgical results from the ORR-PSF experiment with the predictions of the old Reg. Guide 1.99,[17] which is based on formula (2) and the proposed revision[19] which is based on the Guthrie formula (3).[18] The chemistry factor in the old Guide is a linear combination of copper and phosphorus, whereas the new version has the chemistry factor in tabular form with copper and nickel as entries, separate for plate materials and welds. By dividing the Charpy shift by the chemistry factor, all materials can be compared on the same basis having only one upper bound curve for all materials in either Reg. Guide. As the graph in Fig. 13 shows and for the fluence range of 7×10^{18} to 5.5×10^{19} n/cm^2 (E > 1 MeV), the old Reg. Guide is not a good representation of correlation between chemistry, fluence, and NDT shift, since the data points are widely scattered both above and below the boundary line. The revised Guide shows much less scatter and data points from the same material appear to follow the Guthrie curve much better than the square root line in Fig. 13. A safety margin of 34°F for base metal and 56°F for welds which was suggested in (19) was subtracted from the data in Fig. 14 so that most points now lie safely below the boundary line. The two exceptions are the code (K) and (R) materials. Both have higher nickel content than any of the steels in the data base from which the chemistry table was generated.[18,19] It follows that higher safety margins must be imposed on such materials. Or, alternatively, metallurgical irradiation experiments to several different fluences must be performed for such materials to determine the proper chemistry (normalization) factor.

The predictions based on the Reg. Guide are made with fluence (E > 1 MeV) as exposure parameter. Using fluence (E > 0.1 MeV) or dpa changes the values slightly but by less than 10%.[16] The attentuation formula in Ref. 19

$$\Delta NDT_{\text{wall interior}} = \Delta NDT_{\text{wall surface}}\, e^{-0.065x} \qquad (4)$$

where x is the distance of the interior point to the surface in inches, gives also slightly higher values than the predictions based on fluence (E > 1.0 MeV), generally very close to the dpa values. The significance of spectral effects will be discussed below.

APPLICATION TO PV SURVEILLANCE AND REGULATORY PROCEDURES

These preliminary PSF metallurgical Blind Test comparisons show that the various embrittlement prediction formulas are adequate as rough approximations, but that none captures the complex and not-well-understood correlation between radiation embrittlement and fluence, fluence rate, neutron spectrum, chemistry, heat treatment and, perhaps, other factors. None of the current prediction formulas appears clearly superior, but the Guthrie formula captures somewhat better the saturation effect at higher fluences, since the quadratic term adds more flexibility. Improvements are possible in the following areas:

1. Realistic uncertainties need to be established in conjunction with prediction formulas. The Blind Test comparison gives some clues for the size of uncertainties (Table 5). Larger data bases and statistical evaluations, which are more specifically directed towards uncertainties, are needed for more definite results (see Ref. 20).

2. Prediction formulas which were derived from a data base may not be valid for materials whose composition is outside the range of the data base. Substantially higher safety margins must be applied to such materials or test irradiations performed to establish trend curves for the particular material.

EFFECTS OF IRRADIATION TEMPERATURE, FLUENCE RATE, AND NEUTRON ENERGY SPECTRUM

Current damage prediction formulas consider only chemistry and fluence as determining factors. It is well known that ΔNDT is also strongly dependent on the temperature during irradiation, but few quantitative data are available. Most irradiation experiments, including PSF, are performed at only one temperature, either ambient or at 550°F, the operating temperature of power reactors. Temperatures inside surveillance capsules are impossible to monitor during operation and only rough bounds can be determined. Statistical evaluations of the HSST experiments[21] indicate a temperature sensitivity of about 0.5 to 1.5 degree increase in NDT per degree decrease in irradiation temperature. These values are very tentative and may be dependent on the material and fluence. They may serve, however, as guidelines for assessing uncertainties in ΔNDT due to uncertainties in the irradiation temperature.

A dependence of damage on fluence rate has been suspected for some time and the PSF experiment has partly been designed to detect such effects.[22] The Figs. 7-12 show indeed some definite differences in damages between the high fluence rate SSC capsules and the low rate wall capsules at the same fluence levels. These differences appear to confirm qualitatively the model of G. R. Odette[23] for the damage mechanism, but no quantitatively conclusive results can be obtained from the PSF data.[15] The effects are small, barely exceeding the experimental uncertainties. It may be necessary, however, to consider rate effects, when test reactor results are to be applied to damage predictions in power reactors.

The effects of different neutron energies to the total damage are even more difficult to determine. As G. L. Guthrie[15] pointed out, there are only three truly independent spectra in the PSF and all others can be represented as linear combinations of the three. Thus, spectral effects derived from the PSF can be described by at most two parameters (e.g., fast and thermal fluence). In reality, no clear distinction is found in the correlation between fluence and damage for different exposure parameters such as fluence ($E > 1.0$ MeV) and dpa, due to the uncertainties in the data. Thus, the theoretical superiority of dpa cannot be supported experimentally by the PSF experiment.[15] However, the use of dpa leads to somewhat more conservative damage predictions and is, therefore, recommended. It is the basis for the extrapolation formula (4).[19]

RECOMMENDATIONS FOR FUTURE RESEARCH

The PSF experiment has essentially confirmed the broad trends for radiation damage which had been determined from existing data collections. Underneath these general trends lies, however, a bewildering variety of detailed structures which reflect the complexity of the damage mechanism and contributes to substantial uncertainties in predicting radiation damage. Any improvements in prediction will come only from a better understanding of the effects of radiation to the microstructure of the material and from a precise quantification of these effects. Future research planning should consider experiments that are directed to a better understanding of the embrittlement mechanism. For example, small angle neutron scattering can give quantitative information on the changes of the microstructure from neutron irradiation. Information from these techniques complemented by mechanical test procedures will give a better understanding of changes on the mechanical properties produced by changes in the microstructure.[24,25]

REFERENCES

1. W. N. McElroy, et al., LWR-PV-SDIP 1983 Annual Report, NUREG/CR-3391, Vol. 3, HEDL-TME 83-23, U.S. Nuclear Regulatory Commission, Washington, DC, 1984.

2. ASTM Standard E706, "Master Matrix for LWR Pressure Vessel Surveillance Standards," Annual Book of ASTM Standards, Vol. 12.2, American Society for Testing and Materials, Philadelphia, PA, Current Edition.

3. W. N. McElroy and F. B. K. Kam, eds., PSF Blind Test Instructions and Data Packages, distributed to Blind Test participants, March 22, 1983.

4. J. R. Hawthorne, B. H. Menke, and A. L. Hiser, Light Water Reactor Pressure Vessel Surveillance Dosimetry Improvement Program: Notch Ductility and Fracture Toughness Degradation of A 302-B and A 533-B Reference Plates from PSF Simulated Surveillance and Through-Wall Irradiation Capsules, NUREG/CR-3295, MEA-2017, Vol. 1, U.S. Nuclear Regulatory Commission, Washington, DC, 1983.

5. J. R. Hawthorne and B. H. Menke, Light Water Reactor Pressure Vessel Surveillance Dosimetry Improvement Program: Notch Ductility and Tensile Strength Determinations for PSF Simulated Surveillance and Through-Wall Irradiation Capsules, NURFG/CR-3295, MEA-2017, Vol. 2, U.S. Nuclear Regulatory Commission, Washington, DC, 1983.

6. L. F. Miller, Analysis of Temperature Data From the ORR-PSF Irradiation Experiment: Methodology and Computer Software, NUREG/CR-2273, ORNL/TM-7766, U.S. Nuclear Regulatory Commission, Washington, DC, 1981.

7. H. Tourwe, et al., "Interlaboratory Comparison of Fluence Neutron Dosimeters in the Frame of the PSF Start-Up Measurement Program, Proc. of the 4th ASTM-EURATOM Symposium on Reactor Dosimetry," Gaithersburg, MD, March 22-26, 1982, NUREG/CP-0029, Vol. 1, pp. 159-168, U.S. Nuclear Regulatory Commission, Washington, DC, 1982.

8. R. E. Maerker and B. A. Worley, Activity and Fluence Calculations for the Startup and Two-Year Irradiation Experiments Performed at the Poolside Facility, NUREG/CR-3886, ORNL/TM-9265, U.S. Nuclear Regulatory Commission, Washington, DC, 1984.

9. R. E. Maerker and B. A. Worley. "Calculated Spectral Fluences and Dosimeter Activities for the Metallurgical Blind Test Irradiations at the ORR-PSF," presented at the 5th ASTM-EURATOM Symposium on Reactor Dosimetry, Geesthacht, FRG, September 24-28, 1984.

10. E. P. Lippincott, et al., Fabrication Data Package for HEDL Dosimetry in the ORR Poolside Facility LWR Pressure Vessel Mock-Up Irradiation, HEDL-TC-2065, Hanford Engineering Development Laboratory, Richland, WA, 1981.

11. G. L. Guthrie, E. P. Lippincott, and E. D. McGarry, Light Water Reactor Pressure Vessel Surveillance Dosimetry Improvement Program: PSF Blind Test Workshop Minutes, Hanford Engineering Development Laboratory, Richland, WA, April 9-10, 1984.

12. F. W. Stallmann, "LSL-M1 and LSL-M2: Two Extensions of the LSL Adjustment Procedure for Including Multiple Spectrum Locations," presented at the 5th ASTM-EURATOM Symposium on Reactor Dosimetry, Geesthacht, FRG, September 24-28, 1984.

13. F. A. Schmittroth, FERRET Data Analysis Code, HEDL-TME 79-40, Hanford Engineering Development Laboratory, Richland, WA, September 1979.

14. F. W. Stallmann, Determination of Damage Exposure Parameter Values in the PSF Metallurgical Irradiation Experiment, NUREG/CR-3814, ORNL/TM-9166, U.S. Nuclear Regulatory Commission, Washington, DC, 1984.

15. G. L. Guthrie and E. P. Lippincott, "HEDL Analysis of the PSF Experiment," presented at the 5th ASTM-EURATOM Symposium on Reactor Dosimetry, Geesthacht, FRG, September 24-28, 1984.

16. F. W. Stallmann, Statistical Evaluation of the Metallurgical Test Data in the ORR-PSF-PVS Irradiation Experiment, NUREG/CR-3815, ORNL/TM-9207, U.S. Nuclear Regulatory Commission, Washington, DC, 1984.

17. Regulatory Guide 1.99, Effects of Residual Elements on Predicted Radiation Damage to Reactor Vessel Materials, Rev. 1, U.S. Nuclear Regulatory Commission, Washington, DC, 1977.

18. G. L. Guthrie, "Charpy Trend Curves Based on 177 PWR Data Points," LWR-PV-SDIP Quarterly Progress Report, April-June 1983, NUREG/CR-3391, Vol. 2, U.S. Nuclear Regulatory Commission, Washington, DC, 1983.

19. P. N. Randall, "Regulatory Position," Attachment to the Minutes of the ASTM E10.02 Meeting, (draft), San Diego, CA, January 1984.

20. G. L. Guthrie, "Uncertainty Considerations in Development and Application of Charpy Trend Curve Formulas," presented at the 5th ASTM-EURATOM Symposium on Reactor Dosimetry, Geesthacht, FRG, September 24-28, 1984.

21. F. W. Stallmann, Curve Fitting and Uncertainty Analysis of Charpy Impact Data, NUREG/CR-2408, ORNL/TM-8081, U.S. Nuclear Regulatory Commission, Washington, DC.

22. F. W. Stallmann, "PCA-PSF Pressure Vessel Surveillance Program: Accuracy Requirements and Uncertainty Analysis, CAPRICE79, Proc. IAEA Technical Committee Meeting, KFA, Juelich, September 24-27, 1979.

23. G. R. Odette, "On the Dominant Mechanism of Irradiation Embrittlement of Reactor Pressure Vessel Steels," Scripta Metalurgica, 17, pp. 1183-1188, 1983.

24. R. Wagner, "The Influence of Copper on the Radiation-Induced Defect Structure in Ferritic Alloys," presented at the 5th ASTM-EURATOM Symposium on Reactor Dosimetry, Geesthacht, FRG, September 24-28, 1984.

25. D. Schwahn, D. Pachur, and J. Schellen, Neutron Scattering on Neutron Irradiated Steel, Jul-1543, October 1978.

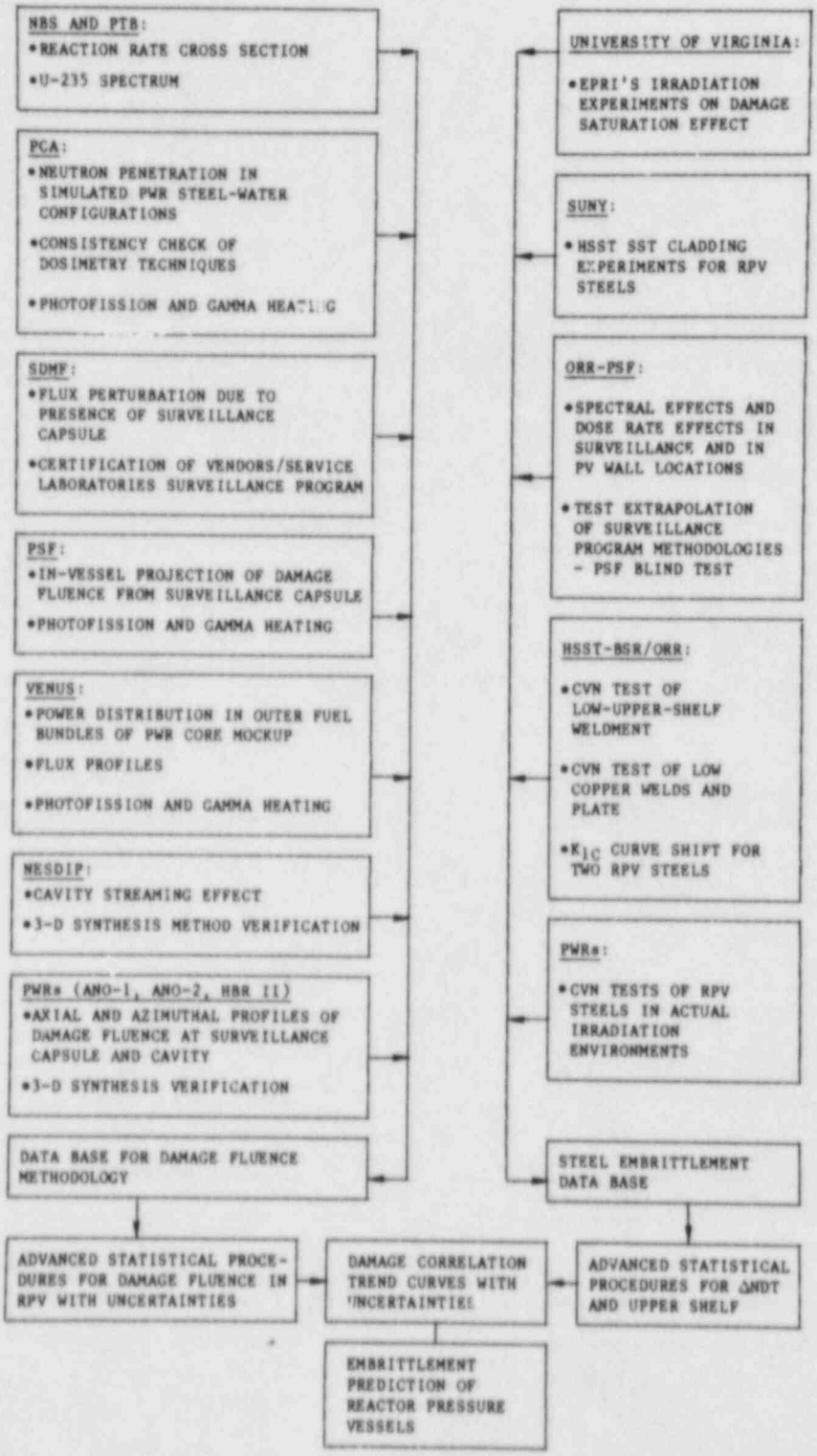

Fig. 1. Benchmark experiments in the framework of the LWR Surveillance Dosimetry Improvement Program.

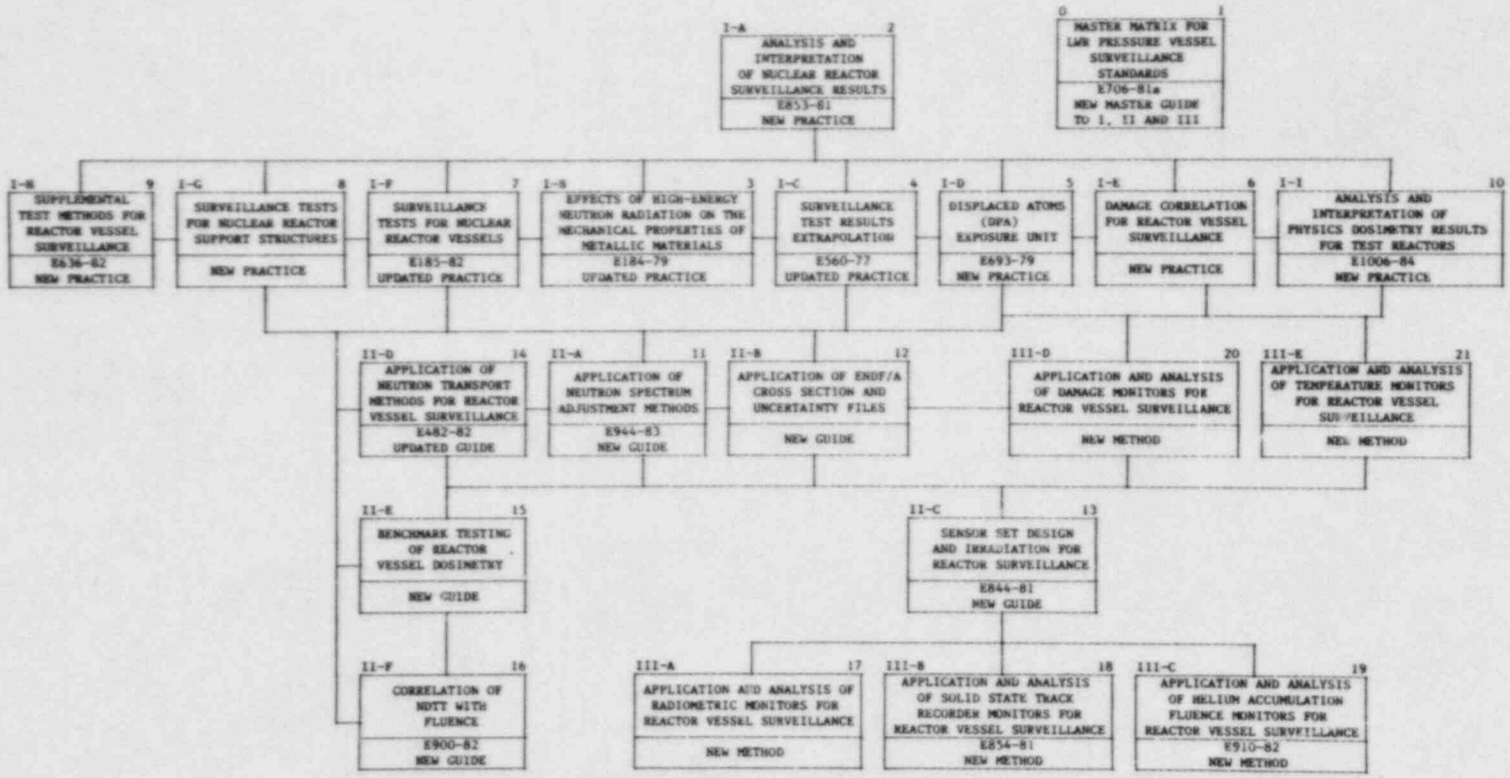

Fig. 2. ASTM Standards for surveillance of nuclear reactor pressure vessels.

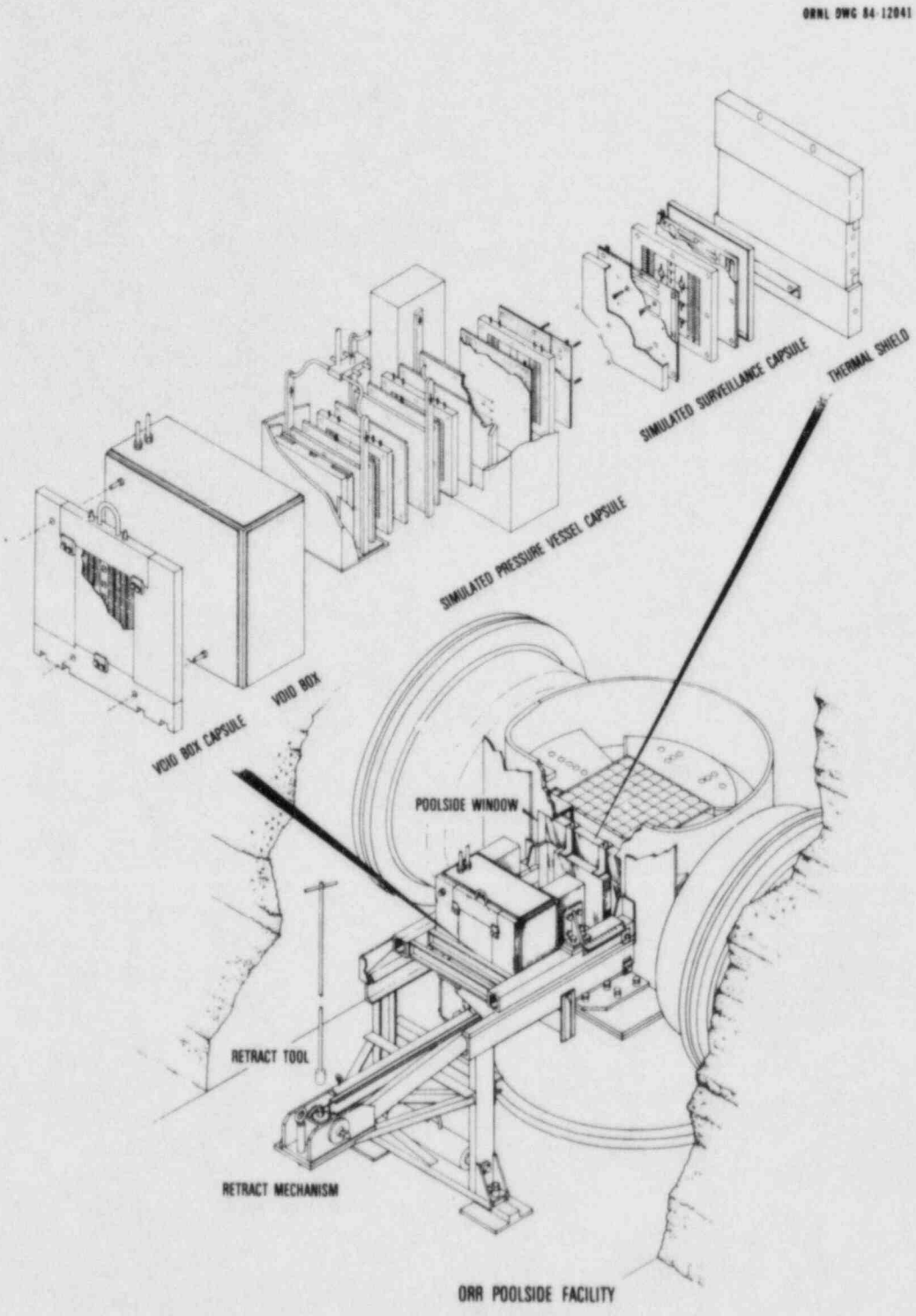

Fig. 3. ORR-PSF Irradiation Facility.

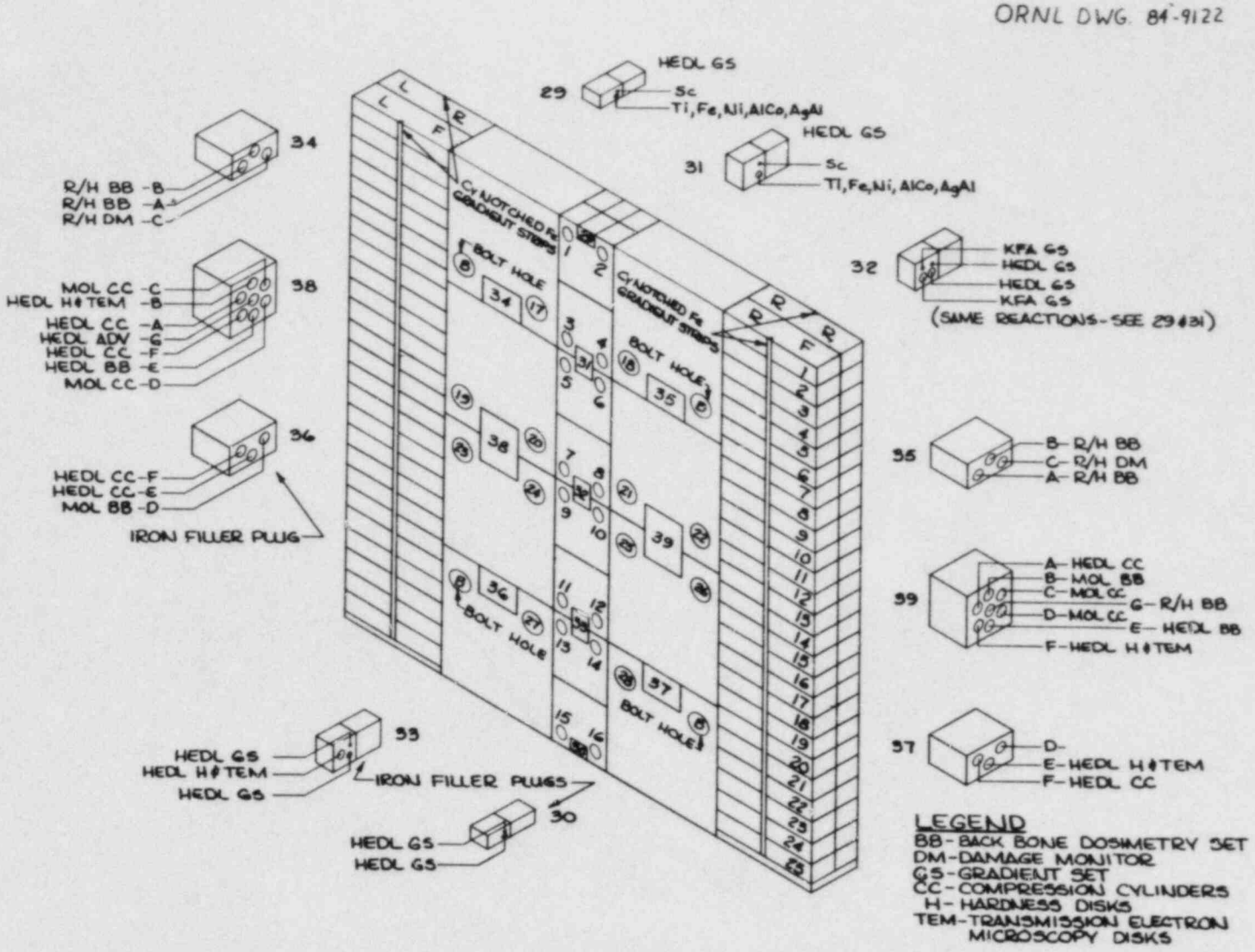

Fig. 4. Illustration of a typical dosimeter and metallurgical specimen assembly in the irradiation capsules.

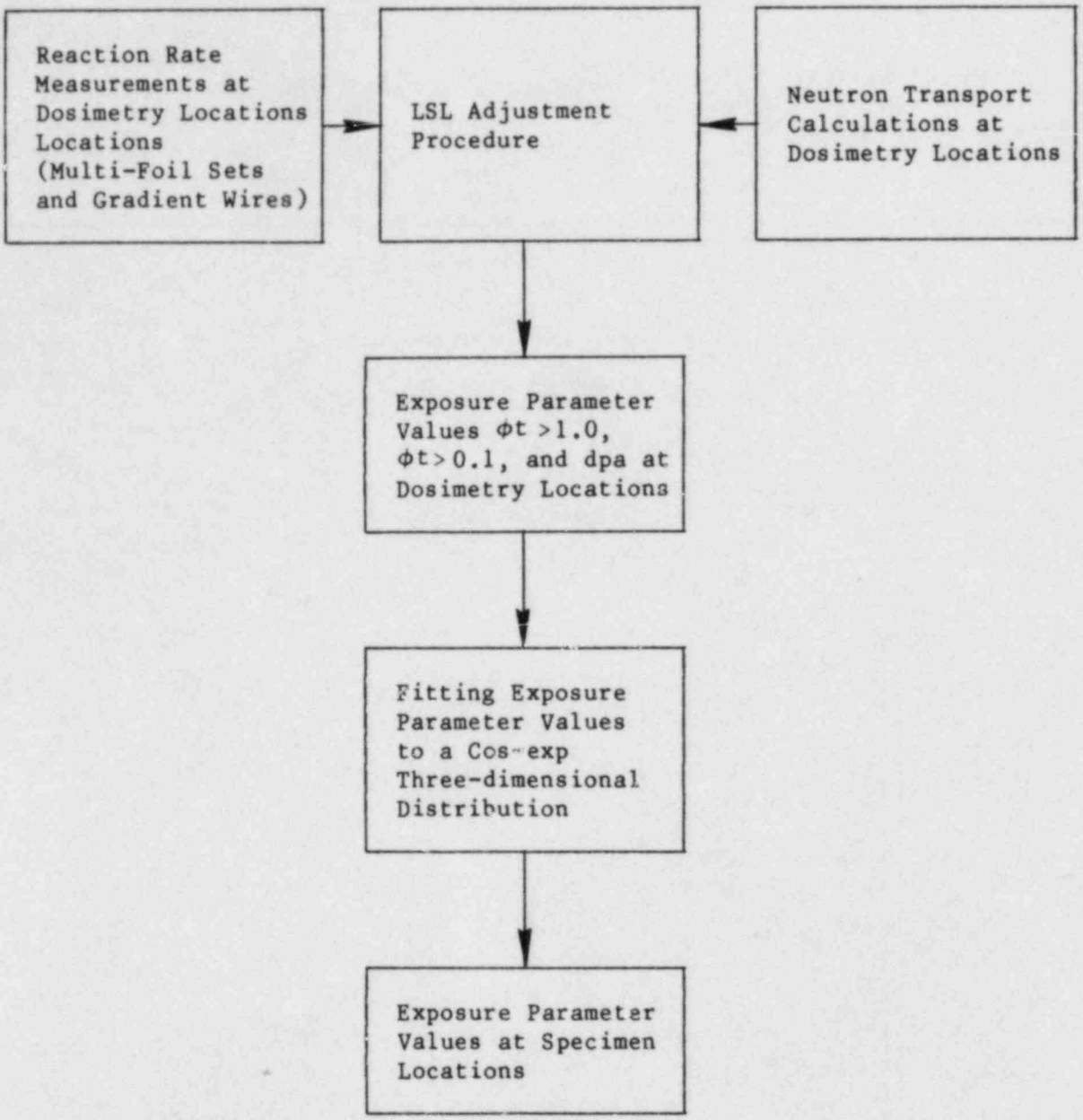

Fig. 5. Methodology for the determination of exposure parameter values and uncertainties.

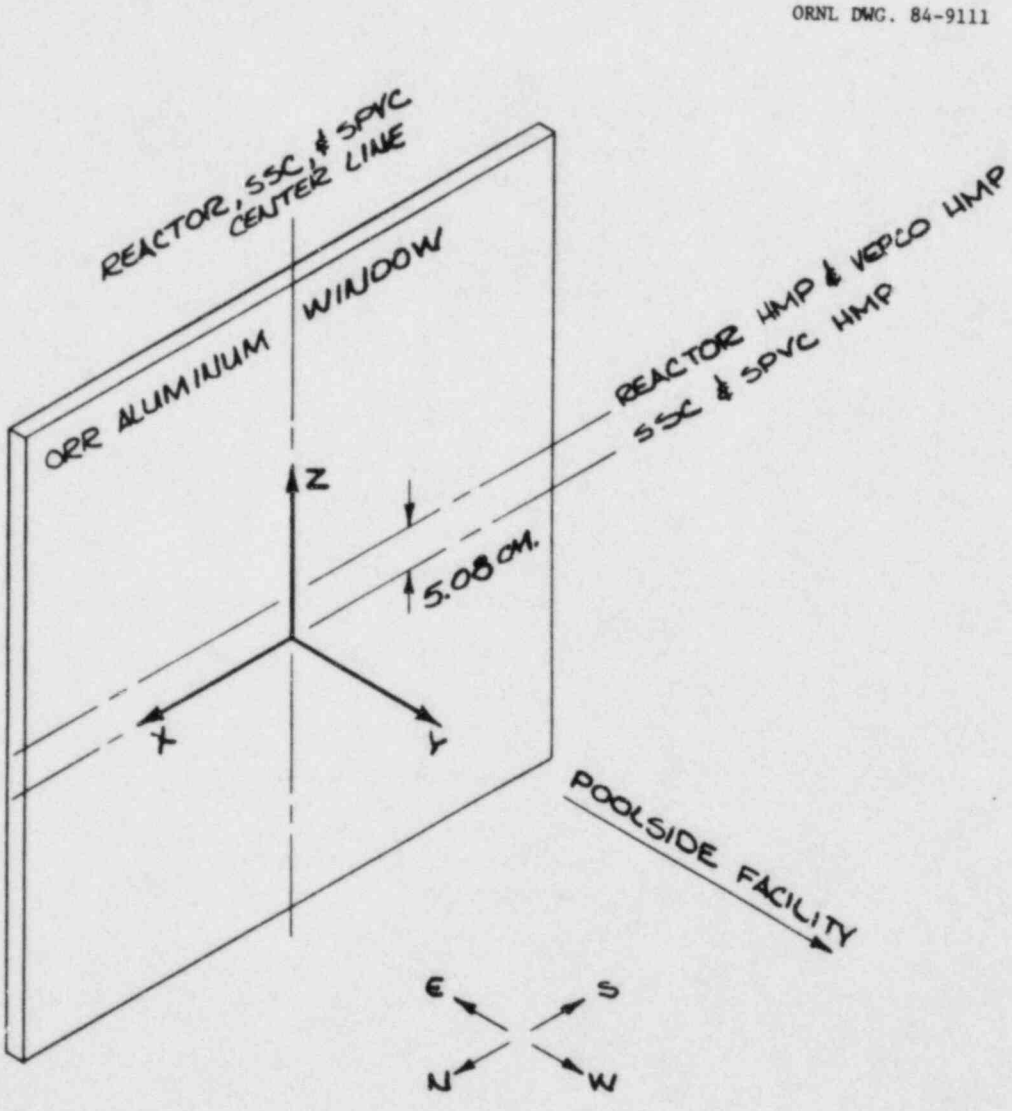

Fig. 6. Coordinate system for the ORR-PSF metallurgical experiment.

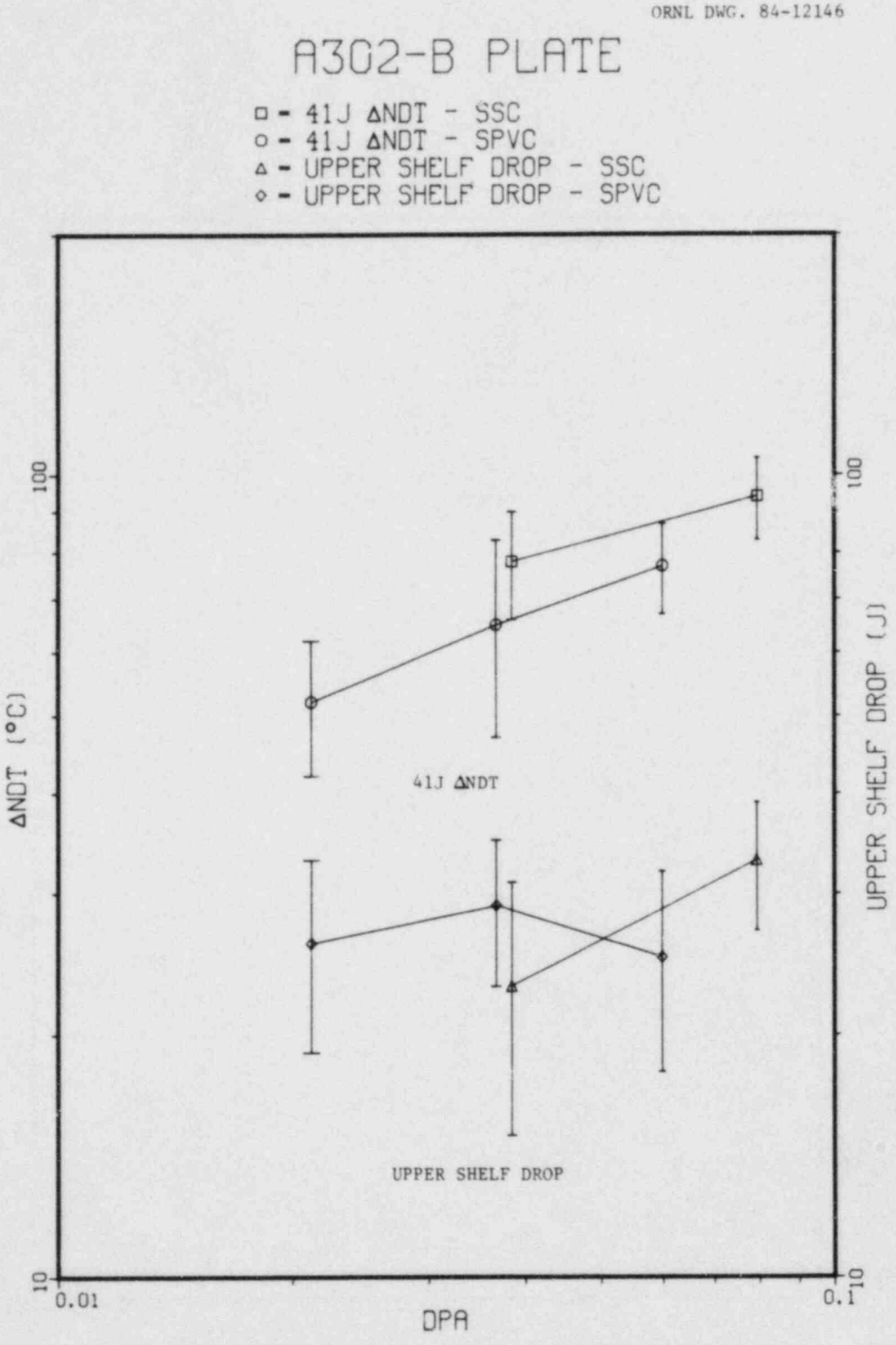

Fig. 7. ΔNDT and upper shelf drop vs. dpa, A302-B plate.

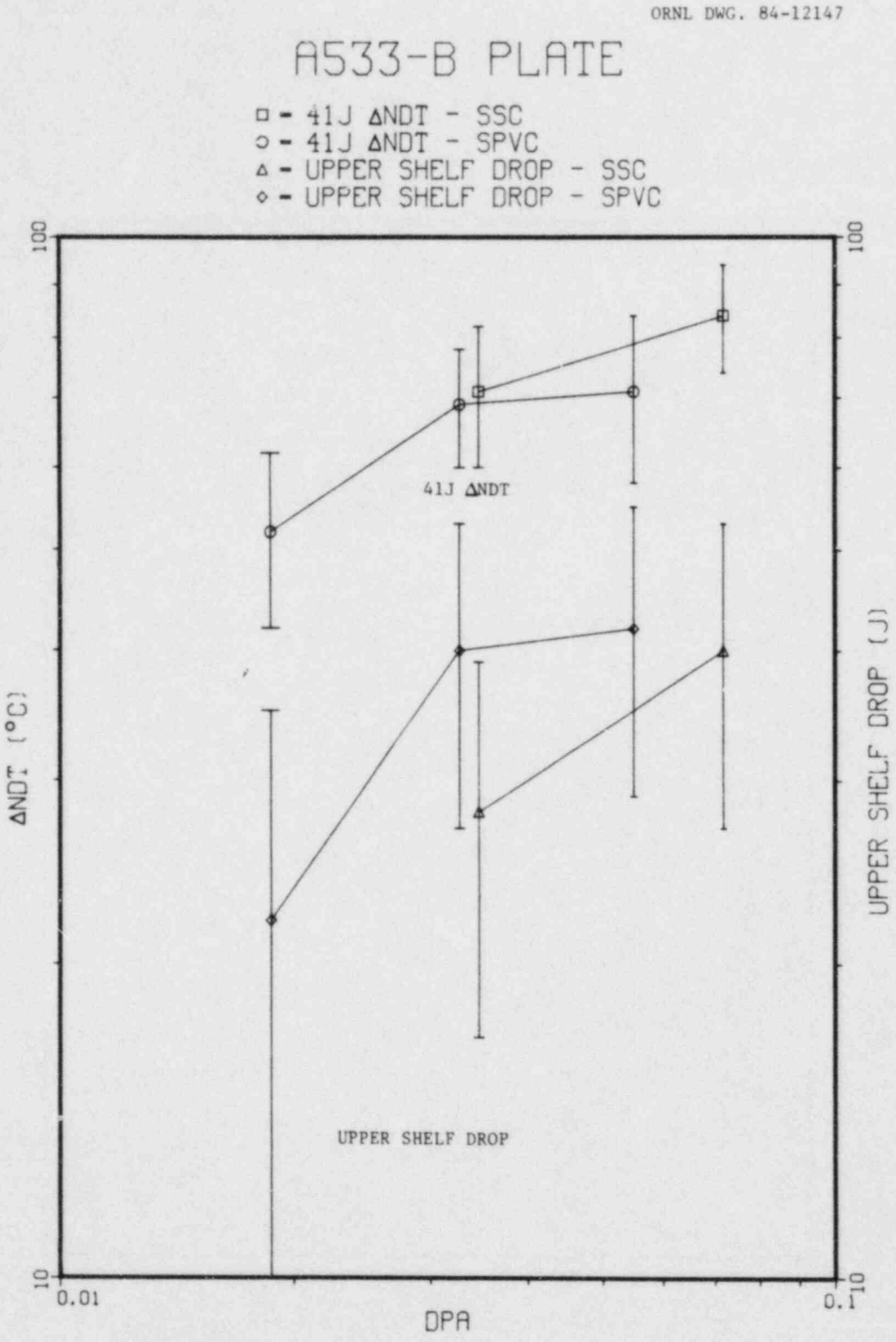

Fig. 8. ΔNDT and upper shelf drop vs. dpa, A533-B plate.

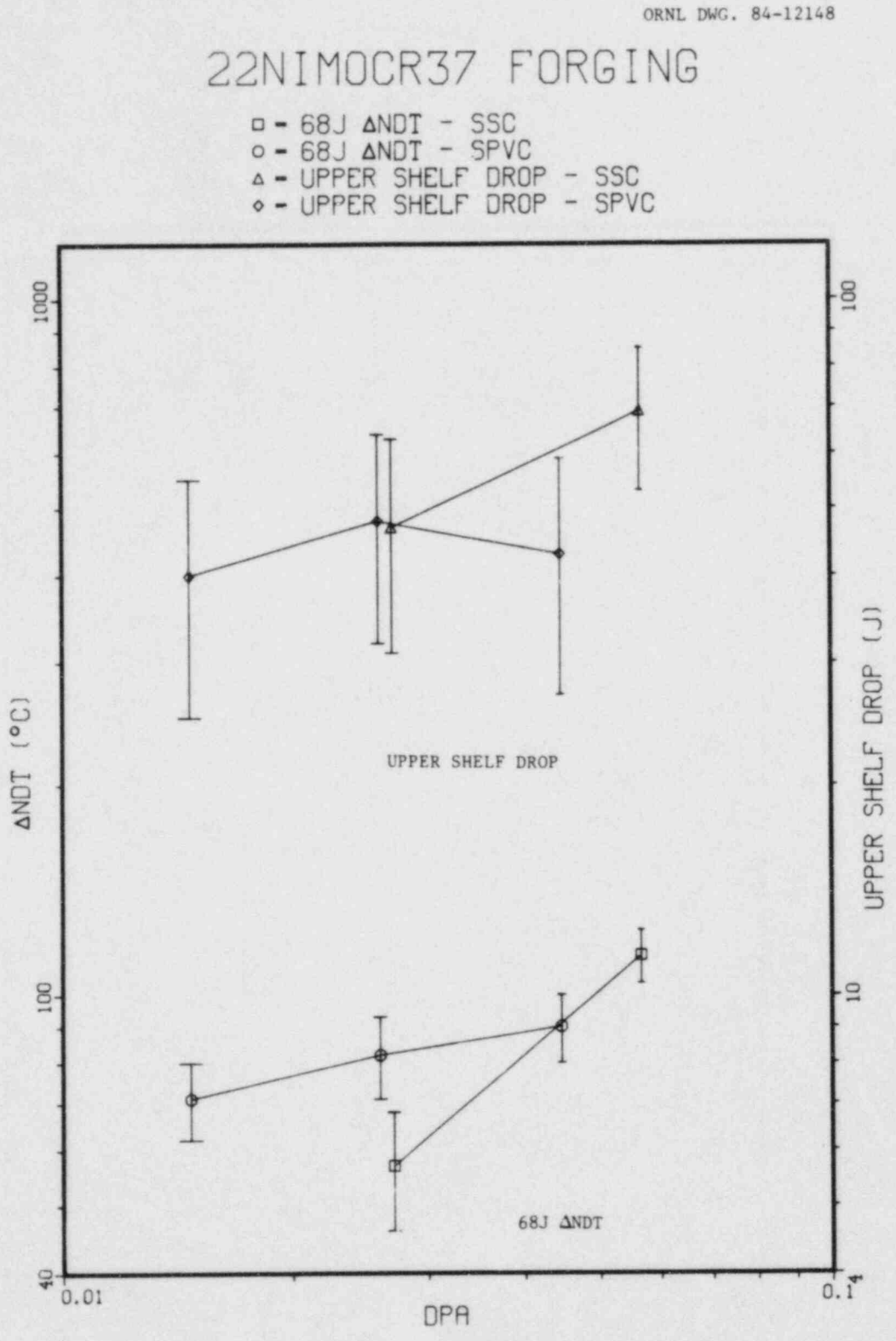

Fig. 9. ΔNDT and upper shelf drop vs. dpa, 22NiMoCr37 forging.

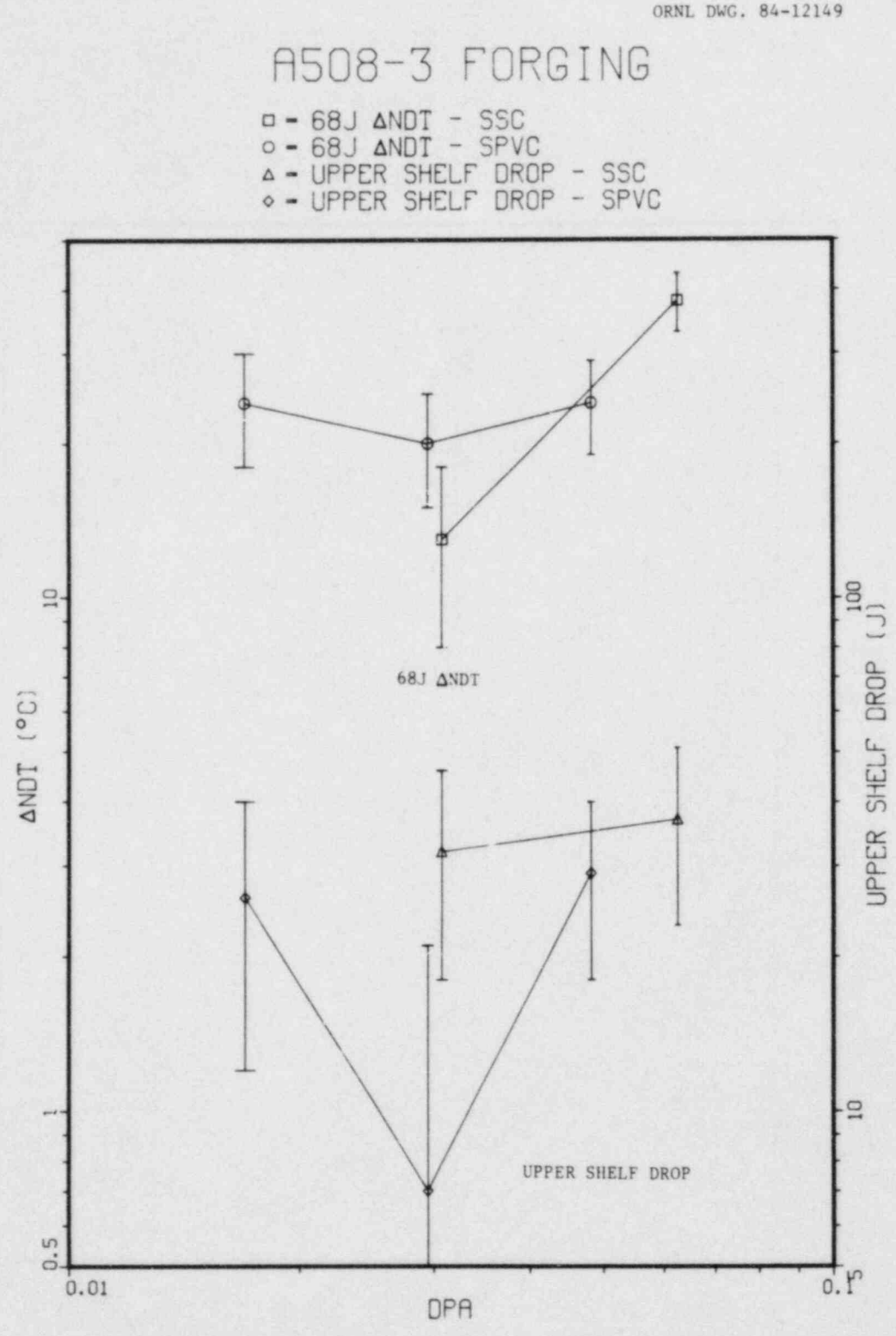

Fig. 10. ΔNDT and upper sheif drop vs. dpa, A508-3 forging.

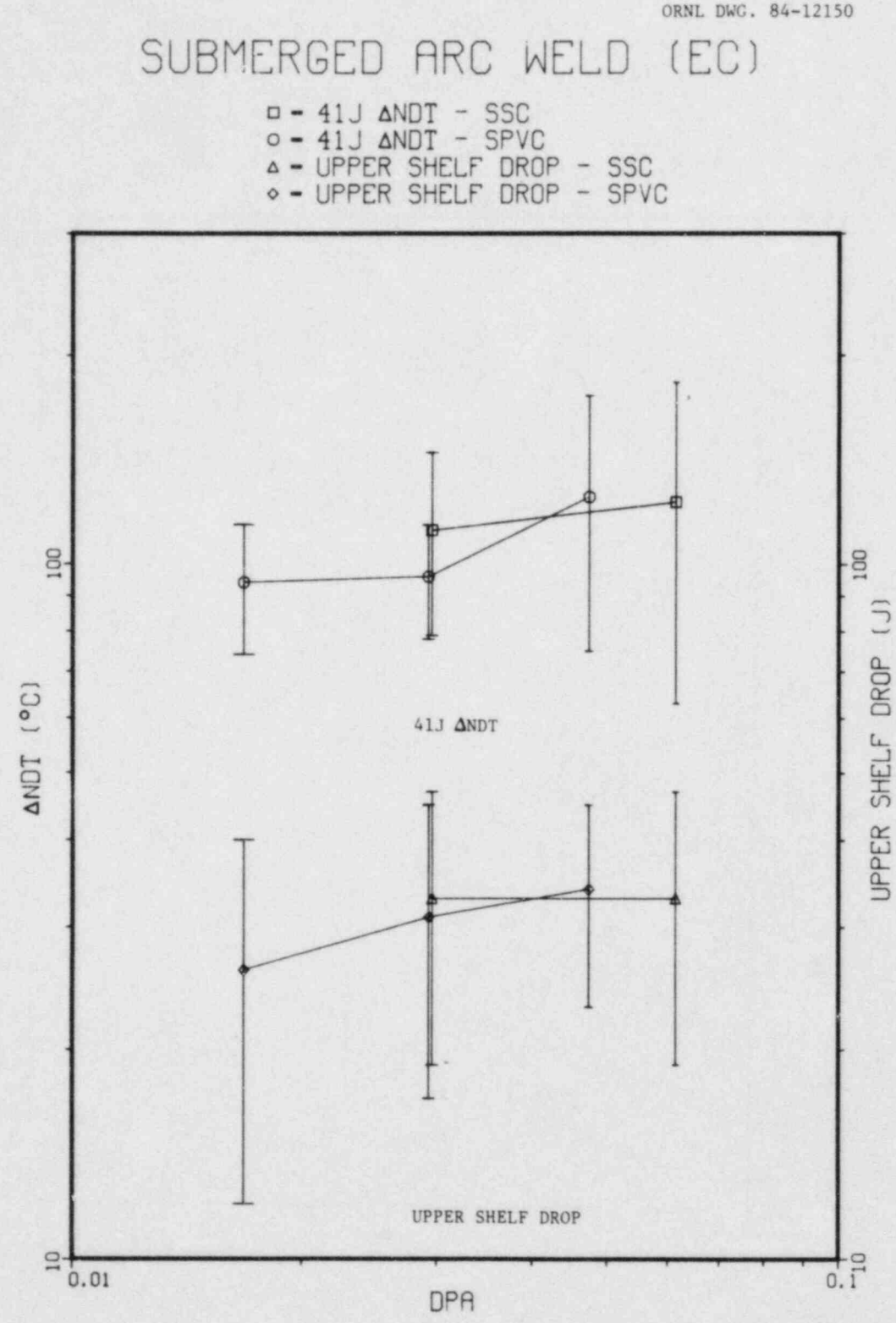

Fig. 11. ΔNDT and upper shelf drop vs. dpa, submerged arc weld (EC).

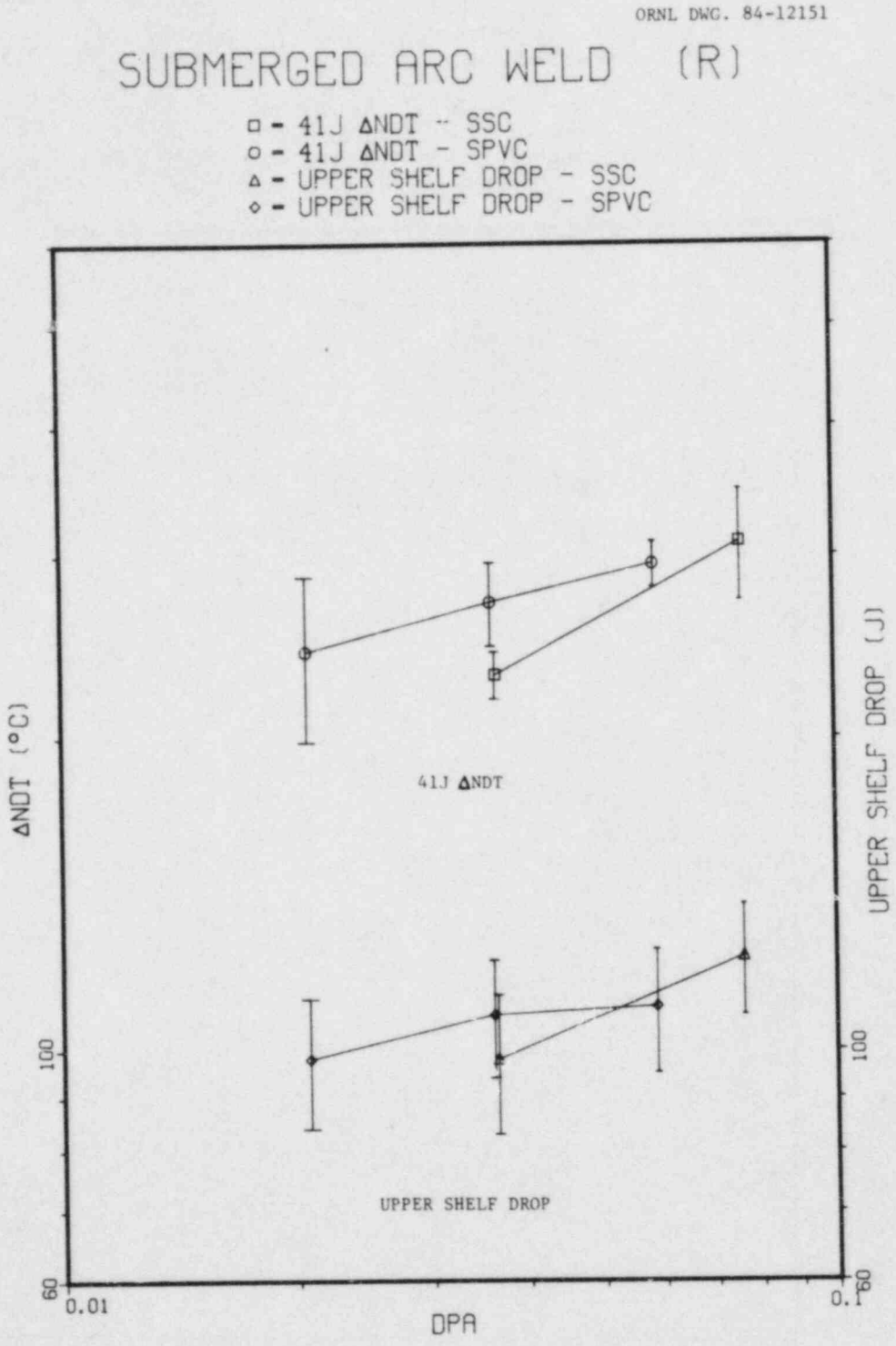

Fig. 12. ΔNDT and upper shelf drop vs. dpa, submerged arc weld (R).

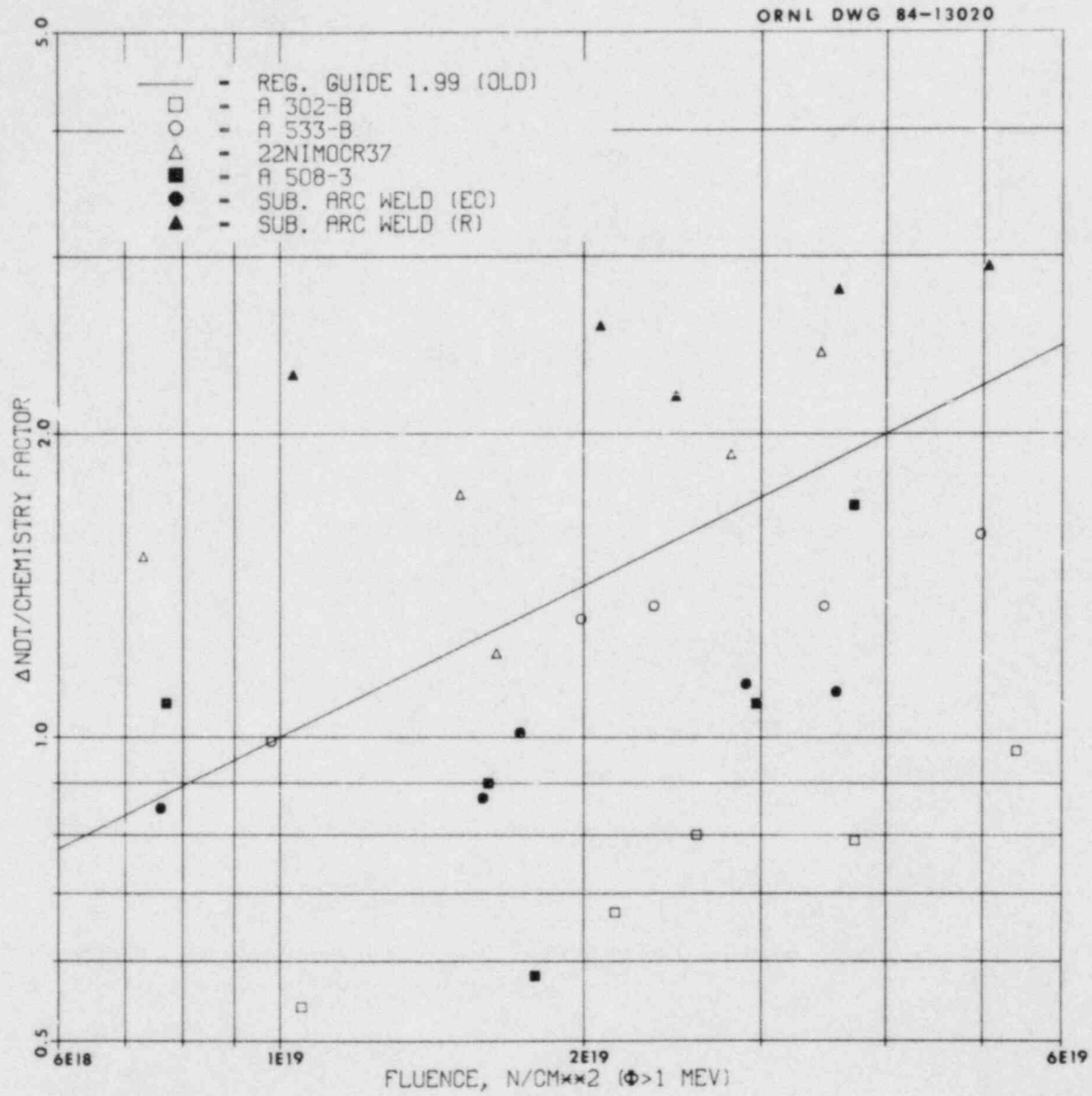

Fig. 13. Positions of ORR-PSF Charpy data relative to Reg. Guide 1.99. Data are adjusted for chemistry factors. Data above the line are underpredicted.

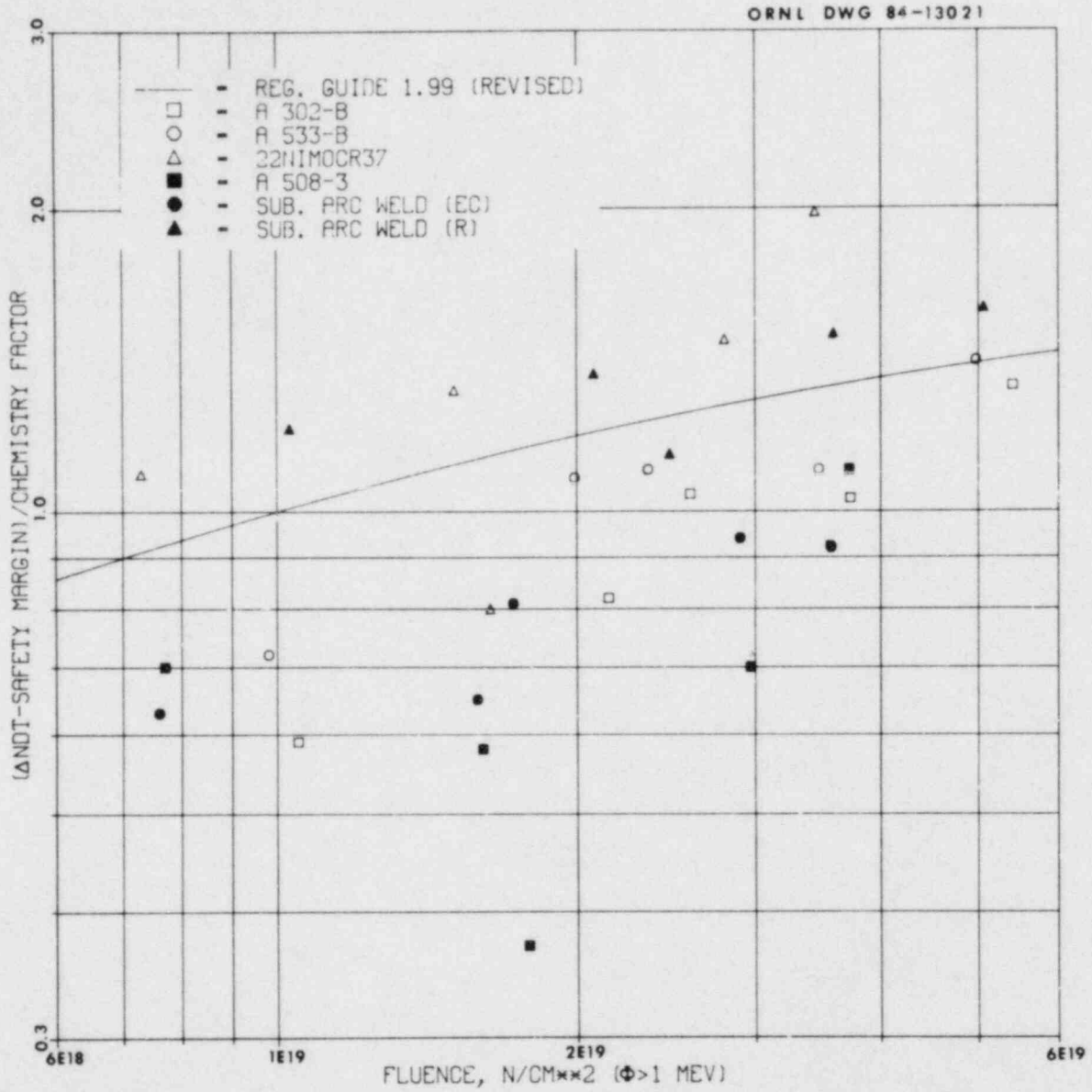

Fig. 14. Positions of ORR-PSF Charpy data relative to the revised Reg. Guide 1.99 (Guthrie formula). Data are adjusted for chemistry factors, and safety margin is added. Data above the line exceed predictions including safety margin.

Table 1. Fluences and dpa at capsule centers

	ϕ>1.0 MeV	Std. dev. (%)	ϕ>0.1 MeV	Std. dev. (%)	ϕ<0.4 eV	Std. dev. (%)	ϕ_{total}	Std. dev. (%)	dpa (10^{-2})	Std. dev. (%)
SSC1 H4	2.56*	5.1	7.74	5.8	1.26	7.4	14.20	5.8	4.07	4.9
SSC2 H9	5.50	5.1	16.84	5.8	2.79	7.4	30.55	5.5	8.80	4.9
0-T H14	4.10	5.1	12.26	5.8	6.29	7.6	27.66	5.8	6.56	4.9
1/4T H19	2.21	5.2	8.98	6.0	0.84	7.9	14.75	5.5	4.13	5.2
1/2T H24	1.05	5.4	5.83	6.0	0.27	8.3	9.17	5.6	2.39	5.4

*Read values for ϕ>1.0 MeV, ϕ>0.1 MeV, ϕ<0.4 eV, and ϕ_{total} as 2.56×10^{19} neutrons/cm^2, etc.

Table 2. Fitting parameters for formula (1)

	P_0*	B_X (cm^{-1})	X_0 (cm)	B_Z (cm^{-1})	Z_0 (cm)	λ (cm^{-1})	Y_0 (cm)
SSC1							
ϕt>1.0 MeV	2.500E+19	0.0499	0.41	0.0436	0.97	0.176	13.29
ϕt>0.1 MeV	7.607E+19	0.0507	0.37	0.0464	0.80	0.134	13.29
dpa	3.995E-02	0.0502	0.38	0.0449	0.90	0.156	13.29
SSC2							
ϕt>1.0 MeV	5.341E+19	0.0528	-0.95	0.0457	0.03	0.176	13.29
ϕt>0.1 MeV	1.648E+20	0.0539	-0.88	0.0484	-0.02	0.134	13.29
dpa	8.580E-02	0.0533	-0.91	0.0470	0.02	0.156	13.29
0-T							
ϕt>1.0 MeV	3.924E+19	0.0517	-0.69	0.0395	0.72	0.107	24.05
ϕt>0.1 MeV	1.214E+20	0.0522	-0.64	0.0432	0.71	0.042	24.05
dpa	6.452E-02	0.0516	-0.67	0.0414	0.71	0.079	24.05
1/4T							
ϕt>1.0 MeV	2.143E+19	0.0478	-0.96	0.0378	1.30	0.134	28.56
ϕt>0.1 MeV	8.823E+19	0.0486	-0.86	0.0425	1.14	0.070	28.56
dpa	4.037E-02	0.0481	-0.91	0.0407	1.21	0.097	28.56
1/2T							
ϕt>1.0 MeV	1.016E+19	0.0441	-0.94	0.0349	1.94	0.146	33.70
ϕt>0.1 MeV	5.727E+19	0.0452	-0.79	0.0413	1.48	0.089	33.70
dpa	2.333E-02	0.0450	-0.83	0.0395	1.59	0.107	33.70

*Values for $\phi t > 1.0$ MeV and $\phi t > 0.1$ MeV are in neutrons/cm^2. Unadjusted spectral fluences $\pm$ 10%.

$$P(X,Y,Z) = P_0 \cos B_X(X-X_0) \cos B_Z(Z-Z_0)\, e^{-\lambda(Y-Y_0)} \qquad (1)$$

None of the estimated standard deviations for damage parameters exceed 10% after adjustment and fit. Interpolation-extrapolation introduced up to 5% uncertainty.

Table 3. List of materials and chemical compositions (wt-%)

Material	Heat code	Supplier	P	Ni	Cu
A302-B (ASTM reference plate)	F23	NRL	0.011	0.18	0.20
A533-B (HSST plate 03)	3PS, 3PT, 3PU	NRL	0.011	0.56	0.12
22NiMoCr37 forging	K	KFA	0.009	0.96	0.12
A508-3 forging	MO	MOL	0.008	0.75	0.05
Submerged arc weld (single vee type, A533-B base plate)	EC	EPRI	0.007	0.64	0.24
Submerged arc weld (single vee type A533-B base plate)	R	Rolls-Royce & Assoc. Ltd.	0.009	1.58	0.23

Table 4. Summary of radiation damage determinations for the Charpy specimen

	$\phi t > 1.0$ MeV ($n/cm^2 \cdot 10^{19}$)*	$\phi t > 0.1$ MeV ($n/cm^2 \cdot 10^{19}$)	dpa (10^{-2})	ΔNDT 41J (°C)	Std. dev. (°C)	ΔNDT 68J (°C)	Std. dev. (°C)	ΔNDT 0.89 mm (°C)	Std. dev. (°C)	Upper shelf drop (J)	Std. dev. (J)
A-302-B											
SSC1	2.59	7.46	3.86	78	±12	84	±17	66	±10	23	± 8
SSC2	5.38	15.35	7.96	94	±11	(101)**	±15	92	±10	33	± 6
0-T	3.95	11.44	6.06	77	±10	(87)	±20	(77)	±16	25	± 7
1/4 T	2.16	8.13	3.70	65	±18	(109)	±83	(72)	±15	29	± 6
1/2 T	1.03	5.27	2.11	52	±10	(57)	±17	56	±10	26	± 7
A-533-B											
SSC1	2.32	6.61	3.44	71	±11	71	±12	85	± 9	28	±11
SSC2	4.83	13.63	7.11	84	±10	86	±11	91	± 7	40	±13
0-T	3.59	10.20	5.46	71	±13	(92)	±25	91	±10	42	±13
1/4 T	1.95	7.13	3.28	69	± 9	65	± 7	74	± 6	40	±13
1/2 T	0.94	4.60	1.87	52	±10	52	± 8	57	± 7	22	±13
22NIMOCR37											
SSC1	1.75	5.69	2.77	(52)	±16	57	±11	78	± 7	47	±16
SSC2	3.64	11.70	5.72	109	±14	114	±10	117	± 8	69	±16
0-T	2.71	8.77	4.40	81	±16	90	±10	97	± 7	43	±16
1/4 T	1.47	6.11	2.64	66	±18	82	±11	93	± 8	48	±16
1/2 T	0.71	3.97	1.51	66	±13	71	± 9	74	± 8	40	±15
A-508-3											
SSC1	1.93	6.32	3.07	15	± 7	13	± 5	18	± 5	32	±14
SSC2	4.02	13.02	6.34	39	± 7	38	± 5	38	± 5	37	±14
0-T	2.95	9.65	4.80	27	± 7	24	± 5	26	± 5	29	±11
1/4 T	1.60	6.84	2.92	23	± 6	20	± 5	23	± 5	7	±14
1/2 T	0.77	4.45	1.67	22	± 7	24	± 6	21	± 6	26	±14
Submerged arc weld (EC)											
SSC1	1.87	6.11	2.97	112	±33	(166)	±120	(142)	±35	33	±14
SSC2	3.90	12.59	6.14	123	±60	(157)	-	138	±20	33	±14
0-T	2.88	9.45	4.71	125	±50	-	-	(171)	±66	34	±11
1/4 T	1.60	6.82	2.92	96	±18	-	-	(118)	±22	31	±14
1/2 T	0.77	4.48	1.68	94	±20	(136)	±65	(129)	±42	26	±14
Submerged arc weld (R)											
SSC1	2.46	7.07	3.66	230	±12	259	±21	260	±17	98	±15
SSC2	5.13	14.56	7.57	309	±38	-	-	352	±64	123	±15
0-T	3.81	10.97	5.83	294	±15	-	-	(364)	±56	110	±15
1/4 T	2.12	7.95	3.62	270	±25	-	-	(321)	±58	108	±14
1/2 T	1.02	5.21	2.09	242	±44	-	-	270	±22	98	±14

*neutrons/$cm^2 \cdot 10^{19}$.

**Values in parentheses are obtained by extrapolation and may be unreliable.

Table 5. Comparison between experimentally determined 41J Charpy shift and Blind Test predictions

	Determined from Charpy curves			Smallest and largest values predicted by Blind Test participants		Difference Blind Test - CV81	
	CV81* (°C)	Std. (°C)	MEA** (°C)	Min. (°C)	Max. (°C)	Min. (°C)	Max. (°C)
A302-B							
SSC1	78	±12	82	71	98	-7	+20
SSC2	94	±11	94	75	112	-19	+18
0-T	77	±10	81	71	96	-6	+19
1/4T	65	±18	67	65	81	0	+16
1/2T	52	±10	50	45	66	-7	+14
A533-B							
SSC1	71	±11	61	45	69	-24	-2
SSC2	84	±10	81	62	99	-22	+15
0-T	71	±13	75	60	87	-11	+16
1/4T	69	± 9	69	54	63	-15	-6
1/2T	52	±10	53	26	52	-26	0
22NiMoCr37							
SSC1	52	±16	61	57	77	-5	+25
SSC2	109	±14	94	65	110	-44	+1
0-T	81	±16	72	63	97	-18	+16
1/4T	66	±18	78	52	76	-14	+10
1/2T	66	±13	56	45	64	-21	-2
A508-3							
SSC1	15	± 7	20	6	43	-9	+18
SSC2	39	± 7	39	11	53	-28	+14
0-T	27	± 7	25	10	49	-17	+22
1/4T	23	± 6	20	8	42	-15	+19
1/2T	22	± 7	14	6	35	-16	+13
Submerged arc weld (EC)							
SSC1	112	±33	108	99	118	-13	+6
SSC2	123	±60	119	130	153	-7	+30
0-T	125	±50	124	121	135	-4	+10
1/4T	96	±18	94	91	115	-5	+19
1/2T	94	±20	89	63	103	-31	+9
Submerged arc weld (R)							
SSC1	230	±12	222	218	227	-12	-3
SSC2	309	±38	289	246	319	-63	+10
0-T	294	±15	286	239	288	-55	-6
1/4T	270	±25	256	180	218	-90	-52
1/2T	242	±44	239	143	189	-99	-53

*ORNL evaluation.
**Evaluation in Ref. 4.

THERMAL AND STRUCTURAL ANALYSIS OF LIGHT-WATER REACTOR VESSEL IN-PLACE ANNEALING[a]

by

W. L. Server
Idaho National Engineering Laboratory
EG&G Idaho, Inc., Prime Contractor

J. P. Houstrup
Combustion Engineering, Inc.

A thermal anneal cycle at a temperature well above the normal operating temperature of a reactor pressure vessel can restore most of the original toughness properties lost due to radiation embrittlement. The heat treatment required for commercial reactor vessels in the United States would involve an annealing temperature of around 454°C (850°F) for one week (168 h); the heat treating method requires radiant heat transfer by dry air to the inside of the evacuated reactor vessel localized in the beltline region.

Critical questions of dimensional stability and residual stresses arise for such a localized heat treating cycle. Prior to actually performing an in-place anneal, detailed elastic-plastic finite element calculations are required. Previous work on in-place annealing only superficially treated these concerns. Therefore, the degree of distortion and residual stresses after an annealing cycle were investigated by Idaho National Engineering Laboratory (INEL) through a subcontract with Combustion Engineering, Inc. (CE).

Two-dimensional axisymmetric calculations were performed using a typical 4.37 m (172 in.) inside diameter CE-design reactor vessel. The finite element thermal model included a thermal simulation of the six

---

a. Work supported by the U.S. Nuclear Regulatory Commission, Office of Nuclear Regulatory Research, Under DOE Contract No. DE-AC07-76ID01570.

nozzles, piping, and three vessel supports. The vessel cover was assumed to be a thermal/radiation shield of 58 cm (23 in.) of reinforced concrete jacketed on both sides with 1.3 cm (0.5 in.) of carbon steel insulated on the bottom. Normal service insulation was used on the inside surface of the vessel between the heated zone and the shield cover as well as the vessel exterior and piping. Vessel cladding was assumed constant at 7.94 mm (0.3125 in.) of stainless steel.

The heat source was divided into five zones of time-dependent heat fluxes imposed over 120% of the core length as shown in the thermal model in Figure 1. Initial attempts at using a uniform heat flux throughout the heated region proved unacceptable in that the temperature profile was not uniform; temperatures at the extremes of the heater were as low as 316°C (600°F) when the inside temperature was held at 454°C (850°F). Therefore, significantly higher heat fluxes were needed at the two end zones of the heater, especially at the top end where relatively large heat losses occur through the nozzles and cover.

It was hoped to achieve temperatures throughout the beltline of 454 ± 14°C (850 ± 25°F); however, since the process of achieving this profile is iterative, once this goal was approached, the computer was stopped. The temperatures at the ends were a little out of tolerance at the beginning and end of the 168-h hold period as shown in Figure 2. A heat-up rate of 14°C/h (25°F/h) was used, but the cooldown rate was less since natural cooling was employed. Vessel isotherms at the end of the 168-h hold period are shown in Figure 3. Temperatures in the nozzle region and the bottom head are very near normal operating temperatures.

The structural model is basically the same as the thermal model except that the cover has been replaced by a simple uniform load and the pipe support modeling has been changed to reflect structural action. Beam elements were carefully used to simulate the actual nozzles, and a gap element was used to simulate the steam generator sliding action. Nonlinear elastic-plastic creep properties were utilized in the analysis. Because of the slow temperature changes and relatively low temperatures (therefore,

low creep rates), long time increments per iteration could be used in the ANSYS computer code. Figure 4 is an exaggerated view of the expansion of the vessel at the end of the 168-h hold period. The axial temperature gradient in the vessel produces a "coke bottle" shape, and the rotation (approximately 0.2 degrees maximum during heat-up) of the vessel wall bends the primary piping connected at the nozzles. Thus, the piping experiences a plastic deformation at the nozzle safe end.

The results with regard to the reactor vessel are very positive. Thermal stresses during the entire cycle were moderate (less than yield), and the residual radial deformations do not exceed 0.036 mm (0.0015 in.). The residual stresses are shown in Figure 5 and do not exceed 39 MPa (5.7 ksi) in the meridianal direction or 32 MPa (4.6 ksi) in the hoop direction. These low residual stresses are secondary in nature and pose no threat to the operating life of the vessel.

The primary problem identified is the plastic bending in the connecting primary piping. One approach to minimize this bending effect is to extend the heating length closer to the nozzles in order to reduce the rotation due to the "coke bottle" effect. However, the temperature profile must be carefully controlled so that the residual stress regions at the edge of the heater do not occur at the nozzle intersection. Summarizing the initial thermal/structural analysis, the following results were obtained: the integrity of the reactor vessel is maintained after the annealing process, temperatures away from the heated area decay rapidly, zones of varying heat flux are needed to obtain an appropriate temperature profile, and rotation at the nozzles during heating causes plastic bending in the attached primary piping system.

Further analytical work has attempted to find a solution to this bending effect by extending the heating length up to the nozzle region in order to reduce the axial thermal gradient. Unfortunately, even by heating the nozzle region to around 343°C (650°F) and reducing the range of the thermal gradient, the actual gradient induced at the nozzles was not significantly reduced.

Using the extended heating zone, the post-anneal residual stresses in the vessel are much less than those shown in Figure 5 due to the more uniform heating with the extended heater length. Future work should be directed to further extension of the heaters to the vessel flange and to increasing the nozzle region temperature. However, individual plants will require separate analyses since variations in the locations of the beltline, nozzles, and flanges exist along with different vessel support arrangements. Precise control of the temperature gradient across the nozzle height is extremely important in order to eliminate the plastic hinge formed at the attachment to the reactor nozzle safe end. An elastic beam algorithm can be used to define the maximum allowable gradient relative to the reference temperature in order to ensure no plastic bending. With proper monitoring and control, the plastic bending at the nozzle safe-end weld region can be solved.

BIBLIOGRAPHY

W. L. Server, "Review of In-Service Thermal Annealing of Nuclear Reactor Pressure Vessels, presented at The Twelfth International Symposium on Effects of Radiation on Materials, Williamsburg, VA, June 1984 (to be published in an ASTM STP)

W. L. Server, In-Place Thermal Annealing of Nuclear Reactor Pressure Vessels, EGG-MS-6708, September 1984 (to be published as a NUREG).

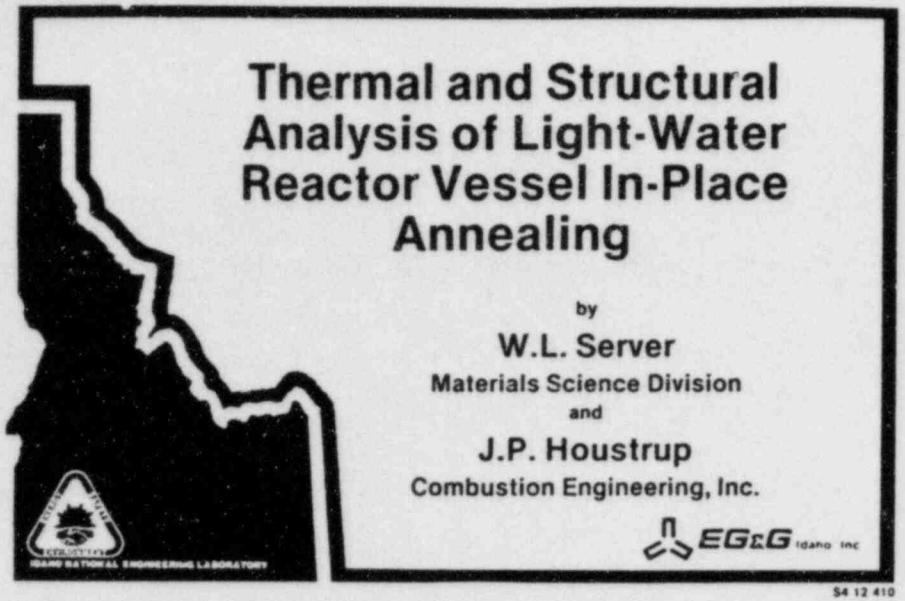

S4 12 410

In-Place Thermal Annealing

- Localized heat treatment in reactor beltline region
- Core and internals removed
- Radiant heat transfer in air ("dry")
- 454°C (850°F) for 1 week (168 h)

S4 12 409

Problem Areas

- Magnitude of thermal stresses
- Dimensional stability after annealing
- Residual stresses due to localized heating
- Temperature distribution and other potential damage due to annealing cycle

S4 12 408

Thermal/Structural Analysis

- Performed at Combustion Engineering, Inc., Chattanooga Tennessee (CE)
- CE-design PWR vessel
- Two-dimensional axisymmetric finite element calculations (ANSYS) considering creep effects
- Simulations of piping, 6 nozzles, and 3 supports used

S4 12 407

Thermal Model of CE Vessel

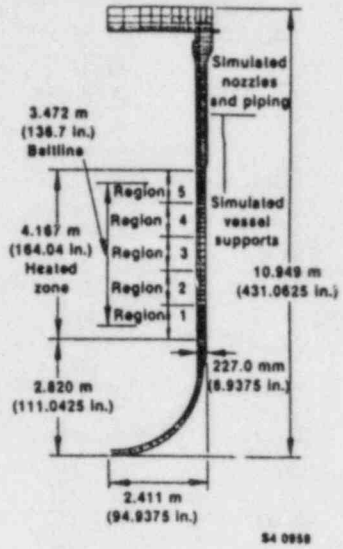

Temperature - Time at the Beltline

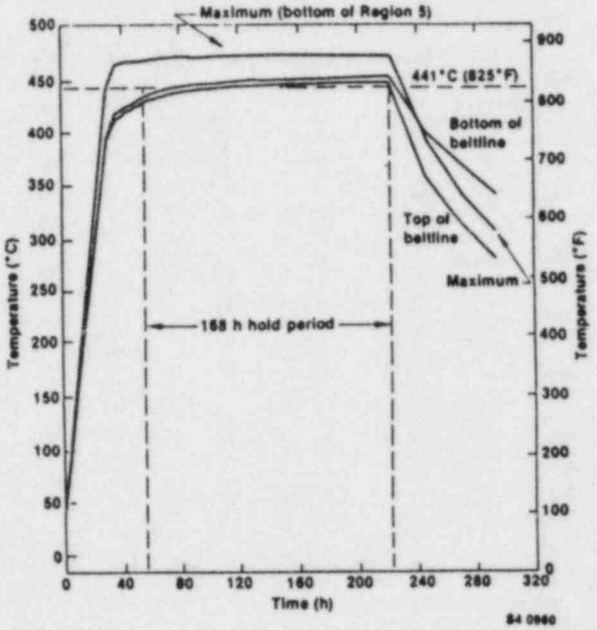

Isotherms at End of 168 Hour Hold Period

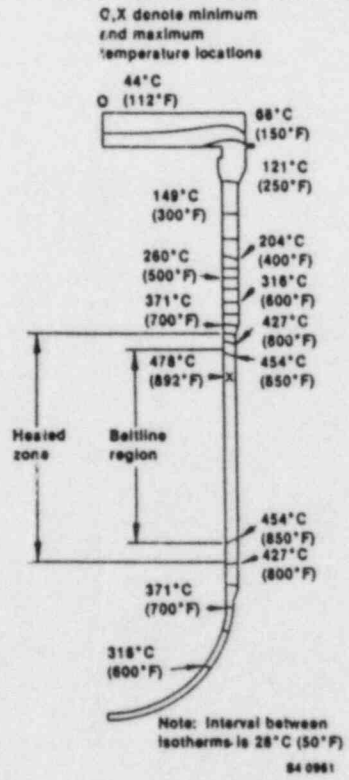

Deformed Vessel at End of 168 Hour Hold Period

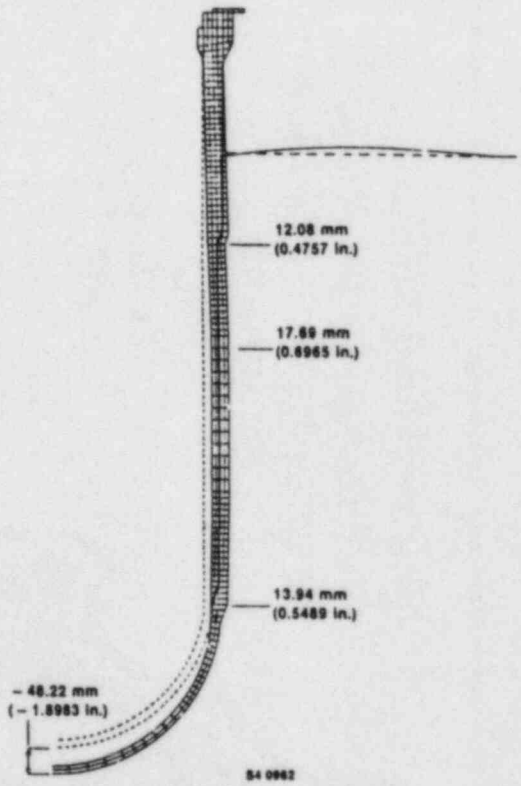

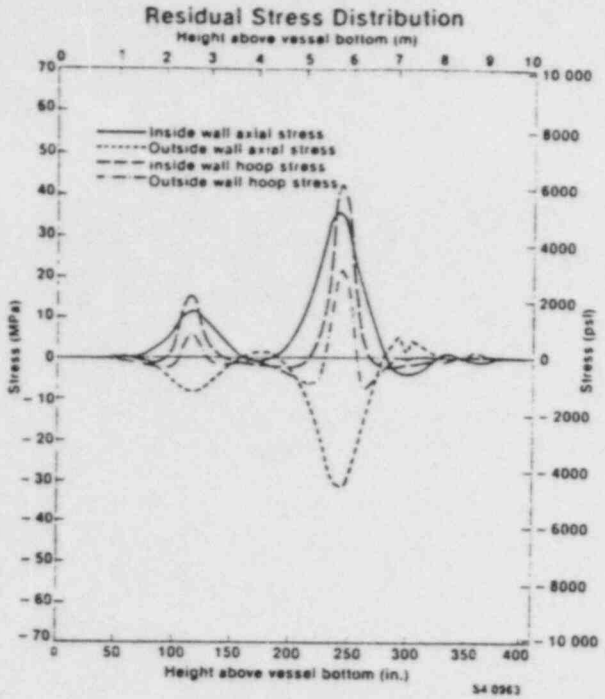

Thermal/Structural Analyses Summary

- Vessel integrity is maintained
  - Thermal stresses below yield
  - Residual deformation <0.036 mm (0.0015 in)
  - Residual stresses <39 MPa (5.7 ksi)
- Temperatures decay rapidly away from heated zone
- Zones of varying heat flux are needed
- Rotation at the nozzles causes plastic bending in attached primary piping

C4 1708

Further Calculations

- Extended heating zone above the nozzles
- Heated nozzle region to nominally 343°C (650°F)
- Produced more uniform heating and reduced residual stresses
- Did not significantly reduce plastic bending of attached piping

Conclusions

- Vessel integrity is maintained
- Plastic bending of primary piping is a problem
- Precise control and monitoring of temperatures across nozzles needed to solve pipe bending problem
- Plant-specific calculations will be needed

ANNEALING OF THE BR3 REACTOR PRESSURE VESSEL

A. Fabry, F. Motte, G. Stiennon and J. Debrue
P. Gubel, J. Van de Velde, G. Minsart and Ph. Van Asbroeck

S.C.K./C.E.N., Mol, BELGIUM

With Consulting or Contractual Contributions by

A. Lowe Jr., J.M. Bloom
(B & W)

J.R. Hawthorne, F. Loss
(MEA)

D. Morris, J. Goodman, G.J. Freeman
(RR & A)

J. Boucau, M. Duprez
(WESTINGHOUSE)

D. Pachur
(KFA, Jülich)

W.L. Server
(EG & G)

SYNOPSIS

The pressure vessel of the BELGIAN BR3 plant, a small (11 MWe) PWR presently used for international fuel testing programmes, and operated at the SCK/CEN, Mol, BELGIUM site since 1962, has been annealed during March 1984. The anneal, an engineering success, was performed under wet conditions for 168 hr. at 650 °F with core removal and within plant design margins /1/. An interim post-anneal operation license has been granted by the BELGIAN Authorities after extensive technical review with experts from the USNRC licensing branch, under the leadership of Dr. W. JOHNSON. The license is presently limited to a period such that the Pressurized Thermal Shock (PTS) screening criterions /2/ should not be exceeded, but it is planned to apply for an extension of this license beyond the generic "warning signal" embodied in these criterions. Actually, owing to a number of plant specificities to be outlined in this paper and already described to some extent elsewhere /3//4/, it is considered that the vessel would have remained fracture-safe till 1987 without anneal; this assessment is not yet entirely demonstrated however with respect to the potential threat associated with a few hypothetized overcooling accidents, for which the current transient definitions /5/ may admittedly be inaccurate. On another hand, under normal, test or upset operation conditions, the vessel integrity in 1987 without anneal cannot be seriously questioned, neither from an engineering assurance standpoint nor in terms of the Regulatory intentions of the applicable Code /6/ and Guidelines /7//8/. The anneal has consequently been viewed as a plant-specific experience readily achievable at low cost and expediently effective in alleviating the timing as well as the financial constraints of a complete PTS safety analysis by 1984. Rather compelling also was the fact that, even though core melt risks potentially stemming from a severe vessel overcooling were deemed acceptably small, the economic penalty of an eventual vessel requalification or plant shutdown may have turned unbearable, should certain hypothetized transients develop, such as the ones entailing crack initiation with arrest before vessel half-thickness (1/2 T) and near upper shelf fracture toughness levels . By contrast, the low plant service temperature of 500 °F (260 °C) was bearing the promise of sufficient embrittlement recovery to remove such concerns till 1987.

The work overviewed in this paper is the result of an interdisciplinary effort, consolidated since 1982 into a coordinated program involving a number of experts and organizations, as identified under the titlehead and by the references /9/ to /18/. The program is not completed yet and consequently, this overview must be seen as a progress report. Furthermore, it must be clearly understood that any information contained herein is provided under the sole responsibility of the SCK/CEN team authorship, and that any position statement made or conclusions drawn do not necessarily reflect the views of other contributing organizations or experts.

The paper is intended at providing a brief review of the various tasks entailed by the evaluation of this vessel anneal, with emphasis on plant-specific metallurgical embrittlement trend curve development and on overall RPV integrity assessment. The engineering aspects of the anneal will be addressed elsewhere /1/.

SUMMARY OF BR3 PLANT CHARACTERISTICS RELEVANT TO RPV SAFETY EVALUATION

As shown by figure 1, BR3 is not comparable to any generic PWR (except maybe to naval propulsion reactors, which are not currently described in the open literature).

The vessel dimensioning to ASME Section I specifications results in significantly lower pressure-induced hoop stresses than for larger commercial plants (diameter-to-thickness ratio /12/); concurrently, thermal stresses for normal heat-up and cool-down conditions are about five times less than in ASME-III designed vessels (because the BR3 wall thickness is about half the one in these larger units). Furthermore, BR3 does not need to be brought critical below the service temperature of 500 °F. The benefit of these various specificities is illustrated by fig. 2 : in short, BR3 can be operated up to a beltline nil-ductility transition temperature RT_{NDT} of 400 °F /19/ without violating 10 CFR50 App. G requirements /6/. Furthermore, it has been established /12//13/ that under normal, test or upset operation conditions, upper shelf safety margins are more than adequate well below the current 10 CFR50 App. G requirement of 50 ft.lb absorbed-energy in the Charpy-V impact

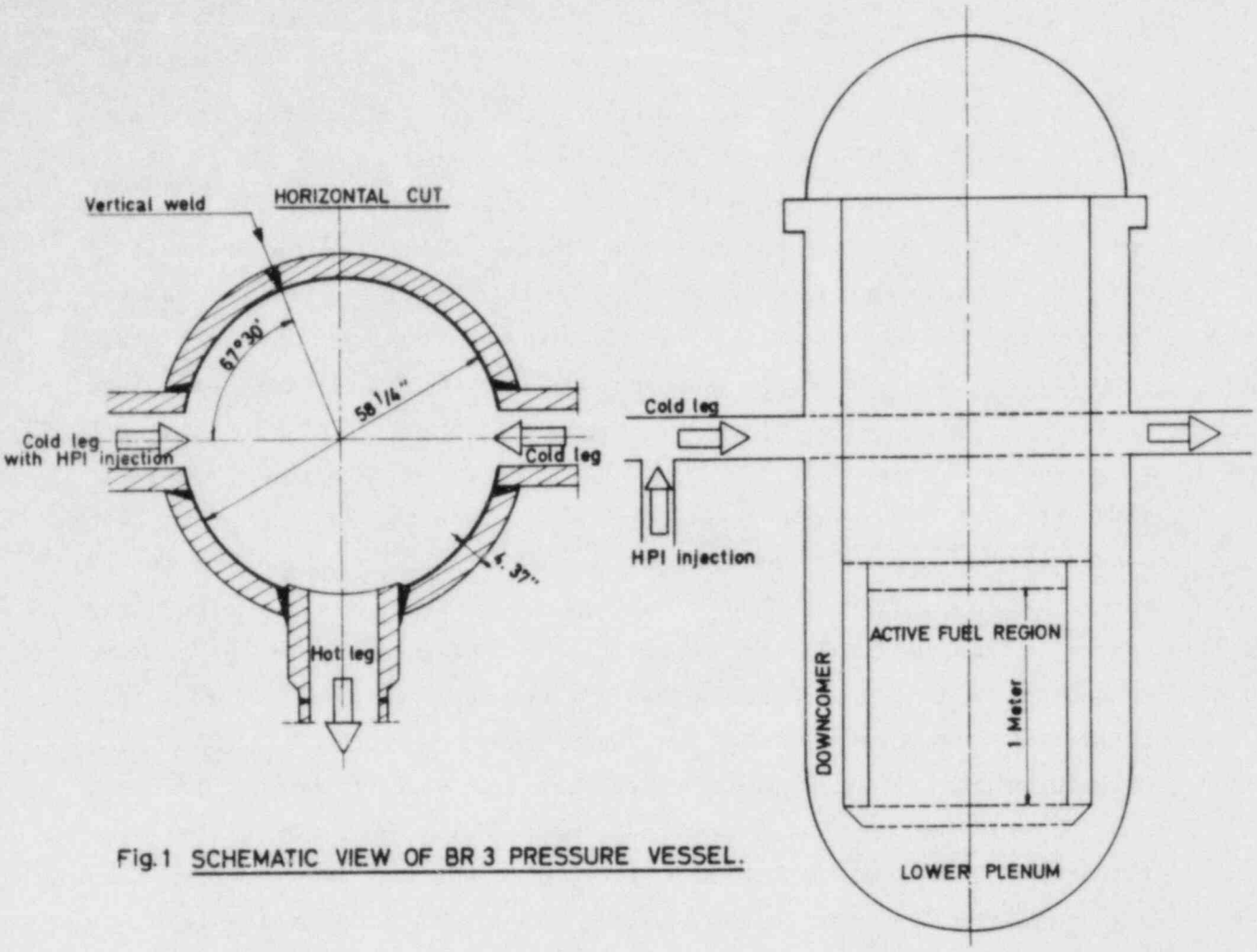

Fig.1 SCHEMATIC VIEW OF BR 3 PRESSURE VESSEL.

Fig. 2 HEAT-UP AND COOLDOWN PRESSURE-TEMPERATURE LIMITATIONS : SCHEMATIC ANALYSIS OF FUNDAMENTAL PLANT-SPECIFICITY

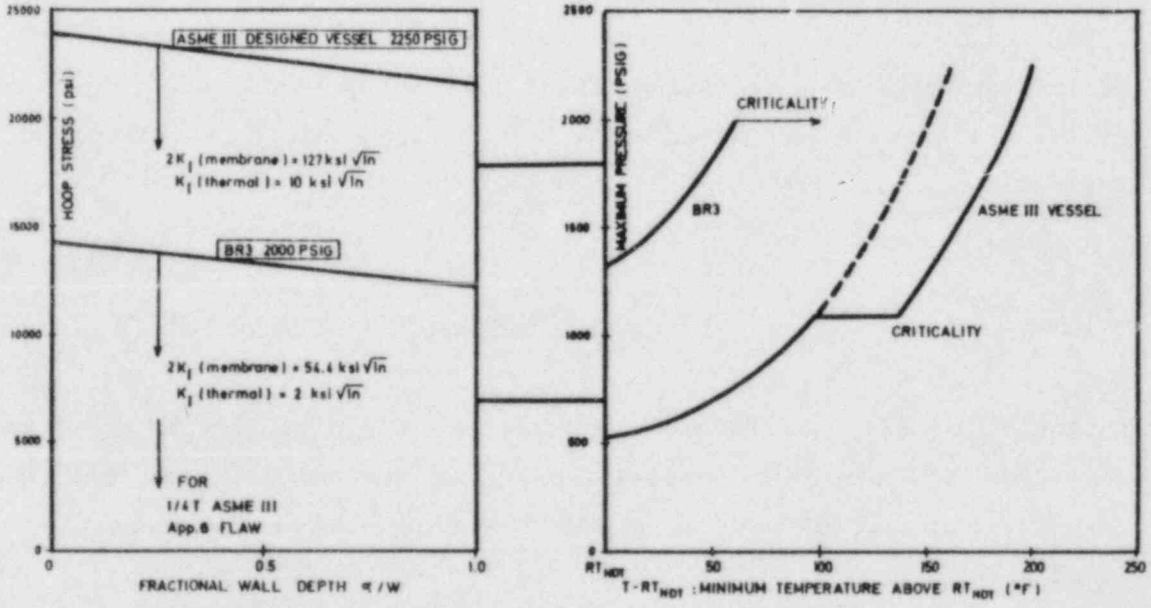

$2K_I\,(\text{membrane}) + K_I\,(\text{thermal}) \leq K_{IR} = K_{Ia} + 26.8 + 1.223 \exp\left[0.0145\,(T - RT_{NDT} + 160)\right]$ (ksi $\sqrt{\text{in}}$).

ADDITIONAL 40°F MARGIN REQUIRED AT REACTOR CORE CRITICALITY.

test (fig. 3); the oldier Regulatory requirement of 30 ft.lb, in vigor even beyond the ASME-I design era, is the one that does apply to BR3 in a perspective of complying with the Regulatory intention. It has been verified, upon NRC suggestion, that these safety margins were still adequate during the 650 °F anneal at the applied pressure, midway between service and design. The concern was the drop of upper shelf properties with temperature /8/, especially for the vertical weld seam (fig. 1). Even when crediting minimal benefit /12/ for fracture toughness increase with eventual stable crack growth, the allowable pressure for the ASME Section III reference 1/4 T flaw was conservatively estimated as 4900 psi, to be compared with 6700 psi under normal service conditions. The anneal has consequently not caused any growth of possibly existing flaws in BR3. Besides improving fracture toughness, the anneal does entail a warmprestressing benefit /20/ sufficient to largely offset any conceivable secondary concern. An evaluation /9/ of fabrication procedures for the BR3 vessel has been made, by the manufacturer BABCOCK-WILCOX. This covers also pre-service inspection. Records dating back to over a quarter of a century have been retrieved and examined. Radiographic evidence is available of an uniquely "clean" weld, one among the first few automatic submerged-arc seams realized for the incipient nuclear energy industry, using LINDE OXWELD 40 wire with nickel bearing LINDE 80 flux. This BR3 vertical weld has been found to govern the RPV safety and is therefore addressed more extensively herein than the plate, an A302B nickel-modified LUKENS STEEL heat.

Thermohydraulic and operation specificities of this one-loop plant (Fig.1) are roughly summarized in a later section dealing with pressurized thermal shock.

BR3 MATERIALS SAMPLING

Essential to RPV embrittlement prediction and/or projection is a good knowledge of materials composition. Complemented by heat treatment documentation, it allows to assess the microstructural interaction of irradiation-induced interstitial and void defect growth with the movement of lattice dislocations.

Fig. 3 Plant-specificity of upper-shelf safety margins:

- failure assessment diagram (Bloom, 1983 : schematic)

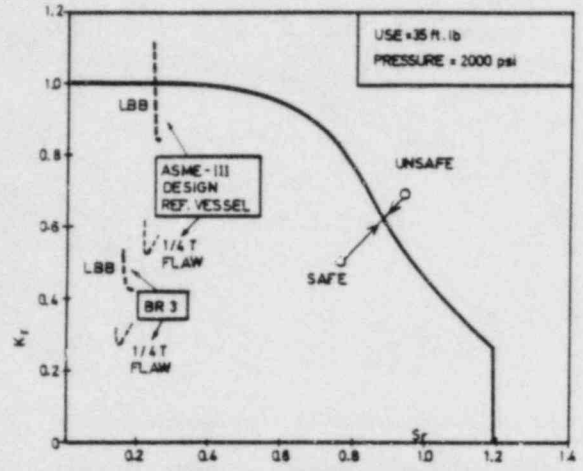

- tearing instability diagram (Fabry, 1981, 1984)

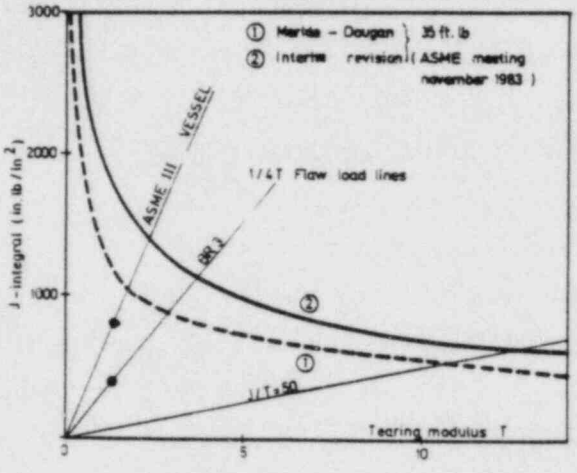

Fig. 4 BR3 VESSEL MATERIALS SAMPLING BY ROLLS ROYCE ASSOCIATES
(Schematic)

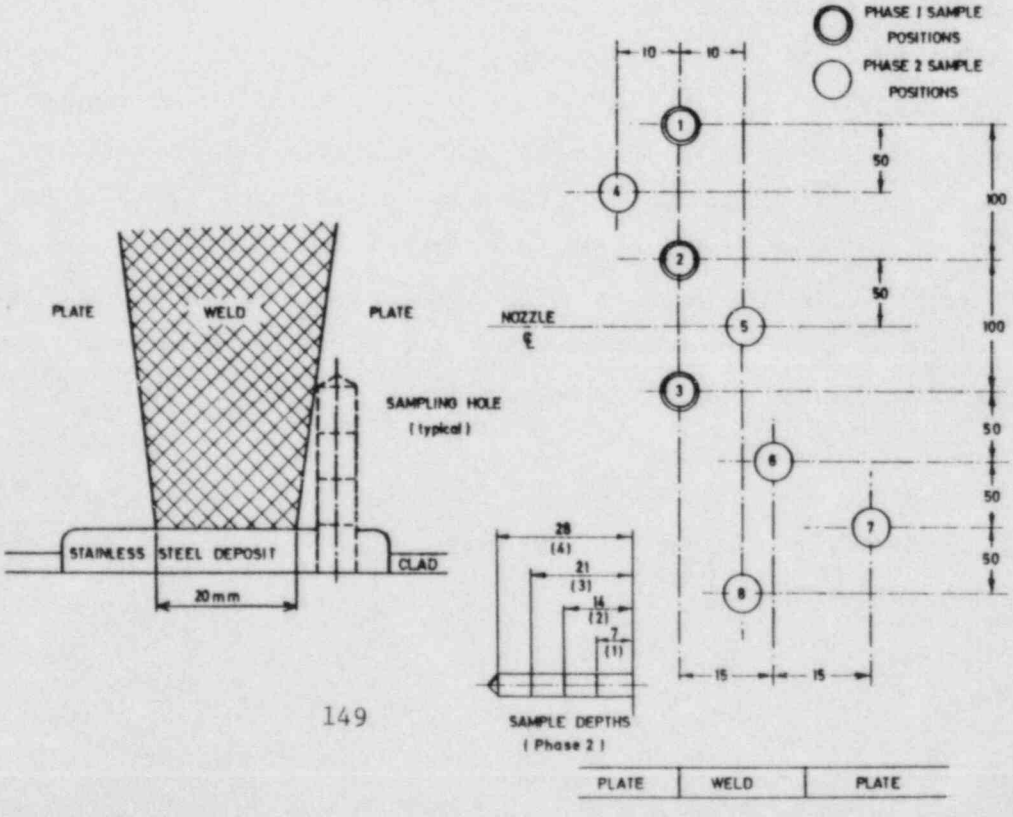

Because the heat number and diameter of the wire used for the BR3 vertical seam weldment is unknown, on-site specimen sampling was decided and executed by a specialist team at ROLLS ROYCE ASSOCIATES (England) under the leadership of Dr. J. GOODMAN. This operation is well documented /10/. It was executed in two phases, the second, decisive one resulting from lessons drawn from the initial one. Figure 4 schematizes the accomplishment. This high-precision drill sampling was limited to an unbrittled zone referred with respect to the nozzle centerline (fig. 1 and 4) and located above the upper top of the thermal shield (essentially unremovable). The primary objective was to obtain valid chemistry data for the weld. Given the fabrication procedure /9/, it was necessary and sufficient to extract specimens at three depths under the stainless steel clad deposit in order to insure that the beltline composition would unambiguously be determined up to the vessel quarter thickness (sampling a representative range of weld beads). Outside of the welding area, the clad is spot-welded to the plate and photographic evidence (localization of the spots) could be obtained by the BR3 team. Combined to engineering drawing tolerance analysis, these photographs allowed to decide that the first sampling (holes 1, 2 and 3 on fig. 4) did not hit the weld centerline, but the heat-affected zone. This had been suggested to be the case on basis of initial chemistry results.

The U.K. team could accept to return in order to sample the holes marked 4 to 8 on fig. 4. This delicate operation was again conducted most precisely and in such way as to insure that no water penetration access would be created in the spot-welded cladding zone. The best chemistry data available at this time are compared in Table I to the ones developed for the archive materials used for the accelerated test program to be outlined in a subsequent section. Reporting the details, including chemistry benchmarking precautions, is beyond the scope of this review. The highlights are :

1) Both weld, plate and HAZ chemistries are spatially uniform (one drilling was through a plate repair zone and displayed marked inhomogeneity)

TABLE I COMPARISON BETWEEN BR3 VESSEL AND ARCHIVE MATERIAL CHEMISTRIES

Material	Chemical Composition (wt. percent)												(ppm)	
	C	Mn	P	S	Si	Cr	Ni	Mo	Cu	V	Al	As	O_2	N_2
BR3 WELD	0.12	1.20	(0.018)*	0.019	0.32	0.06	0.70	0.49	0.18_3		< 0.01		0.10	0.01
W1 [a]	0.09	1.40	0.021	0.020	0.54	0.07	0.56	0.40	0.31	0.008	0.001	0.018		
W2 [a]	0.10	1.42	0.020	0.021	0.52	0.07	0.56	0.41	0.26	0.008	0.003	0.018		
W3 [a]	0.09	1.55	0.017	0.021	0.44	0.09	0.67	0.41	0.32					
W-D [a]	0.08	1.74	0.014	0.013	0.41	0.14	0.60	0.41	0.19	0.008	0.005			
W-E [a][b]	0.10	1.68	0.013	0.016	0.56	0.07	0.56	0.39	0.23					
BR3 PLATE	0.28	1.25	(0.020)**	0.020	0.26	0.06	0.56	0.47	0.19		< 0.04			
PT-A [a][c]	0.22	1.44	0.011	0.021	0.24	0.10	0.55	0.59	0.19	0.004	0.033			
HSST-03 [d]	0.20	1.26	0.011	0.018	0.25	0.10	0.56	0.45	0.13		0.034			

*Best estimate, ref. A.L. LOWE Jr. and L.B. GROSS; BAW-1807 (1983). To be confirmed.

**1957 Mill Report Analysis. Results for other elements agree well with 1983 vessel material sampling data.

[a] Materials procured for BUFFALO Test Reactor Irradiations through contractual agreement with A. LOWE Jr. (B&W).

[b] Cooperative gift from EPRI. Quad Cities II surveillance weld metal (RP 2180-06 and RP 1021-3).

[c] Electrical furnace vacuum degassed melt while BR3 is open-hearth fabrication. Consequently, is not good match on upper shelf (Longitudinal = 124 ft.lb, transverse = 94 Ft.lb, un-irradiated). Because of weak correlations between defects governing shelf and transition ranges, material is considered as reasonably adequate for RT_{NDT} assessment purposes.

[d] C.E. Childress -ORNL-TM-3191 (1971). Specimens from 03 MB block irradiated in BR3 cycle 4C.

2) Copper contents in weld and plate are roughly similar (0.16 - 0.19) but the nickel content of the weld is relatively high (0.70).

3) Good agreement is obtained between the sampling results and the mill analysis report for the plate.

This chemistry analysis work is still being continued. The process is not rapid : attention has to be paid into "benchmarking" the techniques (which differ between laboratories and element groups). The expensively unique BR3 samples are released for analysis when confidence has been obtained that the achievable accuracy meets the requirements.

BR3 PHYSICS-DOSIMETRY

A detailed documentation is available /16/ and the results are illustrated on fig. 5. Accuracy goals /4/ have been met.

The characterization involves the following :

Detailed neutron- and gamma-ray (heating) ex-core transport theory calculations, including cycle-to-cycle variations, and a methodology benchmarked on the PCA /21/ and VENUS /22/ experimental results; the source term description (core analysis) has however been independently provided (BELGONUCLEAIRE) and is not benchmarked in terms of pressure vessel exposure concerns

- In-core accelerated capsule dosimetry (high flux position on fig.5)

- Thermal shield sampling dosimetry, obtained concurrently to the weld chemistry effort outlined in the previous section.

Ex-vessel examination /23/ by means of the JANUS Compton-Recoil Gamma-Ray Spectrometer supports the low-energy part of the neutron transport analysis, which is the most difficult one to predict.
All in all, theory is abut 10 % higher than experiment : this is a remarkable agreement in the present context.

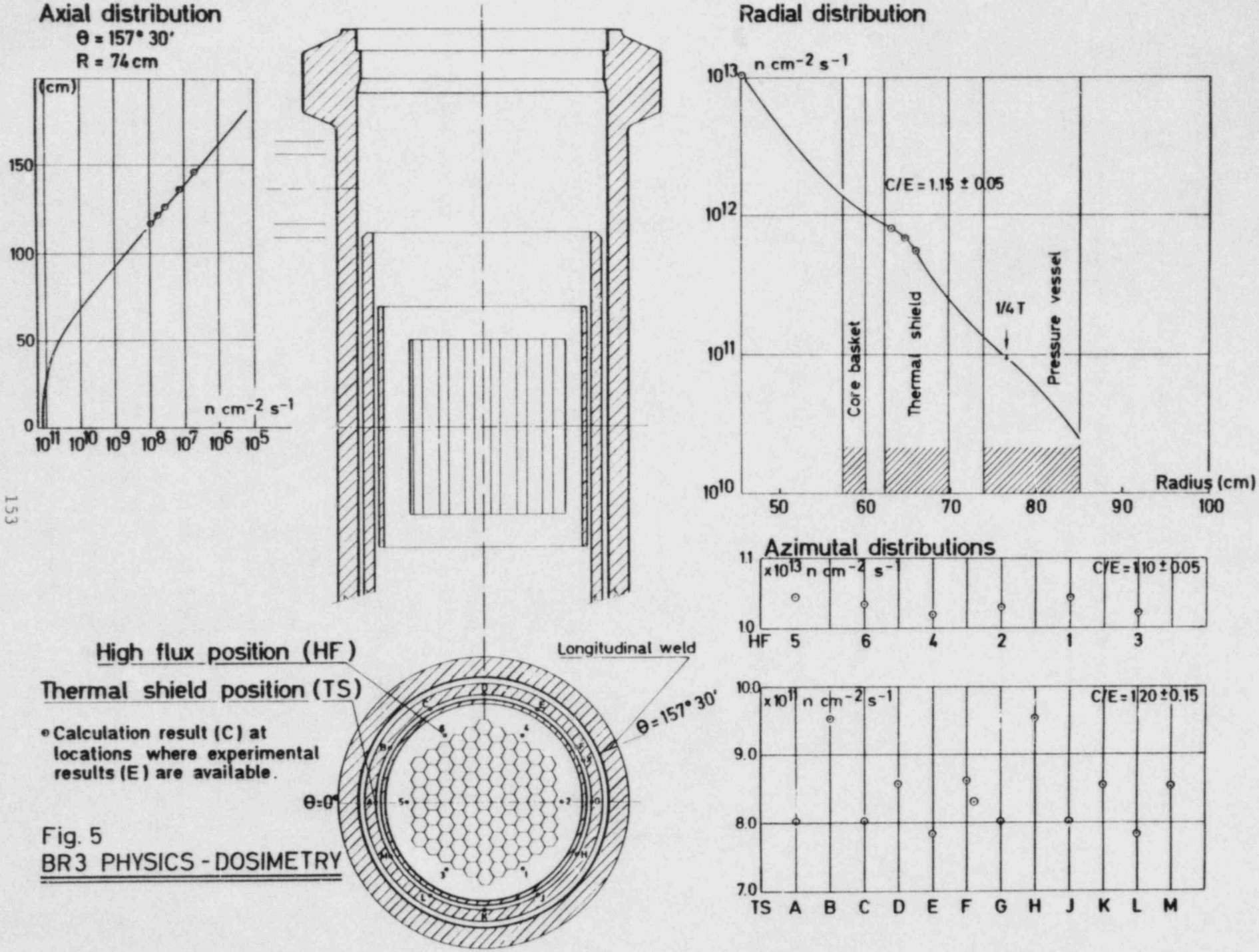

Fig. 5
BR3 PHYSICS - DOSIMETRY

Table II summarizes our evaluation of "best" neutron fluence exposures and their upper bounds for the weld (azimuthal effects are small, i.e. << 20 %). Mean values have been used as objectives for the irradiation-anneal-reirradiation test program. Upper bound values however are conservatively assumed for the vessel structural integrity analysis.

TABLE II. BR3 NEUTRONIC EXPOSURE

WHEN	Vessel Inner Surface		Vessel Quarter Thickness	
	MEAN	UPPER BOUND	MEAN	UPPER BOUND
START CYCLE 4D (1984)	3.43,19	4.22,19	2.45,19	3.01,19
END CYCLE 4D (1987)	4.07,19	5.01,19	2.91,19	3.58,19

DEVELOPMENT OF PLANT-SPECIFIC METALLURGICAL EMBRITTLEMENT TREND CURVES

This objective is most challenging in views of the very limited mechanical testing information directly obtained during the plant commissioning, the lack of an adequate surveillance program and the non-generic irradiation temperature of 500 °F. The difficulties are further compounded by the fact that the vessel has been annealed.

The approach taken to address this task consists of :

1. A dedicated irradiation and testing program conducted by MATERIALS ENGINEERING ASSOCIATES (MEA) at the State University of New York, at Buffalo, using the archive materials identified in Table I .

2. A comprehensive analysis of radiation annealing mechanisms for all materials in the test program in order to provide physically-based projections to the BR3 itself. This work is carried out by

Consultant Dr. Ing. D. PACHUR /24/ and will be finalized by the end of CY 1984; it relies strongly on detailed chemistry information for the test materials and from the vessel sampling, including the assay of gazes (nitrogen, oxygen, hydrogen). The chemical analysis effort has encompassed significant attention to the validation of techniques and is now nearing completion.

The final trend curves are intended at combining all data from this program and from the relevant literature, examined in such way that upper bound recommendations do embody a reliable physical as well as statistical foundation.

In the interim, empirical engineering-type correlations have been proposed and tentatively accepted as decisional guidance for a limited plant operation period. These are briefly reviewed herein. Figure 6 indicates that 19 irradiated Charpy-V impact test curves are presently available for the program materials, with only 6 of them within the embrittlement "space" covered by the B & W Linde 80 flux submerged-arc weld data base of 26 similar curves from surveillance capsules irradiated near 550 °F /25/. (The line drawn through the data is not meant to convey more than historical significance /26/). It is thus clear that if the BR3 data base had not been developed, significant extrapolation beyond current knowledge would have been necessary. As clearly, the question of using test reactor data for PWR application had to be addressed, and our conclusions to this respect are illustrated on fig. 7 for pre-anneal weld trends. The absence of an observable flux level effect is predicted also by mechanistic modelling /24/ for the pre-anneal condition. It must be cautioned that our statement about aging may not be valid for the highly-embrittled RR & A weld data from the PSF program, represented by the five points on the right-hand sides of figures 6 and 7 (at $RT_{NDT} \geq 350$ °F). It is implicit in current trend curve formulations (/25//27//28//29/ for example) that flux spectrum effects are hardly discernible, and this explains well our conclusion to this respect. In particular, the ratios $\phi_{>1\ MeV}$/dpa at BR3 vessel quarter-thickness and in the Buffalo test rigs do not differ by more than 8 %, i.e. an insignificant amount. The exposure unit consequently adopted throughout this paper is the flux of neutrons with energy greater than 1 MeV ($\phi_{>1\ MeV}$).

Fig 6 LOCATION OF THE MOL-MEA-B&W ACCELERATED-IRRADIATION TEST MATRIX IN THE NIL-DUCTILITY TRANSITION TEMPERATURE SHIFT AND C_V-UPPER SHELF ENERGY-DROP SPACE.

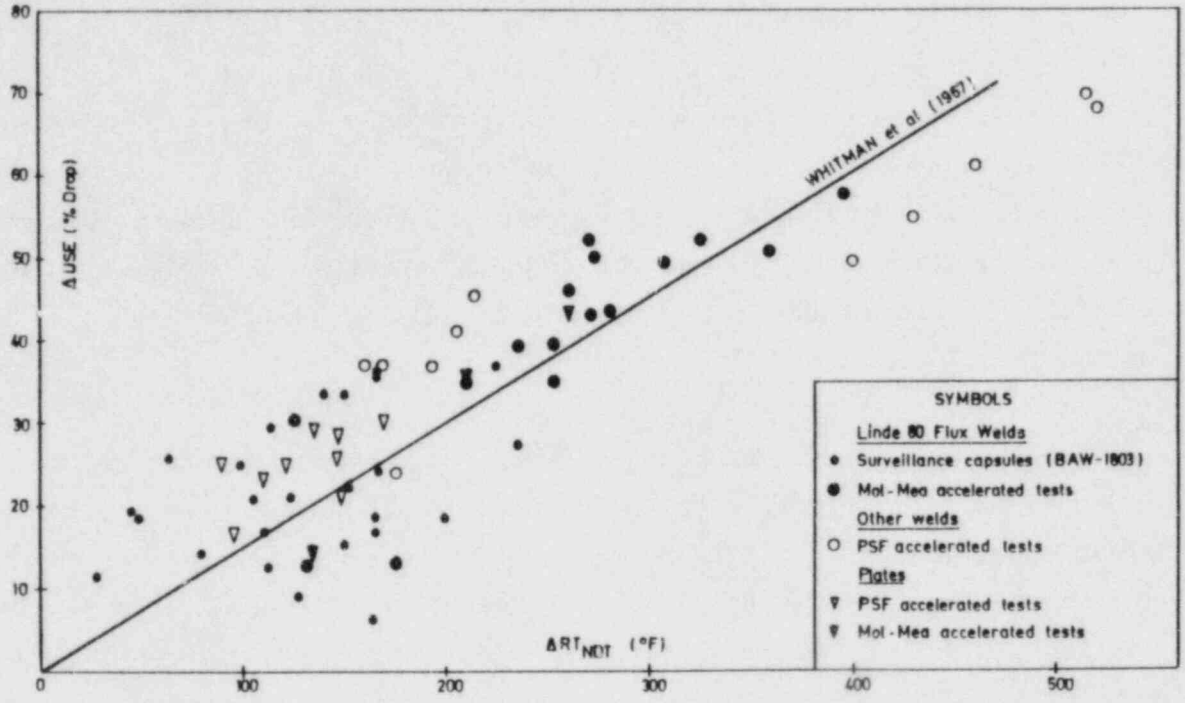

Fig 7 SURVEILLANCE CAPSULE AND TEST REACTOR METALLURGICAL DATA BASES FOR WELDS REVELANT TO BR3 PROGRAM ARE NOT STATISTICALLY DISTINGUISHABLE : NO FLUX LEVEL NOR FLUX SPECTRUM NOR AGING EFFECT (PRE-ANNEAL)

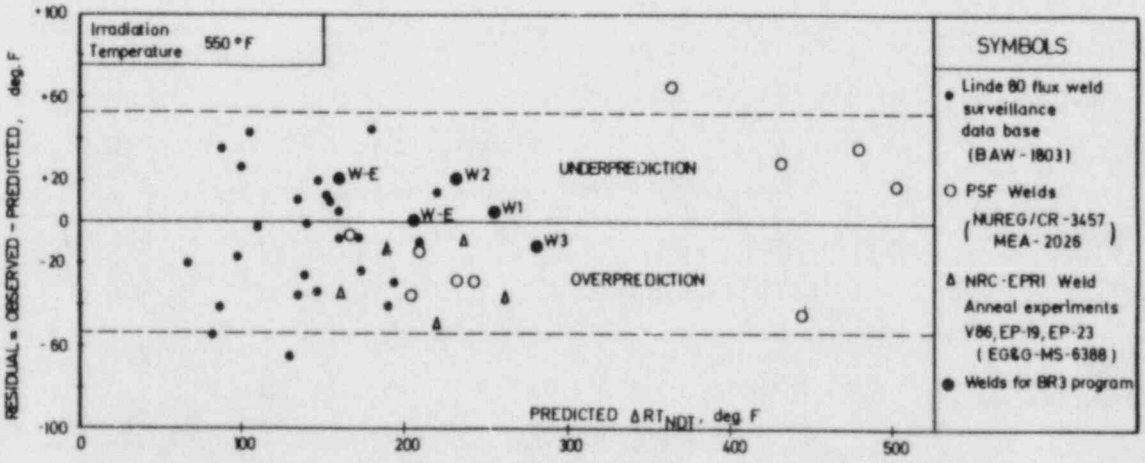

PREDICTION BY GUTHRIE'S EQUATION : $\Delta T_{30ft\,lb} = [590.2\,Cu - 337(Cu.Ni)^{1/2} + 267\,Ni]\,(\phi t / 10^{19})^N$

EXPOSURE UNIT ϕ IS FLUX >1MeV $\quad N = 0.289 - 0.0483 \ln(\phi t / 10^{19}) \quad \sigma = 26.5\,°F$

The next question is the one of irradiation temperature influence, illustrated on figure 8. An equation for the accepted mean trend for both welds and plates is given elsewhere /4/. This has not been found to be affected by the choice of a particular 550 °F correlation among the four ones referred above and in the footnotes to Table III. What is affected however, as shown by the Table, is the judgment about which one from the five program welds does constitute the closiest match to the BR3 weld under 500 °F exposure-assuming that copper and nickel only enter into the chemistry factor of the formulation. We indicate our preferred choice, but must stress that it is tentative at this time.
Our preference is based on the fact that the terms involving nickel in the weld chemistry factors have governing significance and that the BR3 nickel weld content is higher than for all program welds but W3 (Table I); the two preferred correlations are the ones to perform the best at high nickel contents.

However, anneal mechanisms are not traceable to copper and nickel alone, if at all; other alloy or residual elements enter into play, such as chromium, vanadium, gazes ... . This is displayed clearly by the next step of our present derivation : anneal recovery. This has been treated at this stage by means of the recently published correlation of B. McDONALD /30/, as shown on fig. 9. The result for weld W-D is not consistent with the general trend, and it is not to a significant degree. Tentatively the deviation is attributed to the detrimental role of chromium on annealing, as observed in other work by D. PACHUR and as also suggested in reference /31/; this is not to say that in the pre-anneal condition, chromium would have any detectable effect. But we believe that weld W-D is not a good "mock-up" of the BR3 weld after annealing has taken place.

Another significant departure from the correlation has been observed /32/ when annealing HSST-03 plate specimens (Table I) exposed for 8000 hr in BR3 at 525 °F and to a neutron fluence of 2.7, 10^{19} cm^{-2} : essentially 100 % recovery was obtained for the nil-ductility transition temperature shift after 168 hr anneal at 750 °F and 60 % recovery at 650 °F, while prediction ranged from a modest recovery in the first case to a negligible one in the second. By contrast, pre-anneal results

TABLE III. IF 500 °F POST-ANNEAL TREND CURVES CAN BE DERIVED FROM PRE-ANNEAL TREND CURVES AT 550 °F THROUGH OUR EMPIRICAL CORRELATION APPROACH, THE BR3 WELD BEHAVIOUR WILL BE SIMILAR TO THE ONE OF ARCHIVE WELD W2 WHEN USING OUR PREFERRED 550 °F PRE-ANNEAL TREND CURVES

WELD	5.0, 18 cm^{-2} > 1 MeV				1.0, 19 cm^{-2} > 1 MeV				3.0, 19 cm^{-2} > 1 MeV				5.0, 19 cm^{-2} > 1 MeV			
	(1)	(2)	(3)	(4)	(1)	(2)	(3)	(4)	(1)	(2)	(3)	(4)	(1)	(2)	(3)	(4)
W1	208	203	201	182	261	254	246	229	346	329	339	331	382	356	393	392
W2	191	184	184	167	240	230	225	211	318	298	309	305	351	324	359	361
W3	225	224	225	225	283	280	275	284	375	362	378	408	414	393	438	484
W-D	169	167	167	161	213	209	204	204	282	271	281	295	311	294	326	349
W-E	181	174	174	158	227	217	212	200	300	281	292	289	331	305	339	343
BR3*	177	185	184	198	223	232	225	250	295	300	309	360	325	326	359	427

THE QUOTED FIGURES ARE 30 ft.lb T_{CV} SHIFTS AT 500 °F ASSUMING THE FOLLOWING 550 °F TREND CURVE FORMULATIONS :

(1) P.N. RANDALL, G.L. GUTHRIE - ANS Annual Meeting, Detroit, Michigan (June 14, 1983).

(2) G.L. GUTHRIE - NUREG/CR-2805, Vol. 4, p. HEDL-3 to 13 (1983).

(3) J.D. VARSIK et al. - EPRI Report NP-2720 (1982).

(4) A.S. HELLER, A.L. LOWE, Jr. - Report BAW-1803 (1984).

*Using mean copper, nickel contents as given in Table I

Fig. 8 Sensitivity of the ΔRT_{NDT} embrittlement index to irradiation temperature

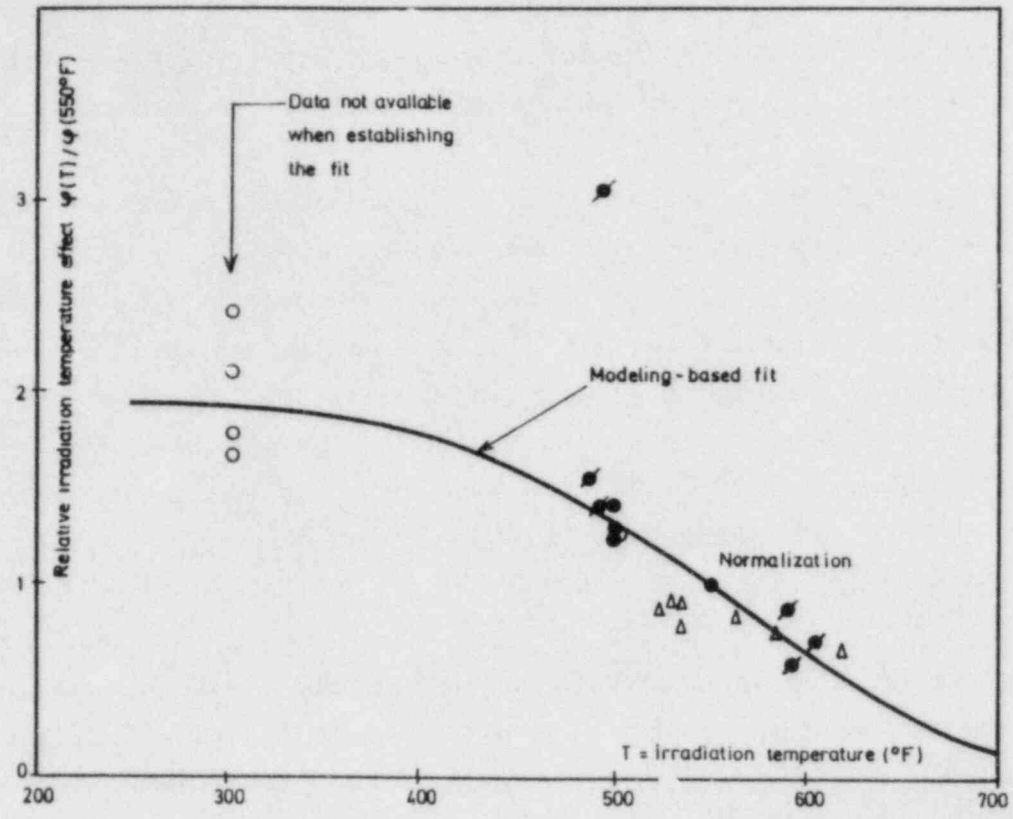

Fig. 9 ANNEALING RECOVERY CORRELATION OF BRUCE MACDONALD : COMPARISON TO RECENT MOL-MEA RESULTS.

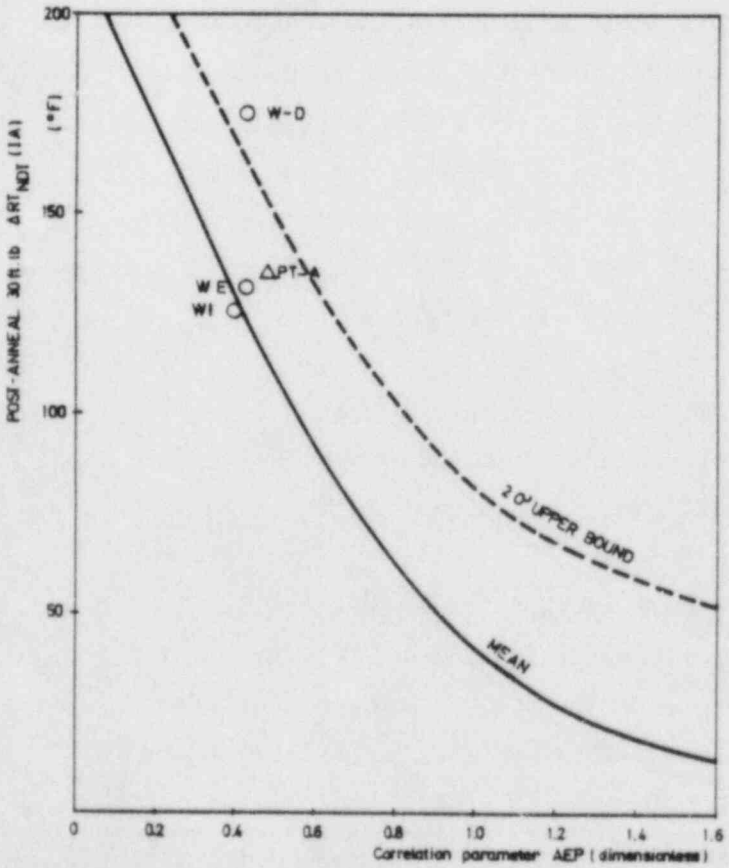

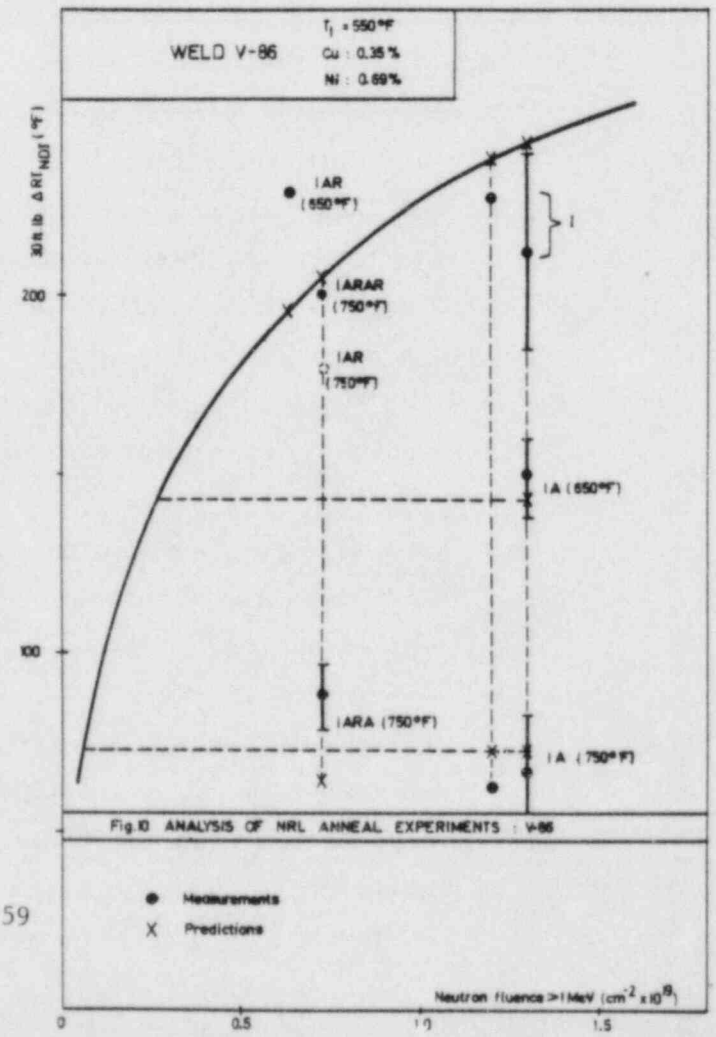

Fig. 10 ANALYSIS OF NRL ANNEAL EXPERIMENTS : V-86

agreed well with the "blind" estimates, strengthening further the correlations preferred in the first two steps of our analysis.

Our empirical look must now turn to post-anneal behaviour. Fig. 10 illustrates how this has been done, starting with the easier case of 550 °F irradiations. Fig. 11 is added for more clarity. Measurements are confronted with prediction and good agreement is noticed. We apply the simple-minded assumption that after anneal, the material will re-embrittle along the pre-anneal trend curve, re-starting at the neutron fluence that would have brought it to the annealed property level. This of course can only be roughly true, in terms of the preceding discussion.

Furthermore, flux level effects are now important : the anneal recovery of the BR3 weld for instance is estimated to be $\sim$ 50 °F less than if measured under test reactor accelerated conditions, while its re-embrittlement under the same accelerated conditions would be initially much faster than in BR3 itself, as suggested for instance by fig. 12. Although we believe that the two flux rate effects tend to compensate each other, we have applied the predicted penalty on the recovery when estimating the BR3 post-anneal weld and plate behaviours. All examined 550 °F irradiated-anneal-reirradiated (IAR) data (EPRI and NRC programs) are reproduced, often conservatively, using this simple correlation method. Unfortunately, the same statement does not apply to all IAR data generated so far for BR3, as can be seen from fig. 13 for weld W-D and, to less an extent, for the plate PT-A. In a licensing perspective however, the following comments are valid :

1. The weld does govern, not the plate. This is the reason why we do not emphasize herein our examination of literature plate data and why we do display modest concern about the plate embrittlement.

2. The available plant-related experimental IAR results for all archive welds at neutron fluences representative of the current BR3 core cycle (end-of-life) do not generally exceed the USNRC pressurized thermal shock screening criterion for longitudinal weldments /2/, even though they reach it in one case (W-D). In a

Fig. 11 NRL CYCLIC ANNEAL TEST REACTOR EXPERIMENTS FOR A B&W ARCHIVE WELDMENT : PREDICTION VERSUS OBSERVATION

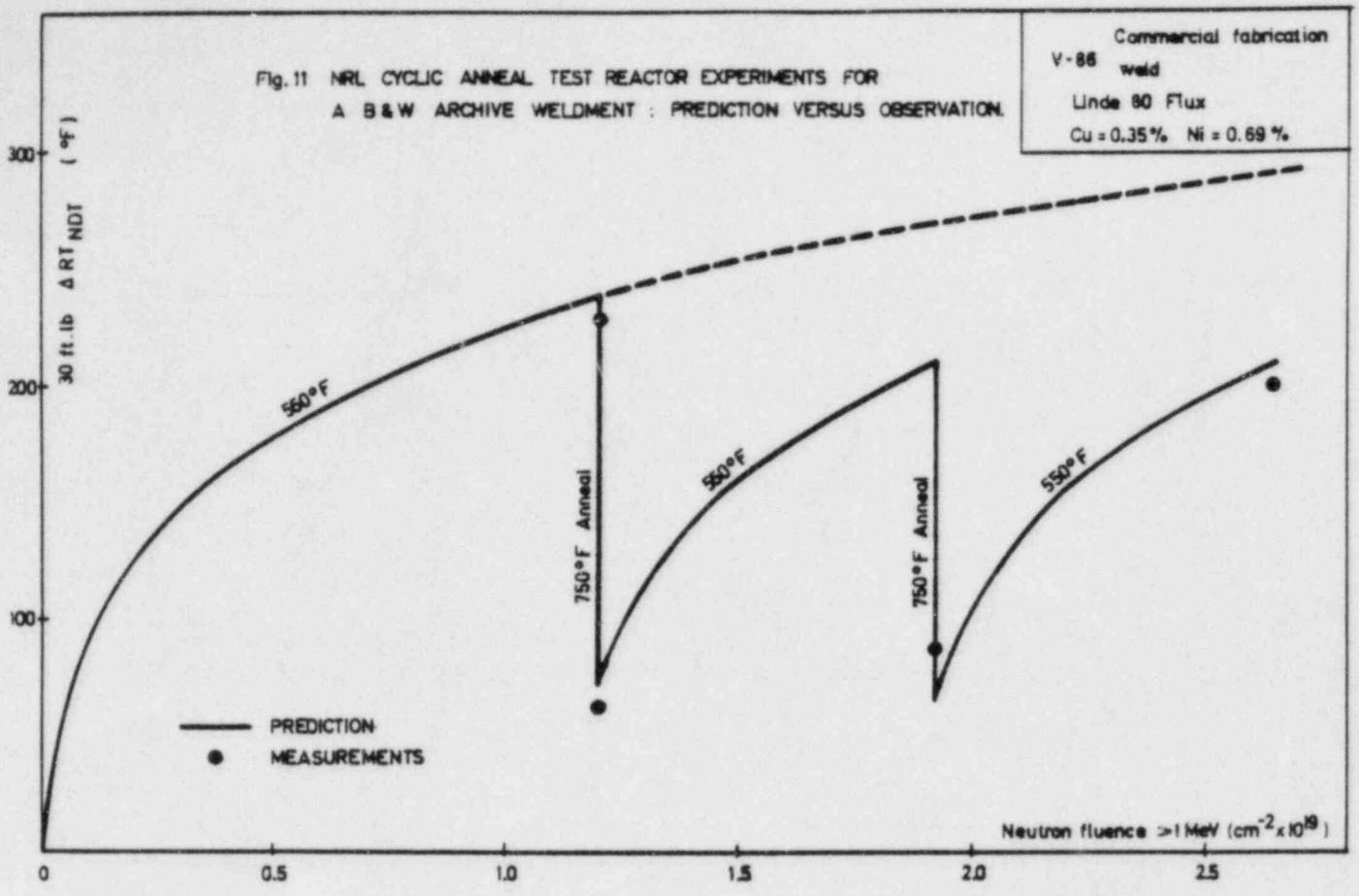

Fig. 12 ANALYSIS OF MEA ANNEAL EXPERIMENTS : WELDS W8 A (Linde 80) AND W9 A (Linde 0091)

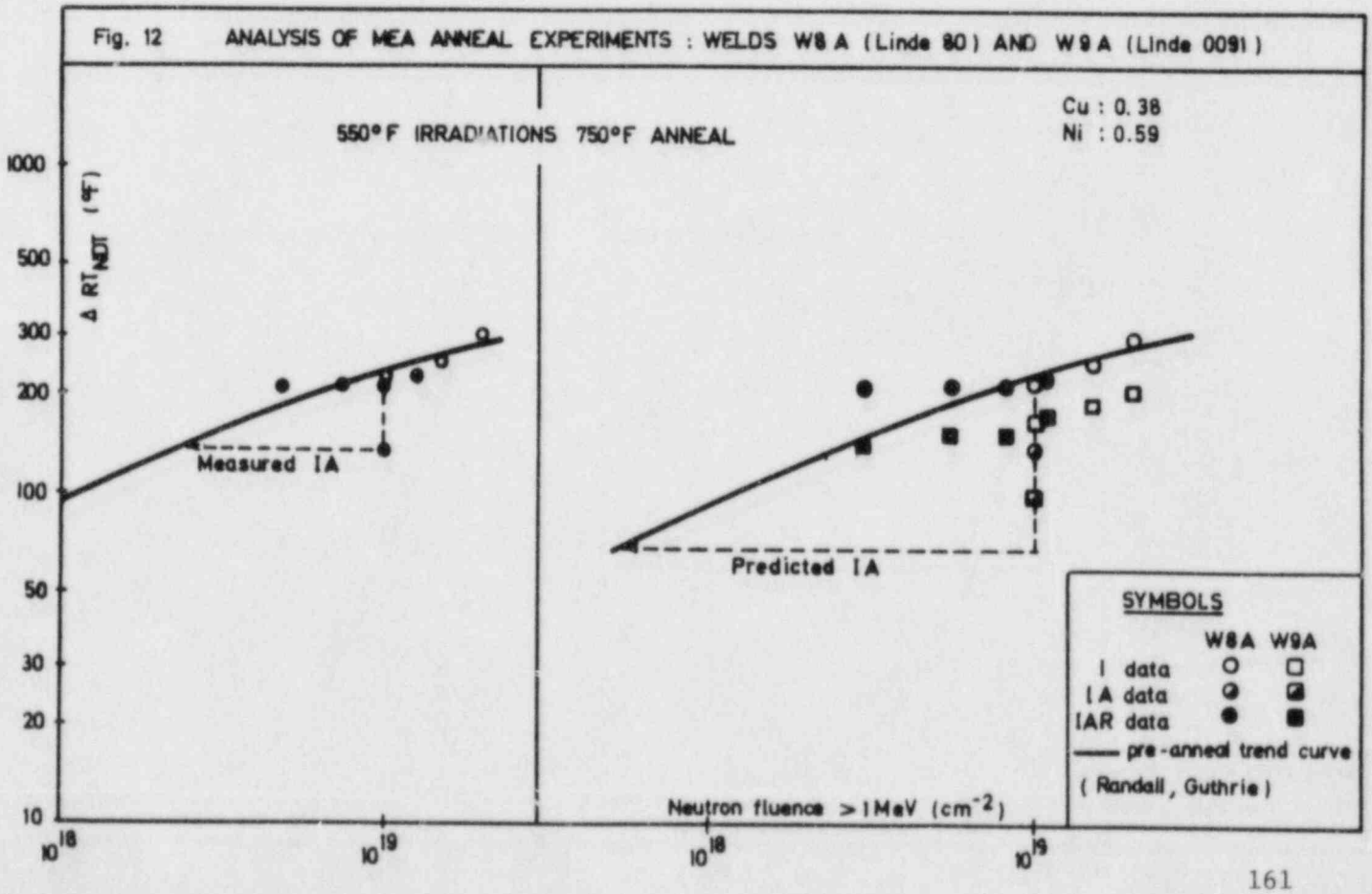

Fig. 13

PRELIMINARY SYNTHESIS OF THE RESULTS OF MOL-MEA-B&W TEST REACTOR ANNEALING EXPERIMENTS IN SUPPORT OF BR3 : IRRADIATIONS AT 500°F, ANNEAL AT 650°F

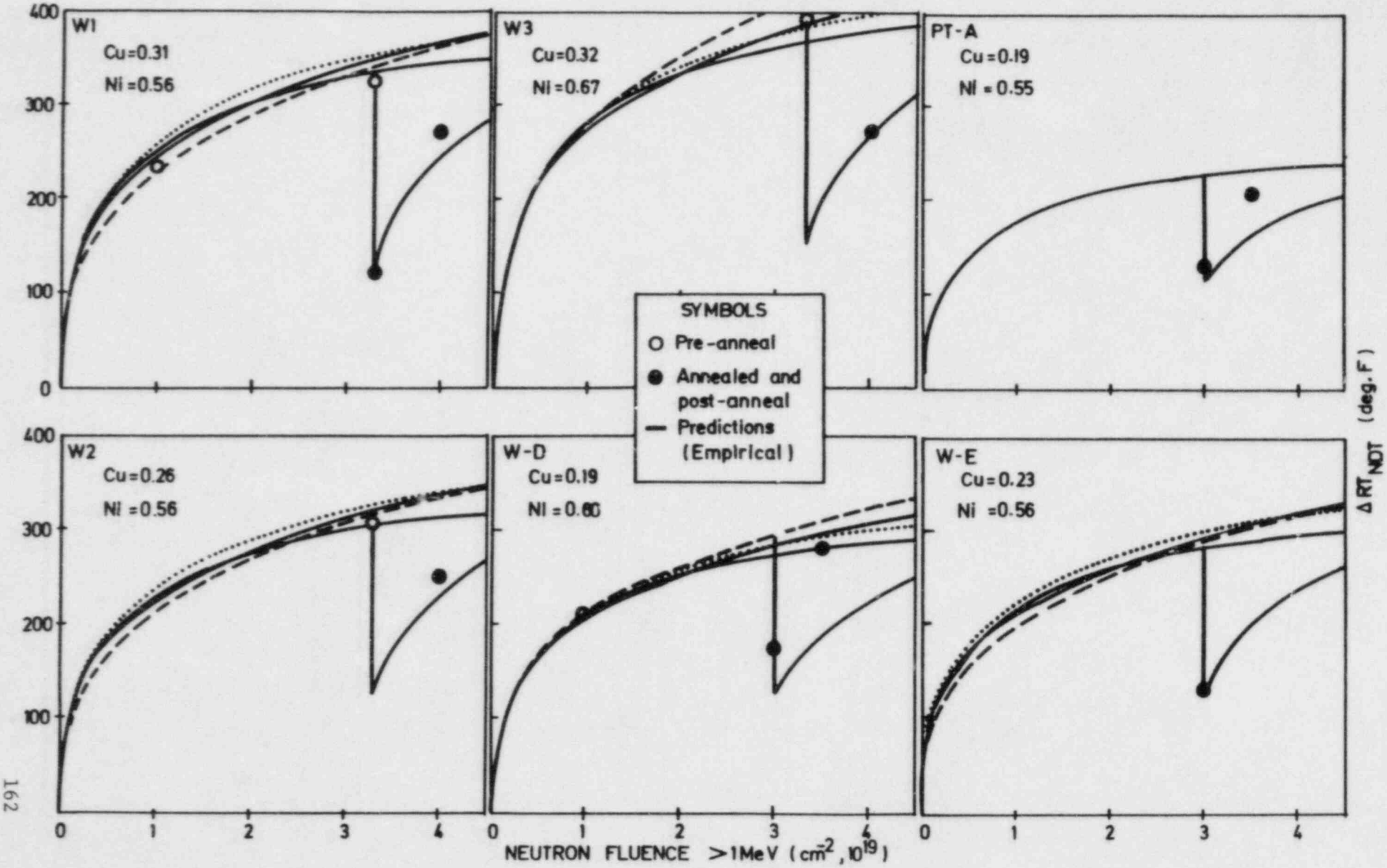

pessimistic view, this isolated case could be interpreted as suggestive of no anneal benefit by end of the considered core cycle.

3. Across the board nevertheless, it is obvious that the vessel anneal has strongly reduced the average expectable RT_{NDT} for the considered core cycle.

As shown by fig. 14, the BR3 related-data are furthermore not inconsistent with literature.

The current balance of all these observations and of previous comments is synthetized by fig. 15 for the BR3 weld. Construction of this figure involves a moderate pile-up of conservatisms : upper bound neutron fluences and weld chemistry, lower bound anneal recovery benefit, incorporating flux level effect penalty, and so on. A similar semi-empirical "construction" has been done for the plate.

An overall summary of current conclusions regarding RT_{NDT} is given in the table below.

TABLE IV. UPPER BOUND RT_{NDT} AT VESSEL INNER SURFACE FOR AN UPPER BOUND 1987 NEUTRON FLUENCE (> 1 MeV) OF $5.10^{19} cm^{-2}$

	PLATE	WELD
IF VESSEL HAD NOT BEEN ANNEALED	333 °F	410 °F
ACTUAL IAR CONDITION	304 °F	330 °F

Figure 16 is self-explanatory with respect to our well-documented position that a 30 ft.-lb absorbed-energy level in the c_V-input test is a wisely conservative requirement in terms of the favourable geometric specificities inherent in the BR3 vessel design : this plant-specific upper shelf safety limitation is satisfied. Further verification is in progress through dedicated J-R curve assessments using 0.5 T-CT specimen testing. Interestingly, closier scrutiny of the figure 16 does highlight again the peculiarity of weld W-D : its upper-shelf anneal

Fig.14 COMPARISON BETWEEN OBSERVED NIL-DUCTILITY TRANSITION TEMPERATURE SHIFTS AND PREDICTIONS BASED ON THE CORRELATION DEVELOPED FOR LINDE 80 FLUX WELDS

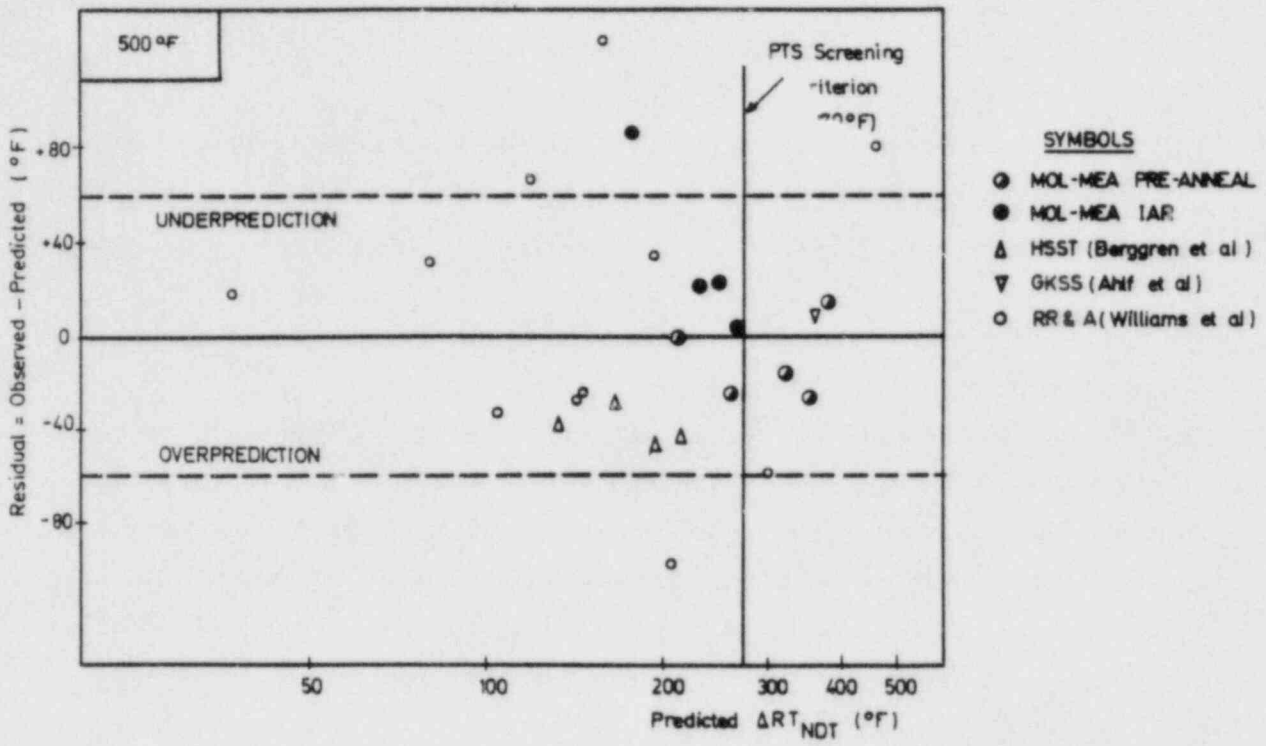

Fig.15 TENTATIVE ESTIMATE OF THE BR3 WELD UPPER BOUND TRANSITION TEMPERATURE SHIFT AT VESSEL INNER SURFACE BY END OF CORE CYCLE 4D (1987)

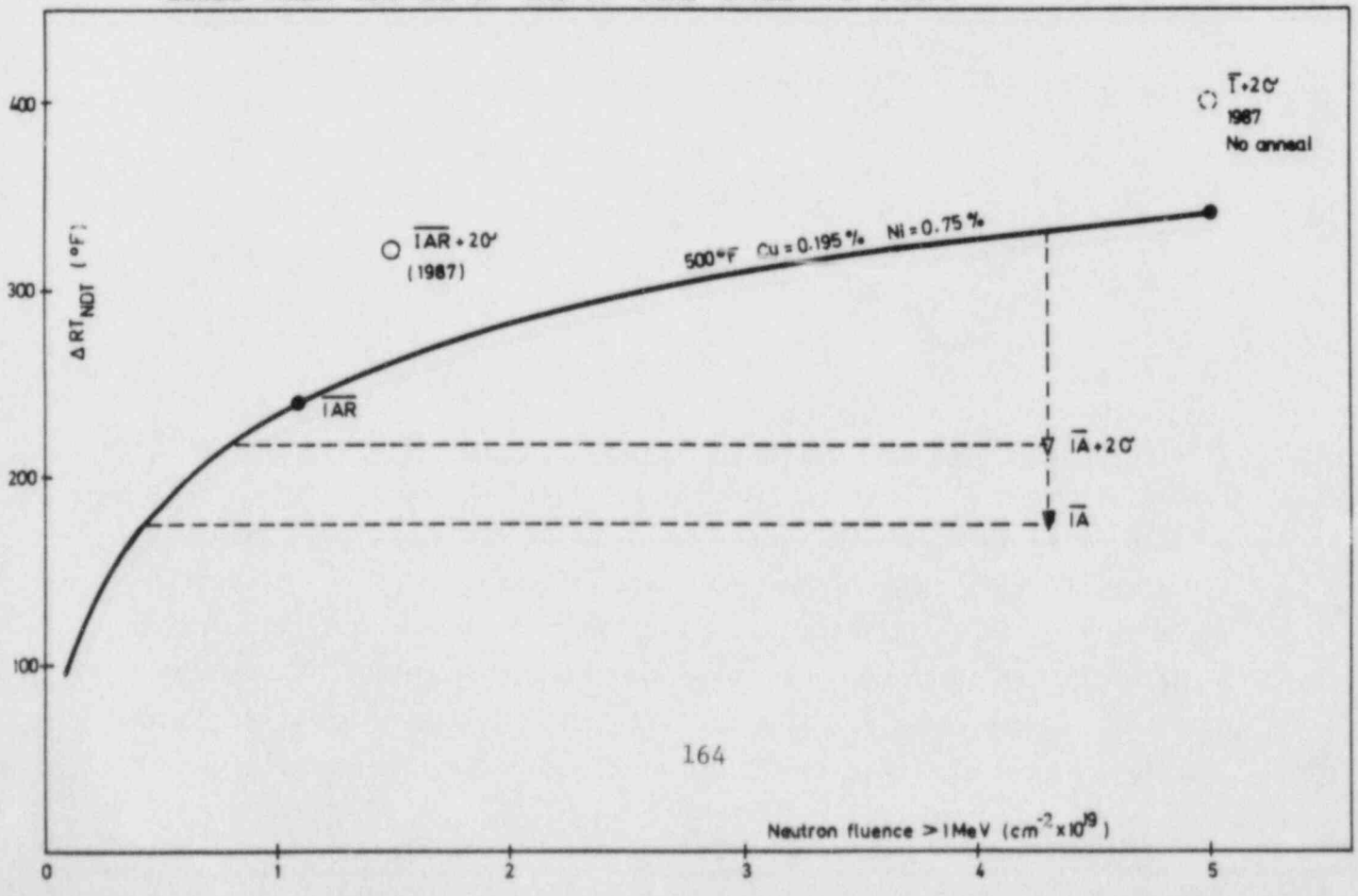

recovery is excellent, by contrast to its RT_{NDT} recovery (compare figures 13 and 16), but its test reactor re-embrittlement is rapid in both cases. It is known /24/ that upper shelf is determined by only one defect mechanism at the temperatures of interest while the transition involves an additional one; this second mechanism is not affected by annealing in our case. All our data are consistent with the view that the relative importance of this second mechanism is greater for weld W-D than for W1, W2, W3, W-E and for the BR3 weld. Here lies the fundamental reason why we consider that archive weld W-D displays an outlier behaviour. A final comment is that test reactor flux rate (acceleration) effects predicted for post-anneal conditions seem confirmed by most of the results of fig. 13, but become less and less evident at increasing neutron fluences, as suggested by fig. 12.

Fig. 16
MOL-MEA-B&W TEST REACTOR EXPERIMENTS INDICATE THAT BR3 WELD UPPER-SHELF CHARPY-V ABSORBED ENERGY WILL ALWAYS EXCEED THE 30 ft.lb. PLANT-SPECIFIC SAFETY LIMITATION (ASME-I DESIGN)

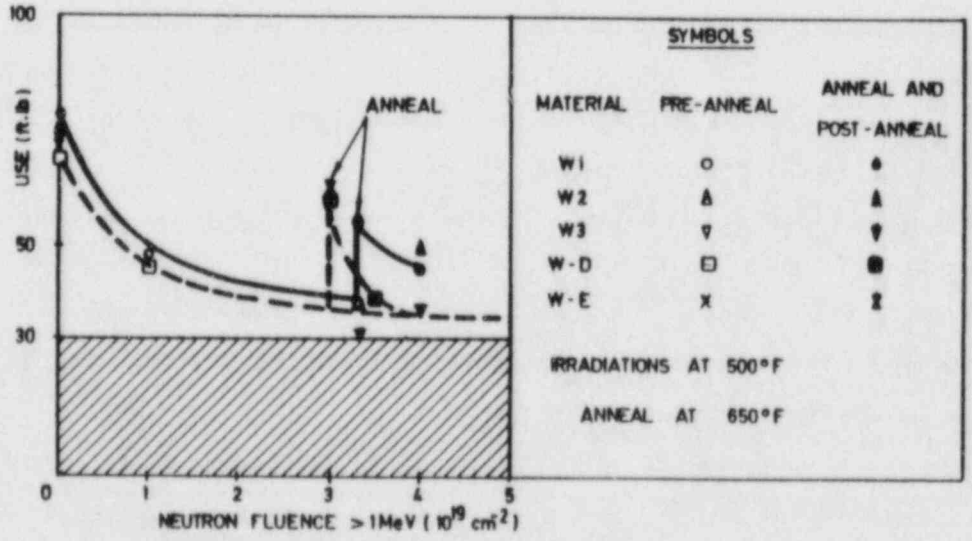

HYPOTHETIZED PRESSURIZED AND OVERCOOLING THERMAL SHOCK ACCIDENTS AT BR3

Four classes of potential event initiators are generally considered :

1. Primary loop failures, such as piping breaks, pressurizer surge line break, stuck-open relief valves reclosing when vessel is cooling, ...
2. Secondary loop failures, i.e. all accidents involving steamline breaks with or without turbine trips etc. ...
3. Excessive feedwater supply to the steam generator(s) for ex. the March 1978 Rancho Seco event /2/
4. Steam-generator tube rupture, eventually combined with other deficiencies.

At BR3, class 3 entails low occurence probabilities ($< 10^{-4}$/year) and mild thermohydraulic transients. Also, steam-generator integrity threats have been shown to be extremely remote /15/. Attention has consequently concentrated on the first two classes, using event-tree methods when appropriate, in order to identify the risk-bounding hypothetized thermohydraulic transient. The current conclusion is that the worse event to be realistically considered would be a main steamline break (MSLB) of 0.4 ft^2 size with the reactor coolant pumps tripped $\sim$ 1 min. after the safety injection signal (steamline isolated by upstream valve), and at full reactor power, not at hot shutdown. The importance of assessing accidental transients on a plant-specific basis could not be better illustrated.

Among BR3 plant system and operation specificities mitigating the PTS risk, the following ones deserve mention :

- Repressurization is limited by the low safety-injection shut-off head pressure of $\sim$ 1000 psi
- Steam-generator feedwater isolation control valve is closed automatically or by procedure at no-load conditions (operator success probability as quantified in /14/, should the automatic actuation train fail)

- Significant fraction ($\sim$40 %) of the total safety injection flow of 120 m^3/hr is diverted over the core by a spray basket designed to protect the fuel
- Metal-stored energy has an important effect in reducing vessel chilling (dimensioning of internals).

Unfavourable are the pressurizer, surge-line and vessel geometrical features in case of SBLOCA. For break sizes in excess of 1.5", rapid and important voidage (up to 65 %) may occur, resulting in loop flow stagnation and potentially poor mixing conditions. However, the break size above which there is no more re-pressurization is small, 0.5", and the associated voidage fraction less than 1 % : natural circulation insures good mixing.

For this case, which still involves maximum re-pressurization, even a very conservative extrapolation of the thermohydraulics calculations does not lead to unacceptable vessel failure risk (fig. 18), for two reasons :

- Warmprestressing (WPS) /20/ is effective in prohibiting crack initiation
- Even if WPS was not credited for, and although crack arrest is not effective here, an utterly unlikely flaw (> 1/4 T) /4/ would be required to result in crack initiation.

The base fracture mechanics analysis, such as the one on fig. 18, is carried out by means of the OCA-1 code /33/, adapted for the BR3 conditions. The code considers only surface flaws infinitely long, and of depth $\underline{a}$ variable from zero to the vessel thickness, $\underline{w}$; the corresponding LEFM stress-intensity factor is labelled here $K_{I\infty}$. The bottom part of fig. 18 is the time-dependent locus of fractional wall penetration values $(a/w)_c$ for which $K_I = K_{Ic}$ (initiation) or = $K_{I\alpha}$ (arrest).

Fig. 19 is intended at carrying two ideas :

1. A BR3 weld IAR condition as estimated here would remove any threat from the potential PTS accident tentatively assessed so far as plant-bounding

Fig. 17

BR3 HYPOTHETIZED PTS TRANSIENTS

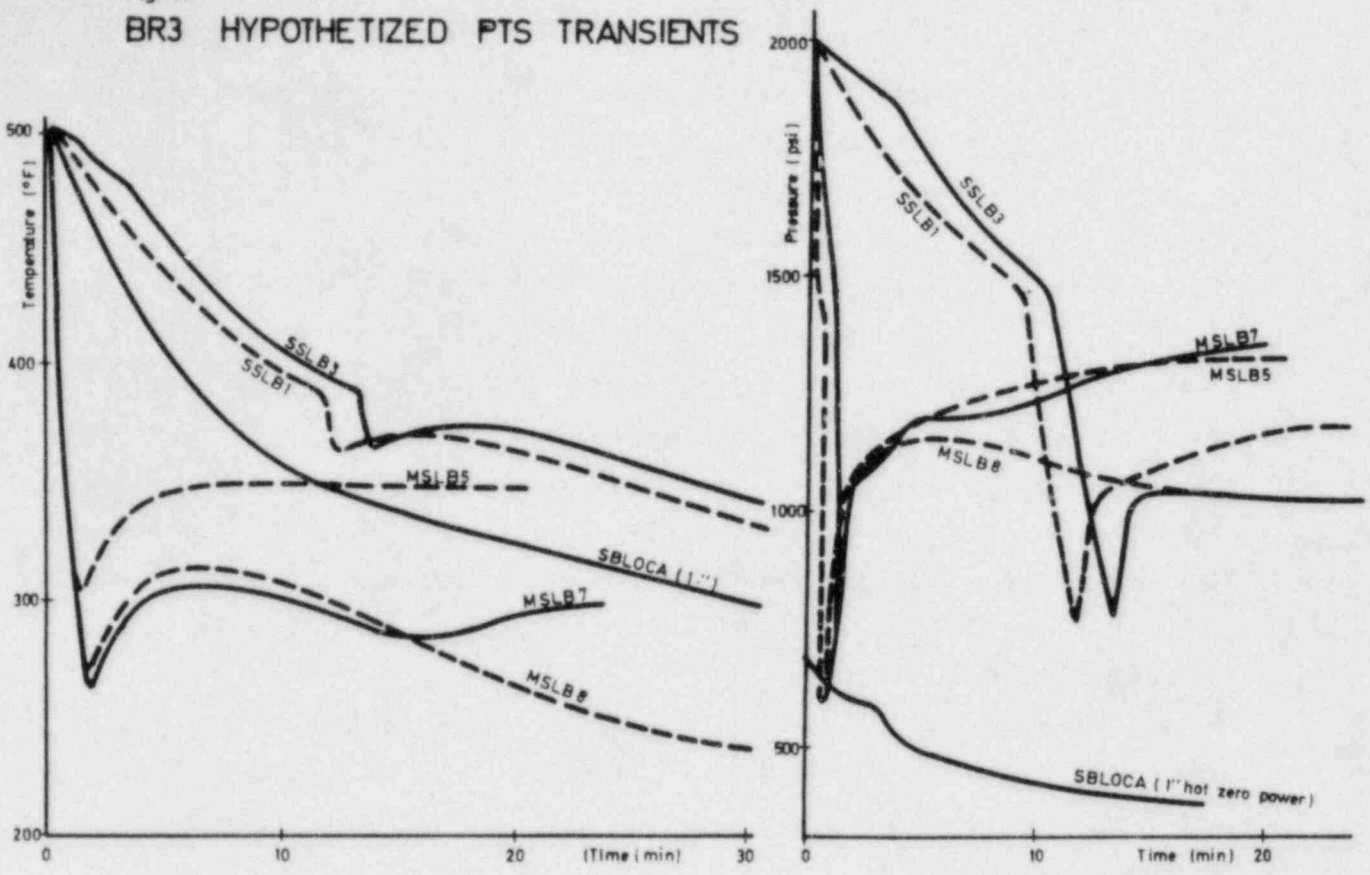

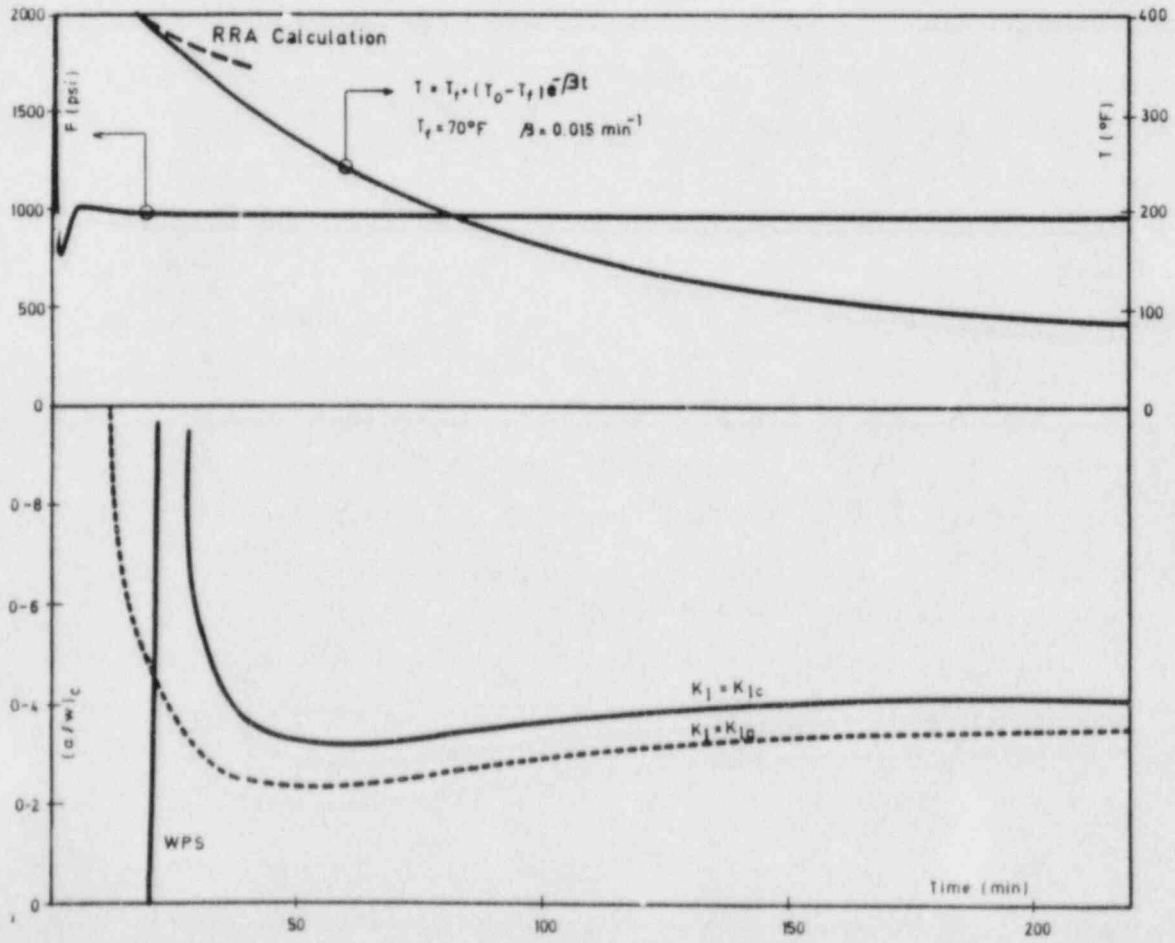

Fig. 18
BR3 WELD
SBLOCA
1/2" leak
HOT SHUT-DOWN
$\phi = 5.10^{19}$ cm^{-2}

2. Under the same materials and transient assumptions, an ASME-III designed vessel would not be fracture-safe to the same obvious degree.

It is extremely rewarding to examine what happens at the most critical time in the transient, i.e. at $t = t_c$ for which $(a/w)_c$ is minimum. For the sake of this paper, we will illustrate such evaluation in the case of one of the worse MSLB transients (MSLB 5 on fig. 17).

This transient is used as example here because it has also been analysed by means of the OCA-P code /34/. The deterministic part of the calculation is in agreement with the runs at MOL, as should be expected; the probablilistic fracture-mechanics part has given the following results :

Crack initiation probability : $2.10^{-3}/Y$
Vessel failure probability : $\underline{9.10^{-4}/Y}$

These are conditional probabilities (i.e. assuming that the transient happens) based on flaw probabilities taken from the MARSHALL report /35/. The interesting points are :

1. Generic conditional failure probability : $\underline{5.10^{-2}/Y}$
2. About 80 % of flaws that initiate do arrest.

It appears thus that the deterministic results on fig. 19 may be unduly conservative - at least if credit is to be taken for crack arrest.

The physical reason under the argument is the small fuel core-height of 1 meter (fig. 1), resulting in vertical exposure and fracture toughness gradients worth accounting for. This in turn entails crack tip driving forces well below $K_{I\infty}$ /36/, as shown on the right-hand side of fig.20. Even considering very pessimistically weld residual-stresses uniformly distributed and as large as 7.5 Ksi /37/, radial crack arrest will occur before 1/2 T and below upper shelf toughness levels. The remaining ligament is sufficient to prevent failure.

Another benefitial consequence of fig. 20 (vertical K_I curve) is that the BR3 effective weld length of concern is less than 2 meter (volume < 8000 cm^3); therefore, the probability of fabrication defects is much

Fig. 19 PLANT-SPECIFICITY OF THE PTS THREAT TO RPV INTEGRITY

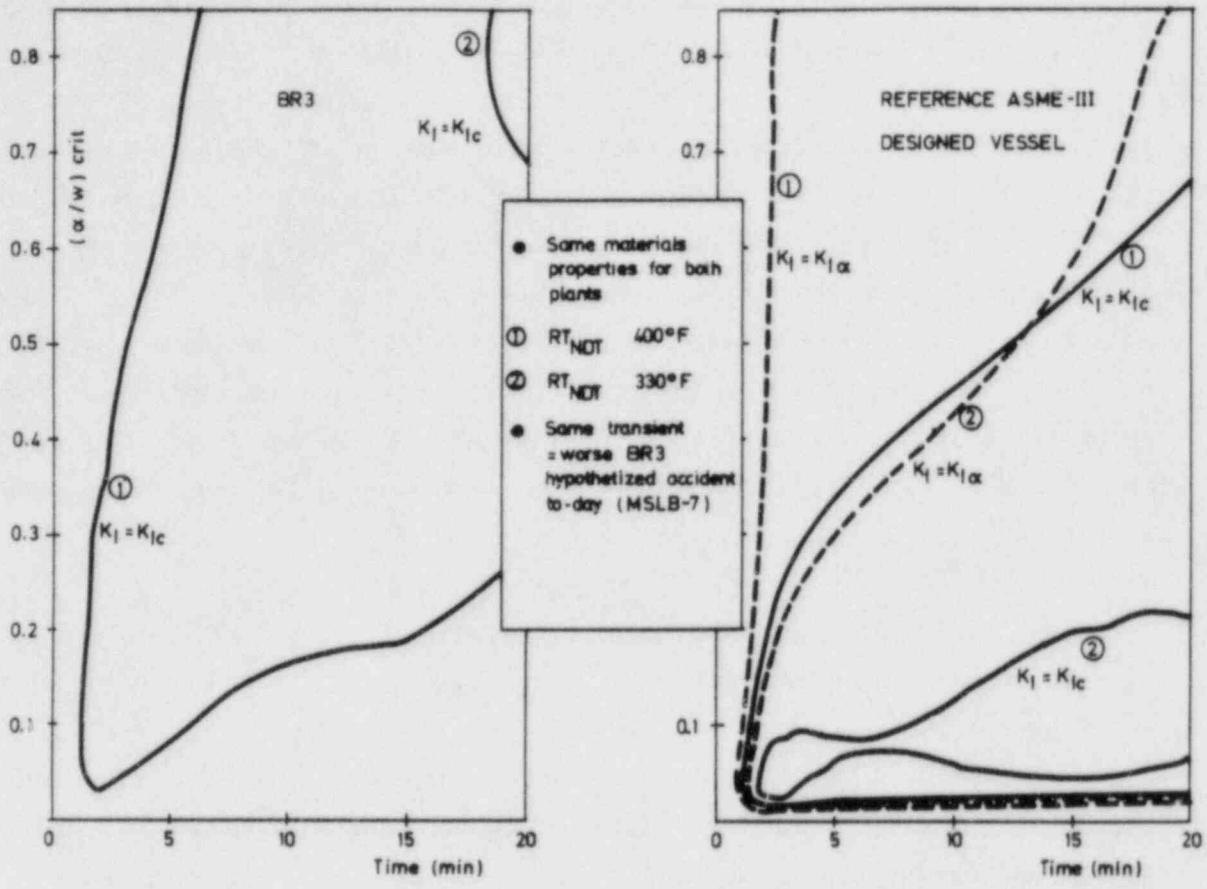

Fig. 20 REALISTIC CRACK-ARREST ANALYSIS FOR TYPICAL HYPOTHETIZED MSLB ACCIDENT AT BR3.
MSLB 5 RT_{NDT} = 400°F

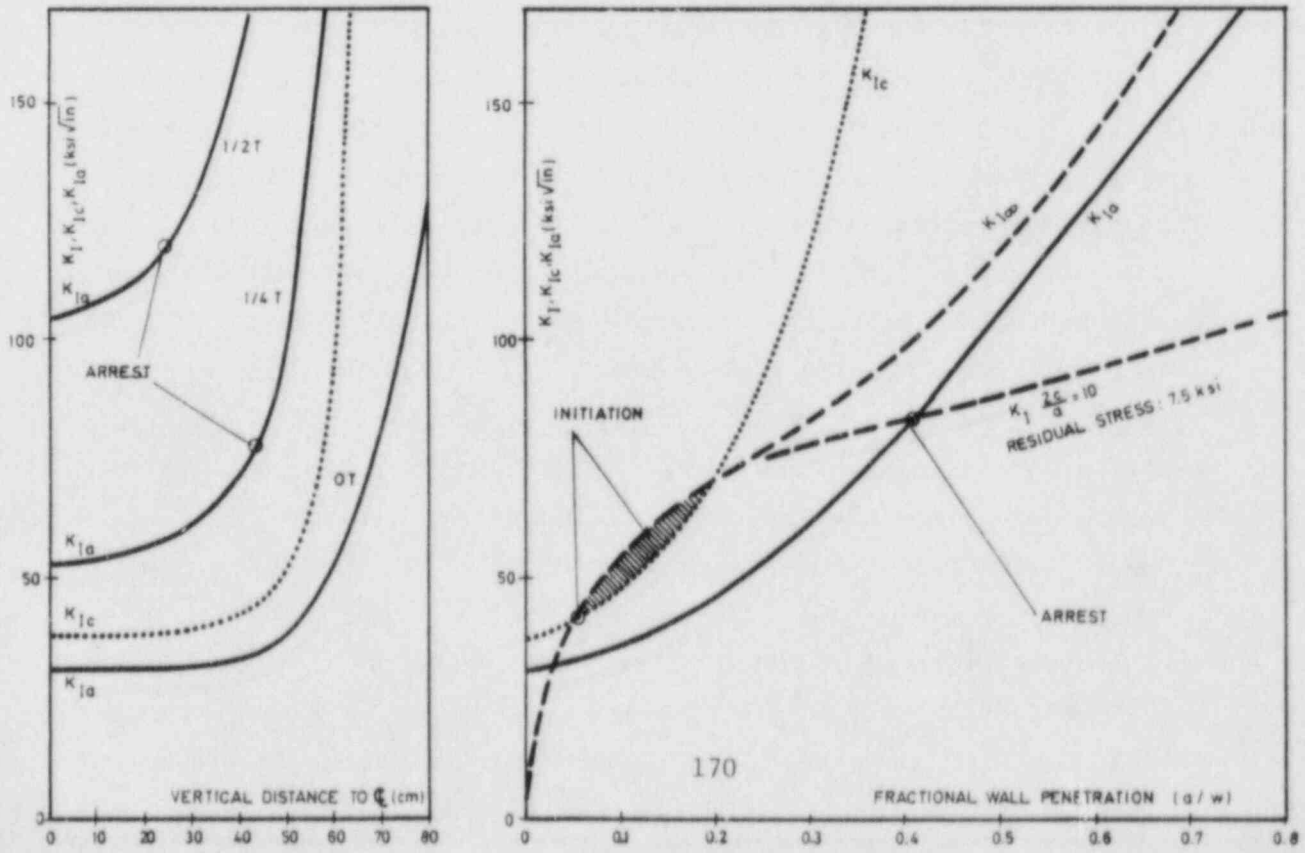

less than for a generic plant beltline. This has been our rationale for discarding the possibility of flaws exceeding 1/4 T (≥8 mm) /4/. It is believed that undetected subclad surface flaws deeper than 6 mm are unlikely in this weld at fabrication and by commissioning time. It must be noted that an enhanced pre-service hydrotest has been successfully performed at 3750 psi (1.5 design pressure) and 86 °F. Also fatigue crack-growth for BR3 materials at beltline has been estimated to be negligibly small.

CONCLUSIONS

- Although the BR3 vessel anneal effectiveness cannot yet be ascertained beyond questioning (until actions in progress are completed), it clearly has enhanced the overall plant safety to an appreciable degree for the next few years.

- Without anneal, it is most likely that the BR3 vessel integrity would not have been jeopardized by 1987.

- The BR3 vessel wet-anneal must be seen as a plant-specific experience. In particular, such approach would obviously be rewardless for commercial PWRs.

- Regulatory requirements to-day must be understood in context : they are adequate for most plants, albeit unacceptably too severe for others, if interpreted as rigid operational barriers. We trust that such is not the Intention of the Regulators.

ACKNOWLEDGMENTS

There would be no reader of this paper if it was not for the dedication and skill of S. ANDRIES, J. THIJS and S. VAESSEN in making a timely edition possible.

But there may not have been any such paper at this time as well without the Advisory Support of the NUCLEAR REGULATORY COMMISSION OF THE UNITED

STATES OF AMERICA : Through its Research Branch and the impetus provided by C.Z. SERPAN; Through its Licensing Branch and the always open, albeit vigilantly critical expertise of Drs. W. JOHNSON, P.N. RANDALL, W. HAZELTON (to name only a few). So much invaluable is this attention (provided despite intense domestic work pressure) that it cannot be acknowledged with just a few words.

The Belgian and U.S. Utilities have helped this effort also. This was done, not only through fingering at potential pitfalls and valid concerns to be addressed, but also by freely providing information and archive test material for BR3.

Dr. T.U. MARSTON (EPRI) and P. HERNALSTEEN (TRACTIONEL) have been most instrumental in these respects.

Last, but not least, we thank Dr. R.D. CHEVERTON and D.G. BALL at Oak Ridge National Laboratory for their help and verification work in having us all set to analyse hypothetized overcooling transients at BR3 and for giving us many constructive guidelines.

REFERENCES

/1/ F. MOTTE et al. - "Engineering Implementation and Quality Assurance of the 1984 Reactor Vessel Anneal at the BR3 Plant" To be published.

/2/ W.J. DIRCKS - Policy Issue (Notation Vote) SECY-82-465 to the USNRC Commissioners and Attachment "NRC Staff Evaluation of Pressurized Thermal Shock", November 23, 1982.

/3/ A. FABRY et al. - "Improvement of LWR Pressure Vessel Steel Embrittlement Surveillance : Progress Report on Belgian Activities in cooperation with the USNRC and other R&D Programs", Fourth ASTM-EURATOM Symposium on Reactor Dosimetry, NUREG/CP-0029, Vol. 1, 45 (1982).

/4/ A. FABRY et al. - "Improvement of LWR Pressure Vessel Steel Embrittlement Surveillance : 1982-1983 Progress Report on Belgian Activities in cooperation with the USNRC and other R&D Programs", Fifth ASTM-EURATOM Symposium on Reactor Dosimetry, Geesthacht, Germany (Sept. 24-28,1984).

/5/ G.J. FREEMAN - "LOCA Analysis of the BR3 Plant at MOL, Belgium", Rolls Royce Associates Report RRA/6784 (1984).

/6/ US Code of Federal Regulations, Title 10, Energy, Part 50, Appendix G, Fracture Toughness Requirements, revised (1983).

/7/ U.S. Nuclear Regulatory Commission Standard Review Plan, Report NUREG-75/087 and Branch Technical Position MTEB 5.2.

/8/ R. JOHNSON et al. - "Resolution of the Reactor Vessel Materials Toughness Safety Issue" NUREG-0744 (1981).

/9/ A. LOWE Jr. - "Evaluation of Fabrication Procedures for BR3 Reactor Vessel" BAW-1807 (1983).

/10/ J. GOODMAN - "Reactor Material Sampling, BR3 Mol Belgium", Rolls Royce Ass. Report RRA/6605 (1983).

/11/ T. MAGER et al. - "Pressure-Temperature Limit Curves for Normal Heat-up and Cool-down of the BR3 Reactor Pressure Vessel" WENX/78/17 (1978).

/12/ A. FABRY - "BR3 Pressure Vessel Safety Margins against Upper Shelf Failure by Plastic Instability or Cleavage Fracture" CEN/SCK 380/81-50, Dec. 4, 1981.

/13/ J.M. BLOOM - "Safety Factor Calculations for the BR3 and Reference Vessels using the Failure Assessment Diagram Approach" BAW-1811 (1983).

/14/ J. BOUCAU, M. DUPREZ - "BR3 - Pressurized Thermal Shock Analysis: Steamline Break Transients" WENX/83/80 (1983).

/15/ F. MOTTE - "BR3 Steam Generator : Elements of judgment on the Integrity of this Equipment" CEN/SCK Internal Document (1983).

/16/ J. DEBRUE and G. MINSART - "Neutron exposure of the BR3 vessel. Status at the start of cycle 4D" (September 1, 1984).

/17/ J.R. HAWTHORNE et al. - "Accelerated Irradiation and Testing of Archive Materials in Support of the BR3 Vessel Anneal" Materials Engineering Assoc. To be published.

/18/ D. PACHUR - "Physically-Based Evaluation of BR3 Materials Metallurgical Trend Curves". To be published.

/19/ T. MAGER et al. - "Pressure-Temperature Limit Curves for Normal Heat-up and Cool-down of the BR3 Reactor Pressure Vessel", Report WENX/78/17 (1978).

/20/ B.W. PICKLES, A. COWAN - "A review of Warm Prestressing Studies",Int. J. Pres. Ves. & Piping 14, 95-131 (1983).

/21/ W.N. McELROY et al. - "Surveillance Dosimetry of Operating Power Plants", Proc. Fourth ASTM-EURATOM Symposium on Reactor Dosimetry, NUREG/CP-0029 (1982).

/22/ A. FABRY et al. - "VENUS PWR Engineering Mcok-up : Core Qualification, Neutron and Gamma Field Characterization" Ibid/4/.

M.L. WILLIAMS et al. - "Calculation of the Neutron Source Distributions in the VENUS PWR Mockup Experiment" Ibid /4/.

A. FERO - "Neutron and Gamma Ray Flux Calculations for the VENUS PWR Engineering Mockup" Ibid /4/.

/23/ R. GOLD et al. - "Non-Destructive Determination of Reactor Pressure Vessel Exposure by Continuous Gamma-Ray Spectrometry and Non-Destructive Measurement of Neutron Exposure of BR3" Ibid /4/.

/24/ D. PACHUR - "Radiation Annealing Mechanisms of Low-Alloy Reactor Pressure Vessel Steels Dependent on Irradiation Temperature and Neutron Fluence" Nucl. Techn. 59, 463-475 (1982).

/25/ A.S. HELLER, A.L. LOWE, JR. - "Correlations for Predicting the Effects of Neutron Radiation on Linde 80 Submerged Arc Welds" Report BAW - 1803 (1984).

/26/ G.D. WHITMAN, Ed. - "Technology of Steel Pressure Vessels for Water-Cooled Nuclear Reactors" Report ORNL - NSCIC 21 (Dec. 1967).

/27/ P.N. RANDALL - "NRC Perspective of Safety and Licensing Issues Regarding Reactor Vessel Steel Embrittlement: Criteria for Trend Curve Development", ANS Annual Meeting, Detroit, June 14 (1983).

/28/ G.L. GUTHRIE- "Charpy Trend Curve Formulas Derived From an Expanded Surveillance Data Base", NUREG/CR-2805, Vol. 4, - HEDL-3 to 13 (1983).

/29/ J.D. VARSIK et al. - "Evaluation of Irradiation Response of Reactor Pressure Vessel Materials" Report EPRI - NP2720 (1982).

/30/ B. MCDONALD - "A Note on Commercial Annealing Experiments" to be published (1984).

/31/ A.P. MAIN, B.L. SHRIVER - "Analytic Predictions of the Annealing Response of A533B Reactor Vessel Steel Welds" Nucl. Techn. 59, 456-462 (1982).

/32/ Ph.VANASBROECK, J. VANDEVELDE - To be published (1984).

/33/ S.K. ISLANDER, R.D. CHEVERTON and D.G. BALL - "OCA-I, A Code for Calculating the Behavior of Flaws on the Inner Surface of a Pressure Vessel Subjected to Temperature and Pressure Transients" Report NUREG/CR 2113, ORNL/NUREG-84 (1981).

/34/ R.D. CHEVERTON and D.G. BALL - Private Communication, July 11, (1983).

/35/ "An Assessment of the Integrity of PWR Pressure Vessels" Second Report of UKAEA Study Group under the Chairmanship of Dr. W. MARSHALL (1983).

/36/ I.S. RAJU, J.C. NEWMAN Jr. - "Stress-Intensity Factor Influence Coefficients for Internal and External Surface Cracks in Cylindrical Vessels" J. Press. Vessel Techn. Trans. ASME V104 no 4, 37-48 (1982).

/37/ D.P.G. LIDBURY - "The Significance of Residual Stresses in Relation to the Integrity of LWR Pressure Vessels" Report to Principal Working Group on Primary Circuit Integrity, Commission on the Safety of Nuclear Installations, CSNI, 1984.

INVESTIGATION OF THE DUCTILE FRACTURE PROPERTIES OF TYPE 304 STAINLESS STEEL PLATE, WELDS, AND 4-INCH PIPE

by

M.G. Vassilaros
R.A. Hays
J.P. Gudas
David Taylor Naval Ship R&D Center
Bethesda, MD 20084

INTRODUCTION

The David Taylor Naval Ship R&D Center has performed two tasks for the Nuclear Regulatory Commission concerning the safety of stainless steel (SS) pipes. The first task dealt with the J-integral fracture toughness of 2-inch thick welded 304 stainless steel plate. The second was the J-integral testing of 4-inch diameter, schedule 80 welded 304 SS pipe that contained circumferential through wall flaws, with and without additional radial flaws. The summary of these two tasks will be presented including the comparison of the maximum loads experienced by the 304 SS pipes and the loads predicted by IWB-3640 for 304 SS pipes.

WELDED 2-INCH PLATE J-INTEGRAL RESISTANCE CURVE TESTS

A 2-inch thick plate of 304 SS was welded by Babcock and Wilcox for use in a weld evaluation task. The weld geometry, welding parameters, and specimen tests on 1T and 2T modified compact specimens of base plate, weld metal, and fusion line. Tests were performed at room temperature (RT), 300°F (149C), and 550°F (288C). The tensile mechanical properties of the weld metal and base plate are given in Table 1. The results of J-integral tests performed on 1T compact specimens are shown in Figure 2. The figure shows the reduction in the J-R curve resulting from the 550°F (149C) test temperature. Additionally, the figure shows that this reduction in toughness has produced a better correlation between the crack length measurements from the elastic unloading compliance method (reference 1), the open symbols, and the final measured crack length, filled symbols. Figure 3 presents the results of the J-integral test performed on a 2T compact specimen at 550°F (288C) compared to the 1T results. Although the 2T specimen appears to have a higher J-R curve, the curve had a significant underprediction of the final measured crack length which was 0.275 inch and therefore off scale on Figure 3. Had the J-R curve been extended to the correct final crack length the curve would

have been lower and agreed well with the 1T specimen data.

The J-R curves for the 1T compact specimens machined from the 304 SS weld metal are shown in Figure 4. These results clearly show the same trends as with the base metal results, that is, an increase in test temperature produces a decrease in the measured J-R curves. The final measured crack lengths were underestimated by compliance from 9 to 22% which would suggest that all of the curves should be lower. However, the relative position of the curves would not change. Figure 5 presents the J-R curves of the 2T weld metal compact specimens tested at 550°F (228C) compared to the 1T specimen results. The figure indicates an apparent increase in the J-R curve behavior of the 2T specimens. This anomaly was the result of machined notch placement which resulted in composite specimens which were approximately 50% weld metal and 50% base plate. Therefore, these 2T specimen J-R curves should be higher than the weld metal curves and less than the base metal curves. The fusion line fracture toughness of the 304 SS weld was evaluated with a 1T compact specimen machined at an angle to the weldment surface so as to have the precrack in the plane of the fusion line. This specimen was tested at 550°F (228C) and the resultant J-R curve is shown in Figure 6 along with representative J-R curves of the weld metal and the base plate. Although the fusion line J-R curve underestimated the final measured crack length (0.270-inch), the curve still would reflect a mixture of the base metal and weld metal toughness. Table 2 has a summary of all the J-integral toughness tests along with the calculated J_{Ic} values and the range of the data used in the linear fit line to calculate J_{Ic}. Also listed in Table 2 are the tearing modulus values calculated using a least squares linear regressive fit of all the data within the ASTM E813 exclusion limits.

4-INCH PIPE J-INTEGRAL RESISTANCE CURVE TESTS AND LIMIT LOAD ANALYSES

The second task is concerned with the fracture toughness and ultimate strength of 4-inch diameter, schedule 80 welded 304 SS pipe at 550°F (288C). The pipe specimens used in this study were supplied by Battelle Pacific Northwest Laboratory (PNL) in two forms, specifically, as welded and welded with a part through radial crack. Both types of pipe were welded with the parameters and geometry shown in Figure 7. The two types of pipe were machined to produce through wall circumferential cracks as shown in Figure 8. The pipe specimens were fatigue precracked and then tested in four point bend as previously described by Vassilaros, et al (reference 2).

The results of the first pipe test are shown in Figure 9 which is a load versus load point displacement record for a welded pipe with a simple crack as illustrated in Figure 8. Also shown in Figure 9 is the predicted maximum load using the equations in Figure 10, the measured initial crack length, and the flow stress obtained from IWB-3640 for 304 SS pipe. As can be seen, the loads on the pipe never reached the predicted maximum load. Figure 11 is the J-R curve produced from the elastic unloading

compliance test on pipe number 1. This curve has an indicated J-initiation of approximately 5000 in-lb/sq.in. The large underestimation of the final crack length is apparent and may have resulted from the large plastic deformation and ovalization of the pipe produced during the test. Figure 12 has the load versus load point displacement record for the second pipe test with a simple crack. This specimen had a longer initial crack length and therefore a lower maximum load. Here again the pipe never reached the predicted maximum load using IWB-3640 flow stress. Figure 13 has two J-R curves produced from the test of pipe number 2. One curve was the result of the elastic unloading compliance technique which again underpredicted the final crack extension. This curve appears to have a J-initiation level of about 7500 in-lb/sq.in. The second J-R curve was from the direct current potential drop (DCPD) technique which fits the J-R curve to the initial and final measured crack length. The J-initiation level from this curve was approximately 3000 in-lb/sq.in. The large difference between the J-initiation levels of these two curves is believed to be a function of the ovalization occurring during the pipe test. This ovalization increases the height of the pipe and decreases the width which effectively produces a stiffer pipe. This increase in pipe stiffness cancels the decrease in pipe stiffness due to crack extension. This condition conceals the crack initiation point from the elastic unloading compliance technique but not from the DCPD technique which is not affected by such geometry changes.

The results of the test performed on a pipe with a complex crack is shown in Figure 14. The load versus load point displacement record of this pipe appears to agree well with the predicted maximum load. However, this specimen had an initial fatigue crack which was at a shallow angle to the pipe wall. This angle gave a difference in inside and outside total crack length (2θ in Figure 10) of approximately 80 degrees. The initial measured crack length was therefore assumed to be the average of the inner and outer crack length. Figure 15 has the two J-R curves produced from pipe test number 4. In this case, the DCPD and unloading compliance test results appear to be in good agreement. This may have resulted from the fact that this pipe test had loads that were low enough to inhibit any significant plastic deformation and ovalization of the pipe section near the crack. This figure indicates that the J-initiation level was lowered to about 1500 in-lbs/sq.in. with a relatively low tearing modulus resulting from the low slope of the resistance curve. Figures 16 and 17 are the summary J-R resistance curves for the three tests with the elastic unloading compliance curves on Figure 16 and the DCPD curves on Figure 17. Both of these sets of curves indicate that the J-integral fracture toughness of the 304 SS pipes is reduced due to the presence of a radial part through crack in addition to the through wall circumferential crack. In addition to the fracture toughness evaluation an analysis was performed to determine the applicability of using limit load concepts to predict the maximum load displayed in the pipe test. A summary of this analysis is listed in Table 3 which has the measured maximum load and the predicted maximum load. Maximum load in the two pipe tests with simple cracks fell short of the predicted maximum load by 11% and 30%. The specimen with a complex crack had measured maximum

loads which were 2.8% to 16% greater than the calculated loads. This set of results may have been the result of error in the estimation of the initial fatigue crack in the complex crack pipe test.

CONCLUSIONS

The tasks described above to investigate the toughness characteristics of 304 stainless steel welds have resulted in the following conclusions:

1. The J-integral fracture toughness of 304 stainless steel plate is reduced when exposed to elevated temperatures of 300°F and 550°F.

2. The J-integral toughness of 304 stainless steel hot wire automatic gas tungsten arc welds is lower than the toughness of the base metal at all test temperatures RT, 300°F, 550°F.

3. The J-integral fracture toughness of gas tungsten arc (GTA) welded 4-inch 304 stainless steel pipe tested with a circumferentially growing through wall flaw is lowered with the presence of a part through radially growing crack.

4. Maximum load prediction of GTA welded 304 SS pipe using limit load analysis and the flow stress from IWB-3640 for 304 SS pipe were unconservative for through wall flaws growing circumferentially.

REFERENCES

1. Joyce, J.A. and J.P. Gudas, "Elastic-Plastic Fracture," ASTM STP 668, J.D. Landes, J.A. Begley, and G.A. Clarke, Eds., American Society of Testing and Materials, 1979, pp. 251-265.

2. Vassilaros, M.G., R.A. Hays, and J.P. Gudas, "J-Integral Tearing Instability Analyses for 8-Inch Diameter ASTM A106 Steel Pipe," NUREG (CR-3740), U.S. Nuclear Regulatory Commission, 1984.

304 STAINLESS STEEL PLATE WELDMENT

- PREPARATION: 2 INCH THICK DOUBLE-VEE BUTT WELDMENT
- PROCESS: HOT-WIRE AUTOMATIC GAS TUNGSTEN ARC WELD (HWAGTA)
- FILLER METAL: SFA-5.9, ER 308L
- HEAT INPUT: 21.7 KJ/IN.

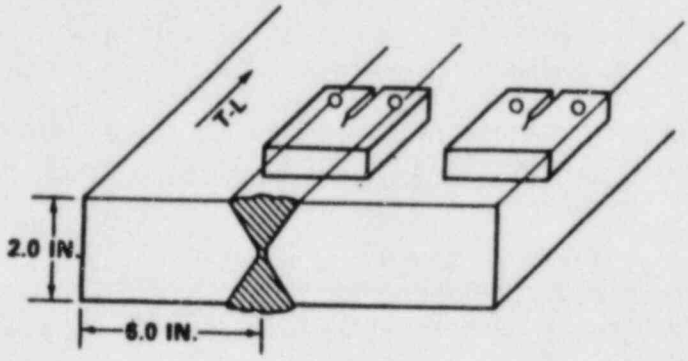

Figure 1 - Weld Parameters and Geometry for Type 304 Stainless Steel Plate Weld

MECHANICAL PROPERTIES OF STAINLESS STEEL BASE METAL AND WELD

		TEMP (°F)	Y.S. (KSI)	U.T.S. (KSI)	% ELONG. (2 IN.)	% R.A.
TYPE 304 STAINLESS STEEL	BASE METAL	RT	36.6	89.0	68	77
		300	27.0	71.8	54	77
		550	22.0	69.9	50	72
	WELD (TRANSVERSE)	RT	67.4	88.7	38	65
		300	51.6	69.1	29	59
		550	49.0	65.6	25	55

Table 1 - Tensile Mechanical Properties of Type 304 Stainless Steel Base Plate and Weld

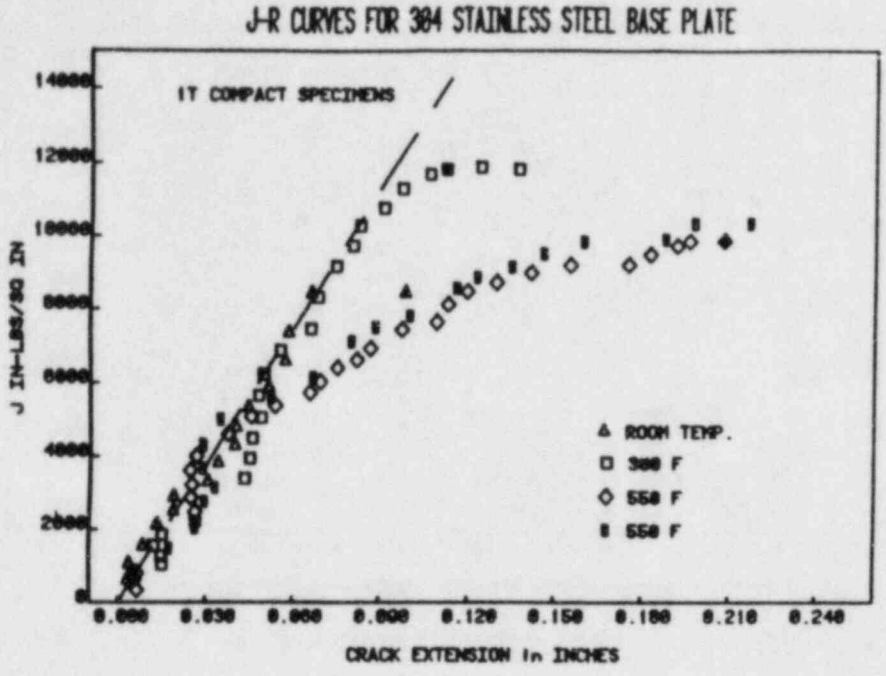

Figure 2 - J-R Curves for 1T Compact Specimens of Type 304 Stainless Steel Base Plate

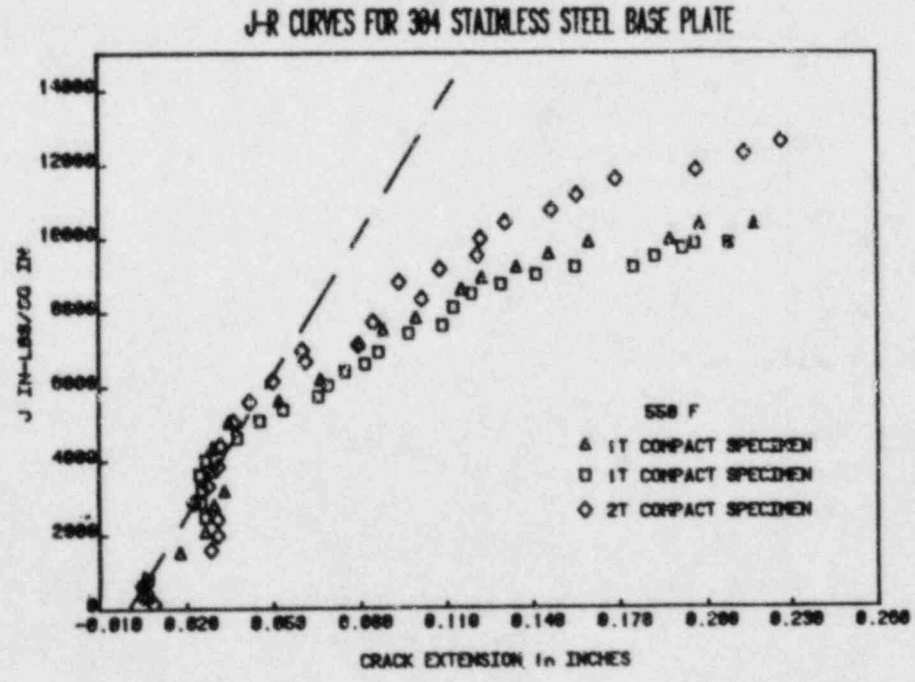

Figure 3 - J-R Curves for 1T and 2T Compact Specimens of Type 304 Stainless Steel Base Plate

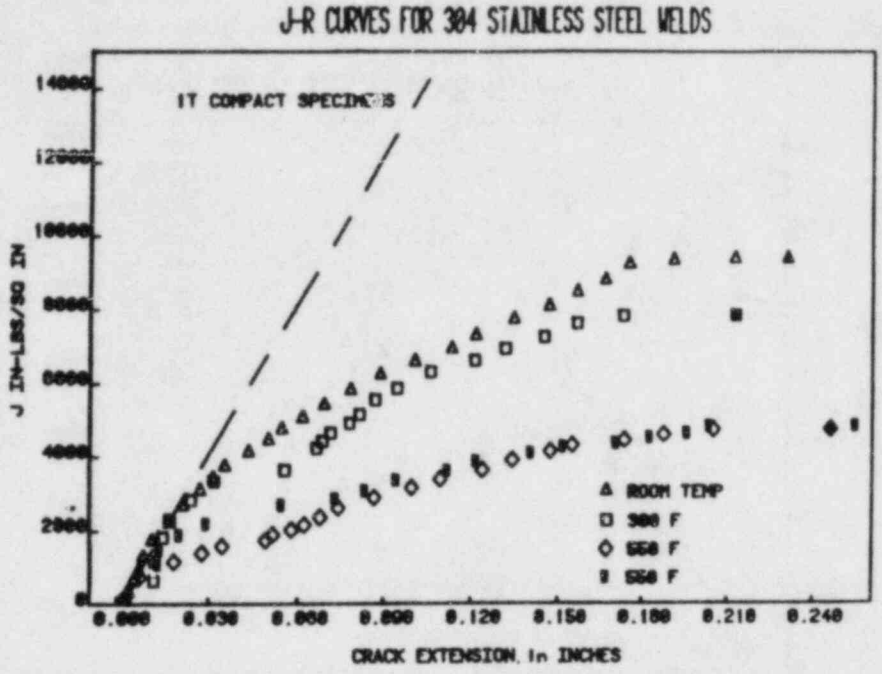

Figure 4 - J-R Curves for 1T Compact Specimens of Type 304 Stainless Steel Weld

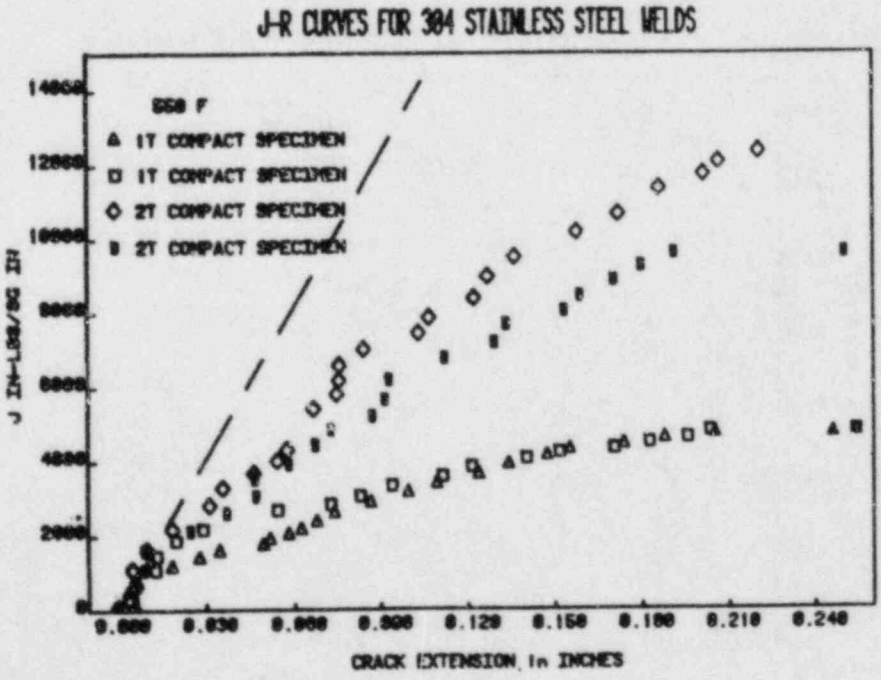

Figure 5 - J-R Curves for 1T and 2T Compact Specimens of Type 304 Stainless Steel Weld

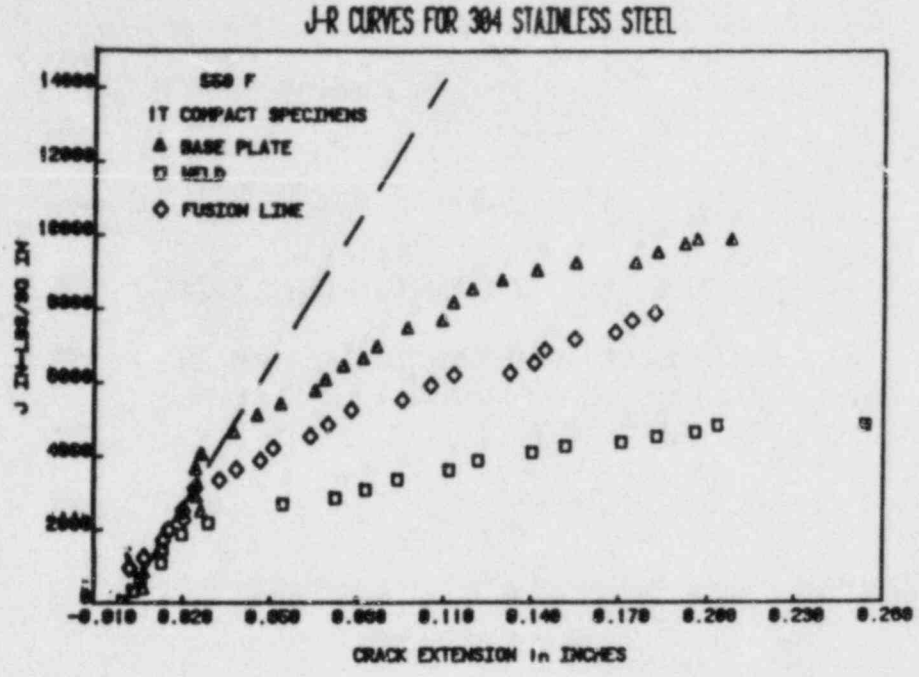

Figure 6 - Comparison of J-R Curves from 1T Compact Specimens of Base Plate, Weld, and Fusion Line for Type 304 Stainless Steel

304 STAINLESS STEEL FRACTURE PROPERTIES

	SPEC #	SPEC SIZE	TEST TEMP (°F)	$\left(\frac{J_{IC}}{\frac{in \cdot lb}{in^2}}\right)$	ΔA FOR CALC (in.)	T_{MAT}
BASE METAL	GAM-1	1T	RT	---		---
	GAM-4	1T	300	---		---
	GAM-2	1T	550	4760	0.088	352
	GAM-3	1T	550	4435	0.097	345
	GAM-8	2T	550	6090	0.102	410
WELD METAL	GAM-19	1T	RT	2974	0.088	289
	GAM-20	1T	300	2283	0.108	277
	GAM-21	1T	550	930	0.062	152
	GAM-22	1T	550	---		---
	GAM-23	2T	550	1297	0.091	353
	GAM-24	2T	550	2144	0.058	437
BASE/WELD FUSION LINE	GAM-35	1T	550	2978	0.776	239

Table 2 - Summary of J-Integral Toughness Tests on Type 304 Stainless Steel

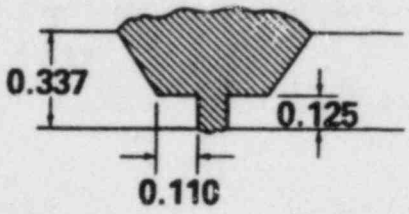

PIPE WELD CONFIGURATION

WELD PROCESS: AUTOMATIC GAS-TUNGSTEN ARC
FILLER METAL: TYPE 308L STAINLESS STEEL
HEAT INPUT: 30 kj/in.

Figure 7 - Weld Parameters and Geometry for 4 in. Diameter Type 304 Stainless Steel Pipe Specimens

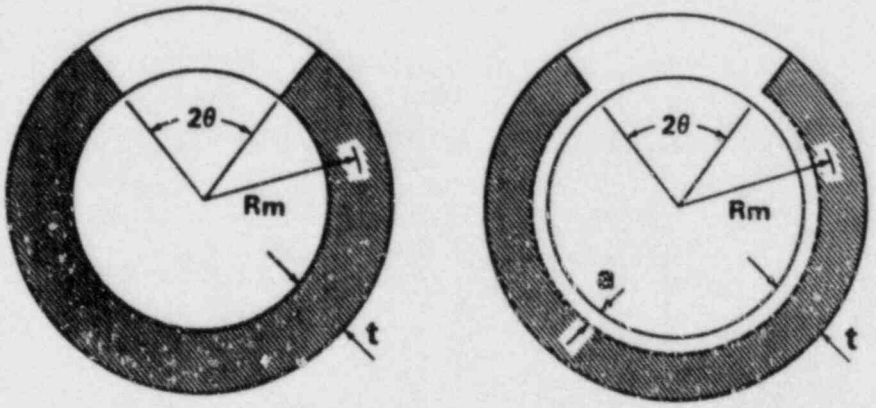

SIMPLE CRACK

2 θ = CIRCUMFERENTIAL CRACK LENGTH
Rm = MEAN RADIUS
t = PIPE WALL THICKNESS

COMPLEX CRACK

2 θ = CIRCUMFERENTIAL CRACK LENGTH
Rm = MEAN RADIUS
t = PIPE WALL THICKNESS
a = RADIAL CRACK LENGTH

Figure 8 - Schematic of Crack Geometries for 4 in. Diameter Type 304 Stainless Steel Pipe Specimens

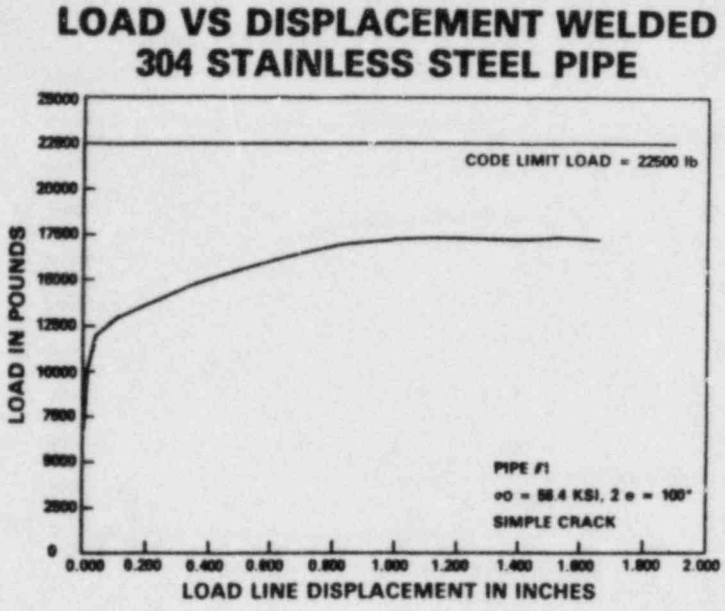

Figure 9 - Load vs. Displacement Record for Pipe Test 1

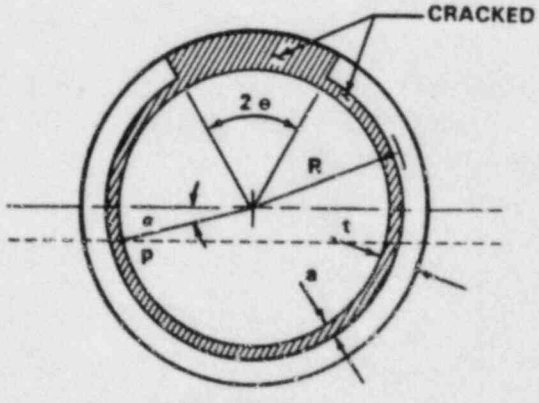

LIMIT MOMENT Mp

$$Mp = 4\sigma_o R^2 t \bar{M}p\ (\theta, \bar{a}, \bar{P})$$

NO CRACK CLOSURE

$$\bar{M}p = (1 - \bar{a})\ (\cos\alpha - 1/2 \sin\theta) + \pi/2\ \bar{P} \sin\alpha$$

CRACK CLOSURE

$$\bar{M}p = (1 - \bar{a}) \left(\frac{1 - 1/2\,\bar{a}}{1 - \bar{a}} \cos\alpha - \frac{1}{2} \sin\theta \right) + \frac{\pi}{2} \bar{P} \sin\alpha$$

Figure 10 - Limit Load Expression for Pipe Geometry

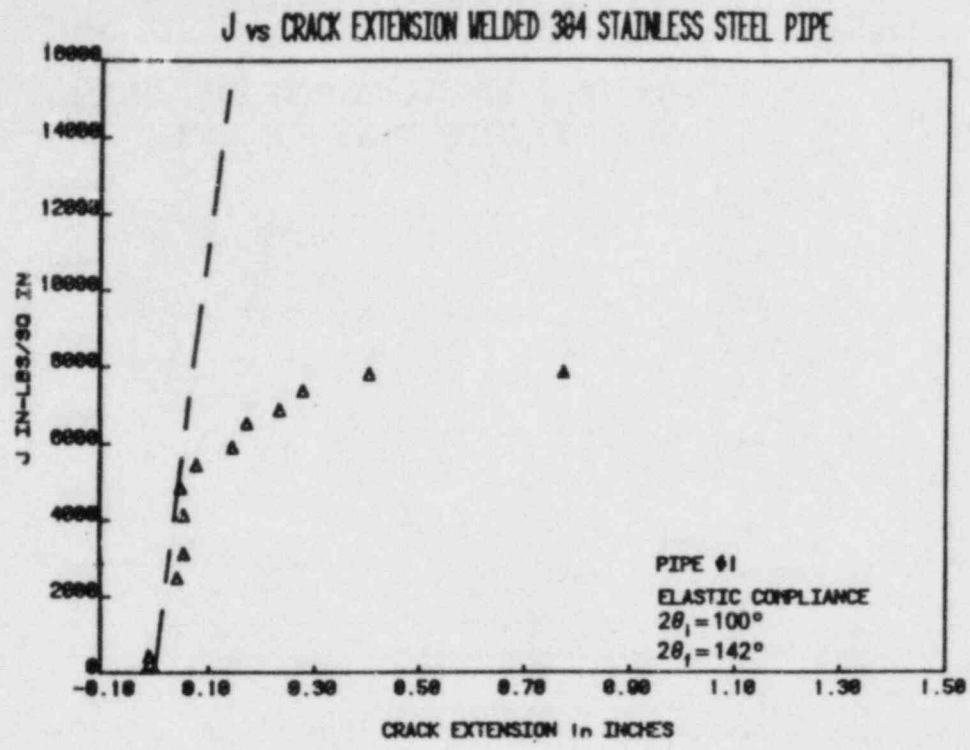

Figure 11 - J-R Curve from Elastic Compliance for Pipe Test 1

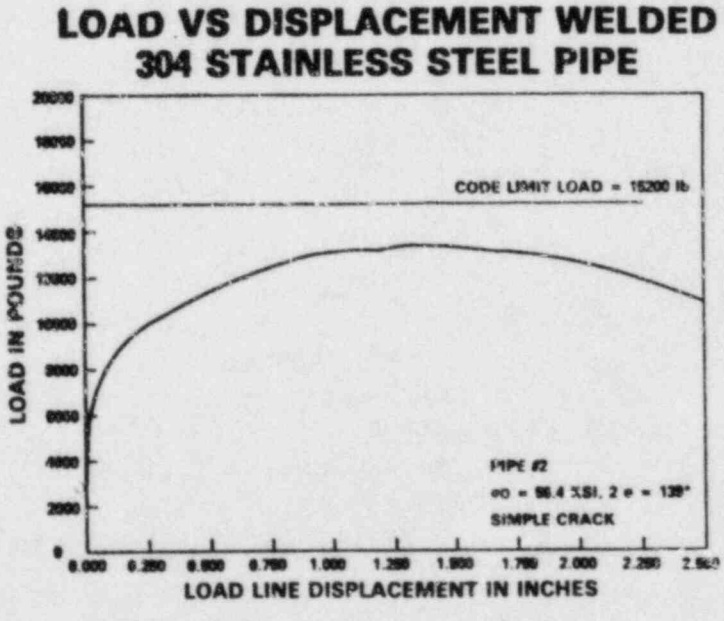

Figure 12 - Load vs. Displacement Record for Pipe Test 2

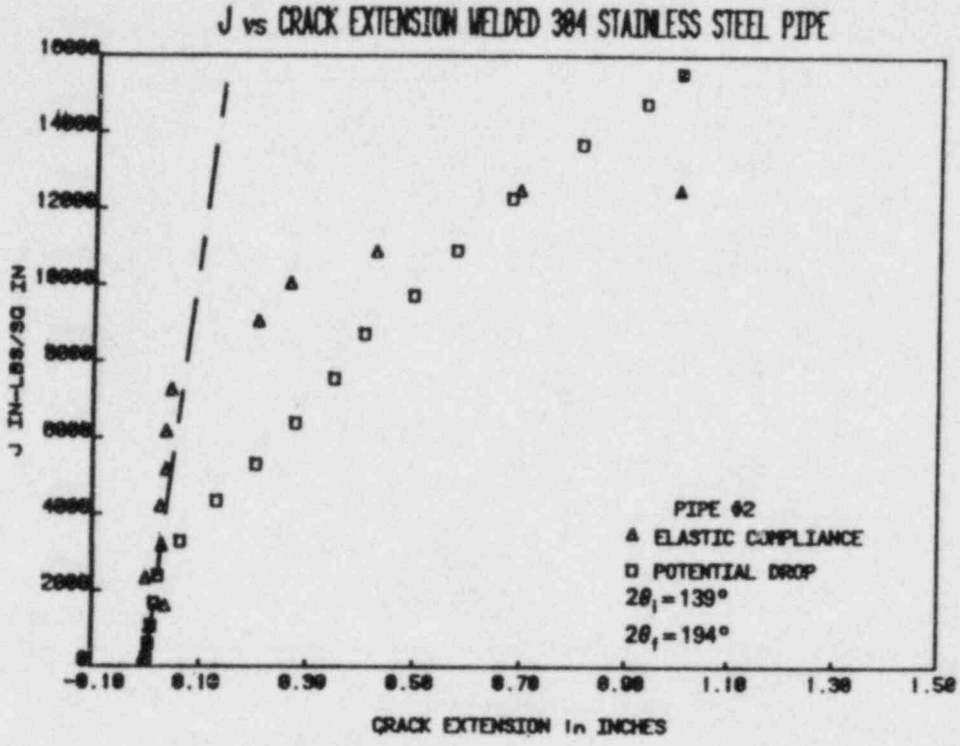

Figure 13 - J-R Curves from Elastic Compliance and DCPD for Pipe Test 2

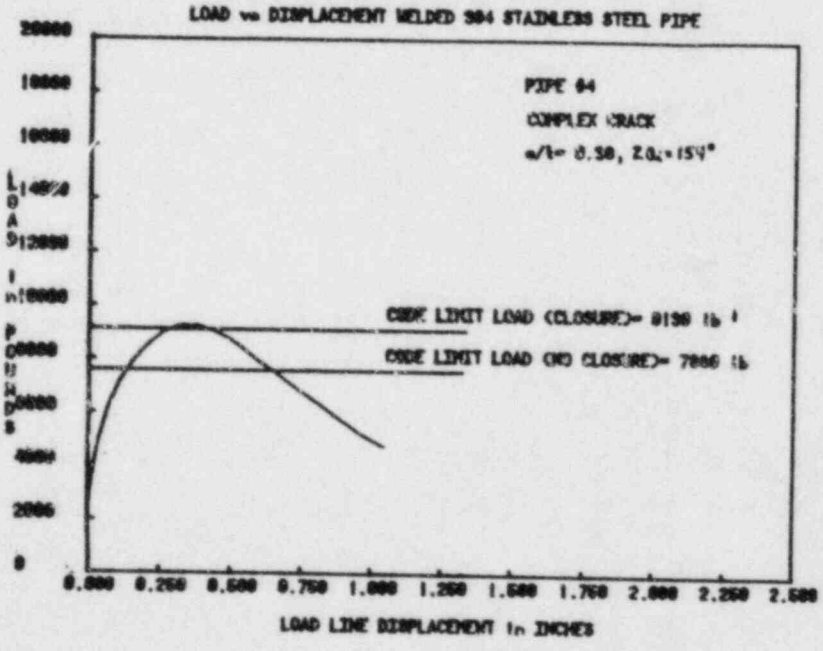

Figure 14 - Load vs. Displacement Record for Pipe Test 4

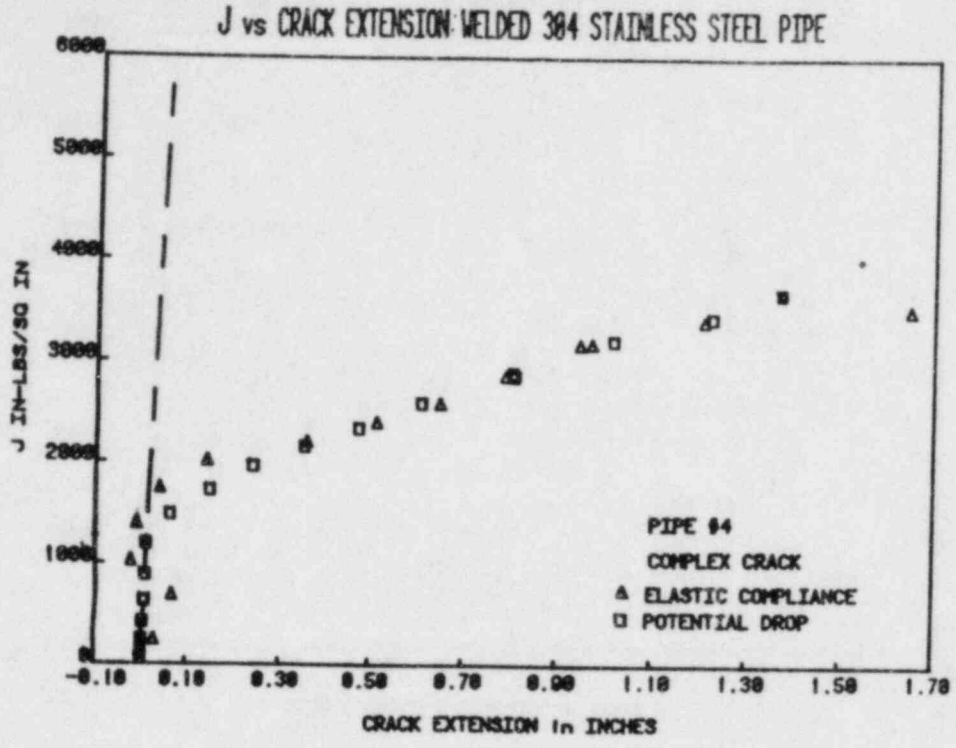

Figure 15 - J-R Curves from Elastic Compliance and DCPD for Pipe Test 4

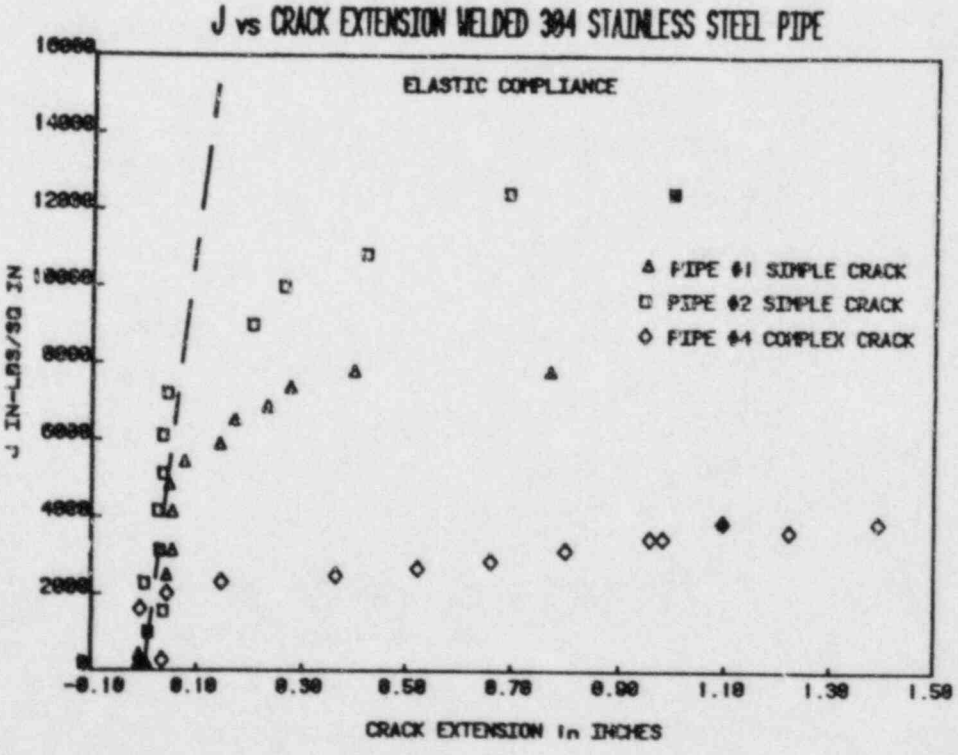

Figure 16 - Comparison of J-R Curves from Elastic Compliance for Pipe Tests

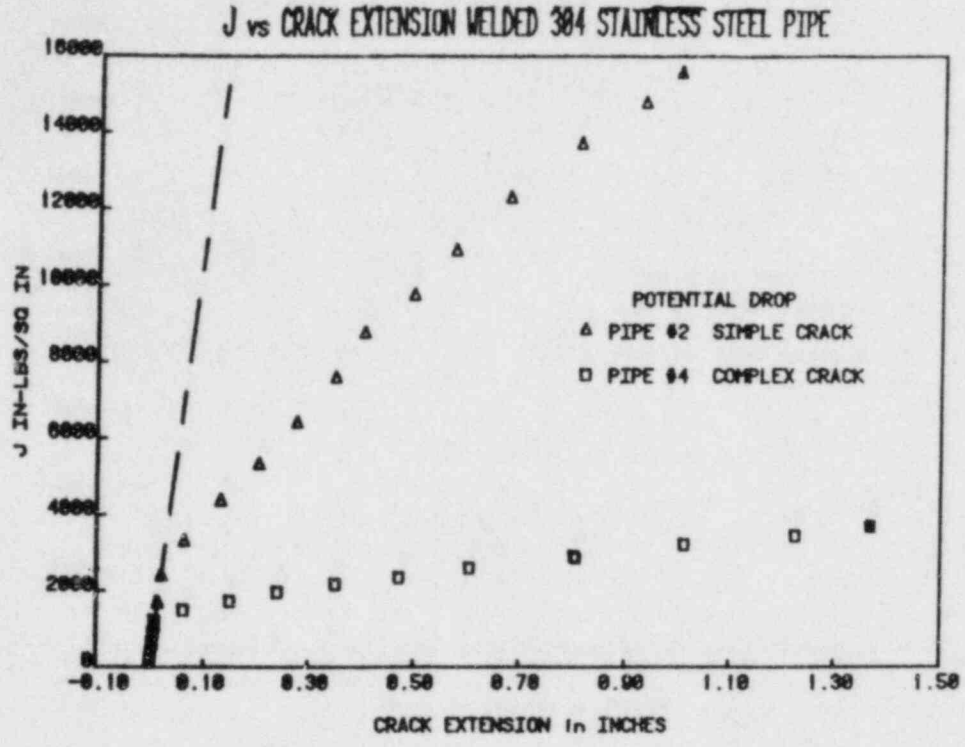

Figure 17 - Comparison of J-R Curves from DCPD for Pipe Tests

WELDED 304 STAINLESS STEEL PIPE

T = 550°F, σ_0 = 55.4 KSI, R_{MEAN} = 2.08 t = 0.33 SPAN = 15

SPEC. ID	2θ (DEG)	A (IN.)	PMAX (lb.)	PLIMIT (lb.)	% DIFF $\left(\frac{P_{MAX} - P_{LIMIT}}{P_{MAX}}\right)$
GAM-100	100	---	17300	22500	-30
GAM-200	139	---	13700	15200	-11
GAM-400 (NO CLOSURE)	159	0.125	9400	7880	16
(CLOSURE)				9130	2.8

Table 3 - Comparison of Measured Maximum Load and Maximum Load Predicted by Limit Load Analysis for Pipe Tests

BWR Pipe Crack and Weld Clad Overlay Studies*

by

W. J. Shack, T. F. Kassner, P. S. Maiya,
J. Y. Park and W. E. Ruther

Materials Science and Technology Division
ARGONNE NATIONAL LABORATORY
Argonne, Illinois 60439

Leaks and cracks in the heat-affected zones of weldments in austenitic stainless steel piping in boiling water reactors (BWRs) due to intergranular stress corrosion cracking (IGSCC) have been observed since the mid-1960s. Since that time, cracking has continued to occur, and indications have been found in all parts of the recirculation system, including the largest diameter lines.

Proposed solutions for the problem include procedures that produce a more favorable residual stress state on the inner surface, materials that are more resistant to stress corrosion cracking (SCC), and changes in the reactor environment that decrease the susceptibility to cracking. In addition to the evaluation of these remedies, it is also important to gain a better understanding of the weld overlay procedure, which is the most widely used short-term repair for flawed piping.

TECHNICAL PROGRESS

The main areas of effort during the past year have been (1) studies of the effects of impurities, dissolved oxygen content, and strain rate on susceptibility to SCC in "Nuclear Grade" Type 316NG and sensitized Type 304 stainless steel, (2) finite-element analyses and experimental measurement of residual stresses in weldments with weld overlays, and (3) analysis of field components to assess effectiveness of in-service inspection techniques and the in-reactor performance of weld overlay repairs. Work at ANL on acoustic leak detection and nondestructive evaluation is reported elsewhere in these Proceedings by D. S. Kupperman et al.[1]

Effects of Impurities and Dissolved Oxygen on the IGSCC Susceptibility of Sensitized Stainless Steels

In addition to dissolved oxygen produced by radiolytic decomposition of the water and corrosion products, other impurity species can enter the coolant through a number of sources (condensate and reactor-water cleanup demineralizers, the condensate storage tank, the suppression pool and reactor heat removal system, etc.). Demineralizer systems on BWRs remove contaminants introduced by condenser in-leakage and unanticipated upsets in water chemistry. However, demineralizer resins are also a source of contamination owing to the leakage of ion-exchange resin fragments to the system during normal operation and to the release of ions to the coolant after regeneration of the resins.

The high temperature and neutron flux in the reactor core cause rapid decomposition of resin fragments that enter the recirculation water. A number

of anion species can be introduced by resin ingress and decomposition (e.g., SO_4^{2-}, NH_3-NH_4^+, NO_2^-, and NO_3^-, as well as by ion exchange (e.g., Cl^-, CO_3^{2-}, and PO_4^{3-}.

The relative effect of these anions, in conjunction with hydrogen and sodium cations (i.e., under slightly acidic or basic conditions, respectively), on the SCC susceptibility of lightly sensitized Type 304 SS has been evaluated in constant-extension-rate (CERT) tests. Anion concentrations in these tests were set at 0.1 ppm. However, the actual concentration of the species will depend on dissociation equilibria at high temperature. These concentrations gave conductivity values of $\leq$1 μS/cm. The effect of the different anions with sodium on the time to failure is shown in Fig. 1. Ductile plus transgranular failures occurred in high-purity water and in water containing nitrate and borate; only a small decrease in the time to failure resulted from the addition of these ions. The other anions were more deleterious. The effects of carbonate and chloride were virtually identical. Phosphate and silicate produced a somewhat greater degree of IGSCC. The sulfur species (viz., sulfate, sulfite, thiosulfate, and sulfide) were the most deleterious.

Added as acids, silicate, borate, nitrate, and phosphate produced the smallest change in CERT parameters; carbonate and chloride were somewhat more deleterious and the sulfur species caused the highest degree of IGSCC. The time-to-failure results shown in Fig. 2 are consistent with those obtained for other CERT parameters.

Comparison of the results for the dilute acids with those for the sodium salts indicates that nitrate, borate, carbonate, and chloride are somewhat more deleterious when added in acid form; however, there is essentially no difference for the sulfur species.

Since the various anion species differ considerably in their effect on IGSCC susceptibility, it is unlikely that susceptibility to cracking can be correlated with conductivity and pH without a knowledge of the specific ions present. The standard instrumentation for routine analyses of reactor coolant is, in general, not adequate to detect the sulfur species that are particularly deleterious from the standpoint of IGSCC even though sulfate is likely to be present in BWR water at low concentrations ($\leq$0.1 ppm) from normal resin leakage and from resin regeneration and replacement operations.

Although CERT tests are very useful for studying the effects of impurities on SCC susceptibility, the severe mechanical loading produced during the tests makes it difficult to use the results quantitatively. Therefore, fracture-mechanics crack-growth-rate type tests are being performed to supplement the CERT tests. Because of the long times required for these tests, only a limited range of conditions can be considered.

Baseline tests were performed in high-purity water with 8 ppm dissolved oxygen at 289°C. Three 1TCT specimens were stressed at a load ratio of 0.95 and an initial maximum stress intensity K_{max} of 28 MPa $m^{\frac{1}{2}}$ under a positive sawtooth waveform. As expected, the most heavily sensitized material had the highest crack growth rate. The crack growth rate increased by about an order of magnitude as the cyclic frequency was increased from $\sim 10^{-2}$ to $\sim 10^{-1}$ Hz. For this heat of material and these test conditions, crack growth rates appear to be

sensitive to small superposed cyclic loading, although the measured crack growth rates are within the scatter band obtained for a number of heats of material under constant loading conditions.[3]

After baseline tests were completed, the effect of dissolved oxygen concentration was evaluated. The dissolved oxygen level was maintained at ∿0.2 ppm for ∿1000 h, decreased to 0.02 ppm for ∿600 h, and then increased back to 0.2 ppm. The crack length as a function of time is shown in Fig. 3. Crack growth virtually ceased over the ∿600-h time interval at the low dissolved oxygen concentration. It resumed at approximately the initial rates after the dissolved oxygen concentration was increased to the 0.2 ppm value.

The crack growth rate for the more heavily sensitized material (EPR = 20 C/cm^2) in water with 0.2 ppm dissolved oxygen is approximately half of that obtained in water with 8 ppm dissolved oxygen, as expected. Surprisingly, the crack growth rate of the lightly sensitized material (EPR = 2 C/cm^2) is approximately an order of magnitude higher at the lower dissolved oxygen concentrations. Measurable crack growth rates were also observed in the solution-annealed specimen. It appears that once a sharp crack (or tight crevice) is introduced (by fatigue precracking in this instance), propagation can occur under conditions that would not normally be considered to lead to environmentally-assisted cracking.

Fractographic examination of the specimens showed that the crack mode was primarily intergranular in the sensitized specimens and transgranular in the solution-annealed specimen. However, the decrease in crack growth rate in the solution-annealed specimen when the oxygen was decreased indicates that even the transgranular growth is strongly influenced by the environment.

A similar crack growth experiment was performed to investigate the effect of an impurity, 0.1 ppm sulfate (as H_2SO_4), on the crack growth rate. After ∿6000 h of testing, the sulfate level in the feedwater was reduced to a very low level for a period of ∿1200 h. After this time interval, the sulfate level was again increased to 0.1 ppm.

The crack lengths as a function of time for this portion of the test are shown in Fig. 4. Stress intensity values for the lightly sensitized specimen (EPR = 2 C/cm^2) at different times are noted on the figure. Removal of the sulfate had virtually no effect on crack growth in the solution-annealed and the more heavily sensitized (EPR = 20 C/cm^2) specimens. The crack growth rate of the lightly sensitized specimen decreased by a factor of ∿4 over an ∿600-h period after sulfate was removed from the feedwater; however, the rate in high-purity water increased over the next 600 h to the initial value observed in the water with 0.1 ppm sulfate. A further increase in the crack growth rate occurred at ∿7300 h when sulfate was again added to the feedwater. Roughly half of this increase in crack growth rate can be attributed to the increase in stress intensity factor due to the growth of the crack. If we assume that the initial decrease in the crack growth rate was due to a change in crack tip chemistry associated with the removal of sulfate from the bulk water, it is possible that sulfate or other sulfur species slowly desorbed from the oxide films, migrated to the crack tip zone, and subsequently accelerated the crack growth process.

The effects of the dissolved oxygen and the sulfate additions observed in the fracture-mechanics crack-growth-rate tests are qualitatively consistent with the crack growth information obtained from CERT tests on the same heat of material.[4] However, reduction of the dissolved oxygen to very low levels causes a much larger relative reduction in crack growth rates in the fracture-mechanics crack-growth-rate tests than in the corresponding CERT tests.[4]

Effects of Impurities on the SCC Susceptibility of Type 316NG Stainless Steel

Our previous work has shown that Type 316NG stainless steel can crack transgranularly in oxygenated water (0.2 ppm O_2) with impurities (0.1 ppm sulfate, added as acid).[5] Additional work has[2] shown that in CERT tests in the strain-rate regime 10^{-6} to 10^{-7} s^{-1}, cracking occurs only when impurities are present. Since an environment containing 0.1 ppm sulfate (added as acid) represents the maximum impurity level currently permitted under normal operating conditions, it is essential to know whether transgranular cracking in Type 316NG stainless steel can occur at lower levels of impurities. Test results for various sulfate impurity concentrations (<0.1 ppm) and strain rates are summarized in Table 1 together with previously reported data. At a strain rate $\dot{\varepsilon} = 1 \times 10^{-6}$ s^{-1}, cracking occurs only when the sulfate level is >0.075 ppm, which suggests that the critical impurity concentration for transgranular cracking at this strain rate is ∿0.1 ppm sulfate. When the strain rate is lowered to 2×10^{-7} s^{-1}, cracking occurs at even lower sulfate concentrations (0.05 ppm). However, the average crack growth rate $\dot{a}_{av}$ decreases by a factor of ∿3 compared to that determined in an environment with 0.1 ppm sulfate.

These results suggest that the critical level of impurity concentration need to produce transgranular cracking decreases with a decrease in strain rate. In conjunction with the complete absence of TGSCC in high-purity water at $\dot{\varepsilon} = 10^{-6}$ to 10^{-7} s^{-1}, they confirm that transgranular cracking in Type 316NG stainless steel is directly related to the impurity level and suggest that significant benefits can be achieved by close control of the coolant chemistry.

Effect of Strain Rate on SCC Susceptibility

A phenomenological model for SCC susceptibility that describes the effects of the applied strain rate $\dot{\varepsilon}$ on SCC has been developed.[6] The model gives simple power-law correlations between $\dot{\varepsilon}$ and parameters such as $\dot{a}_{av}$ and time to failure and is based on an estimate of the crack-tip strain obtained by use of a J-integral approach, the slip-dissolution model of Ford,[7] and a J-integral fracture criterion. The correlations between the SCC susceptibility parameters and the strain rate are of the form

$$\varepsilon_f = (J_c/AC)^{2/3} \dot{\varepsilon}^{1/3} , \quad (1)$$

$$a_f = A(J_c/AC)^{1/3} \dot{\varepsilon}^{-1/3} , \quad (2)$$

$$t_f = (J_c/AC)^{2/3} \dot{\varepsilon}^{-2/3} , \text{ and} \quad (3)$$

$$\dot{a}_{av} = A(AC/J_c)^{1/3} \dot{\varepsilon}^{1/3} , \quad (4)$$

where ε_f, a_f, and t_f are the strain, crack length, and time at failure; $\dot{a}_{av}$ is the average crack growth rate; and A, J_c, and C are constants which depend on the material and environment.

Good agreement is obtained between the results of the analysis and CERT results over a fairly wide range of strain rates, as shown in Figs. 5 and 6.

Analysis of Field Components with Weld Overlays

Laboratory ultrasonic examination, dye penetrant examination, residual stress measurements, metallographic examination, and sensitization measurements were performed on two 12-in.-diameter Type 304 stainless steel pipe-to-elbow weldments (Weld Nos. 2B31-1RC-12BR-C2 and -C3) removed from the primary coolant recirculation piping of the Hatch-2 boiling water reactor (BWR). Overlays were applied to these weldments after ultrasonic in-service inspection (ISI) had indicated cracking. After about one additional year of service, the recirculation piping in Hatch-2 was replaced and the weldments were removed for examination. The weldments were electrochemically polished by Quadrex Inc. to remove corrosion film and reduce radiation levels.

During the original ultrasonic ISI, intermittent indications around the entire circumference on the pipe side were reported for both weldments. The crack depths were estimated to be 28% throughwall for Weld No. 2B31-1RC-12BR-C2 and 30% for Weld No. -C3. However, little correlation was observed between the ISI results and the results of the dye penetrant tests and destructive examinations at ANL. Twenty short penetrant testing (PT) indications were observed on weldment C2 (fifteen on the elbow side and five on the pipe side). The indications were of a variety of types (axial, circumferential, skewed, or point), and most of them were located within 8 mm of the weld fusion lines (WFLs). There were no undercuts at the WFLs that produced PT indications in either weldment. No PT indications were observed on weldment C3. Even after sections from weldment C3 were subjected to three-point bending in order to open tight cracks that might be present, PT again indicated no cracks.

Before destructive examination, blind and partially blind ultrasonic tests (UTs) were carried out. Comparison of the UT results with the results of the PT and the metallographic sectioning indicates that the detection of cracks through the overlay by UT is difficult and at present unreliable.

The weldments were sectioned at a number of selected locations. The cross sections were metallographically polished and examined for cracks, defects, or any other features that might produce UT or PT indications. There was no evidence anywhere on the entire inner surface of the weldments that the counterbore was the cause of the cracking, although some details of the features on the inner surface may have been removed by electrochemical polishing at Quadrex.

The sectioning showed that the circumferential PT indications and the point PT indication were associated with short (<20 mm) circumferential intergranular cracks, and that the axial PT indication was associated with an axial intergranular crack. The depths of the circumferential cracks were 2-13 mm.

The crack profile of the 13-mm-deep (57% throughwall including the overlay) axial crack is shown in Fig. 7. In the interior of the pipe wall, the crack extended about 17 mm from the WFL, which is much further than suggested by the PT indication (1.5 mm long) at the inner surface of the weldment. The profile is somewhat unusual in shape. The crack tip was blunted, as shown in Fig. 8. Blunting of crack tips by weld overlays is predicted by finite-element analyses and would be expected to inhibit further crack growth. There was no evidence of tearing or extension of the crack beyond the blunted region. Metallographic sections were also obtained at a number of positions that produced strong UT signals but showed no PT indications. No cracks or discernible metallographic features (weld defects, inclusions, etc.) or geometrical irregularities were observed.

Experimental Measurement of Residual Stresses Produced by Weld Overlays

Measurements of surface and throughwall residual stresses have been made on three mock-up weldments supplied by Georgia Power and NUTECH for analysis. The weldments were fabricated 12-in. Schedule 100 pipe. One side of each weldment had a long, smooth weld prep geometry typical of that used in the Hatch-1 reactor, while the other side of each weldment had a short weld prep geometry typical of that used in the Hatch-2 reactor. Weld overlays were applied to two of the mock-up weldments after the weldments were fabricated by conventional butt welding procedures. The third weldment was fabricated by Last-Pass-Heat-Sink-Welding (LPHSW).

The two overlays are similar to those actually applied to the recirculation piping in the Hatch-2 reactor and were prepared with identical procedures, but they are slightly different in size. One (the "minioverlay") is ∿100 mm long and ∿5 mm thick. The other (the "standard" overlay) is ∿125 mm long and ∿5 mm thick.

As shown in Figs. 9 and 10, both the overlay procedures and LPHSW were very successful in inducing compressive residual stresses on the inner surfaces of the weldments for both weld prep geometries. The measured results are in general agreement with finite-element predictions supplied by NUTECH and E. F. Rybicki, Inc.

The residual stresses for the LPHSW mock-up are similar to those for the minioverlay and the standard overlay, at least for the region near the weld. On the basis of this set of weldments, differences in the stresses produced by the different procedures are small and appear to be within the range of variations that might be expected from weld to weld with a single procedure. The overlay procedures probably produce larger plastic strains and deformations, but since the stress is a relatively weak function of strain during plastic deformation, the corresponding stresses produced by the different procedures do not differ too greatly.

In Figs. 11-13, the throughwall axial residual stresses ∿2 mm from the WFLs are shown for the LPHSW weldment and the overlays. The depth shown in the figures is nondimensionalized with respect to the total thickness, i.e., wall plus overlay. As expected, the stresses are strongly compressive on the inner portion of the wall and tensile on the outer portion. These distributions should not be interpreted to indicate that the overlay will be effective for

cracks roughly halfway through the wall and ineffective for deeper cracks, since finite-element results[8] show that the presence of a crack strongly perturbs the stresses produced by the overlay process. Although these results do confirm the analytical predictions of strongly compressive stress fields produced on the inner surface by the overlay, other types of tests are needed to verify the predicted stress fields at crack tips.

FUTURE WORK

Work to assess the effect of impurities on SCC in both conventional BWR environments and the low-oxygen environment characteristic of BWRs with hydrogen additions will continue. The emphasis will be on the effect of low levels of impurities well within current water chemistry guidelines. The effects of impurities on crack growth rates in Type 308 weld metal will be examined. The effect of chemistry transients will also be examined further with fracture-mechanics crack-growth-rate tests. Low-stress cyclic pipe tests will be carried out to assess the effect of impurities under more prototypic loading conditions. The effectiveness of low oxygen levels in inhibiting SCC in irradiated materials will be examined. Long-term aging studies on Types 316NG and 304 stainless steel will also continue.

REFERENCES

1. D. S. Kupperman, T. N. Claytor, D. W. Prine, and T. A. Mathieson, Evaluation of Methods for Leak Detection in Reactor Primary Systems and NDE of Cast Stainless Steel, these Proceedings.

2. R J. Kurtz, D. W. Shannon, B. Francis, F. M. Kustas, and P. L. Koelmstedt, Evaluation of BWR Resin Intrusions on Stress Corrosion Cracking of Reactor Structural Materials, EPRI Final Report, NP-3145, Electric Power Research Institute (June 1983).

3. R. Horn et al., The Growth and Stability of Stress Corrosion Cracks in Large-Diameter BWR Piping, EPRI NP-2472, Vol. 2, Electric Power Research Institute (July 1982).

4. W. E. Ruther, W. K. Soppet, and T. F. Kassner, in Environmentally Assisted Cracking in Light Water Reactors: Annual Report, October 1982-September 1983, NUREG/CR-3806, ANL-84-36, Argonne National Laboratory (June 1984), pp. 101-124.

5. P. S. Maiya and W. J. Shack in Environmentally Assisted Cracking in Light Water Reactors: Annual Report, October 1982-September 1983, NUREG/CR-3806, ANL-84-36 (June 1984), pp. 62-75.

6. P. S. Maiya and W. J. Shack, "Effects of Nominal and Crack-tip Strain Rate on IGSCC Susceptibility in CERT Tests," in Embrittlement by the Localized Crack Environments, R. P. Gangloff, ed., The Metallurgical Society of AIME, Warrendale, PA (1984), pp. 199-209.

7. F. P. Ford, "Mechanisms of Stress Corrosion Cracking," in Aspects of Fracture Mechanics in Pressure Vessels and Piping, PVP-Vol. 58, ASME, New York (1982), pp. 229-269.

8. P. S. Maiya and W. J. Shack, in Environmentally Assisted Cracking in Light Water Reactors: Annual Report, October 1982-September 1983, NUREG/CR-3806, ANL-84-36, Argonne National Laboratory (June 1984), pp. 83-92.

Table 1. CERT Test Results for Type 316NG SS (Heat P91576, 1050°C/0.5 h + 650°C/24 h) in Oxygenated Water (0.2 ppm O_2) with SO_4^{2-} Impurity. T = 289°C, ε_o = 1.0%, and a_o = 1 μm.

Test Number	$\dot{\varepsilon}$, s^{-1}	SO_4^{2-}, ppm	Conductivity, μS/cm	t_f, h	σ_{max}, MPa	Failure Mode	$\dot{a}_{av}$, m/s
157	1×10^{-5}	0.1	0.9	9.7	430	Ductile	-
159	2×10^{-6}	0.1	0.9	53.5	453	Ductile	-
186	1×10^{-6}	0.0	~0.1	100.3	457	Ductile	-
206	1×10^{-6}	0.01	0.13	100.6	447	Ductile	-
202	1×10^{-6}	0.05	0.47	123.0	450	Ductile	-
214	1×10^{-6}	0.075	0.72	107.6	438	Ductile	-
160	1×10^{-6}	0.10	0.9	100.6	450	TGSCC	1.51×10^{-9}
154[a]	1×10^{-6}	0.10	0.9	109.4	458	TGSCC	1.50×10^{-9}
169	4×10^{-7}	0.10	0.9	217.4	462	TGSCC	9.74×10^{-10}
207	2×10^{-7}	0.01	0.13	497.3	468	Ductile	-
199	2×10^{-7}	0.05	0.47	588.7	449	TGSCC	2.21×10^{-10}
172	2×10^{-7}	0.10	0.90	474.0	461	TGSCC	7.35×10^{-10}
148	9.5×10^{-8}	0.1	0.9	565.9	472	TGSCC	6.73×10^{-10}

[a] 8 ppm O_2.

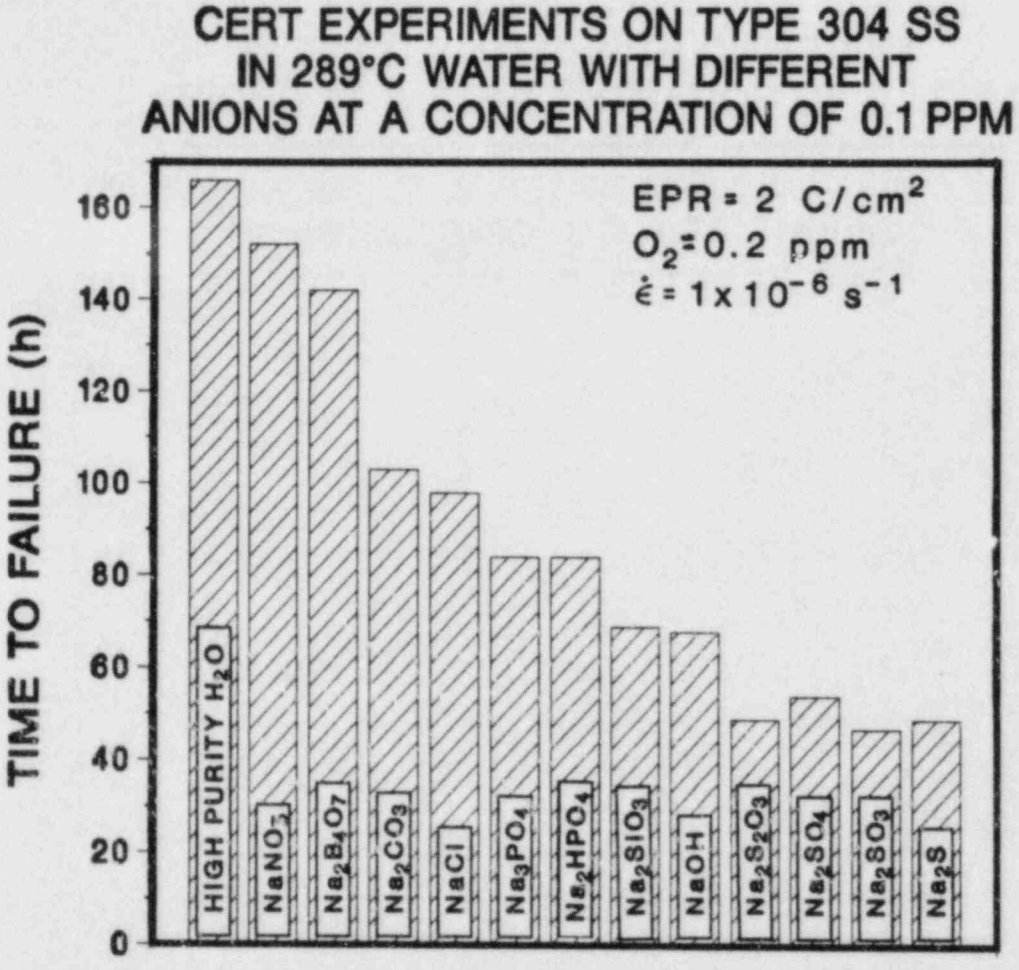

Fig. 1. Effect of Various Sodium Salts at an Anion Concentration of 0.1 ppm in Water Containing 0.2 ppm Dissolved Oxygen on the Time to Failure of Lightly Sensitized Type 304 SS Specimens in CERT Experiments at 289°C and a Strain Rate of 1×10^{-6} s^{-1}

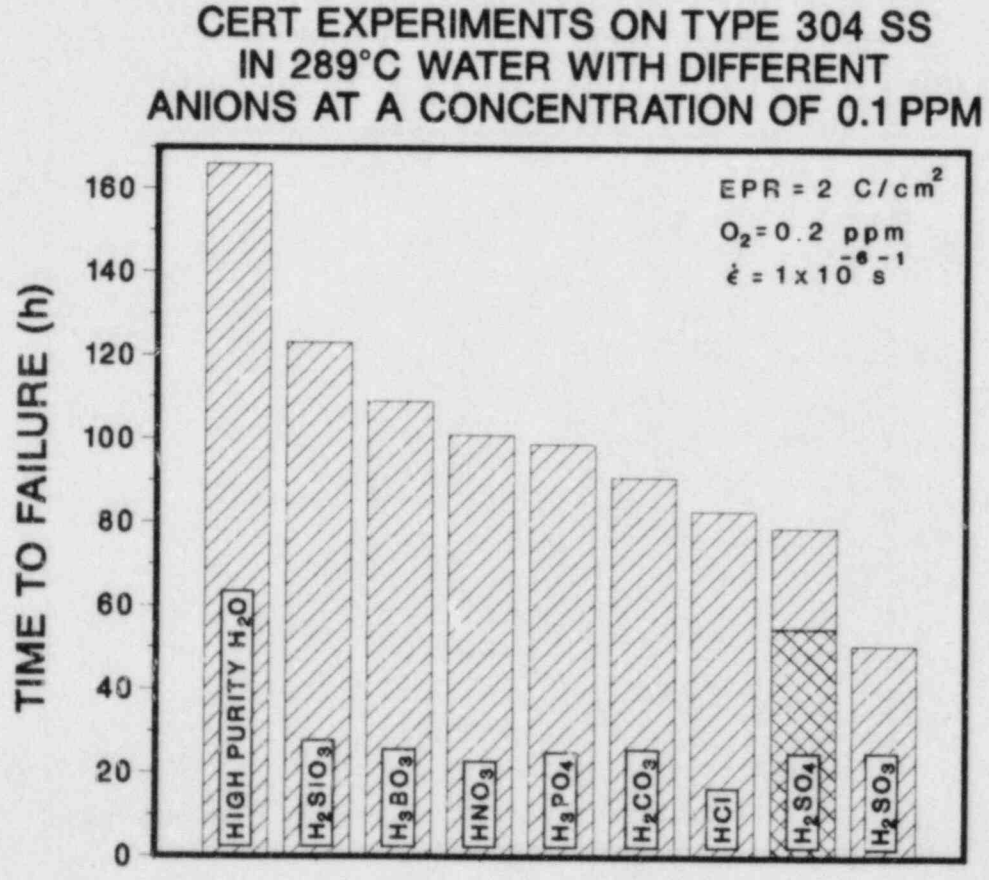

Fig. 2. Influence of Various Acids at an Anion Concentration of 0.1 ppm, in Water Containing 0.2 ppm Dissolved Oxygen, on the Time to Failure of Lightly Sensitized Type 304 SS Specimens in CERT Experiments at 289°C and a Strain Rate of 1×10^{-6} s^{-1}. Two tests were run with H_2SO_4.

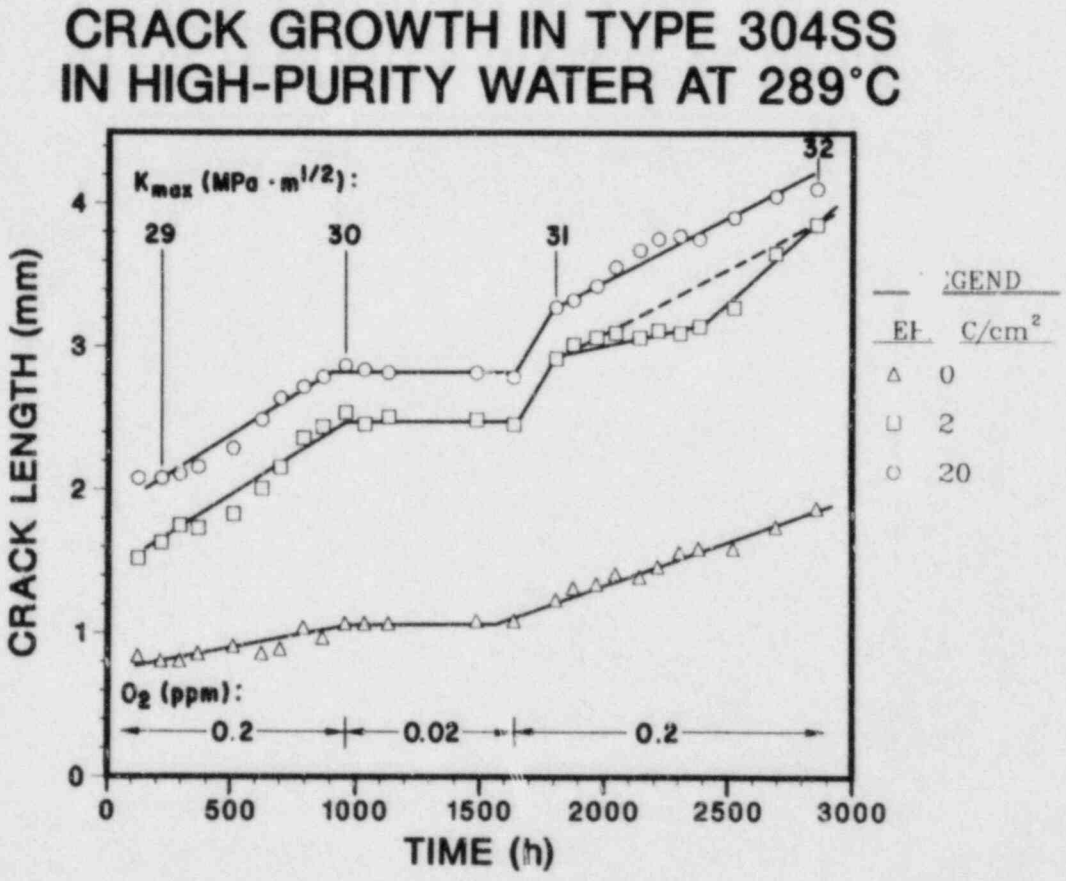

Fig. 3. Crack Length versus Time for 1TCT Specimens of Solution-annealed (EPR = 0) and Sensitized (EPR = 2 and 20 C/cm^2) Type 304 SS in 289°C Water Containing 0.2 ppm Dissolved Oxygen, Except for an Intermediate Period in Which the Oxygen Concentration was Decreased to 0.02 ppm. The loading conditions for the positive sawtooth waveform with a slow loading time (12 s) and a rapid unloading (1 s) are as follows: load ratio R = 0.95, frequency = 8 x 10^{-2} Hz, and K_{max} = 29 to 32 MPa·$m^{\frac{1}{2}}$ for the specimen with the largest crack.

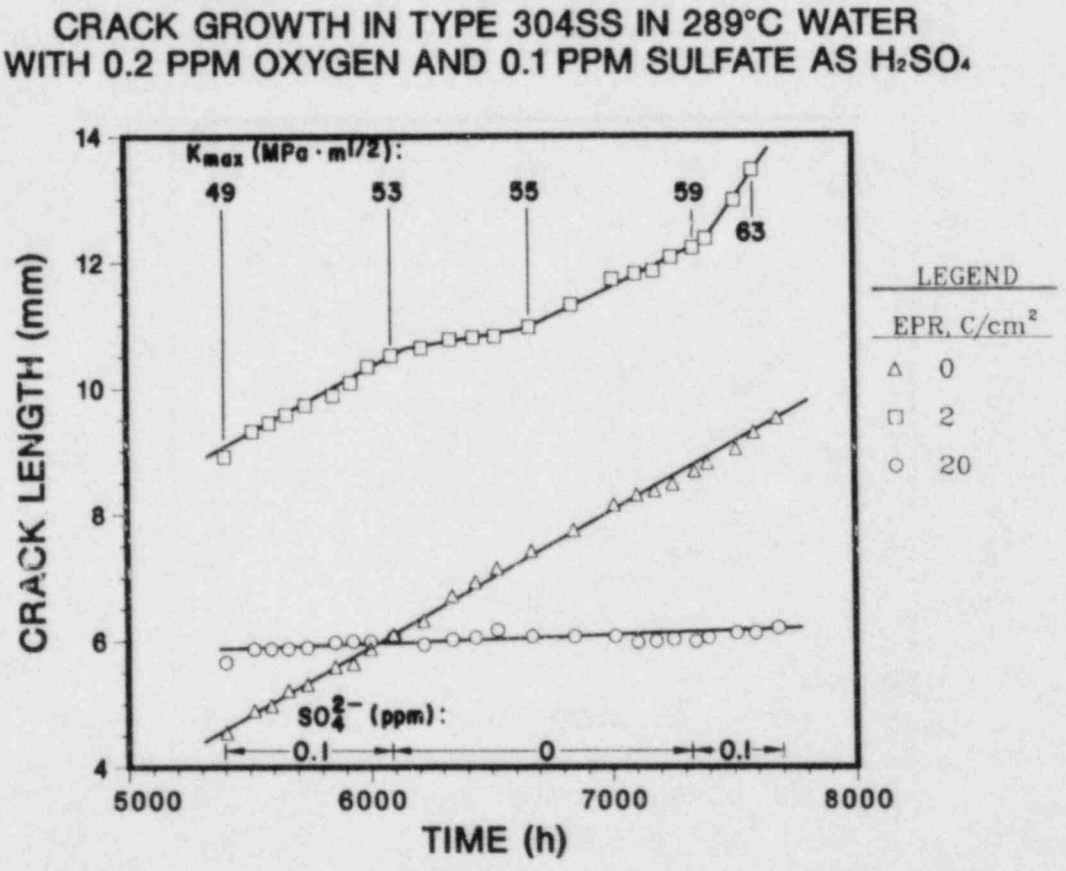

Fig. 4. Crack Length versus Time for 1TCT Specimens of Solution-annealed (EPR = 0) and Sensitized (EPR = 2 and 20 C/cm^2) Type 304 SS in 289°C Water Containing 0.2 ppm Dissolved Oxygen and 0.1 ppm Sulfate as H_2SO_4, Except for an Intermediate Period with High-Purity Water. The loading conditions for the positive sawtooth waveform with a slow loading time (12 s) and a rapid unloading (1 s) are as follows: load ratio R = 0.95, frequency = 8×10^{-2} Hz, and K_{max} = 49 to 63 MPa·m$^{\frac{1}{2}}$ for the specimen with the largest crack.

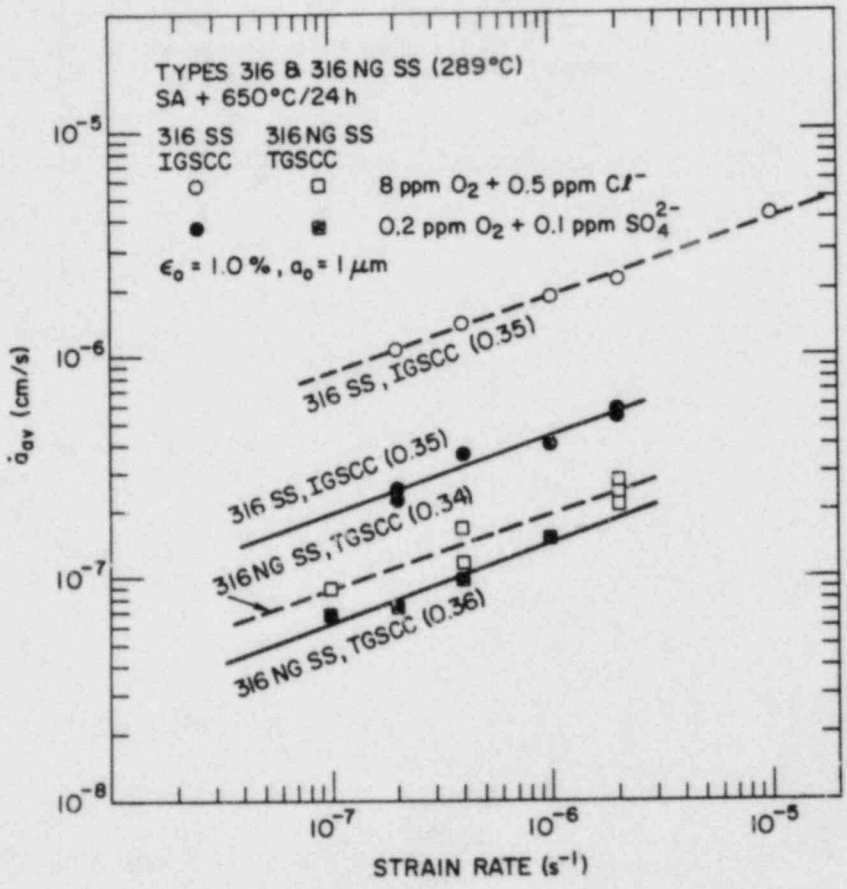

Fig. 5. Correlation between Average Stress Corrosion Crack Growth Rate and Strain Rate.

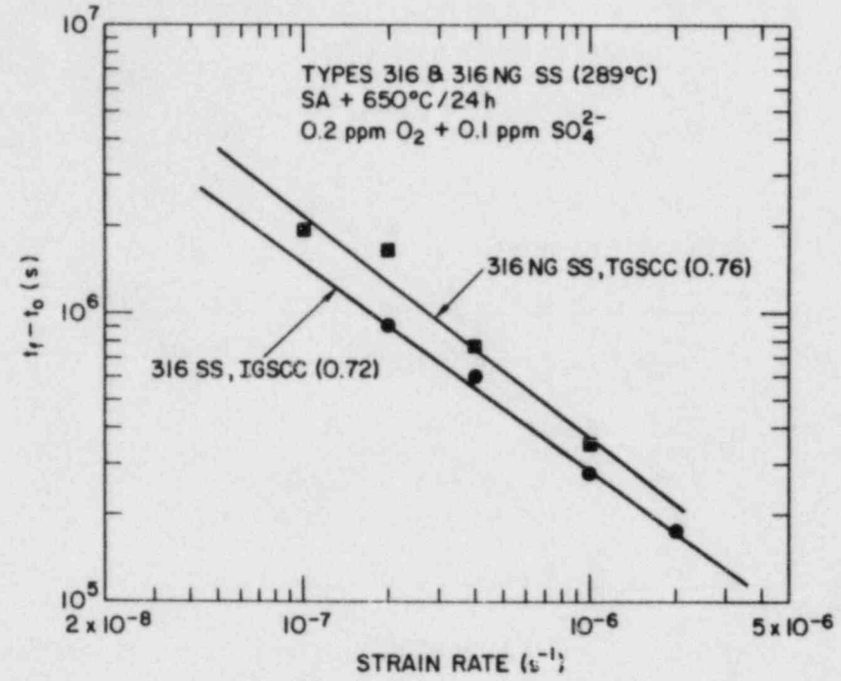

Fig. 6. Correlation between Time to Failure and Strain Rate for Failure by IGSCC and TGSCC.

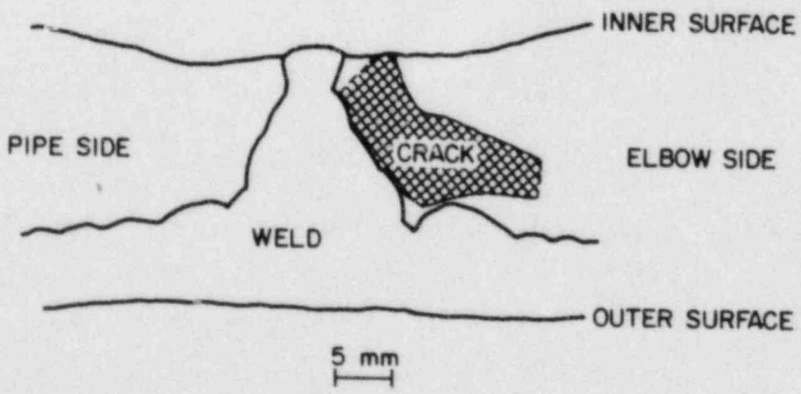

Fig. 7. Mapping of Axial Crack at 81-cm Position in Weldment C2.

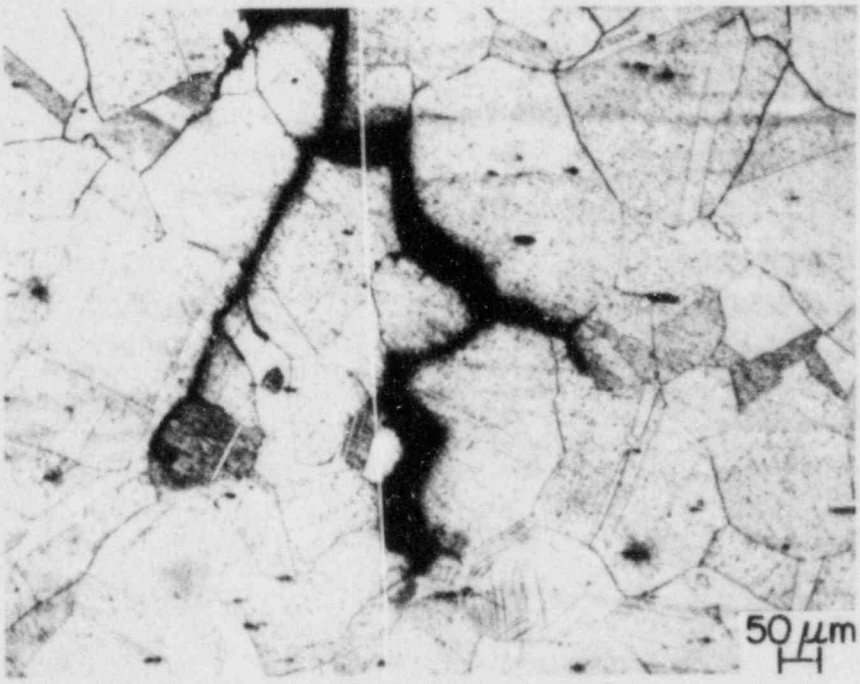

Fig. 8. Crack Tip of Axial Crack at 81-cm Position in Weldment C2.

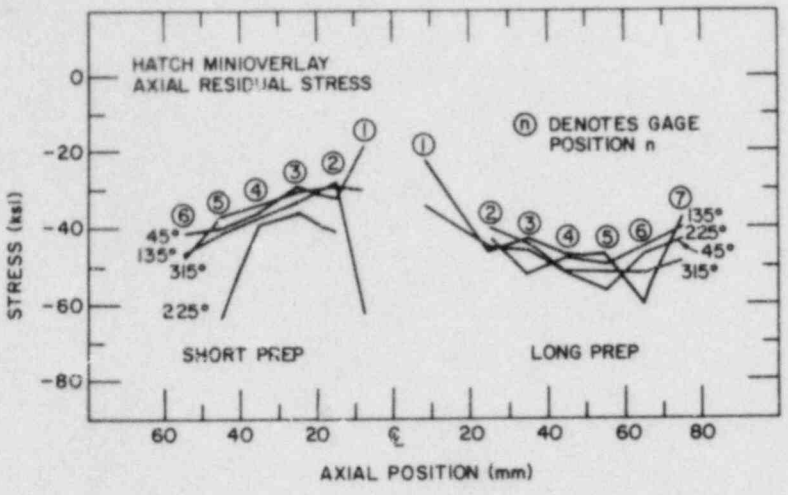

(a)

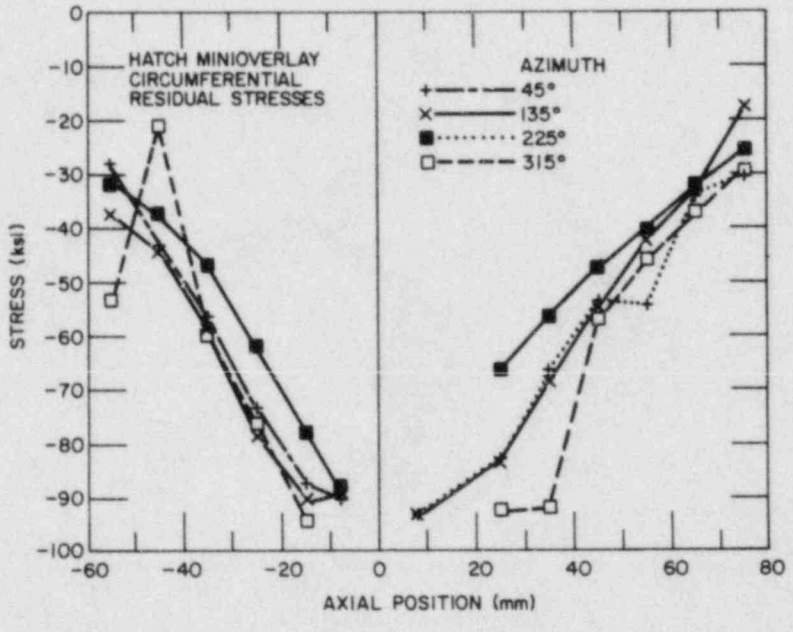

(b)

Fig. 9. (a) Axial and (b) Circumferential Residual Stresses on the Inner Surface at Four Azimuths of the Hatch Minioverlay Mock-up Weldment.

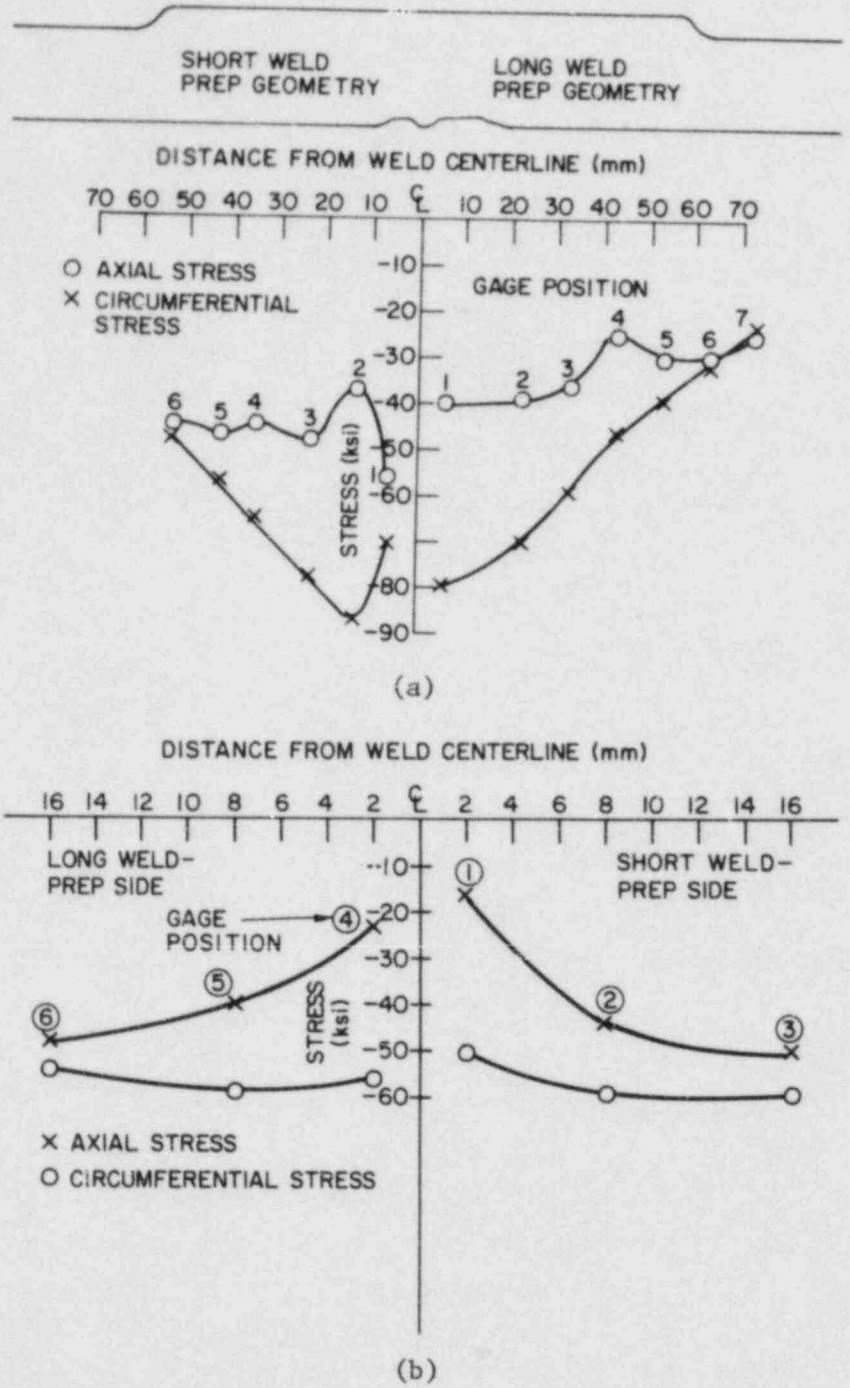

Fig. 10. Axial and Circumferential Residual Stresses on the Inner Surface of the Hatch (a) Standard Overlay Weldment and (b) LPHSW Mock-up Weldment.

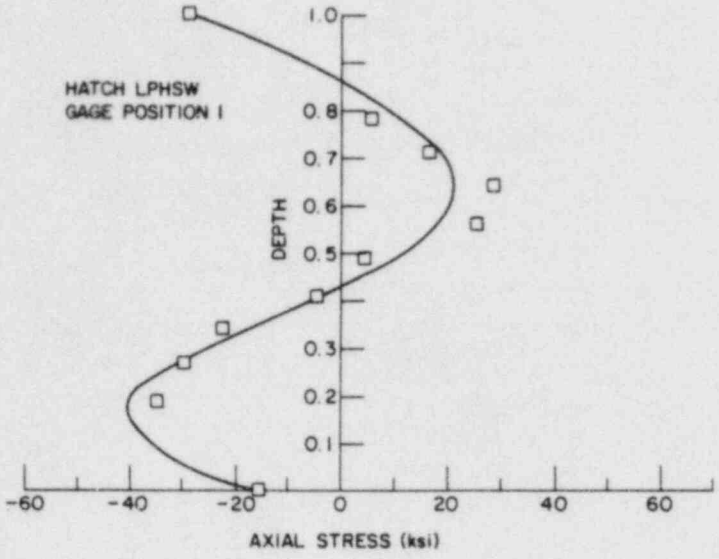

(a)

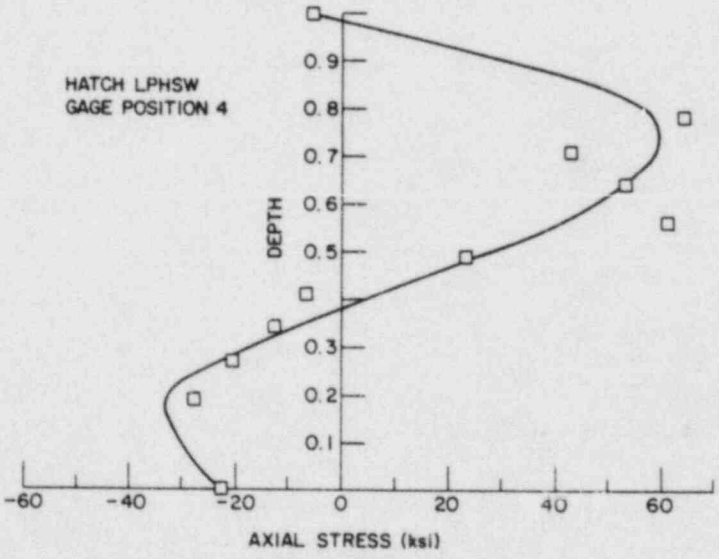

(b)

Fig. 11. Throughwall Axial Residual Stresses ~2 mm from the WFL on (a) the Short Weld Prep Side and (b) the Long Weld Prep Side of the Hatch LPHSW Mock-up Weldment.

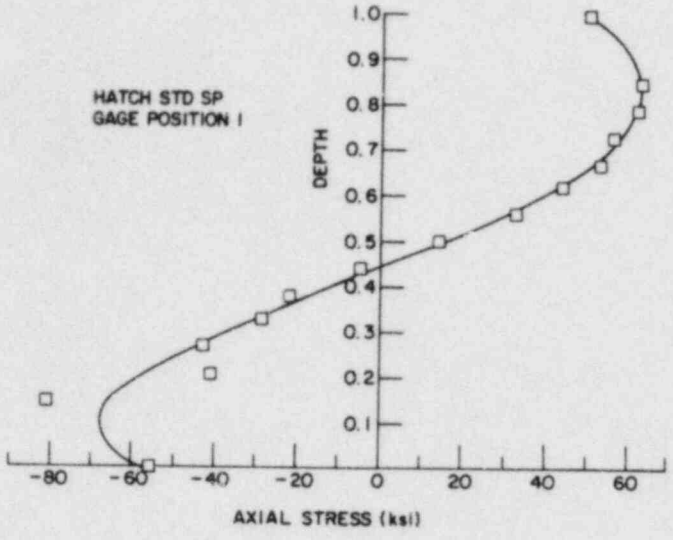

(a)

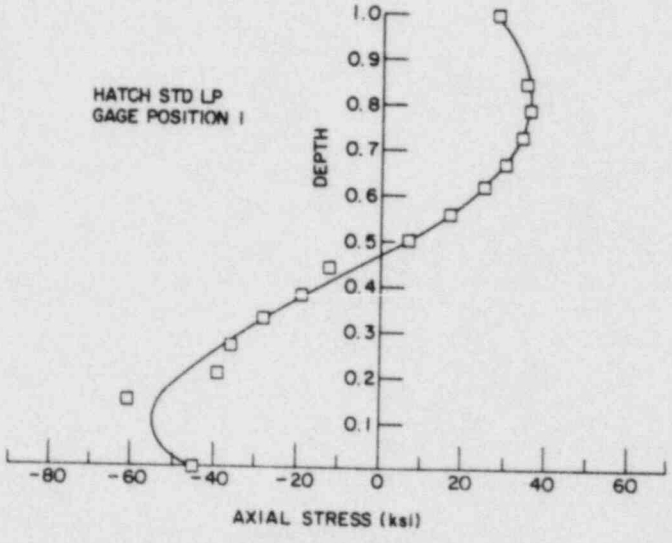

(b)

Fig. 12. Throughwall Axial Residual Stresses ∿2 mm from the WFL on (a) the Short Weld Prep Side and (b) the Long Weld Prep Side of the Hatch Standard Overlay Mock-up Weldment.

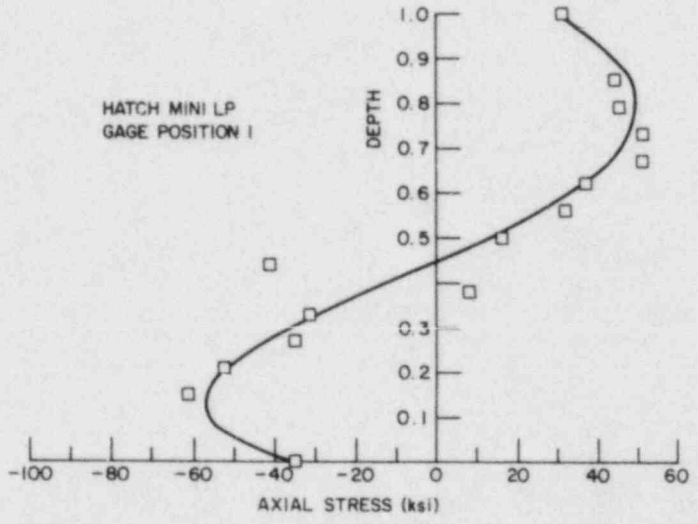

Fig. 13. Throughwall Axial Residual Stresses ∿2 mm from the WFL on the Long Weld Prep Side of the Hatch Minioverlay Mock-up Weldment.

AGING OF CAST DUPLEX STAINLESS STEELS IN LWR SYSTEMS*

O. K. Chopra and H. M. Chung

Materials Science and Technology Division
Argonne National Laboratory
Argonne, Illinois 60439

Abstract

A program is being conducted to investigate the significance of in-service embrittlement of cast duplex stainless steels under light-water reactor operating conditions. The existing data are evaluated to determine the expected embrittlement of cast components during the operating lifetime of reactors and to define the objectives and scope of the investigation. This presentation describes the status of the program. Data for the metallurgical characterization of the various cast stainless steels used in the investigation are presented. Charpy impact tests on short-term aged material indicate that CF-3 stainless steels are less susceptible to embrittlement than CF-8 or CF-8M stainless steels. Microstructural characterization of cast stainless steels that were obtained from Georg Fischer Co. and aged for up to 70,000 h at 300, 350, and 400°C reveals the formation of four different types of precipitates that are not α'. Embrittlement of the ferrite phase is primarily due to pinning of the dislocations by two of these precipitates, designated as Type M and Type X. The ferrite phase is embrittled after ~8 yr at 300°C and shows cleavage fracture. Examination of the fracture surfaces of the impact-test specimens indicates that the toughness of the long-term aged material is determined by the austenite phase.

Introduction

Cast duplex stainless steels are used extensively in the nuclear industry. The ferritic phase in the duplex structure of austenitic-ferritic stainless steels increases the tensile strength and improves weldability, resistance to stress corrosion, and soundness of casting of these steels. However, various carbide phases, intermetallic compounds such as sigma and chi phase, and the chromium-rich BCC phase (α') can precipitate in the ferrite phase during service at elevated temperatures and lead to substantial variations in mechanical properties. It is well known that formation of sigma phase greatly reduces the toughness of cast duplex stainless steels.[1] Long-term aging at relatively low temperatures, i.e., 300 to 500°C, causes drastic reductions in the impact strength of these steels.[2-5] Data on the aging behavior of ferritic or austenitic-ferritic steels show no evidence of sigma-phase formation at temperatures below 550°C. The mottled appearance characteristic of α' precipitates has been observed in material aged at temperatures between 450 and 500°C.[6-8] Microstructural studies on cast duplex stainless steel that were aged for up to 70,000 h at 400, 350, and 300°C revealed the formation of three different types of precipitates which are not α'.[8] At the

*Work supported by the Office of Nuclear Regulatory Research, U. S. Nuclear Regulatory Commission.

operating temperatures of light-water reactors (LWRs), i.e., 280 to 320°C, embrittlement of cast stainless steels is probably caused by the formation of these as yet unidentified precipitates in the ferrite phase.

In general, thermal aging of cast duplex stainless steels at temperatures between 300 and 450°C causes an increase in hardness and tensile strength and a decrease in ductility, Charpy impact strength, and J_{IC} fracture toughness of the material. The low-cycle fatigue properties and fatigue crack propagation are not significantly modified by aging.[4,5] The room-temperature impact strength can be reduced by ~80% after aging for ~70,000 h at temperatures as low as 300°C.[2] The ferrite content of the cast structure has a pronounced influence on the embrittlement behavior, namely, an increase in ferrite content increases the susceptibility to embrittlement.

Extensive data on embrittlement of single-phase binary Fe-Cr ferritic alloys indicate significant effects of chemical composition on the aging behavior. An increase in chromium, molybdenum, or titanium content in the ferrite phase enhances the rate as well as the extent of embrittlement.[6] Interstitial elements, such as carbon and nitrogen, also accelerate embrittlement of single-phase ferritic steels.[9,10] Unfortunately, the bulk of this work has been carried out at temperatures >400°C, and extrapolation of the results to reactor temperatures may not be valid. Furthermore, the influence of metallurgical variables such as grain structure and ferrite morphology has not been established.

The kinetics of embrittlement are evaluated by considering the aging phenomenon to be a thermally activated process described by an Arrhenius relation. The activation energy is determined by examining the degree of embrittlement produced by different time-temperature histories. Arrhenius extrapolations can be used to determine the equivalent aging time at different temperatures:

$$t = 10^{P} \exp\left[\frac{Q}{R}\left(\frac{1}{T} - \frac{1}{673}\right)\right], \qquad (1)$$

where Q is the activation energy, R the gas constant, T the absolute temperature, and P an aging parameter which represents the degree of aging reached after 10^{P} h at 400°C. The activation energy for the process of embrittlement has been described as a function of chemical composition of the cast material.[5] Thus,

$$Q\ (\text{kJ/mole}) = -182.6 + 19.9\ (\%\ \text{Si}) + 11.08\ (\%\ \text{Cr}) + 14.4\ (\%\ \text{Mo}). \qquad (2)$$

Chemical compositions of the various cast materials included in low-temperature aging studies yield activation energies between 65 and 100 kJ/mole (~15 and 24 kcal/mole) for cast CF-8 or CF-3 stainless steels and between 75 and 105 kJ/mole (~18 and 25 kcal/mole) for cast CF-8M stainless steel. The room-temperature impact energies of cast stainless steels that were aged for up to 70,000 h at 300, 350, and 400°C (Ref. 2) are plotted as a function of the parameter P in Figs. 1 and 2. The activation energies for the different materials were calculated from Eq. (2).

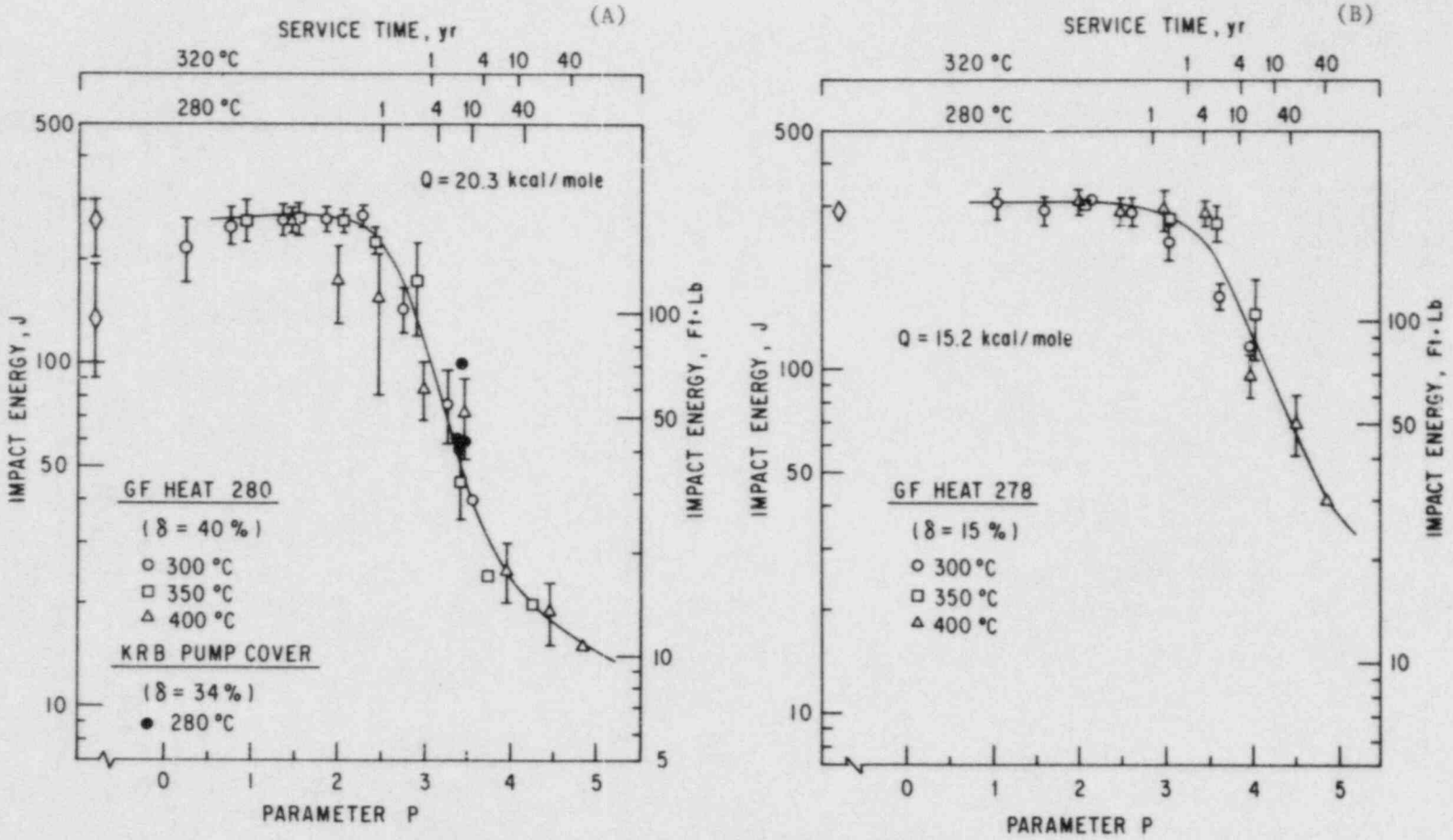

Fig. 1. Effect of Thermal Aging on the Impact Energy of Cast CF-8 Stainless Steels Containing (A) >30% Ferrite and (B) 15% Ferrite.

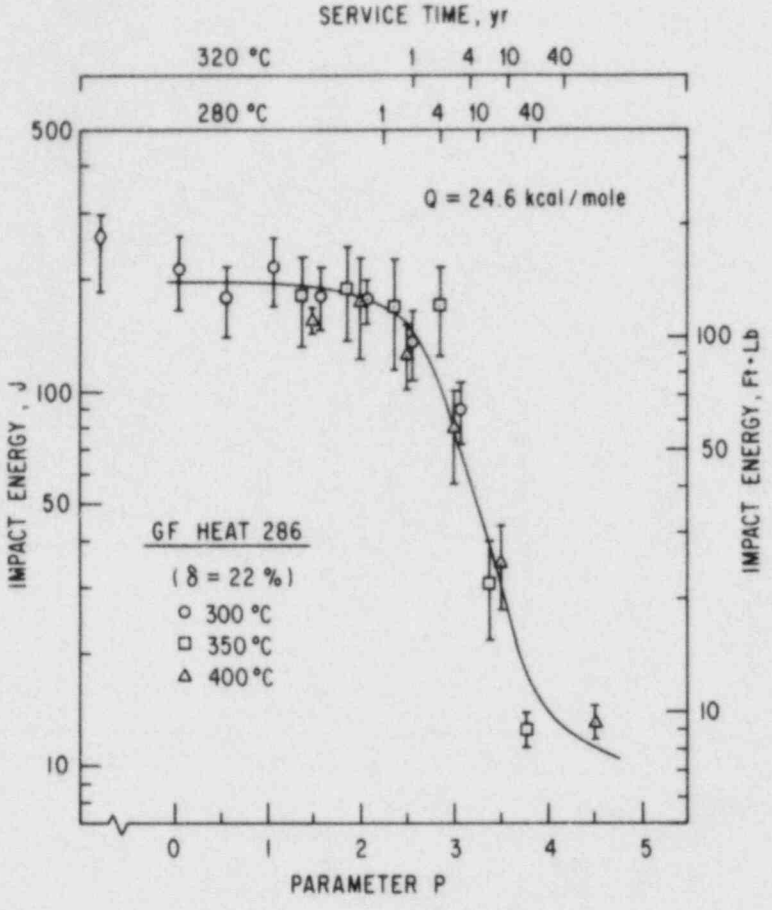

Fig. 2. Effect of Thermal Aging on the Impact Energy of Cast CF-8M Stainless Steel Containing 22% Ferrite.

For each material, the results for an aging temperature of 300°C follow the data for higher aging temperatures. However, the time and temperature for the onset of embrittlement is different for different materials. Cast stainless steels containing >20% ferrite [Figs. 1(A) and 2] show drastic reduction in impact strength for P values >2. Cast CF-8 material containing ~15% ferrite [Fig. 1(B)] shows a reduction in impact strength only above a P value of 3 and the degree of embrittlement is significantly less than for the material containing 40% ferrite. Experimental data obtained on CF-8 steel from the pump cover of the KRB reactor[11] are also plotted in Fig. 1(A). The material was in service for ~8 yr at 280°C. The results show good agreement with data obtained on laboratory-aged material. Figures 1 and 2 may be used to predict the impact energy of cast stainless steels after long-term service at reactor operating temperatures. For example, the impact energy of cast CF-8 steel (containing 30-40% ferrite) or CF-8M steel (containing 20-25% ferrite) will decrease below 70 J (50 ft·lb) after ~2 yr service at 320°C or ~7 yr service at 280°C.

Figure 3 shows the predicted impact strength for various service conditions of CF-8 material (containing 30-40% ferrite), aged at 280 and 320°C during long-term service. The ductile-brittle transition temperature (DBTT) curve was calculated from a tanh function given by

$$K = K_o + B\left[1 + \tanh\left\{\frac{(T - T_o)m + B - B_o}{B}\right\}\right], \qquad (3)$$

where K_o is the lower shelf value of the transition curve and B_o is half the difference between the upper and lower shelf. The coefficients T_o, B, and m depend on aging. Initial values of the constants were determined from DBTT data for the unaged material from the KRB pump cover. The change in coefficients T_o, B, and m with thermal aging is assumed to be the same as that for Heat 280N investigated by Georg Fischer Co. (Ref. 2). The predicted curve for 70,000 h of service at 280°C shows fair agreement with the experimental results, as shown in Fig. 3 (upper panel). The DBTT curve for service at 320°C indicates large reductions in upper shelf values after 70,000 h (~8 yr) of service, and impact energies below 70 J at temperatures up to 120°C. However, the room-temperature impact energy after 300,000 h of service is higher than that indicated by Fig. 1(A). For example, Fig. 3 predicts a room-temperature impact energy of ~40 J after 300,000 h (~34 yr) of service at 320°C, whereas a value of ~20 J is predicted from data shown in Fig. 1(A). The DBTT curves shown in Fig. 3 are current "best estimates" and are subject to large uncertainties. DBTT data for low-temperature aged material are required to accurately establish the change in transition curve due to thermal aging.

To demonstrate the validity of using such an Arrhenius extrapolation of high-temperature data to predict the long-term embrittlement of cast stainless steels at reactor operating temperatures requires a satisfactory understanding of the aging process. The mechanism of embrittlement needs to be established to ensure that the activation energy obtained from the laboratory tests is representative of the actual process. The activation energies determined from the aging data are much lower than that expected for a mechanism controlled by solute bulk diffusion (i.e., activation energy of 230 kJ/mole). This indicates that processes other than precipitation of additional phases in the ferrite matrix contribute to embrittlement of cast duplex stainless steels. For example, microstructural modifications of the austenite phase or changes in the fracture behavior of duplex material may influence the notch toughness of cast stainless steels. The available information is not sufficient to correlate the microstructure with the mechanical properties or to determine the mechanism of low-temperature embrittlement.

The objectives of this program are to (1) characterize the microstructure of in-service reactor components and laboratory-aged material, correlate it with loss of fracture toughness, and identify the mechanism of embrittlement; (2) determine the validity of laboratory-induced embrittlement data for predicting the toughness of component materials after long-term aging at reactor operating temperatures; (3) characterize the loss of fracture toughness in terms of fracture mechanics parameters in order to provide the data needed to assess the safety significance of embrittlement; and (4) provide additional understanding of the effects of key compositional and metallurgical variables on the kinetics and degree of embrittlement.

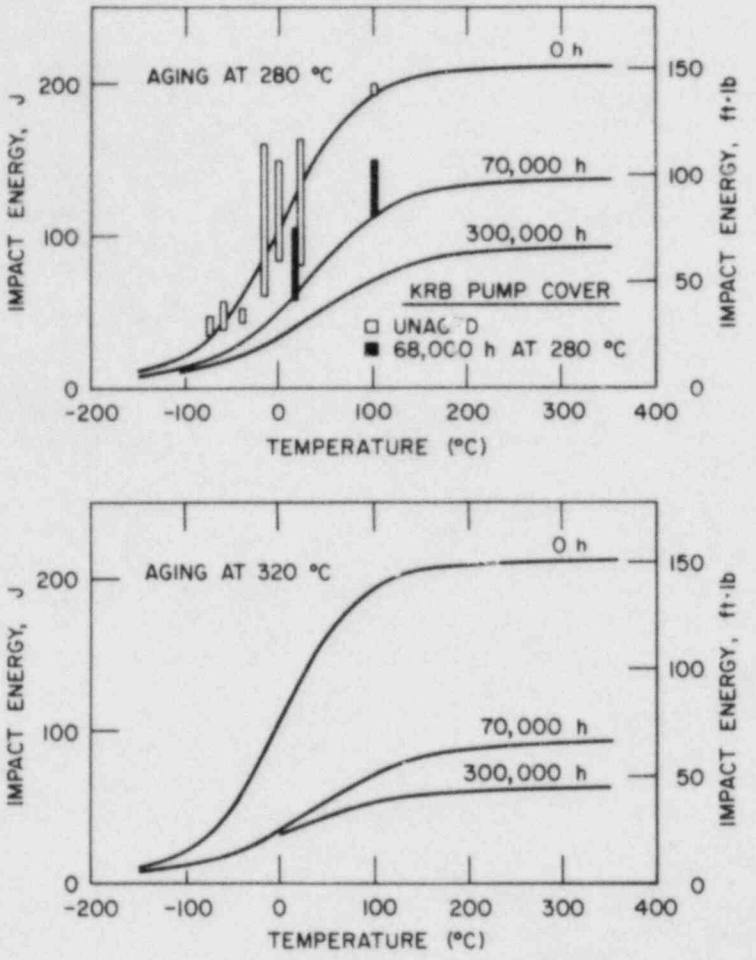

Fig. 3. Effect of Thermal Aging at 280 and 320°C on the Transition Curves for Impact Energy of Cast CF-8 Stainless Steel.

The relationship between aging time and temperature for onset of embrittlement will be determined by microstructural examination and measurements of hardness, Charpy impact strength, tensile strength, and J_{IC} fracture toughness. The kinetics and fracture toughness data generated in this program and from other sources will provide the technical basis to define the aging histories, chemical compositions, and metallurgical structures that lead to significant embrittlement of cast stainless steels under LWR operating conditions. Estimates of the degree of embrittlement will be compared with data obtained from examination of material from actual reactor service. Data pertaining to the effects of compositional and metallurgical variables on the embrittlement phenomenon will help to evaluate the possible remedies for existing and future plants.

Material Procurement and Characterization

Material was obtained from various experimental and commercial heats of CF-8, -8M, and -3 grades of cast stainless steel. Nineteen experimental heats

were obtained in the form of keel blocks approximately 180 mm long and 120 mm high, with a thickness that tapered from 30 to 90 mm. The compositions of the heats were varied to provide different concentrations of nickel, chromium, carbon, and nitrogen in the material and ferrite contents in the range of 3 to 30%. Six large experimental heats, in the form of 76-mm-thick slabs, were obtained for J_R-curve testing. Sections from four centrifugally cast pipes (grades CF-3, -8, and -8M), a static-cast pump impeller (grade CF-3), and a static-cast pump casing ring (grade CF-8) were also procured. The outer diameter and wall thickness of the cast pipes range from 0.6 to 0.9 m and 38.1 to 76.2 mm, respectively.

A cover plate assembly of cast stainless steel from the recirculating pump of the KRB reactor (the same one shown in Fig. 1) was also procured. The material was in service for ~12 yr at 280°C. The cover plate is 0.89 m in diameter and 0.32 m deep. The thicknesses of the various sections range from 60 to 120 mm. The ferrite content of the cast material is ~34%. The cover plate assembly was decontaminated and samples are being obtained from different sections of the plate for mechanical testing and microstructural characterization.

Charpy impact specimen blanks were prepared from keel blocks of the experimental heats and material from the various reactor components. Blanks for compact tension specimens were obtained from sections of two centrifugally cast pipes, the static-cast pump casing ring, the static-cast pump impeller, and the cast slabs. The specimen blanks are being aged at 450, 400, 350, 320, and 290°C for times up to 50,000 h. The test matrices for the various mechanical tests and microstructural examination have been presented earlier.[12] The mechanical test specimens were machined after the thermal aging treatment. The orientations of the notches for the Charpy impact and compact tension specimens were both L-C and C-L.*

The various cast materials were examined to characterize the chemical composition, hardness, ferrite content, ferrite morphology, and grain structure. Energy dispersive x-ray analyses (EDAX) were performed to determine the composition of the α and γ phases (i.e., ferrite and austenite phases) of the duplex structure. All castings were examined in the three orientations, i.e., longitudinal, circumferential, and radial planes, as well as different locations, namely, material near the center and the inner and outer surfaces of the pipes, and top (Row 6) and bottom (Row 3) regions of the keel blocks. Orientation of the material had little or no effect on either hardness or ferrite content and morphology. The ferrite morphology in the various cast materials was globular for ferrite contents of <5%, lacy for ferrite contents between 5 and 20%, and acicular for material with larger amounts of ferrite. The ferrite morphology in the keel blocks was different from that in the centrifugally cast pipes. For the same ferrite content, the islands of ferrite in the keel blocks were smaller and had a finer dispersion than in the pipe material.

The chemical composition, hardness, and ferrite content of the various heats of cast stainless steel are given in Table 1. The results show some

*L = longitudinal or axial and C = circumferential or transverse. The first letter designates the direction normal to the crack plane and the second letter the expected direction of crack propagation.

TABLE 1. Chemical Composition, Hardness, and Ferritic Content of the Various Heats of Cast Stainless Steel

Heat	Grade	Composition,[a] wt %							Location	Hardness, R_B	Ferrite Content,[b] %
		Mn	Si	Mo	Cr	Ni	N	C			
						Cast Keel Blocks					
58	CF-8	0.66	1.21	0.29	19.56	10.37	0.040	0.050	Row 3	76.0	3.6
									Row 6	78.2	2.1
57		0.69	1.24	0.28	18.45	8.94	0.041	0.060	Row 3	80.1	5.1
									Row 6	80.3	2.8
54		0.58	1.08	0.31	19.42	8.91	0.073	0.065	Row 3	82.6	1.2
									Row 6	83.9	2.3
53		0.70	1.28	0.35	19.62	8.86	0.045	0.070	Row 3	82.6	9.5
									Row 6	83.6	7.8
56[c]		0.60	1.16	0.30	19.33	8.93	0.031	0.060	Row 3	81.9	11.9
									Row 6	83.1	8.2
59		0.63	1.14	0.26	20.35	8.95	0.040	0.070	Row 3	83.5	14.2
									Row 6	82.8	12.7
61		0.70	1.20	0.27	20.54	8.59	0.060	0.060	Row 3	85.1	13.0
									Row 6	85.5	13.1
60[c]		0.71	1.01	0.26	21.02	8.07	0.050	0.070	Row 3	86.2	20.4
									Row 6	87.2	21.7
50	CF-3	0.67	1.26	0.28	17.63	8.84	0.064	0.019	Row 3	79.6	5.0
									Row 6	80.6	3.7
49		0.66	1.11	0.29	19.32	10.10	0.064	0.022	Row 3	76.1	8.0
									Row 6	77.2	6.3
48		0.67	1.21	0.26	19.42	9.90	0.071	0.016	Row 3	77.6	8.9
									Row 6	78.6	8.5
47		0.65	1.23	0.45	19.67	10.04	0.027	0.018	Row 3	79.0	16.5
									Row 6	80.3	16.2
52		0.63	1.04	0.31	19.51	9.07	0.049	0.021	Row 3	81.4	10.3
									Row 6	81.8	16.7
51[c]		0.66	1.06	0.28	20.36	8.69	0.048	0.023	Row 3	83.7	18.0
									Row 6	83.9	18.0
62	CF-8M	0.84	0.64	2.46	18.38	11.35	0.030	0.070	Row 3	78.2	6.3
									Row 6	78.0	2.6
63		0.69	0.75	2.52	19.39	11.22	0.030	0.050	Row 3	81.0	10.9
									Row 6	82.1	10.0

TABLE 1. (Contd.)

Heat	Grade	Composition,[a] wt % Mn	Si	Mo	Cr	Ni	N	C	Location	Hardness, R_B	Ferrite Content,[b] %
66[c]	CF-8M	0.71	0.60	2.36	19.41	9.13	0.030	0.060	Row 3	84.6	19.2
									Row 6	85.8	20.5
65		0.66	0.63	2.53	20.95	9.39	0.060	0.060	Row 3	88.4	21.4
									Row 6	89.5	25.4
64[c]		0.70	0.71	2.41	20.87	9.01	0.030	0.050	Row 3	89.7	27.5
									Row 6	89.7	29.3
						Cast Components					
C1	CF-8	1.22	1.19	0.64	19.10	9.32	0.041	0.036	O.D.	78.3	2.3
					18.89	9.42			I.D.	80.6	1.7
P1		0.56	1.07	0.04	20.38	8.00	0.053	0.032	O.D.	84.5	27.6
					20.60	8.20			I.D.	85.3	19.5
P3	CF-3	1.04	0.86	0.01	18.93	8.33	0.159	0.020	O.D.	80.6	2.5
					18.85	8.56			I.D.	83.7	0.9
P2		0.72	0.92	0.16	20.20	9.24	0.041	0.020	O.D.	82.4	15.9
					20.20	9.51			I.D.	85.1	13.2
I		0.46	0.80	0.44	20.08	8.50	0.030	0.016	Vane 3	81.1	20.2
					20.20	0.80			Vane 1	82.2	14.3
					20.34	8.64			Shroud	78.1	16.9
					20.20	8.84			Hub	81.0	19.1
P4	CF-8M	1.07	1.02	2.06	19.63	10.00	0.153	0.039	O.D.	83.0	11.1
					19.65	9.99			I.D.	83.2	9.8

[a]Chemical composition of the keel blocks supplied by the vendor.
[b]Ferrite content measured by Ferrite Scope, Auto Test FE, Probe Type FSP-1.
[c]Chemical composition of the large experimental heats.

differences in hardness and ferrite content for material from different locations in the castings. The ferrite content is lower and the hardness is slightly higher toward the inner surface of the various cast pipes. This behavior appears to be related to the nickel content in the material, i.e., the concentration of nickel is higher near the inner surface. Differences in hardness and ferrite content are also observed for material from different locations in the static-cast keel blocks. Hardness is always higher toward the top of the keel blocks. However, variations in the ferrite content depend on the Cr_{eq}/Ni_{eq} ratio in the material; the ferrite content toward the top of the casting is lower for material with Cr_{eq}/Ni_{eq} <1.13 and higher for material with Cr_{eq}/Ni_{eq} >1.13. In general, the hardness of the cast material increases with an increase in ferrite content. For the same ferrite content, the hardness of CF-8 and -8M material is comparable while the hardness of CF-3 material is lower. An increase in nitrogen content increases the hardness of all grades of cast stainless steel.

The ferrite content and the different structures present in the four pipe sections and pump casing ring are listed in Table 2. The grain structures were examined in the axial, circumferential, and radial planes. Two castings, P1 and P2, contained equiaxed grains across the entire thickness of the pipe.

TABLE 2. Ferrite Content and Grain Structure of Various Cast Stainless Steel Pipes

Heat	OD, m	Wall, mm	Process	Grade	Ferrite Content,[a] % OD	Ferrite Content,[a] % ID	Grain Structure
C1	0.60	57.1	Static	CF-8	2.3	1.7	Banded, columnar/equiaxed; radial to axial growth near ends
P1	0.89	63.5	Centr.	CF-8	27.6	19.5	Equiaxed across thickness
P3	0.58	51.6	Centr.	CF-3	2.5	0.9	Banded, radially oriented columnar; one equiaxed band (~4 mm deep) near ID
P2	0.93	73.0	Centr.	CF-3	15.9	13.2	Equiaxed across thickness
P4	0.58	31.8	Centr.	CF-8M	11.1	9.8	Radially oriented columnar

[a]Ferrite content measured by Ferrite Scope, Auto Test FE, Probe Type FSP-1.

The grain size and distribution were not significantly different in the three orientations. The equiaxed grains were probably produced intentionally by a low pouring temperature or by shear between the liquid and solid. The shear could cause dendrite arms to break off and disperse in the liquid-solid region. These castings are expected to exhibit uniform properties in all directions. The other two centrifugally cast pipes, P3 and P4, showed radially oriented columnar grains. Pipe section P3 also contained a band of small equiaxed grains near the inner surface. This band was relatively thin, i.e., ~4 mm deep, and probably formed accidentally. The columnar grain castings are expected to have uniform properties in the axial and circumferential directions. The static-cast pump casing ring, keel blocks, and slab showed a mixed structure of columnar and equiaxed grains.

EDAX analyses of the various cast materials indicate that the concentration of Cr, Mo, and Si is higher in the α phase and Ni is higher in the γ phase. The concentration of Mn, C, and N is expected to be higher in the γ phase. The results indicate that an increase in the ferrite content of the duplex material has little or no effect on the concentration of Ni in the two phases. For the various cast materials, the average Ni content in the α and γ phases was 4.8 ± 0.4 and 8.7 ± 0.4 wt %, respectively. The concentration of Cr in both phases increases slightly with an increase in the ferrite content. The Cr content in the α phase increases from ~25 wt % for a cast material with 2% ferrite to ~26.1 wt % for a casting with 30% ferrite. The corresponding values of the Cr content in the γ phase are ~19.2 and 20.4 wt %, respectively. These results indicate that the precipitation reactions in the α phase should not be significantly different for cast stainless steels containing different amounts of ferrite. The strong effect of ferrite content on the impact energy

of cast material is most likely due to the different distribution and morphology of the ferrite phase. Precipitate reactions involving the interstitial elements may also influence the mechanical properties of the aged material.

Mechanical Properties of Aged Material

Charpy-impact tests were conducted at room temperature on material that was aged for up to 3000 h at 450, 400, and 350°C. As expected, thermal aging of the cast stainless steels decreased the impact energy. The data indicate that the reduction in impact strength depends not only on the ferrite content, but also on the grain structure and grade of the material. Thermal aging of cast stainless steels with >10% ferrite resulted in substantial reduction in impact energy, whereas cast materials with <10% ferrite showed little or no decrease in impact energy. The CF-3 grades of cast materials exhibit greater resistance to embrittlement relative to the CF-8 and CF-8M grades. For example, the impact energy for Heats 47 and 52 of CF-3 steels decreased by ~25% after aging for 3000 h at 450°C, while Heats 59 and 61 of CF-8 steels showed ~50% reduction in impact energy after a similar aging treatment. Data also indicate superior notch toughness for the centrifugally cast pipe material (e.g., Heat P2) relative to the static-cast keel blocks. Charpy-impact tests are in progress on material that was aged at lower temperatures and material from the pump cover of the KRB reactor.

Microstructural Characterization of the Aged and Impact-tested Material

Results of microstructural characterization by transmission electron microscopy (TEM) of several ferritic alloys and cast duplex stainless steels (aged at 300-475°C) have been reported previously.[8] A total of five different types of precipitates have been identified in the ferrite phase. These can be summarized as follows:

(1) α' - chromium-rich phase giving rise to mottled bright-field images but producing no detectable changes in the diffraction patterns;

(2) Type P - platelet precipitate producing strong strain-field contrast in bright-field images and giving rise to streaking of the ferrite diffraction spots;

(3) Type M - $M_{23}C_6$-like precipitate rich in Ni and Si and exhibiting a distinct diffraction pattern that contains superlattice spots with a lattice constant slightly larger than the $M_{23}C_6$ phase;

(4) Type X - precipitates observed on dislocations giving rise to very weak and streaked reflections as a result of small volume fraction and very fine size;

(5) Type ML - precipitates observed in association with Type M, coating the Type M precipitates and dislocations.

The various materials and aging conditions for which the different precipitates were observed are summarized in Table 3. The α' phase was observed in all alloys aged at 475°C, i.e., 26Cr-1Mo and 29Cr-4Mo-2Ni ferritic steels

TABLE 3. Summary of Types of Precipitates Observed in Ferritic Alloys and Cast Duplex Stainless Steel after Long-term Aging at 300-475°C

Alloy	Aging Conditions		Precipitate Phases				
	Temp., °C	Time, h	α'	Type P	Type M	Type X	Type ML
26Cr-1Mo ferritic	475	1,000	Yes				
	400	1,000	No	No			
29Cr-4Mo-2Ni ferritic	475	1,000	Yes	Yes			
	400	1,000	No	Yes			
Cast duplex stainless steel CF-8, Heat B	475	1,000	Yes		Yes		
	400	1,000	No	No	No	No	No
Cast duplex stainless steel CF-8, Heat 280	400	66,650	No		Yes	Yes	
	400	10,000	No		Yes	Yes	
	300	70,000	No		Yes	Yes	
Cast duplex stainless steel CF-8, Heat 278	400	70,000	No		Yes		
	350	70,000	No		Yes	Yes	
	300	70,000	No		Yes	Yes	
Cast duplex stainless steel CF-8M, Heat 286	400	10,000	No		Yes		Yes

and cast duplex stainless steel CF-8, Heat B. However, two heats of cast duplex stainless steel that were obtained from Georg Fischer Co. and aged up to 8 yr at 300 to 400°C did not show the α' phase. Since long-term aging at the lower temperatures is more prototypic of reactor operating conditions, TEM characterization was focused on the materials obtained from Georg Fischer Co. Characterization by scanning electron microscopy (SEM) was also conducted on the fracture surfaces of the specimens, which were impact-tested at room temperature.

1. TEM Characterization of Precipitates in Aged Cast Duplex Stainless Steel

Examination of the cast duplex stainless steel CF-8 material (Heat 280, ferrite content ~40%), aged at 400°C for 66,650 h, showed another type of precipitate in addition to those indicated in Table 3; this precipitate was designated tentatively as Type S.[13] The presence of the Type S phase could be detected only through a very careful examination of the diffraction patterns. The Type S reflections were extremely weak, indicating a small volume fraction, and could barely be detected on the microscope screen. As a result, no dark-field images could be obtained. The weak spots could be detected only from the developed negatives of the SAD pattern. The specks are very sharp compared to reflections from the matrix or Type M phases,

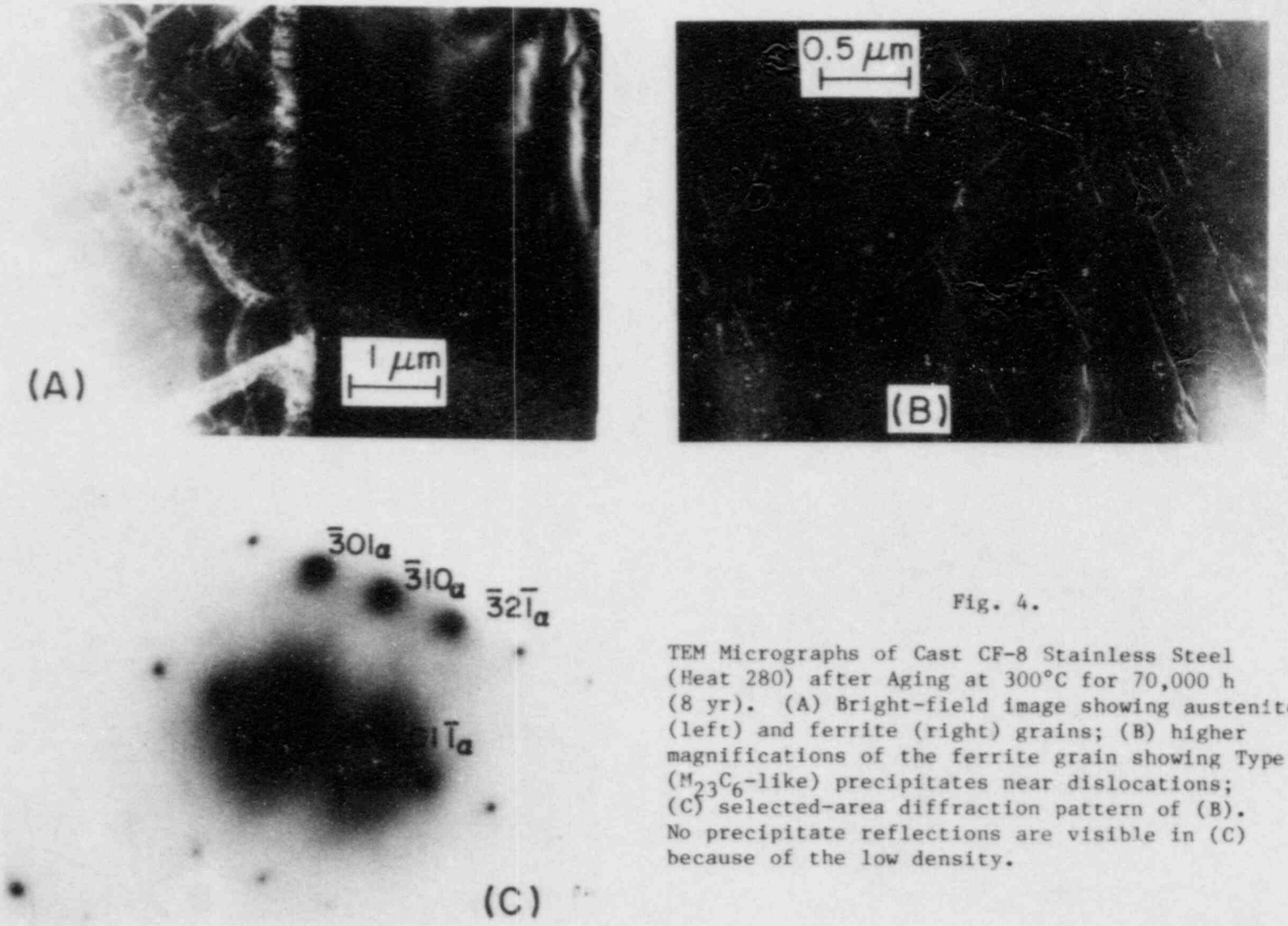

Fig. 4.

TEM Micrographs of Cast CF-8 Stainless Steel (Heat 280) after Aging at 300°C for 70,000 h (8 yr). (A) Bright-field image showing austenite (left) and ferrite (right) grains; (B) higher magnifications of the ferrite grain showing Type M ($M_{23}C_6$-like) precipitates near dislocations; (C) selected-area diffraction pattern of (B). No precipitate reflections are visible in (C) because of the low density.

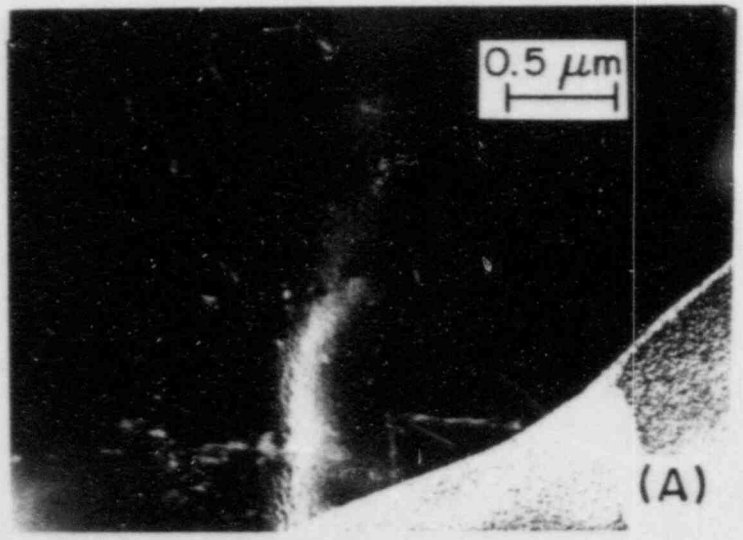

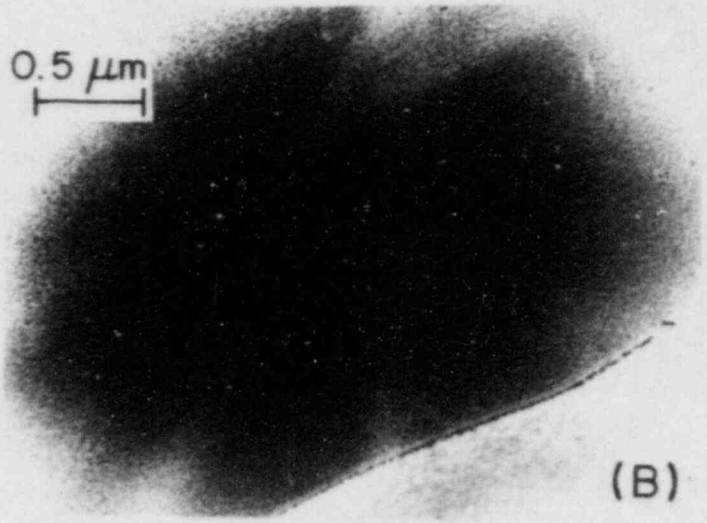

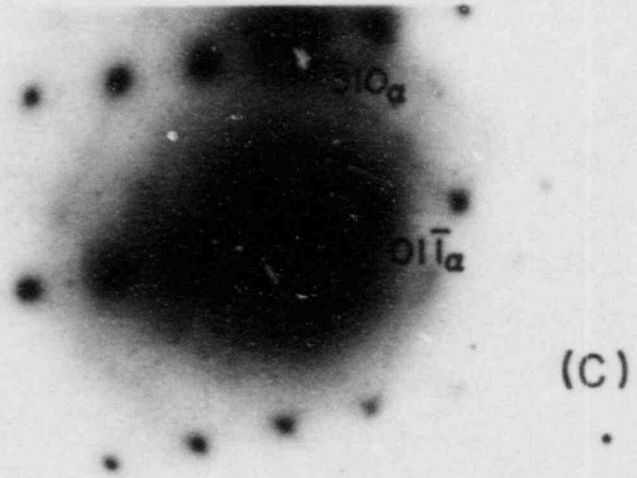

Fig. 5.

TEM Micrographs Similar to Fig. 4 but after Aging at 400°C for 66,650 h (7.6 yr). (A) Bright-field image; (B) dark-field image; (C) selected-area diffraction pattern. Note the high density of Type M precipitates and the negligible number of dislocations.

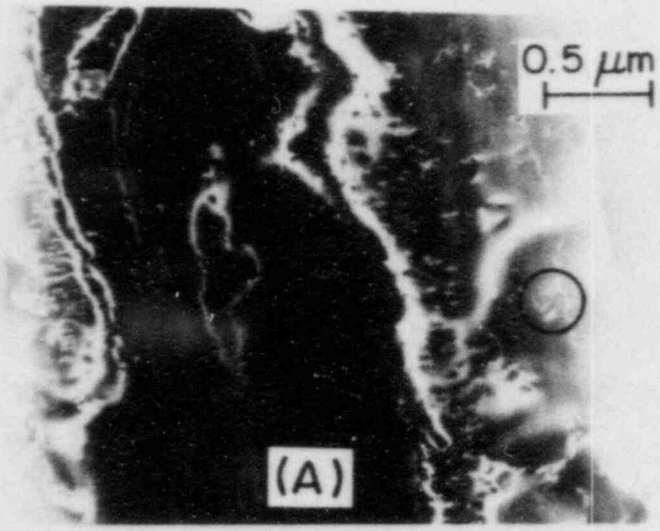

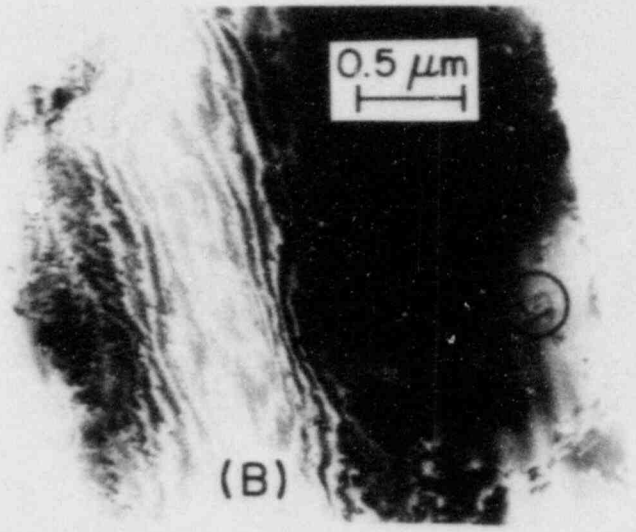

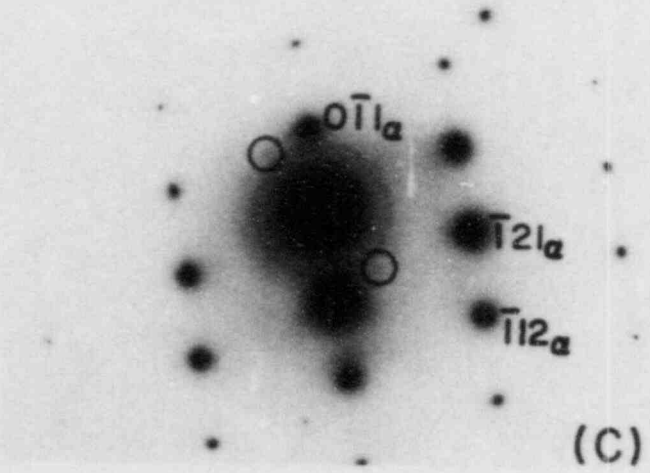

Fig. 6.

TEM Micrographs of Cast CF-8 Stainless Steel (Heat 278) after Aging at 300°C for 70,000 h (8 yr). (A) Bright-field and (B) dark-field images showing short dislocations decorated by Type X precipitates; (C) selected-area diffraction pattern showing diffuse weak Type X precipitate reflections in the circles.

indicating that the reflecting sphere intersects thin, flattened, needle-like reciprocal lattice rods. The Type S precipitates were also observed for specimens of cast duplex stainless steel CF-8, Heat 278 (ferrite content 15%) aged at 300°C for 70,000 h.

TEM examination of material aged for long times at low temperatures indicates that Type M and X precipitates, rather than the α' phase, influence the toughness and fracture behavior of cast duplex stainless steels aged at temperatures of <400°C. Both Type M and X precipitates are present in the ferrite phase of the duplex structure. However, the relative densities of the two types of precipitates are not uniform for the different specimens and ferrite grains. These precipitates are observed primarily near dislocations, indicating some degree of immobilization of the dislocations by the precipitates. Figure 4(B) shows an example of bright-field images of dislocations on the ferrite phase of Heat 280 aged at 300°C for ~8 yr (parameter P = 3.99). A relatively small number of Type M precipitates, ~10 mm in size, can be observed near the dislocations. Because of the low density of the precipitates, no extra reflections are detected in the corresponding selected-area diffraction (SAD) pattern, Fig. 4(C). In contrast, the same material (i.e., Heat 280) aged at 400°C for 7.6 yr (parameter P = 4.83) shows a negligible number of dislocations [Fig. 5(A)], a large density of Type M precipitates [Figs. 5(A) and (B)], and distinct precipitate reflections in the SAD pattern [Fig. 5(C)].

Figure 6 shows an example of dislocations in the ferrite phase, immobilized by Type X precipitates. The bright- and dark-field images of Figs. 6(A) and (B), obtained from a thin-foil specimen of Heat 280 aged at 300°C for 8 yr (parameter P = 3.70), show numerous short dislocations decorated by the Type X precipitates. The diffuse weak reflections of the Type X precipitates are denoted by small circles in the corresponding SAD pattern of Fig. 6(C).

The results from TEM examination of the microstructures of the cast duplex stainless steel materials subjected to long-term aging (e.g., at 300°C for 8 yr) indicate that dislocation glide in the ferrite phase would be significantly limited because of the preferential precipitation of Type M and X particles on or around the dislocations. In contrast, the structure of the austenite phase is characterized by a high density of dislocations and numerous stacking faults and is relatively free of precipitates, as shown in Fig. 4(A). This indicates that the overall ductility of the long-term aged duplex steel will be primarily sustained by the austenite phase. TEM characterization of the material from the pump cover of the KRB reactor is in progress.

2. SEM Fractographic Characteristics

Fracture characteristics of the impact test specimens of cast duplex stainless steel obtained from the Georg Fischer Co. were examined by SEM. Detailed mapping of the fracture surface morphology for Heat 278 aged at 400°C for 10,000 h (parameter P = 4.0) showed that approximately 15-20% of the fracture surface was composed of brittle cleavage and the remainder exhibited a ductile dimple morphology. The cleavage-morphology region revealed river

patterns characteristic of a brittle fracture.[13] In comparison, the extent of cleavage in the fracture surface of the specimen aged at 300°C for 10,000 h (parameter P = 3.14) was minimal.

Similar fracture surface mapping was conducted for specimens of Heats 278 and 280, aged at 300°C for 8 yr (parameter P = 3.99 and 3.70 for Heats 278 and 280, respectively). The fracture surface morphologies of the two specimens are shown in Figs. 7 and 8, respectively. The overall low-magnification morphologies [e.g., Fig. 7(A)] of the fracture surfaces did not indicate any appreciable macroscopic deformation during the room-temperature impact failure. Mapping of the high-magnification fractographs showed that ~15 and 40% of the fracture surfaces of Heats 278 and 280, respectively, were of a brittle-cleavage nature [e.g., Figs. 7(C) and 8(C)]. The rest of the fracture surfaces showed ductile morphologies. The characteristic river patterns could be observed in the cleavage regions.

The fractions of the fracture surfaces of the impact test specimens characterized by the cleavage morphology correspond approximately to the ferrite contents of the material, i.e., ~15 and 40% for Heats 278 and 280, respectively. These observations indicate that the ferrite phase has been embrittled by aging for 10,000 h at 400°C or 70,000 h (8 yr) at 300°C. However, aging for shorter times, e.g., 10,000 h at 300°C, did not embrittle the ferrite phase. The results of the fractographic characterization of the ferrite phase are consistent with the TEM observations which indicated that dislocations in the ferrite phase of the embrittled material were immobilized by Type M and X precipitates. Since the ferrite phase is already embrittled after aging at 300°C for ~8 yr, the toughness of the cast stainless steels after aging for a longer time will be determined by either the austenite phase or interactions between the austenite and ferrite phases of the duplex structure.

References

1. H. D. Solomon and T. M. Devine, "Influence of Microstructure on the Mechanical Properties and Localized Corrosion of a Duplex Stainless Steel," in MiCon 78: Optimization of Processing, Properties, and Service Performance Through Microstructural Control, eds. H. Abrams et al., ASTM STP 672 (1979), p. 430.

2. A. Trautwein and W. Gysel, "Influence of Long Time Aging of CF-8 and CF-8M Cast Steel at Temperatures Between 300 and 500 deg. C on the Impact Toughness and the Structure Properties," Spectrum, Technische Mitteilungen aus dem + GF + Konzern, No. 5 (May 1981); also in Stainless Steel Castings, eds. V. G. Behal and A. S. Melilli, ASTM STP 756 (1982), p. 165.

3. G. Baudry and C. Pichard, "Evolution During Long Holding Times at 300 and 450°C of the Mechanical Properties of Austeno-Ferritic Steel Castings and Welded Joints Used in Pressurized Water Nuclear Reactors," in Troisieme Congres National Sur La Technologie Des Appareils a Bression, Vol. 2, Materiaux, A.F.I.A.P. (1980), p. 673.

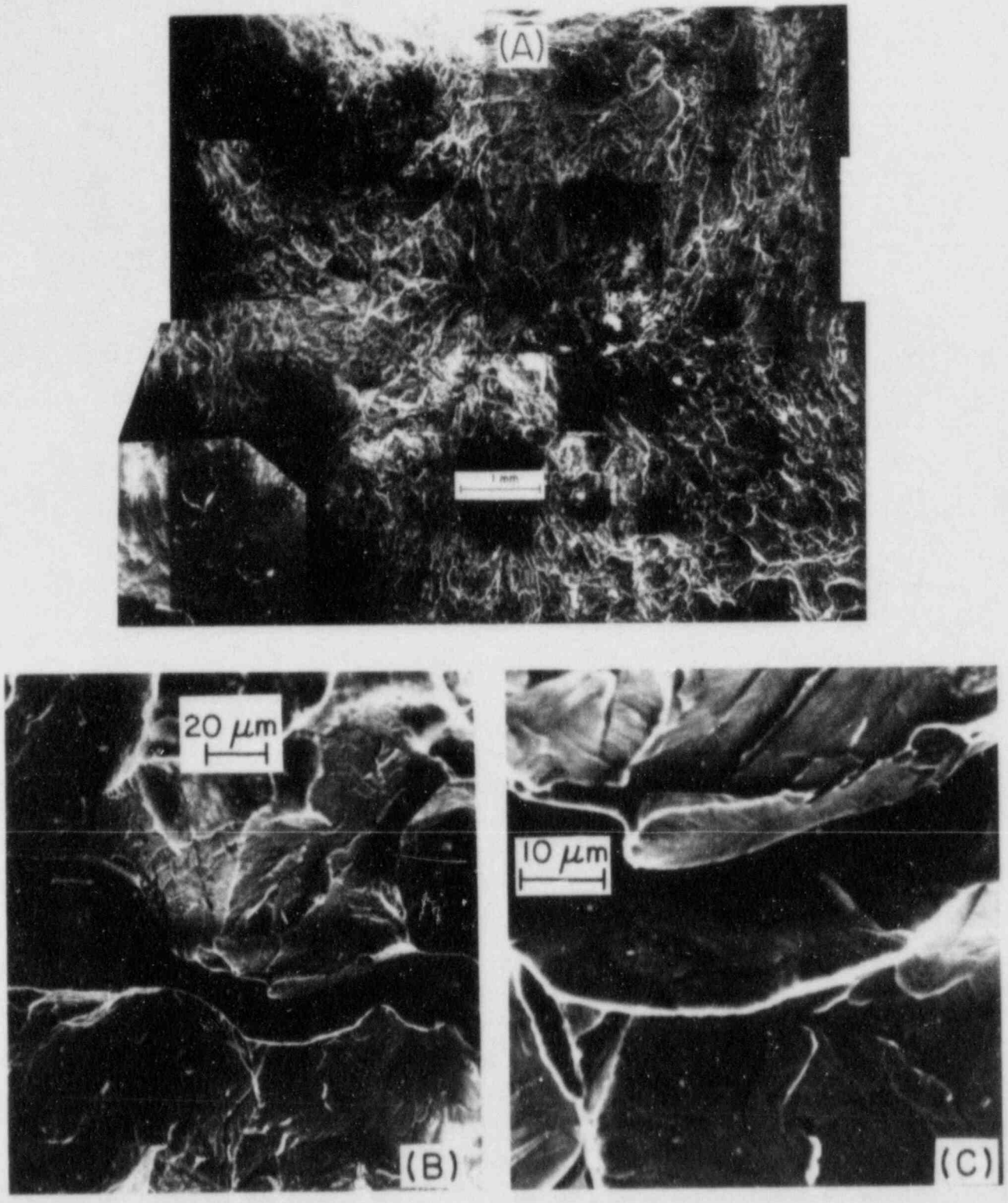

Fig. 7. SEM Fractographs of Cast CF-8 Stainless Steel (Heat 278) after Aging at 300°C for 70,000 h (8 yr) and Impact Failure at 25°C. (A) Overall fracture surface; (B) and (C) higher magnifications of the circled region in (A), showing brittle-cleavage morphology of the ferrite phase.

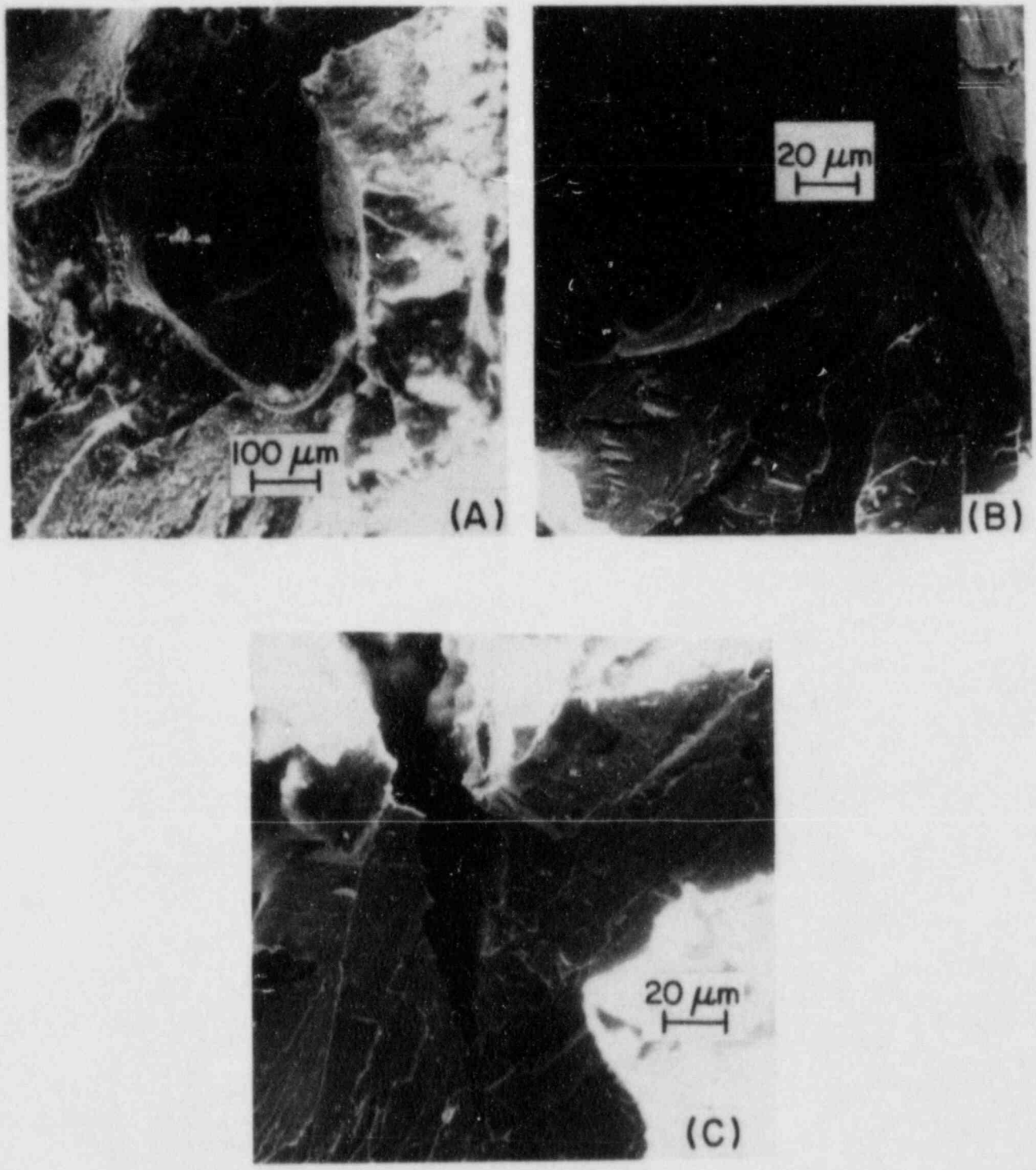

Fig. 8. SEM Fractographs of Cast CF-8 Stainless Steel (Heat 280) after Aging and Impact Failure Similar to Fig. 7. (A) Lower magnification showing both ductile and brittle-cleavage morphologies; (B) and (C) higher magnifications of the cleavage in (A).

4. E. I. Landerman and W. H. Bamford, "Fracture Toughness and Fatigue Characteristics of Centrifugally Cast Type 316 Stainless Steel Pipe after Simulated Thermal Service Conditions," in Ductility and Toughness Considerations in Elevated Temperature Service, ed. G. V. Smith, ASME MPC-8 (1978), p. 99.

5. G. Slama, P. Petrequin, and T. Magep, "Effect of Aging on Mechanical Properties of Austenitic Stainless Steel Castings and Welds," presented at SMIRT Post-Conference Seminar 6, Assuring Structural Integrity of Steel Reactor Pressure Boundary Components, August 29 and 30, 1983, Monterey, CA.

6. P. J. Grobner, "The 885°F (475°C) Embrittlement of Ferritic Stainless Steels," Metall. Trans. 4 (1973), p. 251.

7. T. J. Nichol, A. Dalta, and G. Aggen, "Embrittlement of Ferritic Stainless Steels," Metall. Trans. 11A (1980), p. 573.

8. O. K. Chopra and G. Ayrault, "Aging Degradation of Cast Stainless Steel: Status and Program," in Proc. U. S. Nuclear Regulatory Commission Eleventh Water Reactor Safety Research Information Meeting, NUREG/CP-0048 Vol. 4 (1984), p. 152.

9. A. Hendry, Z. F. Mazur, and K. H. Jack, "Influence of Nitrogen on 475°C Embrittlement of High-Chromium Ferritic Steels," Met. Sci. 13 (1979), p. 482.

10. M. Courtnall and F. B. Pickering, "The Effect of Alloying on 475°C Embrittlement," Met. Sci. 10 (1976), p. 273.

11. Kernkraftwerke Gundremmingen Betriebsgesellschaft, private communication.

12. O. K. Chopra and G. Ayrault, Long-term Embrittlement of Cast Duplex Stainless Steels in LWR Systems: Annual Report, October 1982-September 1983, Argonne National Laboratory, NUREG/CR-3857, ANL-84-44 (1984).

13. O. K. Chopra and H. M. Chung, "Long-Term Embrittlement of Cast Duplex Stainless Steels in LWR Systems," in Light-Water-Reactor Safety Materials Engineering Research Programs: Quarterly Progress Report, January-March 1984, Argonne National Laboratory, NUREG/CR-3998 Vol. I, ANL-84-60 Vol. I (1984), p. 52.

SENSITIZATION DEVELOPMENT IN AUSTENITIC STAINLESS STEEL PIPING[a]

S. M. Bruemmer
R. E. Page
D. G. Atteridge

Pacific Northwest Laboratory
Operated by Battelle Memorial Institute

INTRODUCTION

Pacific Northwest Laboratory and the Division of Engineering Technology of the U.S. Nuclear Regulatory Commission are conducting a program to determine a method for evaluating welded and repair-welded stainless steel piping for light-water reactor service. Validated models, based on experimental data, are being developed to predict the degree of sensitization (DOS) and the intergranular stress corrosion cracking (IGSCC) susceptibility in the heat-affected zone (HAZ) of the SS weldments. The cumulative effects of material composition, past fabrication procedures, past service exposure, weldment thermomechanical (TM) history, and projected post-repair component life are being considered.

Austenitic SS components of commercial boiling-water and pressurized water reactors have experienced IGSCC in the HAZ of SS weldments. Although only a few instances of such cracking have been observed, their potential for causing serious component failure should not be underestimated. Intergranular stress corrosion is caused by combination of a sensitized microstructure, an aggressive environment, and tensile stress. Control of any of these three factors can eliminate IGSCC in most practical situations.

This program will measure and model the development of HAZ TM history and resultant sensitized microstructure in welded and repair-welded piping. An empirical correlation between a material's DOS and its susceptibility to SCC will be determined using slow-strain-rate tensile tests. Mill heat chemistries and processing/fabrication records already required in the nuclear industry will be used as input for initial DOS predictions. Recommendations for increased procedure controls and record changes will be made as required to attain realistic DOS and SCC susceptibility predictions.

This paper briefly reviews specific aspects of the experimental program completed to date. Emphasis is given to three areas: (1) development of composition-based correlations to predict sensitization resistance;

(a) Work supported by the U.S. Nuclear Regulatory Commission under Contract DE-AC06-76RLO 1830.

(2) quantitative measurement and modeling of sensitization development; and (3) measurement of thermomechanical history and sensitization in the heat-affected zone of pipe welds.

COMPOSITION-BASED CORRELATIONS TO PREDICT SENSITIZATION RESISTANCE OF AUSTENITIC STAINLESS STEELS

Background

Sensitization refers to the loss of corrosion resistance after heat treatment in, or slow cooling through, a particular temperature regime. This susceptibility to corrosion results from a change in the local composition at grain boundaries. The primary composition change that occurs is the precipitation of chromium-rich carbides and an associated depletion of chromium in the adjacent region. The importance of chromium depletion was first proposed by Bain, Aborn and Rutherford[1] and was more quantitatively developed by Stawstrom and Hillert[2] and Tedmon et al.[3] Experimental measurements[4-6] have indicated that the chromium-depleted zone is, in most cases, directly responsible for the loss in IGSCC resistance.

The development of a sensitized microstructure is controlled by the thermodynamics of carbide formation and the kinetics of chromium diffusion. Sensitization occurs in a temperature regime in which chromium carbides are thermodynamically stable (<900°C) and chromium diffusion is sufficiently rapid (>500°C) so that precipitates can form in a reasonable period of time. If chromium diffusion occurs too rapidly (>825°C), precipitates will form, but no significant chromium depletion will result. Therefore, sensitization only results from thermal exposure within a relatively narrow temperature range. This range is normally between 550 and 800°C but is strongly dependent on material composition.

The present work has examined a large data base of time-temperature-sensitization (TTS) curves from the literature and measured isothermal sensitization development in a series of Types 304 and 316 SS pipe heats ranging in bulk carbon contents from 0.01 to 0.075 wt%. Material DOS has been determined as a function of thermal treatment using electrochemical potentiokinetic reactivation (EPR) tests. Composition correlations are proposed and evaluated to account for the effect of major alloying elements such as carbon, chromium, nickel, and molybdenum on sensitization development.

Composition-Based Correlations

Cihal[7] rationalized heat-to-heat variability in intergranular corrosion and SCC resistance by normalizing compositional differences with "effective" chromium and carbon concentrations. Chromium concentration was normalized in

relation to molybdenum, and carbon was normalized in relation to nickel. This allows the following expression to be written:

$$Cr^* = Cr + (1.0 \text{ to } 1.7)\ Mo - 100\ C - 0.2\ Ni \quad (1)$$

where Cr* is defined as a "composite" chromium concentration and element designations represent their bulk content in weight percent. The basic form of this equation is identical to that proposed by Fullman[8] and used by Briant et al.[9] This composite chromium term allows the effect of heat-to-heat composition variations on sensitization resistance to be evaluated. Lower composite chromium values indicate an increased potential for sensitization.

A large number of composite chromium formulations, including several based on Cihal's equivalency parameters, had been evaluated by comparison to the literature data base.[10] Some of the results from this evaluation are summarized in Table 1. Linear regression analysis was performed using each of the formulations versus time-to-sensitize data at 600°C, 650°C, and 700°C. These temperatures were the only ones for which sufficient data existed to allow statistical comparisons. The relative "fit" of the particular model prediction to the data is also shown in Table 1 (the lower the variance, the better the fit). Considering the source of these data, the strong positive correlations recorded for several of the predictive equations are promising. Results comparing data at 600 and 700°C were similar to those at 650°C. The best predictive capability was obtained using the Cihal parameters with the molybdenum parameter slightly adjusted. A typical correlation between prediction and the time-to-sensitize data base is shown graphically in Figure 1.

It is important to note from Figure 1 that the scatter in experimental time-to-sensitize data for a particular Cr* can be as much as two orders of magnitude. This scatter is primarily due to variations in initial material condition (e.g., mill annealed, solution annealed, or cold worked), differences in experimental techniques among laboratories (e.g., test time or evaluation criteria to detect sensitization), and difficulties in accurately identifying the time to sensitize from the reported data. Thus, although the Cr* equations fit the trend of the isothermal sensitization data, they cannot be used to quantitatively predict sensitization times.

A significant improvement in the correlation fit was observed by examining TTS curves generated from EPR tests on our program heats. These data are discussed in more detail in the modeling section. Excellent agreement was documented between composite chromium concentrations and time-to-sensitize data, as presented in Figure 2. Variances determined by the linear regression fit were an order of magnitude lower than for the literature data base correlation shown in Figure 1. Thus, the use of calculated composite chromium concentrations

appears to be an effective method of taking into account heat-to-heat composition variations and assessing a material's relative resistance to sensitization.

Factors of Improvement Based on Predicted Sensitization Resistance

The correlation between composite chromium concentration and the time to sensitize demonstrated in the previous section enables the comparative assessment of different heats of Type 304 or 316 SS. Relative sensitization resistance can be determined by calculating the expected time to sensitize from the empirical correlation shown in Figure 1. Linear regression analysis of all data resulted in the equation:

$$\log (t_s) = -3.96 + 0.325\ Cr^* \qquad (2)$$

or

$$\ln (t_s) = -9.108 + 0.748\ Cr^* \qquad (3)$$

where t_s is the time to sensitize in hours (at 650°C) as measured by modified Strauss or EPR tests.

The relationship depicted in equations 2 and 3 allows the prediction of relative sensitization resistance as a function of bulk heat composition (Cr*). In order to compare various heats of material, a factor of improvement (F/I) can be obtained by ratioing the expected times to sensitize of Heat 1 versus Heat 2 using equation 3:

$$F/I = \frac{\exp (-9.108 + 0.748\ Cr_1^*)}{\exp (-9.108 + 0.748\ Cr_2^*)} \qquad (4)$$

where Cr_1^* and Cr_2^* are the composite chromium concentrations of Heats 1 and 2, respectively.

Examples of these factors of improvement in comparison to a high-carbon and a medium-carbon Type 304 SS are listed in Table 2 for Types 304, 304L, 304NG, 316, 316L, and 316NG stainless steels. The significant effect of reducing carbon content is observed by comparing improvement factors within a particular alloy type, either Type 304 or 316 SS. A factor of improvement of about 20 is predicted for Type 316NG over standard Type 304 SS.

Although time-to-sensitize data were obtained from tests on isothermally heat-treated specimens, the data do indicate relative improvements expected in weld-induced sensitization. Thermomechanical cycling during welding had been shown to accelerate sensitization development.[11] Thus, the calculated time to sensitize will be an overestimation of the actual time to sensitize of the HAZ. The factor of improvement may also be changed, but may still reflect the

relative magnitude noted for the isothermal case. Verification tests are required to determine whether such a correlation is possible.

QUANTITATIVE MEASUREMENT AND MODELING OF SENSITIZATION DEVELOPMENT

Background

Sensitization of austenitic stainless steels is dependent on the thermodynamics of carbide precipitation and the kinetics of chromium diffusion. Heat treatment in, or slow cooling through, the temperature range from 550 to 800°C promotes intergranular chromium-rich precipitation and depletion of chromium in adjacent regions. These local chromium-depleted regions are more electrochemically active than the bulk material and may cause intergranular corrosion and/or stress corrosion in many environments. The ability to adequately model and predict sensitization (and IGSCC) behavior of stainless steels requires a better understanding of the development of chromium-depleted regions.

A significant limitation in many studies investigating sensitization development has been the lack of a quantitative method of determining material DOS. The development and application of the EPR test has been an important step in overcoming this limitation. The EPR test and modified Strauss test appear to be the most sensitive to grain boundary chromium depletion and to best correlate to IGSCC susceptibility.[10]

Attempts have been made by several researchers to predict sensitization behavior by modeling chromium depletion at grain boundaries. Most studies have assessed their predictive capability by comparison to corrosion test results. However, more recently, direct comparisons between measured and predicted chromium depletion profiles have been reported. While indirect and direct measurement comparisons show excellent qualitative agreement with prediction, more quantitative correlations over a range of conditions have not been possible.

Model Description for Quantitative DOS Prediction

A model for the prediction of material DOS as a function of bulk composition, initial condition and TM history is being developed. Basic components of the model are shown schematically in Figure 3 and include determination of the equilibrium chromium concentration at the carbide-matrix interface based on the thermodynamics of carbide formation, chromium concentration gradients based on "effective" diffusivities, and an empirical correlation between chromium depletion and DOS as indicated by the EPR test. Several other correlations are also present in the model to account for compositional effects on diffusion and to determine the onset and progression of healing during extended heat treatment.

An important aspect of the model is the prediction of DOS in a form that allows straightforward comparison to experiment. Thus, existing model capabilities and attempts to improve the predictive ability can be evaluated using an inexpensive, yet quantitative technique (i.e., EPR). Examples showing the effect of bulk composition on the predicted equilibrium chromium concentration at the carbide-matrix interface are presented in Figure 4. The four elements displayed--carbon, chromium, nickel, and molybdenum--are the most important in reference to sensitization development in stainless steels.

Sensitization resulting from isothermal or continuous cooling treatments has been modeled in both Types 304 and 316 stainless steel. In addition, several instrumented weldments have been examined on a pass-by-pass basis. Predictions indicate that the model is capable of making realistic estimates of DOS if the thermal history is known. Comparisons between measured and predicted EPR-DOS values are discussed in the following sections for isothermal sensitization. Prediction of HAZ sensitization development is treated after the description of thermomechanical history measurement techniques.

EPR Measurements of Isothermal Sensitization Development

The isothermal TTS behavior of seven heats of Type 304 and seven heats of Type 316 SS has been evaluated. Materials were obtained as 4-in.-diameter pipe, either Schedule 40 or 80. Bulk compositions of each heat and specific experimental details have been reported elsewhere.[12] Alloys were heat treated at temperatures ranging from 500 to 800°C and for times from 0.1 to 100 hours. All heats were initially in the mill-annealed condition.

Sensitization development in both the Types 304 and 316 SS heats tracked reasonably well with the bulk carbon content of the heats. Within a particular alloy type, the higher the carbon content, the higher the measured DOS for a given isothermal heat treatment. Examples of this behavior are shown in Figures 5a and 5b for heat treatment at 700°C. High-carbon heats reach EPR-DOS values of well over 100 C/cm^2 after 100 h at 700°C. An EPR-DOS value greater than 20 C/cm^2 is commonly considered to be "severely" sensitized.

The kinetics of sensitization development are more rapid in Type 304 than in Type 316 SS as seen by comparing the data in Figure 5a to 5b. For a comparable carbon content, the DOS reaches a measurable value at shorter times and reaches higher values at longer times in Type 304 than in Type 316. This is consistent with the reported slower chromium diffusion rate in Type 316 (by about a factor of 4 at these temperatures).[2] The sensitization data obtained after annealing at 500 and 600°C also support this difference in diffusivities.

Another difference between the data for Types 304 and 316 was the onset of "healing" at shorter times and at lower temperatures for Type 304 heats. Healing occurs when chromium diffuses from the matrix into the depleted zone and

reduces its size and thereby the material DOS. All of the Type 316 heats showed increasing DOS through 100 h at 700°C (Figure 5b). However, most of the Type 304 heats exhibited a lower (or comparable) DOS after 100 h than after 10 h at 700°C (Figure 5a). This indicates that the maximum DOS was reached and healing started between these annealing times. At higher temperatures, the disparity between Types 304 and 316 heats due to healing became quite obvious. Very little sensitization was observed in any of the Type 304 heats at 800°C while significant DOS levels were still achieved in higher-carbon, Type 316 heats.[12] Sensitization levels above 2 C/cm^2 were not identified in the low-carbon (L) grades of either alloy as a result of heat treatment at 800°C.

Comparison of Model Prediction to Isothermal Sensitization Measurements

Isothermal sensitization development in more than 20 heats of Types 304 and 316 SS has been measured using the EPR technique. This data base is being used to evaluate model capabilities to predict compositional effects on sensitization. Examples of typical model predictions are shown in Figures 5c and 5d below the experimental measurements. Although some differences can be noted by examining specific heats at certain time/temperature conditions, overall the predictive capability is quite good. Relative ranking of each heat is consistent comparing experiment and model predictions. A more extensive documentation of model predictions have been presented in a separate publication.[13]

One of the most difficult aspects of DOS prediction is the effect of initial material condition. Measured sensitization development at temperatures between 500 and 700°C indicate that apparent chromium diffusivities are significantly more rapid in mill-annealed versus solution-annealed material. Several studies have shown that prior strain or cold work can accelerate sensitization development.[11] The model allows the input of initial material condition, which modifies the effective chromium diffusity equation. This modification was necessary to better predict sensitization development in both mill-annealed and solution-annealed materials.

HEAT-AFFECTED ZONE MEASUREMENTS OF THERMOMECHANICAL HISTORY AND SENSITIZATION IN PIPE WELDS

Background

A weld/repair HAZ is subject to a complicated strain history superimposed over the heating and cooling cycle. Recent work indicates that this strain cycle increases the resultant sensitization of the HAZ over that predicted from strain-free isothermal data or that measured in specimens subjected to a similar but strain-free heating and cooling cycle. It is therefore necessary to precisely determine the strain/temperature history of a HAZ. The HAZ strain history is more complex in a multipass weld/repair than in a single-pass

weld/repair. Strain history is also more complex in a pipe weld/repair than in a plate weld/repair; stresses can be relieved by plate bending, while circumferential restraint restricts metal movement in a pipe weld.

Previous experimentation involving the HAZ TM history concentrated on temperature measurements as a function of time and distance from the fusion line. The present work will determine simultaneously the strain and temperature history in welded/repaired pipe HAZs as a function of time and distance from the fusion line. It is expected that the resultant HAZ TM history will be a complex function of system restraint and heat absorption capability. Variables that can be expected to influence the TM history are pipe diameter and wall thickness, changes in wall thickness from one side of the fusion line to the other, depth of counterbore, weld/repair groove geometry, amount of weld crowning, weld heat input, length and depth of repair, and welding technique.

A major goal of this work is to identify, measure and model the welding and repair-welding variables that have a major effect on resultant DOS. The initial work will be oriented toward experimentally determining HAZ TM histories of welds/repairs as a function of pipe size and heat input. Data will then be used to assess analytical methods for predicting TM histories of generic welds/repairs and the effect of specific welding and repair-welding variables on the resultant TM history.

Instrumentation Development

The decision to measure TM histories dictated the need for fast response signal recording capabilities, strain measurement devices that can withstand temperatures up to the melting point of stainless steels, and signal generation equipment that can withstand an electric welding arc superimposed over the desired strain or temperature measurement device signal. The resultant data must also be deciphered once the test is complete; thus, a Data Retrieval and Analysis System (DRAS) has been developed specifically for this program.

The DRAS begins with the temperature and strain sensors attached in the pipe HAZ. The sensor signals generated during welding are fed through an optically isolated amplifier and noise filtering system and into a high-speed analog-to-digital converter. The signals are then sent to a dedicated computer system where they are displayed in real time on a CRT and stored on magnetic tape. The system is capable of recording 112 independent input signals at a rate of 25 data sets (2800 signal inputs) per second. Data storage on magnetic tape allows post-weld data analysis and also allows easy data transfer from one computer system to another.

Three types of strain-sensing devices have been developed under this program. One type is used to measure strain changes on the pipe surface; another is used to measure strain changes perpendicular to the pipe surface. The third

measures axial shrinkage and expansion. All strain-sensing devices use a standard MTS crack-opening displacement clip gage to measure strain changes.

The clip gages used to measure surface strain are insulated from surface temperature excursions by ceramic extensions. These extensions contain notches on their outside surfaces which mate to knife edges in the stainless steel attachment feet. The feet are connected to the pipe surface by spot welded studs 0.125 in. in diameter and spaced 0.250 in. apart. A spring against the outside surface of the feet counteracts the force exerted by the clip gage legs on the attachment feet. Surface strain-sensing devices are attached parallel and perpendicular to the weld centerline as a function of distance into the expected HAZ. Thermocouples are spot welded to the pipe between the studs to allow simultaneous measurement of strain and temperature.

The strain change measurements perpendicular to the pipe surface require the use of a "stationary" measurement platform above the pipe surface. This was accomplished by constructing a bridge above the counterbore surface and anchored to the pipe surfaces outside the counterbore area. One leg of an MTS clip gage was attached to this bridge and a ceramic pin was forced between the other clip gage leg and the pipe surface. The MTS clip gage thus records any relative movement between the counterbore surface and the bridge. These profilometer surface-movement sensors are placed along the bridge as a function of distance from the weld centerline. The three different types of strain-change measurement devices are shown attached to the 24-in.-dia. pipe in Figure 6.

No problem was encountered in recording the sensor outputs during gas tungsten arc welding (GTAW), but the radio frequency interference (RFI) emitted during high-frequency arc starting was found to disrupt operation of the DRAS. The RFI was capable of locking up the analog-to-digital conversion unit, requiring a system shutdown and restart. It was also capable of scrambling the information on the Winchester hard disk, requiring reprogramming of the disk before system reuse. These RFI-related problems required the development of an arc-starting method that did not emit RFI.

A technique was developed and is presently being used that employs an auxiliary GTAW torch. The auxiliary torch is attached to the ground lead of the welding power supply. It is then brought in contact with the welding electrode. The auxiliary torch is withdrawn once an arc is struck between the two tungsten electrodes. This starting arc transfers from the auxiliary electrode to the work piece during torch removal and welding is initiated without the emission of RFI.

Thermomechanical History Measurements on Pipe Welds

The DRAS was used to record the thermal history on a pass-by-pass basis on three 14-in.-dia. Schedule 160 Type 304 stainless steel pipe welds. Thermal

history, limited strain history, and post-weld DOS measurements were made on a fourth 14-in.-dia. pipe weld. Pass-by-pass thermal, strain, and DOS histories have been determined on a 24-in.-dia. Type 304 schedule 80 SS pipe. Examples of the experimental measurements on the 24-in.-dia. pipe will be presented below. The 14-in.-dia. pipe data have been reported elsewhere.[13]

The 24-in.-dia. pipe is being welded in the 2G position with the pipe axis oriented in the vertical direction and the welding head traveling in a horizontal plane around the pipe, as illustrated in Figure 7. Note that the weld head rides in grooves machined in the pipe surface. The sensor package installed on the 24-in.-dia. pipe included ten surface strain-measurement devices, six profilometer devices, an axial extension gage, and six thermocouples specifically used to define the thermal history of the DOS measurement region. Surface thermocouples were placed between the attachment studs for each of the ten surface strain-measurement gages. Thermocouples were also placed on the legs of the 17 MTS clip gages in order to monitor strain gage temperatures. Placement of the strain-measurement devices and their associated thermocouples for the 24-in.-dia. pipe is shown in Figure 6.

Typical thermomechanical history and resultant DOS plots are shown schematically in Figure 8. Temperature and strain plots represent data collected at a specific distance out from the fusion line as a function of arc-on time for several weld passes. Sensitization is determined after each pass. Typical surface deflection and temperature response during welding of the 24-in.-dia. pipe are superimposed in Figure 9. The temperature is found to remain unchanged until the arc is very close to the thermocouple position. The surface temperature then rises very rapidly, reaches a peak temperature, and then cools down relatively slowly.

The surface strain exhibits a compressive component as the arc approaches, which turns into a tensile component as the area heats up. The tensile strain slowly decreases once the thermal spike has receded. A two-dimensional plot of surface temperatures induced in the 24-in.-dia. pipe by the arc is presented in Figure 10 as a function of distance from the weld and distance along the weld. The arc-induced heat only influences a region of less than one half inch in front of the arc but influences a four to five inch long region behind the arc.

Correlation of Thermomechanical History, DOS Measurements and Model Predictions

One of the primary reasons that pipe HAZ thermomechanical history is being determined is to enable prediction of the expected DOS present in the HAZ. Model predictions are being compared to EPR measurements obtained as a function of distance in the HAZ after each weld pass.

An overview of the thermal history data used to calculate DOS as well as a comparison of the actual and predicted EPR values is presented in Figure 11 for the first (root) and second passes for the 24-in.-dia. pipe weld. The top graph in Figure 11 illustrates the change in maximum temperature as a function of distance from the weld centerline for both passes, while the middle graph illustrates the change in cooling rate. The bottom graph presents the measured and predicted EPR values after the first and second passes.

The first pass reached higher temperatures than the second. Both had relatively equivalent cooling rates at comparable temperatures. Measured and predicted DOS values peaked near the same HAZ location corresponding to a maximum temperature of about 800°C. Comparison of measured and predicted HAZ sensitization in Figure 11 indicates the potential applicability of the model. Further developments through direct correlations to experimental measurements are continuing.

SUMMARY

Several specific aspects of the experimental program, "Evaluation of Welded and Weld-Repaired Stainless Steel for LWR Service" have been reviewed. Three areas are discussed in some detail: 1) development of composition-based correlations to predict sensitization resistance; 2) quantitative measurement and modeling of sensitization development; and 3) measurement of thermomechanical history and sensitization in the heat affected zone of pipe welds.

Calculation of chromium composite concentrations was found to be an effective method to normalize bulk composition effects on sensitization. A simple method is proposed to predict the relative sensitization resistance of individual heats based on correlations to isothermal experimental data. Factors of improvements can be estimated by ratioing predicted times to sensitize for specific heats.

A preliminary model has been developed that enables the prediction of material DOS (as measured by EPR) as a function of alloy composition, condition and thermal history. Comparisons of experimental measurements and model predictions for isothermal sensitization development in Types 304 and 316 SS were in good agreement. The EPR technique allowed an accurate mapping of sensitization development and, thereby, an excellent data base for quantitative correlation to prediction.

Thermomechanical history and sensitization measurements have been performed in the HAZ of pipe welds. Present instrumentation is capable of accurate monitoring of thermal and strain history on a pass-by-pass basis. Strain development is being measured parallel, perpendicular, and normal to the weld

centerline. Preliminary correlations between measured DOS and predicted DOS (using measured thermal histories) as a function of distance within the HAZ are encouraging.

ACKNOWLEDGMENTS

The key contributions of M. Wismer and L. A. Charlot and the technical assistance of B. W. Arey and B. Norton are gratefully acknowledged. J. Muscara is the program monitor for this work and participated in many helpful discussions concerning the planning and execution of the research.

REFERENCES

1. E. C. Bain and R. H. Aborn, Trans. Am Soc. Steel Treat., Vol. 18, p. 837, 1930.

2. C. Stawstrom and M. Hillert, J. Iron and Steel Inst., p. 77, January 1969.

3. C. S. Tedmon, Jr., D. A. Vermilyea and J. H. Rosolowski, J. Electrochem. Soc., Vol. 118, p. 192, 1971.

4. T. M. Devine, J. Electrochem. Soc., Vol. 126, p. 374, 1979.

5. R. L. Cowan and G. M. Gordon, Proc. Conf. Stress Corr. Cracking and Hydrogen Embrittlement, NACE, Houston, p. 1025, 1977.

6. K. Osozawa and H. J. Engell, Corr. Soc., Vol. 6, p. 589, 1966.

7. V. Cihal, "Intergranular Corrosion of Cr-Ni Stainless Steel," presented at Unieux Conference, May 5, 1969.

8. R. L. Fullman, Acta Metall., Vol. 30, p. 1407, 1982.

9. C. L. Briant, R. A. Mulford and E. L. Hall, Corrosion J., Vol. 38, No. 9, p. 468, 1982.

10. S. M. Bruemmer, L. A. Charlot and D. G. Atteridge, NUREG/CR-3918, Oct. 1984

11. H. D. Solomon and D. C. Lord, Corrosion J., Vol. 36, No. 8, p. 395, 1980.

12. S. M. Bruemmer, CORROSION/85, National Association of Corrosion Engineers, Paper No. 106, 1985.

13. D. G. Atteridge, S. M. Bruemmer and R. E. Page, NUREG/CR-3613-2, Annual Report, December 1984.

TABLE 1. Comparison of Predictions from Composition-Based Models to Those from Time-to-Sensitize (t_s) Data Base

Predictive Equation Source	Formula for Composite Chromium, Cr*	Linear Regression Correlation Equation	Variance on Data "Fit" at 650°C
Carbon content	C	$\log t_s = 1.87 - 36.47\ C$	0.55
Cihal-1.0	Cr + 1.0 Mo - 0.2 Ni - 100 C	$\log t_s = -3.82 + 0.326\ Cr^*$	0.473
Cihal-1.3	Cr + 1.3 Mo - 0.2 Ni - 100 C	$\log t_s = -4.03 + 0.338\ Cr^*$	0.388
Cihal-1.5	Cr + 1.5 Mo - 0.2 Ni - 100 C	$\log t_s = -4.00 + 0.330\ Cr^*$	0.350
Cihal-1.6	Cr + 1.6 Mo - 0.2 Ni - 100 C	$\log t_s = -3.96 + 0.325\ Cr^*$	0.341*
Cihal-1.7	Cr + 1.7 Mo - 0.2 Ni - 100 C	$\log t_s = -3.96 + 0.324\ Cr^*$	0.347
Briant[10]	Cr + 1.42 Mo - 0.18 Ni - 100 C	$\log t_s = -4.11 + 0.335\ Cr^*$	0.374
Fullman[9]	Cr + 1.45 Mo - 0.19 Ni - 100 C + 0.13 Mn - 0.22 Si - 0.51 Al - 0.20 Co + 0.01 Cu + 0.61 Ti + 0.34 V - 0.22 W	$\log t_s = -4.07 + 0.332\ Cr^*$	0.364
Nitrogen modified	Cr + 1.6 Mo - 0.2 Ni - 100 C + 9.2 N	$\log t_s = -3.89 + 0.310\ Cr^*$	0.365
Carbon modified	Cr + 1.6 Mo - 0.2 Ni - 110 C	$\log t_s = -3.50 + 0.300\ Cr^*$	0.385
Mn/Si modified	Cr + 1.6 Mo - 0.2 Ni - 100 C + 0.13 Mn - 0.22 Si	$\log t_s = -4.02 + 0.328\ Cr^*$	0.349
Ni modified	Cr + 1.6 Mo - 0.18 Ni - 100 C	$\log t_s = -4.03 + 0.325\ Cr^*$	0.356
Ni modified	Cr + 1.6 Mo - 0.22 Ni - 100 C	$\log t_s = -3.93 + 0.328\ Cr^*$	0.365

TABLE 2. Calculated Sensitization Times and Factors of Improvement for Several Types 304 and 316 Stainless Steels

Alloy	Composition, wt% C	Cr	Ni	Mo	Cr*, %	Time to Sensitize (t_s), h	Factor of Improvement: High Carbon	Factor of Improvement: Standard Carbon
304	0.08	18.5	8.5	0.2	9.12	0.10	1	0.1
304	0.05	18.5	8.5	0.2	12.12	0.96	10	1
304L	0.035	18.5	8.5	0.2	13.62	2.94	29	3
304NG	0.02	18.5	8.5	0.2	15.12	9.04	90	9
316	0.08	17.0	12.5	2.2	10.02	0.20	2	0.2
316	0.05	17.0	12.5	2.2	13.02	1.88	19	2
316L	0.035	17.0	12.5	2.2	14.52	5.77	58	6
316NG	0.02	17.0	12.5	2.2	16.02	17.73	177	9

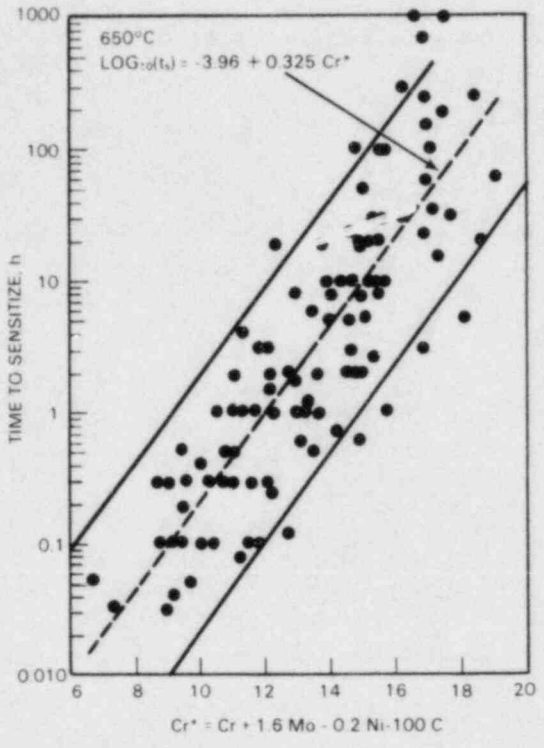

FIGURE 1. Correlation Between Composition Normalization Parameter, Cr*, and Experimentally Measured Time-to-Sensitize Data

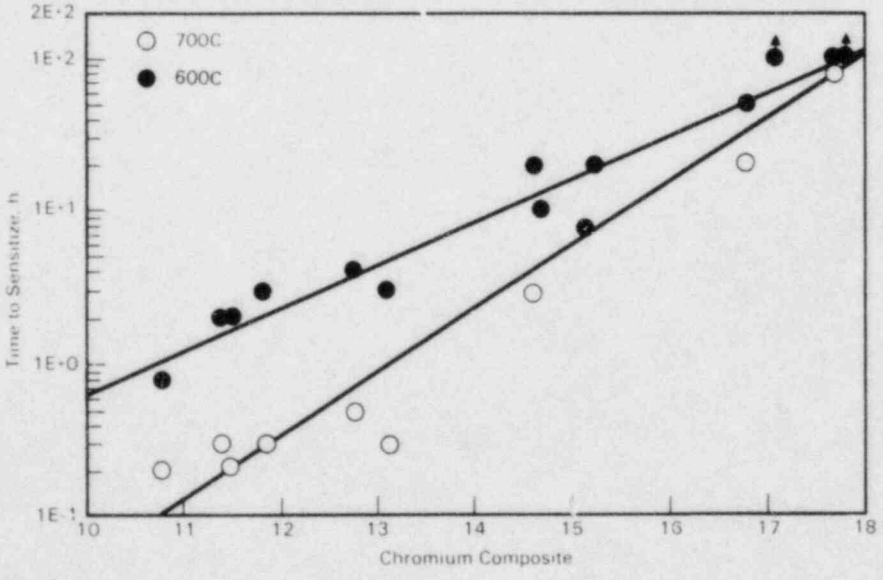

FIGURE 2. Correlation Between Chromium Composite Values and Time-to-Sensitize Data for the Type 304 and 316 SS Heats from the Isothermal Carbon Series Experiments

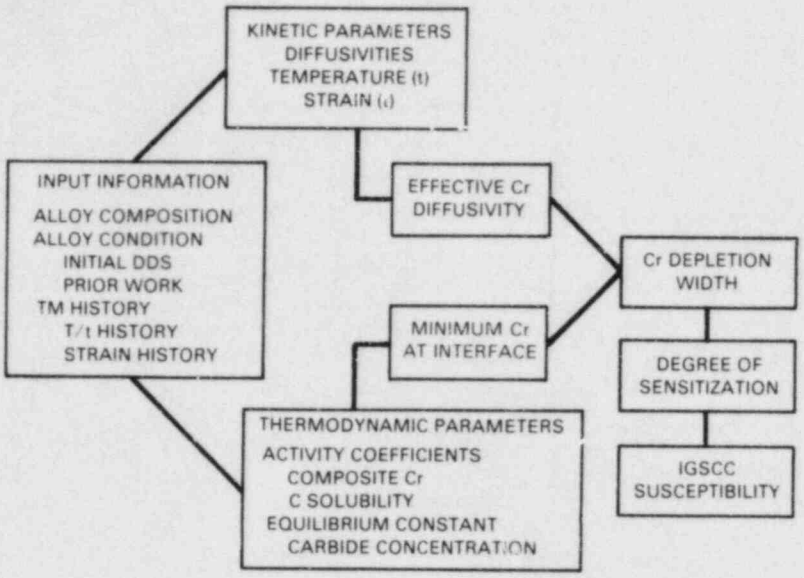

FIGURE 3. Methodology for Prediction of the Degree of Sensitization and IGSCC Susceptibility as a Function of Material Composition and Thermomechanical Treatment

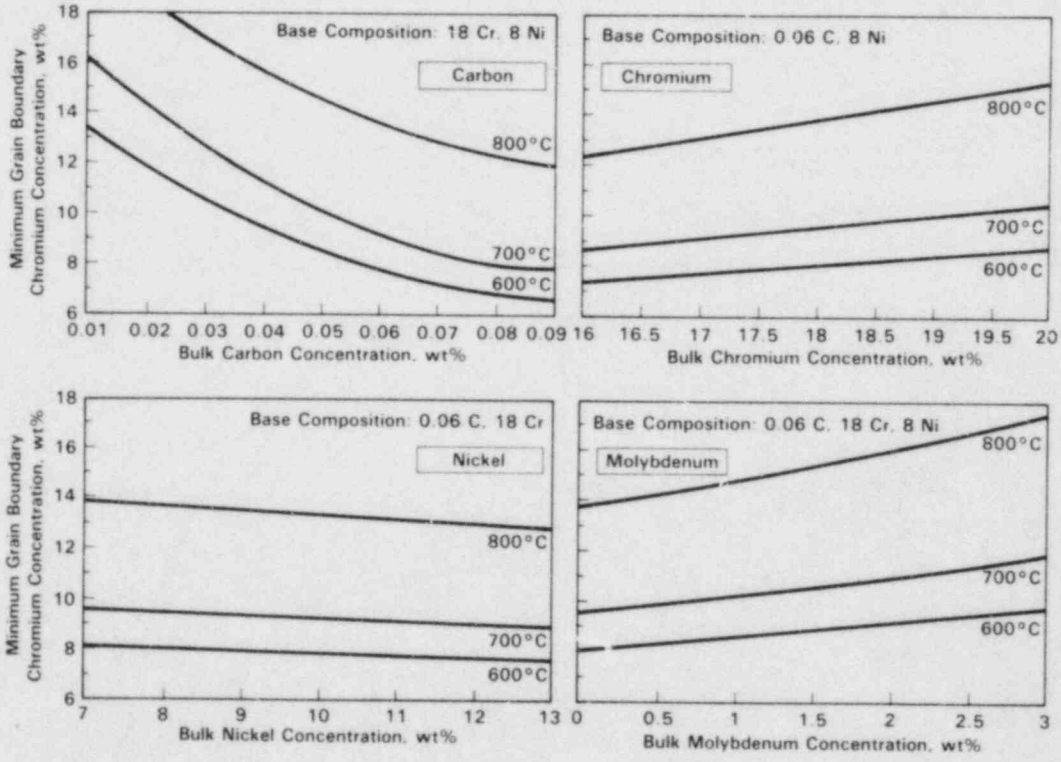

FIGURE 4. Model Predictions Illustrating Bulk Composition Effects on the Interfacial Chromium Concentration in Equilibrium with the Grain Boundary Carbide

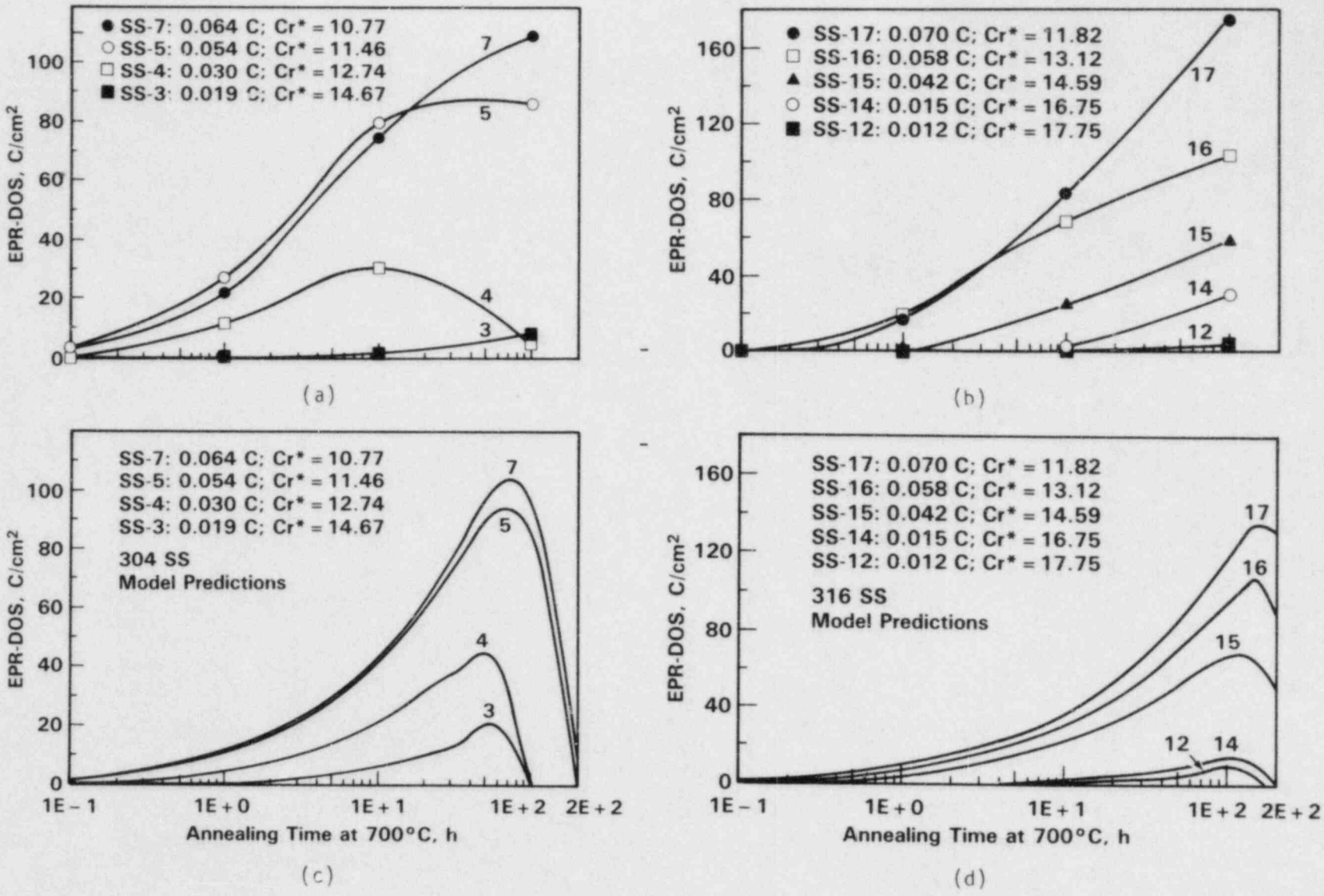

FIGURE 5. Measured and Predicted Sensitization Development for Type 304 (a & c) and 316 (b and d) Heats at 700°C

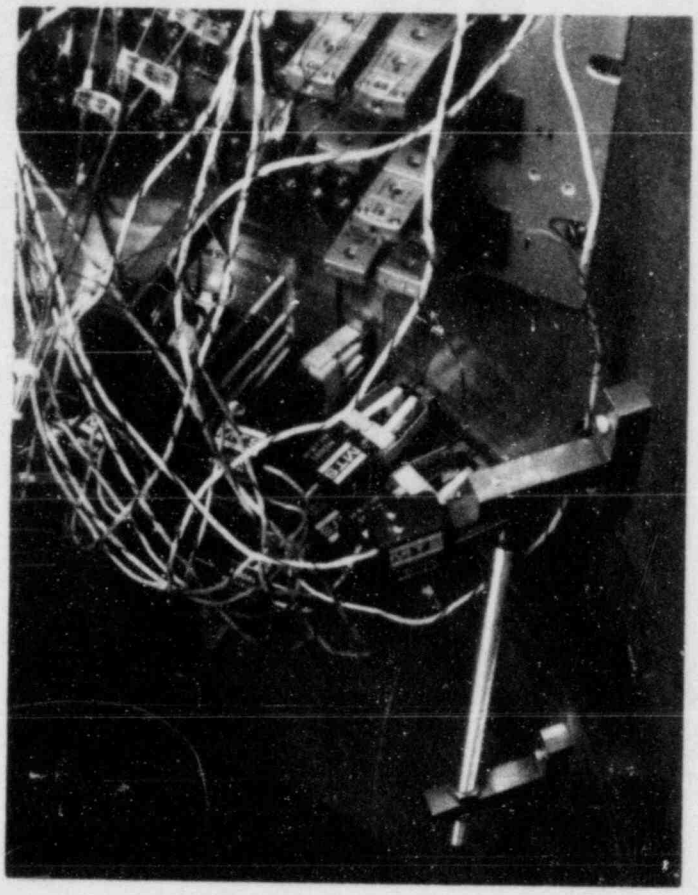

FIGURE 6. Instrumented Heat-Affected Zone in the 24-in.-Diameter Pipe

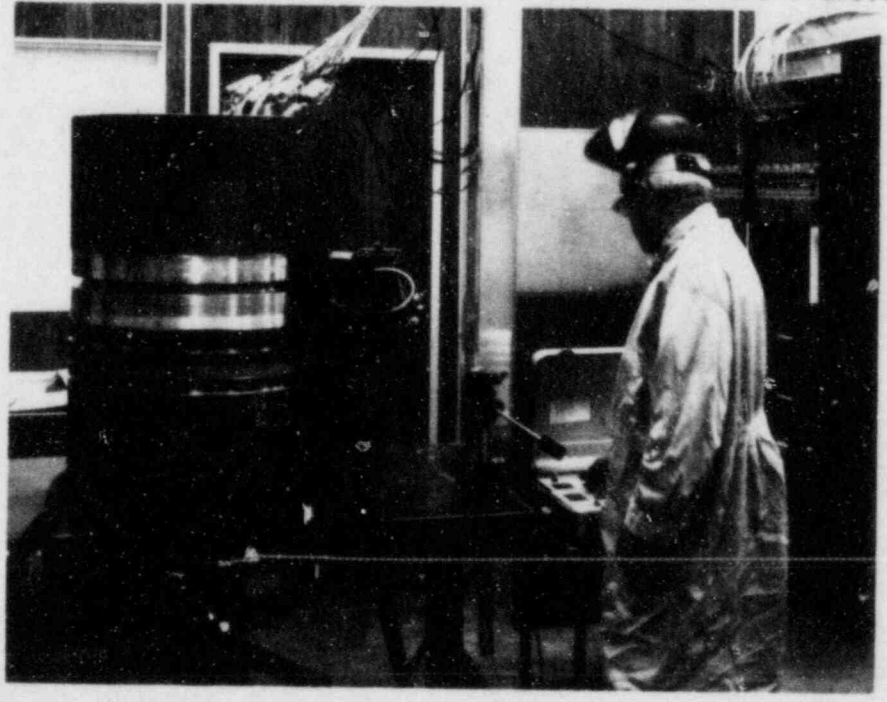

FIGURE 7. Orientation and Setup for Welding of 24-in.-Diameter Pipe

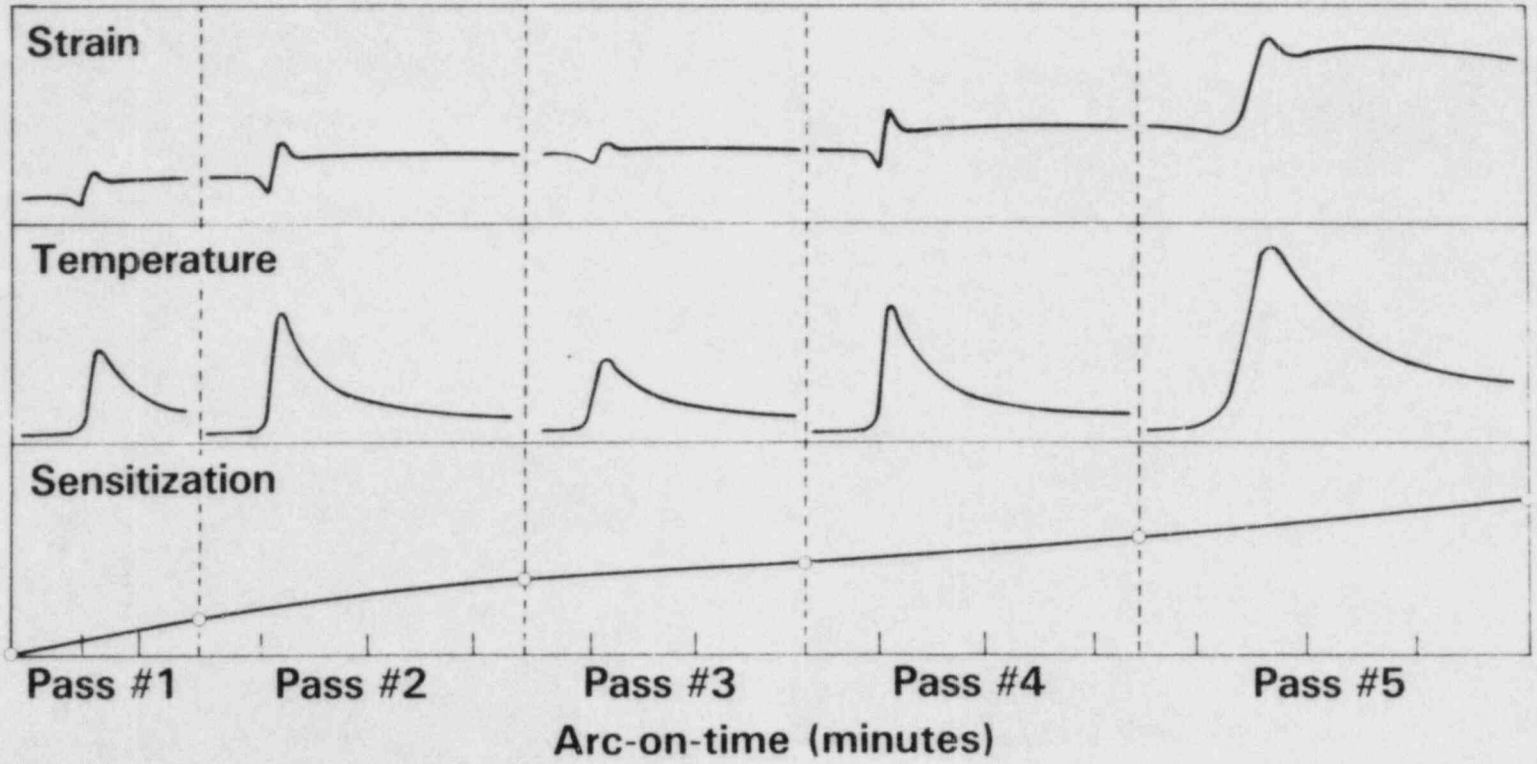

FIGURE 8. Typical Thermomechanical History and Sensitization Development Plots as a Function of Arc-on Time on a Pass-by-Pass Basis

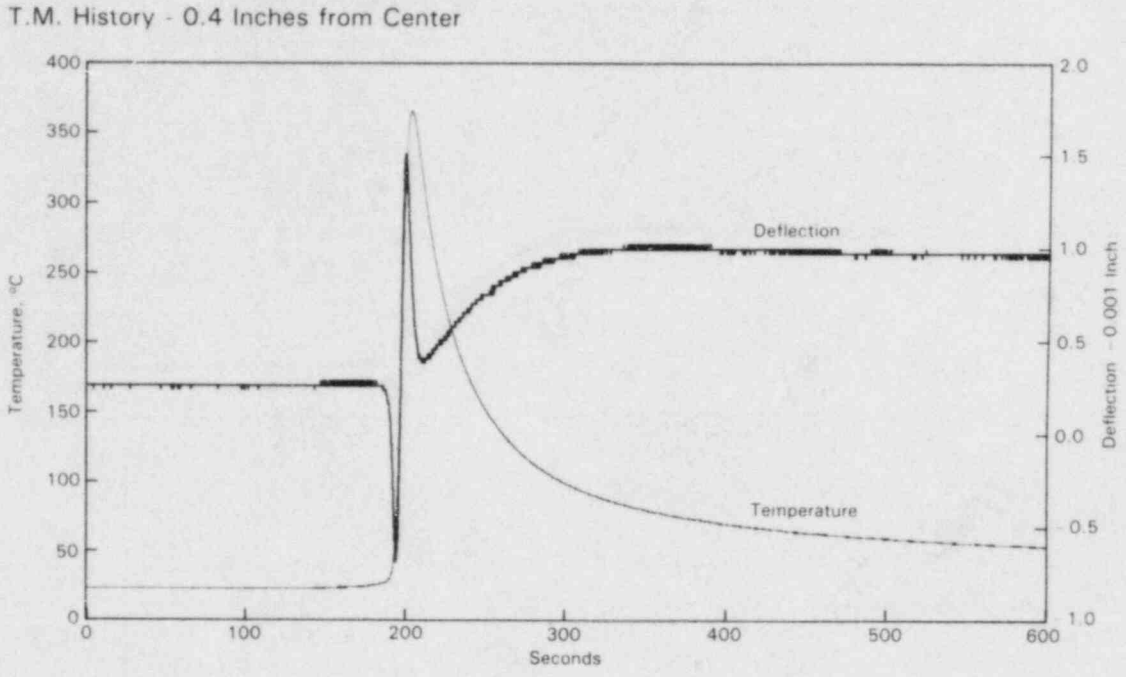

FIGURE 9. Temperature and Surface Deflection Induced 0.4 in. from the Weld Centerline During the Second Pass of the 24-in.-dia. 304 Stainless Steel Pipe Weld

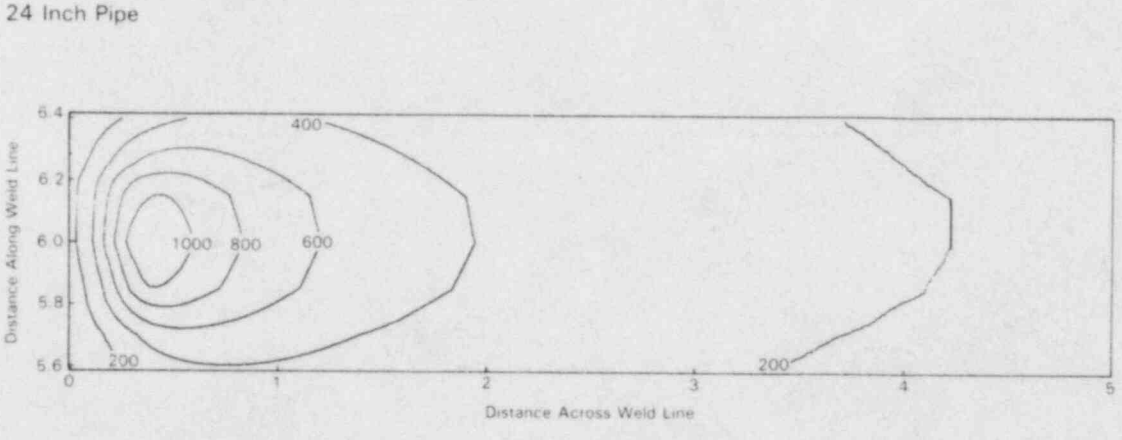

FIGURE 10. Two-Dimensional Plot of Surface Temperatures as a Function of Distance from the Arc

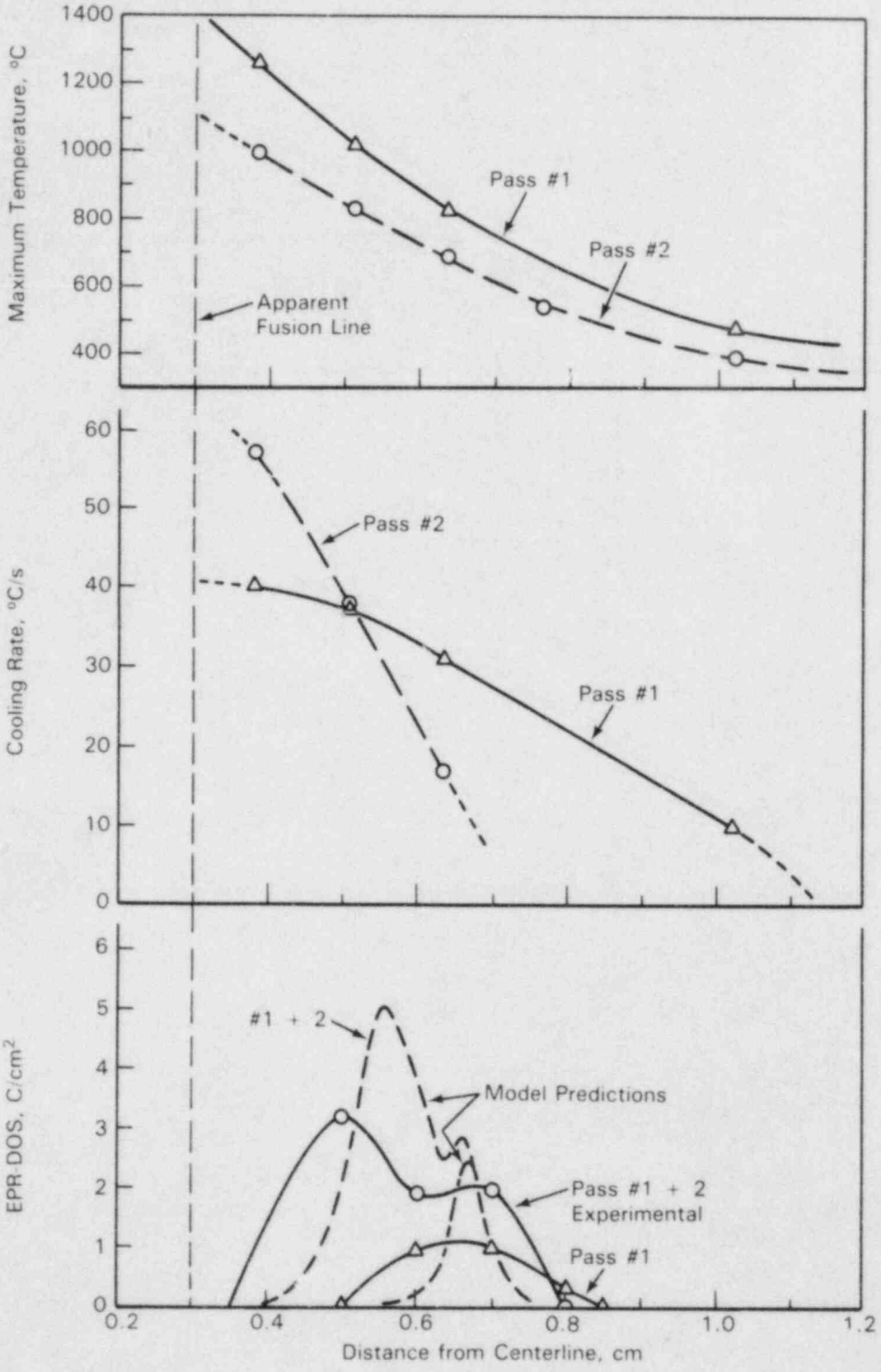

FIGURE 11. Correlation Among Maximum Temperatures (a), Cooling Rates (b), and Measured and Predicted DOS (c) as a Function of Distance from the Weld Centerline for Passes 1 and 2

STEAM GENERATOR TUBE VIBRATION TESTS

Walter I. Enderlin

Pacific Northwest Laboratory

RESEARCH OBJECTIVES

The objectives of this research are 1) to investigate the effects of increased tube/tube-support clearances on rate of tube wear caused by flowinduced vibration in pressurized water reactor steam generators and 2) to provide the U.S. Nuclear Regulatory Commission with criteria to evaluate licensees' specific proposals for chemical cleaning of steam generators.

RELATED SAFETY ISSUE

The overall safety issue related to the objectives of this research is the potential for an increased level of flow-induced vibrations in chemically cleaned steam generators that could lead to high tube wear rates and unacceptable levels of tube failure. The buildup of corrosion products in the steam generators of some pressurized water reactors (PWRs) has led their owners to propose chemical cleaning to remove these corrosion products. The removal of corrosion products includes removal of the magnetite that has formed in the clearances between the Inconel tubes of the steam generator and the carbon steel support plates. In some cases, the volume of magnetite formed by the corrosion of the carbon steel has been sufficient to cause "denting" or reduction of the outer diameter of the tubes where they pass through the support plates. In these cases, the chemical removal of this magnetite would result in enlarged clearances between the dented tube and the support plates.

RELATED RESEARCH BY OTHERS

Research has been performed in both the U.S. and Canada on vibration and wear of PWR steam generator tubes. However, most of the work performed in the U.S. is currently classified as proprietary by its sponsors and is unavailable for general use.

In Canada, P. L. Ko and co-workers have been investigating wear in CANDU steam generators for over 10 years and have published several significant articles on this subject (Ko, Tromp, and Weckwerth, 1982; Ko, 1973; and Ko, 1979). Their activities have included experimental studies to determine the fretting wear mechanisms involved, development of analytical techniques to predict impact forces at the tube supports, and the correlation of tube wear and tube motion parameters. Their studies have included the development of a bench-scale tube fretting apparatus in which they have extensively studied the effects of various tube-support plate parameters on tube wear. Ko et al. found that high wear was not caused by the high-force components such as impact motion that have low probability of occurrence. Instead, the high probability intermediate-range force components (usually combined impact and rubbing motions) were the primary sources of high wear. The amount of wear was observed to increase exponentially with excitation frequency and to increase approximately linearly with diametral clearance and excitation amplitude. However, the data to substantiate the latter were extremely limited. Moreover, this work was not predicated on tube motions and tube support impact forces that were experienced within an actual reactor operating environment. Rather, a computer code (VIBEC) was developed to simulate the motion of a cantilevered beam impacting against supports with clearance, and to predict the midspan displacements and the support impact forces. The difference between the experimental and analytical results using this code was found to be greater for those tubes tested in the presence of water than for those tested in air. This computer code considers only tube motion in air. The fluid damping effect in the tube/support clearance space and the film effect of the water at the contact surface had not been included in the VIBEC simulation at the time of this work (Ko and Rogers, 1979).

TECHNICAL APPROACH

The overall technical approach taken by Pacific Northwest Laboratory (PNL) for this investigation consists of two phases. The first phase is concerned with conducting flow tests designed to conservatively characterize the flow induced vibrations that could occur in a steam generator with clearances representing various conditions following chemical cleaning.

The second phase is devoted to conservatively determining the potential wear rates possible based on the tube vibrations characterized in the flow tests for each of the clearance conditions considered. Figure 1 shows the layout of the tube support plate and tube section being considered in this investigation. For the flow tests to be performed in the first phase, sets of tube support plates will be supplied with 10-, 20- and 50-mil oversized holes to simulate a range of possible clearances. The wear tests in the second phase will be accelerated by increasing the frequency of tube vibration over that experienced in the flow tests. All other test parameters for the wear tests will be matched to those experienced in the flow tests. Both the flow tests and the accelerated wear tests will be performed at elevated temperature and pressure (400°F and 550 psia).

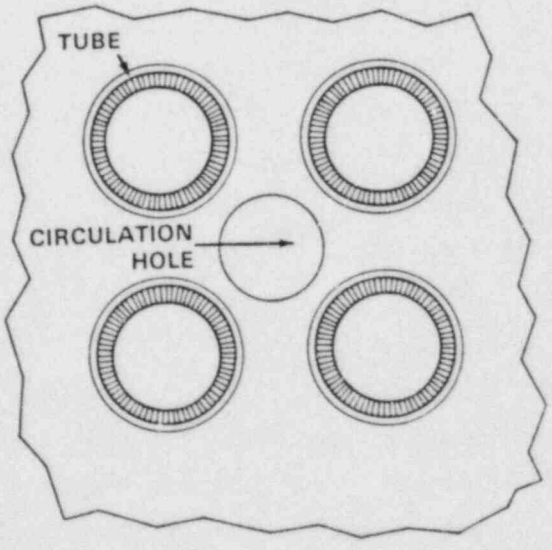

FIGURE 1. Tube Support Section

In the first phase, a full-length scale model of the steam generator (Figure 2) will be built using prototype materials to accommodate the flow tests. This model will be designed such that both the crossflow and axial flow velocities can be regulated independently. The model will be a small section of a prototype tube bundle, necessitating the presence of nontypical flow housing walls. A ring of noninstrumented tubes will be provided around the tubes receiving specific study to "insulate" these tubes from the housing walls. The tube support plate at the tubes receiving specific study will be instrumented so as to determine the pattern of tube motion (displacement), frequency of tube vibration, and the resultant tube contact force. The contact force will be measured using a force ring supported by four miniature piezoelectric force transducers located at 90° intervals. Two inductive type displacement transducers will be mounted orthogonally at the support plate to monitor tube displacement.

Data from the force and displacement measurements will be acquired and stored by a digital data acquisition system. The system will preserve the data on magnetic tape for later processing, and will contain standard interfaces for accessing a variety of large data processors that will be used to analyze the data. A Fast Fourier Transform (FFT) analyzer will be used to generate frequency spectra.

The minimum size bundle that will be tested will be about four tubes by four tubes. Because the flow test will be performed at a temperature and pressure somewhat lower than those of a prototype, the water flow rates in the model will be increased about 16% to obtain equality of Reynolds numbers. The flow loop containing the model of the steam generator is diagramed in Figure 3.

In the second phase, a test apparatus will be fabricated to accommodate the accelerated wear tests at elevated temperature and pressure with water present at the tube/tube support contact surface. As shown in Figure 4, Inconel 600 tube specimen is held at one end by a universal joint mounted at the base of the main frame. The tube is prevented from rotating about its major axis. A tube support plate constructed from prototype material is mounted at the top of the main frame. The tube-support plate contains one round hole in the

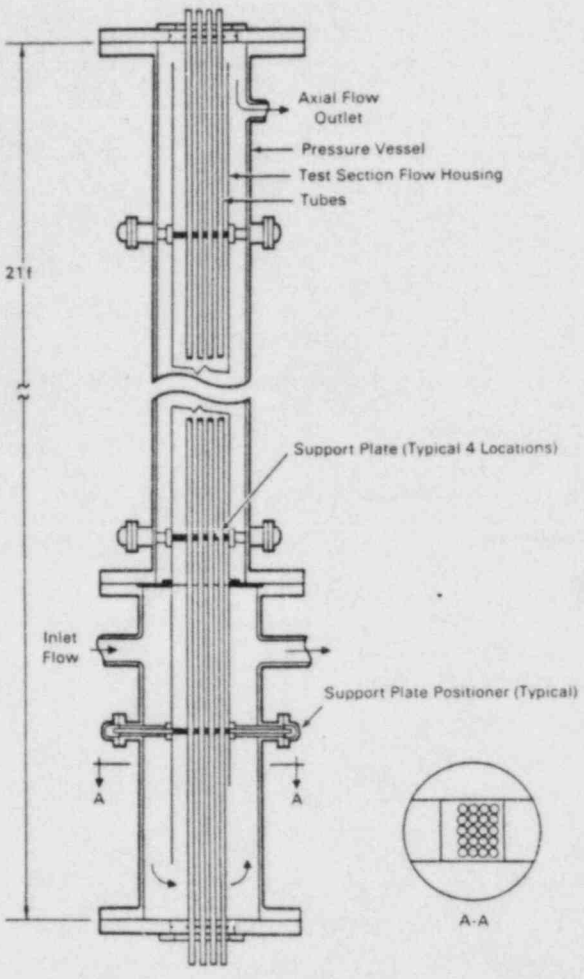

FIGURE 2. Test Assembly for Steam Generator Tests

center which is of sufficient dimension to provide the tube/tube-support plate clearance specified for a particular test. Vibration is imparted to the tube by an air-operated vibrator mounted on the top end of the tube. The vibrator can be adjusted to impart the type of tube motion, frequency, and contact force that was experienced in the flow loop. The test apparatus, including the tube specimen, support plate, and air-operated vibrator, will be contained inside an autoclave.

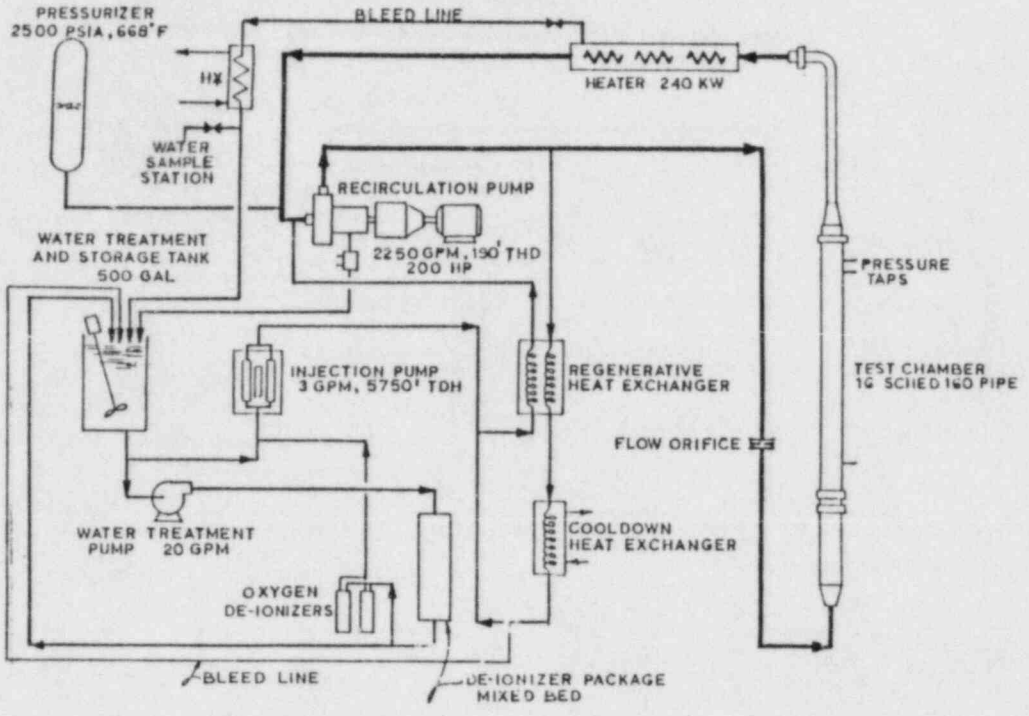

FIGURE 3. Flow Loop Diagram

The instrumentation scheme for the tube-support plate will be the same as for the support plate in the flow loop. Tube wear will be accelerated by conducting the wear tests at a vibration frequency greater than that experienced in the flow loop. The other test parameters will be matched to those experienced in the flow loop. Each test specimen will be subjected to an accelerated wear test equivalent to 1000 hours of reactor operation, based on the frequency of tube vibration experienced in the flow loop. The tube will be removed from the wear test apparatus after each 6.3 million cycles and the diameter of the tube at the contact surface will be measured.

Tube wear will be determined by using an optical noncontact gauging apparatus to measure the tube diameter after a given number of tube cycles. The major components of the optical gauging station are illustrated in Figure 5. The tube sample is illuminated by a filament source that has been approximately collimated using two lenses. Two imaging lenses are used to produce a shadow image of the tube sample that is magnified four times. Because the magnified

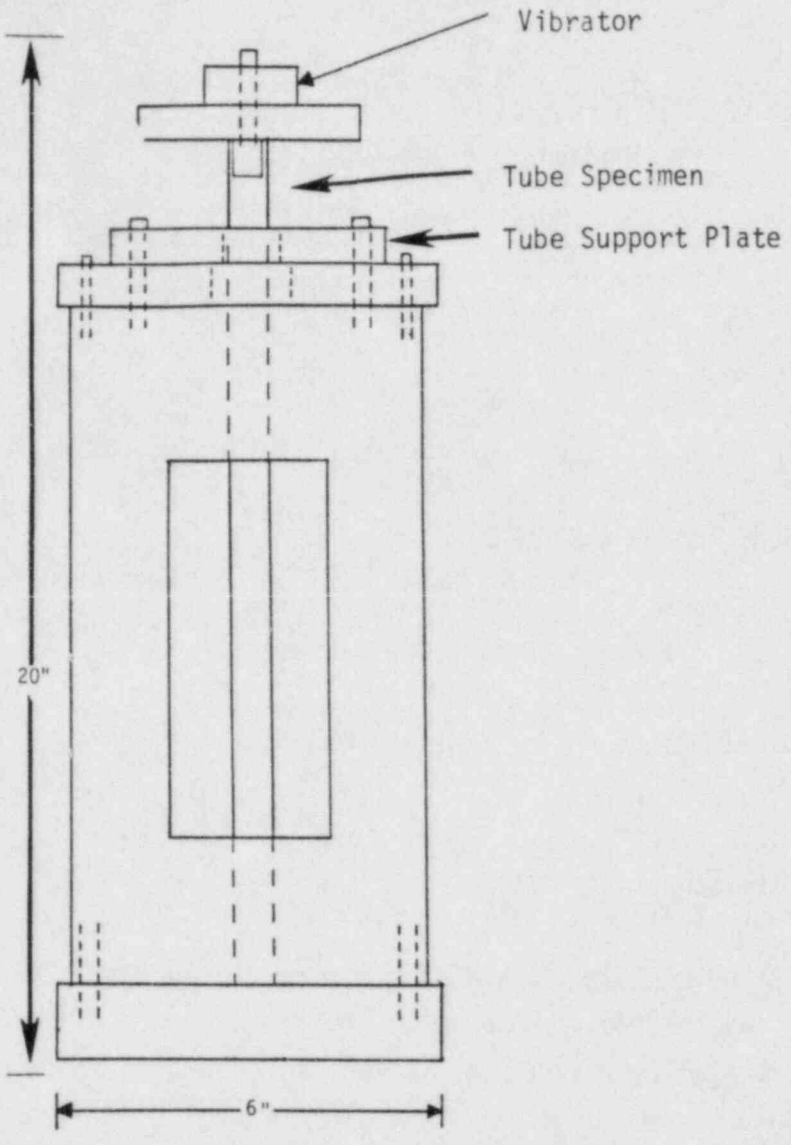

FIGURE 4. Wear Test Fixture

image is greater than the 0.95-inch active area of the linear diode array, two diode arrays are used to detect the two edges of the tube shadow image. Because of the physical size of the printed circuit boards on which the diode array is mounted, a beamsplitter is used to produce two separate tube image planes. One of the image optical paths contains a neutral density filter to balance the image intensities so that both linear diode arrays operate at 80% to 90% of saturation. The system is set up so that the shadow edge (light to

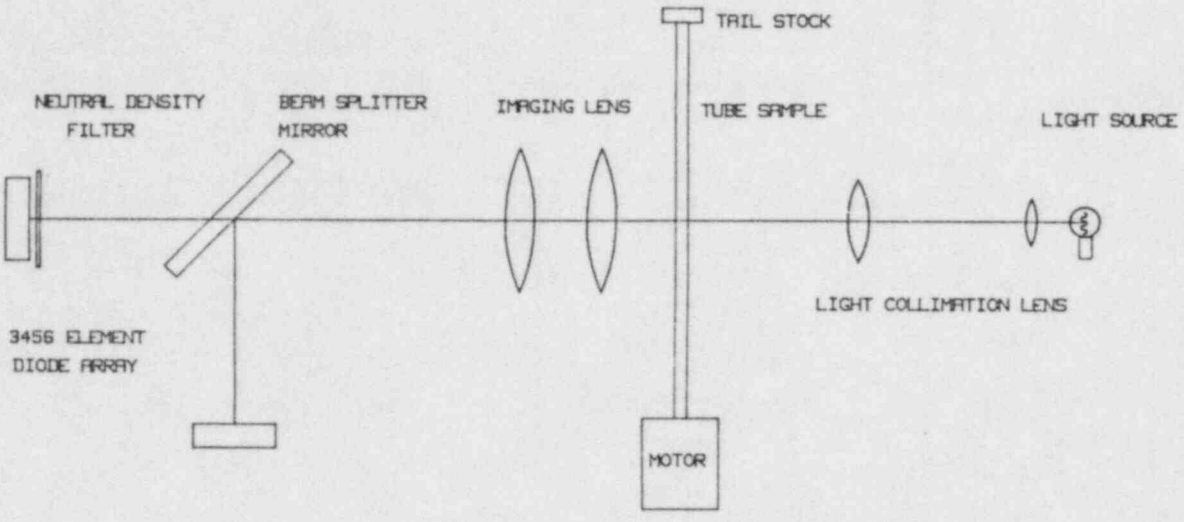

FIGURE 5. Optical Noncontact Gauging Apparatus

dark transition) is at the midpoint of each array. The tube diameter is calculated by subtracting the sum of the illuminated diodes on both diode arrays from the total number of diodes possible. With a magnification of 4x, the system is accurate to 0.000069 inch.

The data will be analyzed to estimate the projected wear over the remaining lifetime of the reference steam generator design. Furthermore, recommendations will be developed regarding the advisability of chemical cleaning under these potential wear conditions.

PROJECT STATUS

The test plan and facility design are completed. The project is currently in the procurement and fabrication phase. Testing is scheduled to commence in January 1985. The project is currently scheduled for completion by the end of September 1985.

ACKNOWLEDGMENT

This work is sponsored by the U.S. Nuclear Regulatory Commission (NRC). The NRC project manager is Dr. Joseph Muscara.

REFERENCES

Ko, P. L., J. H. Tromp, and M. K. Weckwerth. 1982. "Heat Exchanger Tube Fretting Wear: Correlation of Tube Motion and Wear." ASTM STP780, American Society for Testing and Materials, 1916 Race St., Philadelphia, PA 19103.

Ko, P. L. 1973. "Impact Fretting of Heat Exchanger Tubes." ACEL-4653, Chalk River, Ontario, CN.

Ko, P. L. 1979. "Experimental Studies of Tube Fretting in Steam Generators and Heat Exchangers." ASME Journal of Pressure Vessel Technology. Vol. 101, May 1979 pp. 125-133.

Ko. P. L., and R. J. Rogers. 1979. "Analytical and Experimental Studies of Tube/Support Interaction in Multi-Span Heat Exchanger Tubes." Nuclear Engineering and Design, Vol. 65, No. 3, July 1981, pp. 399-409.

SURRY STEAM GENERATOR PROGRAM AND BASELINE EDDY CURRENT EXAMINATION

Robert A. Clark and Pamela G. Doctor

Pacific Northwest Laboratory
Richland, Washington

INTRODUCTION

The Steam Generator Group Project was initiated in January 1982 with formation of a consortium including NRC, EPRI, Japanese, French, and Italian participants. The project utilizes a retired-from-service nuclear steam generator established in a specially designed facility which houses the unit in its normal vertical operating position. The project has multiple objectives during its expected five year duration. The most important objectives deal with validation of nondestructive examination (NDE) techniques used to characterize steam generators during service. This research generator offers the first opportunity to characterize a statistically significant number of service-induced defects nondestructively followed by destructive metallographic confirmation. The project will seek to establish the reliability of defect detection and the accuracy of sizing defects via current state-of-the-art NDE. Other service degraded tubes will be burst tested to establish remaining service integrity. The integrity information and NDE reliability results will serve as inputs to establish a model for steam generator in-service inspections, and provide a data base for evaluation of tube plugging criteria. In addition to NDE validation goals, the project will use the service degraded generator as a specimen for demonstration/proof testing of repair and maintenance techniques, including chemical cleaning/decontamination technologies.

Preparation of the steam generator for research included previously reported tasks to chemically decontaminate the channel head and remove the explosively placed plugs in service defected tubes. This year the program completed post-service eddy current inspections of all accessible tubes. Two widely used technologies were employed in the post-service baseline examinations, Zetec MIZ 12 multifrequency eddy current and Intercontrole IC3FA multifrequency eddy current. The use of these two technologies represents how the majority of in-service inspections are conducted world wide. We were not attempting a comparison of the technologies, rather seeking a consensus on the total defect status in the research generator. The two baseline eddy current examinations did not provide total agreement as to the steam generator's overall condition, largely a result of analytical interpretation divergence on eddy current indications. These differences and our attempts at resolving their sources will be discussed.

The baseline eddy current results were subsequently used, along with other information available about the steam generator from secondary side inspections, from historical operating data, from visual inspections and from operations like the tube unplugging (which established that certain tubes contained primary or secondary side water), to establish a subset of tubes for

more detailed examination. These tubes were first subject to extensive eddy current round robin testing. They are currently being characterized by advanced NDE techniques, utilizing eddy currents and alternate methods. Following this the tubes will be removed in whole or in part for destructive confirmatory testing. This will include destructive metallographic sectioning as well as burst testing of selected tubes to establish remaining integrity. Details on the post-service eddy current baseline examination results, the choice of a round robin subset of tubes, and preliminary results for the data acquisition eddy current round robin will be presented in this paper.

In addition to the efforts associated with NDE examinations, a multitude of other project tasks have been continuing during FY84. Examination and characterization of the steam generator from the secondary side has continued. A large number of additional shell penetrations have enabled access throughout the secondary side for photographic documentation. Sludge samples have been analyzed. Initial tooling has been developed for removing tubing and support plate samples. Several inner row U-bend sections have been removed from the generator to begin characterization of the strains in the sections and the resulting defects in the tubing. A subcontractor has been acquired who, along with Battelle Pacific Northwest Laboratory (PNL) staff, is developing a technique to remove sections from the 21" thick tube sheet. The health physics task has completed a systematic radiological scan through the tubes, to establish how the generator's radioactive inventory is distributed and determine if this scanning technique can aid in nondestructive characterization of the unit. The results of these efforts will be presented in the following pages.

ACCOMPLISHMENTS IN FY84

Health Physics

An experiment was conducted to determine the benefits and/or necessity of multiple dosimetry of channel head workers. This was conducted by monitoring several staff during phases of the tube unplugging operation conducted on the Surry generator. The exposures to the multiple TLD's worn by the PNL personnel working in the channel head during the unplugging operations are given in Table 1. The ratios of the exposures to the TLD's on the various locations on the body to the exposure to the TLD on the front torso were calculated (see Table 2). As expected, the head receives the highest exposure. The ratios of the exposures at the different body locations to the exposure to the front torso seem to fall within a well defined range. These results are similar to ratios published by INPO (1982) for steam generator workers at the San Onofre plant (see Table 3).

The general conclusions which can be drawn from this and other data is that the exposure to the lens of the eye is almost always the limiting exposure. Calculations show that the extremities can never be limiting in channel head work if the radionuclide inventory is uniformly distributed and adequate protection against beta radiation is provided. Under these conditions, the maximum calculated difference between an extremity exposure and a whole body exposure is approximately five to one. Since extremities can receive 75 rem a

year while the whole body can receive only 5 rem a year, the extremities obviously will not be limiting. For most channel head work, a badge on the front torso and a badge at eye level should satisfy the Code of Federal Regulation's (10 CFR 20) criteria of "adequate" dosimetry. The highest reading from the two badges is the dose to the worker.

TABLE 1. Individual Exposure Rates for Torso and Extremities During Unplugging Operations (mR/hr)

Worker	Head	Front Torso	Back Torso	Right Wrist	Left Wrist	Right Ankle
1-A	27	24	20	28	26	30
1-B	48	33	29	41	43	--
1-C	56	35	40	42	49	31
1-D	29	21	20	25	25	22
2-A	94	51	50	62	66	51
2-B	116	66	60	72	86	60
2-C	46	31	28	31	44	28
2-D	117	63	54	66	89	42

TABLE 2. Ratios of Exposure for Various Regions of the Body During Surry Steam Generator Project

Worker	Head	Front Torso	Back Torso	Right Wrist	Left Wrist	Right Ankle	Left Ankle
After First Cycle of Decontamination							
W-1	1.93	1.00	1.28	1.61	1.21	---	---
W-2	1.68	1.00	1.10	1.22	1.23	0.72	0.73
W-3	1.51	1.00	1.27	1.30	1.03	0.81	0.76
Mean	1.71	---	1.22	1.38	1.16	0.77	0.74
Standard Deviation	0.21	---	0.10	0.21	0.11	---	---
After Completion of Decontamination							
1-A	1.13	1.00	0.83	1.17	1.08	1.25	---
1-B	1.45	1.00	0.88	1.24	1.30	---	---
1-C	1.60	1.00	1.14	1.20	1.40	0.89	---
1-D	1.38	1.00	0.95	1.19	1.19	1.05	---
2-A	1.84	1.00	0.98	1.22	1.29	1.00	---
2-B	1.76	1.00	0.91	1.09	1.30	0.90	---
2-C	1.48	1.00	0.90	1.00	1.42	0.90	---
2-D	1.86	1.00	0.86	1.05	1.41	0.67	---
Mean	1.56	---	0.93	1.15	1.30	0.95	---
Standard Deviation	0.25	---	0.10	0.14	0.12	0.18	---

TABLE 3. San Onofre Exposure Ratios for Various Regions of the Body (from film badge results) (from INPO 1982, p.4)

	Average	Range
Steam Generator Workers		
Top of Head-to-Chest	1.65	1.32 - 21.5
Average Head-to-Chest	1.36	1.09 - 1.65
Eyes-to-Chest	1.35	1.06 - 1.68
Hands-to-Chest	1.28	0.26 - 1.78
Upper Back-to-Chest	1.02	0.70 - 1.56
Lower Back-to-Chest	0.83	0.49 - 1.24
Gonads-to-Chest	0.83	0.23 - 1.07
Ankles-to-Chest	0.80	0.43 - 1.03
Platform Workers		
Top of Head-to-Chest	0.99	0.69 - 1.56
Gonads-to-Chest	0.93	0.48 - 1.50

The other experimental activity conducted under this task in FY84 was a through tube radiological mapping. This was conducted using a single crystal CdTe detector mounted into a probe with a signal preamplifier. The 9/16" O.D. probe was capable of being inserted through the steam generator tubes using a standard eddy current pusher-puller. Figure 1 shows the typical result. The technique was readily capable of determining radioactivity distribution throughout the generator. General observations were:

1) The highest field occurs in the center of each hemisphere.

2) Count rates around the outer radius are about 50 percent of the center.

3) The field intensity drops approximately 15 percent adjacent to the divider plate between the hot leg and cold leg side.

4) The relative intensity rises along the flow path as it goes up the hot leg side and makes the U turn and comes back down until it reaches a maximum at the region between support plates 4 and 5 and then slowly decreases down the remainder of the cold leg side.

5) The relative intensities are consistently higher in the manway quadrant.

However, it was determined that defects in individual tubes cannot be located with the CdTe detector due to the overwhelming contribution from surrounding tubes and statistical variations. Pusher-puller speeds down to ~0.3cm a second were used in attempts to utilize radiation field measurements to determine steam generator support structure and/or tube damage.

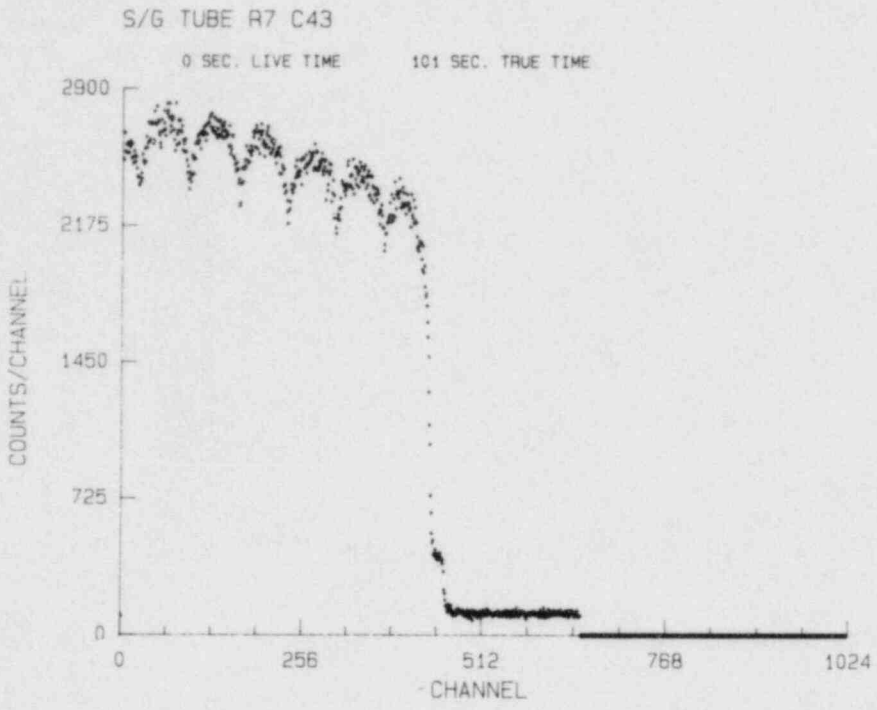

FIGURE 1. Through Tube Radiological γ Scan

Secondary Side Characterization

Secondary side examinations were extended to reach throughout the steam generator during the past year. In order to access all areas, a number of additional shell penetrations were made. The most economic method in terms of time, radiation exposure and costs utilized a Rotabroach to drill through the shell. Utilizing a magnetic based drill, a 2-½" diameter hole could typically be placed in less than two hours. Larger openings were made utilizing a series of overlapping drilled holes. Figure 2 shows an example. Penetration locations were in part determined by the eddy current baseline results, where it was determined that secondary side examinations might assist in resolving discrepancies or in providing additional information. Figure 3 shows a loose part found at the tube sheet, apparently a piece of wire. Figure 4 provides an example of a piece of support plate, again at the top of the tube sheet. Figure 5 shows what we believe to be wastage damage, located just at the top of the current sludge pile. Sludge samples have been taken for analysis, results are summarized in Table 4. These results are from the upper layer of sludge. The generator appears to have two distinct sludge layers, a lower cementitious layer, and an upper granular layer. We have not yet succeeded in removing samples of the lower layer.

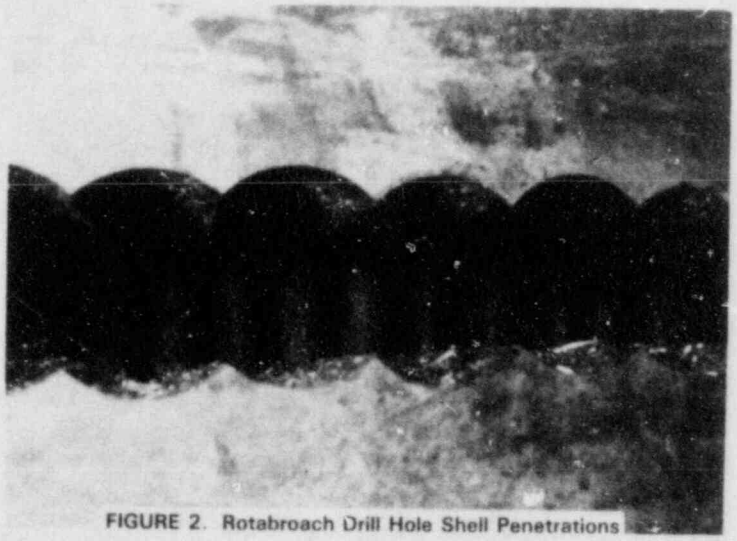

FIGURE 2. Rotabroach Drill Hole Shell Penetrations

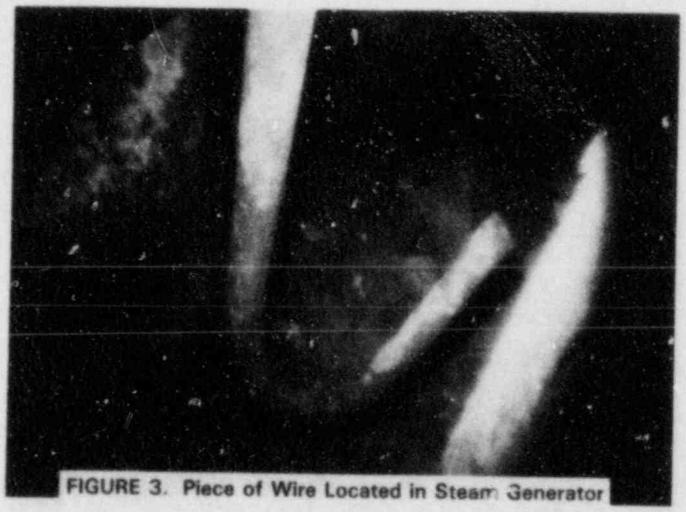

FIGURE 3. Piece of Wire Located in Steam Generator

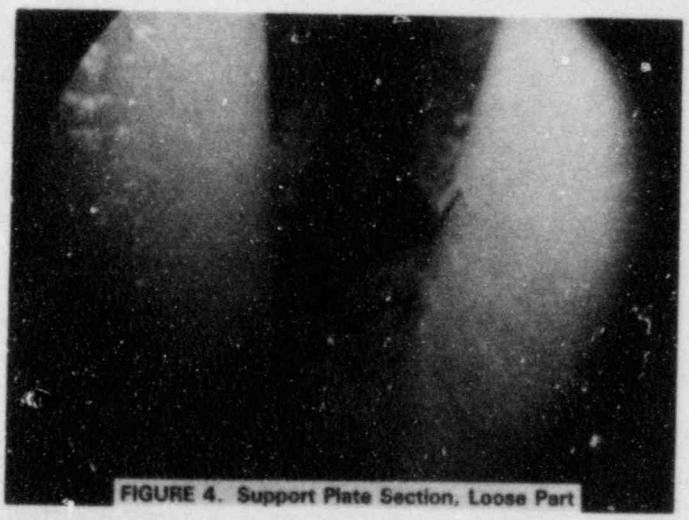

FIGURE 4. Support Plate Section, Loose Part

XRF Semiquantitative Elemental Sludge Composition
(wt.%)

Element	Surry 2A Cold Leg	Surry 2A Hot Leg	Indian Point
Fe	37 - 50	44	49 - 52
Cu	20 - 28	20	10.5 - 13
Ni	1.1 - 1.4	1.3	0.6 - 0.74
Zn	2 - 2.5	2.5	1.6 - 1.7
Cr	0.15 - 0.16	0.18	0.08 - 0.22
Ca + Mg	0.1 - 0.2	0.14	0.08
Cl	0.1 - 0.4	0.28	<0.01
P	0.7 - 0.8	0.43	0.02 - 0.06
Al	1.2 - 1.4	2.1	0.5 - 1.5
S	0.1 - 0.15	0.2	0.02 - 0.06
Ti	0.06 - 0.07	0.05	0.07 - 0.19
Si	1 - 2	1	1.5 - 1.9
Mn	0.23 - 0.27	0.26	0.34
C	0.28	0.21	1.5 - 2.5
Sn	<1	<1	0.01 - 0.03
Ag	<0.1	<0.1	-
B			

Conductivity of Surry Sludge: Dry - 2 Megohm
Wet with D.I. Water 80,000 ohm

TABLE 4.

Generator Specimen Removals

Tooling has been designed and fabricated to allow semi-remote sectioning of the generator. Initial efforts utilize a cut-off wheel that is powered by a remote motor through a flexible shaft. The cutting head is manipulated from an arm that allows the operator to stand away from the generator shell opening (Figure 6). Initial cuts removed a number of U-bends from the inner two rows, with cuts made just above the uppermost tube support plate (TSP). The amount of elastic deformation in the U-bends was determined by measuring the spread of the U-bend legs before and after severing. The amount of remaining plastic deformation was often considerable, as pictured in Figure 7. Here the U-bend on the left was taken from a flow slot region, while the one on the right was from a hard spot. Figure 8 shows cracking damage that has been observed in the U-bends. A current effort is working on establishing a technique for removing a section out of the 21" thick tube sheet. Two methods are under study. One uses the metal disintegration machining technique (MDM) and the other is exploring drilling out the ligaments between adjacent tube holes. Figure 9 illustrates the locations of the first two intended tube sheet sections. The section toward the center of the bundle is to explore conditions where typically the worst corrosion damage in the tube sheet occurs, and where an indication of intergranular attack (IGA) in the tube sheet crevice has been identified during one of our eddy current examinations. The second section, near the tube lane, is intended to remove a leaking plug intact to examine degradation of the plug.

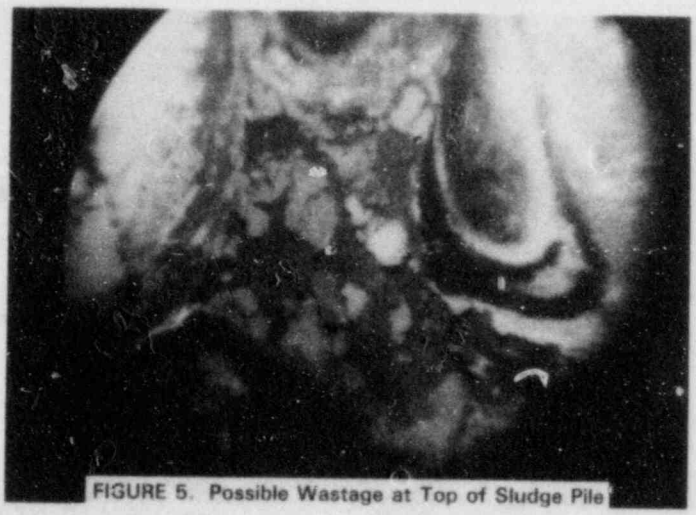

FIGURE 5. Possible Wastage at Top of Sludge Pile

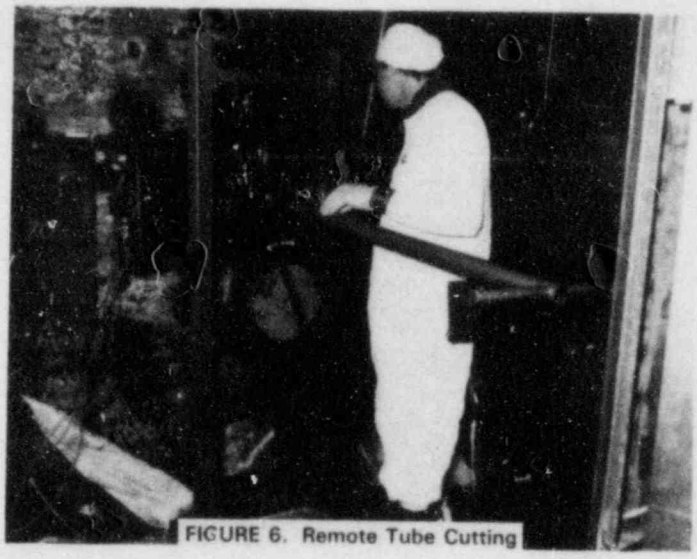

FIGURE 6. Remote Tube Cutting

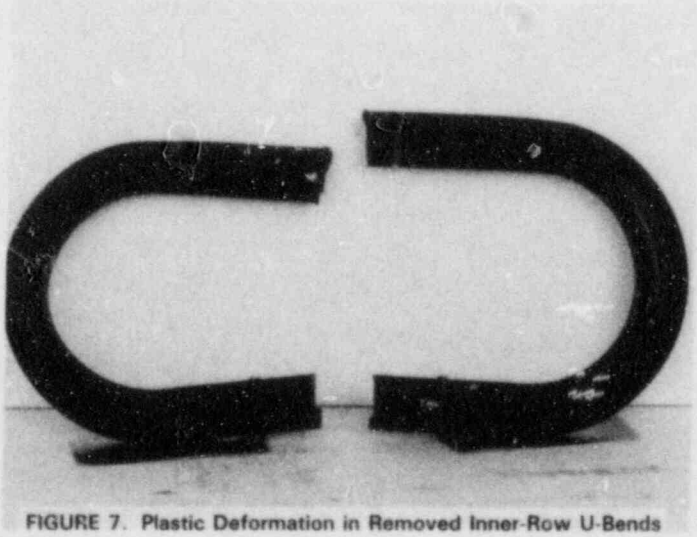

FIGURE 7. Plastic Deformation in Removed Inner-Row U-Bends

FIGURE 8. Crack in Inner-Row U-Bend

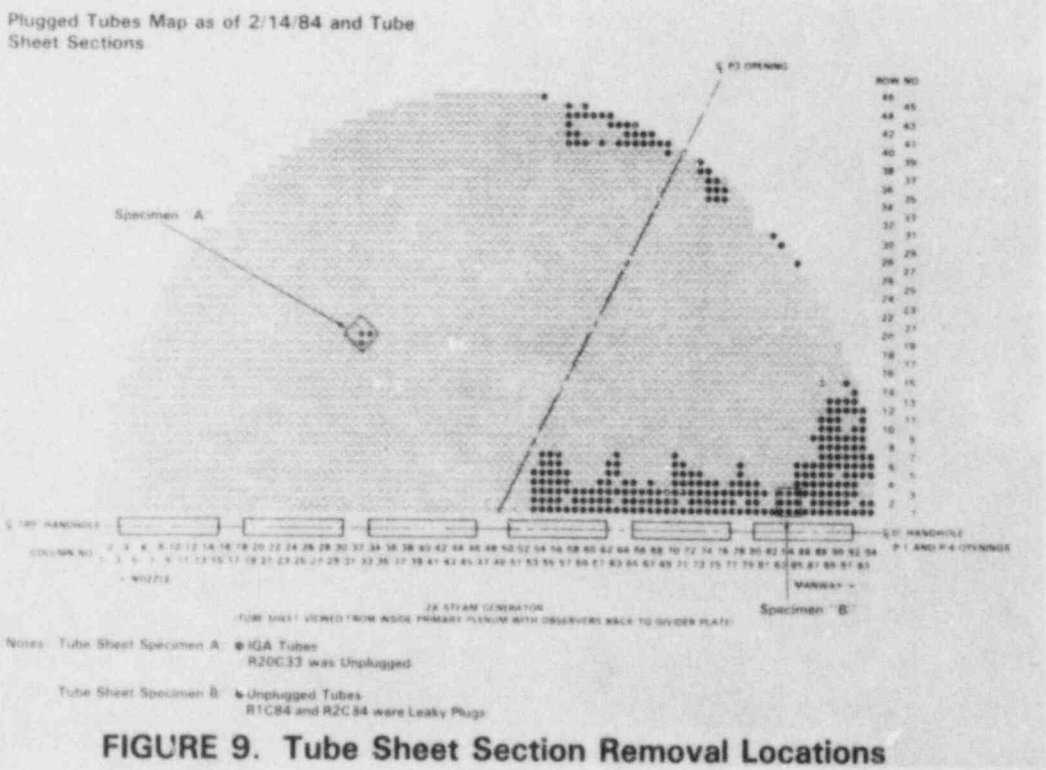

FIGURE 9. Tube Sheet Section Removal Locations

BASELINE EDDY CURRENT INSPECTIONS

The purpose of the post-service baseline eddy current examinations of the generator was to determine as well as possible the condition of the generator. The information on extent and location of defects was subsequently used for selection of a subset of tubes for more detailed examination and round robin inspections. Two separate baseline inspections of the generator were conducted using two commercially-available multi-frequency eddy current inspection systems, the Zetec MIZ-12 and the Intercontrole IC3FA. The two companies use similar technologies; however, their equipment designs and data analysis procedures differ. Zetec and Intercontrole equipment are used for the majority of in-service inspections of steam generators world wide. The reason for using the two inspection systems on the Surry steam generator was not to compare them, but to provide a consensus on the condition of the generator.

Field-experienced teams from Zetec and Intercontrole performed the inspections. The teams were asked to perform the inspections in accordance with ASME code requirements, although it was known to the analysts that we wanted to characterize the condition of the generator as accurately as possible. The test procedures for the inspection of this generator differed between the two teams. Zetec used two frequencies in a total of four modes. They were:

- 400 KHz differential mode, normal gain
- 400 KHz differential mode, reduced gain
- 100 KHz differential mode
- 100 KHz absolute mode

The frequencies and modes used by Intercontrole were:

- 500 KHz differential mode
- 240 KHz differential mode
- 100 KHz differential mode
- 100 KHz absolute mode

The sizes of probes used by the two teams also varied; Zetec used .720", .700", .650", and .610" probes, while Intercontrole used .710", .690", and .670" probes.

Zetec usually records the inspection data on analog tape; however, since an archived database of the baseline inspection of the unit was desirable for further analyses after destructive assay and computerized data processing is necessary, the Zetec inspection data was also digitized during acquisition. A detailed description of the computer data acquisition system that was developed by the project to collect the data is given in Doctor et. al. (1983). The Intercontrole inspection data is customarily recorded digitally; it was also recorded on analog tape for back-up purposes.

Each team provided the results of their analysis of the inspection data in their normal reporting format. Zetec uses a Hewlett-Packard 9836 to perform the data analysis and the results for the inspection of each tube were stored on that computer's storage medium. Intercontrole typed their final report on a personal computer, so the inspection results were available also on computer medium. The inspection data of each team was transferred from the storage media directly to the data analysis computer, which is a Digital Equipment Corporation VAX 11/780, thereby avoiding any transcription errors.

Since it is not our intent to compare the two inspection systems, the teams will be referred to hereafter as Teams A and B.

Of the 3388 tubes in the generator, 3130 tubes were theoretically accessible for inspection after the unplugging. The databases generated by the two baseline inspections were rather large. Team A conducted over 9000 inspections of 3125 tubes, while Team B inspected 2783 tubes with 3392 separate physical inspections. There was quite a bit of preprocessing that had to be done on each of the data files before they could be statistically analyzed, particularly for the Team A database.

The ASME code requires that all indications of wall-loss greater than 20% be reported; however, the inspection teams were asked to report all wall-loss indications regardless of size. In addition to the required reporting items, each team reported conditions existing in the unit but not required by the inspection code. Examples of these conditions are denting of tubes, both at the support plates and between support plates, bulges in the tubes, permeability variations, conductive deposits and loose parts.

The types of wall-loss indications that were reported were O.D., most of which are assumed to be wastage because of their location, and I.D., which are assumed to be cracks. There are two aspects to the analysis of eddy current inspections, the detection of a possible defect and its sizing.

There were a total of 779 indications reported by Team A and 1059 by Team B. Table 5 gives the reference locations of the indications for both teams.

TABLE 5. Locations of Wall-Loss Indications from the Baseline Inspections

Reference Location	Numbers of Indications	
	Team A	Team B
Hot Leg		
Tube End	1	
Tube Sheet Gap		1
Unspecified Tube Sheet		2
Top of Tube Sheet	713	731
Support Plate 1	3	5
Support Plate 2		3
Support Plate 3	2	3
Support Plate 4		1
Support Plate 5	1	9
Support Plate 6		20
Support Plate 7	11	115
U-bend		22
Cold Leg		
Unspecified Tube Sheet		4
Top of Tube Sheet	22	113
Support Plate 1	1	6
Support Plate 2		2
Support Plate 3	2	1
Support Plate 4	2	3
Support Plate 5		1
Support Plate 6	1	20
Support Plate 7	20	10

The reference locations are positions in the tube sheet (tube end, tube roll transition, gap or crevice region and the top of tube sheet), the seven support plates and the U-bend region. Both teams found most of their indications at the top of the tube sheet on the hot leg where tube wastage was expected. Team B called more indications for all locations, except the cold leg seventh support plate, than did Team A. The distribution of the sizes of indications differed between the two teams. Histograms of the sizes of indications called by Teams A and B are given in Figures 10 and 11, respectively. The 12 indications labelled as indeterminate in Figure 10 are ones for which there was a lack of agreement (greater than 10%) of the size from separate inspections by the same team of the same tube. The 100% through-wall indications reported by Team A were caused by drill marks during unplugging and were not reported by Team B. The two histograms appear different, most noticeably because of the 451 indications called by Team B that were less than 10% of wall thickness. However, if the <10% indications are ignored, there are still differences in the histograms. The mode (largest number of indications) for Team A is in the range of 20-30% wall loss, whereas it is in the range of 40-50% for Team B.

PERCENTAGE SIZE	NUMBER OF OBSERVATIONS	
INDETERMINANT	12	***
0% <= x < 10%	54	**********
10% <= x < 20%	130	**************************
20% <= x < 30%	196	**
30% <= x < 40%	151	*******************************
40% <= x < 50%	127	**************************
50% <= x < 60%	45	*********
60% <= x < 70%	32	*******
70% <= x < 80%	14	***
80% <= x < 90%	3	*
90% <= x < 100%	9	**
x = 100%	6	**

EACH * DENOTES 5 OBSERVATIONS

FIGURE 10. Histogram Showing Percentage Size of Defects Found by Team A

PERCENTAGE SIZE	NUMBER OF OBSERVATIONS	
0% <= x < 10%	451	**********
10% <= x < 20%	70	*******
20% <= x < 30%	86	*********
30% <= x < 40%	113	**********
40% <= x < 50%	145	**********
50% <= x < 60%	99	**********
60% <= x < 70%	52	******
70% <= x < 80%	30	***
80% <= x < 90%	12	**
90% <= x < 100%	1	*

EACH * REPRESENTS 10 OBSERVATIONS

FIGURE 11. Histogram Showing Percentage Size of Defects Found by Team B

Matching the indications between the two teams to determine if they were reporting the same physical anomaly required an extensive data analysis effort. Due to differences in the analysis processes of the two teams, one team could locate indications more precisely than the other, so for indications not at the top of the tube sheet, the range of reported locations that were considered to be caused by the same anomaly was 5 inches. At the top of the tube sheet, the 5-inch range was disregarded because of the apparent length of wastage defects and the the fact that the teams reported the locations of these indications differently. Team A reported the location of the largest signal, while Team B referenced their location only as the top of tube sheet. The only reference locations where the two teams detected common indications were the top of the tube sheet on the hot and cold legs, the first support plate on the cold leg, and the seventh support plate on the hot leg. Detection tables for each of these four reference locations are given in Figures 12-15, respectively. The upper left hand cell contains the number of indications called by both Team A and Team B. The upper right hand cell shows the number of indications Team A called that Team B did not. The lower left hand cell contains the number of indications that Team A did not call that Team B did call. The lower right hand cell should contain the number of non-indications called by both teams. To estimate this cell, each inspected tube would have to be divided into segments of some length and the number of segments without indications by both teams tabulated. This count would be very large and would produce misleading conclusions for any statistical techniques applied to these tables. Beneath the table is a count of the number of indications to which each team did not give a specific location. Any indications that fall into this category were not included in the above cell counts. The construction of these tables for the top of the tube sheet posed a problem. There were 87 tubes where one team called more than one indication along the tube and the other team called one or more indications at the top of the tube

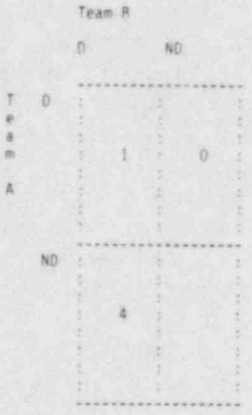

Number of Team B detections without specific locations: 1

Number of Team A detections without specific locations: 0

FIGURE 12. Comparison of Detections for Team A and Team B at Cold Leg Support Plate One

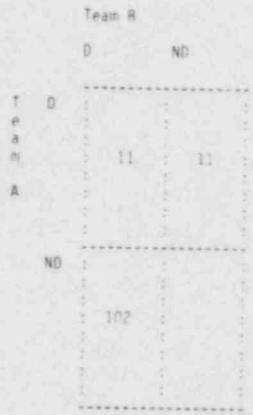

Number of Team B detections without specific locations: 0

Number of Team A detections without specific locations: 0

FIGURE 13. Comparison of Detections for Team A and Team B at Cold Leg Top of Tube Sheet/Tube Sheet Edge

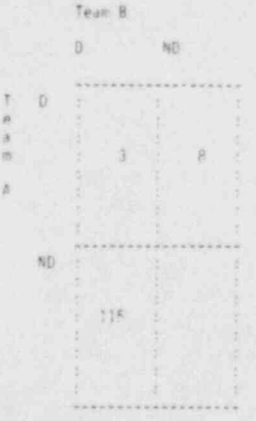

Number of Team B detections without specific locations: 0

Number of Team A detections without specific locations: 0

FIGURE 14. Comparison of Detections for Team A and Team B at Hot Leg Support Plate Seven

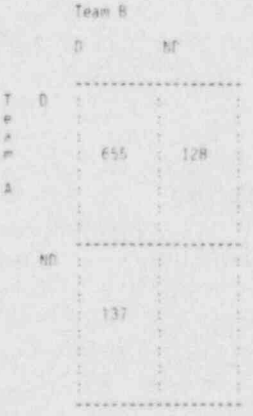

Number of Team B detections without specific locations: 0

Number of Team A detections without specific locations: 0

FIGURE 15. Comparison of Detections for Team A and Team B at Hot Leg Top of Tube Sheet/Tube Sheet Edge

sheet. With no way to identify specific locations, it was impossible to create a one-to-one matching between these indications. The numbers in the upper left hand cell of the detection table contain all possible combinations of these indications and, therefore, are inflated. Figure 12 shows that for the hot leg top of the tube sheet, 655 or 71% of the total number of 920 indications found by the two teams are common detections. Although Team B tended to call more indications, the percentage of each team's calls that are common calls are similar -- 84% for Team A and 83% for Team B. The pattern is different for the cold leg top of the tube sheet (Figure 13). Only 9% of the 124 total reported indications were common calls. Because Team B called over 5 times as many indications, the percentage of each team's calls that were common calls differed: 50% of Team A's calls compared to 11% for Team B.

Figure 16 shows the differences in estimated sizes between the matched indications anywhere in the generator. The horizontal axis of the histogram represents the difference in size (Team B - Team A), with the number representing the middle of the interval. For example, the cell corresponding to 0.0 represents differences in the interval -2.0 to 2.0. Differences less than 0.0 correspond to indications that Team A found to be larger than Team B, and for differences >0.0, the situation is reversed. The shift in the histogram away from a mean of zero shows that Team B consistently sized indications larger than did Team A. The mean of the differences is 5.27%, with a standard deviation of 15.47.

In preparing this histogram, in cases where one team called more than one indication, and the other team called only one indication, a mismatch was calculated for each possible pair of indications. However, when both teams called more than one indication at the same location, the sizes were matched by hand to minimize the size difference. Because this was done, the number of points on the histogram will not match the sum of the elements in the detection figures. In the cases where a team sized an indication as <10%, the size of the indication was called 10%.

After the analyses were completed, there were a sizeable number of discrepancies in the number and locations of indications, and in the sizes of indications that both teams did detect. In order to resolve these discrepancies, each team was asked to re-examine its results in light of the other team's findings. Because of time constraints, the teams were not able to re-examine all of the discrepancies, so they were asked to review only the tubes where there was a difference in detection of indications that were 20% or larger. There were a total of 160 inspections that were to be reanalyzed. Thirty-seven of these were actual agreements in detection between the two teams that had been missed because of the project's data analysis procedures. Only 9 inspections resulted in changes from the original baseline results. These changes consisted of the finding of indications that had been previously missed and the re-locating and the re-sizing of indications. All of these changes are reflected in the tables and figures presented earlier.

```
                PERCENTAGE      NUMBER OF
                DIFFERENCE      OBSERVATIONS
                IN SIZE
                (Number
                represents
                the Middle
                of the
                Interval)
Team A   >      -60.            1   *
Team B         -56.            0
               -52.            1   *
               -48.            0
               -44.            1   *
               -40.            2   *
               -36.            2   *
               -32.            2   *
               -28.            6   ***
               -24.            4   **
               -20.            8   ****
               -16.           21   ***********
               -12.           24   ************
                -8.           36   ******************
                -4.           55   ****************************
                 0.           82   ******************************************
                 4.           90   ********************************************
                 8.           97   **************************************************
                12.           63   ********************************
                16.           41   *********************
                20.           18   *********
                24.           16   ********
                28.           19   **********
                32.            9   *****
                36.           10   *****
                40.           12   ******
                44.            3   **
                48.            3   **
                52.            1   *
                56.            1   *
                60.            3   **
Team B   >      64.            0
Team A         68.            1   *
          EACH * REPRESENTS 2 OBSERVATIONS
```

FIGURE 16. Histogram Showing the Difference in Size of Indications Called by Both Team A and Team B

Although the re-analysis of the data resulted in no more than a 25% decrease in the number of discrepancies in detection, the reasons for the differences between the teams became evident. In all but 11 of the inspections, both teams saw a signal in their data, but differed on its cause. For example, one team called a 45% wall-loss indication, but the other team thought the signal was due to a copper deposit. The differences in the results appear to be more a function of the analysts' interpretation of complex eddy current signals than to any other cause, and the teams' analysts have basically agreed to disagree in their interpretations of the signals.

The status of the results of the two baseline examinations can best be summarized in Table 6. The wall-loss indications for each team are divided into 3 size classes: >40%, 20-40%, and <20%. Within each of the size classes, the indications were further classified according to the level of agreement between the two teams. The class that represents the best agreement between the teams is the one in which both teams called an indication at the same location, and the size difference was within 10%. The next level of agreement is for matched indications where the sizes differ by more than 10%. The third class is the one in which each team saw a signal, but one called it a reportable indication while the other did not. The fourth class consists of the indications for which the other team did not see a signal at the reported location.

TABLE 6. Summary of the Wall-Loss Indications of the Baseline Inspections

	Two Detections Size Difference $\leq$ 10%	Two Detections Size Difference > 10%	Disagree on Type of Detection	Disagree on Signal
Team A Size $\geq$ 40%	132	73	14	7
Team B Size $\geq$ 40%	160	174	20	5
Team A 20% < Size < 40%	158	131	44	11
Team B 20% $\leq$ Size < 40%	125	49	31	2
Team A 0% < Size < 20%	88	41	53	0
Team B 0% $\leq$ Size < 20%	89	44	390	0

If one concentrates on the best agreement category, (both teams detect and size difference <10%) we see that 58% of Team A's and 44% of Team B's indications that are larger than 40% are in that category. For the 20-40% size range, the situation is reversed: 46% of Team A's and 60% of Team B's indications are in this category. This is consistent with the histograms of the sizes of indications called by the two teams. In the <20% size category, the 17% agreement with Team B's indications, as compared to 48% for Team A, is largely due to the very large numbers of small indications that were called by Team B.

If the two agreement-on-detection categories are combined, their proportion of each teams' total number of indications is much larger than if size is also considered. The differences between the teams for each size category tend to even out, except for the <20% category. The percent of matched detections for the >40% size class are 91 and 93%, respectively, for Teams A and B. The percent of matched detections is 84% for both teams for the 20-40% size category. For the <20% size category, the percent of matched detections for Team A is 71%, while it is only 25% for Team B.

ROUND ROBIN TUBE SELECTION

A major goal of the SGGP is to establish the reliability of EC in-service inspections of PWR steam generator tubing using current (multifrequency) technology. The two baseline inspections of the Surry 2A generator were not planned for collecting data to estimate reliability, but to locate indications for selecting a subsample of tubes for the EC round robin, which would generate the data for the reliability analyses. Basing the reliability estimates on a subsample of tubes is necessary because the dented condition of some tubes limits their useful accessibility, and the destructive analysis of even a limited number of tubes is very costly.

Rationale

The ratio of the number of defects expected to be found in the generator to the total number of inches of tubing is small, even for the Surry generator. The temptation is to think that the sample of tubes for the round robin should be representative of the generator as a whole. For most generators, this would imply that there would be very few defects contained in the sample of round robin tubes. However, it must be remembered that the purpose of the round robin is to determine the reliability of detecting defects - this means that there have to be defects to detect in the round robin sample of tubes, and they have to be there in large enough numbers to give the estimates some validity. (This does not, however, imply that there should not be tubes in the round robin sample that do not have defects.) Therefore the composition of the round robin tubes should not be a representative subpopulation of the steam generator from the standpoint of the number of defects. (Swets and Pickett, 1980).

The second point to consider in the selection of the tubes for the round robin sample is that, although the experimental unit for the analysis is a small section of tube (say an inch or two for cracks and perhaps five or six inches for wastage), in terms of EC inspections the experimental unit is the tube. At first thought, it would seem ideal to define a round robin that would have the participants go to a particular section of a particular tube and report what they see. This is very time-consuming and expensive, since many tubes would have to be inspected and removed for destructive analysis. It can also be argued that this type of round robin defeats the purpose of assessing the reliability of detection, because it tells the participants exactly where to look.

Therefore, the two key concepts in designing the sample of tubes for the round robin are that the sample should not reflect the proportion of defects found in the generator, and that there is a difference between the experimental unit for the analysis and the experimental unit for the inspection.

Implementation

There is information on the status of the tubes from two basic sources - in-service history and observations during the SGGP (leakers, defects, plugging reasons, sludge-filled tubes at unplugging) and the baseline inspections. The historical data do not provide much information on defects (except in the crescent/banana zone region), since most of the EC inspection data is from gauging of dents at the support plates. The majority of information on possible defects is from the baseline inspections. The decision was made to select approximately 80% of the round robin tubes which would contain indications observed in the baseline, and about 20% of the tubes to be chosen because of other conditions (leakers, sludge-filled, bulging) or because they exhibited no indications in the baseline. The decision to not base the tube selection solely on the results of the baseline reflects the knowledge that the EC inspection is not error-free and the fact we have useful additional information from secondary side inspections and visual examinations and previous tasks such as tube unplugging.

The initial target number of tubes for the round robin sample was set at 300. The reasons for selecting 300 tubes were two-fold: 1) the cost of removing and examining 300 tubes for defects is the determining factor in the size of the round robin, 2) 300 is also a reasonable number of tubes to inspect in a week, since it is costly to have teams here for extended periods. There is also statistical reasoning for choosing 300 tubes - if there were approximately 300 observations, the probability of being able to detect a difference of 10% in the detection rate between two teams is about 0.80, with a type I error rate of about 5% (Fleiss, 1981).

The analysis of the baseline inspections showed that there were substantial differences between Intercontrole and Zetec in the interpretation of EC signals obtained from the inspection of the generator tubing. The two baseline inspections were not intended to provide estimates of reliability, and they probably were as different as any two inspections of a generator in the field could expect to be. They were conducted with different manufacturer's eddy current equipment, using different frequencies, with somewhat different size probes, different methods of acquiring and analyzing data were employed with different data analysts. In terms of safety issues for steam generator performance, the differences in detection, particularly of indications in the pluggable range (>40% of wall thickness), are of concern. A review of the mismatches in detection of the larger indications by both teams showed that the differences were not due so much to the lack of a signal obtained during the data acquisition by one of the teams, but to different interpretations by the analyst of what the signal represented. Since there are substantial differences remaining in the results of the two baseline inspections which can only be resolved by destructive analyses, the indications for the two teams were combined to produce the most complete picture of the status of the tubes.

The importance of reported indications to the safe operation of a generator is primarily a function of their size and type. Since ASME code and current eddy current practice do not result in defect type information, only defect size data is available. The indications were divided into three size classes based on the current regulations for reporting steam generator indications.

- Indications whose sizes are >40% (the plugging criterion)
- Indications between 20 and 40% (the reportable range)
- Indications <20%

Once the baseline review had been completed, the size classes of indications called by either team were then divided into three agreement subclasses:

- Mismatch on detection - either the teams differed on the source (reportable indication vs copper) of the signal, or one team did not see a signal
- Both teams detected an indication and they agreed on the size within 10%
- Both teams detected an indication and the size difference was greater than 10%

The process of dividing the indications into classes is called stratification, and the classes are called strata. This is the first step in the statistical procedure called stratified sampling (Cochran, 1963). In summary, the tubes that contained indications as a result of the baseline were divided into three size strata, and then each of these strata were further divided into three agreement substrata. The number of indications in each of the strata for the tube selection for each team are given in Table 6.

The next step was to define the composition of the sample to be randomly drawn from these strata. It was decided that the number of indications in each size class in the round robin tube sample should reflect their importance with respect to safety issues, and that the largest indications should receive the most attention. If the indications were selected completely randomly, a large proportion of them would be in the <20% category because of the large number of small indications called by Team B. Therefore, the proportions of indications in each class were selected to be approximately 45%, 35% and 20%, respectively, for the classes (>40%, 20-40%, <20%). In order not to prejudice the results of the round robin by favoring any one agreement class, each class was sampled equally, so a third of each size class was made up of indications in each of the three agreement classes. Because the number of tubes making up 45% and 35% of 240 tubes is not evenly divisible by 3, some adjustment to the number of tubes in each size category was required. Table 7 shows the planned number of tubes to be selected from each category for the round robin.

TABLE 7. Planned Selection of Tubes for the Round Robin

	Numbers of Tubes		
	Matched detection Size diff <10%	Matched detection Size diff >10%	Unmatched detection
>40%	35	35	35
20-40%	30	30	30
<20%	16	16	16
Miscellaneous Tubes Added to the Sample		60	

Because the sizes of the classes varied, nearly all of the tubes with indications in some strata were chosen for the sample. In one case, the sampling plan called for the selection of more tubes than a given class contained. If this situation occurred, a tube from the miscellaneous bin was used as a replacement. Frequently, the same tube was chosen twice because the classes are not completely mutually exclusive. If that happened, another tube was selected from the strata from which it was removed.

The 20% of the tubes with no apparent defects selected for the round robin sample were chosen from the tubes that showed no indications reported by either team from the baseline inspection. In addition, tubes that were leakers, had sludge in them at unplugging, or showed bulges, were considered for added inclusion in the round robin sample. It turned out that many of the sludge-filled tubes and leakers were so badly dented that only a small portion of the tube was accessible for EC inspection. Although these tubes undoubtedly contain through-wall defects, and are therefore some of the most interesting tubes, they were not included in the round robin sample. These tubes will be examined utilizing alternative NDE techniques.

Another 20 tubes were selected from the category containing indications reported by one team where the other team saw no eddy current signal at all in that location. These cases were deemed of enough importance to warrant further examination.

Table 8 shows the final sampling selections, reflecting the changes mentioned above. The actual percentages of each size category are 42.5% for the >40% indications and 37.5% for the 20-40% indications. Considering the amount of variability in the sizing of the indications, the sizes of the two classes may be virtually equal. The total number of tubes selected for the round robin tube sample was 322.

TABLE 8. Actual Selection of Tubes for the Round Robin

	Numbers of Tubes		
	Matched detection Size diff <10%	Matched detection Size diff >10%	Unmatched detection
>40%	36	36	32
20-40%	30	30	30
<20%	16	16	16
Miscellaneous Tubes Added to the Sample		80	

ROUND ROBIN EDDY CURRENT INSPECTION

The objective of the acquisition round robin experiment of the SGGP is to provide estimates of the reliability of detecting, and accuracy of sizing, defects in service-degraded steam generator tubing with Zetec inspection equipment and field-experienced data analysts. The reason the round robin was restricted to Zetec equipment is that it is the equipment used on the majority of inspections done in the U.S. today, and there are not enough inspection companies in the U.S. that are experienced in the use of Intercontrole equipment to even conduct a round robin.

Four teams were selected by competitive bid among those that demonstrated significant field experience in inspecting steam generators, a fifth team has recently been added from a project sponsoring organization. The conditions under which the data acquisition and analysis were to be conducted were standardized as much as possible. The sizes of probes and two frequencies, (400 KHz differential and 100 KHz absolute) were specified. Other frequencies were left to the discretion of the teams. The equipment calibrations were verified by the PNL eddy current expert. Analyses were to be done with the Zetec DDA4 digital data analyzer. Each team was given the same set of instructions that explicitly stated that they were to report safety-related conditions, wall-loss indications and loose parts. The teams were given computer-produced data reporting sheets with the row and column numbers listed on them to standardize reporting practices and minimize errors. The teams were requested to record the channel number (frequency) from which an indication was called, to state its type (wastage, crack, etc.) and their level of confidence in the call. To avoid ambiguity in the location of defects, particularly wastage, the location of the deepest point of an indication was to be reported. A comments column was also provided in case the teams felt further explanation was required.

Since the round robin inspection was conducted this past summer, the analysis of the data is currently not complete. What is reported here are preliminary results that may be subject to change.

For reporting purposes, the round robin teams are simply referred to as Teams 1-4. The numbers of conditions that are related to safety issues called by each round robin team are given in Table 9.

TABLE 9. Safety-Related Conditions Reported by the Zetec Round Robin Teams

	Numbers of Calls			
	Team			
Condition	1	2	3	4
O.D. Indications	265	197	292	263
I.D. Indications	16	3	0	1
Undefined Indications	6	2	0	3
Possible IGA	0	0	20	0
Loose Parts	30	14	18	1
Total number of wall-loss indications, multiple calls within 3 inches deleted, possible tube sheet crevice IGA not included	256	201	226	265

The number of O.D. indications varied from 197 to 265. The number of I.D. indications also varied somewhat, from 0 to 16. The undefined indications were not labelled I.D. or O.D., and are probably inadvertent omissions that were not caught by the data analyst. The number of loose part calls varied also, from 1 to 30. Most interesting are the 20 calls of possible IGA by Team 3. In all but two cases, these were associated with calls of O.D. wastage at the top of the tube sheet. Other conditions noted by the round robin teams were permeability variations, possible sludge, dents and conductive deposits.

Recall that during the baseline examination, there were numerous instances of multiple indications at the top of tube sheet. The instructions for the round robin had explicitly stated that the locations of the deepest part of an indication be reported; however, the decision of when one indication ended and the other began is a subjective judgement of the data analyst. Therefore, for the round robin, the number of multiple indications varied among the teams. To avoid inflation in the number of matched detections, it was decided that if there were multiple calls within 3 inches at the top of the tube sheet, only the largest indication would be retained. That led to a decrease in the total number of indications reported, which are given in the the last row of Table 9. For comparison purposes, it is interesting that the number of indications called during the baseline for the tubes used in the round robin are 239 for Team A and 294 for Team B. The reason that Team B has so many more indications is that the round robin tube sample had many tubes with multiple indications because of the large number of indications referenced to the hot leg seventh support plate.

The round robin teams were required to report the channel number from which a call was made. The channel numbers used by each team to make their calls are given in Table 10. Channel 1 was the 400 KHz differential mode and Channel 2 was the 100 KHz absolute. The other channels are different frequencies or mixes used at the discretion of each team. The term "missing" refers to omissions of channel numbers, and one team appears more prone to this type of behavior than the others. The interesting thing about this table is tnat, despite the fact that the MIZ-12 is a multifrequency instrument with the mixing capability to remove the effects of unwanted signals, most of the interpretations were based on the single frequency of 400 KHz.

TABLE 10. Channel Numbers Used for Calls by the Round Robin Teams

	Numbers of Calls			
	Teams			
Channel Number	1	2	3	4
1	209	164	219	229
2	43	1		
3				1
4				
5	4	34	7	
Missing		2		35

The locations of the loose parts called by the round robin teams is given in Table 11. Although there appears to be some agreement among the teams, Teams 1 and 2 agreed on the location of 3 loose-part calls and Teams 1 and 3 agreed on 1.

TABLE 11. Locations of Loose Parts from the Round Robin Inspections

	Numbers of Calls Team			
Reference Location	1	2	3	4
Hot Leg				
Top of Tube Sheet	10	2	9	
Support Plate 3	1		5	
Support Plate 5	1			
Support Plate 7			1	
Cold Leg				
Top of Tube Sheet	18	12	1	1
Support Plate 1			2	

The locations of the indications called by each team are given in Table 12. Similar to what was observed for the baseline inspections in Table 1, the reported indications for the round robin are scattered among the support plates, but with the majority of indications at the top of the tube sheet on the hot leg. The range of indications for the cold leg top of the tube sheet is similar to the results of the baseline.

TABLE 12. Locations of Indications Based on the Round Robin Inspection

	Numbers of Indications Team			
Location Reference	1	2	3	4
Hot Leg				
Tube End	8			
Tube Sheet Roll	2			
Top of Tube Sheet	216	191	212	222
Support Plate 2	3	1		
Support Plate 3				1
Support Plate 4	1			
Support Plate 5	1			
Support Plate 6	2	1	1	2
Support Plate 7	4	3	1	2
Cold Leg				
Tube End	11	1		
Tube Sheet Roll		1		
Top of Tube Sheet	7	1	8	36
Support Plate 1	1	1	1	1
Support Plate 2			1	
Support Plate 7			1	
Missing		1	1	1

The distribution of indications among the three size classes is given in Table 13. As a point of information, the rows should sum to the number of indications for each team given in the last row of Table 9; there are two exceptions, Teams 2 and 4 had 9 and 3 indications of undetermined size, respectively, so they are not included in Table 13. The number of indications for each size class varies considerably among the teams. It is interesting that three of the teams called many more indications greater than 40% than were in the 20-40% range. The range of the numbers of <20% indications is quite large (50).

TABLE 13. Number of Indications in each Size Category from the Round Robin Inspection

	Size Category		
Team	<20%	20-40%	>40%
1	45	90	121
2	27	76	89
3	24	82	120
4	75	68	119

The pair-wise agreement in detection among the teams is summarized in Table 14. Since the number of indications reported by each team differed, a single percent agreement does not adequately reflect the situation. The table is read as follows: given the indications by the team corresponding to the row, the indications for the team corresponding to the column are compared to them. The fact that the percent agreement between two teams differs depending on which team's indications are the reference set can be seen by comparing Teams 1 and 2. If the Team 1 indications are taken as the point of comparison, the percent of common detections if 61%; if the Team 2 indications are used as the comparison, the agreement is 78%. Of all of the teams, the set of indications reported by Team 3 has the greatest agreement with the other teams. Looking down the columns, it is apparent that Team 2 has the least agreement with the others teams' calls, while Teams 1 and 3 have about the same level of agreement with the other teams' calls.

TABLE 14. Percent of Common Detections of the Round Robin Teams

		Percent Agreement by Team			
		1	2	3	4
For	1	100	61	76	74
Calls	2	78	100	79	79
By Team	3	86	70	100	88
	4	74	60	75	100

More detailed comparisons of the round robin inspection data are currently in progress.

FUTURE ACTIVITIES

Nondestructive examinations and characterization of the generator will continue, with emphasis on advanced and specialized techniques to accurately characterize specific regions and/or defect types. Eddy current data previously acquired will be reanalyzed to determine what additional information is available in the multiple frequencies used by the data acquisition round robin teams. Two data analysis round robins will be conducted, one each using Zetec and Intercontrole data tapes and analysts. This will allow determination of the variability in analysis of common eddy current signals. The previous round robin included variability due to both data acquisition and analysis. The early removal of two tube sheet sections is planned. This will allow early confirmation of tube sheet conditions and provide opportunity for further NDE, if current NDE characterization proves inadequate. Utilizing the extensive NDE database, a plan will be developed for specimen removals. These specimens will be variously used for destructive metallographic confirmation of NDE results, for destructive tests of remaining mechanical integrity, and for preservation for future NDE technology testing and staff training. The program will also conduct laboratory studies on chemical secondary side cleaning and primary side decontamination techniques using specimens from the generator. These studies will examine efficacy of proposed methods and seek to determine long term damage potential from application.

REFERENCES

Cochran, W. G. 1963. Sampling Techniques, Second Edition. John Wiley and Sons, New York.

Doctor, P. G. A Description of the Data Acquisition and Statistical Analysis Computer Systems for the Steam Generator Group Project. March 1983. PNL-3955.

Fleiss, J. L. 1981. Statistical Methods for Rates and Proportions, Second Edition. John Wiley and Sons, NY.

Swets, J. A. 1983. Assessment of NDT Systems - Part I: The Relationship of True and False Detections. Materials Evaluation, 41: October, 1294-1298.

Swets, J. A. 1983. Assessment of NDT Systems - Part II: Indices of Performance. Materials Evaluation, 41: October, 1299-1303.

Swets, J. A. and R. M. Pickett. 1982. Evaluation of Diagnostic Systems. Academic Press, New York, NY.

INTEGRATION OF NONDESTRUCTIVE EXAMINATION RELIABILITY AND FRACTURE MECHANICS*

S. R. Doctor, Program Manager

D. J. Bates
L. A. Charlot
M. S. Good
H. R. Hartzog
P. G. Heasler
G. A. Mart
F. A. Simonen
J. C. Spanner
T. T. Taylor

SUMMARY

The primary pressure boundaries (pressure vessels and piping) of nuclear power plants are in-service inspected (ISI) according to the rules of ASME Boiler and Pressure Vessel Code, Section XI (Rules for In-Service Inspection of Nuclear Power Plant Components). Ultrasonic techniques are normally used for these inspections, which are periodically performed on a sampling of welds.

The Integration of Nondestructive Examination (NDE) Reliability and Fracture Mechanics (FM) Program at Pacific Northwest Laboratory (PNL) was established to determine the reliability of current ISI techniques and to develop recommendations that will ensure a suitably high inspection reliability. The objectives of this NRC program are to:

- determine the reliability of ultrasonic ISI performed on commercial light-water reactor (LWR) primary systems
- using probabilistic FM analysis, determine the impact of NDE unreliability on system safety and determine the level of inspection reliability required to ensure a suitably low failure probability
- evaluate the degree of reliability improvement that could be achieved using improved and advanced NDE techniques

---

*Work supported by the U.S. Nuclear Regulatory Commission under Contract DE-AC06-76RLO 1830; Dr. J. Muscara, NRC Program Manager.

- based on material properties, service conditions, and NDE uncertainties, formulate recommended revisions to ASME Code, Section XI, and Regulatory Requirements needed to ensure suitably low failure probabilities.

The scope of this program is limited to ISI of primary systems; the results and recommendations may also be applicable to Class II piping systems.

The following discussion will cover highlights of both the piping task and the fracture mechanics tasks.

PIPING TASK

TASK 1: INPUT TO NRC PIPE CRACK TASK GROUP

The Executive Director for Operations of the Nuclear Regulatory Commission (NRC) established a committee to review stress corrosion cracking in Boiling Water Reactors (BWRs). As part of their study, the committee requested the support of NRC research in reviewing ultrasonic techniques used for detection and sizing of IGSCC in BWRs. PNL assisted in this review by drafting Chapter Four, which included the following topics:

- Current Ultrasonic Examination Requirements
- Technical Problems of UT Inspection
- Actual Field Experience Before and After the Issuance of IE Bulletins 82-03 and 83-02
- UT Round Robin and Laboratory Experience
- Recent Improvements in Ultrasonic Inspection
- Personnel, Equipment, and Procedure Qualification
- Areas of Needed Research
- Foreign Experience

A short summary of topics from the report follows:

Current Ultrasonic Examination Requirements

Preservice and in-service examination requirements are specified in 10 CFR 50.55a and Section XI of the ASME Code. In general, the applicable ASME Code Edition for a plant's preservice inspection (PSI) program is determined by the con-

struction permit date of issuance, and for the in-service inspection program (ISI) is determined by the operating license date of issuance. Since these issue dates often span a long time period, the intervening changes in Code requirements may negate the primary purpose of the PSI, which is to provide baseline measurements for comparison with later ISI results.

This negative effect can be illustrated by considering the calibration reflectors specified for UT in the 1974 Code (S-75 Addenda) which were side-drilled holes; and the 1977 Code (S-78 Addenda) which were notches. NRC-sponsored reports[1,2] showed that a significant difference in calibration sensitivity resulted when the calibration reference reflector changes from a side-drilled hole to a notch.

NRC Standard Review Plans (SRP's) Sections 5.2.4 and 6.6 may not be adequate because these documents reference Code requirements that are inadequate.

Technical Problems of UT Inspection

The presence of geometrical reflectors at or near the inner weld surfaces, combined with outer surface irregularities (weld crown, etc.) and interferences which limit the overall accessibility for scanning, tend to reduce the overall effectiveness of the ultrasonic inspection. Furthermore, these inspections must often be conducted under uncomfortable working conditions compounded by the time limits imposed on work in high radiation zones. Under these conditions, operator attitudes may also impair examination effectiveness. The anisotropic grain structures found in austenitic stainless steel welds cause severe and variable attenuation of the sound beam, and may also cause the sound beam to bend away from the intended straight line path. These effects occur without the inspector's knowledge and can result in indications that are missed, incorrectly located, inaccurately sized, or all three. The currently employed weld overlay repair process further compounds these problems, and creates an ultrasonic examination situation whose overall effectiveness is questionable, at best.

UT Round Robin and Laboratory Experience

A round robin testing program was conducted by PNL to measure the reliability of crack detection and crack sizing; EPRI also conducted a study to measure the reliability of IGSC crack depth measurements. The PNL round robin showed that for clad ferritic pipe, the probability of detection and correct interpretation (PODCI) was at least 70% for cracks 15% through-wall or deeper, for both near side and far side access. The PODCI for clad ferritic pipe using a PNL improved procedure was nearly

perfect. Thus, the reliability of UT/ISI is considered to be adequate for welds in clad ferritic piping. For both IGSC and thermal fatigue cracks in wrought stainless steel, these six teams achieved an average PODCI of 50-60% when using their own procedures for cracks 15% through-wall or greater. For centrifugally cast stainless steel (CCSS) specimens containing thermal fatigue cracks, the average PODCI dropped to 20-30%, with a corresponding 20-30% false call rate, for cracks penetrating 15% through-wall or greater. Thus, the UT results on welds in wrought stainless steel piping were marginally effective, and the results on welds in CCSS material were categorically ineffective. The teams tended to undersize the length of small cracks and oversize the length of long cracks. All the teams employed the Code-advocated depth sizing method of amplitude drop and did not show good correlation with destructive crack depths.

The results of a 17-team EPRI sizing study to determine IGSC crack depth measurement capability showed that although some teams performed better than others, none achieved a statistically accurate correlation ($\pm$1/4 of wall thickness) between UT measured depth and true crack depth. This study included 13 IGSC cracks and 3 EDM notches, and revealed a general tendency to oversize small cracks (less than 20% through-wall), and to undersize cracks larger than 20% through-wall. This "oversize small/undersize large" tendency was also consistently observed in the results of the PNL round robin.

Recent Improvements in Ultrasonic Inspection

While Inspection and Enforcement Bulletin (IEB) 82-03 was in effect, about 5.4% of the welds examined where classified as cracked; whereas, after IEB 83-02 became effective, some 25% of the welds examined were classified as cracked (not yet verified by destructive evaluations). This five-fold increase in reporting rate may be attributable to the classroom training and performance demonstration requirements contained in IEB 83-02. However, this high reporting rate has resulted in at least several cases of overcall.

The advantages of automated systems include mechanical scanning devices which reduce the radiation exposure to skilled UT operators, automatic data recording processes, and signal processing techniques which improve the repeatability and documentation aspects. The disadvantages of automated systems include limited flexibility and their use is not possible on all piping configurations; physical access precludes their use adjacent to pipe supports, branch connections, etc.; and some scanners are not capable of skewing the search unit for optimum detection of IGSC cracks or other reflectors that are obliquely oriented.

Personnel, Equipment, and Procedure Qualification

The NRC is developing a document which will specify more rigorous qualification requirements than those presently in effect. This document will contain both general requirements and criteria to define overall performance qualification and requalification processes for all required UT in-service examinations. The document will require that: 1) all UT personnel, equipment, and procedures be qualified either individually or in combination, and 2) the qualification processes will include successful completion of a statistically significant performance demonstration. The document will specify that all NDT Level I, II, and III personnel attend nationally-uniform training courses, and the document also describes requirements for conducting "blind test" performance demonstrations of the recording probability, probability of detection and diagnosis, and flaw detection proficiency.

In 1983, an EPRI/Ad Hoc Utility Committee submitted a proposed personnel qualification and certification document (NUC-MR-1A) to the NRC. This document contains an expansion of the ASNT Recommended Practice document (SNT-TC-1A), and establishes a set of "minimum requirements" in lieu of the "guidelines" that are described in SNT-TC-1A. Since NUC-MR-1A requires each user to develop an individualized "Written Practice" to specify how that user will comply with the "minimum requirements" of NUC-MR-1A, a potential weakness exists since users may be more inclined to tailor their written practices to their current programs than to the spirit and intent of NUC-MR-1A. If, and when, this document is adopted by the NRC and implemented by industry, it is expected that the status quo will not change because most employer's written practices will require only minor changes and will, therefore, be inadequate.

The Section XI Working Group on Nondestructive Examination is considering a proposal to add a new qualification appendix to Section XI which will specify requirements for the qualification of UT procedures and personnel. The proposed approach is patterned after the qualification requirements of IEB 83-02. As currently drafted, this appendix will require that each UT procedure be qualified. Thereafter, personnel will be qualified via performance demonstration. Adoption of the proposed appendix XI will only incorporate current personnel qualification requirements (i.e., IEB 83-02) into the Code.

Areas of Needed Research

Applied research is needed to develop: 1) reliable automated UT equipment, 2) better UT techniques for sizing defects, 3) UT techniques for detecting and sizing flaws in pipe repaired

by the weld overlay process and pipe that has been subjected to induction heat stress improvement (IHSI) or last-pass-heat-sink processes, 4) techniques for examining austenitic welds through the weld, 5) techniques for examining cladding, weld overlay buildups, and 6) techniques for scanning centrifugally cast stainless steel piping. Finite element analysis modeling is needed for cracks in austenitic stainless steel materials to provide crack characteristics for use in specifying qualification test samples. Additional research is also needed to identify, isolate, and analyze the human factors aspects of in-service inspection, and their influence on the overall effectiveness of NDT/ISI. The relative influence and relative correctability of these factors should be assessed, and recommendations developed toward mitigating the consequences of the major negative human factors aspects.

Conclusions

Using the information summarized above, the NRC review committee developed the following conclusions and recommendations.

- Code minimum UT procedures result in totally inadequate IGSCC detection. Easily implementable modifications to these procedures can result in some improvement. These have been incorporated into Code Case N-335. Therefore, it is recommended that Code Case N-335 should be immediately mandatory for all augmented inspections until better procedures are developed.

- Although IGSCC detection has improved to the point that it is considered acceptable under optimum conditions and procedures, the detection reliability as impacted by variability in operator procedures and equipment performance along with field conditions needs further study and improvement. While length sizing of cracks is acceptable, depth sizing is inadequate. It is recommended that advanced techniques and procedures for crack detection and depth sizing be developed and incorporated into Code requirements to provide data to reduce the need for extremely conservative fracture mechanics evaluation.

- The current activities in personnel and procedure qualification and performance demonstration represent steps in the right direction, and the resultant process that is implemented is acceptable in this interim; however, they need further improvement. Therefore, it is recommended that ongoing industry

and NRC activities to develop adequate criteria for qualification of the entire inspection process to achieve more reliable field inspection be finalized and implemented on a high priority basis.

- For future plants or for replacement of existing piping systems, the material, design of pipe joints, and accessibility from both sides of the weld should be optimized for UT examinations; this requirement should be mandatory for all components with the exception of existing items such as pumps, valves and vessels in older plants. The uninspectable joints should be subjected to IHSI.

- Inspection techniques should be developed for detection and dimensioning of flaws in pipes repaired by the weld overlay process.

TASK 2: NUREG/CR-3753, PNL-5070 - AN EVALUATION OF MANUAL ULTRASONIC TESTING OF CENTRIFUGALLY CAST STAINLESS STEEL

This report documents the results of a joint PNL and Westinghouse effort to determine the limitations of inspectability of cast stainless steel using manual inspection techniques. Two studies have been conducted in an attempt to determine the degree of inspectability of centrifugally cast stainless steel (CCSS) pipe. One study was an NRC-sponsored Pipe Inspection Round Robin (PIRR) test conducted at PNL. The PNL study reported that less than 30% PODCI was achieved on thermal fatigue cracks ranging from 5% to 50% through-wall. Another study was conducted by Westinghouse. The Westinghouse study reported that 80% detection was achieved for 20% through-wall mechanical fatigue cracks.

A cooperative program between PNL and Westinghouse was conducted to resolve the differences between the two studies. The program was designed as a limited round robin. Detection experiments were performed on samples from both the PNL and Westinghouse studies.

When inspecting the CCSS specimens that were made by Westinghouse, the inspection team performed as follows:

- When considering both cracked and uncracked specimens, 17 of 22 samples were characterized properly.

- When considering cracked and uncracked specimens separately, 9 of 14 cracked samples were characterized properly and all uncracked samples were characterized properly.

The results are in agreement with those reported by Westinghouse in their report WCAP-9894. Detection probability was very good for cracks with depth greater than 15% through-wall.

When inspecting the CCSS specimens that were made by PNL, the results followed the trend of the other four teams that inspected these specimens during the Pipe Inspection Round Robin. Out of 29 inspections of cracked specimens, only two cracks were detected. Again, none of the crack samples produced a recordable signal along its entire length. The only unusual feature of the Westinghouse team's performance was the absence of false calls.

It should be noted that the crack depths indicated for the PNL specimens were based on nondestructive measurements. Limited destructive depth measurements performed to date have indicated that the cracks were probably not this deep; in fact, it is estimated that the depth range of the PNL cracks is about the same as that of the Westinghouse specimens, viz. 0%-30%.

Acoustic Velocity Characterization of Samples

The acoustic velocity of both PNL and Westinghouse test samples was determined. The velocity measurements were made at normal incidence. Table 1 shows the results of the velocity measurements. Sample sets 1 and 2 are from specimens used during the PNL round robin and sample set 3 are specimens used in WCAP-9894.

Table 1. Velocity Measurements (Normal Incidence)

Sample	Microstructure	V_L Max (m/sec)	V_L Min (m/sec)
1 (PNL)	Equiaxed	5932	5875
2 (PNL)	Columnar	5496	5430
3 (Westinghouse)*	Columnar	5800	5420

*Note: Sample set 3 had very significant point-to-point variations (approximately 7%) within a single specimen.

After analyzing the velocity measurements, the following conclusions can be made:

- When considering all test samples, the acoustic velocity of CCSS material shows wide variation.

- The equiaxed and columnar microstructures of the PNL sample set have different, but well behaved velocities. The velocity of the equiaxed microstructure has a maximum variation of 0.9%. The columnar microstructure has a maximum variation of 1.2%.

- The Westinghouse samples, by contrast, have wide variability from point-to-point within each sample and from sample-to-sample.

Conclusions

Metallurgy of Base Material

When analyzing the data with respect to grain structure of the base metal, no trends appeared. Crack detection was either spread evenly between grain structure types (as was the case in the joint study) or, when considering all round robin data, false call rates were so high that trends were not statistically significant after correction for false calls. The variability of velocity did not appear to affect crack detection. It does not appear from the experimental data that either grain structure (equiaxed or columnar) had better properties for ultrasonic inspection.

Weld Access

Similarly, analysis of data from the joint study, PNL round robin, and WCAP-9894 does not show any clear trend for superior detection as a result of near-side or far-side access. However, access to both sides of a weld did improve crack detection.

Defect Type

The most significant factor for crack detection that results from data analysis is flaw type. The PNL samples contained ultrasonically tight, rough cracks. The tightness of the cracks was graphically illustrated when optimized radiographic examination of the samples had difficulty detecting all but the deepest cracks. The Westinghouse samples contain by comparison open and planar type cracks. Both sets of test samples contained no geometric reflectors at the weld root or crown. The only signals interfering with crack detection were metallurgical in nature. Ultrasonic signals from the PNL samples were generally very low amplitude, often no greater than signals reflected from grain boundaries. By contrast, signals from the Westinghouse fatigue cracks were higher in amplitude; in fact, the response from all cracks was greater than or equal to the 3/16 inch side drilled hole calibration reflector located at 1/4T.

Sizing

WCAP-9894 does not address the subject of sizing at all; the PNL PIRR depth sizing data was too sparse for statistical analysis. However, those teams that did attempt to size did not do well. The experimental data shows that no cracks in either set of test samples produced detectable signals along their entire length. Therefore, it is concluded that accurate characterization of cracks with current techniques applied in the field is not possible for either length or depth in CCSS piping.

Inspection Technique

During the PNL PIRR, all teams used dual element longitudinal search units. Some of the search units used a zone isolation principle and some did not. The Westinghouse team used a single search unit designed with a water column. None of the inspection techniques or search units showed superior performance.

Recommendations

The experimental data from the three studies suggest that detection of cracks in CCSS primary piping is highly dependent upon the cracking mechanism. Mechanical fatigue type cracks have a reasonably high probability of detection; tight thermal fatigue cracks are essentially undetectable with current field ultrasonic inspection techniques. The most probable failure mechanism of cast stainless steel pipe is not known at this time. However, because some failure mechanisms (i.e., mechanical fatigue) have proven to be detectable, it is recommended that the requirement of ultrasonic examination of cast stainless pipe be continued. In addition, data from the Westinghouse study indicates that operator training can improve detection proficiency. Therefore, it is recommended that all operators involved in the inspection of CCSS piping be trained on actual flawed specimens and that some demonstration analogous to that described by IEB 83-02 be required as a minimum.

Limited destructive analysis of the PNL PIRR flaws indicates that true flaw depths may be less than the intended depths. Therefore, insufficient data exists to predict the detectability of thermal fatigue cracks deeper than 50% wall thickness. The following recommendations are made to provide a better definition of detectability for safety significant, rough, tight flaws.

1. Using PNL type samples, produce cracks with through-wall depths ranging between 50% and 75% of pipe thickness and determine whether or not crack detection improves significantly for deeper cracks.

2. Establish the critical flaw size (maximum safe length and through-wall depth dimensions) for CCSS pipe.

The most troublesome evidence from all three studies is the conclusive data regarding the inability to properly characterize cracks in CCSS using current field practices. The only area of defect sizing that has not been properly addressed is the potential of more sophisticated techniques such as SAFT, UDRPS, and acoustic holography. Therefore, it is recommended that the potential of these techniques for examining CCSS piping be evaluated.

TASK 3: INTERACTION MATRIX

The objective of this task is to examine the effects of variations in ultrasonic test equipment upon the reliability, repeatability, and quality of the results of inspections of nuclear piping components and develop proposals for improvements in same.

Individual ultrasonic test system components (e.g., transducers, pulsers, and receivers) have been characterized. Mathematical formulas describing their interaction are being developed and based upon those formulas, a computer model of the ultrasonic test system will be constructed. A series of actual test systems have been assembled from characterized components and used to record test results on a set of prepared flaws. These test results will be used to refine and validate the computer model. Because of its speed and ease of use, the computer model will then be used to investigate the effects of a wide range of test system variables upon test results. The results of these investigations will be used to propose standards of improvements for individual test system components.

Test systems will also be characterized as complete systems so that the interaction between test system characteristics and flaw characteristics may be investigated more closely. These investigations will be used to propose standards of improvements for test systems in total.

The majority of the test results of actual test systems have been recorded and analyzed for simple variability of results. Variations in amplitude response of up to 50% for different test systems (each calibrated to the same reference reflector) examining the same flaw show that the problem can easily have a significant impact on the reliability of ultrasonic inspections.

The mathematical formulas describing the physics of the test system have been worked out:

$$\% \text{ FSH} = \text{GARH}_t \; V_p \left(\frac{Z_t}{Z_p+Z_t}\right) \left(\frac{Z_r}{Z_t+Z_r}\right) \qquad (1)$$

where: % FHS = percent Full Screen Height
V_p = pulser internal equivalent voltage
Z_p = pulser output impedance
Z_t = transducer input impedance
Z_t = transducer output impedance
H_t = transducer voltage transfer function
A = test material attenuation coefficient
R = flaw reflectivity coefficient
Z_r = receiver input impedance
G = receiver voltage transfer function gain (displayed as % FSH)

A series of FORTRAN subroutines which form the basis of the computer model have been written. They control the digitization and recording of test results and component characterization data, perform the necessary algebraic array and Fourier transform manipulations, and graphically display and/or record the results.

In order to develop the computer model itself, a second interactive program was written which uses the same subroutines that the model itself will use. The interactive program, through control of the computing process and its ability to display and store intermediate steps, is being used to investigate and refine the characteristics of the group of subroutines that perform the actual calculations. Debugging has been completed and the interactive program is now being used on a series of more complicated calculations.

Significant progress has been made in the transducer segment of the model by the determination of Z_t and H_t, the characteristic parameters of the transducer. Although previous characterizations of the transducer have measured the same or similar parameters, the degree of accuracy (and amount of data) required for accurate waveform prediction were in many cases one to two orders of magnitude greater than the previous characterizations. Not only must these parameters be accurately measured in order for them to be useful in the model, but it must be shown that the transducer does in fact behave in a linear manner over the range of intended operation and that Z_t and H_t are invariant over that range. Our measurements of Z_t and H_t have allowed us to make accurate computer predictions of transducer waveforms given the voltage waveform applied to the transducer. And, although we have not tested the model over the full range of expected applied voltage waveforms, the model has generated good results over a wide range of applied voltage waveforms.

Characterization of the pulser characteristics, V_p and Z_p, has been much more difficult. The initial evaluation of the problem pointed out that the pulser would have non-linearities associated with its operation but that in the best case they might be only associated with the actual off-on and on-off transitions. Given that the transitions are very short in duration and if the on impedance of the transducer is constant, we hoped to be able to model the pulser in a piecewise fashion. Attempts to characterize the on impedance of the pulser were hampered by the brevity of the event of interest and the limited range of frequencies in our static impedance measurements. However, after exhaustive efforts to eliminate other possible causes of our varying measurements of the pulser on impedance, we have concluded that the on impedance of the pulser is also a function of the pulser's output voltage and since that will typically vary while a pulser is driving a transducer, we will not be able to accurately characterize the pulser on impedance.

However, in the case of our square wave pulsers, all of the measurements have indicated that the pulser on impedance is less than 20 ohm magnitude over all frequencies of interest with a typical value of 5 ohms resistance and an inductive reactance of 5 ohm at 10 MHz. Thus, as long as the transducers' impedances are significantly larger than that of the on impedance of the pulser should have little effect on the model and our efforts are currently proceeding on that assumption.

The square wave pulser was investigated first because it was expected that if pulsers could be characterized, it would be easier to characterize by virture of its having, if not a constant on impedance, at least a small on impedance. Shock-type pulsers, particularly if any damping is used, may be much more difficult to characterize because the pulser on impedances are less likely to be significantly smaller than the transducer impedance. This problem casts doubt on ability to characterize the test system piece by piece into a workable model.

An alternative method of ensuring that different test systems in the field give consistent results may merit closer consideration. The present calibration procedure uses a spectral reflector (reflects all frequencies equally well) to adjust the % FSH and construct DAC curves. However, as indicated by our results so far, the cause of a good deal of the differences between test systems is due to variations in the test systems' sensitivity as a function of frequency in conjunction with variations in the material attenuation and flaw reflectivity as a function of frequency. By using frequency specific calibration blocks, a procedure may be developed which would ensure that the variation of a test system's results, as a function of frequency, would fall within certain bounds. The challenge here is to find or construct frequency specific calibration blocks.

TASK 4: ADVANCED UT TECHNIQUE EVALUATION

The objective of this task is to evaluate UT techniques which can effectively reduce in-service inspection unreliability. The performance of each technique is quantitatively compared to the results of the PNL PIRR. In a preliminary evaluation of FLAWSORT (a technique developed by Southwest Research Institute) results have been completed and are presented here to illustrate the analysis methodology used in evaluating candidate techniques.

FLAWSORT is a computerized interpretation algorithm which distinguishes between those ultrasonic inspection results indicative of cracks and those results indicative merely of geometric reflectors.

SwRI ultrasonically inspected selected areas of the circumferential welds in 11 PIRR pipe specimens. The specimens were 10-inch diameter, Schedule 80, Type 304 stainless steel pipes. The inspections utilized a dual-element, 1.5 MHz, 45°, shear-wave transducer. SwRI used FLAWSORT to interpret the inspection results and reported the interpretations to PNL.

PNL evaluated the reported results and the following is a summary of the evaluation. PNL estimated that the false-call probability of FLAWSORT was 0.00, as opposed to 0.09 for the PIRR teams.

PNL evaluated the following probabilities of detection and correct interpretation as cracks (PODCIs) for FLAWSORT:

- for EDM notches, 1.00 versus 0.59 for the PIRR teams;
- for IGSCC, 0.75 versus 0.53;
- for all of the defects taken as an aggregate, 0.68 versus 0.46; and
- for thermall fatigue cracks, 0.50 versus 0.34.

Our evaluation of FLAWSORT results showed a chi-square significance at the 1% level. This is very strong evidence that PNL's test really assessed FLAWSORT's intrinsic performance abilities.

TASK 5: LETTER REPORT ON EVALUATION OF WELD OVERLAY EXAMINATION TECHNIQUES

The objective of this task is to determine the effectiveness and limitations for ultrasonic examinations of stainless

steel piping welds which have weld overlay applied as a countermeasure to SCC.

The project direction is divided in two areas: 1) determine if it is practical to pass ultrasound through weld overlay, and 2) assess if defects in the pipe weld zone can be detected and characterized. Our involvement with weld overlay inspection research began in March 1984. The initial plan was to search for information already published on weld overlay. Secondly, before any research could commence, it would be necessary to collect a group of samples which had weld overlay applied.

A literature search was conducted first, and it revealed there is not a large amount of material on the subject of weld overlay. In March, EPRI published a study prepared by Southwest Research Institute titled "Evaluation of Nondestructive Examinations of Intergranular Stress Corrosion Cracking Countermeasures." This report offered a wealth of information and served as an initial starting point for the work recorded in this report.

There are four different sample categories needed for this project. They are:

1) plate with no weld and no weld overlay

2) plate with full penetration weld

3) pipe with weld overlay and no full penetration weld

   a) unground with no notches on the inside diameter

   b) unground with notches on the inside diameter

   c) ground with no notches on the inside diameter

   d) ground with notches on the inside diameter

4) pipe with weld overlay and a full penetration weld

   a) samples manufactured for use in this project

      - with all conditions listed in 3) above
      - with artificially induced IGSCC

   b) samples procured from nuclear power plants which have been in service.

Samples 1, 2, 3, and 4a have been obtained and sample 4b is an overlaid pipe from Monticello that is at PNL but not decontaminated.

Using a 45° shear wave mode transducer, tests have been conducted to determine how serious an affect weld overlay has on the returned signal from a machined notch on the inside diameter surface. A category 3b sample was used to compare with a pipe section with no weld overlay. Each sample has two notches on the inside surface: one notch is 0.110" deep and one notch is 0.330" deep on each piece. The tests with the 45° shear wave transducer have demonstrated the 0.330" notch can be detected through the weld overlay; however, there is serious energy losses as compared to the 0.330" notch detected through plate with no weld overlay. The 0.110" notch could not be detected with the 45° shear wave transducer through the weld overlay. The above test utilized only a 2.25 MHz, 0.5" diameter transducer. This is the first in a series of selected frequencies, diameters, and angles to be evaluated.

The main body of the program is the detection and evaluation portion which is subdivided into two primary areas: 1) the use of EMATs for sound field measurements, and 2) the comparison of transducers (mode, angle, frequency, and diameter) based on amplitude of the reflected ultrasonic signal. EMAT measurements conducted to date have revealed some expected results - and some unexpected results. Tests through unground weld overlay have revealed that both shear wave mode and longitudinal wave mode transducer angles will be adversely affected. The problem appears to be two-fold on unground surfaces: 1) the lack of surface parallelism, and 2) the metallurgical structure of the weld overlay material. Present sound field tests being conducted with high angle longitudinal transducers using plate with no weld overlay have demonstrated serious loss of energy in the longitudinal mode. Similar tests through weld overlay have yet to be conducted. Other tests, through plate with various angles to determine wave mode energy losses, are also schedule. A report is planned to be out by the end of the calendar year.

TASK 6: QUALIFICATION DOCUMENT TASK

The objective of this task is to develop a document that specifies supplementary criteria, requirements, and processes for qualifying personnel, equipment, and procedures for ultrasonic in-service inspection (UT/ISI) of nuclear power plant components. This document will specify the overall qualification processes that are to be used to achieve a statistically significant performance qualification, and it will also specify the test specimens, environment, and other conditions under which the qualification processes must be conducted.

To date, the overall scope of the qualification criteria and requirements have been defined, the document format has been developed, and three "working draft" versions have been sequentially prepared.

The first working draft contained an extensive review and discussion of the overall qualification issue and its problems, and described the wide variety of approaches and options that should be considered. A broad cross-section of industry and regulatory interests were invited to a workshop meeting which was held in June 1983. Although the controversial nature of this issue was quite evident, the two-day meeting proved to be very productive.

The second working draft included extensive revisions based on input from the workshop meeting. This draft was reviewed with the NRC Project Manager in early March 1984, and the two-part approach involving separate application supplement for each unique, specific application was dropped. The application supplement concept (if used at all) would be limited to only three appendices; one for piping, one for vessels, and one for nozzles. The document has been reformatted using the above concept into a third working draft. This third draft will be presented at a second workshop meeting to be held in November 1984.

The basic document features are:

1. A statistically designed performance qualification demonstration is required.

2. The UT personnel, equipment, and procedures are all considered to be critical inspection elements, and all three are involved in the qualification process.

3. Nationally-uniform classroom training is required prior to initial qualification, and once per year thereafter, for all Level I, II, and III personnel.

4. Level III personnel must successfully complete nationally-uniform Basic and UT Method examinations as one part of the initial qualification requirements.

5. Limited-scope qualifications are permitted for both personnel and equipment.

6. Provisional (reduced) qualification requirements are included to temporarily satisfy unexpected, urgent UT/ISI needs.

The results from other NDE/FM program tasks will be utilized to develop specific criteria and requirements for the test specimens, equipment performance parameters, and performance demonstrations. The major goals of the next workshop meeting will be to obtain general agreement on the scope of this UT/ISI qualification program and to develop a plan for implementing the document.

TASK 7: EVALUATION OF CRACK CHARACTERIZATION TECHNIQUES

The objective is to evaluate UT techniques for accurately characterizing cracks. This task evaluates the capabilities and limitations of techniques used for sizing the depth of cracks in nuclear reactor piping. The operation of the techniques are discussed and a comparison of results from examining cracked specimens is shown. The techniques being evaluated are:

- Shear wave Satellite Pulse Technique (S-wave SPT)
- Longitudinal wave Satellite Pulse Technique (L-wave SPT)
- Outer Diameter Creeping Wave Technique (ODCWT)
- Synthetic Aperture Focusing Technique (SAFT)
- A bi-modal ultrasonic technique (SLIC-40)
- A material resistivity technique (RESTEST)

Our research to date suggests that no single crack sizing technique approaches 100% reliability, in either depth measurement accuracy, or simply yielding a depth measurement. This suggests that the best approach is to use multiple sizing techniques. The material resistivity technique (RESTEST) appears to be uneffective for crack depth sizing (from the OD) at this time.

The following preliminary conclusions are based on the experimental results to date.

- The ODCWT appears reliable for identifying/sizing deep cracks.
- L-wave techniques appear to be effective when attempting crack tip diffraction in austenitic materials (L-wave SPT, SLIC-40, ODCWT).
- S-wave SPT is most effective when applied to ferritic components.

- All crack tip diffraction techniques are best performed using an RF display and high damp transducers.

- Personnel performing crack depth sizing in the field should be required to perform satisfactorily in a qualification test using the same equipment they will be using in the field.

TASK 8: INTERNATIONAL NDE RELIABILITY WORK

Results of previous work by PNL have indicated that standard UT procedures are inadequate for reliable crack detection and sizing in stainless steel piping used in nuclear reactor primary piping systems. As part of a continuing effort to identify nondestructive evaluation methodologies that will have improved ability to reliably detect and more accurately characterize defects, PNL has designed and is presently implementing an international round robin exercise.

The round robin on cast stainless steel has been separated into two phases, with the first phase using presently available test specimens from the PNL PIRR study for initial screening of techniques and allowing direct comparison of results of the PIRR study. This phase of the round robin is already in progress with several U.S. teams completing inspection of the specimens. These specimens are to be shipped to Europe for further study by 14 teams from other countries. The overseas work is being coordinated by the Joint Research Centre in Ispra, Italy as part of the Committee for the Safety of Nuclear Installations. This work will become part of the PISC II program in the fall of 1984.

The planned second phase of the round robin will further characterize appropriate methodologies identified in the screening phase by using a much broader range of cast stainless steel configurations than those available from the PIRR study. Additional studies are also planned for austenitic stainless steel.

TASK 9: SIAMESE IMAGING TECHNIQUE FOR IMAGING PLANAR-TYPE RADIAL DEFECTS IN REACTOR PIPING

Introduction

This report describes a unique acoustical imaging technique (i.e., Siamese imaging) for imaging planar-type, radial defects in reactor pipe weldments, etc. The send/receive imaging configuration consists of two focused probes operating from opposite sides (SROS) or from the same side (SRSS) of the defect to be imaged. The former configuration is usually referred to as the through transmission pitch/catch technique,

and the latter configuration is usually referred to as the tandem technique in NDT jargon. Simple geometrical ray theory is used to derive the basic equations that define the fundamental image parameters that describe the defect: image magnification, defect true height, inclination angle, and depth.

Concept

Send/Receive Scanning Configuration from Opposite Sides of the Defect (SROS)

The siamese image is a bi-symmetrical view of the internal planar object. Figure 1 graphically illustrates the concept of twin image construction using the SROS configuration with the defect onnected to the lower surface. Two focused probes are positioned to view the object at a preselected viewing angle θ. The receiving probe or transducer is represented by the human observer and as the SROS configuration is scanned across the vertical object, one sees first the normal reflected image and then the inverted image. The final integrated image consists of

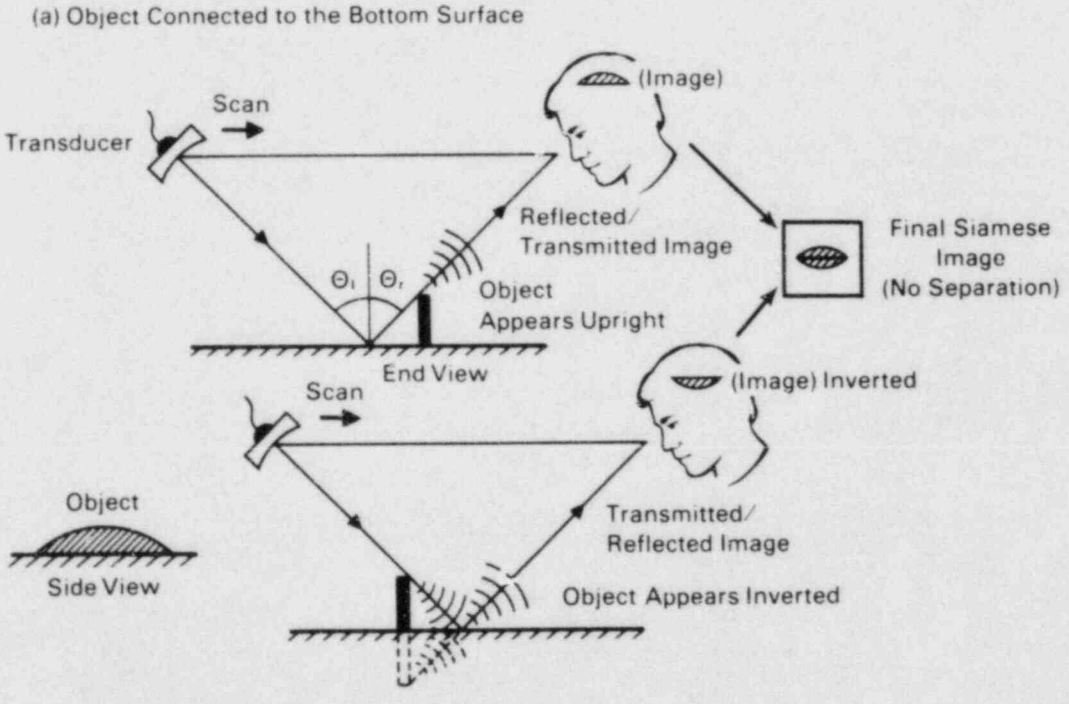

Figure 1. Siamese Image Concept SROS (Object on Lower Surface).

the normal and inverted image connected or separated at the baseline, thus we call it a "siamese image."

Figure 2 illustrates the concept when the object is above the lower surface (i.e., simulating an internal crack). The bi-symmetrical image is now separated indicating the object is above or not connected to the lower surface. Thus, this unique image parameter reveals the object or crack is not lower surface connected.

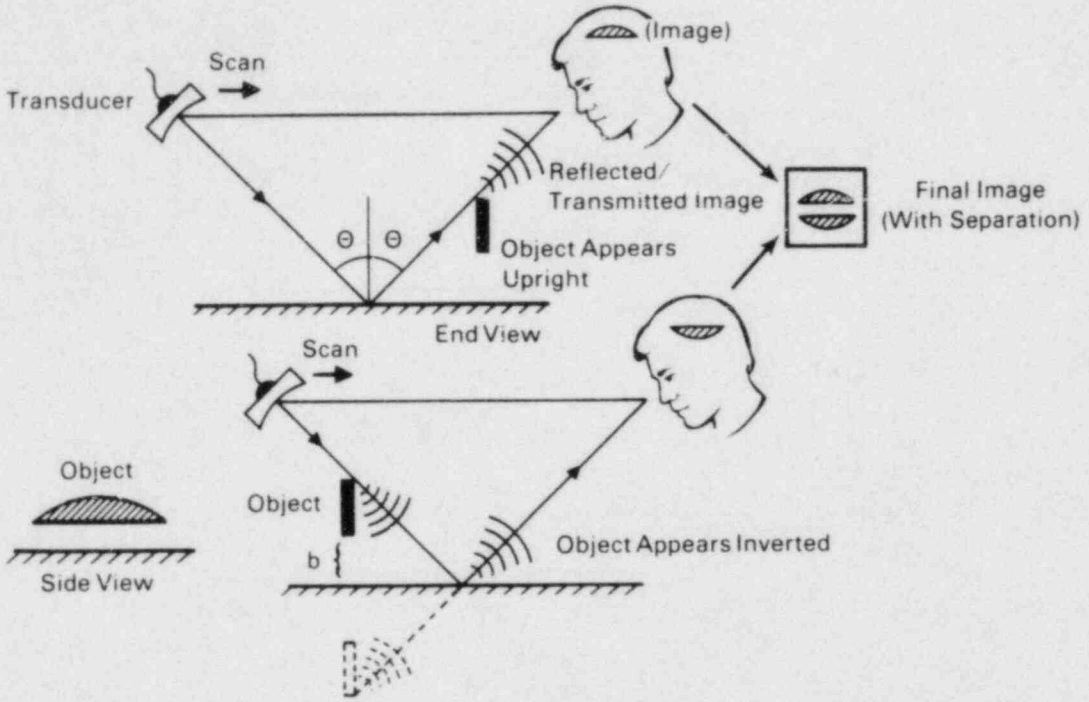

Figure 2. Siamese Image Concept SROS (Object Above Lower Surface).

Send/Receive Scanning Configuration from One Side of the Defect (SRSS)

Imaging a vertical defect from one side using two probes or transducers is usually referred to as the tandem technique. Figure 3 illustrates the basic concept using a scanned source and receiver configuration that generates the siamese image. The scanned source provides object illumination via multiple internal reflections in the block as the receiver scans across the reflected or scattered field above the block and generates the tandem siamese image. Thus, the two scanning configurations (SROS and SRSS) produce approximately the same images with the exception that one sees loss of energy in the image outline

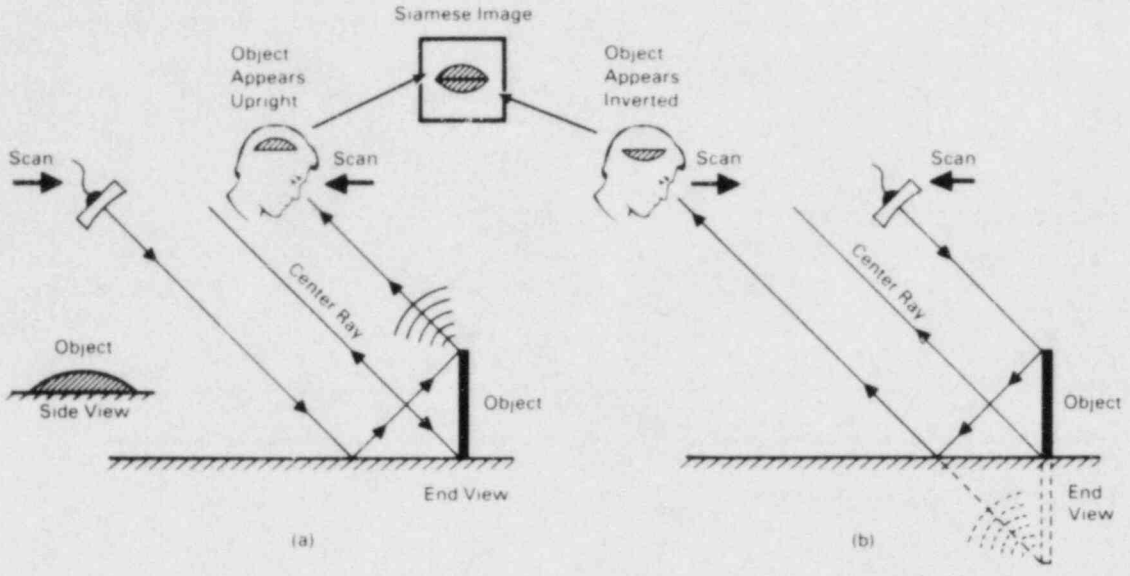

Figure 3. Siamese Image Concept SRSS (Object on Lower Surface).

(SROS) configuration and the presence of energy in the image outline in the tandem (SRSS) configuration.

Geometrical Ray Theory

Simple geometrical ray theory is used to derive the basic equations, as shown in Figure 4, that characterize the defect. The illustration in Figure 4 shows the concept for a non-vertical planar defect above the lower surface (i.e., most general case). The mathematical expressions uniquely define the defect height, inclination, depth, magnification, etc., in terms of simple measurable image parameters and material dimensions. This allows easy calculation of these important defect parameters utilizing only the image, viewing angle, and material dimensions.

Preliminary Experimental Results in Stainless Steel Pipe

Simulated Vertical Cracks in 27 cm Diameter Pipe. The vertical semi-circular type object (i.e., sawcut) simulates a planar crack in pipe weldment and is used to evaluate the system's image resolution capabilities. Figures 5a, b, c, d, and e illustrate the transverse or shear wave pitch/catch construction geometry, and associated siamese images. Broadband pulse illumination centered at 2.42 MHz was used to image the sawcuts.

Figure 5b is the siamese image of the internal sawcut connected to the lower surface. Both images are connected along their baseline as predicted by simple ray theory.

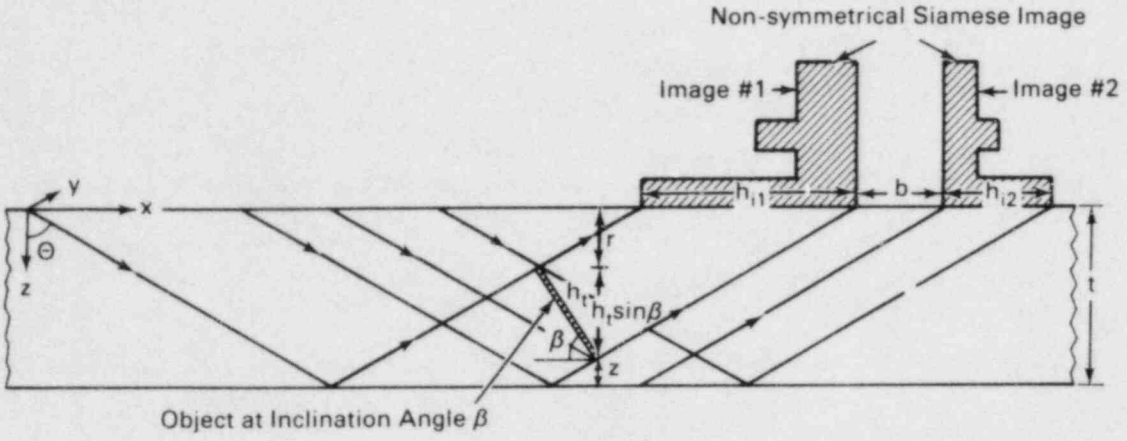

Pitch/Catch Siamese Imaging

True Object Height: $h_t = \sqrt{\frac{(h_{i1} + h_{i2}}{4\sin^2\Theta} - h_{i1}\, h_{i2}}$

Object Inclination Range (β) $\beta = \sin^{-1}\left[\frac{(h_{i1} + h_{i2}}{2h^t\tan\Theta}\right] = \sin^{-1}\left[\frac{h_{i1} + h_{i2}}{2\tan\Theta \sqrt{\frac{(h_{i1} + h_{i2})}{4\sin^2\Theta} - h_{i1}h_{i2}}}\right]$

Object Depth From Upper Surface $r = t - (b/2)\cot\Theta - h_t \sin\beta$

Object Depth From Lower Surface $z = \left(\frac{b}{2}\right)\cot\Theta$

Magnification in "x" Direction: $M_{x1} = \frac{h_{i1}}{h_t} = \left|\frac{\frac{\cos(\pi-\beta) - \tan\Theta\sin\beta}{\cos\beta + \cos(\pi-\beta)}}{2\tan\Theta\sin\beta} - 1\right|$

$M_{x2} = \frac{h_{i2}}{h_t} = \left|\frac{\frac{\cos\beta - \tan\Theta\sin(\pi-\beta)}{\cos\beta + \cos(\pi-\beta)}}{2\tan\Theta\sin(\pi-\beta)} - 1\right|$

Figure 4. Siamese Image Geometry and Associated Parameters.

Figure 5c is the separated siamese image of the external sawcut connected to the upper pipe surface. The exceptionally sharp contrast images define the crack height and length with extremely high resolution. Measurements of through-wall penetration can be easily obtained using simple measurements directly from the image. The predicted internal crack height and length are 8.3 mm and 4.5 mm, respectively. A through-wall penetration of 61% is predicted on the basis of image measurement.

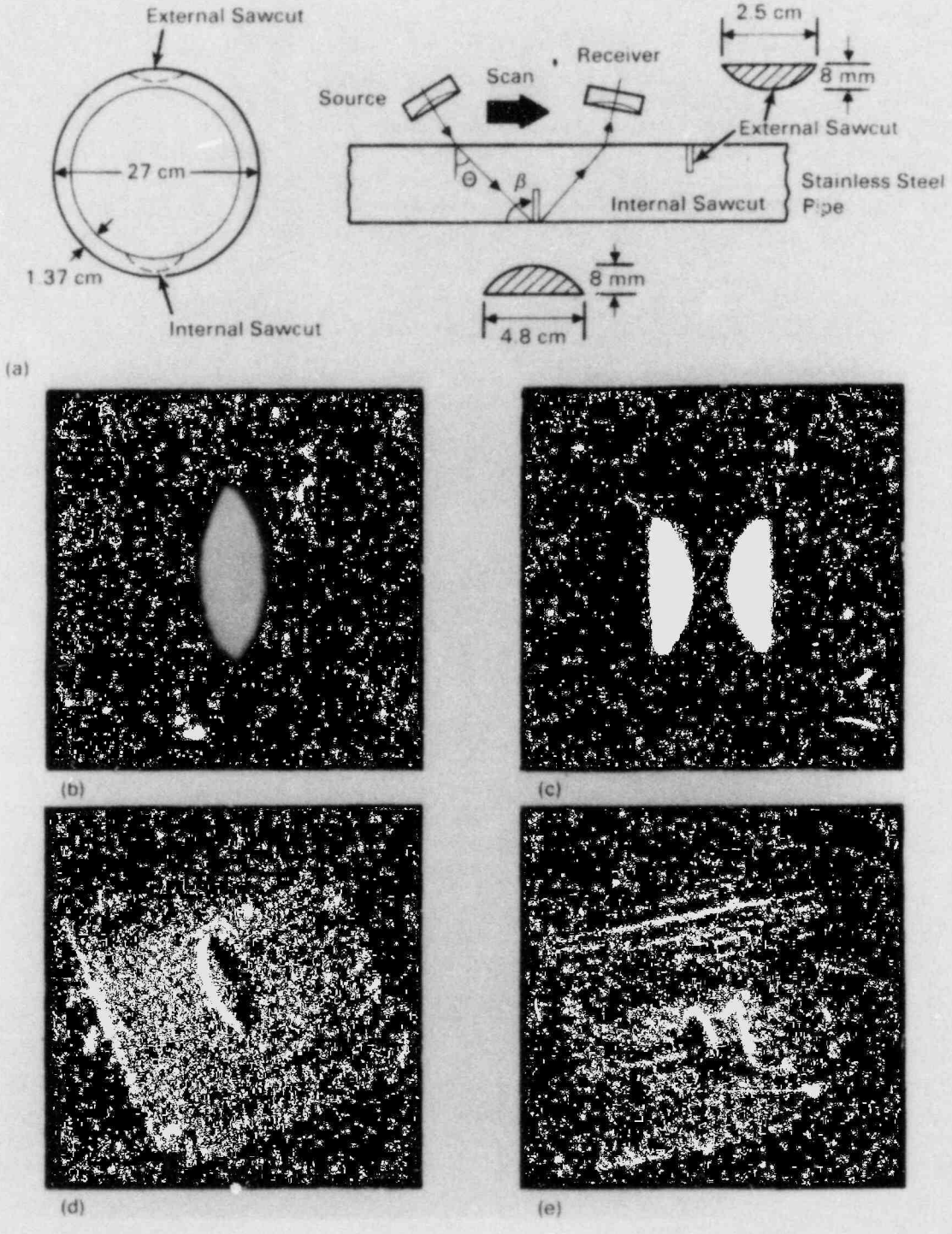

Figure 5. Siamese Image Geometry (SROS) and Shear Wave Images: a) Geometry, b) Internal Sawcut, c) External Sawcut, d) 3-D Internal Sawcut Image, and e) 3-D External Sawcut Image.

Figures 5d and e are the 3-D images of the internal and external sawcuts illustrating the additional information that is available using this format.

Figures 6a, b, c, d, and e illustrate the shear wave tandem construction geometry and associated images of the vertical sawcut in stainless steel pipe. This sequence of tandem images was constructed to compare the image resolution with the previous pitch/catch example. Both the source and receiver are scanned to provide adequate illumination and receiving aperture.

Figure 6a is the tandem geometry showing the multiple skip bounce illumination and the relationship between the source and receiver.

Figure 6b is the siamese image of the internal sawcut showing the typical (normal/inverted) image connected along their baseline. The image is not as sharp as the pitch/catch (see Figure 5b).

Figure 6c is the image of the external sawcut illustrating the unique separation characteristic of a defect not connected to the lower surface.

Figures 6d and e are the 3-D images of the internal and external sawcuts.

In conclusion, the pitch/catch configuration appears to exhibit sharper images with greater resolution, as a result of focusing both the source and receiver. In the tandem example, only the receiver was focused at the defect. Theory predicts greater resolution is achieved when both the source and receiver are focused on the object (i.e., simultaneous source/receiver scanning).

FRACTURE MECHANICS ANALYSES

The objective of the fracture mechanics analyses on this NDE program is to apply deterministic and probabilistic fracture mechanics to guide the development of in-service inspection requirements. Critical factors of concern are NDE sensitivity requirements, inspection intervals, and weld inspection sampling plans.

FRACTURE MECHANICS ANALYSES OF PTS TYPE FLAWS

A series of calculations were performed to consider the types of flaws that are of concern in reactor vessels for Pressurized Thermal Shock (PTS) scenarios. The emphasis was on

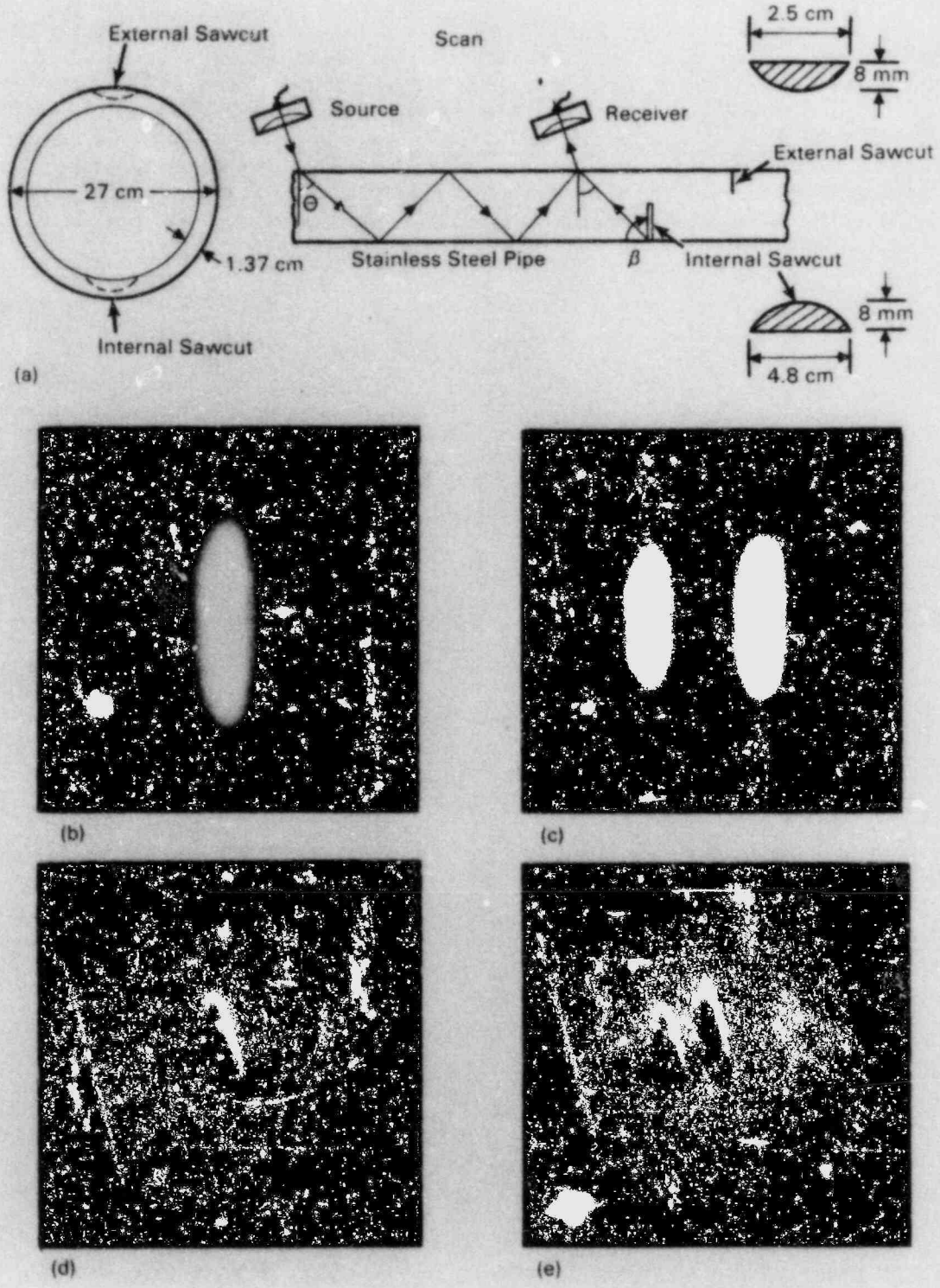

Figure 6. Siamese Image Geometry (SRSS) and Shear Wave Images: a) Geometry, b) Internal Sawcut, c) External Sawcut, d) 3-D Internal Sawcut Image, and e) 3-D External Sawcut Image.

NDE uncertainties, and the implications of incorrect measurements of flaw size and location. Results are reported in Reference 1, which reviews the significant variables of flaw depth, length, location, and orientation required for fracture mechanics evaluations of pressure vessel integrity. Figure 7 shows the range of flaw types considered. The most significant findings of the study showed that cladding effects are important and that flaws well below the cladding to base metal interface need to be considered in PTS evaluations.

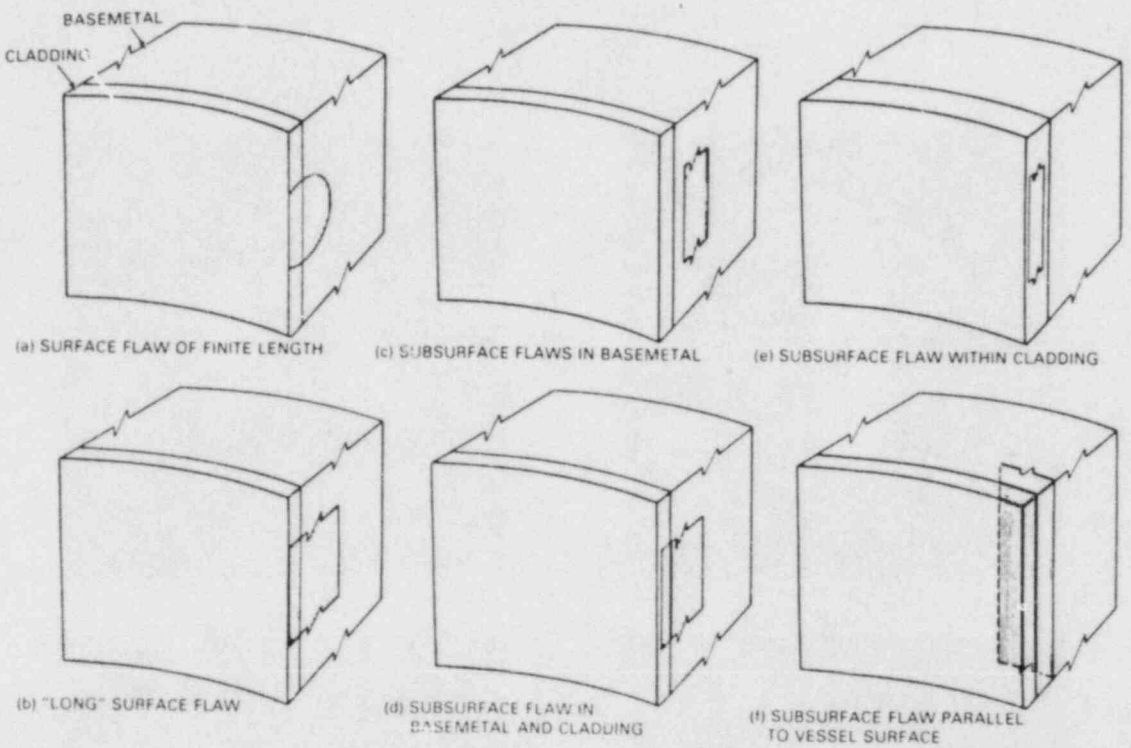

Figure 7. Flaws of Interest to In-service Inspection and Pressure Vessel Integrity.

Figures 8 and 9 show typical results for the critical ratio of crack tip stress intensity factor to the local fracture toughness of the vessel material. Figure 8 indicates the effect of subsurface flaw location and orientation. Clearly flaws with orientations parallel to the vessel surface have no significance to vessel integrity. The predictions also show the relative importance of different subsurface flaws having orientations normal to the surface of the vessel. One can tolerate a flaw at the quarter-wall location that is nearly four times as large as the critical flaw near the inner surface of the vessel. However,

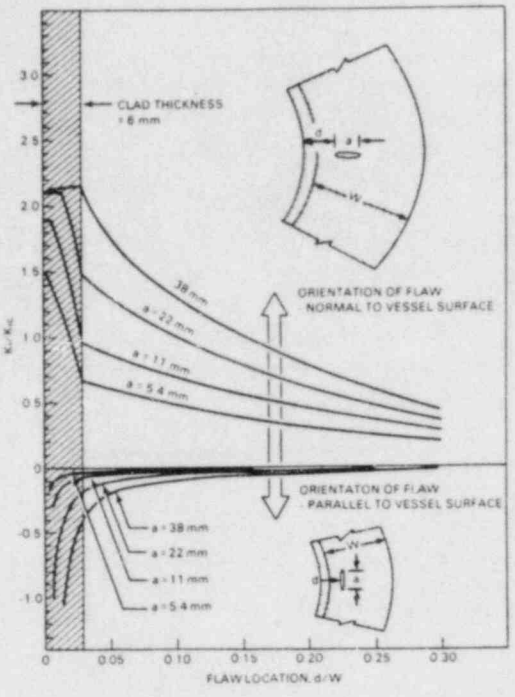

Figure 8. Effect of Subsurface Flaw Location and Orientation on Fracture Evaluation.

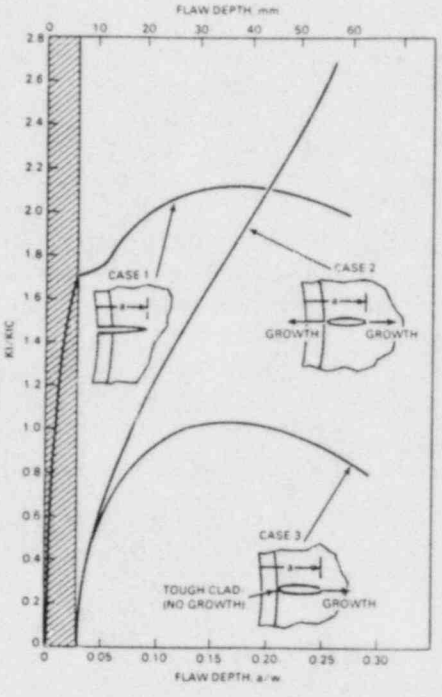

Figure 9. Effect of Cladding on Fracture Evaluation.

flaws at the quarter-wall location are not likely to be detected by the UT methods currently applied in the U.S. for near-surface examination.

Figure 9 addresses the issue of underclad cracks extending into the cladding material. Current NDE methods as practiced in the field are not suited to detect or measure cracking in cladding. These fracture mechanics predictions have been used to evaluate the limitations that result when there are large uncertainties about the presence of cracks in the cladding of a vessel.

The results of these calculations are being used to guide the development of improved NDE methods. The primary conclusions are as follows:

- The importance of flaw depth measurements, as emphasized in current NDE practice, is reinforced by the results of the fracture mechanics analyses.
- It is also important to measure the length and location of flaws becuase these parameters can be as critical as depth in estimates of flaw severity.

- Cracks with orientations parallel to the surface of the vessel are benign. It is thus important that NDE measurements provide a reliable characterization of flaw orientation so that the significance of detected flaws can be correctly evaluated.

- Cladding has a significant effect on crack propagation. Flaws solely or partially in vessel cladding may be more significant than underclad cracks in the base metal of a vessel. It is important that NDE measurements reliably detect and size cracks in cladding to assure that fracture mechanics evaluations are based on realistic assumptions and inputs.

- The most critical subsurface flaws are those near the clad/base metal interface. Priority should continue to be given to detecting and sizing such flaws.

- Flaws located up to a quarter-wall thickness from the vessel inside surface can also impact vessel integrity under thermal shock conditions. Such deeper flaws should not be neglected during in-service inspection. Improvements are required in existing practice to assure the detection and sizing of such deeper flaws. Further analyses should be performed to better define the region of examination and required detection capability. These analyses should consider a broader range of vessel embrittlement conditions and thermal shock transients.

PIPING RELIABILITY USING PRAISE CODE

A series of piping reliability calculations has been completed at Lawrence Livermore Laboratory (LLL). These calculations were performed for PNL as part of the NDE/FM program and were based on data from the PNL piping inspection round robin. Existing fracture mechanics models developed at LLL for the probabilistic fracture mechanics PRAISE code were applied to evaluate the impact of alternate inspection scenarios on piping system reliability. Detailed results of these calculations are given in Reference 2.

The LLL fracture mechanics calculations were for two actual incidents of service cracking:

- thermal fatigue of PWR feedwater line nozzles

- cracking of safe-end nozzles of BWR recirculation lines due to IGSCC.

The detection probabilities described as poor and good were based on PODCI curves which represented the range of performance measured in the round robin on austenitic stainless steel. The advanced detection capability was an estimate of the level of performance that may be achieved within the limitations of field procedures and existing technology.

Figures 10 and 11 provide a summary of the results of the PRAISE code calculations. As can be seen the predicted leak probabilities are high for both cases, and this correlates well with the actual service experience. It can be noted in Figure 11 that there is a clear advantage to the elimination of the poor team by replacement with a team showing a good level of NDE reliability.

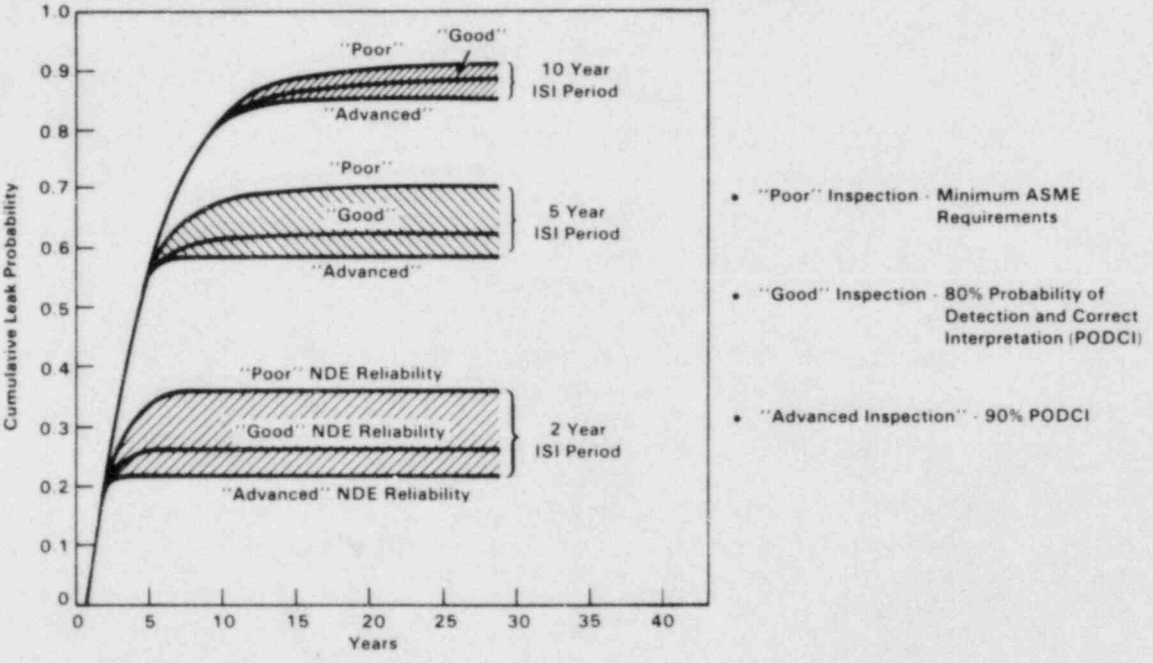

Figure 10. Thermal Fatigue of PWR Feedwater Line Nozzle.

The calculations have evaluated two service failure incidents using the probabilistic fracture mechanics approach. Based on the analysis results for the selected scenarios, the following observations can be made:

1. An effective in-service inspection program requires a suitable combination of flaw detection capability and inspection schedule.

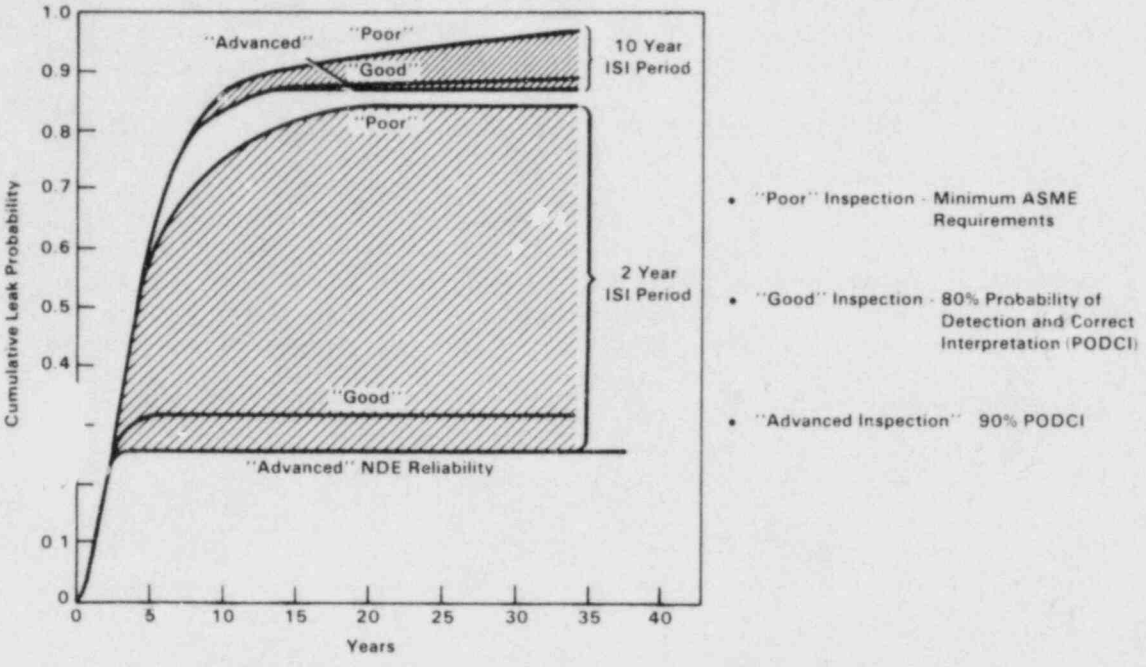

Figure 11. Intergranular Stress Corrosion Cracking of BWR Recirculation Line Nozzle Safe End.

2. An augmented inspection schedule is required for those particular piping lines with fast growing flaws to ensure that the inspection is performed before the flaws reach unacceptable sizes.

3. The first in-service inspection is the most important one, if flaws have the potential to grow to critical size in the early stage of plant life.

4. For the PNL round robin study, the improvement in leak probability reduction from the good team to the advanced team is less than that from the poor team to the good team.

POSITION PAPER ON PIPING ISI

A near term objective of the NDE/FM program at PNL is to draft a comprehensive position paper on in-service inspection of reactor piping. The generation of data from the piping inspection round robin and the associated fracture mechanics calculations to evaluate the implications of these data have been important steps in the evolution of the document. This document will deal with the larger issues of how ISI can improve the safety of systems and components in operating reactors. As such, it will address requirements for weld inspection sampling plans

and inspection intervals, as well as qualification requirements for UT personnel, equipment, and procedures.

Efforts to date have been to identify the general types of criteria that might be used to define acceptable ISI performance. Candidate criteria have been proposed as follows:

1. ISI is employed to reduce the failure rate of a particular component below a specified threshold value.

2. ISI is employed to reduce the failure rate of a component by a specified factor relative to the estimated failure rate for the scenario of no ISI.

3. ISI is employed on a component because it satisfies some cost effectiveness criteria, in that ISI produces a large reduction in failure rate for each safety dollar spent.

4. ISI is employed to find generic failure modes in a reactor population sufficiently early, so that other corrective actions can be performed.

5. ISI is employed as part of the "defense in depth" approach to assure system safety. In this role, ISI provides a means to address the uncertainties that are known to exist in the design and fabrication of components.

In future work PNL staff from the field of Probabilistic Risk Assessment (PRA) will apply the methods of value impact analyses. This effort will help to identify the proper role and justification for piping system ISI within the overall context of reactor safety. Inherent in the value impact type of evaluation is the balance between risk reduction and costs.

Recently completed PRAs for the contribution of intergranular stress corrosion cracking (IGSCC) to piping unreliability in boiling water reactors (BWRs) will be the starting point for evlauations of the role of ISI in reducing risks. These calculations will look at the range of costs and benefits associated with different ISI options.

FUTURE WORK

The major activities to be addressed during FY85 include: complete the qualification document, complete the equipment interaction matrix study, extend pipe inspection round robin results to other pipe diameters and wall thicknesses, complete

advanced UT technique evaluation, complete the study on inspectability of IGSCC through weld overlay, continue support of international NDE reliability activities include CSNI and PISC II, and extend probabilistic fracture mechanics and probabilistic risk assessment to aid in evaluating criteria for defining acceptable ISI performance.

ACKNOWLEDGEMENTS

The authors wish to gratefully acknowledge contributions from other PNL staff members. Foremost among these other PNL staff are R.L. Bickford, D.A. Buelt, S.H. Bush, J.D. Deffenbaugh, G.J. Posakony, D.A. Spanner, L.G. Van Fleet, and K.E. Williamson.

REFERENCES

1. Simonen, F.A., The Impact of Nondestructive Examination Unreliability on Pressure Vessel Fracture Predictions, NUREG/CR-3743, PNL-5062, May 1984.

2. Simonen, F.A. and H.H. Woo, Analyses of the Impact of Inservice Inspection Using a Piping Reliability Model, NUREG/CR-3869, PNL-5149, July 1984.

DEVELOPMENT AND VALIDATION OF A REAL-TIME SAFT-UT SYSTEM FOR INSERVICE INSPECTION OF LWRs*

S.R. Doctor, H.D. Collins, L.P. Van Houten, S.L. Crawford,
T.E. Hall, A.J. Baldwin, R.E. Bowey, R.P. Gribble
Pacific Northwest Laboratory
Operated by Battelle Memorial Institute

1.0 INTRODUCTION

A three-year program is underway at Pacific Northwest Laboratory (PNL) to move the synthetic aperture focusing technique from the laboratory into the field to inspect light water reactor (LWR) components. The objectives of the program are:

- Design, fabricate, and evaluate a real-time flaw detection and characterization system based on SAFT-UT for inservice inspection of all required LWR components.
- Establish calibration and field test procedures.
- Demonstrate and validate the system through actual field reactor inspections.
- Generate an engineering data base to support Code acceptance of the real-time SAFT-UT technique.

The program scope is defined by the following:

- Conduct laboratory tests to provide engineering data for defining SAFT-UT system performance.
- Complete the development of a special processor to make SAFT a real-time process for ISI application.
- Fabricate and field test a fieldable real-time SAFT-UT system on nuclear reactor piping, nozzles and pressure vessels.

This report is a summary of highlights from the second year's efforts. The major areas of work to be presented here are the field trips, the efforts to implement the tandem method, the various attempts at decreasing the SAFT processing computation time, methods to expedite envelope detection, and next year's efforts.

*Work supported by the U.S. Nuclear Regulatory Commission under Contract DE-AC06-76RLO 1830; Dr. J. Muscara, NRC Program Manager.

2.0 TVG AMPLIFIER FABRICATION AND IMPLEMENTATION

The field SAFT system requires digitization of the acoustic RF signal (not detected). The range of the digitizer is 8 bits, which relates to 255 levels or a 48-dB dynamic range. Because a focused beam is used, the signals received from flaws cover a much greater dynamic range. If a conventional linear fixed gain amplifier is used, the large signals will be saturated when high gains are used to see the small signals.

To keep all the signals within the dynamic range of the digitizer, a Time Variable Gain (TVG) amplifier must be used. This TVG amplifier has two parts: 1) a gain controller which generates the control function, and 2) a voltage controlled amplifier.

Preliminary specifications for the voltage controlled amplifier portion were developed covering the following:

- Packaging
- Preamplifier input impedance and protection
- Total system gain and voltage controlled range
- Bandwidth
- Input noise, output swing, and dynamic range
- Overload recovery
- Documentation

A company experienced in supplying state-of-the-art hybrid and discrete amplifier modules to industry agreed to develop a voltage controlled amplifier to our preliminary specifications. After considerable effort, this company delivered a prototype.

Preliminary tests have shown the prototype to perform closely to the specifications. Further tests and the development of the gain controller module is currently being carried out. Upon completion of the tests, the TVG amplifier shall be installed and tested in the field SAFT system. The results of these tests shall be used to develop the final specifications for a new TVG amplifier.

3.0 LABORATORY EXPERIMENTS USING TANDEM SAFT-UT

The sizing of vertically oriented defects using conventional UT and SAFT-UT has not been successfully demonstrated, even though detection of these defects is quite reliable.[1] The difficulty with sizing these defects appears to be related to the fact that most of the ultrasonic energy returned to a transducer, operating in a pulse-echo mode, follows a "corner bounce" path. The time of flight of a pulse following this path is nearly the same as a direct propagation path to the back surface. These two paths are illustrated in Figure 1. Because the time-of-flight profiles produced by these two paths are nearly identical, all of the corner bounce information is placed at the back surface, yielding good detection reliability and poor sizing reliability.[2]

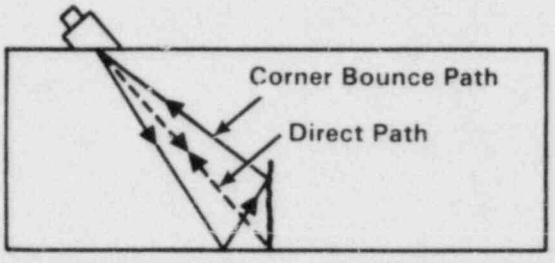

Figure 1. Direct and Corner-Bounce Propagation Paths for Ultrasonic Energy from a Pulse-Echo Transducer.

An experimental program is underway to improve the sizing reliability of SAFT by making use of an alternate means of data collection, called "Tandem".[3] The tandem technique is a transmission technique for producing SAFT images and is illustrated in Figure 2. A small transmitting transducer, producing

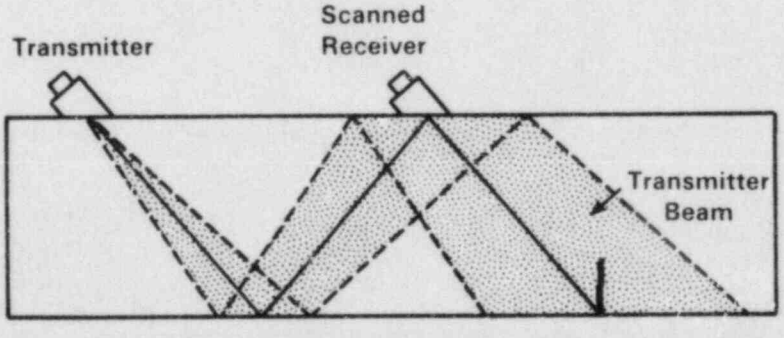

Figure 2. Tandem Transmission Technique for Producing SAFT Images.

a divergent sound field, is used to illuminate a volume to be imaged. Some number of skip bounces are used for this illumination, usually three or five half-V paths. Data is collected using a scanned receiving transducer and an image is formed using SAFT processing by taking the bounce paths into consideration when calculating the time shifts used for processing.

To SAFT process each image point using tandem data, four different propagation paths must be considered as illustrated in Figure 3. The time of flight associated with all four of the paths must be calculated and to do this the absolute thickness of the specimen and the location of the transmitting transducer

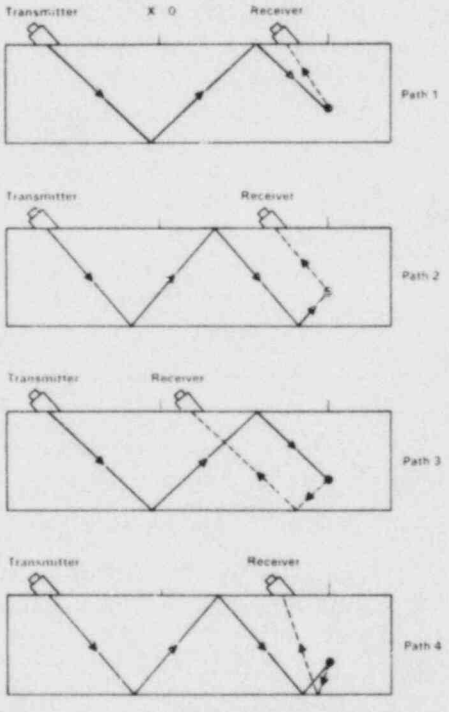

Figure 3. Four Different Propagation Paths for Ultrasonic Energy Produced by the Tandem Transmission Technique.

with respect to the scanned receiver aperture must be known. Analysis of Figure 3 shows that two transmit propagation paths and two receive propagation paths must be considered. Figure 4 illustrates the transmitter paths more clearly. Let X_T and X_P represent the X coordinates of the transmitter and processing points within a specimen of thickness T. To process the image point at D, the two time of flights needed are:

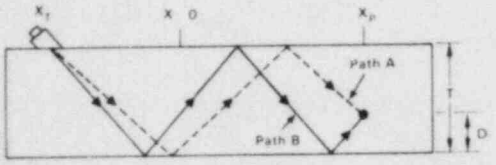

Figure 4. Two Propagation Paths (A and B) from Transmitter to a Point at D.

$$T_A = \sqrt{(X_P - X_T)^2 + (NT + D)^2}\ /v \qquad (1)$$

$$T_B = \sqrt{(X_P - X_T)^2 + (NT - D)^2}\ /v \qquad (2)$$

where T_A and T_B represent the times associated with transmitter paths A and B, respectively; v is the velocity of sound in the material; and N is the number of skip bounces used (in this case N=3).

Figure 5 shows the two receive paths which must be considered for a receiver located at X_R. To process the image point at D, two receiver times needed are:

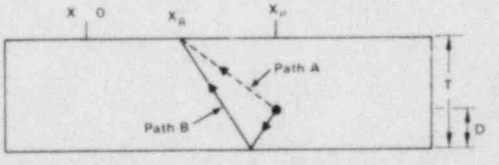

Figure 5. Two Propagation Paths (A and B) from a Point at D to the Receiver.

$$R_A = \sqrt{(X_P - X_R)^2 + (T - D)^2}\ /v \qquad (3)$$

$$R_B = \sqrt{(X_P - X_R)^2 + (T + D)^2}\ /v \qquad (4)$$

It should be noted that the receiver time shifts are dependent only on the position of the receiver relative to image point and not to any absolute position. It is possible, therefore, to store the times R_A and R_B in look up tables to minimize the amount of computation required.

A program called TSAP has been written which implements the tandem processing procedure outlined above. The program has been written specifically to handle the signals produced by corner reflectors (i.e., machine defects and vertically oriented cracks) and so it makes use of only paths 2 and 3 as

described in Figure 3. The program allows the user to choose between (either or both) of these paths at run time.

Figure 6 shows preliminary results of TSAP using a machined defect. The defect consisted of a 1.0-in.-deep sawcut located in a 2.5-in.-thick aluminum test block. From the reconstruction shown, it is evident that TSAP properly orients the defect vertically. The defect appears as a continuous indication 1.0-in. in depth. (The reader will recall from previous reports that normal SAFT processing for this type of defect produces images which consist of two separated indications: one bright indication at the back surface and a second weaker indication near the top of the defect.) The image in Figure 6 was produced using TSAP and specifying path 2 for processing.

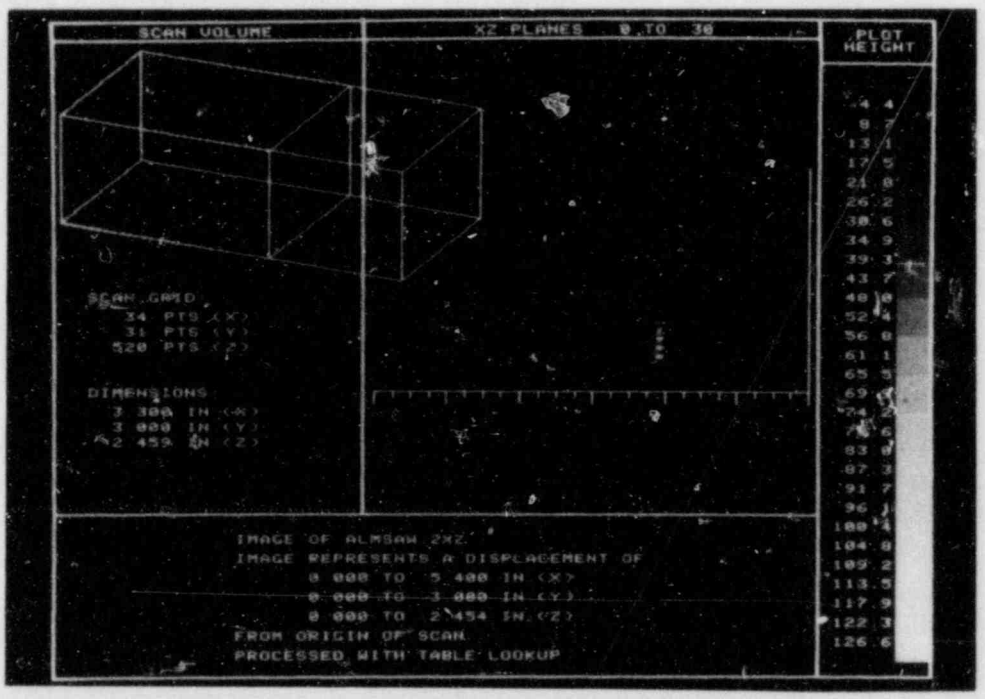

Figure 6. Preliminary Results of TSAP Output (one inch sawcut in 2.25 inch thick aluminum test block). SAFT pulse-echo technique used.

For planar defects which are not vertically oriented or for diffuse reflectors, it may be necessary to also include paths 1 and 4 of Figure 3. Further experimental work is planned in this area using thermal fatigue cracks and ultimately IGSCC.

4.0 SAFT SOFTWARE PROCESSING EFFICIENCY - ATTEMPTS TO REDUCE PROCESSING TIME

In this section a variety of issues and techniques which were considered to improve the SAFT processing speed are reported. The issues studied can be divided into two sections: 1) hardware/operating system and 2) application specific software. Under this second item a number of subtopics will be addressed such as data storage format and software processing logic. Improvements in SAFT processing speed have been achieved as a result of this work.

4.1 HARDWARE/OPERATING SYSTEM ISSUES

SAFT processing of UT data is being performed on a VAX 11/780. This machine is operated using a virtual memory operating system (UNIX at the University of Michigan and VMS at PNL), which provides the computer with the ability to simultaneously handle very large programs and very large data sets. To be specific each process or program running on the computer might, for example, allocate 20 Mbytes of memory, even though only two Mbytes of physical memory are present within the machine. The characteristics of the operating system handle the swapping of needed data and instructions from virtual memory (physically located on disk) into physical memory (RAM). This swapping is handled transparently as far as the user application program is concerned.

Since the swapping (sometimes called paging) operations required in a virtual memory operating system requires input/output (I/O) with the disk, they can significantly affect the performance of the SAFT data processing programs. Two attempts were made to change operating characteristics of the computer that would minimize the amount of swapping required. First, the physical memory was expanded from 2.5 Mbytes to approximately 4 Mbytes. Second, more physical memory was allocated to the batch job area in which SAFT data processing was usually performed. The combined effect of these two changes produced a slight improvement in the processing speed of the machine. Programs ran about 10 percent faster; however, the amount of swapping (page faults) did not apparently decrease. One marked benefit of these changes was that response time for other interactive users of the system was noticeably improved. As a result of this work, it became obvious that some modification of the specific application software was required in order to achieve significant improvements.

4.2 APPLICATION SOFTWARE ISSUES

Over the past year much effort has been directed toward optimizing the SAFT processing as performed on the VAX 11/780.

It was evident from the onset that the processing software, as it existed at that time, was not efficiently utilizing the architecture of the VAX. A number of software modifications were considered in an attempt to reduce the time required for SAFT data processing. Three modifications are described.

4.2.1 Reduced Data Storage

The software developed at the University of Michigan evolved over a period of about seven years. During that time much of the hardware used for SAFT-UT data collection was changed. One change involved switching from a 10-bit transient recorder to an 8-bit transient recorder. To accommodate the data taken by the 10-bit transient recorder, each waveform datum was stored in a 16-bit (short) integer format. The most recent data acquisition systems have made use of an 8-bit transient recorder. Data can be stored in an 8-bit, unsigned character format, thereby reducing the data storage and I/O requirements by a factor of two without affecting data accuracy. This new data format was implemented upon the data acquisition programs, as well as all of the University of Michigan processing programs and related libraries. This change has resulted in about a 10 percent improvement in data processing speed because less swapping is required during the processing phase. The change has resulted in a greater improvement in computer throughput and operator productivity, because data handling requirements have been reduced substantially.

4.2.2 Software Processing Logic

Because the above modifications and additions resulted in only modest improvements in SAFT processing speed, serious redesign of the programming logic was undertaken in an effort to reduce the amount of disk swapping and hopefully increase processing speed. In this section, we describe in some detail, the logic of two programs: a University of Michigan written program (SAP) designed to perform SAFT processing, and a PNL version of the same program (FSAP), which subtantially reduces the amount of virtual memory swapping required for SAFT data processing.

A general purpose synthetic aperture processing program called SAP was analyzed. A skeleton of the processing portion of this program is shown in Figure 7. A two-dimensional look-up table is calculated at each depth and then this table is applied to process all center A-scan points at this depth. The data is processed plane by plane. This logic minimizes the amount of calculation which must be performed and relies on memory management of the computer to access all needed data points. The difficulty with this approach lies in the order in which raw data files are stored: raw data files are stored

```
For each depth:
{
     Calculate a two-dimensional look-up table of shift
     information at this depth

     For each center A-scan x and y position
     {
          For each off-center A-scan x and y position
          {
               Use look-up table to fetch and add all contri-
               buting points
          }
     }
}
```

Figure 7. Skeleton of Logic of the Processing Portion of a General Purpose Synthetic Aperture Focusing Program (SAP).

sequentially as A-scans, and this processing logic forces the data to be accessed as planes. In other words, as a page of data is swapped into physical memory to access a particular point on an A-scan, it is unlikely that any of the other data on that page will be of use in the immediate future. A paging operation is therefore needed to access each data point.

A second version of SAP, called FSAP, was implemented with somewhat different programming logic. Figure 8 shows a skeleton of this new version. Before the main processing loop is entered, a large three-dimensional look-up table is generated containing all of the appropriate time shifts for every point within the transducer sound field. The main processing loop picks a center A-scan position and then processes for each depth. In effect, the data is processed as A-scans (as it is stored) rather than as planes. As a page of memory is swapped into physical memory to access a particular point on an A-scan, the following data points will be used in the processing which immediately follows.

A comparison of SAP and FSAP was performed on a data file containing 1281 A-scans, each 585 points in length. SAP processed this file in 105 minutes and generated nearly 2,000,000 instances when the CPU had to wait for disk swapping (page faults). FSAP processed this same data file in 32 minutes and generated only 8500 page faults. By reducing the memory management and paging tasks, a factor of three improvement in processing speed was achieved. Images produced by both processing programs looked the same.

```
For each depth:
{
     For each off-center A-scan x,y position in local aperture
     {
          Calculate a three-dimensional look-up table of shift
          information
     }
}
For each center A-scan x,y position
{
     For each depth
     {
          For each off-center A-scan x,y position in local
          aperture
          {
               Use look-up table to fetch and add contributing
               points
          }
     }
}
```

Figure 8. Skeleton of Logic of the Processing of FSAP.

4.2.3 Selective Processing

In analyzing the data collected by the SAFT system, it is apparent that there is a very large volume of data. It is also apparent that a large fraction of this data contains very little information, since most of the volume being inspected contains no defects. To take advantage of this frequent occurrence of null data, a selective processing technique was implemented to significantly reduce processing time.

The method chosen to achieve selective processing is relatively simple. For any given flaw, the A-scan centered on that flaw will typically receive the largest reflection. Therefore, it is logical to analyze the center A-scan of a given aperture to make a decision concerning processing. The magnitude of the center A-scan signal is tested prior to processing of that point. If this value is not above an operator selected threshold (typically -20 dB of maximum value), then no off-center A-scans are summed and the single center A-scan is retained for the processed value. However, if the value tested is above the threshold, then processing occurs normally and all associated off-center A-scans are summed into the processed value.

The operator may choose not to implement selective processing simply by entering a threshold level of -40 dB or less.

The results of selective processing are quite significant. A typical pipe data file was used for speed comparisons. The old program (SAP) processed and envelope detected the data in 71 minutes, while the new technique performed this in 6 minutes (a ratio of 12 to 1). The resulting images were comparable in quality and provided the same characterization information.

In pipe situations (typically 1.3 inches in thickness) approximate real-time speeds are achievable on the VAX 11/780. The previous example was processed at a rate of 7 A-scans per second, while real-time is considered to be something greater than 10 A-scans per second.

The field system will be utilizing a VAX 11/730 rather than a 780 which will reduce the actual field processing speed some. It is anticipated that the field system, using the current software without a hardware SAFT processor, will perform pipe SAFT processing at a rate of 2 to 3 A-scans per second. This is an estimate based on the comparable speed of the two processors, but trial test runs have not been performed to date.

5.0 ENVELOPE DETECTION TECHNIQUES

Envelope detection is required by the SAFT-UT process to transform the bipolar, RF ultrasonic waveforms (either raw or processed data) into unipolar, video waveforms. The objective of this section is to review the digital signal processing theory behind envelope detection techniques. The purpose of this review is to document the technique as implemented by the University of Michigan and to describe a related technique based on the use of digital filters. Another technique has been shown to run in software approximately five times faster than the previous technique based on Fourier transforms.

5.1 BACKGROUND

A measured ultrasonic signal $v(t)$ can be represented mathematically as some complicated, real envelope function $e(t)$ modulating a sinusoidal carrier frequency $\sin(2\pi ft)$

$$v(t) = e(t) \sin(2\pi ft) \qquad (5)$$

where f is the center frequency of the pulse and t is time. One means of deriving the envelope function from the measured signal makes it necessary to subject $v(t)$ to a Hilbert transformation.[4] In the time domain, the Hilbert transformation is defined as the convolution of the original signal with the kernel $(-1/\pi t)$:

$$V_{HIL}(t) = \frac{1}{\pi} \int_{-\infty}^{\infty} \frac{v(t')}{(t'-t)}\, dt' \qquad (6)$$

In the frequency domain, the Hilbert transform can be expressed as a multiplicative filter where positive frequency components are multiplied by +i and negative frequency components are multiplied by -i. The Hilbert transformation is equivalent to an allpass filter where the amplitudes of spectral components are left unchanged, but their phases are altered by plus or minus $\pi/2$ depending upon the sign of f. The mathematical representation of this filter is [i sgn (f)]. In effect then

$$V_{HIL}(t) = e(t) \sin (2\pi ft+\pi/2) = e(t) \cos (2\pi ft) \qquad (7)$$

where we have phase shifted the carrier by $\pi/2$.

At this point the envelope function can easily be derived from the original signal

$$e(t) = [v^2(t) + V_{HIL}{}^2(t)]^{1/2}. \qquad (8)$$

From the above discussion, it is clear that the Hilbert transform, which is needed to produce the envelope function, can be implemented in either the frequency domain or the time domain.

5.2 FREQUENCY DOMAIN TECHNIQUES

By far the most efficient means for implementing the Hilbert transform in the frequency domain is to make use of the Fast Fourier Transform (FFT). This process can be represented as follows:

$$V_{HIL}(t) = FFT^{-1}[[i \text{ sgn } (f)] \text{ FFT } [v(t)]]. \qquad (9)$$

The forward FFT transforms v(t) into the frequency domain, where it is multiplied by the Hilbert transform filter and then transformed back to the time domain by means of the inverse FFT. The computational complexity of this process depends on the number of points used to represent the waveform v(t). If M points are used to represent the waveform, then M $\log_2$ M multiplications and additions are needed to perform the two FFTs and M multiplications are needed to perform the frequency domain filtering operations.

5.3 TIME DOMAIN TECHNIQUES

In the time domain, the Hilbert transform can be implemented as a finite impulse response (FIR) digital filter (h) which can be represented as a series of N coefficients. Such a filter is applied by time domain convolution:

$$V_i = \sum_{j=-N/2}^{N/2} v_{i-j} * h_j \qquad (10)$$

where V represents the output and v represents the filter input. An FIR filter is noncausal because the present output V_i is dependent upon the present input (j=0), as well as past (j>0) and future (j<0) values of the input. Implementing an FIR filter requires M x N multiplication and additions where M is the number of points in the total waveform and N is the number of points in the FIR filter.

By comparing the complexity of time and frequency domain techniques, it is evident that the time domain will be more efficient for short length FIR filters and the frequency domain technique will be more efficient than long FIR filter lengths. The break even point occurs when

$$M + 4M \log_2 M \simeq M \times N. \qquad (11)$$

For typical waveforms processed, M = 1024 and so the break even point occurs for N less than 40. Performing envelope detection using an FIR filter less than 40 points in length will be faster than an FFT implementation of the same algorithm.

5.4 FIR FILTER DESIGN

A general FIR filter design algorithm was implemented so that an envelope detection scheme based on digital filters could be designed and tested.[5] The test program allows for a variety of FIR filters (lowpass, highpass, bandpass, bandstop, differentiators, and Hilbert transformers) to be designed.

Figure 9 shows the performance of a combined bandpass and Hilbert transform filter. The coefficients of the filter are represented graphically in the upper right corner of the figure, and the power spectral density of these coefficients are shown in the major portion of the figure. The filter was designed to eliminate the low and high frequency portion of the signal and to perform a $\pi/2$ phase shift on the central portion of the spectrum.

Figure 10 shows an envelope detection algorithm implemented using two digital filters. The "Hilbert and Bandpass" module was demonstrated in the previous figure. The Bandpass module was designed to have the same spectrum; however, the bandpass filter does not produce any phase shift.

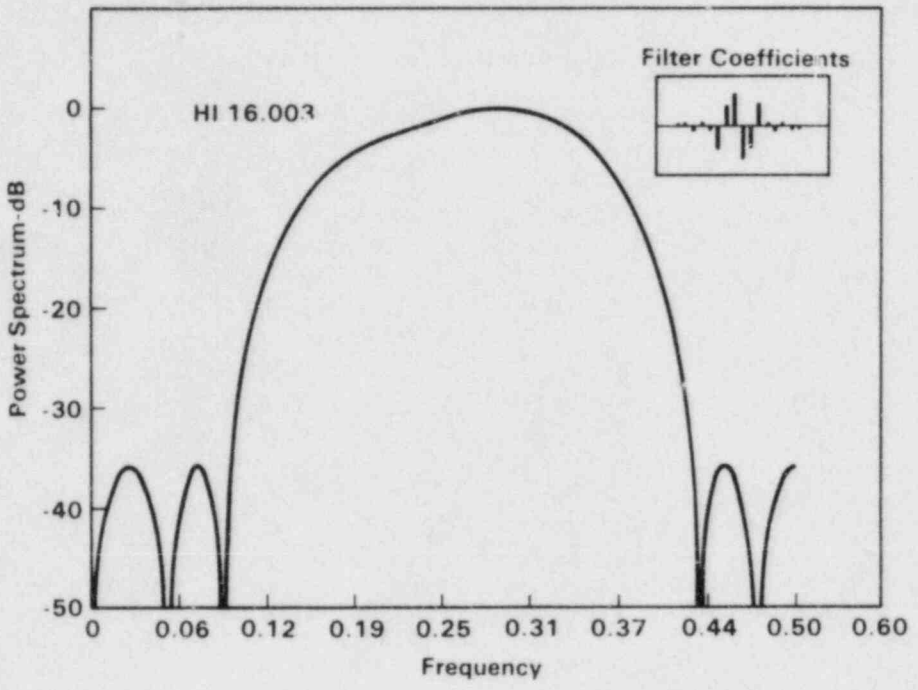

Figure 9. Graph of Performance of a Combined Bandpass and Hilbert Transform Filter.

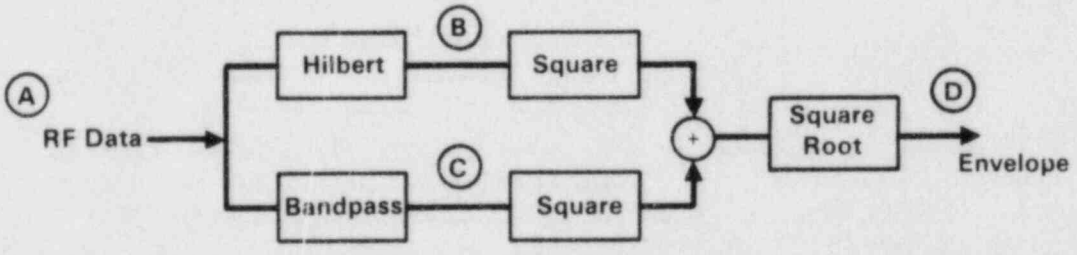

Figure 10. Envelope Detection Algorithm Implemented Using Two Digital Filters.

Figure 11 shows the performance of this algorithm at various stages of the detection process. Panel A shows the input signal, an RF pulse within the passband which has been added to continuous high and low frequency noise. Panels B and C show the outputs of the Hilbert and Bandpass modules. Their filtering characteristic is obvious; however, the relative phase shift is hard to detect. Panel D shows that the output of the detection algorithm produces the true envelope of the input pulsed signal. Panel E shows the result obtained when the absolute value of the filter outputs are simply summed. This is not the true signal envelope in the rigorous mathematical sense, but it does provide a more easily calculated representation of the envelope by avoiding the squaring/square root function.

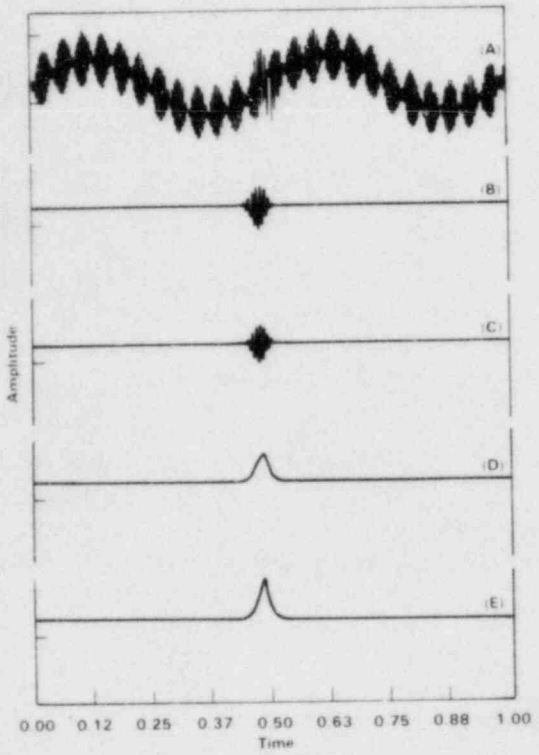

Figure 11. Performance of Envelope Detection Algorithm: a) RF signal, b) and c) Hilbert module and band-pass module output, d) output of detection algorithm, and e) summed absolute values of filter outputs.

This digital filter envelope process has been implemented in current SAFT processing and benchmark tests have shown it to be five times faster than the FFT implementation of the same algorithm. It should be noted that the particular filter coefficients chosen will only perform properly with waveforms sampled at 4 to 6 points/wavelengths.

6.0 FIELD SYSTEM DEVELOPMENT

At the outset of this year, the data acquisition system had been assembled and initial tests on the system were complete. This year has been spent testing and enhancing the field system. The testing effort consisted of many laboratory trials, but most important were the field tests. The system was taken to the field for data acquisition in the real world environment three times. These trips were to:

- General Electric BWR training facility for inspection of the PISC II block.

- Dresden Unit 3 for inspection of the recirculation system piping.

- Vermont Yankee for inspection of the recirculation system piping.

These field trips were extremely valuable for pointing out the system deficiencies as well as reinforcing our confidence in the capabilities of the overall system concept. Although the complete SAFT field system is not complete, the data acquisition system works well.

Although the trip to General Electric BWR training facility did not give us experience in an actual nuclear power plant, it was valuable for testing the portability of the system. Also, it gave us experience scanning flaws in pressure vessel material.

Prior to this trip several changes were made to the system to accommodate data acquisition on thick material. The record length for data storage was increased from 512 bytes to 1024 bytes. This allowed longer A-scans to be stored. The scanner was extensively modified to allow a larger scanned aperture. This was important since larger synthetic apertures are possible with thick material - larger apertures yield higher resolution. This modification, lengthening the scan axis, has proven valuable in subsequent field trips for increasing the flexibility of the scanner. One other enhancement had been previously planned - the use of a square wave pulser in the ultrasonic system. This produces a more broadband ultrasonic pulse in the material which, in turn, enhances depth resolution of the entire system.

Several problems involving low line voltages with periodic voltage drops and motor pulses from the positioning motors coupling through to the received RF signal were encountered in San Jose. After these were overcome, routine scanning was begun.

Due to our lack of familiarity with scanning on 10" thick material, many more views than absolutely necessary (six per volume of interest) were taken. In addition to several calibration scans done on side drilled holes, seven volumes were scanned with a variety of flaw depths. Because of a backlog of data from other sources and the amount of PISC II data, processing and analysis of this data is not complete. Of the portion that has been completed, results have been very good.

So with the confidence that the system was indeed portable and that it would work in an environment where conditions are not carefully controlled, we returned to PNL to improve the system and prepare for our first field exercise to a nuclear power station. Changes to the system included the addition of 200 feet

of cable so that the electronics package could remain outside of the containment area. Since a transducer cannot drive a long cable, it was necessary to add a remote pulser and preamp for the UT system. This addition enhanced the signal quality considerably when compared to the conventional methods used previously.

During this period, the SAFT field system was extensively tested on pipe samples in the laboratory that contain IGSCC defects. This gave us experience in image analysis and helped us define the actual system capabilities. Data collection was performed in the pulse echo mode using the highest frequency possible while retaining a high signal-to-noise ratio. The frequency was 5 MHz or 2.25 MHz depending on the ultrasonic quality of the stainless steel and the material thickness. As the tests went on, a trend developed: detection of flaws became relatively routine, and crack length could be accurately determined. Crack depth information using this technique was not routinely available. It was expected that the tip information of IGSCC would be enhanced by the SAFT technique. However, any enhancement was not sufficient to make these features visible in the processed images. This lack of depth information would later be addressed using the new technique of SAFT-Tandem, which uses two transducers and does not depend on crack tip diffraction for depth sizing as does the pulse echo method.

With confidence in our detection capability and little expectation for crack sizing, we embarked on a field exercise to scan some selected problem areas in the recirculation system of Dresden Unit 3. These welds were areas where two separate teams disagreed over whether or not indications were due to geometry or IGSCC. Four volumes were scanned in 28" pipe and one scan was done on 12" pipe. Four out of the five volumes showed no indications that could be attributed to cracking.

One questionable area did exist in one of the scans. There was a small (1/4" long) crack-like indication in one image. There were also considerable low level indications that occurred up to one inch away from the weld and extended the length of the scan, at or near the back surface. A core sample was taken in this area and no crack was found. Instead, it was found that the back surface had been ground, clad, and ground smooth again.

The system operated flawlessly at Dresden, but some deficiencies were identified. The regions near the welds were often obstructed, making scanner placement difficult at times and impossible in one case. For this reason, the scanner has been shortened by over 5" in length, while still maintaining the capability for a 6" scan length. It was also determined that voice communication between the system operator and the person placing the scanner was absolutely necessary. Prior to this,

communication consisted of relaying information from the operator through a helper to the scan head placer, or gestures over the closed circuit TV system.

While changes were being made to the system, the SAFT-Tandem technique was developed and implemented. This included extensive changes to the SAFT algorithm to allow for the new geometric assumptions used in the two transducer mode. The images from this technique are far better than the images from the pulse echo method. Not only do they give depth information, the reconstructed image is easier to analyze. Also, the weld root indications, which were sometimes difficult to separate from the crack indications, are not imaged well and no longer pose a problem.

One other important change was made to the system at this time. Time variable gain (TVG) and a receiver with exceptionally high signal to noise ratio was added to the system. The high S/N greatly enhanced our imaging capabilities in materials where high gain settings are required. This made the resultant images clearer. TVG was necessitated by the front surface ringdown affect caused by excessive reflection as the ultrasonic energy enters the test piece. This control allows us to image nearer to the front surface.

Other equipment changes were made during this period. A new motor and power supply were added, allowing axial scan speeds as high as 1.25" per second. A parallel gimbal transducer mounting was added giving better transducer-to-pipe contact and orientation. Contact transducers were tested and found to be adequate (but not superior) for imaging in pipe using the pulse echo method. Testing using the SAFT-Tandem method and contact transducers has not been completed.

In July we had our most demanding test of the SAFT data acquisition system, and SAFT in general. We went to Vermont Yankee to develop an independent evaluation of the condition of certain recirculation system welds. These were regions where indications identified as IGSCC in 1983 had decreased in extent or had been reclassified as geometry or metallurgical indications in 1984. The 1984 inspection was far more extensive than the 1983 inspection, involving more advanced equipment such as the ALN-4060 and a P-scan system. Also the inspectors were more experienced with IGSCC detection in the 1984 ISI.

The equipment once again came through the trip unscathed even though the field system crate was damaged when an airline worker dropped the system off of a forklift. As further testimony to the portability of the system, it started up with no problems. We proceeded to scan nine welds with the pulse echo

technique. SAFT-Tandem was used on three welds where substantial indications were located and where clearance was adequate for proper positioning of the scanner.

Analysis of this large volume of data was accelerated by the use of very fast programs developed prior to the trip. This made possible the timely report that followed the trip. Typical examples of results can be seen in Figures 12 to 15. The report basically substantiated the results of the 1984 ISI. However, there was one exception where we called a small region cracked that was called not cracked in the 1984 ISI. The area we disagreed on could easily confuse a manual UT inspection since, in addition to the crack, there were substantial geometry indications.

Figure 12 shows an image from weld 59 at Vermont Yankee (1.25 inch thick stainless steel) and is typical of the images using the pulse-echo method. This is a cross-section view of a crack present. Toward the bottom of the image (the 1.75 inch to 2.0 inch region) is the crack indication. The cloudy region to the right is due to the weld material.

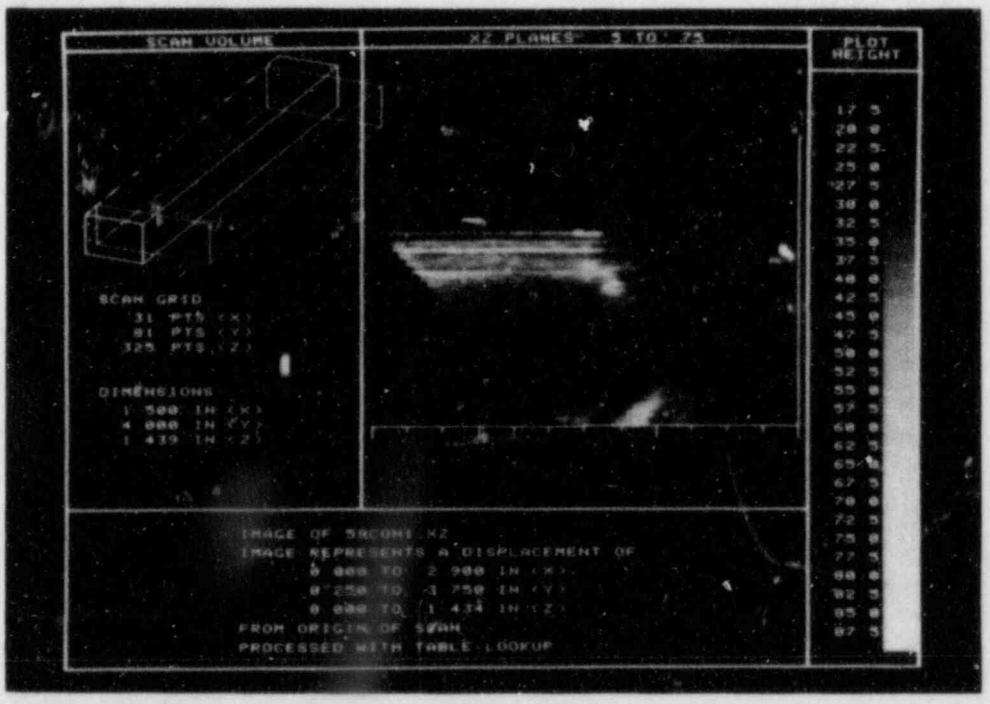

Figure 12. Cross-sectional View of Weld 59 at Vermont Yankee. SAFT pulse-echo technique used.

Another view of the same crack indication is shown in Figure 13. This view is perpendicular to the weld and shows the length characteristic of this particular crack.

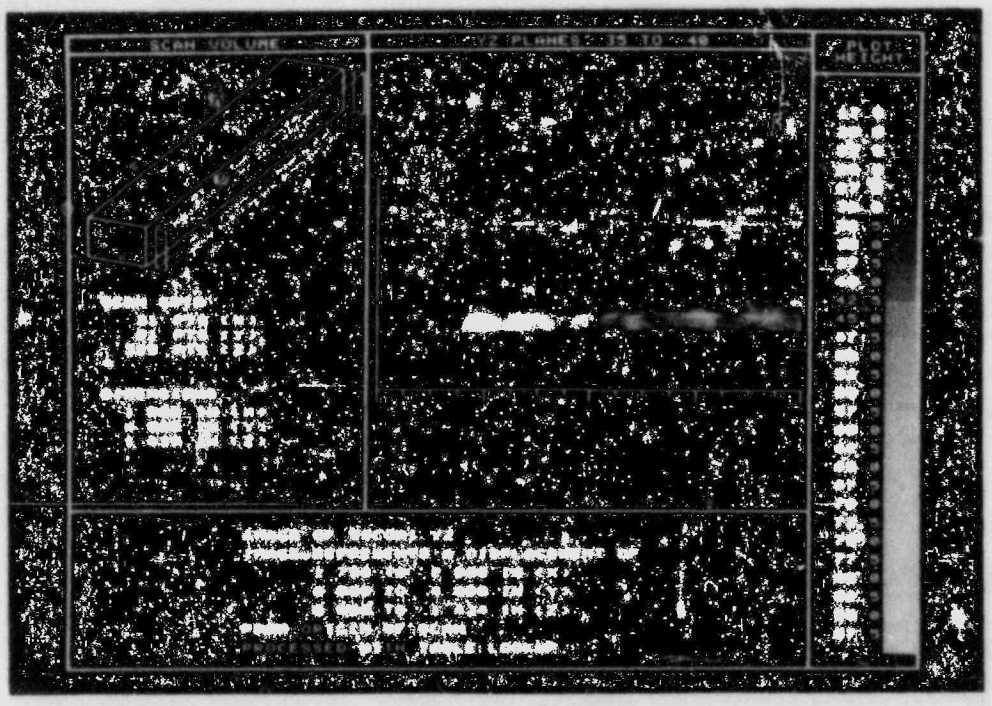

Figure 13. View Perpendicular to Weld Area of Vermont Yankee Weld 59.

SAFT-Tandem technique results are shown clearly in Figures 14 and 15. The material, again, is weld 59 at Vermon Yankee. Figure 14 shows a cross-sectional view, while Figure 15 shows a view perpendicular to the weld area. Note that this method provides sufficient detail to characterize accurately, both the length and depth of the crack indication.

At the review session following this trip, a long list of changes to the system was drawn up. Analysis of this list showed many convenience items and few major problems. The most substantial problem encountered was electronic equipment overheating in the very warm environment. This problem was taken care of in the field with a few fans. A more long-term approach has been to heat sink some high current components and rework some modules to allow more adequate air flow. A need was also identified for easier implementation of the SAFT-Tandem technique. The solution to this problem is presently in progress and involves redesign of the scan axis of the scanner, to allow scanning of both transducers.

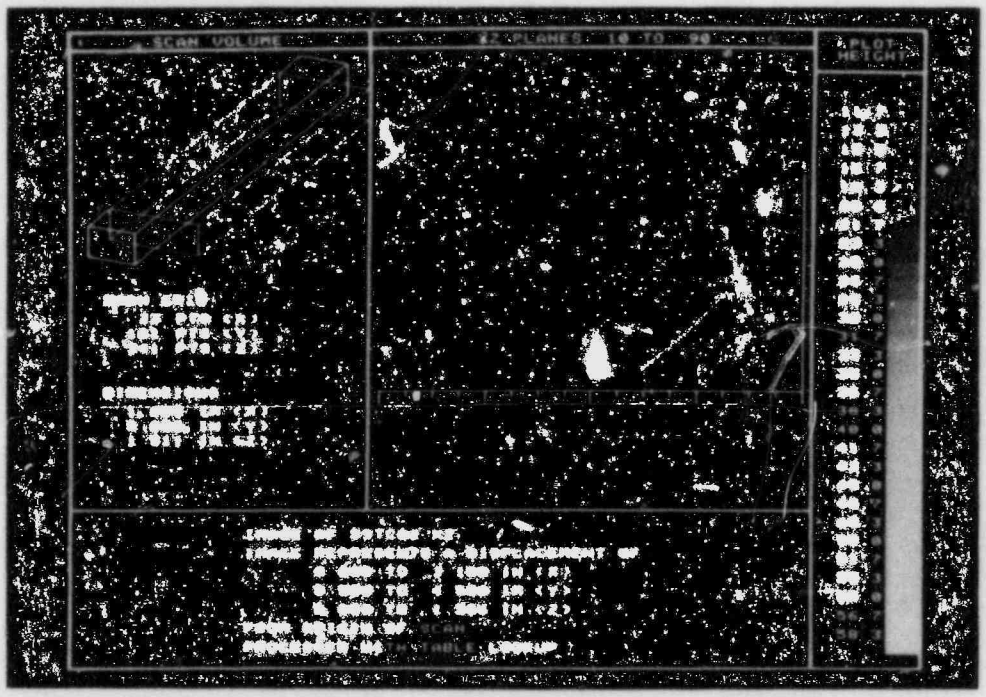

Figure 14. SAFT-Tandem Image of Vermont Yankee Weld 59. Cross-sectional view.

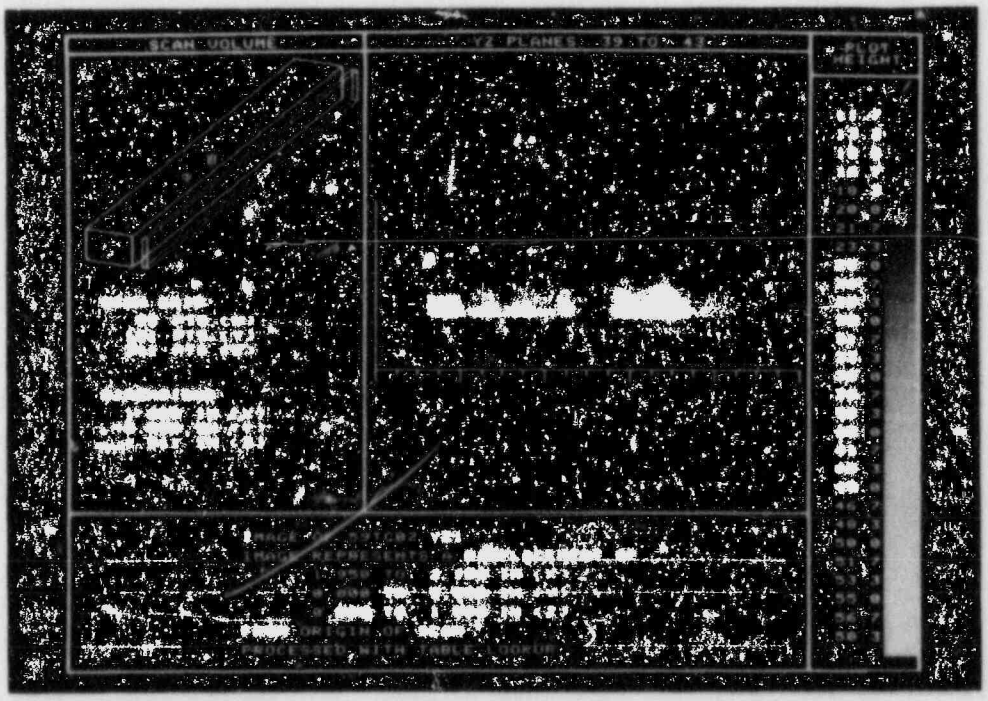

Figure 15. SAFT-Tandem Image of Vermont Yankee Weld 59. Viewed perpendicular to weld.

Other work presently underway but not complete include:

- Analysis of CCSS data previously taken. Initial results look very promising for detection of IGSCC and CCSS.
- Inspection of IGSCC in 10", Schedule 80 pipe samples.
- Analysis of transducer combinations for the SAFT-Tandem technique.
- Analysis of the correlation between image and crack depth in SAFT-Tandem.

In summation, the most important point is that the SAFT data acquisition system is a mature and flexible system that can be used for ISI. It is well prepared for integration into the final real-time SAFT system when the processing and display modules are prepared. The system has had many tests and the equipment and procedures have had many substantial modifications. Some of the more important of these developments were:

- Three successful field exercises
  - Inspection of PISC II at General Electric BWR training facility in San Jose, California.
  - Inspection of recirculation piping at Dresden Unit 3.
  - Inspection of recirculation piping at Vermont Yankee.
- Establishment of the pulse echo technique as a detection technique.
- Development of the SAFT-Tandem technique for sizing.

7.0 FUTURE ACTIVITIES

- Complete assembly of field analysis equipment and software.
- Develop field calibration procedures.
- Redesign scanner for tandem mode implementation.
- Finalize optimum inspection procedures for IGSCC and CCSS.
- Further field trials on nuclear reactor components.
- Reduced processing time.

- Workshops on SAFT technology.
- Code activities.

8.0 REFERENCES

1. Busse, L.J., H.D. Collins, and S.R. Doctor, Review and Discussion of the Development of SAFT-UT, NUREG/CR-3625, 1984.

2. Krautkramer, J. and H. Krautkramer, Ultrasonic Testing of Materials, 3rd Ed., p. 469-470, Springer-Verlag, 1983.

3. Bracewell, R.N., The Fourier Transform and Its Application, p. 267-272, Academic Press, 1978.

4. Rabiner, L.R. and B. Gold, Theory and Application of Digital Signal Processing, Chapter 3, Prentice-Hall, 1975.

5. Busse, L.J., H.D. Collins, and S.R. Doctor, "The Emerging Technology of Synthetic Aperture Focusing for Ultrasonic Testing," presented at the 1984 Pressure Vessel and Piping Conference, San Antonio, TX, 84-PVP-122, June 18-20, 1984.

EVALUATION OF METHODS FOR LEAK DETECTION IN REACTOR PRIMARY SYSTEMS AND NDE OF CAST STAINLESS STEEL

D. S. Kupperman and T. N. Claytor
Materials Science and Technology Division
Argonne National Laboratory
Argonne, Illinois 60439

and

D. W. Prine and T. A. Mathieson
Chamberlain Mfg. Corporation
GARD Division
Niles, Illinois 60648

ABSTRACT

No currently available, single leak-detection method combines optimal leakage detection sensitivity, leak-locating ability, and leakage measurement accuracy. Technology is available to improve leak detection capability at specific sites by use of acoustic monitoring. However, current acoustic monitoring techniques provide no source discrimination (e.g., to distinguish between leaks from pipe cracks and valves) and no leak-rate information (a small leak may saturate the system). Leak detection techniques need further improvement in the following areas: (1) identifying leak sources through location information and leak characterization, to eliminate false calls; (2) quantifying and monitoring leak rates; and (3) minimizing the number of installed transducers in a "complete" system through increased sensitivity.

Six cracks, including two field-induced IGSCC specimens and two thermal-fatigue cracks, have been installed in a laboratory acoustic leak detection facility. The IGSCC specimens produce stronger acoustic signals than the thermal-fatigue cracks at equivalent leak rates. Despite significant differences in crack geometry, the acoustic signals from the two IGSCC specimens, tested at the same leak rate, are virtually identical in the frequency range from 200 to 400 kHz. Thus, the quantitative correlations between the acoustic signals and leak rate in the 300-400 kHz band are very similar for the two IGSCC specimens. Also, acoustic background data have been acquired during a hot functional test at the Watts Bar PWR. With these data, it is now possible to estimate the sensitivity of acoustic leak detection techniques. In addition, cross-correlation techniques have been successfully used in the laboratory to locate the source of an electronically simulated leak signal.

The adequacy of current inspection techniques for cast stainless steel (CSS) piping has not been demonstrated. For the near term, improvements that may increase the reliability of ultrasonic inspection include (1) the development of methods to establish the microstructure of the material (to help optimize the

*Work supported by the U.S. Nuclear Regulatory Commission, Office of Nuclear Regulatory Research.

inspection technique), (2) calibration standards that are more representative of the material to be inspected, and (3) the use of cracked CSS samples for training purposes. For the long term, it will be necessary to establish (1) the variability of the microstructure of CSS, (2) the effect of microstructure on inspection reliability, and (3) the degree of improvement possible with techniques and equipment designed specifically for CSS, e.g., focused transducers and lower frequencies than those used conventionally.

I. LEAK DETECTION IN REACTOR PRIMARY SYSTEMS

A. Background

No currently available single leak-detection method combines optimal leakage detection sensitivity, leak-locating ability, and leakage measurement accuracy. For example, while quantitative leakage determination is possible with condensate flow monitors, sump monitors, and primary coolant inventory balance, these methods are not adequate for locating leaks and are not necessarily sensitive enough to meet regulatory guide goals. The technology is available to improve leak detection capability at specified sites by use of acoustic monitoring or moisture-sensitive tape. However, current acoustic monitoring techniques provide no source discrimination (e.g., to distinguish between leaks from pipe cracks and valves) and no leak-rate information (a small leak may saturate the system). Moisture-sensitive tape provides neither quantitative leak-rate information nor specific location information other than the location of the tape; moreover, its usefulness with "soft" insulation needs to be demonstrated. Hence, leak detection techniques need further improvement in the following areas: (1) identifying leak sources through location information and leak characterization, to eliminate false calls; (2) quantifying and monitoring leak rates; and (3) minimizing the number of installed transducers in a "complete" system through increased sensitivity.

B. Objectives

The objectives of the leak detection program are to (a) develop a facility for the quantitative evaluation of acoustic leak detection (ALD) systems; (b) assess the effectiveness and reliability of ALD techniques; (c) evaluate a prototype ALD system; (d) establish the sensitivity, reliability, and decision-making capability of a prototype system through laboratory testing; and (e) assess the effectiveness of field-implementable ALD systems. The program will establish whether meaningful quantitative data on leak rates and location can be obtained from acoustic signatures of leaks due to IGSCC and fatigue cracks in low- and high-pressure lines, and whether these can be distinguished from other types of leaks. It will also establish calibration procedures for acoustic data acquisition and show whether advanced signal processing can enhance the adequacy of ALD schemes.

C. Review of Current Practice

Regulatory Guide 1.45 recommends the use of at least three different detection methods in reactors to detect leakage. Monitoring of both sump-flow and airborne-particulate radioactivity is mandatory. A third method can involve either monitoring of condensate flow rate from air coolers or monitoring of airborne gaseous radioactivity. Although the current methods used for leak detection reflect the state of the art, other techniques may be developed and used. Regulatory Guide 1.45 also recommends that leak rates from identified and unidentified sources be monitored separately to an accuracy of 1 gal/min,* and that indicators and alarms for leak detection be provided in the main control room.

Since the recommendations of Regulatory Guide 1.45 are not mandatory, the technical specifications for 74 operating plants including PWRs have been reviewed by the present authors to determine the types of leak detection methods employed, the range of limiting conditions for operation, and the surveillance requirements for the leak detection systems.

All plants use at least one of the two systems specified by Regulatory Guide 1.45: All but eight use sump monitoring, and all but three use particulate monitoring. Monitoring of condensate flow rate from drywell air coolers and monitoring of atmospheric gaseous radioactivity are also used in many plants.

The allowed limits on unidentified coolant leakage are shown in Fig. 1 (upper panel). The limit for all PWRS is 1 gal/min, whereas the limit for most BWRs is 5 gal/min. The limits on total leakage (Fig. 1, lower panel) are generally 10 gal/min for PWRs and 25 gal/min for BWRs. (Regulatory Guide 1.45 does not specify leakage limits, but does suggest that the leakage detection system should be able to detect a 1-gal/min leak in 1 h.) In some cases, limits on rates of increase in leakage are also stated in the plant technical specifications. Two BWRs have a limit of 0.1 gal/min/h; four have a limit of 0.5 gal/min/h.

Surveillance periods for BWRs and PWRs are indicated in Fig. 2 (upper panel). Leakage is checked every 12 h in most PWRs, and every 4 or 24 h in most BWRs. One BWR specifies that a continuous monitor with control room alarm shall be operational. The intervals between successive system calibrations and checks are indicated in Fig. 2 (lower panel). For BWRs, calibration is generally performed at 18-month intervals; functional tests are performed every month.

Generally speaking, reactors rely on sump pump monitoring to establish the presence of leaks. Other methods appear to be less reliable or less convenient. In most reactors the surveillance periods are too long to detect a 1-gal/min leak in 1 h, as suggested by Regulatory Guide 1.45, but it appears that this sensitivity could be achieved if monitoring procedures were modified. None of the systems provides any information on leak location, and leaks must be located by visual examination after shutdown. Since cracks may close when the reactor is shut down, reducing flow rates considerably, it would be desirable to be able to locate cracks during plant operation.

*Conversion factor: 1 gal/min = 3800 cm^3/min.

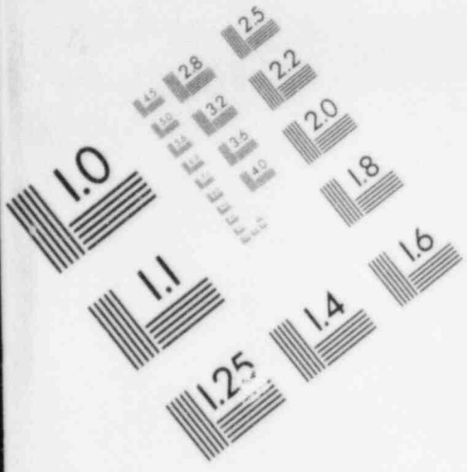

IMAGE EVALUATION TEST TARGET (MT-3)

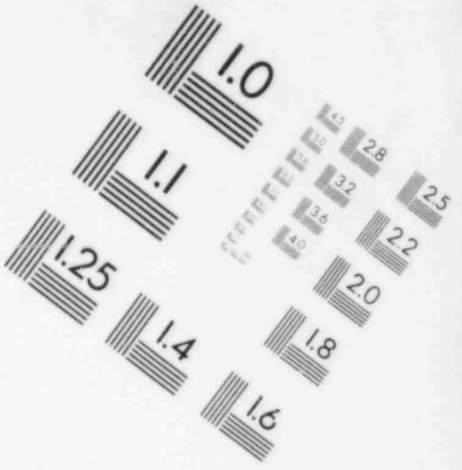

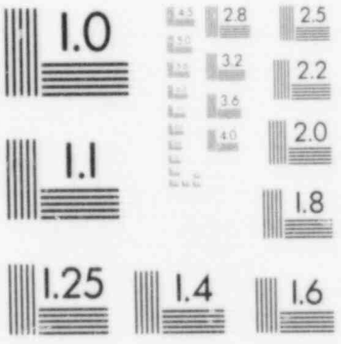

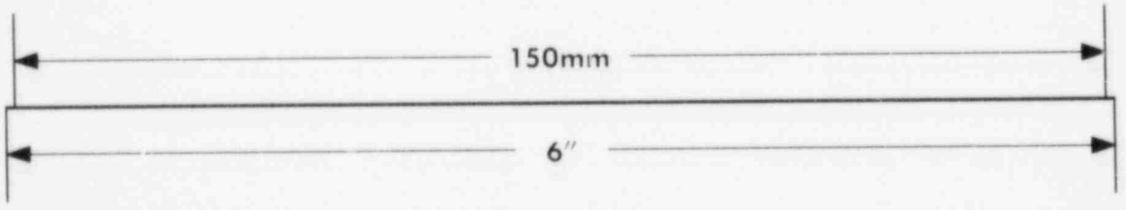

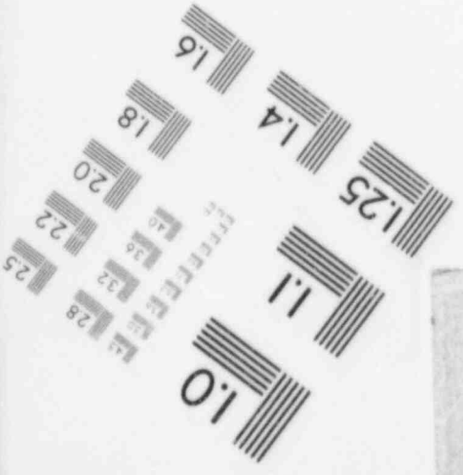

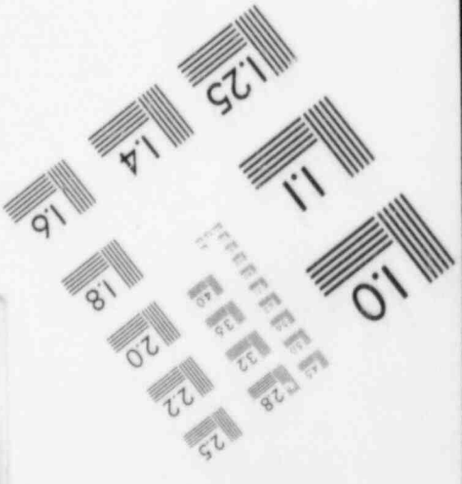

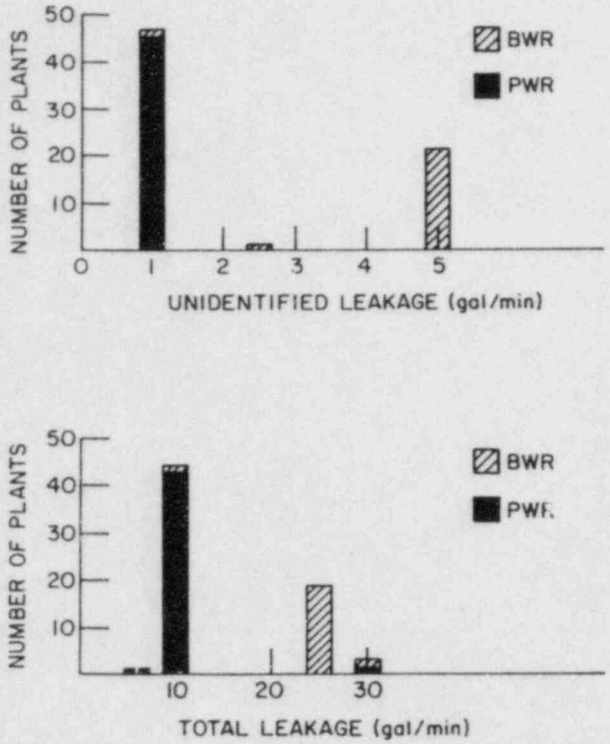

Fig. 1. Amounts of Unidentified and Total Coolant Leakage Allowed at BWRs and PWRs. Conversion factor: 1 gal/min = 3800 cm^3/min.

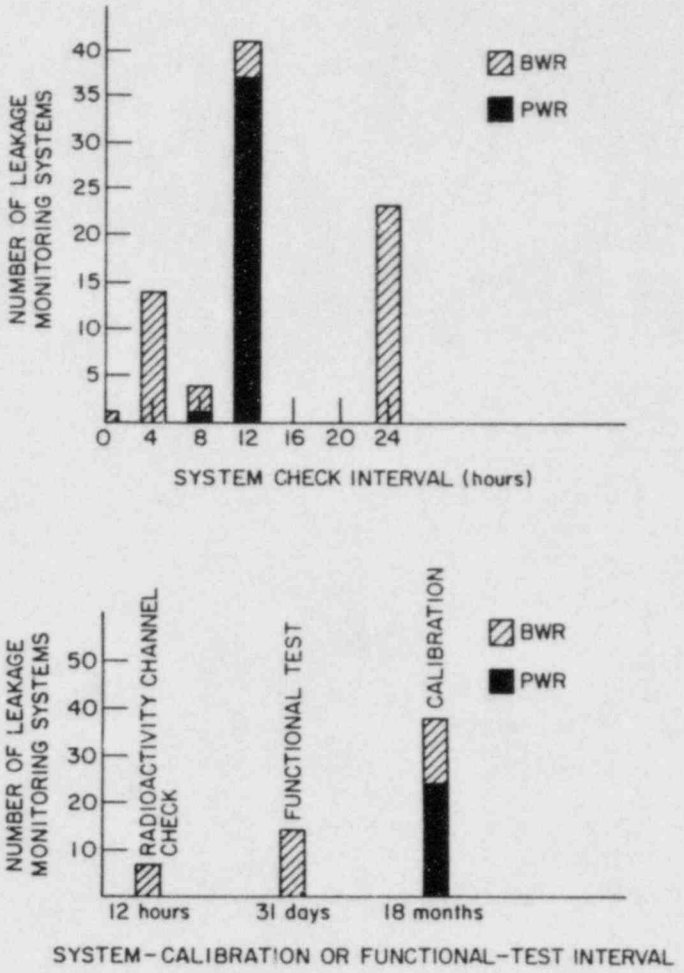

Fig. 2. Surveillance Periods (Top) and Test Calibration Intervals (Bottom) for BWRs and PWRs.

The estimated sensitivity of leakage monitoring is occasionally addressed in the technical specifications. For example, one specification indicates that air particulate monitoring can, in principle, detect a 0.013-gal/min leak in 20 min, that the sensitivity of gas radioactivity monitoring is 2-10 gal/min, and that the sensitivity of condensate flow monitoring is 0.5-10 gal/min. Continuous sump pump monitoring appears capable of detecting a 1-gal/min leak in 10-60 min.

The impact of Reactor Coolant Pressure Boundary leakage detection systems on safety was evaluated for eight reactors as part of the Integrated Plant Safety Assessment-Systematic Evaluation Program (SEP) and described in eight SEP reports (NUREG-0820 through -0827). In four of the eight reactors evaluated, a 1-gal/min leak could not be detected within 1 h; and four of the eight reactors did not have three leakage monitoring systems, contrary to the suggestions in Regulatory Guide 1.45. The fracture mechanics and leak rate calculations in the SEP reports are consistent with other studies which indicate that (1) current leak detection systems will detect through-wall cracks 10-25 cm (4-10 in.) long in 12- to 28-in. piping within one day, and (2) current leakage limits will necessitate plant action after such a detection event. Since these cracks are much smaller than those required to produce failure in tough reactor piping, improved leak detection systems may offer little safety benefit for this particular class of flaws when crack growth occurs by a relatively slow mechanism. However, the SEP reports state that local leak detection systems may be necessary for some postulated break locations where separation and/or restraint is not a practical way to mitigate the effects of a high-energy pipe break.

Although current leak detection systems are adequate to ensure a leak-before-break scenario in the great majority of situations, the possibility that large cracks may produce only low leak rates must also be considered. This could arise because of corrosion plugging or fouling of relatively slowly growing cracks or the relatively uniform growth of a long crack before penetration. In such cases the time required for a small leak to become a significant leak or rupture could be short, depending on crack geometry, pipe loading, and transient loading (a seismic or water hammer event). Furthermore, with existing techniques such as sump pump monitoring, no information on leak location is available.

The shortcomings in existing leak detection systems are not simply a matter of conjecture. The Duane-Arnold safe-end cracking incidents and Indian Point Unit 2 fan cooler leakage indicate that the sensitivity and reliability of current leak detection systems are clearly inadequate in some cases. In the Duane Arnold case, the plant was shut down on the basis of the operator's judgment when a leak rate of 3 gal/min was detected; however, this leakage rate is below the required shutdown limit for almost all BWRs (see Fig. 1). Examination of the leaking safe-end showed that cracking had occurred essentially completely around the circumference. The crack was throughwall over about 20% of the circumference and 50-75% throughwall in the non-leaking area.

Simply tightening the current leakage limits is not an adequate solution to these shortcomings, since this might produce an unacceptably high number of spurious shutdowns owing to the inability of current leak detection systems to identify leak sources.

One other safety-related aspect of improved leak detection systems concerns radiation exposure of plant personnel. Improved systems with leak location capability could reduce the exposure of personnel inside the containment and could present an attractive alternative to augmented ISI. Improved leak detection is consistent with the defense-in-depth philosophy of the NRC and would lead to earlier detection of system degradation.

D. Technical Progress

1. Comparison of Acoustic Leak Data from Different Crack Types

Two IGSCC specimens, two thermal fatigue cracks (TFCs), and one mechanical fatigue crack (FC) have been installed in the ALD facility at ANL. The crack widths and lengths at the pipe outer surface are indicated in Table 1. Figure 3 shows acoustic leak data acquired from these five cracks. These data are normalized to a 375-kHz acoustic emission (AET-375) transducer on a waveguide with a water temperature of 260°C (500°F) and pressure of 7.7 MPa (1100 psi). The largest correction is for the mechanical fatigue crack FC #1. Corrections for the other data are less than 6 dB. Transducer signals indicated in Fig. 3 are for a 300-400 kHz bandwidth and represent the signal after electronic noise levels are subtracted. The acoustic signals from the fatigue cracks vary approximately as (leak rate)$^{0.7}$, whereas the signals from the IGSCC vary approximately as (leak rate)$^{0.37}$. Frequency analysis also indicates less dependence of acoustic signal on frequency for the IGSCC specimens than for the fatigue cracks. An analysis of the frequency spectrum may provide information on the source of acoustic leak signals. The excellent matching of acoustic leak data in the 300-400 kHz range for the two IGSCC specimens, despite their different geometries, suggests that it may be possible to derive leak rate information from the amplitude of the acoustic leak signal in this frequency range.

Table 1. Outer-Surface Lengths and Widths of Cracks Used in ALD Studies

Crack	Length, cm	Width, μm
IGSCC #1	0.23	90
IGSCC #2	1.10	60-80
TFC #1	2.64	75-100
TFC #2	1.24	40-100
FC #1	0.52	150-200

Detection of a leak requires that $S_e = S_l - T_l - N_l + PG > 0$, where S_e = signal excess at detector output, S_l = source level (affected by waveguide geometry, insulation, and circumferential position), T_l = transmission loss down pipe, N_l = background noise level, and PG = system gain (all in dB). The acquisition of acoustic leak data, background noise estimates (from Hatch and Watts Bar), and attenuation data allows a rough estimation of the sensitivity of an ALD system under field conditions. Figure 4 shows predicted signal-to-noise ratios (in dB) vs distance along a 10-in. Schedule 80 pipe for three leak rates and three levels of estimated acoustic background noise.

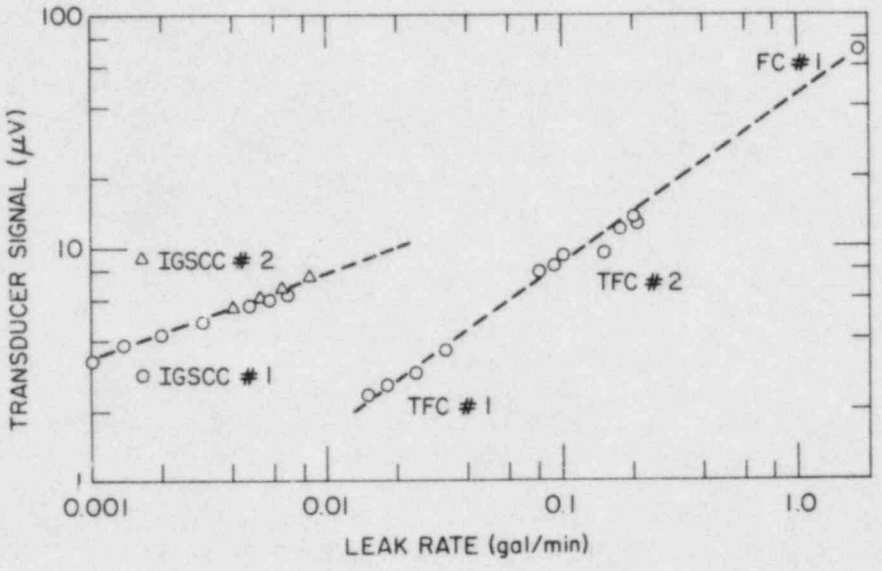

Fig. 3. Acoustic Leak Data from the Cracks Listed in Table 1. Data are normalized as described in the text. Signal amplitudes are for a 300-400 kHz bandwidth after electronic background noise is subtracted.

The highest level is estimated from the maximum acoustic level obtained during the Watts Bar hot functional test when the reactor was at operating temperature and pressure. The lowest level is obtained from an indirect estimate of background noise from Hatch and the assumptions that the reactor acoustic background level will vary by a factor of 10 in the plant and that the measurement at Watts Bar was an upper-limit value. The striped area suggests possible enhancement of the acoustic signal for a 0.1-gal/min leak rate in a situation where the leak plume strikes the reflective insulation. Results of laboratory experiments suggest that for leak rates greater than 0.02 gal/min but less than 0.2 gal/min, signals could be enhanced significantly, given the correct circumstances. The following equation has been used to generate the curves of Fig. 4:

$$S = 20 \log_{10} \left(\frac{70R^{0.32}}{B} \right) - \begin{Bmatrix} 4.5D \text{ for } D < 3 \text{ m} \\ 5.6 + 1.7D \text{ for } D \geq 3 \text{ m} \end{Bmatrix} + \begin{Bmatrix} 6 \text{ if } 0.01 < R \leq 0.1 \end{Bmatrix} , \quad (1)$$

where S is the signal-to-noise ratio in dB, R is the leak rate in gal/min, B is the acoustic background level in μV (4, 20, or 40), and D is the distance from the leak in meters. Equation (1) assumes a signal loss of 4.5 dB for the first 2 m, followed by a further loss of 1.7 dB/m. The acoustic signal is assumed to vary as $(\text{leak rate})^{0.32}$. A 6-dB signal enhancement is added to the 0.1-gal/min curve to indicate how the presence of reflective insulation could improve the signal-to-noise ratio. For low acoustic background levels, a 1-gal/min leak would be detected at a distance of 11 m. With a high background level, this leak would be detected only at a distance of 1 m.

Acoustic leak data have also been obtained from a small (3-mm-diam) valve with a stem leak. An AET-375 transducer, on a waveguide attached directly to the valve body, was employed to acquire data from a 0.01-gal/min, 270°C (520°F) leak. The signal obtained was 35 dB above the electronic background level.

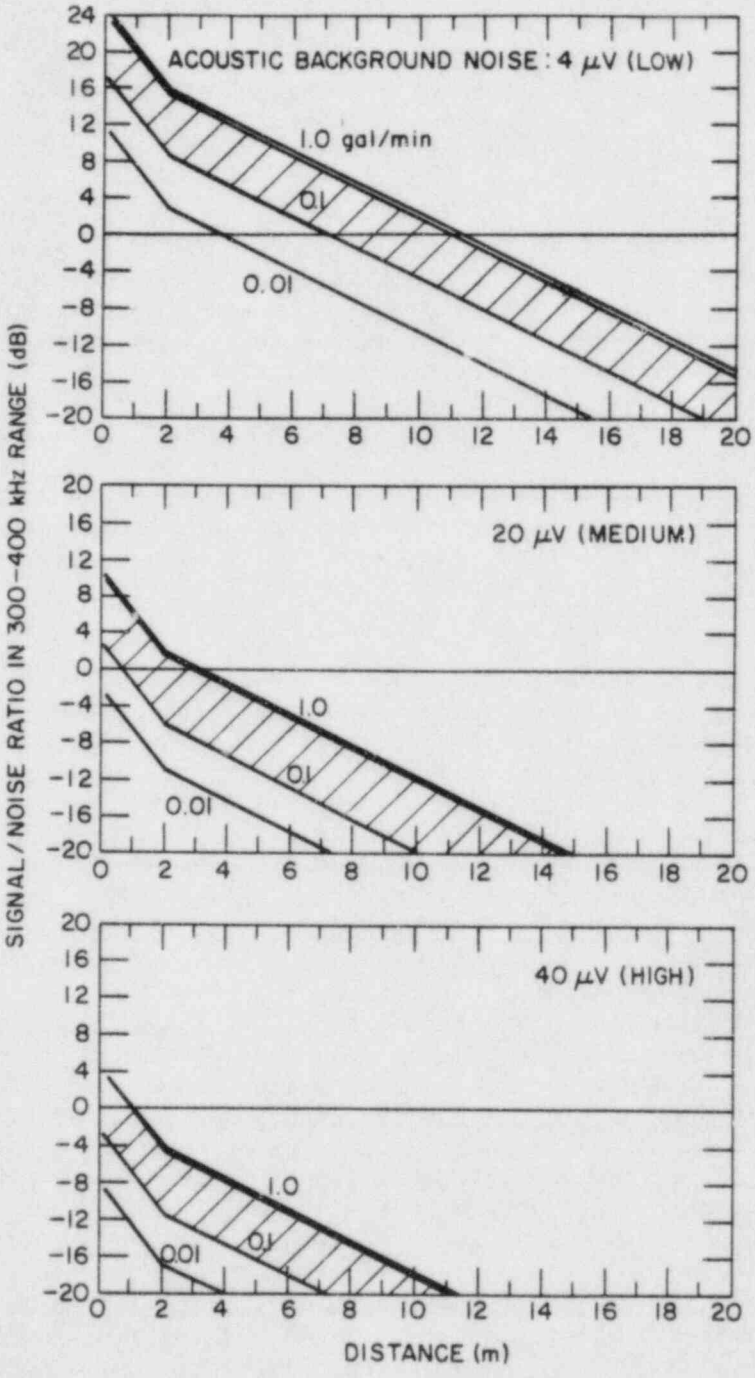

Fig. 4. Predicted Acoustic Signal-to-Noise Ratios vs Distance along a 10-in. Schedule 80 Pipe for Three Leak Rates and Three Levels of Estimated Acoustic Background Noise. The striped areas indicate possible enhancement of the signal for the 0.1 gal/min leak because of the presence of reflective insulation.

This is considerably higher than signals obtained from IGSCC specimens with similar leak rates. Further analysis of valve leak signals is in progress to establish whether valve leaks can be distinguished from crack leaks.

Studies have also been carried out to establish the effect of "Nu-Kon" fiberglass insulation on the generation and attenuation of acoustic leak signals. Analysis of the results suggests that this "soft" insulation has very little effect on the generation or propagation of acoustic leak signals.

2. Spectral Analysis of Acoustic Background Noise

The background noise data acquired during a hot functional test of the TVA's Watts Bar Reactor in Tennessee has been evaluated with regard to spectral content. In this test, an AET-375 transducer was mounted on the accumulator safety injection pipe on the cold leg of loop 2. A 25.4-cm-long waveguide was employed. The responses of this transducer to the acoustic background noise and an acoustic leak signal were compared. The acoustic leak signal response of the very-broadband NBS-designed IQI-501 transducer served as a reference. The frequency spectrum of the acoustic background noise showed a slight (<2 dB) drop in amplitude in the 250-kHz region when compared with a monotonically decreasing background noise curve. This adds some further support to the belief that the optimum frequency window for acoustic leak monitoring is 200-400 kHz.

3. Cross-Correlation Analysis

Results of recent experiments on the application of cross-correlation analysis for acoustic leak location have been encouraging. Electronically generated white noise, simulating acoustic waves from leaks, was injected into the 10-in. piping of the ALD facility. Strong correlations were obtained in the 200-400 kHz range with "matched" AET-375 transducers on waveguides separated by a distance of about 1 m. These tests were carried out on a part of the pipe run that was filled with water and included an elbow with two welds. Figure 5 shows the cross-correlation function for a simulated leak signal and waveguides separated by 1.4 m. The acoustic source consisted of a white noise generator driving a PZT-5 pressure-bonded crystal on a rod threaded into the pipe between the waveguides, 0.1 m from one waveguide. The peak is slightly off center, as expected. The radio frequency signals were envelope detected before being analyzed by a Spectral Dynamics 375 signal processor. A wave velocity of 1400 m/s was calculated from the 0.86-ms transit time difference and the 1.2-m difference in waveguide/signal-source separation. This is close to the velocity of longitudinal waves in water (1500 m/s). When the pipe is filled with water, the acoustic leak signal is propagated predominantly through the water. With the pipe drained, the measured velocity is close to the velocity of surface waves in steel, as expected. Correlations for leaks through field-induced cracks were evident, but they were much weaker than for the electronically generated acoustic waves. This may be the result of the complex geometry in the vicinity of the IGSCC (pressure vessel below the crack, heating bands, and extensive welding in the vicinity of the crack).

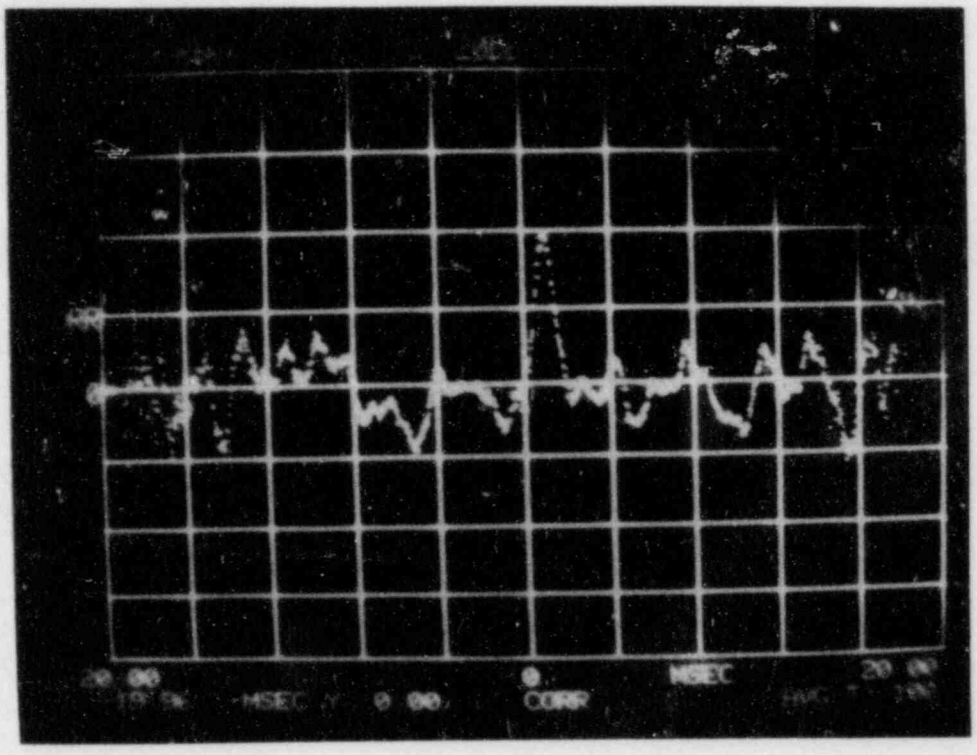

Fig. 5. Cross-Correlation Function for Simulated Leak Signal. The source is located between two AET-375 transducers on waveguides, which are separated by 1.4 m; one waveguide is 0.1 m from the source. The radio frequency signals were envelope detected before being analyzed by a Spectral Dynamics SD 375 signal processor.

4. Calibration Procedures

Three calibration procedures are being considered for checking transducer-waveguide systems after field installation. They are the pencil-lead-breaking method, the gas jet method, and electronic pulsing.

In the lead-breaking technique, the 0.5-mm-dia lead of a Pentel mechanical pencil is extended 5 mm beyond the end of the pencil body and is pressed against the pipe, at an angle of 30° to the pipe, until it breaks. (If this technique is demonstrated to be useful, fixtures will be fabricated to standardize the procedure.) The breaking of the lead was detected by an AET-375 transducer mounted on a waveguide at a distance of 0.2 m from the pipe surface. Excellent reproducibility of the captured acoustic transient signal was evident from a comparison of the digitized and stored transient pulses of four successive breaks. This technique may be useful as a convenient and rapid way to check the ALD system after installation. However, the method would not be applicable to remote in-situ calibration. This could be carried out by the gas jet technique or by electronic pulsing.

In preliminary work on the gas jet technique, a jet of nitrogen gas from the 1.5-mm-dia exit hole of a Swagelok fitting was directed normal to the pipe surface from a distance of 6 mm. An rms signal (50 kHz to 1 MHz) with a magnitude 4 times that of electronic background was detected at a distance of 1 m. The broadband IQI-501 transducer was employed to obtain information on

frequency spectra. The acoustic spectrum from the gas jet shows greater frequency dependence than does the spectrum from a leak through an intergranular crack. Relatively more signal at lower frequencies is present in the gas jet spectrum. Furthermore, most of the detected gas-jet acoustic signal is in the form of surface waves; this is not the case for crack leaks. It has also been determined that the acoustic signal is relatively insensitive to the exact height of the gas jet above the surface for heights of about 10 mm. This technique appears to be well suited to remote calibration. Its chief disadvantages are the inconvenience associated with setting up the system and problems associated with the presence of insulation.

The sending of electronic pulses to a calibrating transducer is also under investigation as a technique for remote calibration. In this technique, an electronic signal is used to pulse a transducer (on a waveguide) which then generates an acoustic signal in the pipe. Since a different transducer is used to receive acoustic leak signals, a method would have to be established for distinguishing anomalous behavior of receivers from anomalous behavior of pulsers. The electronic pulsing technique is a relatively simple procedure for continuous in-situ monitoring of an ALD system. The disadvantage is the need for additional transducers on the pipe and possible problems in coupling the waveguides of the transmitting transducers to the pipe.

5. Processing of Acoustic Leak Data

Progress has been made in the evaluation of an ALD system that could be employed in the field. Software accomplishments have included the establishment of a precise test procedure for correlogram computation, the writing of a new correlation subroutine, and the discovery and elimination of "bugs" in the operator interaction routines. The leak detector's internal function generator was enhanced to include exponential enveloping and linear frequency modulation capabilities. With the aid of the latter, functions with characteristic correlogram patterns were generated and used as data sets for testing the IEEE FFT-based correlation routines. Autocorrelograms were computed as expected, but cross-correlograms rarely yielded the expected results. However, FORTRAN programs computing the straightforward time domain solution for the same data set yielded the expected results.

Because time domain computations written in FORTRAN take so long to execute (5 minutes in our test case) and because the time expenditure in analyzing the IEEE correlator insufficiency was felt to be unpredictable at best and prohibitive at worst, a time domain correlation routine callable from a FORTRAN program was written in 68000 assembler language. This routine has been tested and found to give excellent results. It also executes in one-quarter of the time required by the IEEE FFT-based correlator.

A serious bottleneck in the processing of ALD data is in the transfer of the raw data from the transient signal recorders in the CAMAC crate to the host computer system. Currently, the communications link consists of a Kinetic Systems Model 3989 RS-232 crate controller interfaced to our Dual Systems 83/20 computer system through a Dual SIO/DMA Intelligent Four-Port Serial I/O board.

The main problems faced are as follows: (1) The serial I/O board allows direct memory access (DMA) transfer on output only; on input, the host CPU must transfer the data one byte at a time into primary memory. (2) Since the host computer's operating system is a multiuser, multitasking system, we are allotted only small "time slices" in which to accomplish the transfer. Apparently, the duration of one such time slice is not sufficient to allow the transfer of an entire block of data from the transient signal recorders to the host computer.

To overcome these problems, we have decided to use a bit-parallel rather than an RS-232 byte-serial interface. A parallel interface is, with proper handshaking, inherently faster than a serial interface. A brief investigation of the commercially available systems for parallel interfacing of a CAMAC crate controller to an IEEE-696-standard backplane computer showed these to be generally too expensive and too inflexible for our needs. For this reason, we intend to add a parallel port to the existing (serial interface) crate controller. The crate controller PROM firmware will be partially rewritten to support parallel transfers. In addition, we will design an I/O channel controller for the host computer system. This controller will have the ability to drive the host's buses on both output and input operations. Since the controller will have complete control of the host system's resources during CAMAC crate I/O operations, the interference from the host's operating system will be completely avoided. Using the CAMAC block transfer protocol, we will be able to transfer an entire block of data at one time, without concern for operating-system housekeeping activities.

Additional efforts to speed up the data processing are being applied in the area of special-purpose signal processing hardware. As it now stands, the transfer of acoustic leak data from the transient signal recorder to S-100 RAM is the single most time-consuming operation in the entire data reduction process. This situation will change appreciably when we have modified the CAMAC crate controller-to-S-100 bus interface so that data can be transferred in parallel rather than serially; a 50-to-1 improvement in transfer time is expected. At that point, the main cause of delay will become the correlation algorithm itself.

6. Evaluation of Moisture-sensitive Tape

Tests have been carried out to help assess the effectiveness of moisture-sensitive tape for leak detection. Tapes were supplied by Techmark. Figure 6 shows a schematic representation of the facility used for these tests. Leaks are simulated by feeding water through a copper tube to the surface of a 10-in. Schedule 80 pipe. The tapes are located at three positions on the bottom of the pipe, which is tilted approximately 1° as indicated. The pipe is wrapped with either reflective insulation or "soft" insulation (Nu-Kon). The "soft" insulation allows water vapor to penetrate to its outer surface and severely limits the useful range of the tape. Table 2 shows the response time of the tape under various experimental conditions. With Nu-Kon in place and the tape placed directly below the leak (test 10), a 0.05-gal/min leak could be detected in about 12 min. With the tape 2 m away (test 11), the leak could not be detected. However, when the reflective insulation was used (test 7) with the same combination of leak and tape positions as in test 11, the leak was detected in about 10 min. The relative positions of leak and tape on a slightly tilted pipe can have a significant effect on the response

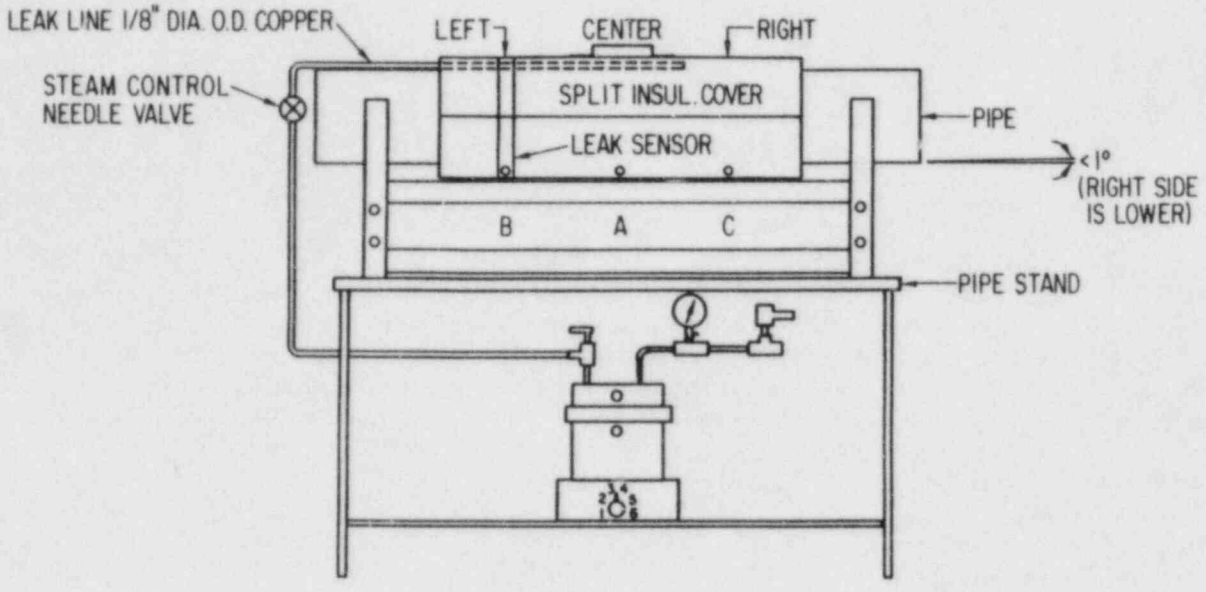

Fig. 6. Schematic Representation of Facility Used to Evaluate Moisture-sensitive Tape. The leak source is placed at one of the indicated positions along the top of the pipe; the leak sensor is placed at one of the three corresponding positions along the bottom. The distance between the center position and the left or right position is about 1 meter.

time, as indicated by the data from tests 1-3. In this case, the tape was able to detect a 0.01-gal/min leak in about 60 min when it was 1 m downstream of the leak, but it did not detect the leak even after 150 min from a location 1 m upstream of the leak. As indicated in tests 5 and 7, however, larger leaks can be detected upstream over these relatively short distances.

The analysis of these results suggests that moisture-sensitive tape may be useful for the detection of leaks in reactors. Under the right conditions, the tapes can detect leaks of the order of 0.01 gal/min. The tapes, however, will be significantly more effective in systems that employ reflective insulation. Despite the sensitive nature of the tapes, they do not provide any quantitative data other than the location at which the system has been triggered. A large leak a long distance from the tape could cause the same response as a small leak at a short distance.

E. Summary

Current leak detection practices in 74 operating nuclear reactors have been reviewed. Although the current leak detection systems are adequate to ensure a leak-before-break scenario in most situations, there is the possibility that large cracks may produce low leakage rates (from corrosion fouling, for example). In such cases, the time required for a small leak to become large could be short. In addition, no leak location information is available with existing systems. Simply tightening current leakage limits may produce an unacceptably large number of unnecessary shutdowns.

Table 2. Response of Moisture-sensitive Tape to Small Leaks

Test	Tape Location[a]	Leak Location[a,b]	Type of Insulation[c]	Flow Rate, gal/min[d]	Water Temperature, °F[d]	Water Pressure, psi[d]	Response Time, min
1	center	center	R	0.01	500	1000	3.8
2	right	center	R	0.01	500	1000	60.2
3	left	center	R	0.01	500	1000	>150.0
4	center	right	R	0.01	500	1000	>270.0
5	center	right	R	0.05	480	770	9.7
6	left	right	R	0.01	500	1000	>270.0
7	left	right	R	0.05	480	770	10.5
8	center	left	R	0.05	500	800	0.3
9	right	left	R	0.05	500	800	0.5
10	left	left	S	0.05	450	900	12.0
11	left	right	S	0.05	500	1000	>65.0

[a] See Fig. 6.

[b] Right end of pipe was lower than left (1° tilt).

[c] R = reflective insulation; S = soft insulation (Nu-Kon).

[d] Conversion factors: 1 gal/min = 3800 cm^2/min; °C = (°F - 32)/1.8; 1 psi = 7 x 10^3 Pa.

Characterization of acoustic leak signals from IGSCC, combined with information on acoustic background noise levels, allows acoustic signal-to-noise ratios to be estimated for a 10-in. Schedule 80 pipe as a function of distance from the leak. Under ideal conditions, leak rates as low as 0.1 gal/min may be detectable at distances on the order of 10 m. Tests with various types of cracks indicate that quantitative correlations between leak rates and acoustic signals in the 300-400 kHz band are possible for IGSCC. Recent cross-correlation results with simulated acoustic leak signals and 375-kHz acoustic-emission sensors on 3-mm-dia waveguides indicate that correlations should be possible.

Preliminary tests have also been carried out at ANL to evaluate a breadboard ALD system that can carry out cross-correlation analyses (including averaging), monitor acoustic leak signals, and provide spectral information.

An evaluation of moisture-sensitive tape suggests that under the right conditions the tapes can detect leaks on the order of 0.01 gal/min when reflective insulation is used. Despite the sensitivity of the tapes, they do not provide quantitative leak data and a large leak at a long distance can result in the same response as a small leak near the tape.

F. Future Efforts

The capability of acoustic techniques to detect, locate, and size leaks will be further studied. A breadboard ALD system will be used to evaluate field-implementable concepts. Leaks larger than those examined thus far will be studied. These will include IGSCC, thermal fatigue, and, in particular, valve leaks. These data will form a more significant basis for estimating the sensitivity and reliability of ALD.

The monitoring of Watts Bar (in collaboration with PNL) will continue. Additional background noise data will be acquired, along with data from any seal leaks appearing during reactor start-up procedures.

II. NDE OF CAST STAINLESS STEEL

A. Background

It is well known that the coarse grain size and elastic anisotropy of cast stainless steel (CSS) make ultrasonic inspection difficult. Although the ASME code requires inspection of cast stainless piping, it has not been possible to demonstrate that current inspection techniques are adequate.

B. Objectives

For the near term, improvements that may increase the reliability of ultrasonic inspection include (a) the development of methods to establish the microstructure of the material (to help optimize the inspection technique), (b) calibration standards that are more representative of the material to be inspected, and (c) the use of cracked CSS samples for training purposes. For the long term, it will be necessary to establish (a) the variability of the microstructure of CSS, (b) the effect of microstructure on inspection reliability, (c) the degree of improvement possible with techniques and equipment designed specifically for CSS, e.g., focused transducers and lower

frequencies than those used conventionally, and (d) qualification of requirements for CSS inspections. Recent work carried out at ANL to address some of these points is presented below.

C. Technical Progress

1. Variation of Sound Velocity with Microstructure

When CSS material is isotropic (equiaxed grains), the variation in velocity is small (<2%), whereas for anisotropic material (columnar grains) the variation in velocity can be as large as 100% for shear waves. The magnitude of the velocity of sound may also be used as a measure of the degree of anisotropy and thus as an indicator of microstructure. Relatively low longitudinal velocities indicate a columnar grain structure, whereas high velocities indicate an equiaxed (isotropic) structure. Intermediate values indicate the presence of both microstructures. The validity of this concept has been demonstrated on CSS samples with different microstructures. Figure 7 shows the longitudinal velocities of sound for seven 400 x 180 x 60-mm samples of a 28-in. pipe provided by Battelle PNL and 18 samples of a comparable large-diameter pipe provided by Westinghouse. The Battelle samples were fabricated from a weldment in which material with a well-defined equiaxed grain structure was joined to material with a well-defined columnar grain structure. The Westinghouse samples were also made from a weldment. These specimens, however, were machined flat and have a coarse and poorly defined grain structure. The velocity of sound was measured by standard pulse-echo methods with a 37-mm-dia, 1-MHz transducer. Echo transit times were measured with a Tektronix oscilloscope. In all cases the longitudinal waves propagate in a radial direction through the pipe wall. As shown in Fig. 7, the equiaxed and columnar sides of the Battelle samples can be easily distinguished by measurements of the longitudinal sound velocity. Also, the sample-to-sample variation is relatively small. The Westinghouse samples, however, show large variations in sound velocity from sample to sample as well as within a sample (two measurements were made on each sample). The wide range of the values is indicative of large variations in the microstructure of these samples. This complex microstructure could cause significant, unpredictable distortion of the ultrasonic waves used to interrogate the material and lead to an unreliable result.

During a visit to the Commonwealth Edison Byron Station, sound velocity was measured in a CSS/carbon steel reference block and two CSS elbows (one each on the steam-generator and pump side of the loop 4 crossover).

On the cast portion of the 7.6-mm-thick reference block, the longitudinal sound velocity was measured by the pulse-echo technique at 11 points covering about 0.01 m^2. No significant difficulties were encountered in making these measurements. The average velocity was 6090 m/s, with a variation of about $\pm$1.5% due to the microstructure. The relatively high sound velocity strongly suggests that the calibration block has an equiaxed grain structure, which may be significantly different from the grain structure of the plant piping and elbows. As a check on the accuracy of the measurement, the carbon steel portion of the reference block was also examined. A sound velocity of 5890 m/s was obtained, which is consistent with previous data for this material.

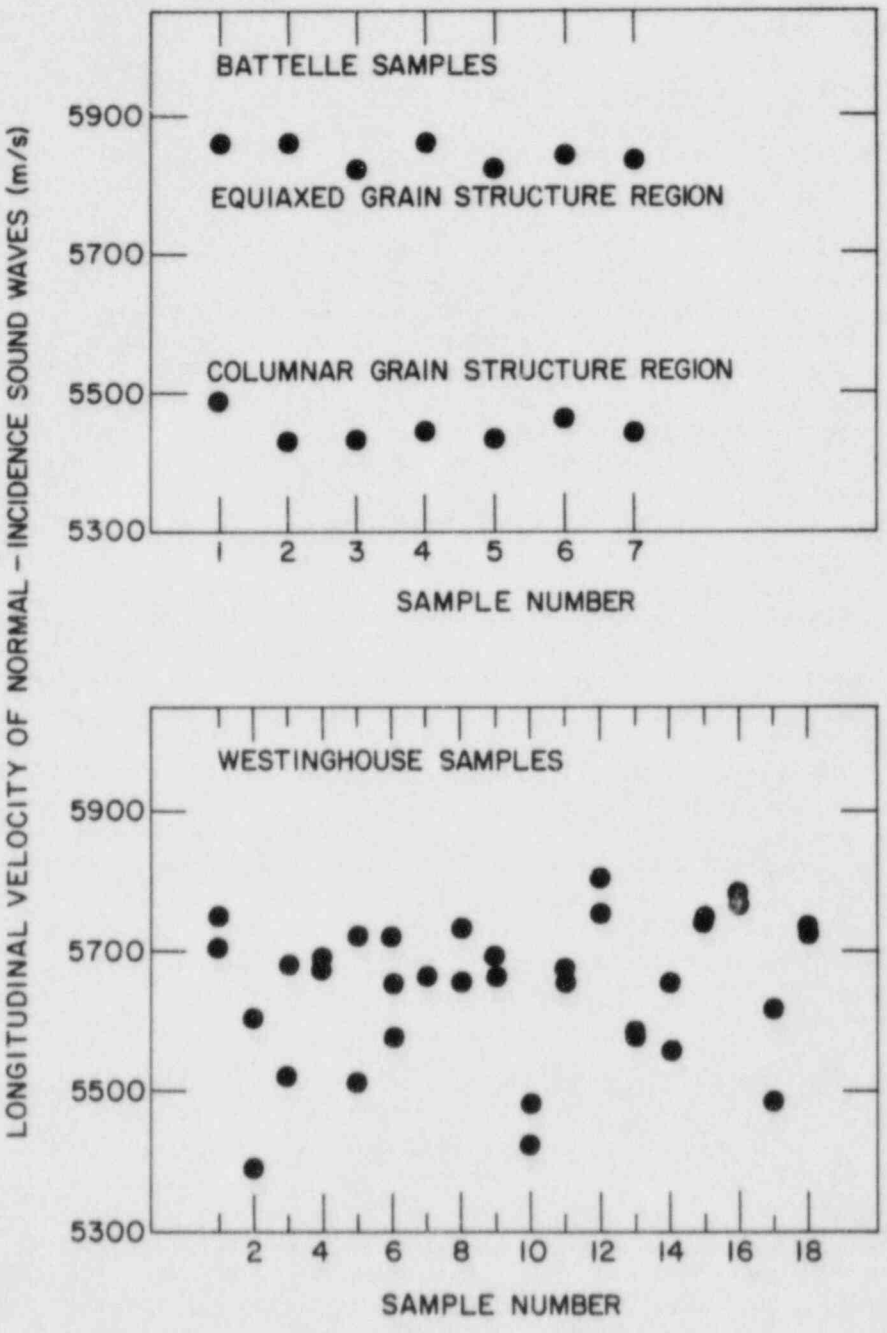

Fig. 7. Variation of Longitudinal Sound Velocity in Large-Diameter CSS Pipe Sections. (Upper panel) samples with both columnar and equiaxed regions; (lower panel) samples with a poorly defined, coarse grain structure. Two measurements were made on each sample. Sample wall thicknesses are nominally 60 mm. 1-MHz, longitudinal waves in a pulse-echo mode were propagated normal to the pipe outer surface.

The surfaces of the CSS elbows were, in most areas, too rough for efficient propagation of ultrasonic waves. Only the smoothly ground areas adjacent to the elbow-to-pipe welds were amenable to pulse-echo examination; ultrasonic backwall echoes could be detected in most, but not all, of these areas. On the pump-side elbow, echoes were detectable at several locations away from the top of the elbow. Since the elbow and pipe appeared to have the same wall thickness, the wall thickness stamped on the pipe section was used as a "best guess" value for the elbow wall thickness. On the basis of this assumption, the sound velocity in the elbow varied from 5200 to 5860 m/s. This suggests that the microstructure of the elbow was quite different from the reference block. The wall thickness of the generator-side elbow could not be estimated because of the elbow geometry, so absolute velocities were not determined; however, it appeared that the velocity varied by about 5%. The velocity of sound in the straight (wrought) section was found to be 5760 m/s, which is consistent with previous measurements on stainless steel.

Attempts were also made to propagate 1-MHz, 45° longitudinal waves in the cast material with two transducers in a pitch-catch mode. No backwall echo was detected in the reference block, which is consistent with the conclusion that the material is equiaxed. No echo signal could be detected on the pump-side elbow, but echoes were present in the generator-side elbow. Thus, the two elbows have distinctly different wave propagation characteristics. However, in both cases there was considerable ultrasonic noise.

These results are consistent with the suppositions that ultrasonic inspections of CSS are very unreliable at best, that ultrasonic-wave propagation characteristics vary considerably from component to component and within an individual component, and that reference-block material may not be representative of the material to be inspected.

2. Microstructure and Deviation of Ultrasonic Beams

In an elastically isotropic material (equiaxed grains), the energy in an ultrasonic beam propagates in the direction of the wavefront normal, as expected. However, in elastically anisotropic material (columnar grain structure), the direction of propagation of ultrasonic energy in a beam can be different from the direction of the wavefront normal. Because of this phenomenon, it may be possible to distinguish columnar from equiaxed grain structures nondestructively by examining the propagation behavior of 45° longitudinal waves in the material. Figure 8 shows the predicted propagation behavior in 60-mm-thick specimens. For an equiaxed specimen with the transmitter and receiver placed on opposite sides (Fig. 8a), the maximum acoustic signal will be detected ∿60 mm from the point directly opposite the beam entry point. For a specimen with columnar grains (Fig. 8b), the energy in the beam deviates markedly from the expected 45° path, such that the maximum signal will be detected at only ∿16 mm from the point opposite the beam entry point. As shown in Fig. 8c, the beam in the equiaxed material will be reflected to a point ∿120 mm from the transmitting transducer (following the expected "full-V" path), while the maximum reflected-beam intensity in the columnar material will be found much closer to the transmitting transducer (∿32 mm away).

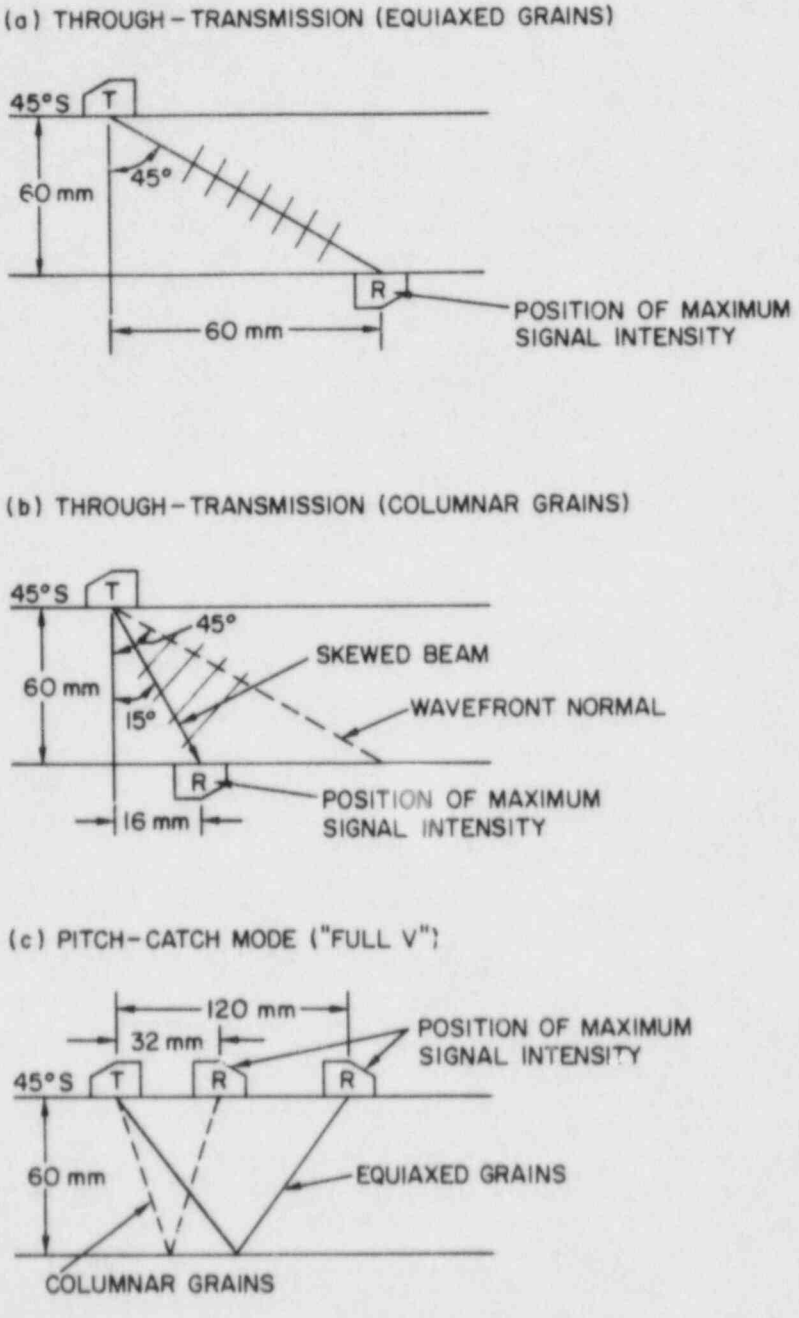

Fig. 8. Schematic Representation of the Path of Ultrasonic Energy in Cast Stainless Steel with Equiaxed and Columnar Grain Structures. (a) Transmit from outer surface and receive at inner (equiaxed grains), (b) transmit from outer surface and receive at inner (columnar grains), and (c) transmit and receive at outer surface.

Experiments were carried out on one columnar and one equiaxed pipe section to verify these predictions. Two 1-MHz, nominally 45° shear-wave transducers (1-in. dia) were placed on the outer surface of each pipe section, and the separation between the two transducers was varied to maximize the received signal. Table 3 compares the optimum separations determined in these experiments with the corresponding predicted values. The agreement is reasonable.

Table 3. Transducer Pair Separation[a] for Maximum Received Signal on Outer Surface of 60-mm-Thick CSS Pipe Sections

Grain Structure	Predicted Value, mm	Measured Value, mm
Columnar	32	42
Equiaxed	127	105

[a] 45° shear waves in pitch-catch "full-V" configuration at 0.5 MHz

D. Summary

Although the ASME code requires inspection of CSS piping, it has not been possible to demonstrate that current inspection techniques are adequate. For the near term, improvements that may increase the reliability of ultrasonic inspection include (a) the development of methods to establish the microstructure of the material (to help optimize the inspection technique), (b) calibration standards that are more representative of the material to be inspected, and (c) the use of cracked CSS samples for training purposes. For the long term, it will be necessary to establish (a) the variability of the microstructure of CSS, (b) the effect of microstructure on inspection reliability, (c) the degree of improvement possible with techniques and equipment designed specifically for CSS, e.g., focused transducers and lower frequencies than those used conventionally, and (d) qualification of requirements for CSS inspections.

SUMMARY OF DETECTION, LOCATION, AND CHARACTERIZATION CAPABILITIES OF AE FOR CONTINUOUS MONITORING OF CRACKS IN REACTORS*

P.H. Hutton, R.J. Kurtz, R.A. Pappas,
J.R. Skorpik, M.A. Friesel, and J.F. Dawson
Pacific Northwest Laboratory
Operated by Battelle Memorial Institute

INTRODUCTION

A brief review of the program background and format will serve to establish a context for the results discussed.

Objective

Develop acoustic emission (AE) methods for continuous monitoring of reactor pressure boundaries to detect and evaluate crack growth.

Approach

The approach involves three phases:

1) Develop relationships to identify crack growth AE signals and to use identified crack growth AE data to estimate flaw severity.

2) Evaluate and refine AE/flaw relationships through fatigue testing a heavy section vessel under simulated reactor conditions.

3) Demonstratc continuous AE monitoring on a nuclear power reactor system.

The first phase, which is essentially completed, utilized laboratory test specimens of A533B steel to develop the needed relationships. Recognizing the difficulty of theoretical extrapolation of these relationships to full size structures, the program incorporated Phase 2 to accomplish the transition experimentally. Phase 2 was performed on an intermediate scale vessel (ZB-1) tested in collaboration with the German Materialpruefungsanstalt (MPA) in Mannheim, West Germany. Demonstration of reactor monitoring (Phase 3) is in progress, through the cooperation of the Tennessee Valley Authority, on the Watts Bar Unit 1 reactor.

*Work supported by the U.S. Nuclear Regulatory Commission under Contract DE-AC06-76RLO 1830.

DISCUSSION

The focus of this paper is on the current capabilities derived from this program for continuous AE monitoring to detect and characterize flaw growth in reactor pressure boundaries. The subject will be treated in the following sequence:

- Instrumentation
- Flaw detection and location
- Noise interference
- AE signal identification
- Flaw severity estimate
- Inservice hydrostatic testing
- Leak detection

Instrumentation

Obviously, a fundamental requirement is an AE instrument system capable of operating continuously over a long period (one year minimum), capable of withstanding the reactor environment, and capable of mass data storage. Such an instrument system has been developed.

The AE monitor system used in the ZB-1 vessel test performed with very limited problems during the one year duration of the test and has continued in use on laboratory tests since. An engineering prototype system for installation at Watts Bar, Unit 1 has been developed based on the ZB-1 experience. The instrument concept is shown in Figure 1.

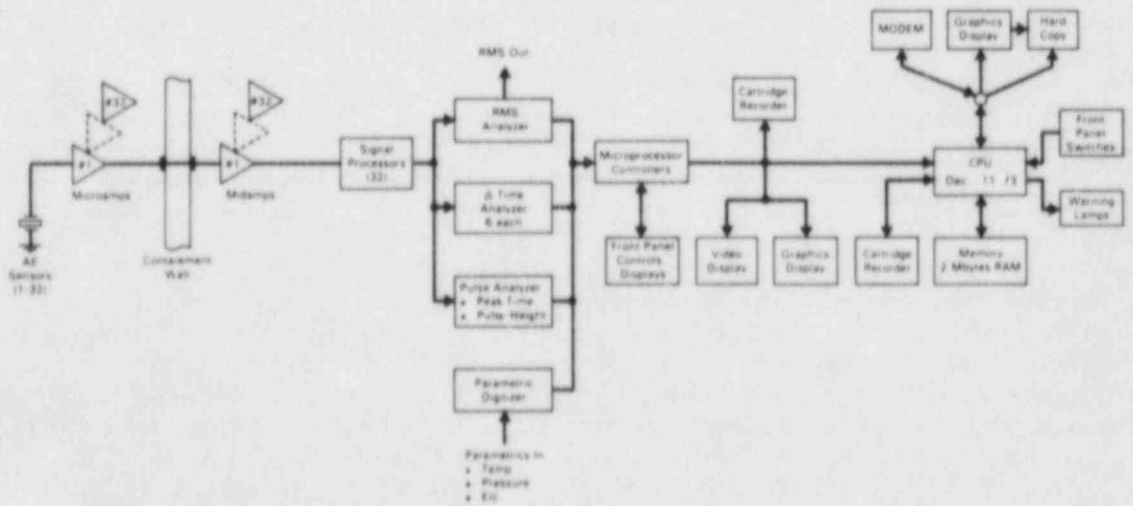

Figure 1. Functional Diagram of Engineering Prototype AE Monitor System.

The acquisition subsystem, which receives data from the sensors, is composed of 24 channels divided into six arrays. Arrays may be composed of 1, 2, 3, or 4 channels. Each channel has a maximum electronic amplification of 90 dB, which can be reduced with channel attenuators in 1 dB steps to 14 dB. A 20 dB microamp is used in close vicinity of the sensor to provide sensor impedance matching and cable driving. All amplifier stages are linear.

Data collected from each array consists primarily of 1) delta-times, 2) RMS, 3) peak time, 4) pulse height, and 5) sensor hits. Delta-times are used for source location and are measured with 1 microsecond resolution. RMS is measured on each channel for leak detection analysis. Peak time and pulse height are measured only on one channel of each array. Sensor hit totals are used to determine both sensor functional condition and signal propagation affects.

All data is recorded on a 67 Mbyte cartridge tape for long term storage. The data is also passed on a high speed buss to a DEC 11/73 for real-time analysis.

The system is operated on a menu approach wherein a video display shows function choices to the operator and a keyboard lets the operator enter his choice. Once a choice is made, a series of questions and prompts follow for operator guidance.

Data analysis is performed in a separate subsytem which is designed to maximize speed and information accessibility with a minimum of operator intervention. It operates in both an on-line mode with data directly from the data acquisition subsystem or in an off-line mode receiving data from cartridge tape.

High processing speeds are attained with the use of DEC's 15 MHz, 32-bit J-11 CPU and over 2 Mbytes of RAM memory. System software resides in battery backed nonvolatile memory eliminating the need for the slower mechanically based mass storage devices.

The analysis subsystem allows easy access to information for personnel not experienced in the details of acoustic emission monitoring techniques and instrumentation. Front panel lamps and gauges serve to direct the operator to monitoring conditions and to instrument conditions such as data storage device full or hardcopy paper empty. Information concerning acoustic activity is presented in the form of graphic displays on a CRT screen. The selection of display type, reactor area of interest, and information screening is accomplished through the use of front panel switches. With minimal training, the operator can characterize acoustic activity according to its location,

rate, and characteristics (amplitude, rise time, and pattern recognition classification).

Several automated features are integral to the analysis subsystem to facilitate unattended operation. Periodically, hard copies of a select group of principle displays are generated by the system. A modem can be used for remote system access. A 67 Mbyte cartridge tape unit used for off-line analysis also serves as a backup real-time data storage device when the primary storage device in the acquisition system has been filled. The data processing rate is about 150 events per second maximum. Data rate can be reduced by several variables such as the size of the sensor array, the length of time that a high data rate is sustained, and buffer capacity.

The instrument system hardware is illustrated in Figure 2. The modules will be installed in existing racks at Watts Bar, Unit 1.

A key element of the AE monitor system is a high temperature sensor. Two problems have been experienced in attempts to develop high temperature AE sensors to be mounted directly on a 500-600^{o}F surface: 1) the high temperature piezoelectric materials have poor sensitivity to AE signals, and/or 2) the sensors are very costly. Long term acoustic coupling of these sensors to the structure surface that is acceptable for reactor use can also be a problem. These problems have been overcome by using metal waveguides with a sensing crystal (PZT5A) and a preamplifier mounted on the outer end. Figure 3 shows one of these sensors mounted on an inlet nozzle at Watts Bar, Unit 1. It is pressure coupled to the surface with a pressure of about 15,000 psi which requires 30 pounds force with the tip design used. The waveguides are 0.130 inches in diameter which is a compromise between minimizing acoustic signal dispersion and retaining needed mechanical strength. These sensors have been used effectively on both the ZB-1 vessel test and on hot functional testing at Watts Bar. These sensors have been exposed to 1.13 and 1.33 meV gamma radiation at 1.7 x 10^{3} R/hr for a cumulative dose of 6 x 10^{5} R with no degradation.

Summarizing, an instrument system capable of long term monitoring under reactor conditions with a mass data storage feature has been demonstrated.

Flaw Detection and Location

Given the needed instrument system, the next topic to be considered is the effectiveness of flaw detection and location. In the ZB-1 vessel test,[1] fatigue crack growth from machined flaws was detected consistently during both low temperature

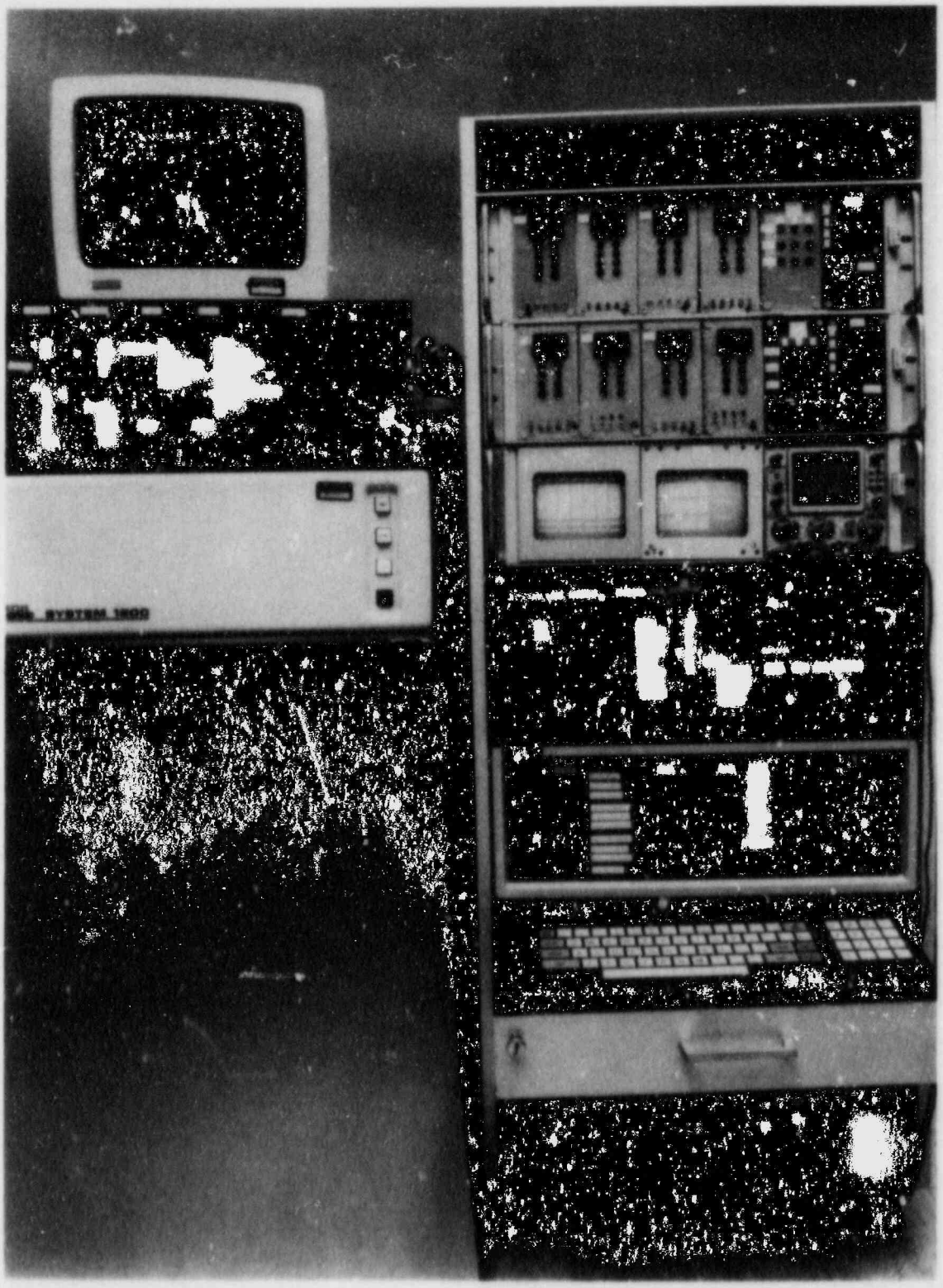

Figure 2. Engineering Prototype AE Monitor System for Watts Bar, Unit 1 Reactor.

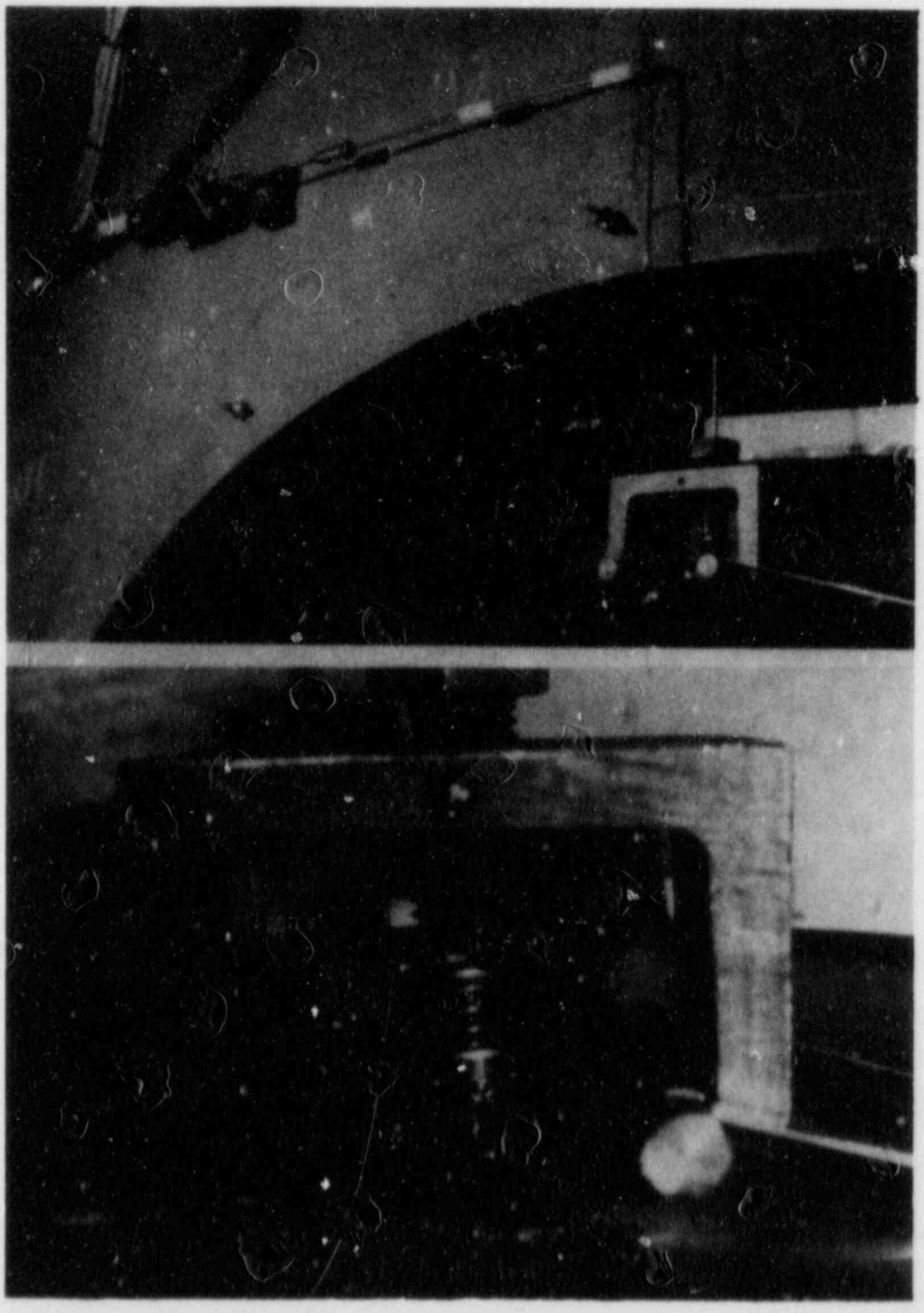

Figure 3. Waveguide AE Sensor Installed on No. 2 Inlet Nozzle - Watts Bar, Unit 1.

(65°C) testing and during high temperature (288°C) testing. The most significant example of fatigue crack detection during the ZB-1 vessel test, however, involved an unexpected crack along an insert weld. In Figure 4, the weld crack is associated with the KS07R insert. The illustration is a roll-out of the vessel cylinder with the match line (M/L) running through the KS07R insert. The presence of a growing fatigue in the weld region was identified early in Step 9 by the AE data and called out as such. This was well ahead of confirmation of the flaw by ultrasonic inspection. Another significant aspect is the fact that the signals had to be received by AE sensors ten feet from the source in order to be accepted and located by the monitor. This provides a calibration of the range of AE detection for 400 kHz tuned waveguide sensors pressure coupled to the vessel surface.

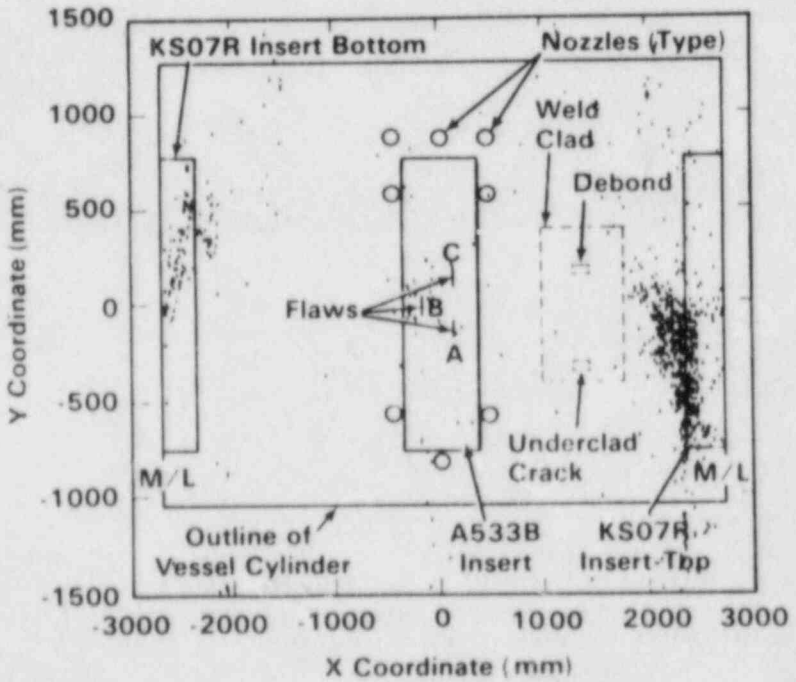

Figure 4. AE Source Locations, Step 9, Array 3 (65-80 L.P.), ZB-1.

Stress corrosion cracking (SCC) is another cracking process of major interest. All of our information to date on detection of SCC by AE methods has come from laboratory specimens ranging from 4 inch to 26 inch diameter austenitic stainless steel pipe. SCC has been successfully detected by AE in all of these tests. Figure 5 gives an example of the relatively small cracks detected. This information is from a test performed with 4 inch Schedule 80 stainless steel pipe.

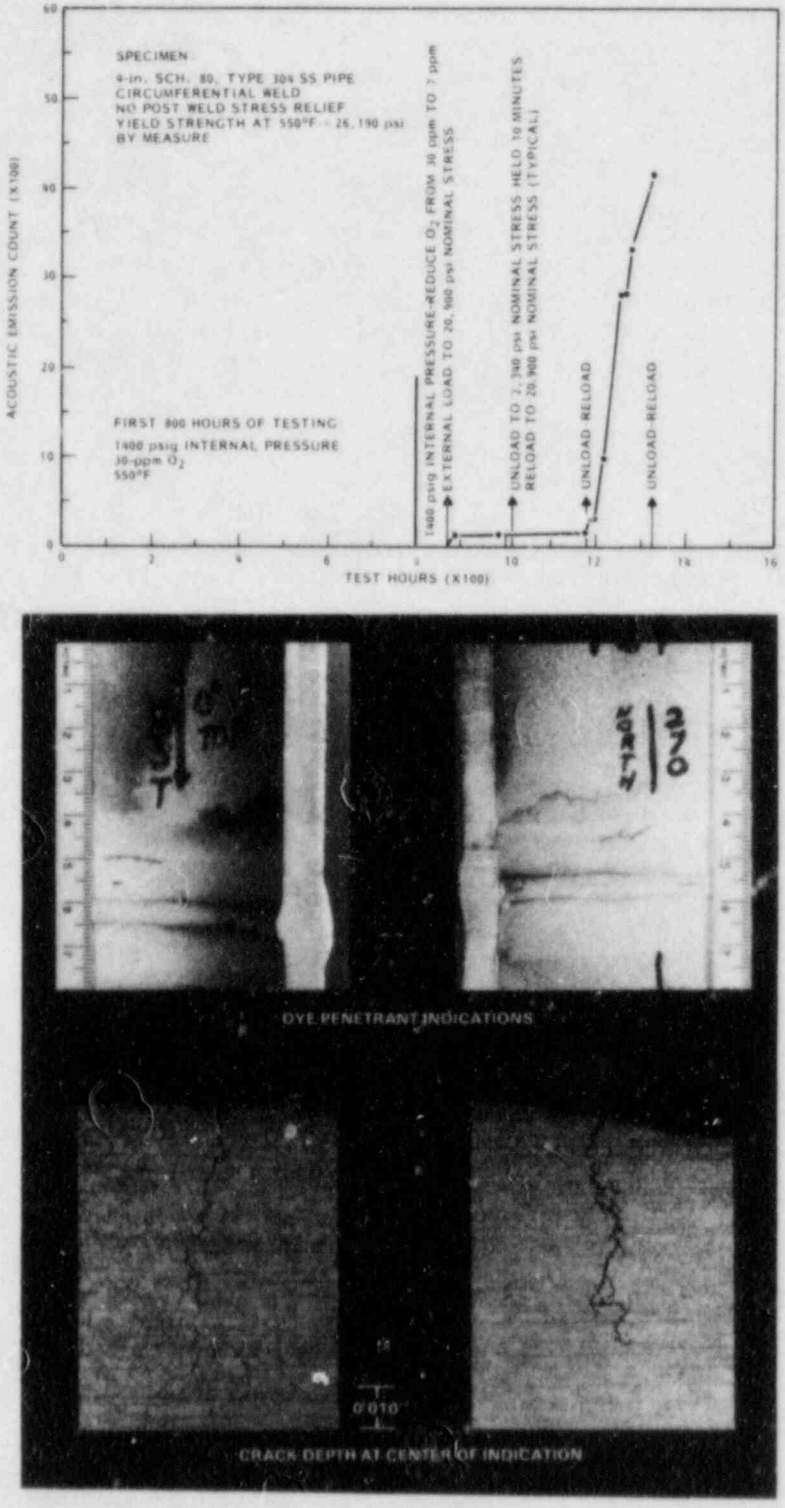

Figure 5. Stress Corrosion Cracking Associated with Detected AE.

Further characterization of AE from SCC is in process in the laboratory. In addition, a special eight channel AE monitor unit has been fabricated for the purpose of monitoring selected piping locations on an operating reactor. We are still searching for an effective location where this unit can be installed on a test basis.

In summary, effective detection and location of fatigue crack growth under simulated reactor conditions has been demonstrated. Fatigue cracking has been detected by AE prior to detection/confirmation by ultrasonic inspection. Stress corrosion cracking has been repeatedly detected in laboratory tests using techniques compatible with reactor monitoring.

Noise Interference

One of the major concerns with continuous AE monitoring on an operating reactor has been the background noise from reactor coolant flow. Coolant flow noise for both PWRs and BWRs has been characterized in the past.[2,3,4] Required sensor characteristics to avoid interference from flow noise were developed using that information. Results from hot functional testing at Watts Bar, Unit 1[5] showed (Figure 6) that the tuned waveguide sensors do overcome the problem of noise interference at coolant temperatures above about 300°F. The sensors used on Watts Bar are the same as those used in the ZB-1 testing waveguide sensors tuned to 400-500 kHz and pressure coupled to the structure. At full cold flow (150°F-400 psig), even the tuned sensors are ineffective. Increasing coolant temperature brings about a drastic reduction in noise in the 400-500 kHz frequency range.

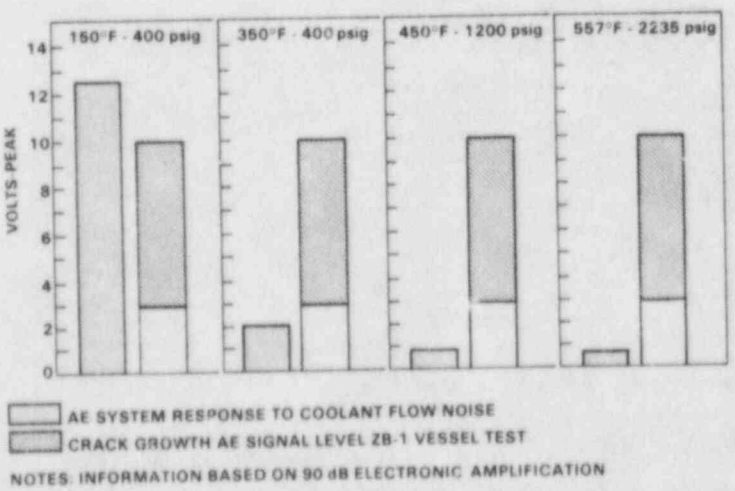

Figure 6. AE System Response to Coolant Flow Noise - Watts Bar, Unit 1.

In summary, the coolant flow noise problem can be overcome using high frequency tuned waveguide sensors. These same sensors have shown capability to detect AE at a distance of at least 10 feet.

AE Signal Identification

One of the key elements of this program is to develop a method of separating AE signals produced by crack growth from acoustic signals produced by innocuous sources. Signal pattern recognition is the technique chosen for this purpose.[6] The approach taken is to use signal processing techniques to generate features related to spectral content of the signals. These features provide a reduced set of information that describes characteristics of the waveform of interest. Standard pattern recognition techniques are used to calculate decision rules for classifying the waveforms using these features.

The original set of features used in the ZB-1 test did not produce satisfactory results. Analysis using waveforms recorded on the ZB-1 test showed that it was working to separate many of the signal types but several of the more similar signal types were not being correctly identifed.

A second set of features consisting of the parameters of a 10th order autoregressive model of each waveform was developed out of this analysis. The results using the second set of features showed some improvement but correct classification was still only about 75-80%.

In the course of reassessing the problem, visual examination of recorded waveforms showed evidence of a consistent three-pulse signal pattern present in practically all waveforms originating near known and suspected regions of crack growth (Figure 7). It was determined experimentally that the three pulses are wave modes, traveling at different group velocities, and that separation of these wave modes takes place in the waveguide as a response to a high frequency, short duration input pulse - i.e., an AE signal. Incorporation of this feature into a pattern recognition approach has resulted in correct classification rates of about 95% when applied to recorded waveforms from the ZB-1 vessel test.

Current emphasis is on incorporating the pattern recognition technique into the engineering prototype system to perform analysis on acoustic signals as they are received.

Summarizing, the original pattern recognition method was not satisfactory; however, a modified approach utilizing characteristics of the metal waveguide sensors produces a correct

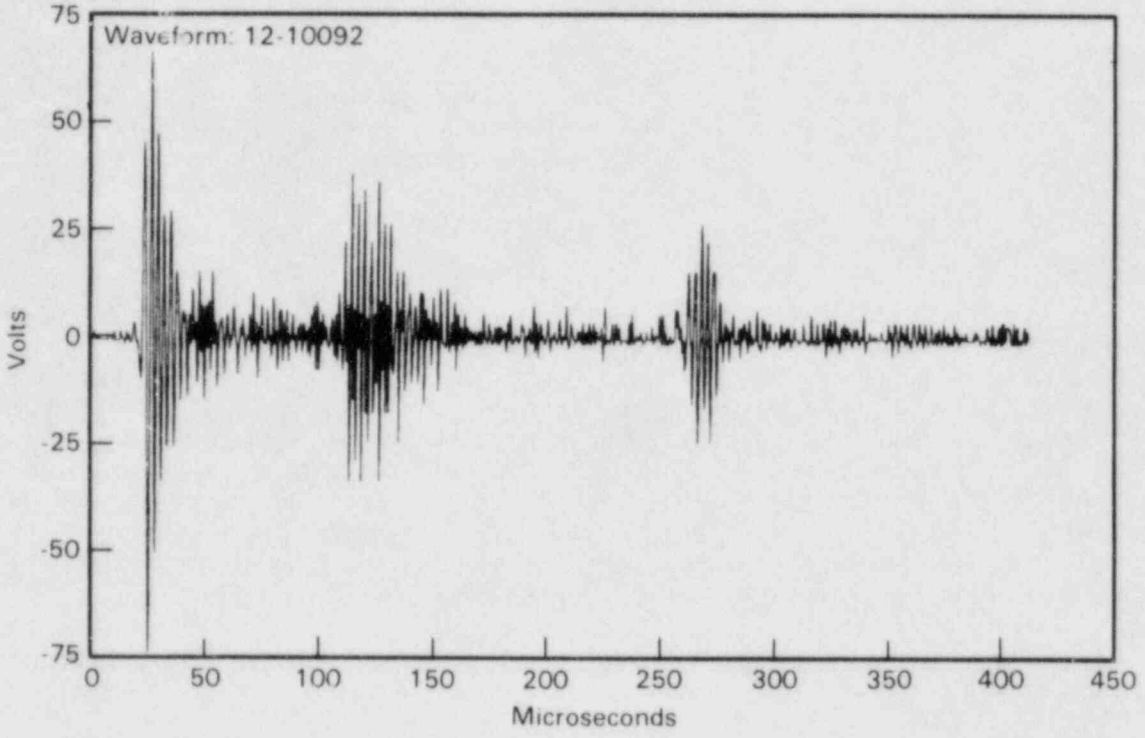

Figure 7. Three Pulse Response of Waveguide Sensor to AE Signal.

classification rate of about 95% on ZB-1 vessel test data. Emphasis is now on implementation.

Flaw Severity Estimate

A major program objective is to develop a relationship to estimate flaw severity from AE data. The ZB-1 vessel test is the principal vehicle for evaluating a flaw severity relationship developed in the laboratory. To test the flaw severity relationship, AE data for each flaw was filtered with respect to source location, load position, and signal amplitude. This was done to remove noise sources from the data. With the filtered information for each flaw, AE rate values were established for each of the cyclic loading steps. The AE rate in events/second was then used in conjunction with the lower bound flaw severity relations developed from laboratory data to estimate crack growth rates in micro-inches/second. Figure 8 gives the experimental AE/fatigue crack growth rate relationship. Figure 9 shows the crack growth rates determined from the AE data for Flaws A, B, and C plotted against the crack growth rates determined from COD and fracture surface measurements. The line in Figure 9 shows where the two crack growth rates are equal to each other. The results indicate that the flaw severity relationship under predicted the crack growth rates during the low tempera-

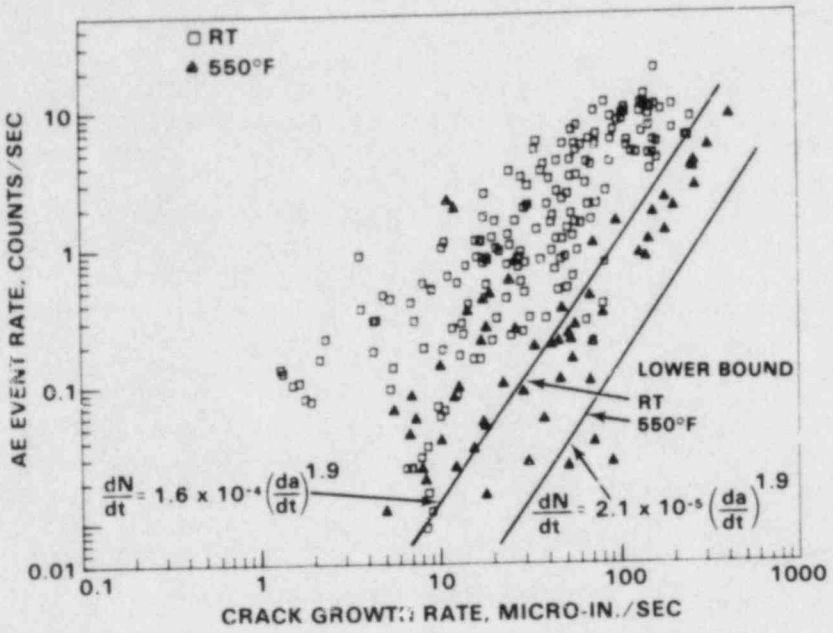

Figure 8. Experimental Fatigue Crack Growth/AE Data.

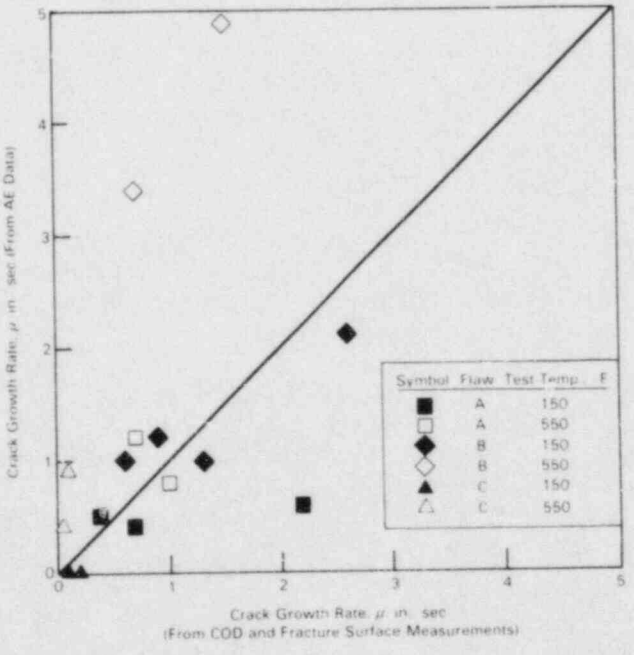

Figure 9. AE/Crack Growth Rate Relation - Machined Flaws, ZB-1 Vessel Test.

ture portion of the test. The under prediction may be caused by the extrapolation of the laboratory relationship to very low crack growth rates for which there is no laboratory data. There may also be a cycle rate dependency on the AE data at low crack growth rates in a water environment. For the high temperature portion of the test, the relationship tended to over predict the crack growth rate. Results from Flaw B at 550°F seem quite high relative to the other data in Figure 9, but these results represent normal variations in the AE data as can be seen in Figure 8.

Flaw severity estimates were also made for the KS07R weld crack during Step 11 of the test. This was the period of maximum AE activity. The flaw severity relationship significantly overpredicted the crack growth rate in this case. AE activity from the weld crack was extremely high for reasons not yet understood.

In summary, flaw growth characteristics for Flaws A, B, C, and KS07R weld cracking have been determined from NDE, crack-opening-displacement and fractographic measurements. This information was used to establish crack growth rates for comparison with predictions derived from the AE/flaw severity relationship. A test of the relationship using data from Flaws A, B, and C indicates that the model gave reasonably good predictions. When applied to the KS07R weld crack, the model significantly over predicted crack growth rates. Analysis will be performed to determine an explanation for this.

In-service Hydrostatic Testing

The ZB-1 vessel test sequence[1] was designed to provide an evaluation of the effectiveness of AE monitoring to detect flaws during in-service hydrostatic testing of reactor systems. The results fall into three categories.

One of the original inserts in the vessel wall was degraded steel which the Germans wished to test. It contained a high population of micro and macro cracks. In the course of a hydro test (1.0 x operating pressure) which was Step 1 of the vessel test sequence, it became evident from AE data and audible sounds that the insert was nearing failure as operating pressure was approached. Figure 10 shows the AE response during the final portion of the hydro. The key feature is the continuing AE with pressure hold on the last two pressure increments. The vessel test was stopped and the insert was replaced with sound material. Although examination of the degraded insert has not yet been completed, there is definite evidence that a sizeable crack had generated in the region indicated by AE. This result simply reiterates the long known ability of AE to signal impending

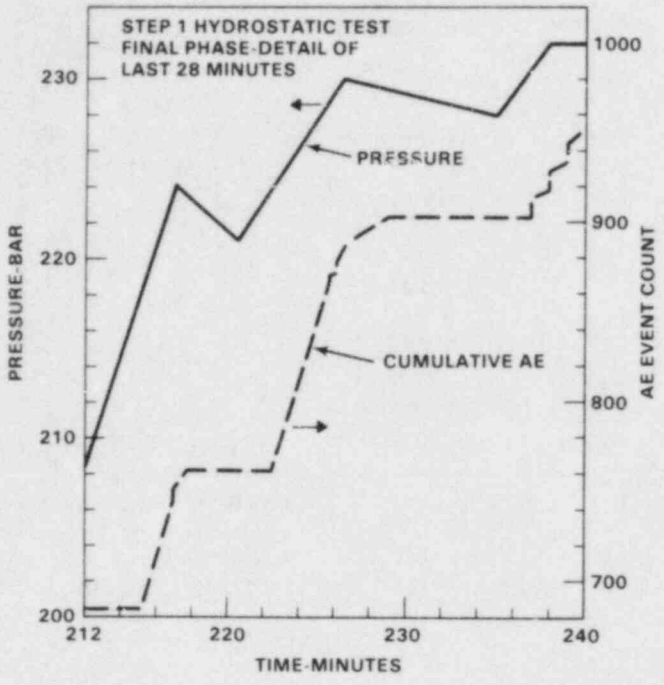

Figure 10. AE Response From Degraded Steel Insert During Hydro Test, ZB-1 Vessel Test.

failure in a structure using an elementary criterion.

In the course of the ZB-1 test, five hydro tests were performed with increasing over pressure ranging from 1.0 to 1.4 x operating pressure. The first four of these covered the over pressure range up to 1.15. No notable AE was detected from any of the flaws during the hydro test. Figure 11 which shows the results from the 1.15 hydro is typical. The largest ID machined defect had grown to a surface length of 195 mm and a depth of about 85 mm (70% through wall) and the natural crack in the KS07R weld was about 20 mm deep (20% through wall). These results suggest that the flaw detection resolution using AE during in-service hydro up to 1.15 x operating pressure will be rather poor.

The final hydro test went to an over pressure of 1.4 x operating pressure. By this point, the largest ID machined defect had grown to a surface length of 207 mm and a depth of 99 mm (83% through wall). The natural crack in the KS07R weld ranged in depth from 10 to 40 mm over a 1500 mm length (maximum of 33% through wall). As shown in Figure 12, considerable AE was detected during this hydro with the machined flaws and the weld crack becoming defined contributors. Although Figure 12 is a composite of the full hydro, data from the flaws started to

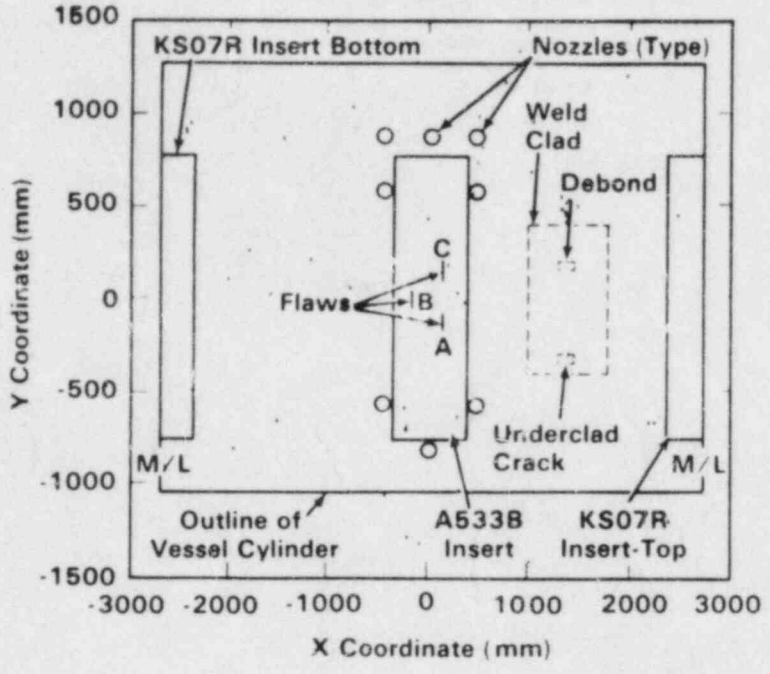

Figure 11. Source Locations, Array 3 - Step 10, Part 2, ZB-1 Vessel.

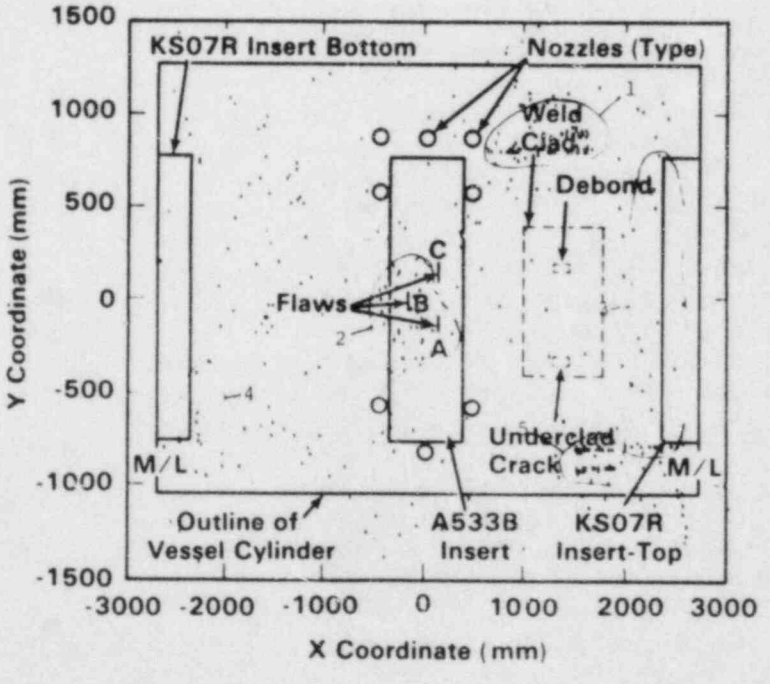

Figure 12. AE Source Locations, Array 3 - Step 13, ZB-1 Vessel Test.

appear between 1.0 and 1.1 x operating pressure. The correlation of stress at the crack front versus AE indications has not been completed, but it appears that the data is available to establish a criterion in terms of crack front stress needed to produce detectable AE during a hydro.

In summary, AE monitoring during in-service hydros would detect an impending failure condition or a major flaw; however, detection of small flaws particularly in a 1.15 over pressure hydro is questionable. It must be emphasized that these conclusions do not apply to preservice tests where the structure has not been previously stressed to a significant level. Resolution of flaw detection by AE should be much better in that case.

Leak Detection

Leak detection is an inherent capability of AE systems with their high sensitivity. A comprehensive program is in progress at Argonne National Laboratory funded by NRC to establish interpretation criteria for leak detection. The PNL program has collaborated with Argonne to the extent of making provision in the engineering prototype system to deliver raw data that Argonne needs to apply their analytical methods.

CONCLUSIONS

The conclusions drawn as to the current capabilities for continuous AE monitoring to detect flaw growth in reactor pressure boundaries are:

- Instrumentation has been developed for long term monitoring.
- AE sensors capable of withstanding reactor environment which can be mounted in a manner acceptable to reactor requirements have been developed.
- Fatigue crack growth in pressure vessels can be detected and located over a distance of at least 10-15 feet.
- Stress corrosion cracking in stainless steel piping can be detected at least in localized areas.
- Problems associated with reactor flow noise interference have been overcome.
- A computer-aided method for identifying crack growth AE signals has been developed.

- Flaw severity estimation has been partially successful; however, there are some inconsistencies that remain to be resolved.

- Large flaws and impending failure can be detected by AE during inservice hydrotests to 1.15 over pressure. Small flaws probably will not be detected.

- Coolant leaks during reactor operation can be detected.

- On-reactor experience is the major requirement to refine and establish the technology.

Beneficial uses of continuous AE monitoring at this time in addition to loose parts monitoring are:

- Piping - Detection of pipe crack growth, surveillance of pipe weld repairs for crack growth, and leak detection.

- Pressure Vessels - Surveillance of the vessel belt line for indications of crack growth.

- Nozzles - Monitoring vessel nozzles for crack growth.

FY-85 PLANS

The major tasks planned for FY-85 are:

- Install the prototype AE monitor at Watts Bar Unit 1 reactor and perform continuous monitoring during start-up and operation.

- Perform continuous monitoring of a location on reactor primary piping to test detection of stress corrosion crack growth.

- Test the potential for monitoring weld overlay pipe repair.

- Implement pattern recognition method in hardware to use with prototype AE monitor.

- Finalize AE data interpretation method.

- Complete IGSCC testing of stainless steel piping.

- Complete refinement of engineering prototype AE monitor and document.

- Continue work to establish an ASTM standard for continuous AE monitoring and to gain ASME Code acceptance.

PUBLICATIONS

Quarterly Report, October 1983 - March 1984, P.H. Hutton, R.J. Kurtz, NUREG/CR-3825, PNL-5125, Vol. 1 and 2, June 1984.

Quarterly Report, April - September 1984, P.H. Hutton, R.J. Kurtz, NUREG/CR-3825, PNL-5125, Vol. 3 and 4, to be published November 1984.

Acoustic Emission Monitoring of Hot Functional Testing, Watts Bar Unit 1 Nuclear Reactor, P.H. Hutton, et al., NUREG/CR-3693, PNL-5022, June 1984.

Acoustic Emission Results Obtained from Testing the ZB-1 Intermediate Scale Pressure Vessel - An Interim Report, P.H. Hutton, et al., NUREG/CR-3915, PNL-5184, to be published December 1984.

AE/Flaw Characterization for Nuclear Pressure Vessels, P.H. Hutton, R.J. Kurtz, R.A. Pappas, Review of Progress in Quantitative Nondestructive Evaluation, Vol. 3B, Plenum Press, 1984.

Acoustic Emission Monitoring of ZB-1 Intermediate Scale Vessel Test, P.H. Hutton, R.J. Kurtz, R.A. Pappas, Proceedings of the 9th MPA Seminar, October 13-14, 1983.

REFERENCES

1. P.H. Hutton, et al., Acoustic Emission Results Obtained from Testing the ZB-1 Intermediate Scale Pressure Vessel - An Interim Report, NUREG/CR-3915, PNL-5184, to be published December 1984.

2. P.H. Hutton, "Summary Report on Investigation of Background Noise at the San Onofre Nuclear Power Reactor as Related to Structural Flaw Detection by Acoustic Emission," published in Southwest Research Institute Project 17-2440, Biannual Progress Report No. 6, Vol. I, Projects I through IV, January 7, 1972.

3. J.R. Smith, G.V. Rao, and J. Craig, Acoustic Monitoring Systems Tests at Indian Point Unit 1, C00/2974-2, Westinghouse Electric Corp., NTIS, PC A06/MF A01, December 1979.

4. S.P. Ying, J.E. Knight, and C.C. Scott, "Background Noise for Acoustic Emission in a Boiling Water and a Pressurized Water Nuclear-Power Reactor," The Journal of the Acoustical Society of America, 53 (6), 1973.

5. P.H. Hutton, et al., Acoustic Emissio Monitoring of Hot Functional Testing, Watts Bar Unit 1 Nuclear Reactor, NUREG/CR-3693, PNL-5022, Pacific Northwest Laboratory, Richland, WA, June 1984.

6. P.G. Doctor, T.P. Harrington, and P.H. Hutton, Pattern Recognition Methods for Acoustic Emission Analysis, NUREG/CR-0910, PNL-3052, Pacific Northwest Laboratory, July 1979.

NRC FORM 335 (7-77)

U.S. NUCLEAR REGULATORY COMMISSION

BIBLIOGRAPHIC DATA SHEET

1. REPORT NUMBER *(Assigned by DDC)*
NUREG/CP-0058, Volume 4

4. TITLE AND SUBTITLE *(Add Volume No., if appropriate)*
Proceedings of the Twelfth Water Reactor Safety Research Information Meeting

2. *(Leave blank)*

3. RECIPIENT'S ACCESSION NO.

7. AUTHOR(S)
Compiled by: Stanley A. Szawlewicz, Consultant

5. DATE REPORT COMPLETED
MONTH: December | YEAR: 1984

9. PERFORMING ORGANIZATION NAME AND MAILING ADDRESS *(Include Zip Code)*
Office of Nuclear Regulatory Research
U. S. Nuclear Regulatory Commission
Washington, DC 20555

DATE REPORT ISSUED
MONTH: January | YEAR: 1985

6. *(Leave blank)*

8. *(Leave blank)*

12. SPONSORING ORGANIZATION NAME AND MAILING ADDRESS *(Include Zip Code)*
Same as Item 9.

10. PROJECT/TASK/WORK UNIT NO.

11. CONTRACT NO.

13. TYPE OF REPORT
Collection of Conference Papers

PERIOD COVERED *(Inclusive dates)*
October 22-26, 1984

15. SUPPLEMENTARY NOTES

14. *(Leave blank)*

16. ABSTRACT *(200 words or less)*

The papers published in this six volume report were presented at the Twelfth Water Reactor Safety Research Information Meeting held at the National Bureau of Standards, Gaithersburg, Maryland during the week of October 22-26, 1984. The papers describe progress and results of programs in nuclear safety research conducted in this country and abroad. Foreign participation in the meeting included twenty-six different papers presented by researchers from seven European countries, Japan, and Canada.

17. KEY WORDS AND DOCUMENT ANALYSIS

17a. DESCRIPTORS

17b. IDENTIFIERS/OPEN-ENDED TERMS

18. AVAILABILITY STATEMENT
Unlimited

19. SECURITY CLASS *(This report)*
Unclassified

21. NO. OF PAGES
385

20. SECURITY CLASS *(This page)*
Unclassified

22. PRICE
$